JPL Publication 03-4

Proceedings of the 11th JPL Airborne Earth Science Workshop

Robert O. Green
Editor
Jet Propulsion Laboratory
California Institute of Technology

National Aeronautics and Space Administration

Jet Propulsion Laboratory
California Institute of Technology
Pasadena, California

December 2002

This publication was prepared at the Jet Propulsion Laboratory, California Institute of Technology, under a contract with the National Aeronautics and Space Administration.

Reference herein to any specific commercial product, process, or service by trade name, trademark, manufacturer, or otherwise, does not constitute or imply its endorsement by the United States Government or the Jet Propulsion Laboratory, California Institute of Technology.

Contents

Introduction 1

An Algorithm for De-Shadowing Spectral Imagery
S. M. Adler-Golden, M. W. Matthew, G. P. Anderson, G. W. Felde, and J. A. Gardner 3

Validation of Water Quality Parameters Retrieved from Inverse Modeling
S. Bagheri, K. Stamnes, S. Jiang, W. Li, and T. Yu 11

Quantitative Mapping of the Soil Rubification Process on Sand Dunes, Using Field and Airborne Sensors
E. Ben-Dor, N. Levin, A. Singer, A. Karnieli, and O. Braun 19

Combining S-Space and Image Spatial Information for Characterization of Land-Cover Elements Using AVIRIS Data
C. M. Bielski 25

Synthesis of Multispectral Bands from Hyperspectral Data: Validation Based on Images Acquired by AVIRIS, Hyperion, ALI, and ETM+
S. Blonski, G. Gasser, J. Russell, R. Ryan, G. Terrie, and V. Zanoni 33

Surface Reflectance Calibration of Terrestrial Imaging Spectroscopy Data: a Tutorial Using AVIRIS
R. N. Clark, G. A. Swayze, K. E. Livo, R. F. Kokaly, T. V.V. King, J. B. Dalton, J. S. Vance, B. W. Rockwell, T. Hoefen, and R. R. McDougal 43

Mapping the Invasive Plant *Arundo donax* and Associated Riparian Vegetation Using AVIRIS
D. DiPietro, S. L. Ustin, and E. Underwood 65

Detecting Spider Mite Damage in Cotton Through Spectral Mixture Analysis of AVIRIS Imagery
G. J. Fitzgerald, S. J. Maas, and W. R. DeTar 75

Mapping Forest Composition in the Central Appalachians Using AVIRIS: Effects of Topography and Phenology
J. R. Foster and P. A. Townsend 83

Ecosystem Carbon Flux in a Disturbed, Fragmented Southern California Landscape
J. Gamon, D. Fuentes, D. Sims, S. Houston, A. Moyes, H.-L. Qiu, and W. Oechel 91

A Curve-Fitting Technique to Improve Wavelength Calibrations of Imaging Spectrometer Data
B.-C. Gao, M. J. Montes, and C. O. Davis 99

Acquisition of Underwater Reflectance Measurements as Ground Truth
J. A. Goodman and S. L. Ustin 107

Initial Estimates from AVIRIS of the Temperature and Fractional Areas of Fires at the World Trade Center Disaster
R. O. Green, R. N. Clark, J. Boardman, B. Pavri, and C. Sarture 113

AVIRIS Inflight Calibration Experiment Results for 2001
R. O. Green and B. Pavri 125

Hierarchical Segmentation of Hyperspectral Data
J. A. Gualtieri and J. C. Tilton 139

Characterization of Land Degradation at the Ñacuñán Biosphere Reserve in Argentina with AVIRIS Data
A. Huete, T. Miura, X. Gao, C. Borghi, and R. Ojeda 153

Leaf Area Index and Cover of Shortgrass Steppe Using AVIRIS Imagery
E. R. Hunt, Jr. 163

Comparison between AVIRIS and Hyperion for Hyperspectral Mineral Mapping
F. A. Kruse 171

Integrated Multispectral and Hyperspectral Mineral Mapping, Los Menucos, Rio Negro, Argentina, Part I: Landsat TM Reconnaissance and AVIRIS Prospect Mapping
F. A. Kruse, S. L. Perry, and A. Caballero 181

Integrated Multispectral and Hyperspectral Mineral Mapping, Los Menucos, Rio Negro, Argentina, Part II: EO-1 Hyperion/AVIRIS Comparisons and Landsat TM/ASTER Extensions
F. A. Kruse, S. L. Perry, and A. Caballero 185

Comparison of AVIRIS and Landsat ETM+ for the Estimation of Leaf Area Index
K.-S. Lee and W. B. Cohen 189

Characterizing Mineral Alteration Using Airborne Visible-Infrared Imaging Spectrometer Data at Questa, New Mexico
K. E. Livo and R. N. Clark 199

Decision Tree Classification of a Forest Using AVIRIS and Multi-Seasonal TM Data
S. Mannel, D. Hua, M. Price, A. Knobloch, and X. Chen 207

The Evolution and Present State of Tree-Kills on Mammoth Mountain, California: Tracking Volcanogenic CO_2 and Its Lethal Effects
B. A. Martini and E. A. Silver 213

Constrained Least Squares Linear Spectral Unmixture by the Hybrid Steepest Descent Method
N. Ogura and I. Yamada 223

Deriving Quantitative Monitoring Data Related to Acid Drainage Using Multi-Temporal Hyperspectral Data
C. Ong and T. Cudahy 231

Using AVIRIS Imagery to Map Invasive Plants on Rangelands: Leafy Spurge in Northeastern Wyoming
A. Parker Williams and E. R. Hunt, Jr. 237

Band Ratios as a Reconnaissance Tool for Hyperspectral Data
B. S. Penn 245

Using the Semi-Automated Plug-In Tool for Feature Identification, Recognition, and Extraction (SPITFIRE) Tool to Extract Roads and Surface Material Types from AVIRIS Imagery
B. S. Penn and K. E. Livo 257

A Comparative Analysis of Endmember Extraction Algorithms Using AVIRIS Hyperspectral Imagery
A. Plaza, P. Martinez, R. M. Perez, and J. Plaza 267

COMANCHE and COCHISE: Two Reciprocal Atmospheric Codes for Hyperspectral Remote Sensing
L. Poutier, C. Miesch, X. Lenot, V. Achard, and Y. Boucher 277

Leaf Area Index Mapping Using Retrieved Reflectance from AVIRIS Data
R. Pu, P. Gong, and G. S. Biging 287

Comparison of AVIRIS and Eo-1 Hyperion for Classification and Mapping of Invasive Leafy Spurge in Theodore Roosevelt National Park
R. Root, S. Ustin, P. Zarco-Tejada, C. Pinilla, R. Kokaly, G. Anderson, K. Brown, K. Dudek, S. Hager, and E. Holroyd 297

Environmental Processes in the Monterey Bay National Marine Sanctuary: Studies Integrating AVIRIS and Synoptic In Situ Sensing
J. Ryan, F. Chavez, J. Bellingham, E. Rienecker, H. Dierssen, R. Kudela, A. Vander Woude, R. Maffione, and A. Fischer 307

Hyperspectral Image Analysis for Oil Spill Detection
F. Salem, M. Kafatos, T. El-Ghazawi, R. Gomez, and R. Yang 319

Effects of Geo-Atmospheric Preprocessing on Imaging Spectroscopy Data Quality and Methods
D. Schläpfer, P. Meier, and M. Schaepman 327

Coupling Hyperspectral Remote Sensing with Fieldspectrometer to Monitor Inland Water Quality Parameters
N. A. Shafique, F. Fulk, S. M. Cormier, and B. C. Autrey 335

Multiscale Opponent Approach for Hyperspectral Texture Recognition Using AVIRIS Data
M. Shi and G. Healey 345

Hyperspectral Remote Sensing of the Brazilian Pantanal Lakes
L. Soares Galvão, W. Pereira Filho, M. de Moura Abdon, E. M. M. L. Novo, J. S. V. da Silva, and F. J. Ponzoni 355

Low-Altitude AVIRIS Data for Mapping Landform Types on West Ship Island, Mississippi
J. P. Spruce, E. G. Otvos, and M. J. Giardino 363

Mineral Mapping Mauna Kea and Mauna Loa Shield Volcanos on Hawaii Using AVIRIS Data and the U.S.G.S. Tetracorder Spectral Identification System: Lessons Applicable to the Search for Relict Martian Hydrothermal Systems
G. A. Swayze, R. N. Clark, S. J. Sutley, C. A. Gent, B. W. Rockwell, D. L. Blaney, J. L. Post, and B. P. Farm 373

Terrain Normalization of AVIRIS and Hyperion Imagery in Forested Landscapes
P. A. Townsend and J. R. Foster 389

Mapping Non-Native Plants Using Hyperspectral Imagery
E. Underwood, S. Ustin, and D. Dipietro 395

An Integrated Approach to the Discrimination of Riparian Vegetation in the Navarro River Watershed, Mendocino County, California, U.S.A.
J. H. Viers, C. T. Sailer, C. M. Ramirez, J. F. Quinn, and M. L. Johnson 403

Introduction

This publication contains the proceedings of the JPL Airborne Earth Science Workshop—a forum held to report science research and applications results with spectral images measured by the NASA Airborne Visible/Infrared Imaging Spectrometer (AVIRIS). These papers were presented at the Jet Propulsion Laboratory from March 5–8, 2001. Electronic versions of these papers may be found at the AVIRIS Web site noted below.

Note

Our budget this year allows for only a few color reproductions, even though they now often prove necessary for a complete understanding of figures presented here in black and white. For full color versions of the papers, please go to the AVIRIS Web site at http://makalu.jpl.nasa.gov/docs/workshops/toc.htm

AN ALGORITHM FOR DE-SHADOWING SPECTRAL IMAGERY

Steven M. Adler-Golden,[1] Michael W. Matthew,[1] Gail P. Anderson,[2] Gerald W. Felde,[2] and James A. Gardner[3]

1. INTRODUCTION

The interpretation of visible-near infrared spectral imagery of the earth's surface can be complicated by illumination variations due to shadowing, sloped terrain, or other causes. In atmospherically "corrected" (spectral reflectance) data, these variations mainly affect the spectrum amplitude. However, in deep shadows where the illumination is mainly skylight, the spectrum is not only dimmer but also skewed to short (blue-violet) wavelengths. Either or both of these effects can impede the classification of surface materials and the detection of targets with standard methods. Recently, some classification and detection algorithms have been developed that are insensitive to illumination (Healy and Slater 1999; Adler-Golden et al., 2001). However, for many applications, and for visual inspection of the image, it is very beneficial to normalize all the pixels to a common illumination, such as full sun and skylight. This requires the ability to characterize the illumination for each pixel, and in particular to identify shadows and quantify their depths. Knowledge of shadow depths can also be valuable as a source of elevation information for terrain, surface objects, and clouds.

Several methods have appeared in the literature for identifying and correcting for shadowing. The standard approach is based on linear unmixing of atmospherically corrected data (Boardman, 1993) using spectral endmembers, which represent the distinguishable pure materials in the scene. The shadow is defined as a "black" (zero reflectance) endmember, and a sum-to-unity constraint is imposed on the endmember weights. A positivity constraint may also be imposed. Upon unmixing, the reflectance spectrum is approximately "de-shadowed" by dividing by one minus the shadow weight (or, equivalently, the sum of the non-shadow endmember weights), provided that this quantity is not too small. There are several limitations to this approach. One is that by defining the shadow as black, the blue-skewed skylight illumination of the shadow is ignored, leading to under-correction for shadow at long wavelengths and overcorrection at short wavelengths. Another is the dependence of the results on the specific endmembers used, and hence on the method of endmember selection (e.g., by clustering, convex hull, convex cone, or other methods).

Recently, more sophisticated shadow removal methods have been developed as part of atmospheric correction processing. Davenport and Ressl (1999) obtained excellent results with visible channels of the HYDICE sensor using an algorithm that models the illumination spectrum as a function of shadow depth, which is extracted using an endmember-finding and fitting method. Another method, developed by Portigal (2002), avoids endmember complications by determining the shadow fraction with a matched filter. The filter is constructed using a shadowed pixel in the radiance image; the filter output to adjust the amount of direct solar illumination in the atmospheric correction while maintaining full sky illumination. Potential pitfalls include sensitivity to the choice of shadow spectrum and limitations of the full-sky assumption.

In this paper we describe a rather simple matched filter-based de-shadowing algorithm for spectral reflectance images that builds upon several ideas from the previous work. At present the algorithm is partially supervised, in that the best results are achieved with manual adjustment of a parameter that controls the sky brightness. The de-shadowing method can also be applied to the general illumination-compensation problem, including terrain "flattening," a topic that will be reserved for a future paper. The algorithm uses iterative application of the matched filter, an approach that may be suitable for a broader class of problems that involves a non-linear effect (in this case, the skylight blue-skewing).

All of the de-shadowing approaches mentioned presume that differences caused by illumination variation are spectrally distinguishable from differences in material composition. In the black shadow approximation, this amounts to an assumption that all pure spectra in the image are linearly independent. As this is often untrue, particularly in complex scenes, many instances of mis-correction (i.e., when a fully illuminated pixel is assigned as a

1 Spectral Sciences, Inc., 99 South Bedford Street, Suite 7, Burlington, Massachusetts 01803 (sag@spectral.com)
2 AFRL/Space Vehicles Directorate, 29 Randolph Street, Hanscom AFB, Massachusetts 01731
3 University of Arizona, Tucson, Arizona 85721

shadowed pixel of another material or combination of materials) are to be expected. Nonetheless, we have found that useful and, for the most part, visually realistic de-shadowed images can be obtained with this method under a wide variety of conditions.

2. DESCRIPTION OF METHOD

The method consists of (1) atmospherically correcting the original radiance data to reflectance with the usual assumption of full sun and sky illumination, (2) applying a matched filter for a black surface to the reflectance data to infer an initial shadow fraction for each pixel, (3) rebalancing the data to remove the skylight skewing effect, (4) refining the shadow fraction by reapplying the matched filter, and (5) using the shadow fraction, de-shadowing the data by dividing by the ratio of the inferred to full illumination. The procedure was implemented in IDL code using the Research Systems, Inc. ENVI software.

Atmospheric Correction. A number of atmospheric correction algorithms have been developed. For de-shadowing, especially accurate results are needed for dark pixels. We have employed the FLAASH algorithm (Matthew et al., 2000, Adler-Golden et al., 1999), which uses MODTRAN4 (Berk et al., 1998) for radiation transport modeling and includes an adjacency effect correction and an automated aerosol retrieval method based on the work of Kaufman et al. (1997).

Matched Filtering. A matched filter for a zero reflectance target is generated and applied to the reflectance image. In the following discussion we provide some mathematical motivation for the matched filtering step and qualitatively compare the matched filter and endmember unmixing approaches.

As described in the Introduction, each pixel reflectance spectrum y is assumed to be a mixture of linearly independent, fully-illuminated endmember spectra, $\boldsymbol{e}_i$:

$$\boldsymbol{y} = \sum_i w_{iy}\boldsymbol{e}_i \tag{1}$$

where w_{iy} is the ith endmember weight for the pixel (here bold face denotes a column vector). Let $\boldsymbol{a}$ be a fully illuminated pixel, whose weights w_{ia} sum to 1. If shadow is considered as a zero reflectance endmember, then the shadow fraction f can be written as the difference between the total weights for pixel $\boldsymbol{a}$ and pixel $\boldsymbol{y}$:

$$f_y = \sum_i w_{ia} - \sum_i w_{iy} = -\sum_i (w_{iy} - w_{ia}) \tag{2}$$

In unconstrained least-squares unmixing, the ith endmember weight may be extracted from each spectrum by taking its dot product with a filter vector $\boldsymbol{v}_i$ that is orthogonal to all endmembers except $\boldsymbol{e}_i$; that is, $w_{iy} = \boldsymbol{v}_i^T\boldsymbol{y}$ and $w_{ia} = \boldsymbol{v}_i^T\boldsymbol{a}$. Eq. (2) can then be written as

$$f_y = -\sum_i \boldsymbol{v}_i^T(\boldsymbol{y} - \boldsymbol{a}) = \boldsymbol{g}^T(\boldsymbol{y} - \boldsymbol{a}) \tag{3}$$

where $\boldsymbol{g}$ is a filter vector. If we furthermore assume that shadow is rare, the scene mean spectrum can be used for $\boldsymbol{a}$. Thus, according to Eq. (3) the shadow fraction can be unmixed by applying a linear filter to mean-subtracted spectra. One such linear filter is the matched filter. Instead of being constructed from explicit endmembers, the matched filter $\boldsymbol{q}$ is defined in terms of the covariance matrix $\boldsymbol{C}$:

$$\boldsymbol{q} = \boldsymbol{C}^{-1}(\boldsymbol{t} - \boldsymbol{a})/[(\boldsymbol{t} - \boldsymbol{a})^T\boldsymbol{C}^{-1}(\boldsymbol{t} - \boldsymbol{a})] \tag{4}$$

where $\boldsymbol{t}$ is the target spectrum to be detected and $\boldsymbol{a}$ is the scene mean spectrum. Taking $\boldsymbol{t} = 0$ for shadow, the shadow matched filter is given by

$$q_{shadow} = -\boldsymbol{C}^{-1}\boldsymbol{a}/(\boldsymbol{a}^T\boldsymbol{C}^{-1}\boldsymbol{a}) \tag{5}$$

The matched filter, like the CEM filter (Farrand and Harsanyi, 1997), yields a minimum RMS target abundance for the scene as a whole. However, instead of using the covariance and mean-subtracted reflectance signal, the CEM filter uses the correlation matrix and the reflectance signal. This results in a singularity when $\boldsymbol{t} = 0$ and makes the CEM filter unusable for shadow detection

In the limit of zero shadow abundance and linear independence of all materials in the scene, the outputs of both the matched filter and the endmember-based filter g should be zero, and the two filters should be equivalent. In real scenes the outputs differ. In particular, the matched filter generates negative as well as positive shadow outputs, whereas the endmember filter, if constructed from outlying endmembers (such as from a convex-hull or convex-cone algorithm), should in principle generate only non-negative outputs. A negative output may be interpreted as indicating either an anomalously bright material or excess illumination in the pixel compared with the nominal full sun plus sky illumination of a horizontal surface. With flat terrain, it would generally not be appropriate to "correct" the illumination for a negative shadow output. However, with sloped terrain it may be desirable to do so in order to remove the excess illumination of surfaces tilted towards the sun.

As the amount of shadow in the scene increases, the behavior of the matched filter increasingly deviates from what would be obtained with linear unmixing. As the mean spectrum becomes contaminated with shadow, the filter's response to partial shadow is reduced and the negative outputs become larger and more numerous. Very dark materials that can be confused with shadow, such as bodies of water, produce the same contamination effect. A remedy is to remove as much water and deep shadow from the scene as is practical before constructing the matched filter. A simple method is to set a low threshold for the average spectral reflectance, such as 0.03, and to eliminate all pixels falling below this threshold when calculating the mean and covariance.

Spectral Rebalancing. Application of the matched filter to the image yields a first estimate of the shadow fraction f for each pixel. The spectra are then rebalanced to simulate illumination by a spectrally uniform source, namely, $1-f$ times the direct sun plus sky spectrum, as follows. Let $d = d(\lambda)$ be the spectrum of the direct sun illumination and $s = s(\lambda)$ the spectrum of the sky illumination, and define $g = 1-f$ as the fractional illumination of each pixel by the direct sun. Then the rebalancing factor applied to the spectrum is

$$F(\lambda) = g(d(\lambda) + s(\lambda))/(gd(\lambda) + s(\lambda)) = g(1 + s(\lambda)/d(\lambda))/(g + s(\lambda)/d(\lambda)) \quad (6)$$

The spectral ratio $s(\lambda)/d(\lambda)$ is, strictly speaking, a quantity that depends on the detailed three-dimensional geometry of the terrain and surface objects. However, we assume that it can be adequately modeled with the full sky to sun illumination ratio as calculated from MODTRAN (Adler-Golden et al., 2001) or some other radiation transport code, multiplied by an empirical scaling factor that accounts for the average sky fractional subtense in the shadows. The ratio can often be reasonably approximated by the power law expression $c\lambda^{-N}$, where c is an empirical constant and N is an Angstrom-law exponent for the atmospheric scattering.

Re-application of the Matched Filter. The matched filter is applied to the rebalanced spectra, resulting in refined shadow fraction estimates. The rebalancing and filter application steps may be iterated a few times to insure convergence.

De-shadowing. The de-shadowed spectrum for each pixel is obtained by multiplying the rebalanced spectrum by the factor $1/g$.

3. SAMPLE RESULTS

We have applied the de-shadowing method to a total of around a half-dozen images to date, including AVIRIS, HYDICE and Landsat TM data. In this discussion we focus on two atmospherically corrected scenes: a forested scene taken by AVIRIS that contains a broken cloud field and an urban scene taken by HyMap that contains building shadows.

3.1 AVIRIS Scene

The AVIRIS scene, f960628t01p02_r04_sc07, is of the White Mountains region near North Conway, New Hampshire. Good removal of the cloud shadows was obtained using either the original spectral data or the data binned to the six Landsat TM spectral channels. For simplicity we focus here on the Landsat TM representation, which allows us to show the complete data cube in two color images: a true-color image of the blue, green and red channels 1 to 3 and a false-color image of the infrared channels 4 to 6. The scene was atmospherically corrected using FLAASH. Little difference was found in performing the atmospheric correction or de-shadowing steps before or after the spectral binning.

Figure 1 shows the reflectance image prior to de-shadowing. To emphasize the darker pixels, a non-linear

scaling has been applied to these and other color images in this paper, which sets the mean brightness level at 50%. Figure 2 shows the retrieved shadow fraction as a grayscale image; black denotes 100% shadow and white denotes zero shadow. Figure 3 shows the final de-shadowed image using c=0.07 and N=2 in the power-law expression for the full sky to sun illumination ratio; N=2 represents a compromise between the wavelength dependences of Rayleigh and aerosol scattering. Despite some residuals, appearing as a slight darkening in the infrared and a slight grayish cast in the visible, the cloud shadow removal is quite effective. Contrast is slightly enhanced compared to Figure 1 due to the non-linear display. The most serious artifacts are an artificial brightening of water bodies (streams and a small pond) and paved roads. Details of the scene shown in Figure 4 highlight the dramatically improved visualization of surface features upon de-shadowing.

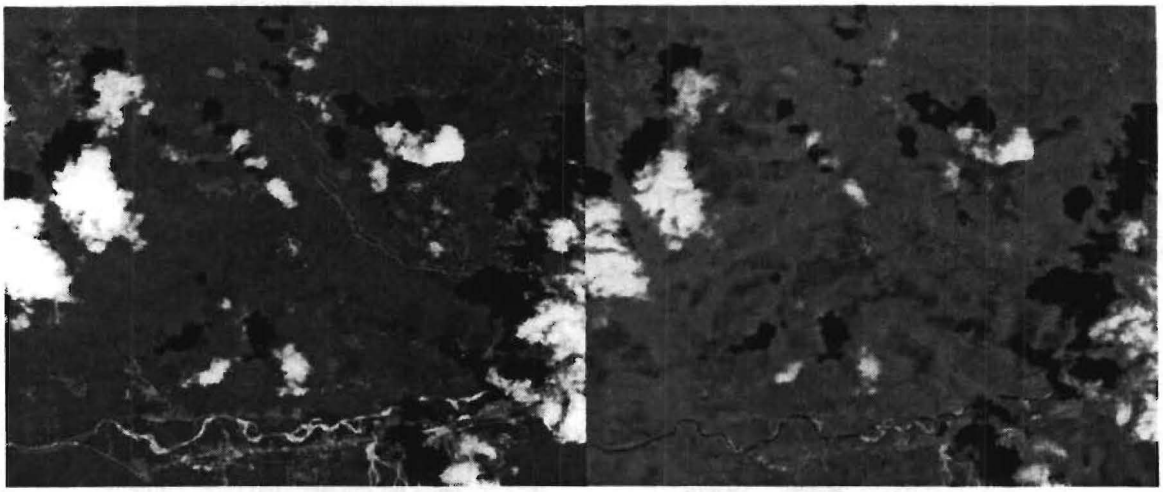

Figure 1. AVIRIS White Mountains scene displayed in Landsat TM channels; (blue, green, red) = visible channels 1,2,3 at left, infrared channels 4,5,6 at right.

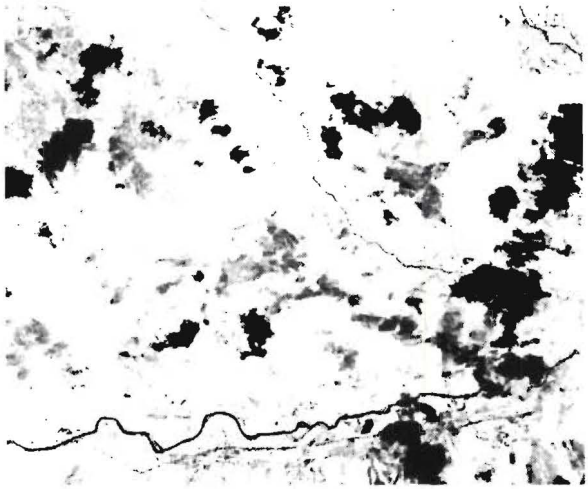

Figure 2. Retrieved shadow image for the White Mountains scene.

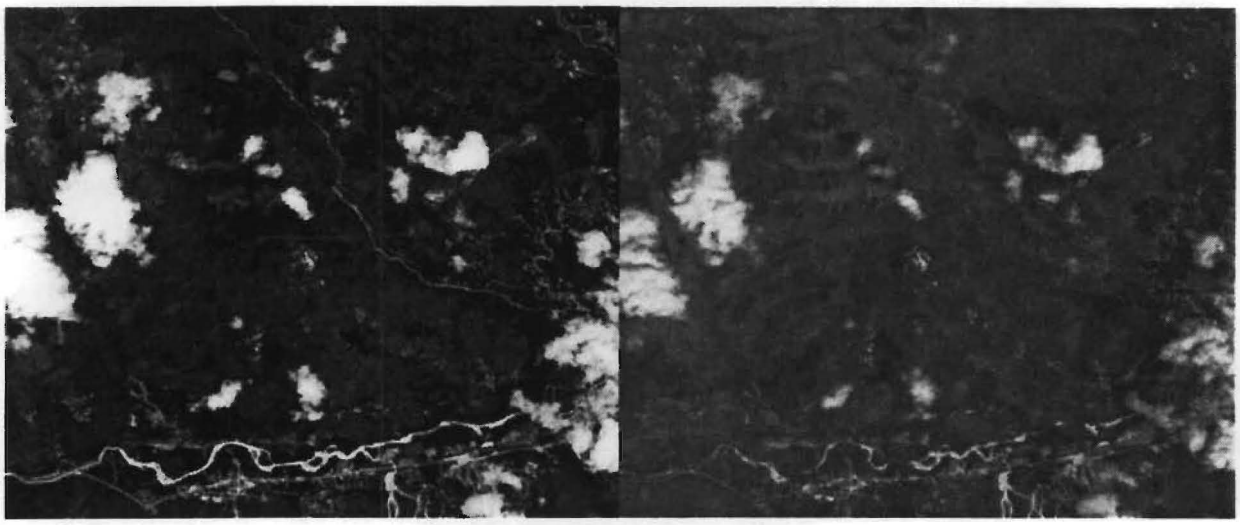

Figure 3. White Mountains scene after de-shadowing, displayed as in Fig. 1.

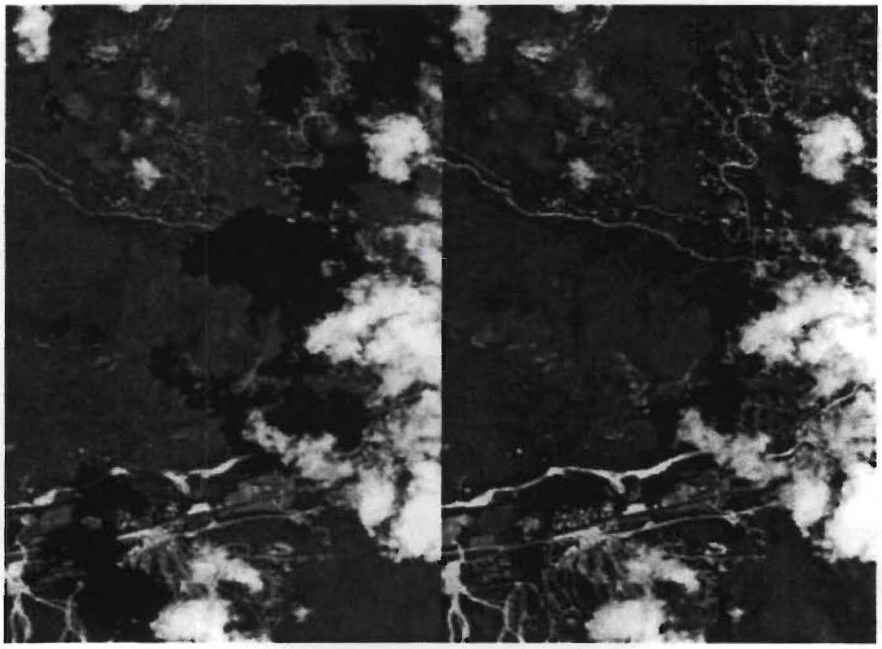

Figure 4. Details from Figures 1 and 3.

The effect of ignoring the sky illumination of shadows (by setting c=0) is seen in Figure 5. In the visible the illumination is underestimated and the image is noticeably over-corrected. In the infrared the illumination is slightly overestimated and the channels are slightly under-corrected.

Convergence of the algorithm was investigated by comparing the results for one and two iterations of the spectral rebalancing and matched filtering steps. Differences of a few percent in the de-shadowed spectra were found (Figure 6); this effect is too small to be noticed in the images, however.

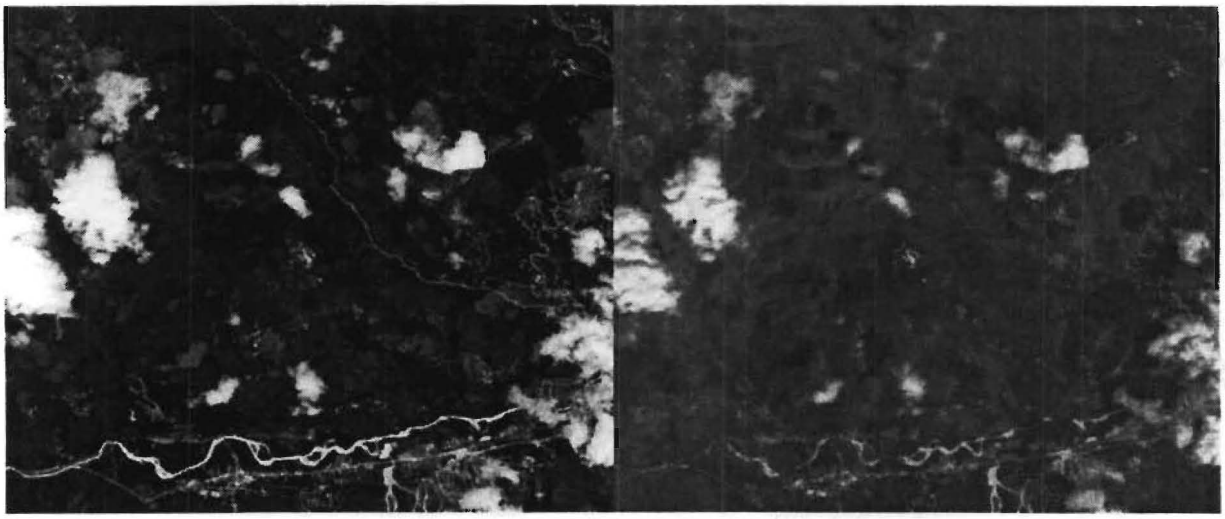

Figure 5. De-shadowed image ignoring the sky illumination.

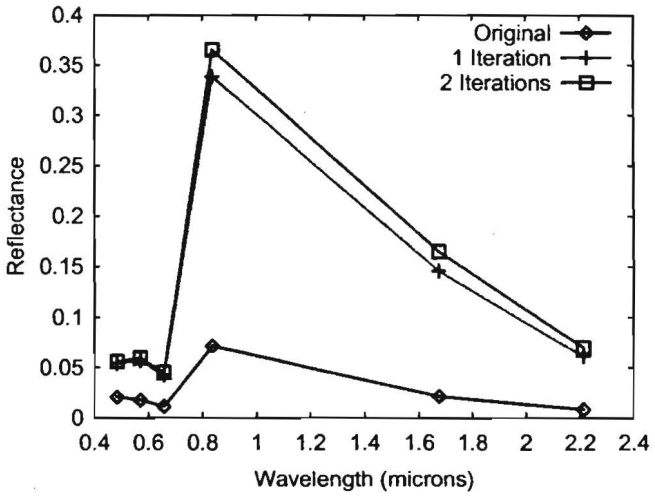

Figure 6. Shadowed vegetation pixel in the White Mountains scene before (original) and after de-shadowing (1 and 2 iterations).

3.2. HyMap Scene

An atmospherically corrected HyMap image of downtown San Francisco from the archives of Analytical Imaging and Geophysics LLC was kindly provided to us by the Boeing Company. Special handling was needed to process this data cube because of what appears to be a sizable baseline of residual atmospheric scattering. To minimize its effect on the shadow detection, the matched filter was restricted to wavelengths from 1.4-2.5 μm. While we did not attempt to create a full de-shadowed data cube, we were able to generate a good de-shadowed true-color image by baseline-subtracting the displayed red, green and blue channels, using their minimum values as the baseline, and by increasing the green and blue sky-to-sun spectral ratios relative to the N=2 predictions (this might be compensating for an especially clear sky, dominated by Rayleigh scattering).

The results from a portion of this scene are shown in Figure 7. The removal of the building shadows is quite striking and gives the scene a strangely flat appearance. The water is brightened, as usual, but otherwise there appear to be no major problems. There is a tendency for under-correction in the deepest shadows, next to and between tall buildings, where there would be less than the usual amount of skylight. Even so, the shadow removal is sufficient to discern a wealth of new detail.

Figure 7. HyMap scene of San Francisco before (left) and after (right) de-shadowing.

4. CONCLUSIONS

A simple de-shadowing method based on iterative matched filtering has been developed for atmospherically corrected spectral imagery. In initial tests with a handful of data cubes, generally realistic and quantitative de-shadowed images and spectra have been obtained for non-water surfaces. The method has the basic shortcomings inherent in a purely spectrally-based approach, which does not take advantage of spatial context or ancillary information that might distinguish between shadowed and fully lit surfaces that are spectrally similar. In addition, the assumption that all of the shadows are illuminated by a uniform skylight spectrum is not very realistic, and can cause problems in very deep shadows as well as in shadows that are lit by sources other than the sky, such as a transmissive plant canopy. Nevertheless, this simple model for shadow illumination provides a dramatic improvement over ignoring the illumination completely, as is done with standard linear unmixing. Although the initial applications have involved removal of cast shadows, the de-shadowing method also has potential for terrain "flattening," which we hope to explore in the future. Further work is needed to test the algorithm on additional data and against other algorithms such as those of Davenport and Ressl (1999) and Portigal (2002).

5. ACKNOWLEDGEMENTS

This work was supported by the Air Force Research Laboratory under Contract No. F19628-00-C-0022.

6. REFERENCES

Adler-Golden, S.M., R.Y. Levine, M.W. Matthew, S.C. Richtsmeier, L.S. Bernstein, J. Gruninger, G. Felde, M. Hoke, G.P. Anderson, and A. Ratkowski, 2001, "Shadow-Insensitive Material Detection/Classification with Atmospherically Corrected Hyperspectral Imagery," Proc. of SPIE, Orlando, Florida, Vol. 4381.

Adler-Golden, S.M., M.W. Matthew, L.S. Bernstein, R.Y. Levine, A. Berk, S.C. Richtsmeier, P.K. Acharya, G.P. Anderson, G. Felde, J. Gardner, M. Hoke, L.S. Jeong, B. Pukall, A. Ratkowski and H.K. Burke, 1999, "Atmospheric Correction for Short-wave Spectral Imagery Based on MODTRAN4," in Summaries of the Eighth Annual JPL Earth Science Workshop, Vol. I, available at http://makalu.jpl.nasa.gov.

Berk, A., L.S. Bernstein, G.P. Anderson, P.K. Acharya, D.C. Robertson, J.H. Chetwynd, and S.M. Adler-Golden, 1998, "MODTRAN Cloud and Multiple Scattering Upgrades with Application to AVIRIS,' Remote Sens. Environ., **65**, 367-375.

Boardman, J.W., 1993, "Automated Spectral Unmixing of AVIRIS Data Using Convex Geometry Concepts," in Summaries, Fourth JPL Airborne Geoscience Workshop, JPL Publication 93-26, v. 1, pp. 11-14.

Davenport, M. R. and W. Ressl, 1999, "Shadow Removal in Hyperspectral Imagery," Proceedings, International Symposium on Spectral Sensing Research, Las Vegas, Nevada, October 1999.

Farrand, W.H. and J.C. Harsanyi, 1997, "Mapping the Distribution of Mine Tailings in the Coeur d'Alene River Valley, Idaho, Through the Use of a Constrained Energy Minimization Technique," Remote Sens. Environ., vol. 59, pp. 64-76.

Healy, G. and D. Slater, 1999, "Models and Methods for Automated Material Identification in Hyperspectral Imagery Acquired Under Unknown Illumination and Atmospheric Conditions," IEE Trans. Geosci. Remote Sensing, Vol. 37, pp. 2706-2717.

Kaufman, Y.J., D. Tanre, L.A. Remer, E.F. Vermote, A. Chu, and B.N. Holben, 1997, "Operational Remote Sensing of Tropospheric Aerosol over Land from EOS Moderate Imaging Spectroradiometer," J. Geophys. Res. **102**, 17051.

Matthew, M.W., S.M. Adler-Golden, A. Berk, S.C. Richtsmeier, R.Y. Levine, L.S. Bernstein, P.K. Acharya, G.P. Anderson, G.W. Felde, M.P. Hoke, A. Ratkowski, H.-H Burke, R.D. Kaiser, and D.P. Miller, 2000, "Status of Atmospheric Correction Using a MODTRAN4-based Algorithm," SPIE Proceeding, Algorithms for Multispectral, Hyperspectral, and Ultraspectral Imagery VI, Vol. 4049, pp. 199-207.

Portigal, F., 2002, "Adaptive Reflectance Calibration" method; see http://www.ultraspectral.com.

VALIDATION OF WATER QUALITY PARAMETERS RETRIEVED FROM INVERSE MODELING

Sima Bagheri,[1] Knut Stamnes,[2] Shigan Jiang,[2] Wei Li,[2] and Ting Yu[1]

1. INTRODUCTION

Understanding the relationship between reflectance, absorption and backscattering of water is essential for developing the analytical and multitemporal algorithms necessary to use remote sensing as a management tool in the estuarine/coastal environment. The objective of this paper is to demonstrate utility of bio-optical modeling and retrieval techniques to derive the concentrations of important water properties (chlorophyll, color dissolved organic matter, etc.). This is a prerequisite to retrieve water quality parameters from the AVIRIS data acquired in July 13th 2001 over the Hudson/Raritan Estuary of NY-NJ. Atmospheric correction algorithm, coupled atmosphere ocean (CAO) system based on discrete ordinate method (DISORT) is applied to compensate for the atmospheric effects and to infer the water-leaving radiance. We used the linear matrix inversion model developed by Hoge and Lyon (1996) for retrieval of the inherent optical properties (IOPs) from which the water constituent concentrations are obtained. Validation was performed using the insitu measurements collected simultaneously with the AVIRIS overflight.

The study area is the Hudson/Raritan Estuary located south of the Verrazano Narrows and bordered by western Long Island, Staten Island and New Jersey (figure 1) Fresh water flows into the estuary mainly from the Hudson and Raritan Rivers and ocean waters enter tidally across the Sandy

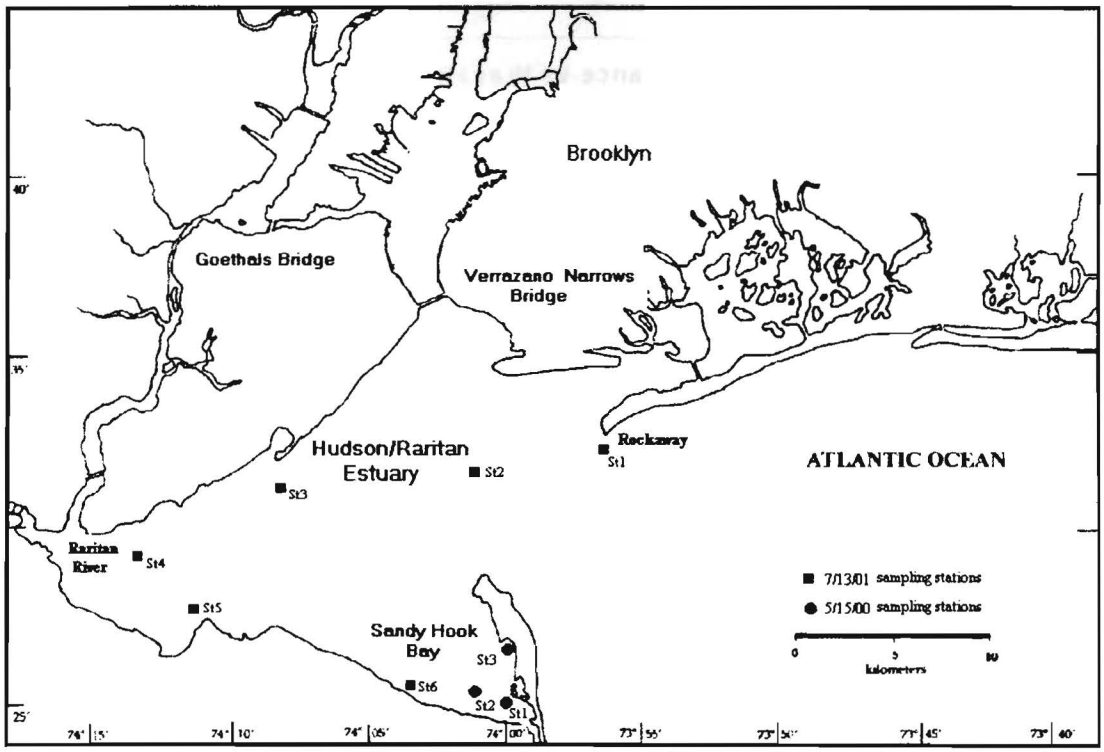

Figure 1. Map of the study area and locations of the sample points surveyed on 7/13/01

[1] New Jersey Institute of Technology, Newark, New Jersey (bagheri@adm.njit.edu)
[2] Stevens Institute of Technology, Hoboken, New Jersey

Hook-Rockaway transect. The tidal water is mixing with fresh water inflows, in highly dynamic environments where there are major conflicting interests on the use of these waters. This shallow (< 8 m) and eutriphicated interface of the Hudson and Raritan Rivers and Atlantic Ocean was cruised during the field seasons in 1998-2001 with RV Walford and Blue Sea (MAST).

2. RESEARCH MATERIALS AND METHODS

2.1 AVIRIS

On July 13th, 2001, the AVIRIS, was flown over the study area. The AVIRIS images the earth's surface in 224 spectral bands approximately 10 nm wide covering the region 400-2500 nm from a NASA ER-2 aircraft at an altitude of 20 km. The ground resolution is 20m*20m. A geometric correction algorithm is applied to the AVIRIS data for correlation with in situ measurements. Atmospheric correction is required for retrieval of the inherent optical properties (IOPs) from which the water constituent concentrations are obtained.

2.2 Spectroradiometer

An OL 754 scanning, submersible spectroradiometer was deployed at six sampling stations as marked in figure1 simultaneously with the AVIRIS overflight. It uses a double monochromator for low stray light and measures spectral data from 300 nm to 850 nm. Upwelling (E_u (λ)) and downwelling ($E_d(\lambda)$) irradiances are measured and used to calculate the subsurface irradiance reflectance R(0-) for comparison with modeled reflectances. Figure 2 depicts the reflectance spectra recorded by the OL-754 at stations 2-6 on Jul. 13th, 2001. (Note that the reflectance data from Station 1 is not included due to pronounced effect of wave propagation.)

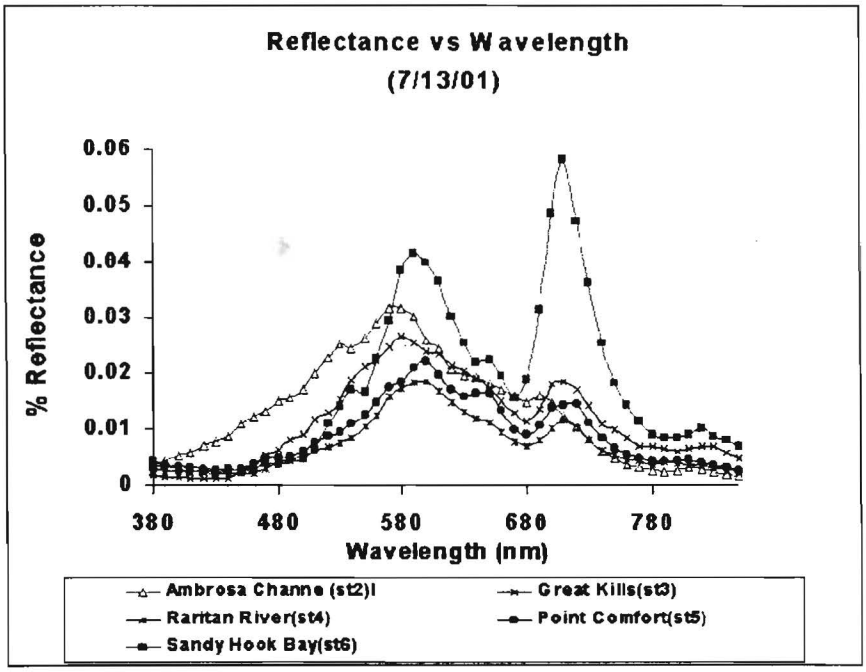

Figure 2. The reflectance spectra recorded by the OL-754 at designated sampling stations

2.3 Attenuation-absorption meter

Measurements of spectral absorption and beam attenuation coefficients were made using the ac-9 instrument. The ac-9, with one absorption flow tube and one attenuation flow tube, measures beam

absorption (a) and attenuation (c) coefficient at 9 wavelengths (412, 440, 488, 510, 532, 555, 650, 676, 715 nm). The scattering coefficient (b) is obtained from a and c, since b = c - a. Use of the ac-9 has enabled us to model the backscattering coefficient (b_b), which is an important input parameter for establishing the IOPs of the estuary (in preparation). Figure 3 shows the absorption spectra recorded by the ac-9 at station 5 (Point Comfort) on July 13, 2001.

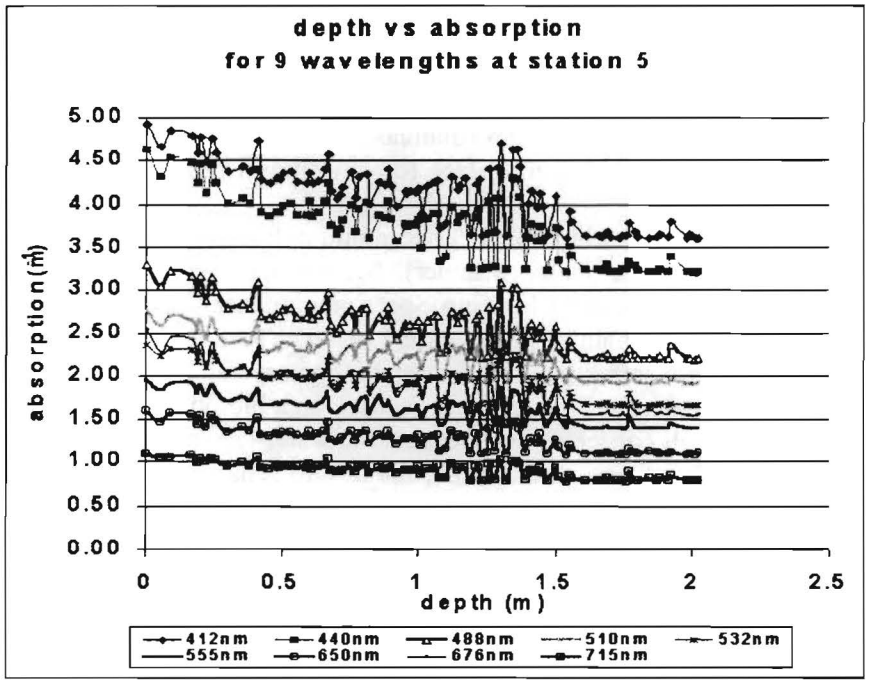

Figure 3. The absorption spectra for 9 wavelengths recorded by the ac-9 at station 5

2.4 Shipboard sampling

Water samples were collected (0.2 to 0.5 m depth) from selected sample stations as marked in figure 1 for laboratory analysis. Standard procedures were used to determine the concentrations of total chlorophyll_a (TCHL) (as indication of concentration of phytoplankton) and total suspended matter (TSM) (NEN 6520 (1981)) and NEN 6484 (1982)) respectively. The samples were analyzed for their IOPs as well as the identification/enumeration of the phytoplankton species. This was done to demonstrate the variety and composition of phytoplankton populations for input into library spectra of the estuary, which is currently in progress (Bagheri et al., 1999). The most abundant organisms identified were the Diatoms; Skeletonema sp. in high/moderate counts (7520-540 cells/ml). Also present in low counts were Flagellates; Eutreptia sp. (60 cells/ml) and Prorocentrum minimum (60 cells/ml). The TCHL concentrations varied between 73mg m^{-3} and 17 mg m^{-3} indicating that the measurements did not coincide with any major outbreaks of phytoplankton blooms. Likewise, the TSM ranges (23-5 g m^{-3}) were within the expected values for the time of year when the measurements taken.

3. DATA ANALYSIS and MODEL DEVELOPMENT

3.1 Atmospheric correction of the AVIRIS data

The remote sensing signal received by the AVIRIS is the sum of the water-leaving radiance and contribution from atmospheric aerosols and molecules. Comparison of the AVIRIS measured radiance and in-situ reflectance measurements reveals the effect of the atmosphere on the total upwelling spectral radiance measured by AVIRIS (Green et al., 1996). In atmospheric correction, the most challenging issue

is to remove the impact of the highly variable aerosol component on top of the atmosphere (TOA) to convert remote sensing measured radiance into normalized water leaving radiance. This is the required input to algorithms designed to retrieve phytoplankton pigments or suspended solid concentrations. The aim is to calibrate the AVIRIS data spectrally and radiometrically to radiance/reflectance for bio-optical and inverse modeling and generation of thematic maps of water quality parameters. We use a comprehensive radiative transfer model for the coupled atmosphere-ocean (CAO) system based on the discrete-ordinate method (DISORT) to compute the radiance within and backscattered from the atmosphere-ocean system (Jin and Stamnes, 1994; Thomas and Stamnes, 1999). This CAO-DISORT model, in which multiple scattering by ocean particles are properly treated, is also suitable for constructing an atmospheric correction algorithm (Stamnes et al., 2002), and it can be used to calculate the amount of light incident above the water surface (downwelling irradiance) for a given geographic location and a chosen atmosphere.

Algorithms for retrieving the chlorophyll concentration from space have been developed for sensors such as CZCS (coastal Zone Color Scanner), SeaWiFS (the Sea-viewing Wide Field-view Sensor), MODIS (the Moderate-Resolution Imaging Spectroradiometer) and others. However, most of these algorithms have been applied mainly to the case I water. These algorithms usually include two steps. The first step is atmospheric correction, which is applied to separate the atmospheric radiance from the radiance that comes from the ocean. The next step is based on a bio-optical model to relate the water-leaving radiance to the chlorophyll concentration. Because the water-leaving radiance typically comprises at most about 10% of the total radiance at the TOA, the key to reliable retrieval of the water-leaving radiance from the measured total radiance is an accurate correction of the effects of aerosol scattering and absorption.

Based on the CAO-DISORT radiative transfer model for the coupled atmosphere-ocean system (CAO-DISORT, Stamnes et al., 1988; Jin and Stamnes, 1994; Thomas and Stamnes, 1999) and a complete bio-optical model of Case I waters (Li and Stamnes, 2002), we have developed a new algorithm for SeaWiFS data processing (Stamnes et al., 2002). The CAO-DISORT code computes multiple scattering effects in a rigorous manner, and automatically and accurately takes into account the anisotropic behavior of the water-leaving radiance. The SeaWiFS channels 765 nm and 865 nm are used for retrieval of aerosol optical depth and aerosol model due to the small contribution from the case I water in the NIR. Then, the retrieved aerosol model and optical depth are used to predict the water leaving radiance in the visible, and subsequently to retrieve the chlorophyll concentration from the SeaWiFS channels at 490 nm and 555 nm. This approach provides simultaneous retrieval of atmospheric aerosol properties and chlorophyll concentrations in Case I waters. This new algorithm has been tested on synthetic datasets as well as match-up data. The results show that our new algorithm provides self-consistent and accurate retrievals.

Now this algorithm is being modified for use with the AVIRIS data to retrieve marine parameters for coastal waters. The AVIRIS data should be ideal for coastal water retrieval due to the many spectral channels available, and the wide spectral range from 400 nm to 2500 nm. The channels at 765 nm and 865 nm are no longer suitable for aerosol retrieval in the coastal water, because of the strong scattering of coastal water. The longer wavelength channels, such as 1040 nm and 1240 nm, will be selected to retrieve aerosol properties. In contrast to Case I waters where the optical properties are assumed to covary with the chlorophyll concentration, a bio-optical model for coastal waters must include other parameters. At a minimum we should include 3 different components: chlorophyll (CHL), color dissolved organic matter (CDOM) and total suspended solids (TSM). Because the different components have different spectral scattering/absorption characteristics, the wide spectral range of the AVIRIS instrument provides a good opportunity for retrieval of multiple components. Feasibility studies based on a three-component model (Frette et al., 1998; Frette et al., 2001) show promising results. Based on the field measurements obtained over the Hudson/Raritan Estuary area (Bagheri et al., 1999, 2000 and 2001). We have used a three-component bio-optical model in conjunction with the CAO-DISORT code to compute the radiance both at the surface and at the top of the atmosphere. Figure 4 shows comparison of reflectances measured and computed from CAO-DISORT code using a bio-optical model consistent with the measurements.

Building such bio-optical models for special coastal locations will be very important step for developing reliable algorithms to retrieve the coastal water parameters. The high spatial resolution of the AVIRIS data will also be very advantageous for coastal water property retrieval, because coastal waters usually have high spatial and temporal variation. Thus, the AVIRIS data has suitable resolution data for coastal water quality estimation.

3.2 Bio-Optical and Inverse Modeling

The ongoing research is based on imaging spectrometer data from AVIRIS, field spectroradiometer and water samplings. Based on these measurements optical water quality models are constructed linking the water constituent concentrations to (i) the inherent optical properties (IOP), using the specific inherent optical properties (SIOP), and (ii) to the subsurface (ir)radiance reflectance (Bagheri and Dekker , 1999 and Bagheri et al., 2000 and 2001).

The subsurface irradiance reflectance R(0-) are generated from the constituent concentrations using the linear backscattered albedo model based on the work of Gordon et al. (1975):

$$R(0-) = r \cdot \frac{b_b}{a + b_b} \tag{1}$$

Where:

a is the total absorption coefficient

b_b is the total scatter coefficient

r is a factor based on the geometry of incoming light and volume scattering in the water body.

This model is then validated with the R(0-) measured in the study site (figure 4). The validation of subsurface irradiance reflectance measured by the spectroradiometer is an important step for establishing the optical properties of the waters of the study site. Modeling of reflectance spectra based on the IOP will explain the variability in water quality concentrations and inverse modeling can be used for monitoring water quality conditions in the estuarine waters using remotely sensed data.

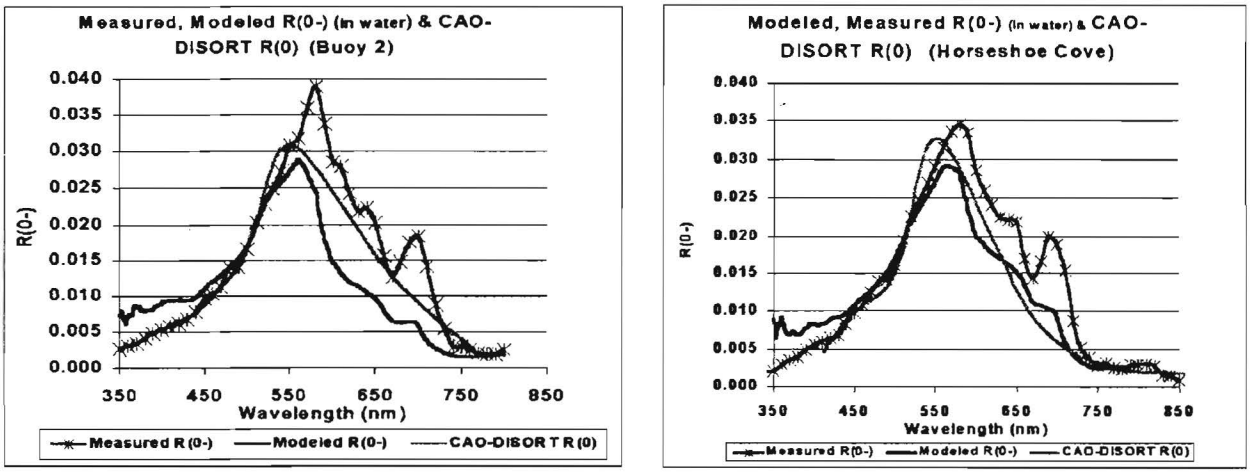

Figure 4. Modeled, Measured R(0-) and CAO-DISORT R(0) computed for Stations 2&3 (5/15/2000)

The linear matrix inversion developed by Hoge et al. (1996) was applied to in situ measurements collected simultaneously with the AVIRIS overflight. The radiance models describe the generation of upwelled water-leaving spectral radiance caused by backscatter and absorption of incident downwelling solar irradiance (Hoge et al., 2001). The algorithm was then applied to the atmospherically corrected AVIRIS data acquired over the study area to retrieve the IOPs (from which the constituent concentration

are obtained). The linear matrix inversion for retrieval of IOPs was based on the work of Gordon et al. (1988).

The inversion matrices (2) are used for solving for three unknown $a_{ph}(\lambda_1)$, $a_d(\lambda_1)$ and $b_{bt}(\lambda_1)$ at any wavelength λ_i:

$$\begin{bmatrix} 1 & 1 & v(\lambda_1) \\ D_{21} & e^{[-S(\lambda_2-\lambda_1)]} & (\lambda_1/\lambda_2)^n v(\lambda_2) \\ D_{31} & e^{[-S(\lambda_3-\lambda_1)]} & (\lambda_1/\lambda_3)^n v(\lambda_3) \end{bmatrix} \cdot \begin{bmatrix} a_{ph}(\lambda_1) \\ a_d(\lambda_1) \\ b_{bt}(\lambda_1) \end{bmatrix} = \begin{bmatrix} h(\lambda_1) \\ h(\lambda_2) \\ h(\lambda_3) \end{bmatrix} \tag{2}$$

where:

$\lambda_1 = \lambda_g$----peak wavelength for Gaussian phytoplankton absorption model (nm)

λ_1=440, λ_2 = 500, λ_3 =560 nm

S = 0.025, n = 1.2, g = 30

V--- a factor to separate absorption and scattering components of water

$$D_{21} = e^{(\lambda_2-\lambda_1)^2/-2g^2} \qquad D_{31} = e^{(\lambda_3-\lambda_1)^2/-2g^2}$$

The $a_{ph}(\lambda_i)$, $a_d(\lambda_i)$ and $b_{bt}(\lambda_i)$ at all wavelengths are computed using the following:

$$a_{ph}(\lambda_i) = a_{ph}(\lambda_g) \cdot e^{[(\lambda_i-\lambda_g)^2/(-2g^2)]} \tag{3}$$

$$a_d(\lambda_i) = a_d(\lambda_d) \cdot e^{[-s(\lambda_i-\lambda_g)]} \tag{4}$$

$$b_{bt}(\lambda_i) = b_{bt}(\lambda_b)(\lambda_b / \lambda_i)^n \tag{5}$$

The results of the linear matrix inversion were input into Equation (1)-- the bio-optical model of the estuary for retrieval of water quality parameter concentration (figure 5).

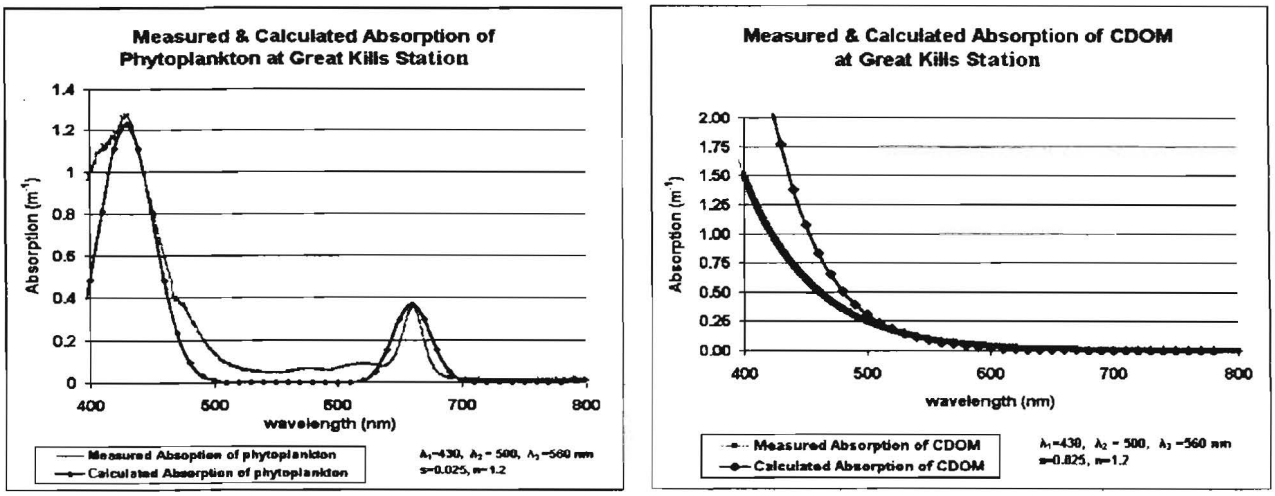

Figure 5. Measured and Retrieved Phytoplankton and CDOM absorptions at Great Kills (St 3) (7/13/2001)

4. DISCUSSION AND CONCLUSION

Atmospheric correction of ocean color imagery is commonly based on the assumption that the water-leaving radiances at NIR are negligible. Over the open ocean an aerosol model and aerosol optical depth can be derived from the NIR channels. The aerosol information can be extrapolated into the visible range for retrieval of the water leaving radiance and the estimation of the chlorophyll concentration. Unfortunately, these algorithms cannot be used in case 2 waters because the suspended material in case 2 waters have strong scattering in the NIR part of the spectrum. Development of a robust algorithm for simultaneous retrieval of atmospheric aerosol optical properties, chlorophyll concentration and colored dissolved organic matter is a very challenging task. Nevertheless, such an algorithm is needed to make progress in this area.

The AVIRIS is capable of measuring hydrologic optical properties at a level of detail unmatched by any existing satellite instrument. The AVIRIS hyperspectral data provide us with an opportunity to develop such algorithms based on the different spectral reflectances characterizing aerosol and ocean particles. This can be used as a basis for distinguishing between atmospheric and oceanic effects and to set the estimated turbidity for each region within the image for retrieval of water constituents. The methodology described here provides a baseline for better understanding of how sunlight interacts with estuarine/coastal water necessary in establishing the IOP characterization of the estuary and setting a foundation for the future research. The products of remote sensing data derived from AVIRIS analysis in forms of thematic maps representing the spatial/temporal distributions of water quality parameters are important input into a GIS for better management of the water resources of the study site and other estuaries nationwide.

5. ACKNOWLEDGEMENT

This project is funded by the National Science foundation (Grant # 9806982). Support of the NASA/Headquarters-Biology and Geochemistry Program and the AVIRIS Experiment Team is greatly appreciated. Review of the paper by Dr. F. Hoge is greatly appreciated.

6. REFERENCES

Bagheri, S., and Dekker, A., 1999, Remote Sensing of Nearshore Water Quality Using Bio-Optical Modeling and Retrieval Techniques, *8th AVIRIS Workshop*. Pasadena, California.

Bagheri, S., Zetlin, C., and Dios, R., 1999, Estimation of optical properties of nearshore water, *International Journal of Remote Sensing*, Vol. 20, No. 17, 3393-3397.

Bagheri, S., Rijkeboer, M., Pasterkamp, R., and Dekker, 2000, A Comparison of Field Spectroradiometers in Preparation of Bio-Optical Modeling, *9th JPL AVIRS Workshop*. Pasadena, California.

Bagheri, S., and Stamnes, K and Li, W., 2001, Application of Radiative Transfer Theory to Atmospheric Correction of AVIRIS Data, *10th JPL AVIRS Workshop*. Pasadena, California.

Frette, O., Stamnes, J. J., and Stamnes, K., 1998, Optical remote sensing of marine constituents in coastal waters: A feasibility study, *Applied Optics*, 37, 8218-8326.

Frette, O., Erga, S. R., Stamnes, J. J., and Stamnes, K., 2001, Optical remote sensing of waters with vertical structure, *Applied Optics*, 40, 1478-1487.

Gordon, H. R., Brown O. B., and Jacobs, M. M., 1975, Computed Relationships between Inherent and Apparent Optical Properties of a Flat Homogeneous Ocean. *Appl. Optics*, 14:417-427.

Gordon, H. R., Brown, O. B., Evans, R. H., Brown, J. W., Smith, R. C., Baker, K. S., and Clark, D. K., 1988, A semianalytic radiance model of ocean color, *J. Geophys. Res.*, 93, 10,909-10,924.

Green, R. O., 1996, Summaries of the 6th Annual JPL Airborne Earth Science Workshop. Vol. 1, *JPL AVIRIS Workshop*. Pasadena, California.

Hoge, F. E., and Lyon, P.E., 1996, Satellite retrieval of inherent optical properties by linear matrix inversion of oceanic radiance models: An analysis of model and radiance measurement errors, *J. Geophys. Res.* 101, 16,631- 16,648.

Hoge, F.E., Wright, C. W., Lyon, P.E., Swift, R. N., and Yungel, J.K., 2001, Inherent optical properties imagery of the western North Atlantic Ocean: Horizontal spatial variability of the upper mixed layer, *J. Geophys. Res.* 106, 31129-31140.

Jin, Z., and Stamnes, K., 1994, Radiative transfer in nonuniformly refracting media such as the atmosphere/ocean system, *Appl. Opt.*, 33, 431-442.

Li, W., and Stamnes, K., 2002, Inherent optical properties of case I waters: A complete model suitable for use in radiative transfer computations, *J. Geophys. Res.*, submitted.

NEN 6484, 1982, Water: Determination of the content of not dissolved material and its ignition residue, *Nederlands Normalisatie instituut, Delft, The Netherlands (in Dutch)*

NEN 6520, 1981, Water: Spectrophotometric determination of chlorophyll a content, *Nederlands Normalisatie instituut, Delft, The Netherlands (in Dutch)*

Stamnes, K., Tsay, S.-C., Wiscombe, W.J. and Jayaweera, K., 1988, Numerically stable algorithm for discrete-ordinate-method radiative transfer in multiple scattering and emitting layered media, *Appl. Opt.* 27, 2502-2509.

Stamnes, K., Li, W., Yan, B., Barnard, A., Pegau, W. S., and Stamnes, J. J., 2002, A new ocean color algorithm: Simultaneous retrieval of aerosol optical properties and chlorophyll concentrations, *Appl. Optics,* submitted.

Thomas, G. E., and Stamnes, K., 1999, Radiative Transfer in the Atmosphere and Ocean, *Cambridge University Press.*

Quantitative Mapping of the Soil Rubification Process on Sand Dunes, Using Field and Airborne Sensors

Eyal Ben-Dor,[*] Noam Levin,[*] Arie Singer,[**] Arnon Karnieli,[***] and Ofer Braun[****]

[**]Department of Geography and Human Environment, Tel-Aviv University, Ramat Aviv, P.O.B. 39040, Israel 69978
[**]The Soil and Water Science Department, Faculty of Agriculture, Hebrew University of Jerusalem, Israel
[***]Bloustein Center for Desert Research, University of Ben-Gurion, Negev, Israel
[****]Bar-Kal Systems Engineering, Ltd., Netania, Israel

1.0 INTRODUCTION

Remote sensing of soils plays a major role in both soil survey and soil mapping applications. Traditional methods such as air photos and satellite images suffer from low spectral resolution and, thus, provide only limited spectral information about the targets explored. For soil survey applications, high-resolution imaging spectroscopy may be a key factor in implementing accumulated spectral-soil knowledge. Because the IS technology provides a near-laboratory-quality reflectance and emittance spectrum for each single picture element (pixel), it allows the identification of objects based on the spectral absorption features of the chromophores (Goetz et al. 1985, Clark and Roush 1984). In this regard it can be used to assess mineral changes on the soil surface and to better provide spatial view of pedogentic processes. One of the fundamental pedogenesis processes taking place along the coastline of Israel is the soil rubification of the sand dunes. The soil rubification is defined as a pedogenesis stage in which iron is released from primary minerals to form free iron oxides that coat quartz particles with a thin reddish film (Buol et al., 1973). The Fe in the free iron oxides is active across the VIS-NIR region via the electron transition of ($^6A1 \rightarrow {}^4T1g$ between 0.75-0.95μm and $^6A1 \rightarrow {}^4T2g$ between 0.55-0.65μm) and is responsible for the red soil color. We thus applied a careful study to account for the iron oxides content on the sand dune surfaces using spectral information both from laboratory and airborne sensors. This was done in order to demonstrate that rubification processes on costal environment can be done using imaging spectroscopy technology.

2.0 MATERIALS AND METHOD

In October 1999 the CASI 48 channel sensor (covering the VIS-NIR) was mounted onboard an Piper Aztec two-engine aircraft and acquired data from an altitude of 10,000 feet over the area of Ashdod City, Israel. Two flight lines were acquired from south to north, each having a spatial swath of 1.2 km and ground resolution of about 2 meters. During the flight coverage, ground truth data were collected. These data included atmospheric conditions (optical depth, humidity and water vapor content) and soil sample collections for laboratory measurements. The soils were dried and measured for reflectance in the laboratory, using a LICOR spectrometer. For each soil sample, two replications were used for the DCB extraction (Mehra and Jackson 1960). The radiance CASI data were atmospherically rectified into reflectance using the EL calibration

method (Roberts et al., 1985), using 5 selected targets. Validation of this correction was performed using samples that were not incorporated in the EL process, and by comparing the similarities between the imaging spectra and the laboratory spectra. Geometrically correction took place using image the image correction technique that extract about 160 GCP from ortho-photo of the area.

3.0 RESULTS AND DISCUSSION

a. General

The sand material is brought to the Israeli coast from the Nile delta by the west-east circle stream along the east bank of the Mediterranean Sea. The study area located near the city of Ashdod, consists of a dune mass of about 350,000 m^3/year as received from the above stream. The resulting dune strip at the selected areas is about 5 km in width. Viewing historical air photos (taken over the past 60 years) shows that a significant diminishing of dune area coverage is occurring. These changes, significantly observed in the north, are due to the massive urbanization activity. Careful measurements of the entire sand dune area show that the sand dunes occupied an area of about 40 km^2 in 1945 and diminished to 25 km^2 in 2001. The sand motion envelope as identified by the 60-year air photo archive showed that the dune masses have tended to significantly diminish over the years, from 2.7 m/year in 1945 to 0.6 m/year in 1997. Based on this finding, we selected soil samples (for spectral and chemical analyses) that were allocated on the cross section that best represents the southwest to northeast dune development. As can be observed from both the satellite image and the ground observations, no significant natural reddish chrome occur at the selected west–east cross sections, except in several discrete pockets (vegetation surrounding area). For the most part, the absence of a reddish color on the rest of the dune area is based on the fact that the dune stabilization process is rather young (about 50 years) and the climate conditions (500 mm of annual precipitation) do not effectively permit a massive extraction of free iron oxides in those areas during this time period. The free iron oxide content (DCB-Fe) that was chemically measured in the laboratory, showed relatively low iron oxides amount (0-0.03 %) that agrees with the previous observation that showed no red color sequence in the study area. The first step toward adopting the spectral information to account for the DCB-Fe content was to examine the laboratory spectral information and then to apply it on the image data.

b. Laboratory (Field) Dune Spectra

In this stage, the original laboratory spectra was resampled into the CASI spectral configuration (consisting of 48 bands) and then used to extract the iron absorption parameters after applying the continuum removal (CR) algorithm. As can be seen in Figure 1a,b, a spectral sequence exists between the selected samples (for both laboratory (a) and air (b) domains), which calls for the extraction of the quantitative relationship between the entire DCB-Fe sand sample, using spectral parameters. The two selected spectral parameters were 1) the slope between 590 and 511 nm (termed as [SLOP] and 2) and the absorption peak at 499 nm after applying the CR treatment (termed as ABS). The above-mentioned spectral parameters provided correlation values (r) of 0.79 for the SLOP 0.88 for the ABS parameters. Examining the slope and aspect effects showed that significant variation occur within close areas as a result of the micro-topography variation. Also, non-lambertian effects, especially in the low incidence angle, were found to be significant. Correction for those effects (using DEM and Minnaret correcting factor respectively) still provided errors in the spatial domain, suggesting that BRDF effects may be introduced within the data. To remove these effects, a second polynomial curve fit, between the spectral differences of

the laboratory and the image reflectance data, for each ground point, across the entire spectra region, was employed. As the ground sampling were taken across track the flight lines, the correction for the BRDF effects was found to provide a sufficient solution for the entire sensor's FOV. Validation data confirmed the previous corrections, allowing us to move forward to the next quantitative stage.

c. Quantitative Mapping of the Rubification Process using the Image Spectra
Assuming that each spectral parameter describes a different mechanism, and that all of the external effects were removed, we prepared a multiple correlation using both SLOP and ABS parameters to extract the following equation:

(1) $Fe = 0.80929 + 0.00975(SLOP) - 0.86681\ (ABS)$ $r2=0.88$

Applying this equation on a pixel-by-pixel basis produces a gray scale image, in which the intensity level of each pixel refers to the iron concentration. Figure 2 shows the two georectified flight lines after applying the above equation and after the gray scale image was encoded with a color table that represents the iron oxide occurrences in a natural view, i.e., reddish pixels represent high, and white pixels represent low DCB-Fe content. In contrast to the manipulated DCB-Fe image, areas in the gray scale image that are not characterized as dune or soil were not encoded with the selected color table, because their calculated values lie outside the DCB-Fe calibration scale. From the DCB-Fe images, it can be seen that the reddish chroma increase while going from the coastline (west) toward the inner land (east), whereas the greatest amount of reddish chroma occurred at the southeastern boarder of the sand dune area. Because the direction of the wind regime in the study area is WSW to ENE, and there is a decreasing wind gradient toward the east, sand particle movement decreases while going east, resulting of sand stabilization processes. At the reddish locations, the sand particles are more stable and are exposed more to soil-forming factors than at the light locations, forming the free iron oxides that coat the quartz particles. It is interesting to note that the reddish spots observed previously (exposed paleosol and vegetation pockets) were also encoded a strong red in the processed DCB-Fe image.

4. SUMMARY AND CONCLUSIONS

Reflectance spectroscopy offers new insight into the pedogenesis process, long before it is visible to the naked eye. The imaging spectroscopy technique, which provides near-laboratory-quality reflectance information, also has the capability to observe nonvisible information and thus to produce a special view of the pedogenesis processes in large areas. Caution must be paid however to micro topographic and non-lambertian effects as well as to BRDF effects in spectral imaging sand dunes ecosystem. We can conclude that spectral information from field or air domains can provide valuable information regarding the premature stages of the rubification process. This information can also shed light on sand dune stabilization as well as on possible obstacles that might control dune development.

5. REFERENCES

Buol, S.W., F.D. Hole, R.J. McCracken 1973, Soil Genesis and Classification, The Iowa State University Press, Ames, pp. 360.

Clark, R.N. and T.L. Roush, 1984, reflectance spectroscopy: Quantitative analysis techniques for remote sensing applications. Journal of Geophysical Research, 89:B7:6.

Goetz, A.F., H.G. Vane, J. Solomon, and B.N. Rock, 1985, Imaging spectrometry for earth remote sensing, *Science*, **228**, 1147-1153.

Mehra, O.P. and M.L. Jackson, 1960, iron oxide removal from soils and clays by dithionite-citrate system buffered with sodium bicarbonate. Clays and Clay Minerals, 7:317-327.

Roberts D.A., Y. Yanaguchi, and R.J.P Lyon, 1985, Calibration of airborne imaging spectrometer data to the percent reflectance using field spectral measurements. Proceedings of the Nineteenth International Symposium on Remote Sensing of Environment, Ann Arbor, Michigan, 21-25 October, pp. 463-472.

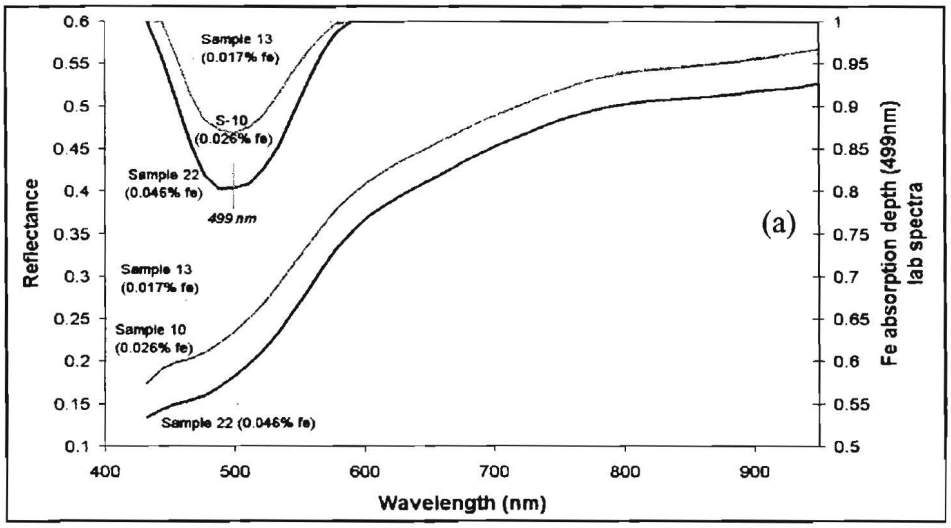

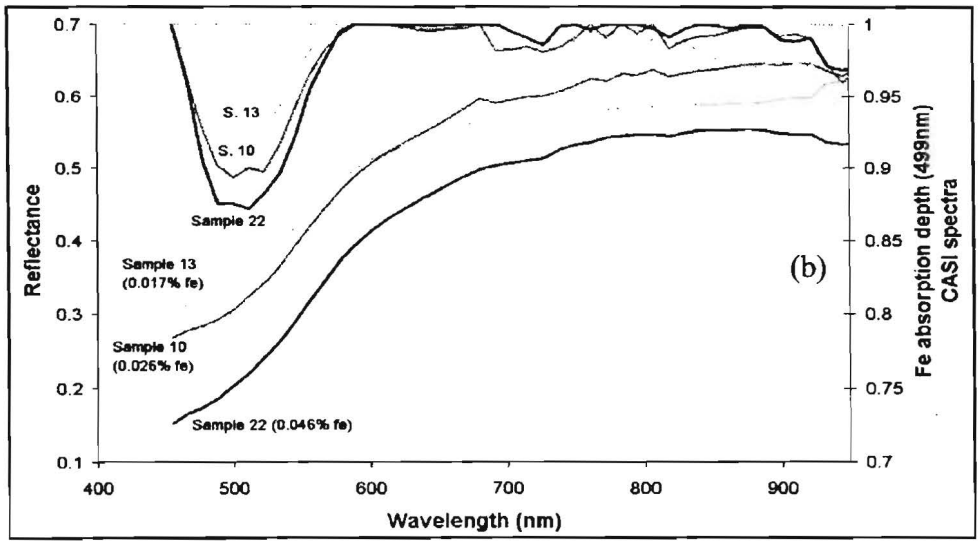

Figure 1: The reflectance spectra of three selected sand samples, with relative high, moderate and low DCB-Fe content before and after applying the continuum removal algorithm. Both the field (a) and airborne (b) measurements are provided.

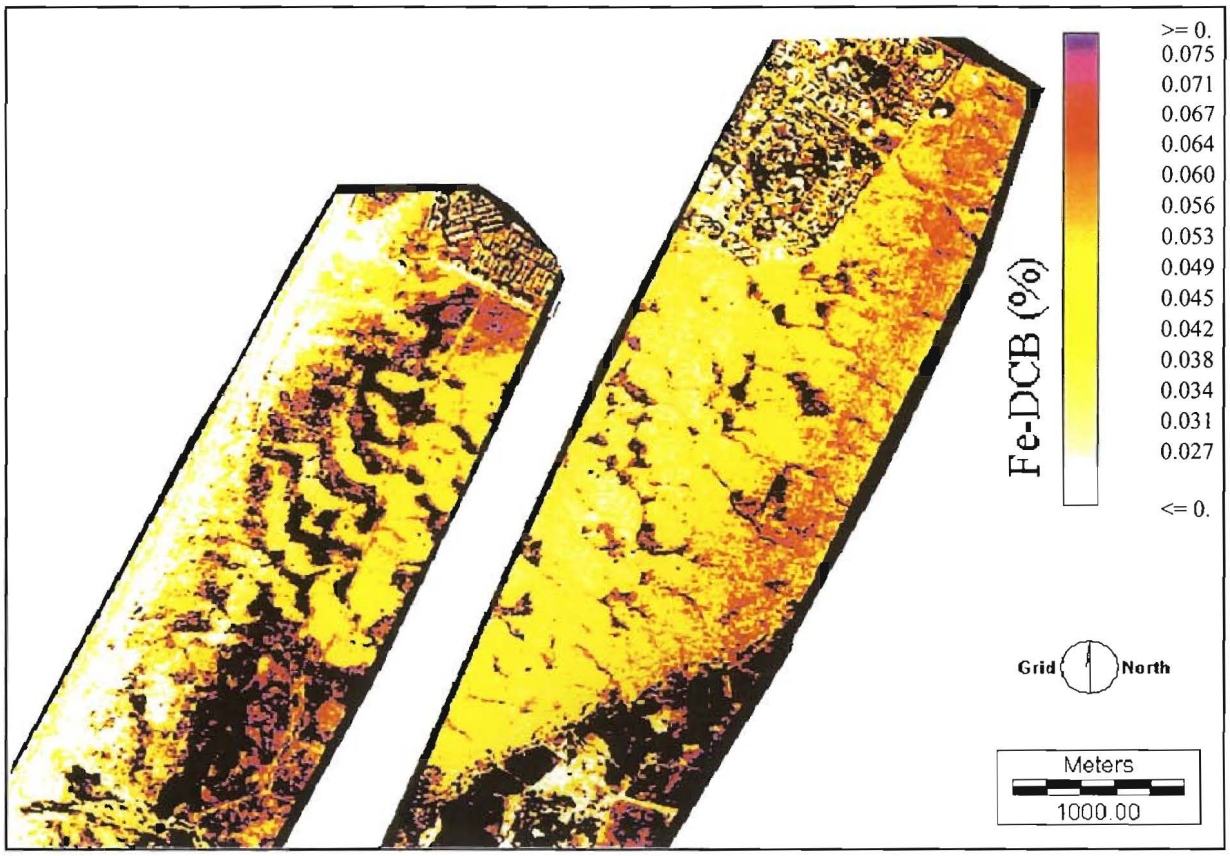

Figure 2: The DCB-Fe image as obtained after applied equation 1 on a pixel-by-pixel basis on the CASI 48 atmospherically rectified image

COMBINING S-SPACE AND IMAGE SPATIAL INFORMATION FOR CHARACTERIZATION OF LAND-COVER ELEMENTS USING AVIRIS DATA

Conrad M. Bielski
Jet Propulsion Laboratory, California Institute of Technology
4800 Oak Grove Dr., Pasadena, California 91109
conrad.m.bielski@jpl.nasa.gov

Abstract: Imaging spectroscopy data provides information that is both spatially and spectrally rich. However, hyperspectral classification and identification procedures are generally based solely on the spectral data. The S-space concept treats the spectrum as a 'spatial' dimension thereby facilitating the exploration of a relationship between the spectral and spatial image domains. This paper presents the ideas that will be researched as well as some preliminary results.

1. Introduction

Imaging spectroscopy data is becoming more available to the remote sensing community due to the increased number of sensors put into commission over the last few years. This is favorable news for the land-cover community because the increase in potential information that can be obtained from such data is promising. However, the tools currently available are generally based solely on the spectral signature even though the spatial content can provide a significant amount of information. A reason for not combining the two types of data into the information extraction process is the unknown relationship between the spatial and spectral dimensions. For example, the standardized Airborne Visible/Infrared Imaging Spectrometer (AVIRIS) Processing Methodology (Kruse, 1999) proposes calculation of the Pixel Purity Index and N-dimensional Visualization for endmember definition, which are solely based on the spectral signature at each measured location.

This paper introduces the ideas that were put forth for post-doctoral research with the AVIRIS lab at the Jet Propulsion Laboratory. These ideas were based on the observation that a spectral signature resembles quite closely many other spatial-type measurements. Even though the electromagnetic (EM) spectrum itself is not considered as a spatial domain, this similarity to the spatial dimension could be explored and more easily associated to the spatial dimension. A first attempt at examining the spectral variability of imaging spectrometer data using geostatistical tools is presented. Geostatistics is concerned with the study of phenomena that fluctuate in space (Olea, 1991) and has been widely applied in the remote sensing context to understand and model the spatial variability inherent in remote sensing scenes. One example is Curran and Dungan's (1989) work on estimating the per-band signal-to-noise ratio in AVIRIS data, using the semivariogram model nugget information.

Four sections make up the remainder of this paper. Section 2 introduces the S-space concept, followed by a section dedicated to describing the quantification of the spectra using the semivariogram. The next section presents examples and preliminary results based on AVIRIS imaging spectrometer data. The final section describes some ideas and future work.

2. Spectral Space or S-Space

As mentioned above, the spectral signature recorded by an imaging spectrometer very closely resembles other types of spatial measurement. In figure 1, a comparison was made between a measure of soil pH along a transect (Figure 1, left side) and a hypothetical measure of radiance or reflectance taken at different wavelengths (Figure 1, right side). Envisioning the spectral signature in this manner gives one the spatial sense of the EM spectrum. Furthermore, the idea that measured point B is closer to point A than point C reinforces this idea of 'spatial distance.' In order not to confuse this type of space with spectral space that can also mean spectral feature space, S-space was coined in order to differentiate the two (Bielski et al., 2002). The spatial measures in S-space are wavelengths or frequency. Since S-space is one dimensional, distance between measurements are analogous to the difference in wavelength or frequency.

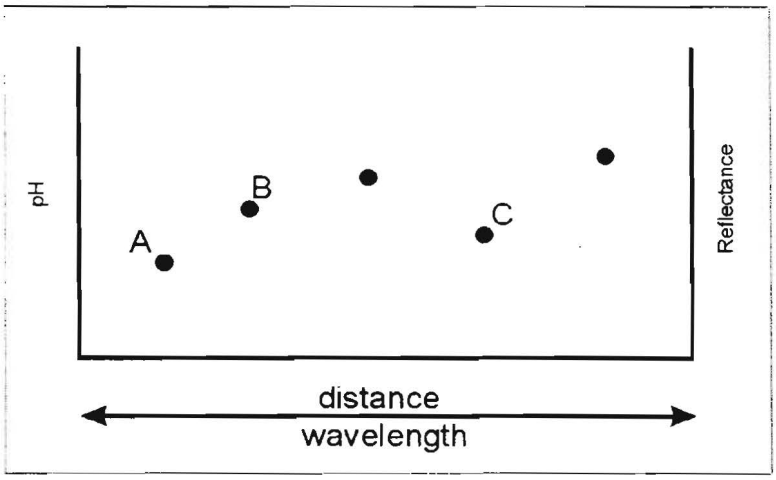

Figure 1 – S-space illustration: a theoretical profile was compared with a sampling transect in order to show similarities between geographical space and S-space. Point A is closer to point B, both in S-space and geographical space when compared with point C.

3. Quantifying Spectral Variability

The variability in S-space was computed using the variogram, a geostatistical tool. Previous work has demonstrated the applicability of the semivariogram for the quantification of the spatial variability inherent in remotely sensed imagery (Curran, 1988; Woodcock et al., 1988a,b; Jupp et al., 1988). The experimental semivariogram is a univariate statistic that measures the average dissimilarity between data separated by a lag h. The lag in S-space was considered to be the spectral distance between image bands. Mathematically, the semivariogram is computed as half the average squared difference between the components of every data pair:

$$\gamma(\mathbf{h}) = \frac{1}{2N(\mathbf{h})} \sum_{i=1}^{N(\mathbf{h})} [z(u_\alpha) - z(u_\alpha + \mathbf{h})]$$

where z is the radiance or reflectance at the spectral space location u, and N(h) is the number of data pairs at a spectral distance h apart. In the two-dimensional case, location pairs are found by jumping the necessary h pixels apart for each lag (Figure 2). Since the spectral signature is one dimensional, the semivariogram is computed along a transect, as in Figure 2. This method of computing the S-space semivariogram was used as a means of generating initial results even though in reality imaging spectroscopy data does not necessarily provide equidistant bandwidths. The bandwidths making up AVIRIS imagery are not equidistant and should therefore be taken into account in the computation of the experimental semivariogram.

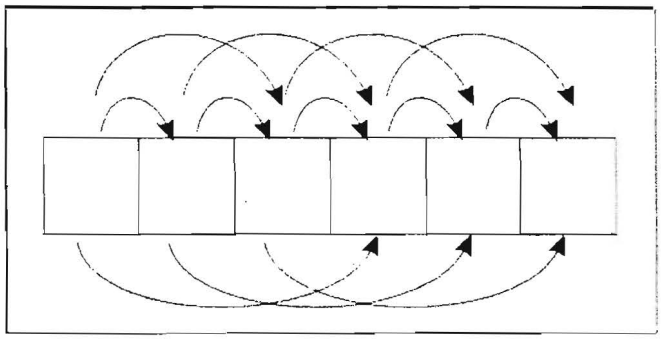

Figure 2 – Computing the experimental semivariogram along a transect of pixels. Each arrow designates a different size h. In S-space, the varying bandwidth must be taken into account.

Computing the experimental semivariogram is but the first step. Since the data acquired by the sensor does not have infinitely small distances between samples, the second step is to fit a mathematical model to the experimental model. The modeled semivariogram will then have variance values for any lag h, which is necessary for solving interpolation equations (e.g., kriging). Another reason for modeling the experimental semivariogram was to diminish the number of resulting bands even further. A modeled semivariogram (single model) is made up of three parameters: the nugget, sill and range (Figure 3). The nugget is a description of the unknown variability between the smallest sampling interval. The sill is the plateau of the variance and the range is the distance at which the sill is attained.

The expected shape of a typical semivariogram is that variances at shorter lags are smaller because objects that are closer together tend to be more similar. As the distance increases between pairs of points, objects become less similar, thereby increasing the variance. A horizontal semivariogram indicates no spatial variability because the variance of close data pairs is the same as with data pairs further apart.

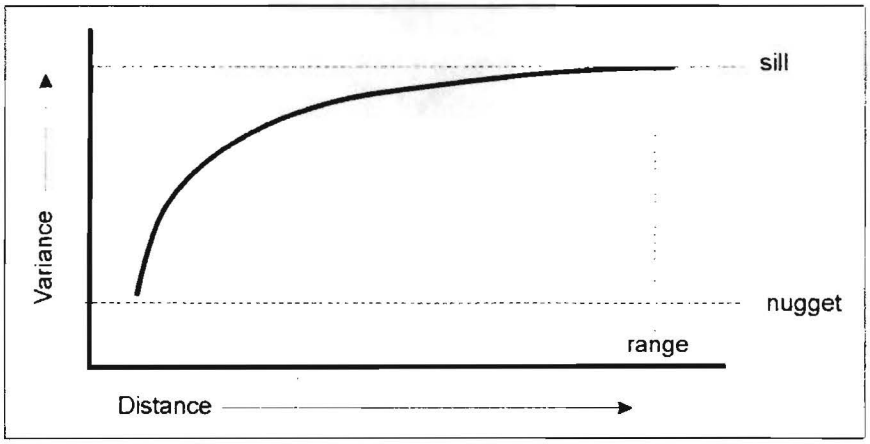

Figure 3 – The ideal semivariogram. Three parameters modeling a single model semivariogram: the nugget, sill and range.

4. Results of Initial Experiments

This section presents results of computing the experimental semivariogram on AVIRIS imagery acquired on October 9, 1998 (Figure 4). The image is of an experimental agricultural field in the Salinas Valley region of California. The image shows rows of broccoli at different stages of growth as well as lettuce and senescent corn. The perfect rows of planted vegetation were easily discerned and also have a distinct spatial pattern that was easily observed in the computed experimental variogram.

A set of two-dimensional semivariograms was computed on ten bands of the AVIRIS data set. The first semivariograms were computed for band 20 and then for every 20th band after that. Three directional semivariograms were computed from top/bottom, at a 45° angle and side/side. The results are shown in Figure 5 and presented an interesting view of how the bands differed spatially. The close resemblance between the top/bottom and 45° angle semivariograms was due to the fact that the rows do not exactly run at a 45° angle and therefore had a similar spatial variability as the top/bottom semivariogram. The side/side semivariogram (Figure 5, right side) showed that a sill was reached and then the pixel pairs began to resemble each other again at increasing lags. This was most likely due to the fact that the most mature vegetables were found at the sides of the image where the largest lags would reach.

The one band that had the same semivariogram shape across all three plots was band 160. This band continuously produced an almost horizontal plot in all three cases. As mentioned previously, this occurs when there is a lack of quantifiable spatial variability. It turns out that the AVIRIS band number 160 was within a water vapour absorption band.

Figure 6 presents the actual images from which each of the above semivariograms was computed. The bands with the well-defined semivariograms did have an obvious spatial component. However, band 160 did not and this resulted in a horizontal experimental semivariogram.

The images in Figure 6 also showed the variability inherent spectrally for each of the row crops. It is precisely this variability that needs to be harnessed and related to the spatial dimension.

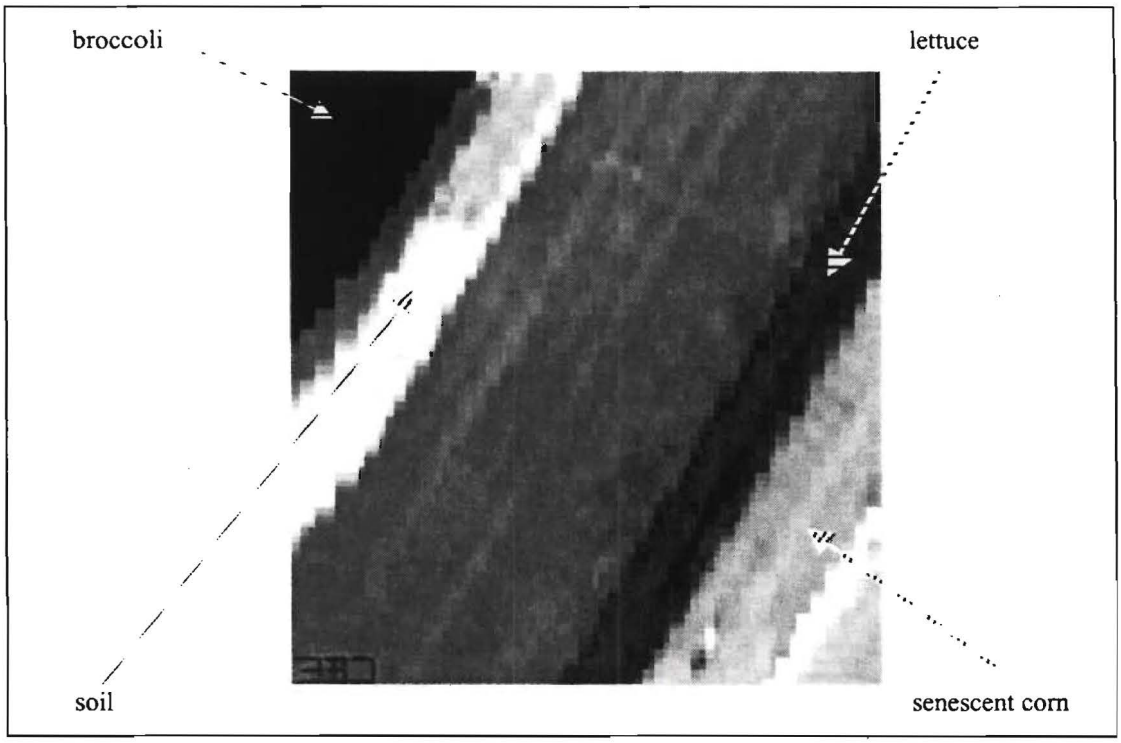

Figure 4 – AVIRIS image of Salinas Valley agricultural field taken October 9, 1998. Shown are mature broccoli, bare soil, senescent corn and lettuce.

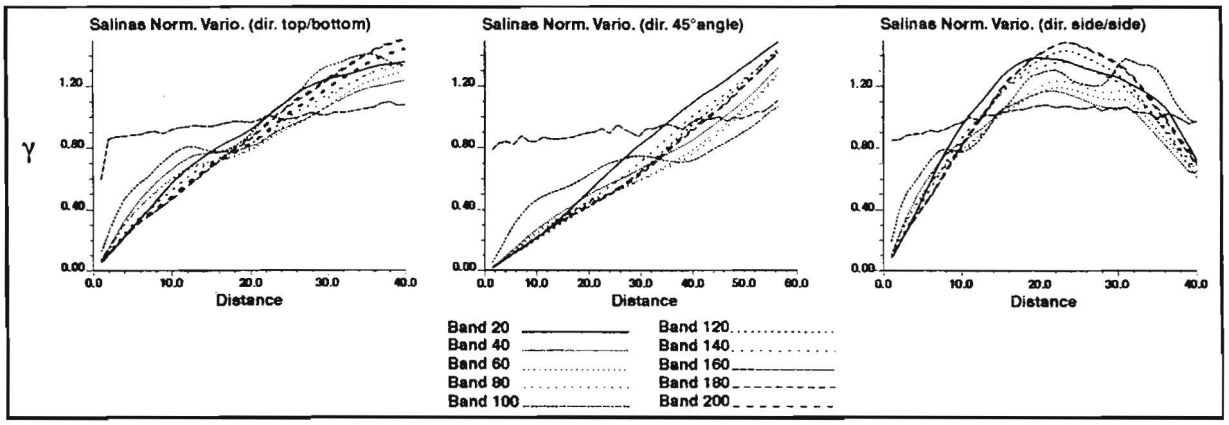

Figure 5 – Computed semivariogram in three directions: top/bottom (left), 45° angle (center) and side/side (right) for 10 AVIRIS spectral bands.

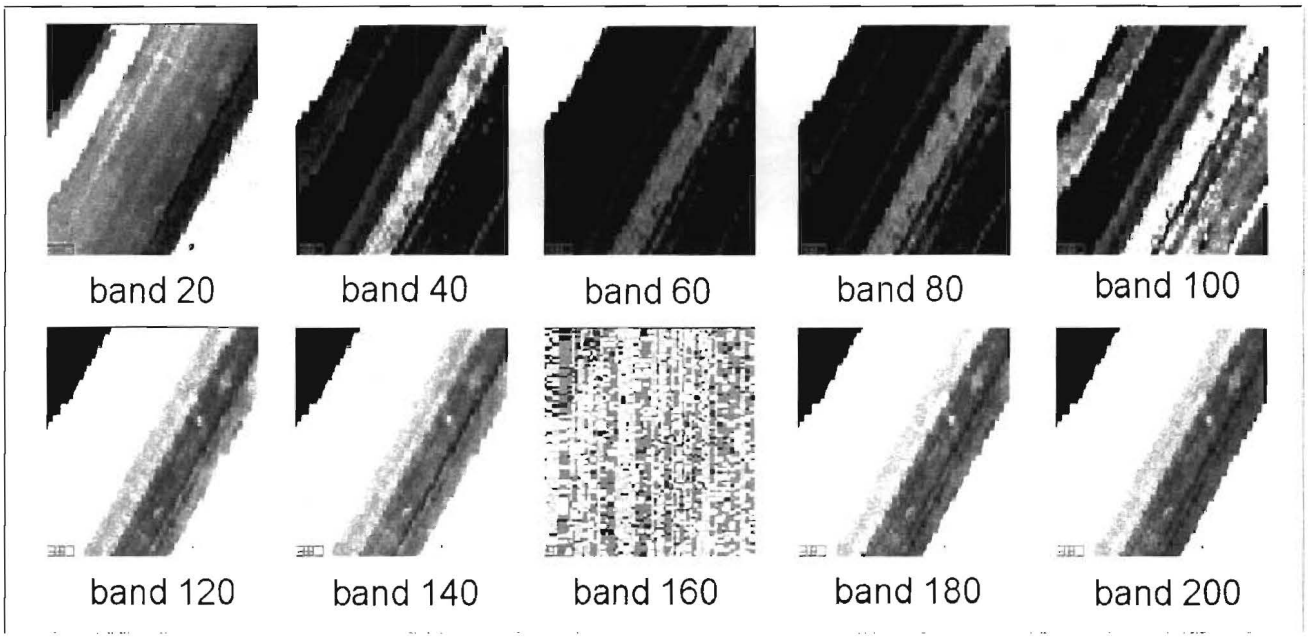

Figure 6 – The bands corresponding to the computed two-dimensional semivariograms in figure 5.

S-space was first explored with a simple computation of the average spatial variability across the entire Salinas image. Specifically, the experimental semivariogram was computed in the z-direction (i.e., along the spectrum) and averaged across all the pixels within the image. This resulted in a single plot (Figure 7). A quick analysis of the computed semivariogram over the entire spectrum recorded by AVIRIS showed that as the distance between bands increased, so did the S-space variability. This first analysis also showed that there was spatial variability in S-space. Upon closer examination, three distinct features were observed. A nugget effect was present but very small, and around lag 20, a small but evident plateau was observed that indicated small-scale variability between lags 0 and 20. A second plateau was observed between lags 40 to 45 that indicated a second scale of S-space variability.

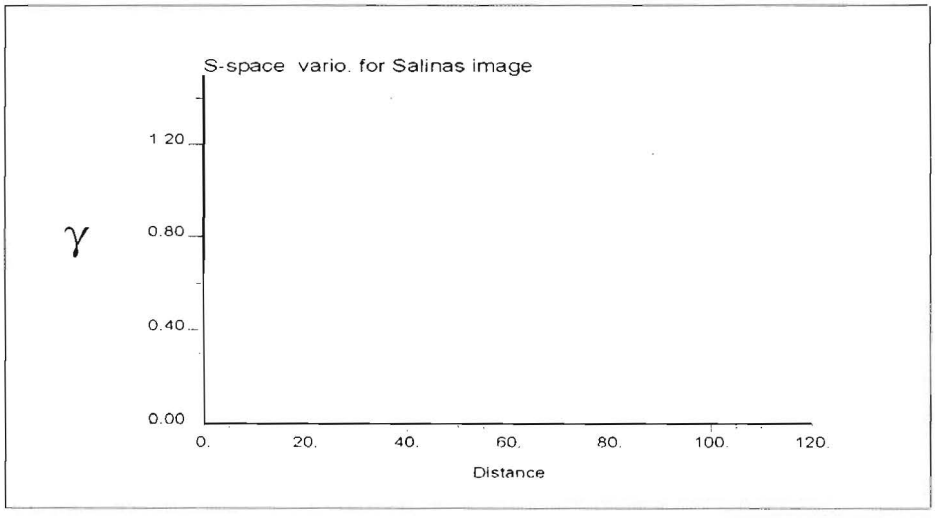

Figure 7 – The semivariogram computed in S-space (z-direction) for the Salinas Valley image.

Averaging all the spectral signatures over the entire image lost many details. Subsequently, four pixels were chosen from different land-covers for a more detailed look at the S-space variability. A single pixel from each of mature broccoli, bare soil, senescent corn and lettuce were chosen. Their spectral signatures are presented in

Figure 8. The S-space experimental semivariogram was computed based on these four spectral signatures (Figure 9, top). The first observation noted the very high variance for all of the computed semivariograms. This was due to the fact that radiance measures were used in the computation. Another interesting result was the relationship between the S-space variability and the resulting experimental semivariogram. Those spectral signatures with large variations produced the highest sills, i.e., broccoli and lettuce. The lower plot in Figure 9 showed the normalized semivariograms. The shapes of these semivariograms were more defined, with broccoli and lettuce having larger bumps than the senescent corn and soil.

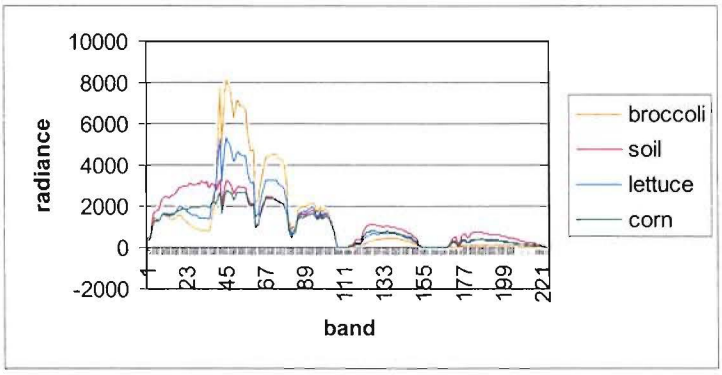

Figure 8 – Four pixels representing mature broccoli (orange), bare soil (pink), senescent corn (green) and lettuce (blue) and their associated spectral signature (left plot).

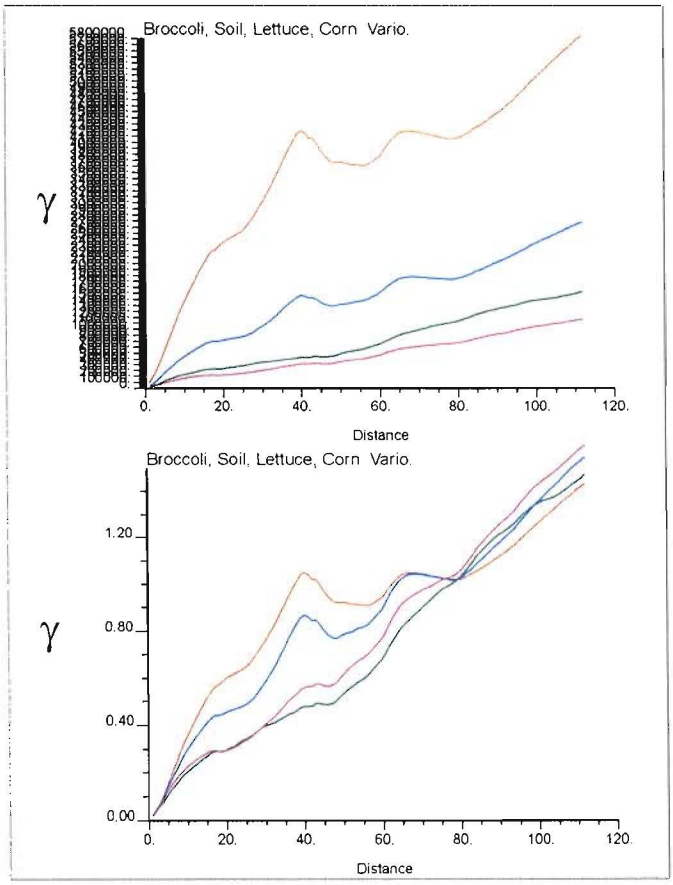

Figure 9 – Computed experimental semivariogram (top) and normalized experimental semivariogram (bottom) based on the four spectral signatures in Figure 8.

5. Future Directions

The above results were preliminary and served to provide insight into the use of geostatistical tools to quantify S-space. An important result was that the spectral signatures did in fact have quantifiable spatial variability. This fact alone is interesting enough to continue the investigation further. One possible use of modeling the spatial variation is to interpolate the spectral signature in areas where there is no data available or the data has been corrupted.

Ultimately, the direction of this research is to study the relationship between the spectral component of remotely sensed imagery and that of the spatial component. While both are distinct, they are the most important components making up a remotely sensed image for information extraction purposes. Combining the two types of information should increase the performance of automatic classification algorithms.

6. References

Bielski, C. M., Dubé, P., Cavayas, F., and Marceau, D. J., 2002, S-space: a new concept for information extraction from imaging spectrometer data. International Journal of Remote Sensing, 23(10), 2005-2022.

Curran, P.J., 1988, The semi-variogram in remote sensing: an introduction. Remote Sensing of Environment, 37, 493-507.

Curran, P.J., and Dungan, J.L., 1989, Estimation of signal to noise: a new procedure applied to AVIRIS data. IEEE Transactions of Geoscience and Remote Sensing, 27, 620-628.

Jupp, D. L. B., Strahler, A. H., and Woodcock, C. E., 1988, Autocorrelation and regularization in digital images: I. Basic Theory. IEEE Transactions on Geoscience and Remote Sensing, 26, 463-473.

Kruse, F.A., 1999, Visible-Infrared Sensors and Case Studies. Chapter 11 in Manual of Remote Sensing, Third Edition, Volume 3, Remote Sensing for the Earth Sciences, Andrew N. Rencz editor. John Wiley & Sons, Inc.

Olea, R. (ed.), 1991, Geostatistical Glossary and Multilingual Dictionary (New York: Oxford University Press).

Woodcock, C. E., Strahler, A. H., and Jupp, D. L. B., 1988a, The use of variograms in remote sensing: I. Scene models and simulated images. Remote Sensing of Environment, 25, 323-348.

Woodcock, C. E., Strahler, A. H., and Jupp, D. L. B., 1988b, The use of variogram in remote sensing: II. Real digital images. Remote Sensing of Environment, 25, 349-379.

Acknowledgment

The research described in this paper was carried out at the Jet Propulsion Laboratory, California Institute of Technology, under a contract with the National Aeronautics and Space Administration.

SYNTHESIS OF MULTISPECTRAL BANDS FROM HYPERSPECTRAL DATA: VALIDATION BASED ON IMAGES ACQUIRED BY AVIRIS, HYPERION, ALI, AND ETM+

Slawomir Blonski,[1] Gerald Gasser,[1] Jeffrey Russell,[1] Robert Ryan,[1] Greg Terrie,[1] and Vicki Zanoni[2]

1. INTRODUCTION

More systematic studies are needed for a better understanding of how multispectral data properties such as ground sample distance (GSD) and spatial resolution, extent and shape of spectral bands, signal-to-noise ratio (SNR), data quantization, and band-to-band registration affect performance of remote sensing imagery in real-world applications. However, because the number of available multispectral data sources is still limited, parametric studies with varying image properties are difficult to conduct. In the case of panchromatic imagery, the amount of data collected at various scales and other parameters facilitated development of the General Image Quality Equation (GIQE) that allows predicting values of GSD, edge response, and SNR necessary to detect and identify objects of interest (Leachtenauer et al., 1997). To support systematic studies of multispectral data requirements, the Applications Research Toolbox (ART) has been developed at NASA's Stennis Space Center. The ART software provides the capability to generate simulated multispectral images with predefined properties from data acquired by existing sensors with higher spatial and spectral resolution. Multiple datasets simulated with key data characteristics varied parametrically can be then evaluated by potential end-users for utility in real-world applications.

Spectral band synthesis is a key step in the process of creating a simulated multispectral image from hyperspectral data. In this step, narrow hyperspectral bands are combined into broader multispectral bands. Such an approach has been used quite often, but to the best of our knowledge accuracy of the band synthesis simulations has not been evaluated thus far. Therefore, the main goal of this paper is to provide validation of the spectral band synthesis algorithm used in the ART software. The next section contains a description of the algorithm and an example of its application. Using spectral responses of AVIRIS, Hyperion, ALI, and ETM+, the following section shows how the synthesized spectral bands compare with actual bands, and it presents an evaluation of the simulation accuracy based on results of MODTRAN modeling. In the final sections of the paper, simulated images are compared with data acquired by actual satellite sensors. First, a Landsat 7 ETM+ image is simulated using an AVIRIS hyperspectral data cube. Then, two datasets collected with the Hyperion instrument from the EO-1 satellite are used to simulate multispectral images from the ALI and ETM+ sensors.

2. SPECTRAL BAND SYNTHESIS ALGORITHM

Equations governing the spectral band synthesis process are shown here for completeness of the presentation. Although the band synthesis process has been proposed and applied previously, it is not clear if the applied formulae were the same as in the current work (Anderson et al., 2000). Band synthesis, applying an algorithm that compares more closely to the one presented here, was conducted during a cross-calibration of a satellite multispectral instrument with AVIRIS (Green and Shimada, 1997), as well as in simulations of future sensors (Esposito et al., 1999). In all the methods, each band of a multispectral image is simulated by a weighted sum of the hyperspectral image bands. Differences between the methods are in the ways the weights are determined. In the current approach, calculation of the weights is based on finding the best approximation of a multispectral response by a linear combination of the hyperspectral responses. This method is consistent with the goal of accurately modeling a sensor with a predefined spectral response.

[1] Lockheed Martin Space Operations, Stennis Space Center, Mississippi (sblonski@ssc.nasa.gov)
[2] NASA Earth Science Applications Directorate, Stennis Space Center, Mississippi

Consider a multispectral instrument (MSI) with N_{MSI} bands and a hyperspectral instrument (HSI) with N_{HSI} bands. Spectral response of the ith MSI band R_i^{MSI} is defined at n wavelengths λ_k. Spectral response of the jth HSI band R_j^{HSI} is also known for these wavelengths. The linear combination coefficients c_{ij} are derived by solving in the least-squares sense the following set of band-synthesis equations:

$$R_i^{MSI}(\lambda_k) = \sum_{j=1}^{N_{HSI}} c_{ij} R_j^{HSI}(\lambda_k) \quad \text{for} \quad k = 1,...,n; \;\; i = 1,..., N_{MSI}$$

Spectral responses of existing hyperspectral instruments such as AVIRIS and Hyperion are accurately approximated with Gaussian functions. For the HSI bands with the Gaussian shape and full width at half-maximum Δ_j, the coefficients c_{ij} are used in the following weighted-sum formulae to calculate (for each pixel) spectral radiance of the synthesized multispectral image bands L_i^{MSI} from the hyperspectral radiances L_j^{HSI}:

$$L_i^{MSI} = \frac{\sum_{j=1}^{N_{HSI}} c_{ij} \Delta_j L_j^{HSI}}{\sum_{j=1}^{N_{HSI}} c_{ij} \Delta_j} \quad \text{for} \quad i = 1,..., N_{MSI}$$

An example of the band synthesis is shown in Figure 1 for the case of Landsat 7 ETM+ Band 1 simulation from AVIRIS 1999 data. The figure also illustrates that although the synthesized bands and the actual bands closely overlap, some artifacts such as ripples at band plateaus, shoulders at band edges, and negative values outside bands do occur. Evaluation of effects of those artifacts on simulation results is presented in the following section.

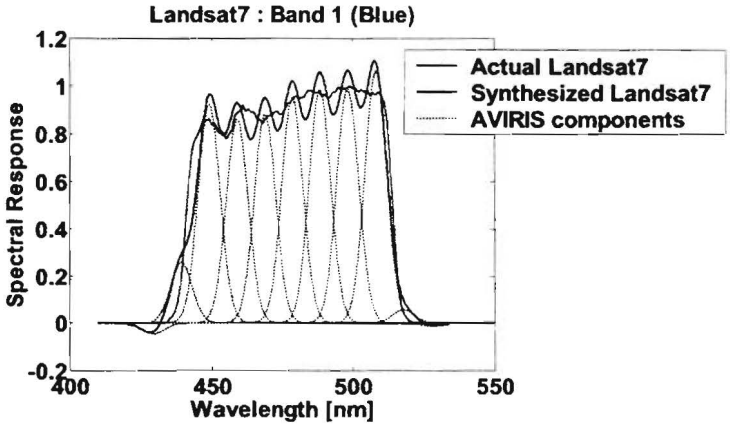

Figure 1. Comparison of actual and simulated spectral response of Landsat 7 ETM+ band 1: hyperspectral components used in the band synthesis are shown as dotted lines.

3. MODTRAN MODELING

To evaluate effects of differences between actual and synthesized spectral bands, extensive atmospheric radiative-transfer modeling was undertaken using the MODTRAN4 software (Berk et al., 1998). The calculations included the correlated-*k* option and the Isaacs approximation for the multiple scattering. About 30,000 MODTRAN calculations were conducted for each sensor: AVIRIS, Hyperion, ALI, and ETM+. The calculations were based on 1,287 surface reflectance spectra selected from the ASTER library, which comprises spectra collected at Johns Hopkins University, the NASA Jet Propulsion Laboratory (JPL), and U.S. Geological Survey (USGS) (Hook, 1999), as well as from the USGS Spectroscopy Lab collection (Clark et al., 1993). The selected spectra were measured mainly for minerals, but vegetation, soils, and man-made materials such as concrete were also included. For each reflectance spectrum, 24 MODTRAN calculations were conducted, i.e., for 6 atmospheric models combined with 4 aerosol conditions. The atmospheric models spanned a wide range of climates and seasons:

- tropical at 30°N on June 22
- tropical at 30°N on Dec. 22
- mid-latitude summer at 45°N on June 22
- mid-latitude winter at 45°N on Dec. 22
- sub-arctic summer at 60°N on June 22
- sub-arctic winter at 60°N on Dec. 22

The aerosol models were diverse as well, using the specified values of the meteorological range parameter (VIS):

- rural, VIS = 23 km
- rural, VIS = 5 km
- urban, VIS = 5 km
- tropospheric, VIS = 50 km

For all the sensors (even AVIRIS), the calculations were performed with the nadir viewing geometry from space with sensor altitude set to 100 km and ground at sea level. Solar illumination was specified by longitude of 0° and acquisition time at 10:00 UTC. To generate in-band mean spectral radiance values, convolution of the calculated atmospheric radiance spectra and the instrument spectral response functions was conducted internally within MODTRAN. The same convolution procedure was applied for the multispectral sensors, ALI and ETM+, and the hyperspectral sensors, AVIRIS and Hyperion. The calculations were based on spectral response functions obtained from existing data on spectral calibration of the instruments. Results of the MODTRAN calculations for the hyperspectral sensors were further processed with the band synthesis algorithm to simulate response of the multispectral sensors. Radiance values generated by the band synthesis were compared with those created directly in the MODTRAN modeling for the same surface reflectance and atmospheric conditions.

Synthesis of Landsat 7 ETM+ band data has been conducted from the AVIRIS and EO-1 Hyperion hyperspectral bands. The Hyperion bands were also used to synthesize the EO-1 ALI band data. Results of the band synthesis for all three cases are shown in Figure 2. In this figure, the graphs comparing the actual and synthesized spectral responses are set against scatter plots created from the MODTRAN generated data. Despite the artifacts occurring in the synthesized spectral responses, almost all the scatter plots display very high correlation between radiance values simulated from hyperspectral data by band synthesis and those generated directly in the MODTRAN modeling. Although the figure shows only data for bands 2 (green) and 4 (NIR), results for the other bands, not shown here due to limited space, are very similar to the best ones presented. The least accurate band synthesis occurs for the ETM+ band 2 simulations from Hyperion data; dispersion of points on the scatter plot suggests the possibility of 10 to 15% radiometric errors. This is in clear contrast to the very accurate simulations of the same ETM+ band from the 1999 AVIRIS data, and it is an illustration of possible effects of spectral aliasing. Although synthesis of the ALI band 4 is more challenging because of its narrow width, the respective scatter plot proves that the simulation is still quite accurate.

4. IMAGES

The AVIRIS image used for the band synthesis experiment presented in this paper was obtained from the JPL archive as a radiometrically calibrated, but not geometrically corrected, image product. The image was acquired from the high-altitude platform (ER-2) over a Maryland area at 15:35 UTC on May 11, 2000. GSD of the image was estimated to be approximately 18 m. A relatively cloud-free area of 592 × 656 pixels was selected from the AVIRIS image for the comparison with the Landsat 7 ETM+ image acquired near coincidentally. The ETM+ image was acquired for the Worldwide Reference System (WRS) path 15 and row 33 at 15:38 UTC on the same day as the AVIRIS image. The image was obtained from the USGS EROS Data Center (EDC) on level 0R and processed in-house to level 1G using the LPGS-lite software with the following parameters: UTM projection, GSD of 30 m, and cubic-convolution resampling. An area of 353 × 372 pixels, having the same extent as the AVIRIS image subset, was selected from the Landsat image.

EO-1 images selected for the presentation were obtained from NASA Goddard Space Flight Center. Both ALI and Hyperion images were only radiometrically corrected (level 1R). The first pair of the images was acquired over an Arizona area (WRS path 35, row 38) at 17:42 UTC on March 23, 2001 (day 82). The second pair was acquired over a New England area (WRS path 12, row 31) at 15:17 UTC on May 9, 2001 (day 129). Respective Landsat 7 ETM+ images were acquired one minute before the EO-1 data. Those Landsat 7 images were obtained from the EDC on level 0R as well, but they were processed only to level 1R using the LPGS-lite software. Areas of overlap between the Hyperion, ALI, and ETM+ images were selected from the images. Due to small GSD differences between the instruments, pixel sizes of the image subsets are slightly different, for example, 197 × 6094 pixels for Hyperion and 201 × 6234 pixels for ALI.

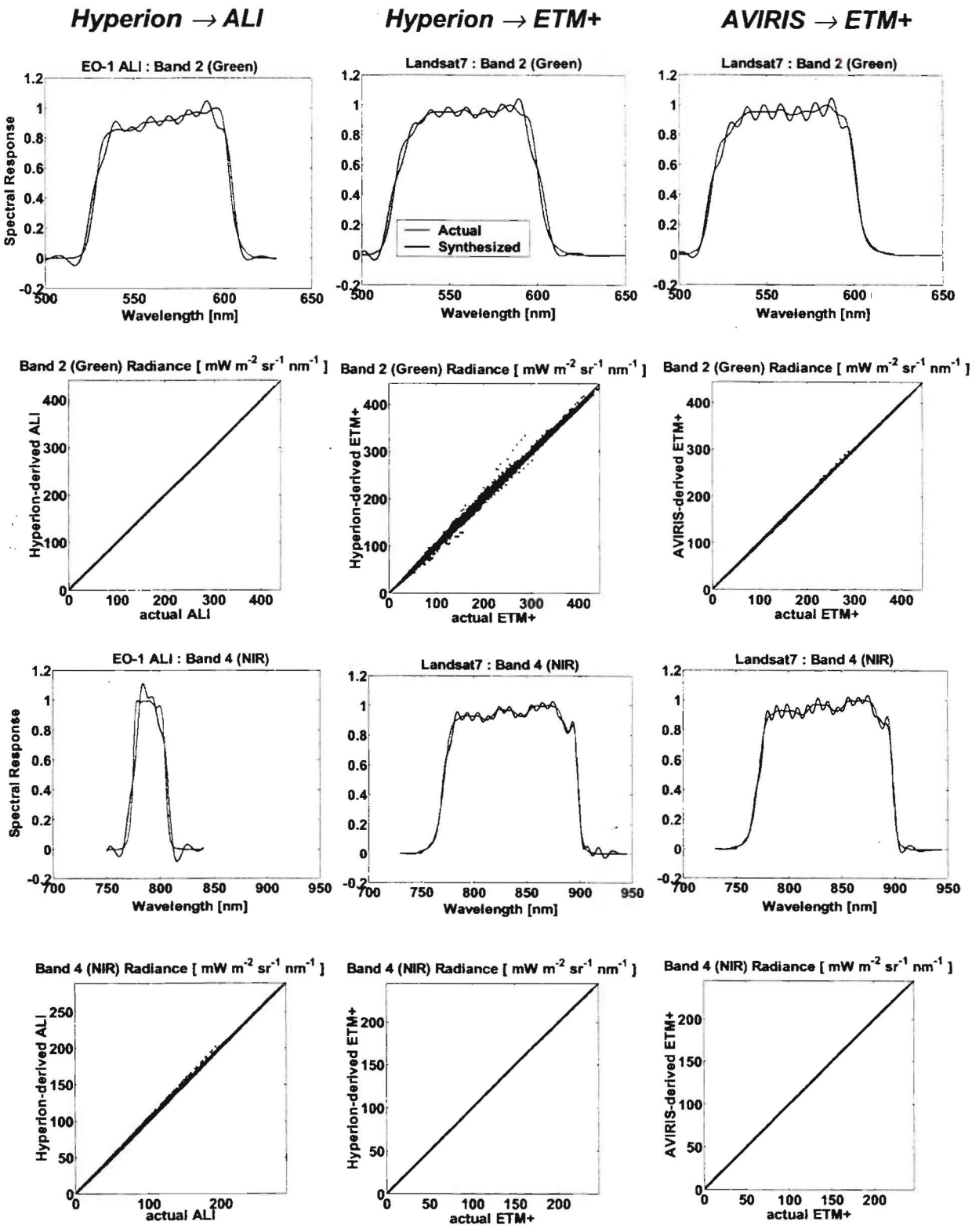

Figure 2. Comparison of spectral band synthesis results and actual spectral responses for band 2 (top row of the upper panel) and band 4 (top row of the lower panel) of the ALI and ETM+ instruments. Scatter plots created from the MODTRAN-generated data (bottom rows of both panels) show moderate effects of the band synthesis artifacts on the simulated images.

5. AVIRIS-BASED ETM+ SIMULATIONS

An image with the Landsat 7 ETM+ bands synthesized from the AVIRIS data is shown in Figure 3 together with the actual ETM+ image. Because of the GSD difference, only histograms of the images are compared in Figure 4. Despite the GSD difference, the histograms of the actual and simulated data still agree. Not only are the shapes of the histograms generally the same, but also the positions of the peaks closely match.

Figure 3. True color Landsat 7 ETM+ image of the Laurel, Maryland, area (right) and the image synthesized from the AVIRIS data (left). The suburban area contains not only numerous roads, but also vegetated spaces and a noticeable water surface, of which a dark signature is apparent in histograms for the infrared bands.

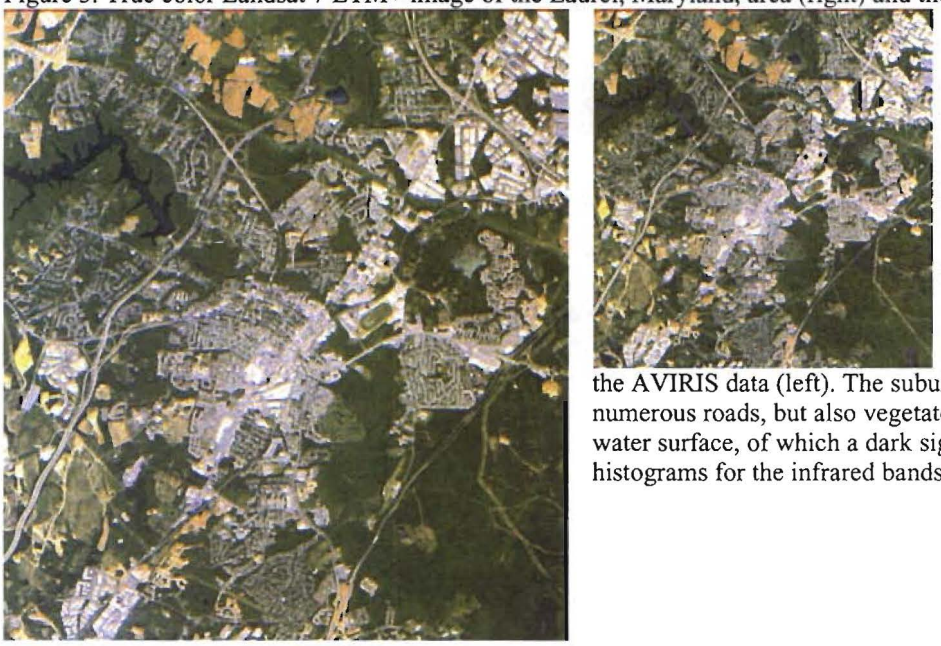

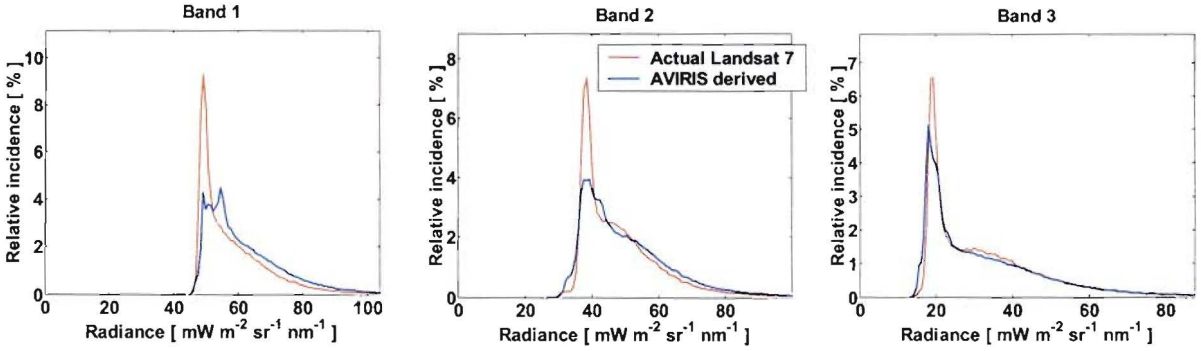

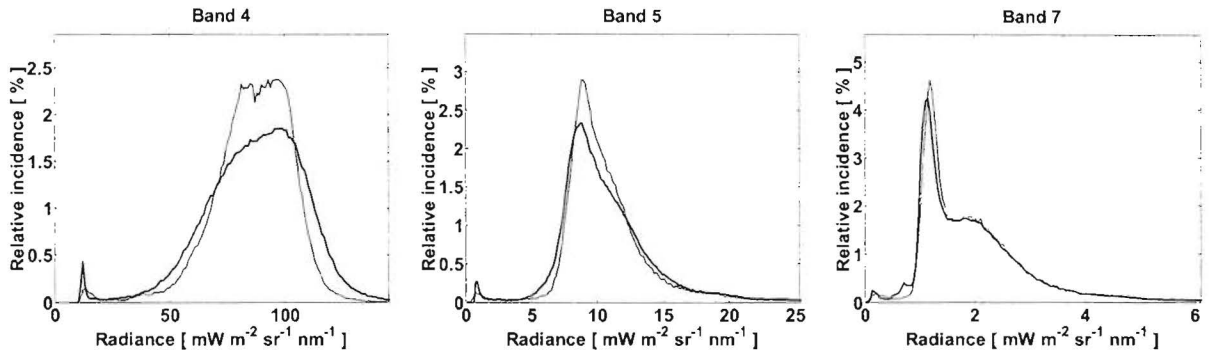

Figure 4. Histograms of radiance values for the actual Landsat 7 ETM+ image and for the image simulated by spectral band synthesis from the AVIRIS hyperspectral data.

6. HYPERION-BASED ALI AND ETM+ SIMULATIONS

EO-1 Hyperion data from Arizona and New England were used to simulate both Landsat 7 ETM+ and EO-1 ALI images. Examples of the actual and simulated images are shown in Figure 5 (New England) and Figure 6 (Arizona). The VNIR images demonstrate very good qualitative agreement between the actual and simulated data. Radiance histograms presented in Figure 7 allow for quantitative comparisons of the images. The best agreement is achieved for the simulations of bands 2 and 3 of the ALI images. Only small radiometric differences occur for the other VNIR bands. While actual ETM+ data in the VNIR bands differ a little more from the Hyperion-derived values than the ALI data, shapes of the histograms still match very closely. Hyperion-derived data diverges more significantly from the original ALI and ETM+ images in the NIR band 4, but the difference is still quite moderate. Decisively, large differences occur solely for the SWIR bands 5 and 7. Although the relative differences are close to 20-30%, the huge discrepancy observed for band 5 of the ALI image from Arizona seems to be a result of some accidental error during ground processing of that image.

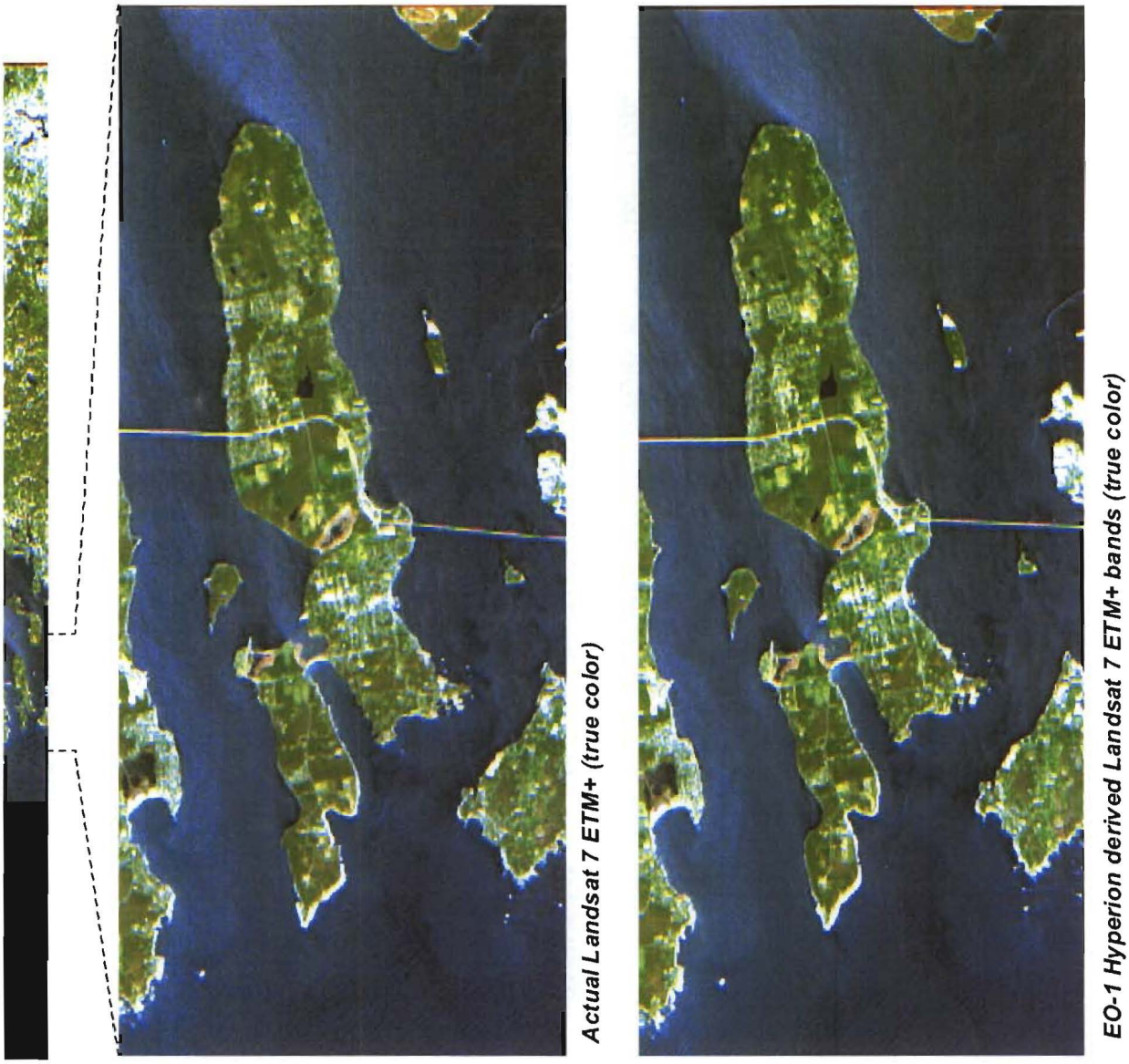

Figure 5. True color Landsat 7 ETM+ image of the New England swath (left), full-scale subsets of the ETM+ image (center) and its simulation from the EO-1 Hyperion data (right).

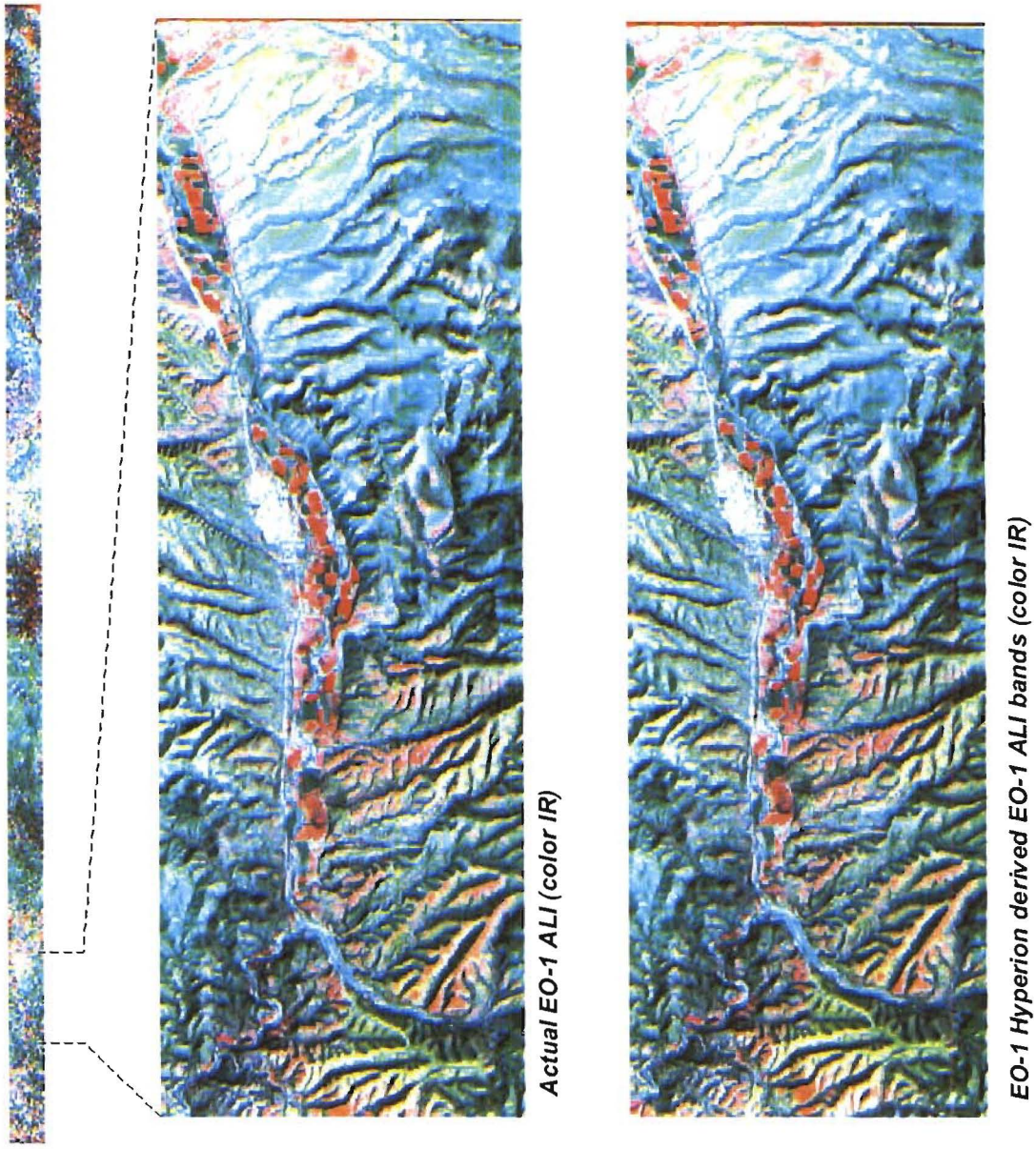

Figure 6. Color IR EO-1 ALI image of the Arizona swath (left), full-scale subsets of the ALI image (center) and its simulation from the EO-1 Hyperion data (right).

7. DISCUSSION

Overlap area of the New England images stretches from Boston, Massachusetts, to Rhode Island Sound in the Atlantic Ocean (see Figure 5). The coverage includes many urban areas, abundant vegetation (both forests and agriculture), and an extensive seawater surface. Overlap areas of the Arizona images cover mainly desert with mountains (minerals) and sparse vegetation (see Figure 6). Therefore, the two images represent quite different environments and allow for the band synthesis algorithm testing with various spectral features. Surface constituents of the Arizona images are similar to the ones used in the MODTRAN modeling. Based on the MODTRAN results presented above, a very good agreement between the actual and simulated data has been expected for the Arizona images. Although such an agreement occurs only for some spectral bands, these results and those from the AVIRIS-based simulations fully validate the presented band synthesis method.

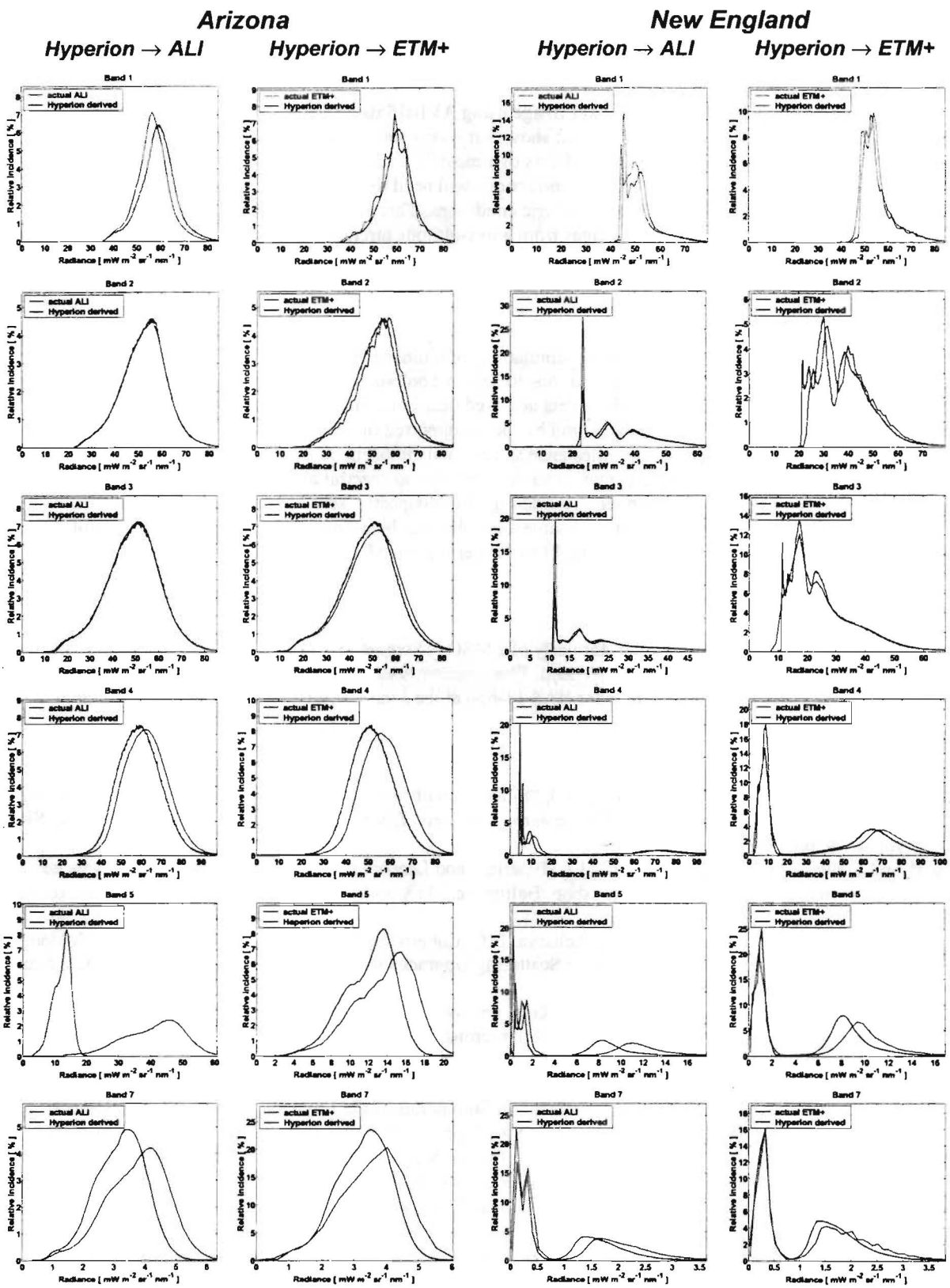

Figure 7. Histograms of radiance values for the actual EO-1 ALI and Landsat 7 ETM+ image as well as for the respective images simulated by spectral band synthesis from the Hyperion hyperspectral data.

Differences observed for the other spectral bands do not contradict the band synthesis method, but only suggest that radiometric calibration of the sensors needs to be improved. Similar results have been reported by others (Jarecke et al., 2001; Barry and Ong, 2001).

The simulations of the Landsat 7 ETM+ image using AVIRIS data acquired near-coincidently (within minutes of each other) from a high-altitude aircraft show that a very satisfactory radiometric agreement can be achieved even without applying corrections for effects of atmospheric radiative transfer processes occurring above the airplane altitude. However, in most cases the corrections will need to be applied to account for differences in viewing geometry, solar illumination, and atmospheric conditions. This becomes especially important when data from a hyperspectral instrument acquiring images from a low-altitude aircraft are to be used in modeling of satellite multispectral sensors.

8. CONCLUSIONS

A spectral band synthesis algorithm for simulations of multispectral images from hyperspectral data has been formulated and implemented in the Applications Research Toolbox software package. High correlation achieved between the simulated images and the data acquired near-coincidentally by actual remote sensing instruments has validated the algorithm. Validation has been supported by results of MODTRAN modeling conducted with an extensive set of surface reflectance spectra and atmospheric conditions. The modeling has also shown that band synthesis may be less accurate, in some cases, due to spectral aliasing. Nevertheless, the band synthesis algorithm can be effectively applied in modeling of multispectral sensors in the remote sensing applications research and development area. The same algorithm can be used as well for cross-calibration of hyperspectral and multispectral instruments (e.g., EO-1 Hyperion and ALI vs. Landsat 7 ETM+).

9. ACKNOWLEDGEMENTS

Discussions with Amanda Warner, formerly of LMSO -- Stennis Programs, and her help with the selection of AVIRIS and EO-1 images are greatly appreciated. This research was supported by the NASA Earth Science Applications Directorate under contract number NAS 13-650 at the John C. Stennis Space Center, Mississippi.

10. REFERENCES

Anderson, D.S., B. Keaffaber, and R. Wasky, 2000, "Simulation of MSI Imagery from HIS Data," in *Algorithms for Multispectral, Hyperspectral, and Ultraspectral Imagery VI*, S.S. Shen and M.R. Descour, eds., Proc. SPIE, vol. 4049, pp. 76-81.

Barry, P. and L. Ong, 2001, "Comparison of ALI, Hyperion, and Landsat Data," EO-1 Hyperion and Advanced Land Imager (ALI) Data Users Workshop, Baltimore, Maryland, November 28-29, 2001 (available on-line at http://eo1.gsfc.nasa.gov/)

Berk, A., L.S. Bernstein, G.P. Anderson, P.K. Acharya, D.C. Robertson, J.H. Chetwynd, and S.M. Adler-Golden, 1998, "MODTRAN Cloud and Multiple Scattering Upgrades with Application to AVIRIS," Remote Sens. Environ., vol. 65, pp. 367-375.

Clark, R.N., G.A. Swayze, A.J. Gallagher, T.V.V. King, and W.M. Calvin, 1993, "The U. S. Geological Survey, Digital Spectral Library: Version 1: 0.2 to 3.0 microns," U.S. Geological Survey Open File Report 93-592, 1340 pages.

Esposito, E.S.C., T. Krug, and R.O. Green, 1999, "Simulation of the Spectral Bands of the CCD and WFI Cameras of the CBERS Satellite Using AVIRIS Data," in Summaries of the Eight JPL Airborne Earth Science Workshop, R.O. Green, ed., JPL Publication 99-17, pp. 93-102.

Green, R.O. and M. Shimada, 1997, "On-Orbit Calibration of a Multispectral Satellite Sensor Using a High Altitude Airborne Imaging Spectrometer," Adv. Space Res., vol. 19, no. 9, pp. 1387-1398.

Hook, S.J., 1999, "ASTER Spectral Library," Jet Propulsion Laboratory, California Institute of Technology, CD-ROM.

Jarecke, P.J., P. Barry, J. Pearlman, and B.L. Markham, 2001, "Aggregation of Hyperion Hyperspectral Spectral Bands into Landsat-7 ETM+ Spectral Bands," in *Imaging Spectrometry VII*, M.R. Descour and S.S. Shen, eds., Proc. SPIE, vol. 4480, pp. 259-263.

Leachtenauer, J.C., W. Malila, J. Irvine, L. Colburn, and N. Salvaggio, 1997, "General Image-Quality Equation: GIQE," Appl. Opt., vol. 36, no. 32, pp. 8322-8328.

Surface Reflectance Calibration of Terrestrial Imaging Spectroscopy Data: a Tutorial Using AVIRIS

Roger N. Clark, Gregg A. Swayze, K. Eric Livo, Raymond F. Kokaly,
Trude V.V. King, J. Brad Dalton, J. Sam Vance, Barnaby W. Rockwell,
Todd Hoefen, and Robert R. McDougal

U.S. Geological Survey, Mail Stop 964, Box 25046 Federal Center, Lakewood, Colorado 80225

This tutorial is designed to help others understand how we calibrate terrestrial imaging spectroscopy data. This paper, along with the full resolution images can be found at: http://speclab.cr.usgs.gov/PAPERS.calibration.tutorial

1. Introduction

Remote sensing data are routinely used to characterize vegetation, minerals and other materials on the surface of the Earth. The demands for better characterizations have increased as the technology of remote sensing, the complexity of biophysical models, and the sophistication of scientific studies and land management applications have advanced. As a result, there is a need for accurate correction of atmospheric effects and conversion from radiation measured at the sensor to reflectance arising solely from the imaged surface materials. Sensors known as imaging spectrometers have the capability of resolving the intensity of atmospheric absorption features and the shapes of scattering curves and, thus, allow for a better correction of remotely sensed spectra to values of reflectance.

Calibrating imaging spectroscopy data to surface reflectance is an integral part of the data analysis process, and is vital if accurate results are to be obtained. The identification and mapping of materials and material properties is best accomplished by deriving the fundamental properties of the surface, its reflectance, while removing the interfering effects of atmospheric absorption and scattering, the solar spectrum, and instrumental biases. Calibration to surface reflectance is inherently simple in concept, yet it is very complex in practice because atmospheric radiative transfer models and the solar spectrum have not been characterized with sufficient accuracy to correct the data to the precision of some currently available instruments, such as the NASA/JPL Airborne Visible and Infra-Red Imaging Spectrometer (AVIRIS, see Green *et al.*, 1998).

The objectives of calibrating remote sensing data are to remove the effects of the atmosphere (scattering and absorption) and to convert from radiance values received at the sensor to reflectance values of the land surface. Figure 1a shows a sample radiance spectrum from an imaging spectrometer. The overall level and shape of this radiance spectrum is strongly a function of the solar illumination and absorption by atmospheric gases. The advantages offered by calibrated surface reflectance spectra (e.g., Figure 1b) compared to uncorrected radiance data include: 1) the shapes of the calibrated spectra are principally influenced by the chemical and physical properties of surface materials, 2) the calibrated remotely-sensed spectra can be compared with field and laboratory spectra of known materials, and 3) the calibrated data may be analyzed using spectroscopic methods that isolate absorption features and relate them to chemical bonds and physical properties of materials. Thus, greater confidence may be placed in the maps of derived from calibrated reflectance data, in which errors may be viewed to arise from problems in interpretation rather than incorrect input data.

The consequences of poor surface reflectance calibration can be costly. For example, an artifact in the calibration could be seen as a dip in the derived surface reflectance spectra, and that dip might be interpreted as representing a material that does not really exist at that location. Such an error could have serious implications, for example, if the misidentified material has hazardous properties indicating a need for environmental cleanup, or if it indicated a new mineral deposit discovery. Investigating such a false lead could result in wasted time and money.

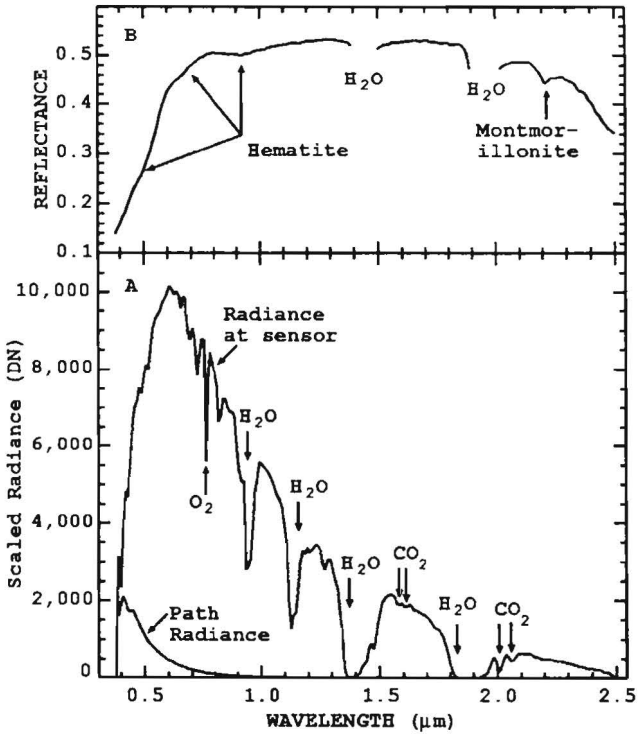

Figure 1. A typical radiance spectrum of a non-vegetated area (Figure 1a) is strongly influenced by the solar function and absorption features caused by atmospheric gases. After calibration to surface reflectance, the spectrum (Figure 1b) reveals the absorption feature(s) caused by minerals on the surface. Subsequently, lab spectra of minerals can be examined to identify the mineral(s) causing the absorption feature(s), in this case hematite and montmorillonite. The water features in the radiance spectrum in (A) is due to gaseous atmospheric water, while that in the surface reflectance in (B) is due to liquid water in the soil. The gaps in (B) are where the Earth's atmosphere is too opaque to derive surface reflectance in from the radiance spectrum in (A).

The following tutorial documents the methods used by scientists at the USGS Spectroscopy Lab to provide the best calibration given the technology available. This tutorial is based on methods and experience developed from calibrating dozens of AVIRIS data sets. While the discussion here is focused on the calibration of AVIRIS data, the concepts apply to other sensors as well. Because AVIRIS data are delivered to the investigator calibrated to radiance at the sensor, instrumental biases are already removed and will not be discussed in this tutorial.

2. Review of Calibration Approaches

Many approaches have been developed for atmospheric correction and calibration to surface reflectance of imaging spectroscopy data. These approaches may be grouped into four broad categories: scene-derived corrections, radiative transfer models, ground-calibration methods, and hybrid radiative-transfer-ground-calibration procedures.

The appeal of the scene-derived and modeling approaches is the potential ability to atmospherically-correct remote sensing data without the dependence on external information or measurements. The Internal Average Reflectance (IAR) approach of Kruse (1987) uses the mean radiance of all the pixels in the image as a correction factor. The individual radiance values in each pixel are divided by this mean radiance to estimate reflectance. The flat field correction method (Roberts *et al.*, 1986, and Carrere and Abrams, 1988) assumes that there is an area in the scene that is spectrally neutral (no variation in reflectance with wavelength). The average radiance of this "flat field" may then be used as an estimate of irradiance. As with IAR, this average radiance is used as a correction factor to convert the radiance in each pixel to reflectance. While essentially independent of external information or measurements, these approaches rely on assumptions about the surface materials in the scene which are rarely encountered and, thus, result in apparent reflectances which show deviations from spectra of comparable materials measured in the field or laboratory (Clark and King, 1987, and Kruse, 1987).

The calibration of remote sensing data using physics-based radiative transfer models has been the subject of vigorous research efforts. Theoretically, models may be developed which describe the radiative transfer of sunlight in its physical interaction with the gases and particles in the atmosphere, its interaction with the surface, and its transmission along a different path upward through the atmosphere to the sensor (e.g., Gao *et al.*, 1993, Leprieur *et al.*, 1995, Zagolski and Gastellu-Etchegorry, 1995, Adler-Golden *et al.*, 1999, Schlapfer *et al.*, 2000, and Qu *et al.*, 2000). These models describe the solar irradiance function, the absorption and scattering processes of atmospheric gases, and the reflection from surface materials, all

as a function of the wavelength of electromagnetic radiation and the directional angles of the sun and sensor with respect to pixels of remote sensing data as they are located on the Earth's surface. The full solution of the equations which describe the physics of this radiative transfer problem are complex and, thus, numerical models of radiative transfer use simplifying assumptions to achieve results in reasonable computation times.

Although theoretically well-described, the methods of radiative transfer calibration produce apparent surface reflectance values which show residual atmospheric absorptions and scattering effects. These residual errors may affect the identification, characterization, and/or mapping of surface materials. Indeed an examination of the results of radiative transfer models show errors in the calculated reflectance (see Clark *et al.*, 1993 and 1995). These errors arise from inadequate definition of the solar irradiance function, variations in the source illumination, and simplified assumptions in the physics that describe absorption by atmospheric gases. While the models have been steadily improving with time, they are not yet at the level where artifacts are smaller than sensor noise.

The use of field and/or laboratory measurement of reflectance from surfaces and materials within an image of remote sensing data represents another approach to atmospheric correction and calibration. The need for such measurements to be made during a field survey of the study area places demands on the conduct of a remote sensing study. The field measurements require the availability of an appropriate field spectrometer and a field crew to use the instrument to measure an area of ground within the image at the time that the remote sensor passes overhead, or, at least, at a time close to the overpass. The empirical line calibration (Conel *et al.*, 1987) was applied to an early imaging spectrometer, the Airborne Imaging Spectrometer (AIS). This approach uses field measurements of two or more areas within an image in order to correct the radiance data using a linear equation. The average field measurements of reflectance for the calibration areas are used in a linear relationship with the corresponding average radiance values over the calibration areas in order to derive additive and multiplicative correction factors. Conel *et al.* (1987) describe the application of the procedure using calibration areas of differing albedo, at least one bright target and one darker target.

A similar approach, but using only a single calibration site, described by Clark *et al.* (1988, 1993, and 1995) has been applied to Airborne Visible/InfraRed Imaging Spectrometer (AVIRIS) data over a wide range of study sites. This approach uses both an additive correction factor (an estimate of path radiance) and a multiplicative correction factor derived from the ground measurements of reflectance of the single calibration site. These empirical approaches based on field measurements result in well-calibrated surface reflectance values near the calibration sites. The drawbacks of these methods include the increase in atmospheric residual absorptions for pixels remote from the calibration site and for pixels with different path lengths through the atmosphere as caused by a changing scan angle of the sensor.

This paper describes a hybrid approach that uses ground measurements and radiative transfer models. First described by Clark *et al.*(1993 and 1995), this method uses a combination of the ATmosphere REMoval Program (ATREM; CSES, 1997) and field spectral measurements of a single ground calibration site. The use of the ATREM model allows better atmospheric correction at elevations that are different from the calibration site, while the ground calibration removes the residual errors common with most radiative transfer approaches. We have termed this method "radiative-transfer-ground-calibration (RTGC)." In a comparison of several methods, the use of field measurements in conjunction with radiative transfer models has been found to give the best calibration results for imaging spectrometers by Clark *et al.* (1993 and 1995).

3. Method Summary

Our calibration process involves two steps. In the first step, the flight data are corrected using a radiative transfer algorithm that examines the imaging spectroscopy data pixel by pixel, adjusting atmospheric absorptions in the model and removing the absorptions from the data. This step also includes characterizing and removing the effects of Rayleigh and aerosol scattering in the atmosphere (called "path radiance") and a correction for the solar spectral response relative to wavelength. However, the resulting surface-reflectance-corrected spectra have residual artifacts due to imperfect radiative transfer models,

and the imperfect knowledge of the detailed spectral response of the sun. A second step is necessary to remove these artifacts.

The second step requires *in situ* spectral characterization of an area that is also measured by the sensor, *i.e.* a ground calibration site. The reflectance of a ground calibration site may be characterized using a field-portable spectrometer and/or the careful collection of samples of the materials covering the surface of the site and their subsequent measurement with a laboratory spectrometer. A comparison of the field or lab spectral measurements with the corresponding spectra from the imaging spectroscopy flight data may show differences which indicate that additional corrections are necessary. On the basis of this comparison, a set of multipliers (a multiplication factor for each spectral channel) can be derived. When the correction is applied to the data, the resulting spectra are similar in quality to laboratory reflectance spectra. Additional areas in the data set can be used to verify and further refine the accuracy of the multipliers and to derive any residual path radiance correction.

Achieving a high quality calibration is difficult. It requires careful planning, multiple visits to the field, time to reduce field and laboratory data, examination of flight data and comparison to the field data, and verification of the results. Our experience has shown that the high signal-to-noise of recent AVIRIS data (since 1995) typically requires 1 to 2 person months per study site to achieve a quality calibration. Table 1 shows a summary of our calibration steps, and the following presentation shows how a quality calibration can be achieved.

Table 1. Summary of Calibration Steps

Planning for calibration. Include at least one calibration site as part your flight data set.
Near the time of data acquisition, characterize the calibration site using field portable spectrometers. Collect samples and measure their spectra in the laboratory to back up the field data. Numerically convolve field and lab spectrometer data to the bandpass and sampling of the flight data.
After data receipt, remove solar and atmospheric response using a radiative transfer algorithm.
Derive residual path radiance correction and subtract it from the flight data. Trick: Use vegetation in shaded areas to determine residual path radiance issues.
Derive a set of multipliers as a function of wavelength to correct residuals from the radiative transfer algorithm.
Apply the offset correction and multipliers to the flight data set.
Examine spectra and large averages of spectra from the flight data set for artifacts. If artifacts are discovered, trace their origin and repeat the above analyses.

4. Planning for Calibration

An important preliminary step, before the calibration process is even started, is in planning for the acquisition of the imaging spectroscopy data. The planning should be conducted with these important considerations in mind in order to select good calibration sites.

1) It is important to visit the study area *before* establishing the exact location of the flight lines to ensure inclusion of at least one suitable calibration site.

2) If at all possible, the region of data coverage should include some spatially uniform, "spectrally bland" area. A spectrally bland area is one that does not have strong absorption features in the wavelength region to be measured.

3) High reflectance level is required. A high reflectance gives the best sensitivity to multiplicative corrections. A target with low reflectance will be more sensitive to additive offsets such as atmospheric scattering (which will be discussed later).

4) The site should be large enough so that many sensor pixels cover the site; thus, many spectra can be averaged to minimize noise in the flight data calibration. Regardless of the number of pixels averaged, some noise will remain in the average spectrum. The larger the calibration site, the more pixels that can be averaged to reduce that noise level. The noise decreases as the square root of the number of pixels averaged. So, for example, averaging 16 pixels results in a fixed pattern residual noise of 1/4th of the noise in any one pixel. A 100 pixel average reduces the pattern to 1/10th of the pixel noise. The high signal to noise of AVIRIS data since 1995 requires at least 25 pixels in the average for good corrections, and many more is certainly better. This many pixels implies large, spatially uniform calibration sites for accurate AVIRIS calibration.

5) The site should be accessible to a ground crew.

6) The site should be at a similar elevation to the prime study area.

The considerations of high reflectance and large area for the calibration site affect the overall signal-to-noise of the spectra that will be used to derive a set of multipliers, one for each spectral channel, to correct the flight data to surface reflectance (examples will be shown below). This set of multipliers will be applied to each pixel in the imaging spectroscopy data set. A residual noise pattern in the calibration site reflectance spectrum will propagate into the set of multipliers which are derived from the field data. Because the same set of multipliers are applied to the spectrum for each pixel, the noise pattern will impart a fixed residual pattern into the entire final data set. Thus, care must be taken to minimize noise, and that can be best achieved by averaging numerous measurements.

We have used playas, salt flats, dam faces, dirt or gravel parking lots, rock outcrops, sand beaches, building construction sites, rock talus slopes, plowed fields (free of vegetation), building roofs, and dry grass fields as calibration sites, with varying degrees of success (the list is in approximate order of best to worst in our experience). Figures 2a-n show some of these sites.

5. Atmospheric Correction Using A Radiative Transfer Model

Because imaging spectroscopy data sets are typically large, organization for easy use is an important preliminary step. We divide the data into manageable chunks to fit on our removable optical media. For AVIRIS studies, we divide the data into 1024- line Vicar-format data cubes which are 282 megabytes in size (Appendix A).

We assume in this report that the flight data are delivered to the user already calibrated to radiance (e.g. Figure 3). If that is not the case, the data must be corrected to radiance before radiative transfer calculations are performed.

The next step in calibrating imaging spectroscopy data is to remove the solar spectral response, atmospheric absorptions and atmospheric scattering using a radiative transfer program. Initially, the calibration is applied to the 1024-line data cubes that contain the ground calibration site(s). Currently we are using ATREM (Gao *et al.*. 1990, 1992, 1993) from the University of Colorado, with custom modifications to read Vicar headers, to perform this radiative transfer calibration step. ATREM estimates the average O_2, CO_2, ozone and others gases in the scene, but does not adjust the amounts on a per-pixel basis. Thus as the atmospheric path length changes with elevation, residual features caused by these gases will be observed in the ATREM-corrected data.

Once the data are radiative transfer corrected, spectra from the AVIRIS data set are extracted from pixels over the ground calibration site covering the same area as was measured with the field spectrometer (e.g. Figure 4). These ATREM-extracted pixels are averaged (Figure 5) and compared to the average field spectrum (Figure 6). Because the solar irradiance function has not been modeled with sufficient accuracy to correct imaging spectroscopy data to surface reflectance, and because the radiative transfer corrections are imperfect, the ATREM-corrected data contain significant artifacts (Figure 6). The magnitude of residual features caused by imperfect water corrections by ATREM depends on the wavelengths selected to characterize the 0.95 and 1.15 micron water absorptions in the ATREM user command file. We use a different set of wavelengths in our ATREM corrections which give a more consistent correction than the wavelengths in the command file distributed by the University of Colorado.

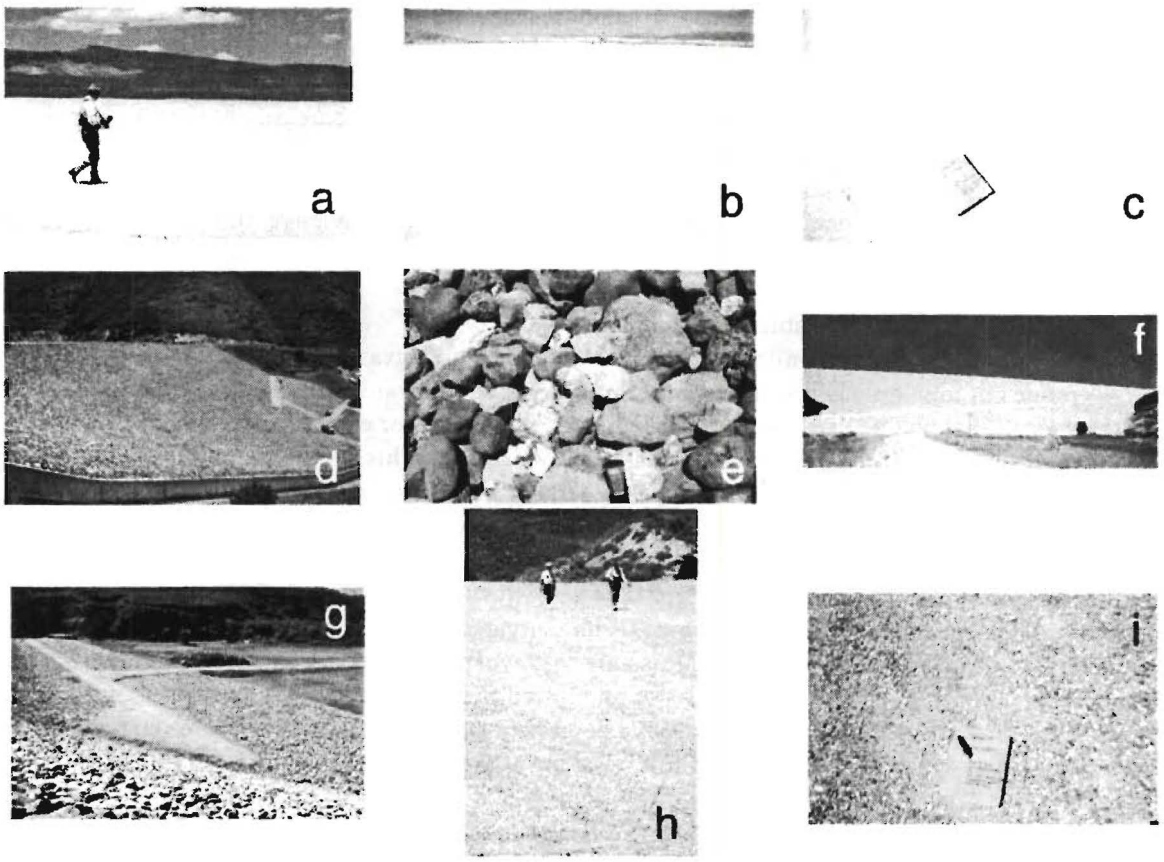

Figure 2a - Cuprite Calibration. Stonewall Playa, located southeast of the main hydrothermal centers at Cuprite, Nevada, is very large and uniform and provides an excellent calibration site, but must be characterized well because of weak Fe^{3+} absorptions in the visible and a weak montmorillonite absorption at 2.2-microns. **2b - Salt Flat Calibration A**. The shores of the Great Salt Lake provide for excellent calibration sites. This area, located next to Old Saltair west of Salt Lake City, Utah, is very large and uniform. High reflectance and no significant absorptions make this one of the best calibration sites we have encountered. Eric Livo is in the distance with the field spectrometer, walking a grid over the calibration area and obtaining hundreds of spectra. **2c - Salt Flat Calibration A**. Close up of the Old Saltair salt flat. The surface is so uniform that field sampling and measurement of the samples on a laboratory spectrometer should be able to give a good representation of the surface. Contrast this surface to the Deer Creek dam face. **2d - Deer Creek Dam Calibration A.** The Deer Creek dam, southeast of Salt Lake City, Utah, provides an excellent calibration site, if it can be characterized well. **2e - Deer Creek Dam Calibration B.** Close up of the Deer-Creek dam face. One can see large variations from rock to rock, making it difficult to collect rocks in the correct proportions for measurement on a laboratory spectrometer. A field spectrometer is required to accurately characterize the site. **2f - Jordanelle Dam Calibration A.** The Jordanelle dam face, located east of Salt Lake City, Utah, is much larger and appeared to be more uniform than the Deer Creek dam face. **2g - Jordanelle Dam Calibration B**. The toe of the Jordanelle dam appears excellent as a calibration site. The rocks are bright. The area is just barely large enough for AVIRIS coverage, giving only about 10 pixels on the toe. Despite appearances in the field, and with the field spectrometer, it turned out that the reflectance levels from spectrum to spectrum and weak absorptions in the field spectra were quite variable. Also, the spectra of the toe and dam face were slightly different. Thus, the Deer Creek dam face turned out to be a better calibration site than the Jordanelle dam face. **2h - Piute Parking Lot Calibration A.** An example of a gravel parking lot calibration site: the Piute reservoir boat launch parking lot in central Utah. Ray Kokaly (left) walks with Eric Livo (right, with the field spectrometer) to provide the Spectralon reflectance standard for re-calibration as soon as the spectrometer calibration begins to drift. **2i - Piute Parking Lot Calibration B.** Close up of the Piute Reservoir boat launch parking lot in central Utah. The average spectrum (in Figure 3) shows the mixture of muscovite in the rocks and the clay montmorillonite in the dirt.

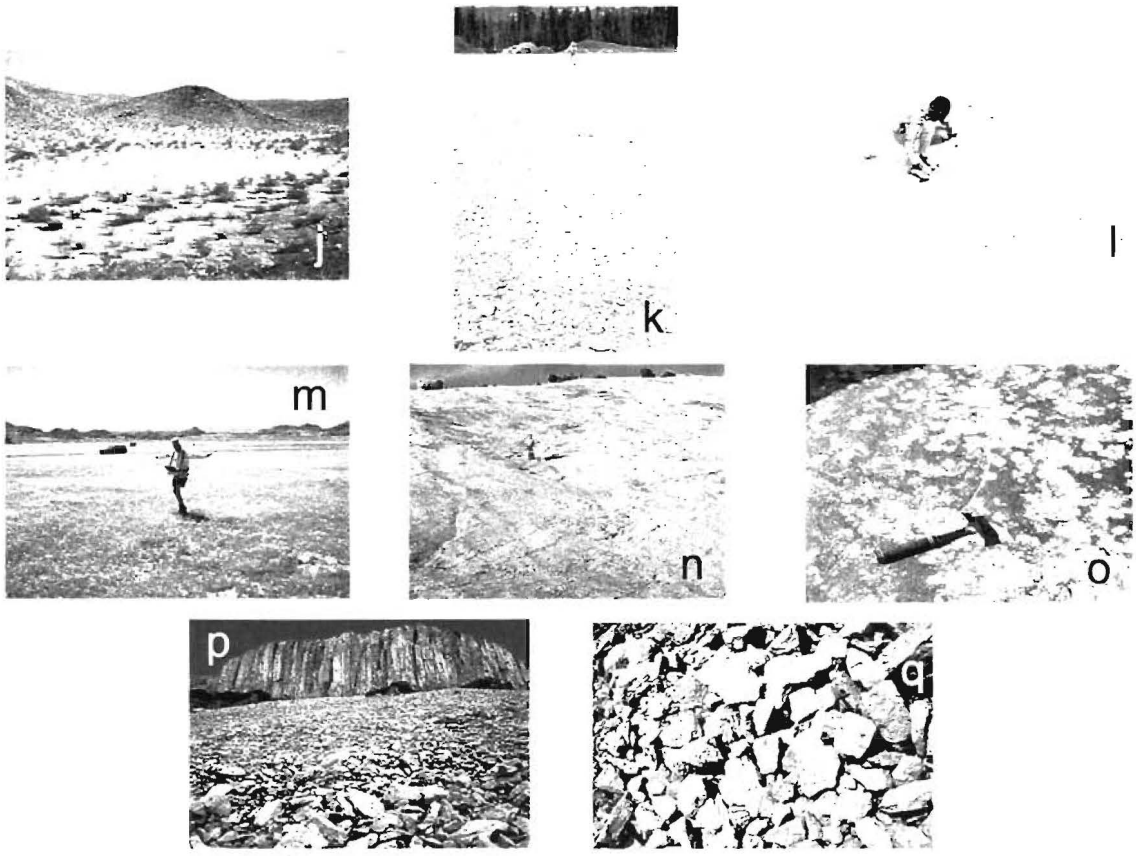

Figure 2j - Joshua Tree Calibration. This small playa was the most vegetation-free area we found to calibrate the 1995 AVIRIS data. **2k - Yellowstone Calibration.** At Yellowstone National Park we used a road construction gravel staging lot for calibration. Ray Kokaly is in the distance with the field spectrometer. While the area is large and uniform, the source rock for the road construction periodically changes, and thus the site must be re-measured near the time of each flight. **2l - Arches Calibration A.** The calibration for the 1995 AVIRIS data acquisition at Arches National Park was particularly well planned. This image shows Gregg Swayze collecting a sample of the Yellow Cat Flat playa, just outside of the Park boundary, on April 27, 1995. The site was well characterized with our field spectrometer. The flight was tentatively planned for May to July. **2m - Arches Calibration B.** On June, 19, 1995, the day of the flight, we arrived at the Yellow Cat Flat playa and found that in the previous month and a half, weeds had grown all over the playa, rendering it unusable as a calibration site. Nearby was the cheatgrass field shown here. While the field was uniform enough to work as a calibration site, cheatgrass (see Figure 3) has strong absorption features. If the site was not well characterized, residual cheatgrass features would appear in all the calibrated AVIRIS data. Because of this potential difficulty, additional calibration sites were characterized. Gregg Swayze is shown operating the field spectrometer. **2n - Arches Calibration C.** The calibration site used for the Arches 1995 data was this large outcrop of Moab Tongue Formation in Arches National Park just north of the Wolf Ranch parking lot and along the Delicate Arch trail (shown). **2o.** Closeup of the rock in Figure 2n. **2p.** Site used for AVIRIS animas Colorado calibration. The rocks are andesitic and spectrally bland, meaning they have few spectral features. **2q**. Closeup of the rocks in Figure 2p. While the rocks show variability on a small scale, on the large scale of many AVIRIS pixels, the site is relatively uniform.

Figure 3. A typical AVIRIS radiance spectrum. The general shape, including the peak near 0.5 microns and the overall decrease toward 2.5 microns, is due to the solar spectrum. Major atmospheric water absorptions occur at 0.95, 1.15, 1.4 and 1.9 microns. Oxygen absorption occurs at 0.76 micron, and CO_2 at 2.0, 2.08, and the weak doublet near 1.6 microns. The 1.9 to 2.5 micron region is scaled a factor of 2 higher relative to the data at shorter wavelengths to better show the details. Sixteen-bit AVIRIS data are distributed with this scale factor applied to avoid data number (DN) quantization errors.

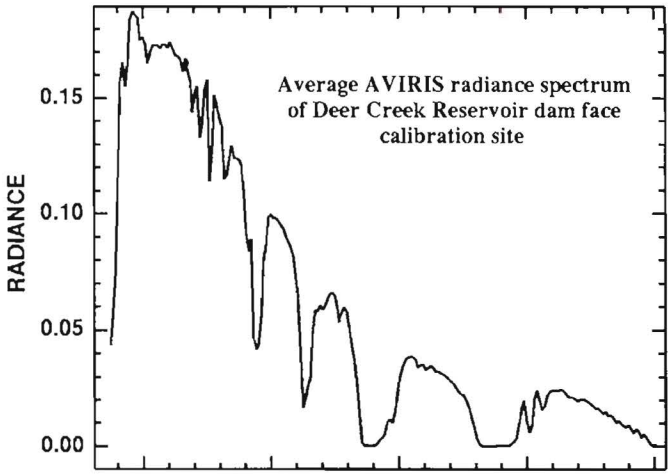

Figure 4. The AVIRIS pixels sampled to characterize the Deer Creek dam calibration site for comparison with the ground field spectra.

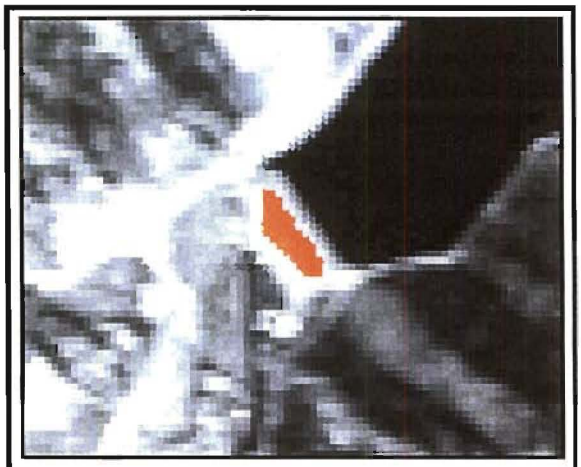

Deer Creek Reservoir dam, Utah

Red area indicates AVIRIS pixels selected and averaged to characterize calibration site

AVIRIS scene f980805t01p02_r02_s01
Image acquired August 5, 1998

Note in Figure 6 the difference in reflectance level between the field and the ATREM spectra. Because the dam face consists of large boulders, shadowing plays a significant role. If the field spectrum was obtained under lighting conditions different from that of the AVIRIS flight, the levels could be different. In the case shown in Figure 6, however, the levels match closely near 0.8 to 1.1 microns, but differ more beyond 1.4 microns. This is due to some calibration difference with the AVIRIS and/or the solar spectrum used in the ATREM software. For the August 1998 Utah AVIRIS flight, we observed similar discrepancies at all our calibration sites, including those such as the Old Salt Air salt flat where shadowing is negligible. However, the ground calibration step removes these discrepancies.

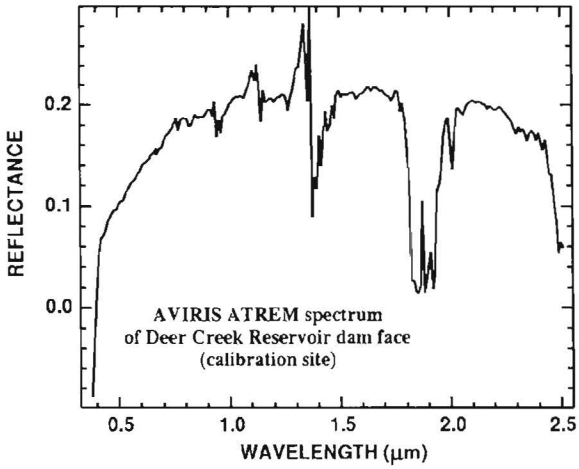

Figure 5. The ATREM-corrected spectrum sampled from the area shown in Figure 4. While ATREM corrects the data to approximate surface reflectance, there are too many artifacts for detailed surface material identifications and mapping. Note the reflectance is negative in the UV (<0.4 micron). ATREM overcorrects for the path radiance (described below).

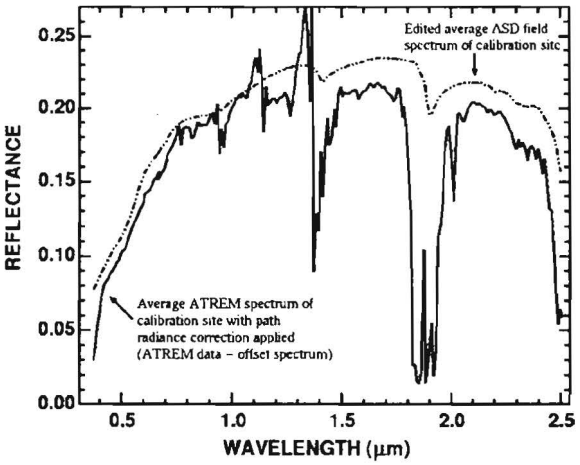

Figure 6. The ATREM-corrected spectrum from Figure 5 is compared to the edited average field spectrum for the Utah Deer Creek dam face. Note the field spectrum is smooth, as would be expected for the minerals present in the rocks, as compared to the ATREM-corrected spectrum. The ATREM-corrected spectrum has had the over-correction of the path radiance fixed using the methods described below. Besides the artifacts around atmospheric water absorptions, there are many small-scale spikes in the ATREM-derived spectra which must be corrected before material identification can begin.

After seeing the ATREM-derived surface spectra, one might ask why use ATREM at all? Water vapor in the atmosphere is highly variable, even over dry desert sites. Changes in elevation result in large variations in the atmospheric gas absorption depths. If a radiative transfer program was not applied first, the artifacts would be much greater than seen in Figure 6. The artifacts from ATREM are largely consistent between all pixels, and include those caused by the imprecisely known solar spectrum, possible errors in the AVIRIS radiance calibration, and relatively repetitive errors in the radiative transfer code in deriving the atmospheric water absorption profiles. Thus, these artifacts can be satisfactorily removed. Of course it would be better to use more accurate models, and we will test them when they become available.

6. Path Radiance Correction.

We have found that ATREM overcorrects for the path radiance scattering in the atmosphere at blue to UV wavelengths. The atmosphere scatters more light at shorter wavelengths (blue to UV--that is why the sky appears blue), so the path radiance portion of the measured signal that a radiative transfer routine must correct is largest in the UV. This type of scattering is called Rayleigh scattering and is caused by light scattering from molecules and particles much smaller than the wavelength of light. The information to derive the necessary correction can be found in the imaging spectroscopy data of a spectrally dark target whose reflectance is known. Larger particles, such as dust and water droplets (aerosols), cause Mie scattering at UV as well as at longer wavelengths (sometimes there is significant scattering in the infrared at 2.5 microns), but such conditions have not been a significant factor in our study areas in the western United States to date.

There is a simple strategy for deriving the UV path radiance levels. The main problem is in separating the surface reflectance component from the atmospheric path radiance. An accurate surface reflectance level is critical for determining the path radiance component. Ideally, a spot on the ground with zero reflectance would give a direct measurement of the path radiance. Traditionally, water has been used as a spectrally dark target. However, water also scatters blue light more than longer wavelengths (deep water also looks blue), so water is not usually UV-dark. The best UV-dark target we have found is green plants. From about 0.4 microns and shorter wavelengths, plant reflectance is very low, about 2% or less, and is either flat or decreases toward shorter wavelengths (e.g. Clark *et al.*, 1993, and Figure 7a). The north side of a hill or mountain (in the northern hemisphere) will be in shadow or at least lower solar intensity, so the apparent reflectance is lower than vegetation in full sunlight. It is common to find vegetated north sides of mountains with apparent reflectance in the UV of < 0.2% (Figure 7a&b). This provides an excellent UV dark comparison for the path radiance correction. Such areas are simply found by choosing a channel at UV wavelengths from the data (e.g. AVIRIS channel 3) and stretching the image brightness to show the darkest areas.

In some desert areas, where there is no vegetation in shadow areas in the imaged area, the above method cannot be used. In such cases an accurate measurement in the field is required. For example, some dark rocks on the north side of a hill might be used. It is important to make such measurements under the same lighting conditions as the flight data so the shadows will be the same.

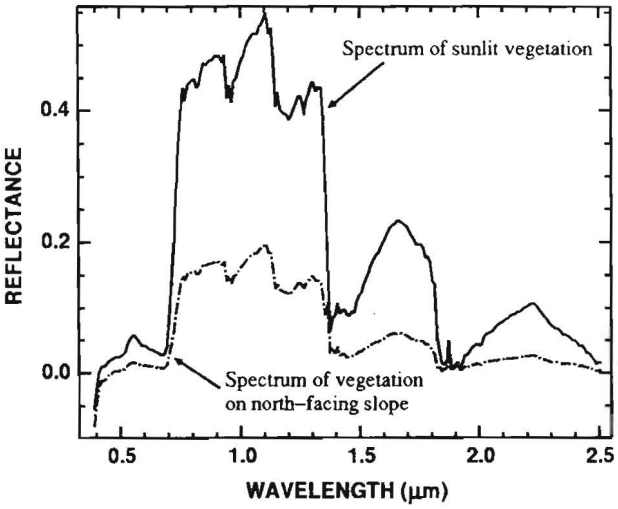

Figure 7a. Vegetation spectra from ATREM-corrected AVIRIS data. Two spectra are shown: one in sunlight, and another on the north side of a hill, largely in shadow. The reflectance in the UV is low and decreasing toward shorter wavelengths. ATREM has overcorrected the reflectance at wavelengths shorter than about 0.45 microns, and the data are negative at wavelengths short of 0.4 microns, which is not physically possible.

Figure 7b. Same two spectra as in Figure 7a, except showing details in the visible and ultraviolet portions of the spectrum.

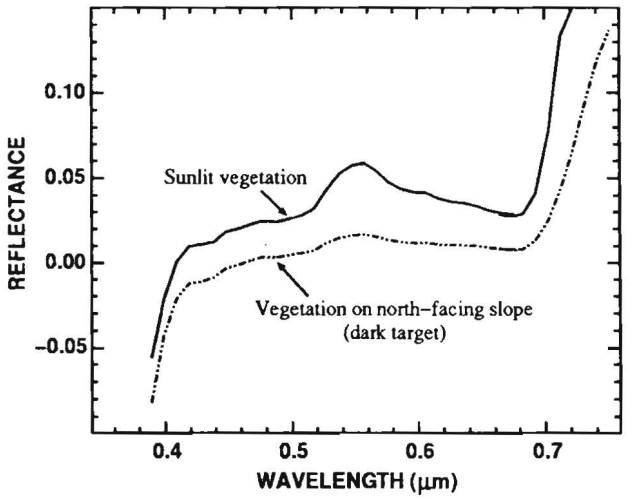

The ATREM-corrected data typically are negative in the UV, so the UV spectrum of vegetation in shadow is used to estimate the ATREM over-correction (Figure 8a). The difference between ATREM derived spectrum and the estimate (Figure 8a) becomes an offset correction to the ATREM data (Figure 8b). The offset correction is typically zero at wavelengths longer than about 0.5 microns (Figure 8b). This is called the "offset spectrum."

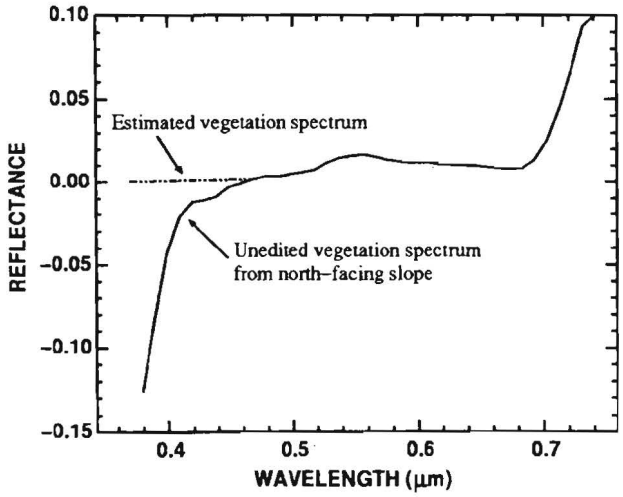

Figure 8a. Estimate of a normal vegetation-in-shadow spectrum shown in Figures 7a and 7b. This estimation is used to remove the effects of the ATREM overcorrection for path radiance as shown in the un-edited vegetation spectrum.

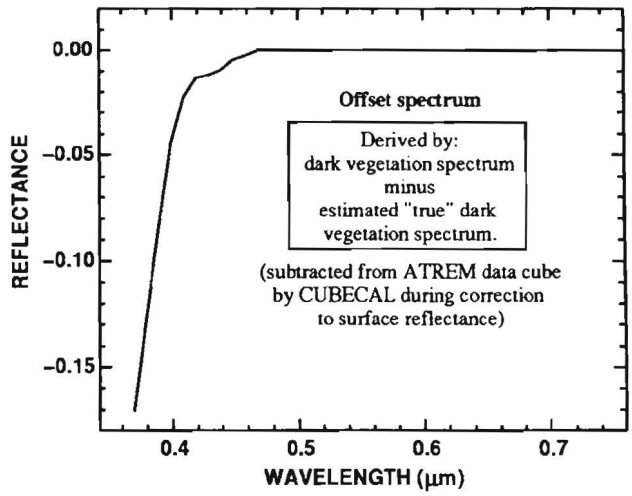

Figure 8b. The derived ATREM offset spectrum: the difference of the two spectra shown in Figure 8a.

7. Correction Using A Calibration Site

7.1 Calibration Site Surface Reflectance Characterization

At the time of data acquisition, it is very important to characterize the calibration site with a field spectrometer. Examples of field measurement activities at some calibration sites are given in Figures 2a-n and Figures 9a-d. A calibration site can change in a relatively short time (e.g. with rain or vegetation growth). For example, as a part of our calibration of the AVIRIS 1995 data over Arches National Park, we located an excellent playa just outside the park in April. It was a site we had used for calibration of previous AVIRIS data sets. While vegetation growth in the region seemed to be at its peak (relatively lush for that year), the playa had essentially no vegetation on it, and we had not seen significant vegetation on it during our previous visits. We measured it with our field spectrometer and sampled it for measurement on our lab spectrometer. However, on the day of the flight in mid-June, we went to the site and found it covered with weeds. As a result, it would no longer serve as an adequate calibration site. Fortunately, we had backup sites, and scrambled to characterize them. First we characterized a cheatgrass-covered field near the Playa (Figure 2m), and a rock outcrop just after the flight (Figure 2n).

Figure 9a - Salt Flat Calibration. Spectralon calibration.

Figure 9b - Deer Creek Dam Calibration A. Ray Kokaly operates the field spectrometer on the Deer Creek dam face. Obviously, such a measurement is tricky because walking on large boulders is difficult.

Figure 9c - Deer Creek Dam Calibration B. Frequent calibration of the field spectrometer is important. The constantly changing atmosphere and heat load on the instrument from sun and shadow as one moves around making measurements cause continual drifts. Here, Ray Kokaly operates the field spectrometer while Eric Livo holds the Spectralon reflectance standard. Eric hold the standard high and away from his body to reduce secondary reflections, and tries to position the standard so the shadow side of his body is seen by the standard.

Figure 9d - Jordanelle Dam Calibration. Calibration of the reflectance target with the field spectrometer is important. Roger Clark holds the target high to minimize reflections from clothes, and makes his shadow side face the target. Roger's green Gortex hat has distinctive and sharp absorption bands. If any light from the hat contributed to the signal, inverse Gortex features would be seen in the spectra of the dam face, but no such features are seen in the data. Such checks are important to verify the accuracy of the calibration.

It is also important to characterize the sky conditions at the time of the flight. While the water, oxygen, and carbon dioxide contents of the atmosphere are derivable from the imaging spectroscopy data, cirrus or other thin cloud formations are harder to assess. While clouds might be recorded by the sensor in the image area, clouds outside the edges of the imaged area may reflect light into the scene, resulting in increased water features

apparent in the data. Thus it is important to record sky conditions (note sky conditions in Figures 2a-n) at the time of calibration site field characterization. Also record sky conditions overhead at the time of the overflight (e.g. Figure 10).

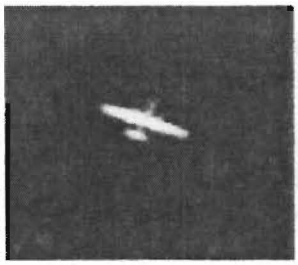

Figure 10. This photo shows the AVIRIS ER-2 aircraft flying over Arches National Park on June 19, 1995, and illustrates sky conditions at the time of the overflight. The rest of the sky was similarly clear. The photo was taken with a tripod-mounted 300 mm lens, Fujichrome Velvia (ISO 50) film, by Roger Clark. The aircraft velocity is so fast and the airplane is so high that the sound appears to come from about 60 degrees behind the plane. A quiet location is required to find the plane in the sky at the time of the overflight. Listen for the engines, and then, keeping in mind the flight line directions, look about 60 degrees ahead of the sound.

7.2 Spectrally Uniform and Spectrally Bland Sites

A calibration site is ideally spectrally uniform and spectrally bland. A site that is not spectrally uniform requires more thorough sampling. For example, the above discussion regarding the playa calibration for the Arches National Park AVIRIS flight illustrates a spectrally non-uniform site: weeds with strong green vegetation spectral signatures on a playa spectral background. While it is possible that an adequate field spectrometer measurement strategy could have been devised to characterize such a variable site, the possibility of residual artifacts is nevertheless increased.

Imaging spectroscopy pixels are almost always much larger than what you can measure in the field, and certainly larger that what can be measured in the lab. For example, AVIRIS pixels are about 20 meters square (area = 400 square meters). Our field spectrometer has about a 20 degree field of view so it measures a spot only about 0.5 meters in diameter from a distance of shoulder height. Such a spot corresponds to an area of only 0.2 square meters, or only 0.05 % of the area of an AVIRIS pixel. Even if one measures 300 spots, the equivalent area covered is only about 15% of an AVIRIS pixel (although the field spectra could be statistically scattered over many AVIRIS pixels). Thus, if the calibration site has spectral features which vary across the site, even 300 (or 3000) field spectra may not be representative of the large area seen by the AVIRIS instrument.

An improved method of spectrally sampling a calibration site involves the use of a rapid sampling spectrometer, which acquires a spectrum every fraction of a second. With such an instrument, hundreds of spectra can be obtained during a continuous traverse of the site. For example, at the USGS we use a field spectrometer that obtains a spectrum every 0.1 second. We typically configure the field computer to average 60 0.1-second integrations before recording the spectrum (6 seconds). Six seconds reduces the recorded data volume while still providing feedback often enough for the operator to evaluate data quality. During those six seconds, the spectrometer operator is traversing the calibration site (note the operators in Figures 2a-n). Depending on the roughness of the terrain, a person will traverse from 1 to 8 meters every six seconds. Assuming an average of 4 meters traversed per six seconds, and a 0.5 meter spot for the spectrometer field of view, one integration covers about 2 square meters. Thus, 300 field spectra cover about 600 square meters, or about 150% of an AVIRIS pixel. If those spectra are spread over the large area of a typical multi-pixel calibration site, then it can be assumed that a reasonable representation of the site has been recorded.

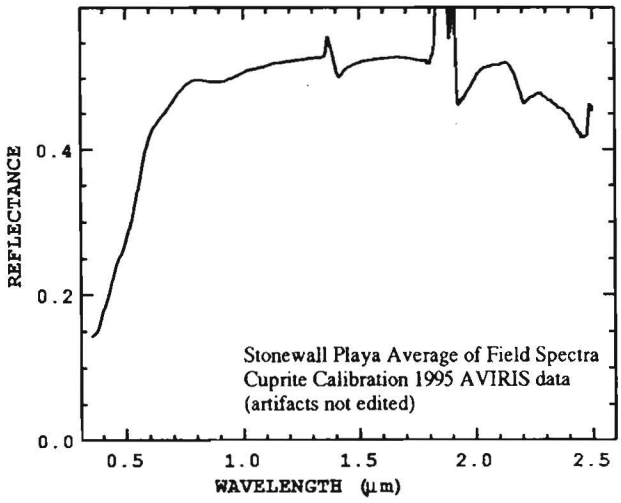

Figure 11a - Cuprite. Stonewall playa calibration site average field spectrum.

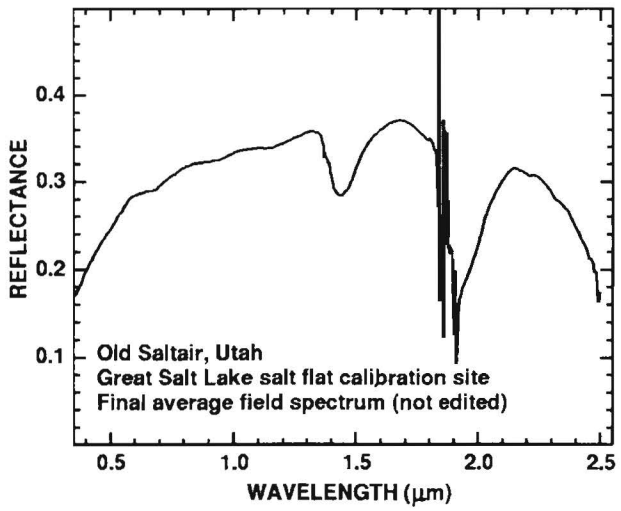

Figure 11b - Salt Flat. Calibration site average field spectrum near Old Saltair west of Salt Lake City, Utah. The high reflectance and relatively bland spectral nature of the salt flat make it one of the best calibration sites we have encountered.

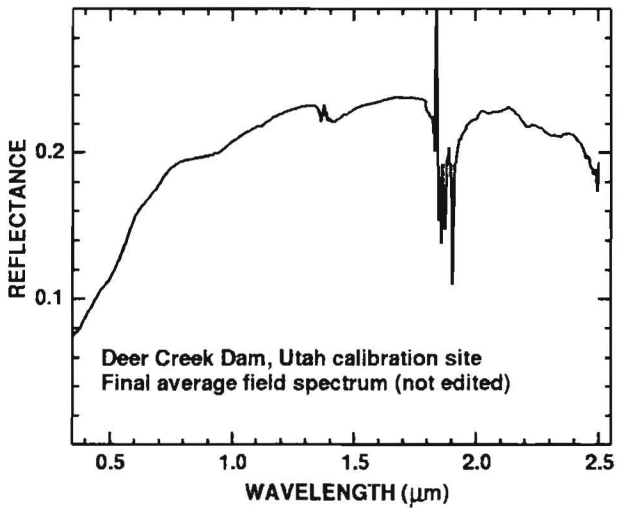

Figure 11c - Deer Creek Dam. Deer Creek dam face calibration site average field spectrum.

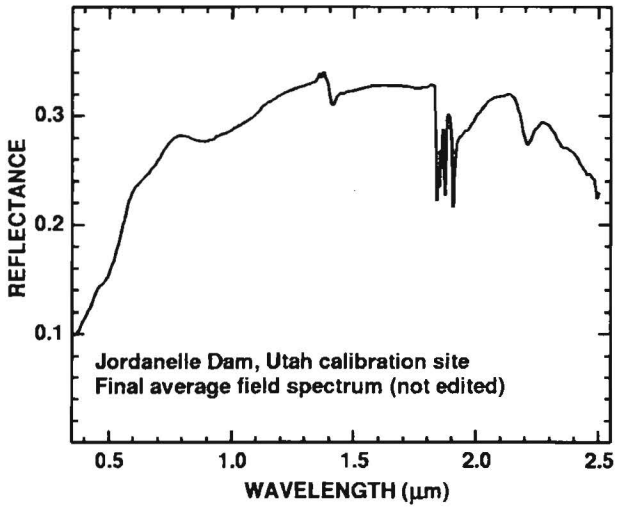

Figure 11d - Jordanelle Dam. Jordanelle dam calibration site average field spectrum. In the field, the dam appeared quite uniform and we thought it would be better than the Deer Creek dam site. However, note the strong muscovite feature at 2.2 microns, and the strong iron Fe^{3+} absorptions in the visible and NIR regions of the spectrum compared to the Deer Creek dam spectrum. The Jordanelle dam spectra had more variability than was obvious in the field. The Deer Creek dam is the better calibration site despite the variability in visual color between cobbles (Figures 2d-e).

The characterization of a calibration site becomes more difficult with a laboratory spectrometer, which measures an area of only about a square centimeter (~$3x10^{-7}$ of the area of an AVIRIS pixel). If the ground characterization does not exactly agree with the spectral features observed by AVIRIS, there will be residual features in all the reflectance-calibrated imaging spectroscopy data. Such artifacts can produce errors in identification and mapping of materials, as mentioned above.

A spectrally bland calibration site is ideal because any spectral features that are not well characterized might result in residual spectral features added to all pixels in the final calibrated data set. For example, montmorillonite (clay) and

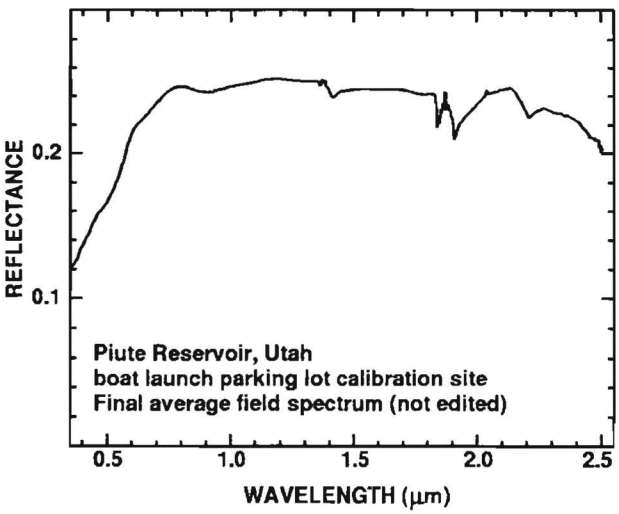

Figure 11e - Piute Parking Lot. The Piute Reservoir boat launch parking lot calibration site average field spectrum.

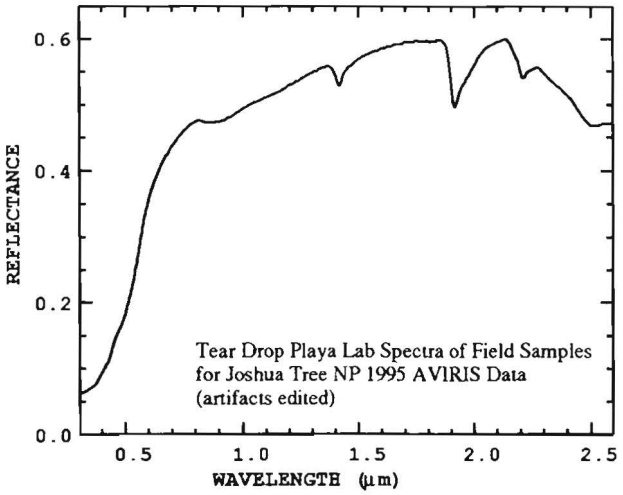

Figure 11f - Joshua Tree Playa. Calibration site average field spectrum.

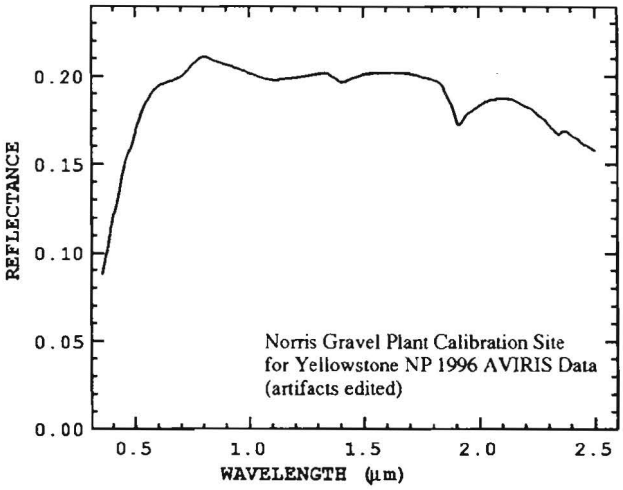

Figure 11g - Yellowstone. Yellowstone National Park road construction gravel staging lot calibration site average field spectrum.

t

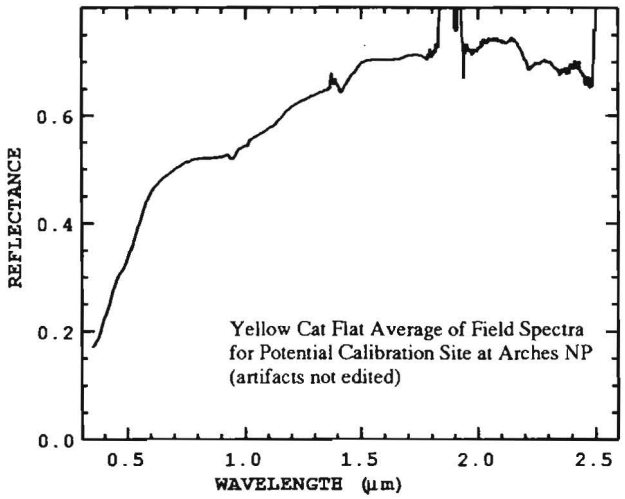

Figure 11h - Arches A. The Yellow Cat Flat playa calibration site average field spectrum acquired on April 27, 1995, about 2-months before the AVIRIS flight.

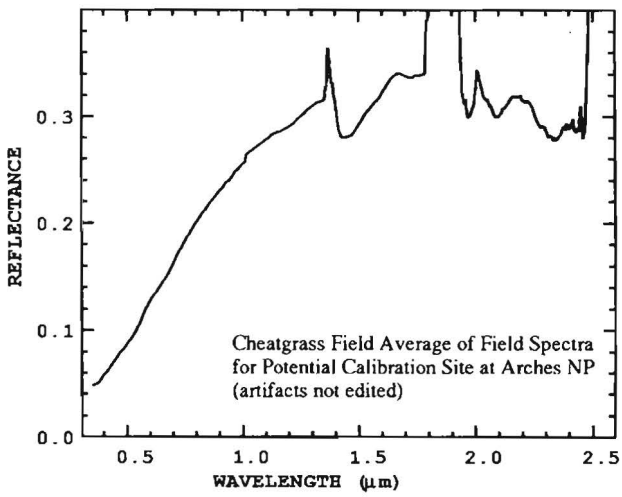

Figure 11i - Arches B. Calibration site average field spectrum of cheatgrass field, located just outside of the Arches national Park boundary.

trace iron oxide (or iron hydroxide) are common components of playa surfaces (see Figure 11a). If the field spectral measurement of the playa does not accurately characterize the site, there could be a residual spectral signature imparted to the final calibrated data that is either not enough of a particular absorption feature, or too much of a feature. Such residuals are a result of different sampling between the remote sensing instrument and the ground study. If the site has no spectral features (e.g. no 2.2 micron montmorillonite absorption, and no iron absorption in the ultraviolet or visible), then there would be no error in sampling.

The probability of residual spectral artifacts is reduced if the calibration site spectrum has few or no spectral features. If the spectrum is flat, and thus there are no residual features to impart to the data, then even a laboratory spectrometer could be effectively used (assuming disturbing the surface to take the sample to the lab does not change the spectral characteristics). For the AVIRIS spectral range (0.4 to 2.5 microns), quartz sand is ideal: it has high reflectance at all wavelengths and no significant absorption features. Playas often have high quartz content and usually only weak clay or iron absorption bands, thus they are usually spectrally bland. Bright white rocks or sandy areas are often ideal if not covered with

vegetation (even sparse vegetation). Feldspar-bearing rocks also have little to no absorption features in the AVIRIS spectral range. Figures 11a-j show spectra of the calibration sites shown in Figure 2. Note that just because a site appears bright and white does not mean it is a good spectral calibration site. It may have strong UV or infrared spectral features (such was the case with the Jordanelle dam spectra, Figure 11d).

A spatially uniform calibration site is an area on a scale which can be characterized in the field, on the ground and by the remote sensor, where the pixel to pixel variations in the reflectance spectra are low. If a site is composed of many different pebbles, for example, but both the field spectrometer and the flight data measurements average many pebbles together, the site is most likely acceptable and can be considered spatially uniform. Many dam faces are composed of large boulders, some larger than a person's head, but a field spectrometer with a half-meter diameter spot can average over many boulders, thus providing a uniform site. Such was the case of the Deer Creek dam site shown in Figure 2d-e.

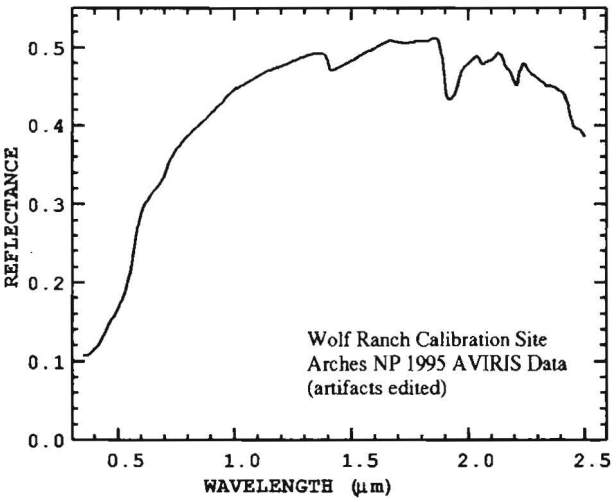

Figure 11j - Arches C. Calibration site average field spectrum of Moab Tongue Formation in Arches National Park.

7.3 Field Spectra Verification

Field spectra commonly have artifacts due to constantly changing conditions. The atmosphere and local air temperature can vary with time. Wind, sun, and shadow impacting on the instrument vary as the operator moves around making measurements, and battery power constantly decreases. Dark and gain levels also vary with time, producing offsets in measured spectra. Atmospheric water vapor varies with time resulting in residual water absorptions. The atmospheric path length constantly changes as the sun moves across the sky, necessitating continual re-measurements of local reference standards. Given these conditions, it is very difficult to keep the field spectrometer in a stable environment and therefore in good calibration. Example spectra with typical artifacts are shown in Figure 12.

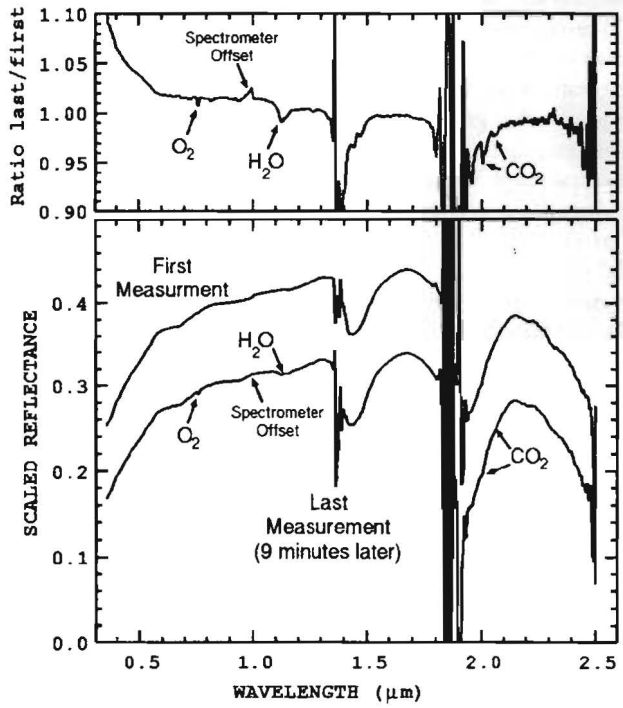

Figure 12: Example sample spectrometer drift over 9 minutes is shown. The residual features after 9 minutes are small in this case because the atmosphere and the instrument were relatively stable. The features are small enough they would be barely noticed on a field spectrometer computer screen. However, when the first and last spectra are ratioed, one sees residual features several percent in strength. Each spectrum is a six-second integration. These residual features must be hand-corrected if present in the final average for the site (discussed below).

There is no simple solution to the above problem. Even if the field spectrometer remained in perfect calibration, the atmosphere will not remain constant. The best conditions in which to make field measurements are clear skies, near solar noon, at temperatures that do not stress the instrumentation (no extreme heat or cold). A field spectrometer that

measures a reference spectrum to provide continuous corrections to varying atmospheric conditions at the same time as measuring the surface is needed to avoid some of these problems, along with low sensitivity to temperature and power fluctuations.

Another way to reduce atmospheric effects is to use an artificial light source, powerful enough to measure a large spot in an enclosure to minimize solar and atmospheric effects. However, batteries to power lights and the spectrometer, which last long enough to measure many spots, would be cumbersome to carry, especially on rough terrain.

So how does one determine if a spectral feature in a calibration site spectrum is real or a field spectrometer artifact? One solution to this difficulty with field measurements is to sample the surface materials and measure their spectra in the laboratory. We have found that for some calibration sites, the laboratory spectra of field samples usually measure enough of the site's spectral characteristics to enable determination of what are artifacts and what are real features in the field data. Thus, the laboratory spectra provide a secondary check to establish the quality of the *in situ* field data (e.g. Figure 13). Multiple calibration sites also help answer this question. When compared to the airborne imaging spectroscopy data, multiple calibration sites should indicate the same residual differences between the flight data and the calibration site spectra. Ideally, those differences are zero for the flight data converted to surface reflectance and the field reflectance data.

Once artifacts are identified, the spectrum is corrected by numerous methods depending on the artifact. An offset in the spectrum might be corrected by multiplying one part of the spectrum by a constant to adjust the level. If the correction can be determined to be a zero-level error, a constant could be added or subtracted. Spikes and residual features can be interpolated across, or other the correct values can be estimated from a graph and the data values edited by hand. Laboratory comparison spectra are sometimes spliced into the field spectrum, most commonly where the terrestrial atmosphere is nearly opaque around the 1.4 and 1.9 micron water absorptions. There are no simple software packages for these manipulations. We commonly use the tools available in the SPECPR package (Clark, 1980, 1993).

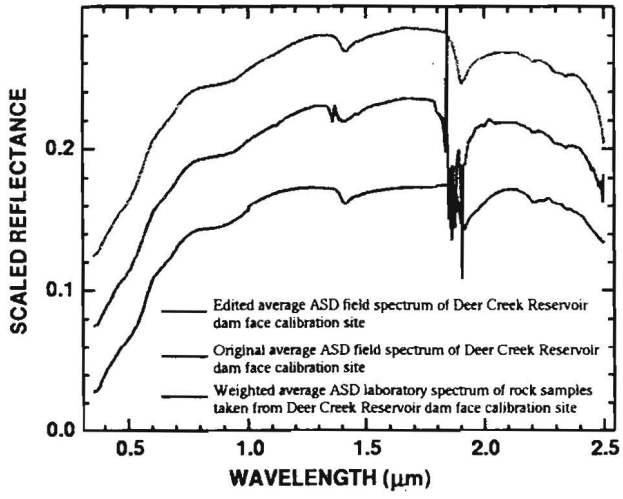

Figure 13. Example calibration site spectra and the correction of artifacts. Spectra are offset for clarity. The average field spectrum from the Deer Creek dam calibration site is shown (middle). Artifacts include residual atmospheric water features at 1.15, 1.4, 1.9, and 2.5 microns, and residual CO_2 features near 2 microns. A weak offset at 1 micron (a grating and detector change in the instrument) is also present but at a level too small to appear in this graph. Spectra of rock samples from the site were measured in the lab (lower spectrum) to confirm spectral features. Note the difference in the 2.2-micron feature depth between lab and field spectra. This is due to variation in the proportions of materials sampled in the field and lab. The lab spectrum is relatively smooth in the regions of atmospheric water, and was used to fix/interpolate the average field spectrum across the regions of atmospheric artifacts. The final edited spectrum is shown at the top. The quality of the final spectrum shows that field spectra can be of laboratory quality. This is the quality we try to achieve at each of our calibration sites.

7.4 Spectralon Correction.

Spectra obtained by both the field and laboratory spectrometers must be fully corrected to absolute reflectance before any analysis can be performed. Laboratory and field reflectance measurements are made relative to a "white" reference material, such as Spectralon (available from Labsphere, a commercial derivative of the reflectance standard developed by the National Institute of Standards and technology, NIST: Weidner and Hsia, 1981). However, no currently known material has a 100% diffuse

reflectance in the UV to near infrared (0.3 to 2.5 microns). The reflectance of Spectralon is shown in Figure 14, derived according to methods similar to that used by Clark *et al.*. (1990) to derive the reflectance of Halon. It is obvious from Figure 14 that Spectralon has a several percent absorption feature near 2.13 microns. Because reflectance with a field or laboratory spectrometer is derived by the ratio of sample / reference, the result with a Spectralon reference will result in a spectrum with a positive feature near 2.13 microns. Thus, the corrected reflectance, R_{absref} is:

$$R_{absref} = (I_{sample} / I_{ref}) R_{ref},$$

where I_{sample} is the light intensity measured by the instrument from the sample, I_{ref} is the light intensity measured by the instrument from the reference under the same incident lighting conditions, and R_{ref} is the absolute reflectance of the reference material (e.g. Figure 14 if Spectralon).

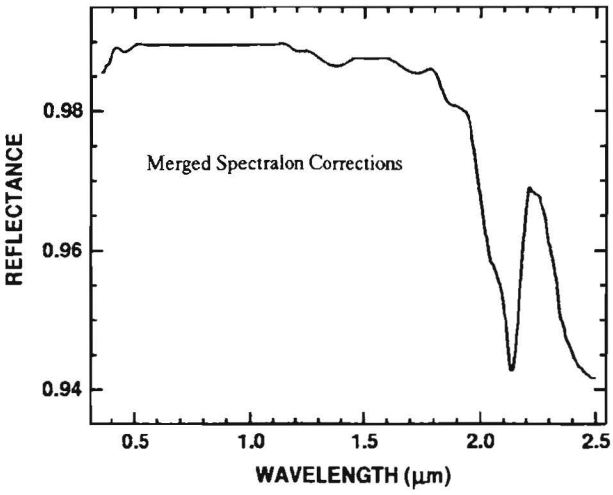

Figure 14. The reference used with the field spectrometer, Spectralon, is not a perfect 100% reflectance standard. The spectral features of the field reference standard must be removed, or residual reference material spectral features will be propagated into the imaging spectroscopy data.

7.5 Spectral Convolution.

Before actual comparisons are done between different spectrometers, the field spectra to be used in the comparisons should be convolved to the bandpass and sampling of the flight instrument. If there are absorption features in the spectra that are on the same order or less in width than the bandpass of the spectrometer, the spectrometer will broaden the feature and give a width wider by approximately the sum of the squares of the widths of the feature and the spectrometer. The measured width, W_m is

$$W_m = (W_f^2 + W_s^2)^{0.5},$$

where W_f is the width of the feature and W_s is the bandpass width of the spectrometer. Thus, the field and/or lab spectrometer should have narrower bandpasses than the flight instrument. Note, however, that if the spectra being compared have no spectral features, then all spectrometers will give the same answer. Spectral convolution software that tracks the finite bandwidth of spectrometers is available in the SPECPR package (Clark, 1980, 1993).

The variation of wavelength accuracy between instruments will result in disagreements between spectra measured by those instruments. Because field instruments get rough treatment relative to laboratory instruments that remain in the lab, the wavelength accuracy should be monitored often in the field and confirmed in the laboratory. We measure mylar plastic in the field with our field spectrometers and confirm the wavelength position of the mylar absorption features with our Fourier Transform laboratory spectrometer. The bandwidth of the spectrometer can also be monitored by use of the mylar absorption features and the above formula. The narrowest features in a spectrum provide for the highest accuracy when determining wavelength accuracy and bandwidth.

7.6 Multiplier Correction.

The offset spectrum (e.g. Figure 8b) is subtracted from ATREM-corrected data (e.g. Figure 5) from the ground calibration area. The edited field spectrometer average of the ground calibration site (Figure 6) is spectrally convolved to the AVIRIS sampling and bandpasses and ratioed to the offset-corrected ATREM data. This ratio becomes the multiplier for the ATREM data cube to correct the data to surface reflectance (Figure 15).

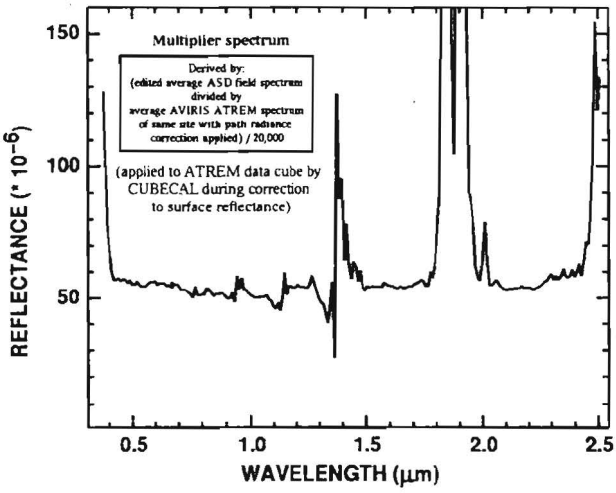

Figure 15. The derived multiplier spectrum. Our ATREM-corrected data are scaled integers where a reflectance level of 1 is a data number (DN) equal to 20,000. The multiplier corrects the DN back to reflectance in our software, so the multiplier should be approximately 1/20,000 (or $50x10^{-6}$). If the ATREM data matched the field spectrometer data, the multiplier would be a flat line on this graph at $50x10^{-6}$.

The imaging spectroscopy data are corrected by running a computer program that subtracts the offset and multiplies by the multiplier for each pixel. This simple math can be done with commercial software such as IDL or small custom programs or other public domain software such as REMAPP. We scale the AVIRIS data souch that a derived reflectance of 1.0 is scaled to a DN = 20,000, so the multiplier shown in Figure 15 should have a level approximately equal to 1/20,000. The resulting surface-reflectance-calibrated data set is called "radiative transfer ground calibrated" and we use a file extension of "rtgc" on the output file name.

The final "rtgc" data are stored as signed 16-bit integers so that the 0 to 1.0 reflectance range must be scaled. Because of the very high signal-to-noise of current AVIRIS data (which can be several thousand), with seemingly continuous improvements from year-to-year by the AVIRIS engineering team, we use a high scale factor, 20,000, to be sure we do not run into any DN quantization problems. Thus all "rtgc" calibrated data from our lab is scaled so a DN of 20000 is a reflectance of 1.0 (reflectance 0.5 has a DN=10000, a reflectance of 0 is DN=0). If any value in the data set is out of range, or the processing steps indicated bad data, the data point is marked deleted. Deleted point values are set to a value of -32767.

Example spectra from well-calibrated data cubes are shown in Figure 16a-c. Ignoring the regions of low signal through the Earth's atmosphere, near 1.4 and 1.9 microns, the derived surface reflectance data are excellent.

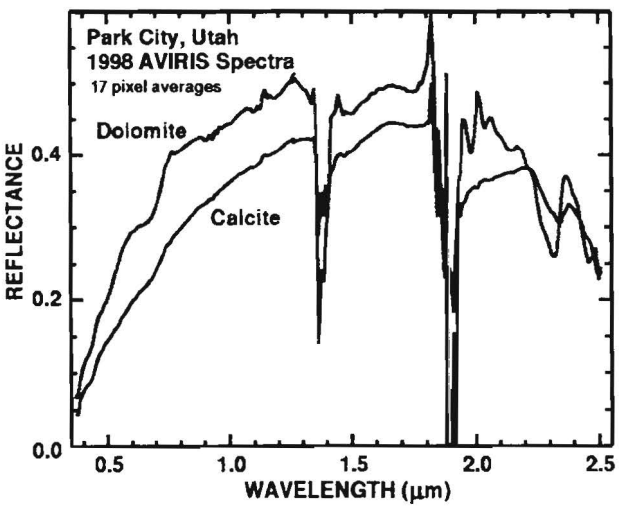

Figure 16a. Radiative transfer, ground calibrated (rtgc) calibrated AVIRIS spectra from the August, 1998 flight over Park City, Utah. Comparison of calcite and dolomite spectra. Ignore the 1.4 and 1.9 micron regions where the terrestrial atmosphere is mostly opaque. The dolomite spectrum shows residual CO_2 absorptions near 2-microns because the area from which it was sampled is at a much higher elevation than the calibration site and ATREM does not correct for localized CO_2 effects.

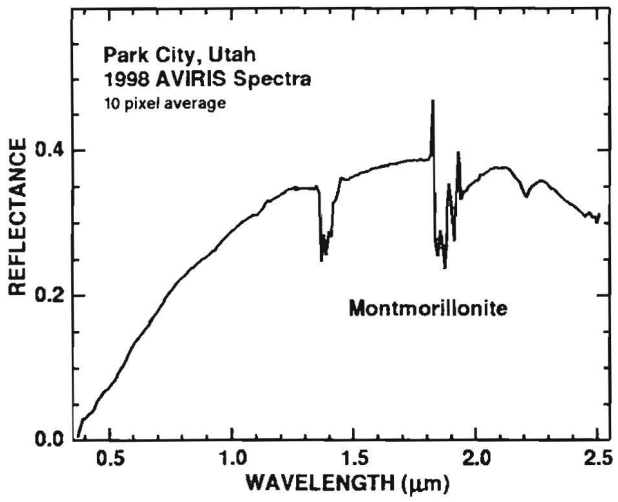

Figure 16b. Radiative transfer ground calibrated (rtgc) AVIRIS spectrum from the August, 1998 flight over Park City, Utah. The clay mineral montmorillonite shows a 2.2-micron absorption feature. Ignore the 1.4 and 1.9 micron regions where the terrestrial atmosphere is mostly opaque.

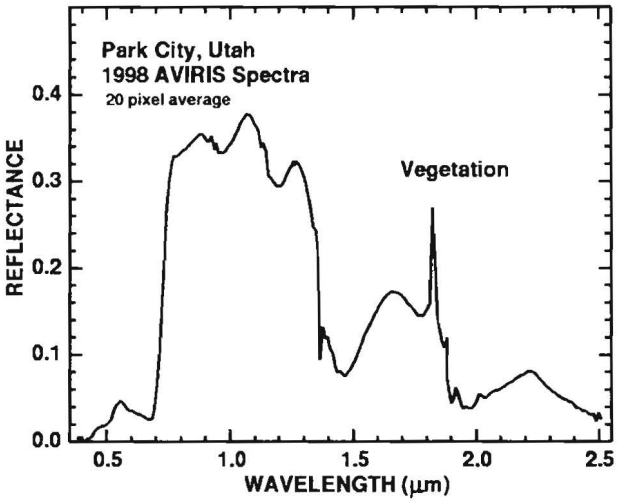

Figure 16c. Radiative transfer ground calibrated (rtgc) AVIRIS spectrum from the August, 1998 flight over Park City, Utah. Example vegetation spectrum. Ignore the 1.4 and 1.9 micron regions where the terrestrial atmosphere is mostly opaque.

8. Summary

Imaging spectroscopy data, such as AVIRIS, can be corrected to surface reflectance by using a two step correction. A radiative transfer correction tracks changing atmospheric water absorptions from pixel to pixel and removes the absorptions due to water and other atmospheric gases, scattering in the atmosphere and the solar spectrum. The second step uses the reflectance of known targets in the scene to correct the artifacts from the imperfect radiative transfer correction. Critical to the success of this method is the accurate reflectance characterization of field calibration sites.

The quality of the calibration to surface reflectance is important for accurately identifying materials. A small calibration artifact could distort an absorption feature, causing a misidentification. An accurate calibration shows the fundamental properties of surface materials, and is key to linking remotely sensed surface properties with laboratory data.

The effort to do the calibration is significant. The steps involved are many, including pre-assessment of calibration sites before the flight, measurements with a field spectrometer near the time of the flight, sampling of the materials at the site, measurement of those samples on laboratory spectrometers, reduction of the field data, radiative transfer corrections of the flight data, extraction of imaging spectroscopy data over the same area as the field measurements, comparison of the radiative transfer data with the field data, correction of artifacts in the field data, evaluation of path radiance scattering in the imaging spectroscopy data, derivation of offsets and multipliers to correct the radiative transfer calibrated imaging spectroscopy data, application of the offsets and multipliers to the flight data, and then evaluation of the resulting calibration to see if it is adequate. If the calibration is not adequate, the data need to be re-evaluated and some steps re-done. Our experience has shown that the calibration of one site involves about 1 to 2 person months to calibrate, and sometimes more. One of our recent experiences was with the Utah EPA study where a person week was spent pre-assessing calibration sites, 3 person weeks spent in the field making measurements near the time of the flight, and about 7 person months working in the lab and at the computer doing the above steps for 3 sites. The average is about 2.7 person months per site, and the calibration for all 3 sites is not yet complete.

While the effort is substantial, the results are worth the effort as the "radiative transfer ground calibrated" spectra are near laboratory quality. The remaining artifacts are mainly due to elevation differences because the current radiative transfer code we use does not correct elevation effects for all

atmospheric gases. More sophisticated code should result in even better corrections for all pixels in the imaging spectroscopy data set.

9. References

Adler-Golden, S.M., Matthew, M.W., Bernstein, L.S., Levine, R.Y., Berk, A., Richtsmeier, S.C., Acharya, P.K., Anderson, G.P., Felde, G., Gardner, J., Hoke, M., Jeong, L.S., Pukall, B., Mello, J., Ratkowski, A., and Burke, H.-H. (1999), Atmospheric correction for short-wave spectral imagery based on MODTRAN4. In *Summaries of the Eighth JPL Airborne Earth Science Workshop* (R.O. Green, Ed.), **JPL Publ. 99-17**, Jet Propulsion Laboratory, Pasadena, California, pp. 21-29.

Carrere, V. and Abrams, M.J. (1988), An assessment of AVIRIS data for hydrothermal alteration mapping in the Goldfield mining district, Nevada. In *Proceedings of the Airborne Visible/Infrared Imaging Spectrometer (AVIRIS) Performance Evaluation Workshop* (G. Vane, Ed.), **JPL Publ. 88-38**, Jet Propulsion Laboratory, Pasadena, California pp. 134-154.

CSES (Center for the Study of Earth from Space), (1997), ATmosphere REMoval Program (ATREM) Version 3.0 User's Guide, 27 p.

Clark, R.N., A Large Scale Interactive One Dimensional Array Processing System, Pub. Astron. Soc. Pac., 92, 221-224, 1980.

Clark, R.N., SPECtrum Processing Routines User's Manual Version 3 (program SPECPR), U .S. Geological Survey, Open File Report 93-595, 210 pages, 1993.

Clark, R.N., and King, T.V.V. (1987), Causes of spurious features in spectral reflectance data. In *Proceedings of the Third Airborne Imaging Spectrometer Data Analysis Workshop* (G. Vane, Ed.), **JPL Publ. 87-30**, Jet Propulsion Laboratory, Pasadena, California, pp. 132-137.

Clark, R.N., Middlebrook, B.J., Swayze, G.A., Livo, K.E., Knepper, D.H., King, T.V.V., and Lee, K. (1988), Calibration and evaluation of AVIRIS data: Cripple Creek in October, 1987. In *Proceedings of the Airborne Visible/Infrared Imaging Spectrometer (AVIRIS) Performance Evaluation Workshop* (G. Vane, Ed.), **JPL Publ. 88-38**, Jet Propulsion Laboratory, Pasadena, California, pp. 49-61.

Clark, R.N., T.V.V. King, M. Klejwa, G. Swayze, and N. Vergo, High Spectral Resolution Reflectance Spectroscopy of Minerals, *J. Geophys Res.* **95,** 12653-12680, 1990.

Clark, R.N., G.A. Swayze, A. Gallagher, T.V.V. King, and W.M. Calvin, The U. S. Geological Survey, Digital Spectral Library : Version 1: 0.2 to 3.0 m, *U.S. Geological Survey, Open File Report 93-592,* 1326 pages, 1993.

Clark, R.N., Swayze, G.A., Heidebrecht, K.B., Green, R.O., and Goetz, A.F.H. (1995), Calibration to surface reflectance of terrestrial imaging spectrometry data: Comparison of methods. In *Summaries of the Fifth Annual JPL Airborne Earth Science Workshop* (R.O. Green, Ed.), **JPL Publ. 95-1**, Jet Propulsion Laboratory, Pasadena, California, pp. 41-42.

Clark, R.N., Swayze, G.A., Heidebrecht, K.B., Goetz, A.F.H., and Green, R.O. (1993), Comparison of methods for calibrating AVIRIS data to ground reflectance. In *Summaries of the Fourth Annual JPL Airborne Geoscience Workshop* (R.O. Green, Ed.), **JPL Publ. 93-26**, Jet Propulsion Laboratory, Pasadena, California, pp. 35-36.

Conel, J.E., Green, R.O., Vane, G., Bruegge, C.J., and Alley, R.E. (1987), AIS-2 radiometry and a comparison of methods for the recovery of ground reflectance. In *Proceedings of the Third Airborne Imaging Spectrometer Data Analysis Workshop* (G. Vane, Ed.), **JPL Publ. 87-30**, Jet Propulsion Laboratory, Pasadena, California, pp. 18-47.

Gao, B.C., and A.F.H. Goetz, Column atmospheric water vapor and vegetation liquid water retrievals from airborne imaging spectrometer data, *J. Geophys Res.* **95**, 3549-3564, 1990.

Gao, B.C., K.B. Heidebrecht, A.F.H. Goetz, ATmospheric REMoval Program (ATREM) User's Guide, version 1.1, Center for the Study of Earth From Space document, University of Colorado, 24 pp. 1992.

Gao, B.-C., Heidebrecht, K.B., and Goetz, A.F.H. (1993), Derivation of scaled surface reflectances from AVIRIS data. *Remote Sensing of Environment* **44:** 165-178.

Green, R.O., Eastwood, M.L., Sarture, C.M., Chrien, T.G., Aronsson, M., Chippendale, B.J., Faust, J.A., Pavri, B.E., Chovit, C.J., Solis, M., Olah, M.R., and Williams, O. (1998), Imaging spectroscopy and the Airborne Visible/Infrared Imaging Spectrometer (AVIRIS). *Remote Sensing of Environment* **65:** 227-248.

Kruse, F.A. (1987), Mapping hydrothermally altered rocks in the northern Grapevine Mountains, Nevada and California with the Airborne Imaging Spectrometer. In *Proceedings of the Third Airborne Imaging Spectrometer Data Analysis Workshop* (G. Vane, Ed.), **JPL Publ. 87-30**, Jet Propulsion Laboratory, Pasadena, California, pp. 148-166.

Leprieur, C., Carrere, V., and Gu, X.F. (1995), Atmospheric corrections and ground reflectance recovery for Airborne Visible/Infrared Imaging Spectrometer (AVIRIS) data: MAC Europe'91. *Photogrammetric Engineering and Remote Sensing* **61:** 1233-1238.

Qu, Z., Goetz, A.F.H., and Heidebrecht, K.B. (2000), High-accuracy atmosphere correction for hyperspectral data (HATCH). In *Summaries of the Ninth Annual JPL Airborne Earth Science Workshop* (R.O. Green, Ed.), **JPL Publ. 00-18**, Jet Propulsion Laboratory, Pasadena, California.

Roberts, D.A., Yamaguchi, Y., and Lyon, R.J.P. (1986), Comparison of various techniques for calibration of AIS data. In *Proceedings of the Second Airborne Imaging Spectrometer Data Analysis Workshop* (G. Vane and A.F.H. Goetz, Eds.), **JPL Publ. 86-35**, Jet Propulsion Laboratory, Pasadena, California, pp. 21-30.

Schläpfer, D., Bojinski, S., Schaepman, M., and Richter, R. (2000), Combination of geometric and atmospheric correction for AVIRIS data in rugged terrain. In *Summaries of the Ninth Annual JPL Airborne Earth Science Workshop* (R.O. Green, Ed.), **JPL Publ. 00-18**, Jet Propulsion Laboratory, Pasadena, California.

Weidner, V.R. and Hsia, J.J., Reflection properties of pressed polytetrafluoroethylene powder, *J. Opt, Soc. Am.* **71,** 856-859, 1981.

Zagolski, F., and Gastellu-Etchegorry, J.P. (1995), Atmospheric corrections of AVIRIS images with a procedure based on inversion of the 5S model. *International Journal of Remote Sensing* **16:** 3115-3146.

APPENDIX A

Obtaining and Organizing Imaging Spectroscopy Data

The first step to organizing data is to acquire digital copies of the imaging spectroscopy data (e.g. AVIRIS data are obtained from JPL). The data may not come in a form that will be easy to work with and will have to be reformatted. For example, new AVIRIS data are sometimes shipped as one flight line per tape, with AVIRIS data in 512-line scenes (files) in band-interleaved-by-pixel (BIP) format. Our processing requires band interleaved by line (BIL) format. We read the data tapes onto disk, and convert the imaging spectroscopy data to BIL format and add ascii Vicar headers. Table 1 shows a sample Vicar header. Important for software use, including easy access by FORTRAN programs, the header should have a length equal to a logical record length. For example, AVIRIS has 614 pixels across one scan line and 2 bytes per pixel, thus the header is (2x614=) 1228 bytes. Note that a valid vicar header has at least two blank spaces between key words.

```
LBLSIZE=1228 FORMAT='HALF' TYPE='IMAGE' BUFSIZ=19648 DIM=3 EOL=0 RECSIZE=1228
ORG='BIL' NL=1024 NS=614 NB=224 N1=614 N2=224 N3=1024 N4=0 NBB=0 NLB=0 TASK='dd
to combine scene1,2' USER='rclark' DAT_TIM='Aug 19 19:35:05 1992 UTC'
TITLE='Chesler Park flight 920819B run 6 scene 1,2'
```

We concatenate the AVIRIS scenes into 1024-line segments because the size of a segment is about 281 megabytes, enabling convenient viewing on a terminal screen and so that two scenes plus some data products can fit onto a CD-ROM disk (650 megabyte capacity). Two scenes on an optical disk are required because the radiance data and the reflectance calibrated cubes are stored together so that they can both be used for mapping. In the future, the many-gigabyte capacity of Digital Versatile Disk (DVD) technology will allow archiving of an entire flight line on a single disk as one file each for the radiance and reflectance cubes.

MAPPING THE INVASIVE PLANT *ARUNDO DONAX* AND ASSOCIATED RIPARIAN VEGETATION USING AVIRIS

Deanne DiPietro,[1] Susan L. Ustin,[1] Emma Underwood[1]

1. INTRODUCTION

It is now widely recognized that invasions by non-native plants present a serious ecological threat to the already greatly reduced native ecosystems of California (Barbour et al., 1993; Bossard et al., 2000). In response to the expanding ranges and increasing damage done by harmful non-natives, control of invasive species has become a priority for environmental management and an integral component of many habitat conservation efforts. This is especially true for riparian ecosystems in southern California, where invasive species threaten the last vestiges of remaining native habitat and associated species already reduced to precariously small and fragmented populations (Zembal, 1989). This study focuses on an invasive plant that has proven very destructive to riparian ecosystems, *Arundo donax* (Arundo, giant cane). An aggressive invader, the plant successfully out-competes all surrounding vegetation, completely converting large areas into solid, impenetrable cane fields that deplete water resources, trap sediment, and burn readily (Jackson et al., 1993). Arundo is present in large stands in the study area on the Santa Margarita River on Camp Pendleton Marine Corps Base and has been the target of an ongoing eradication effort since 1996 using a combination of mechanical and herbicide control methods (Omori, 1996).

A key requirement for the effective management of invasive plants is the ability to identify, map, and monitor invasions as well as the invaded plant communities. Hand-mapping in the field or from aerial photos are techniques commonly used in support of eradication efforts, but these methods are labor intensive and limited. Hand-mapping from field observation requires access to the site from the ground, a prospect that is not always practical, safe, or timely, especially on an active military base. Interpretation of aerial photos is extremely time-intensive and often necessitates interpretation of large numbers of photographs (Avery, 1992). In addition, it can be difficult to distinguish the weed species in the photos even with magnification, making the interpretation process highly subjective and likely to differ from one analyst to another. Because of these constraints, weed mapping is usually done on an as-needed basis, and comprehensive maps that would support time-series evaluation are not generally made. There is the need, therefore, to develop repeatable and reliable automated techniques for monitoring the spread of weeds and the effects of eradication efforts as well as changes in the habitats being managed. Imaging spectrometry data offers the spectral resolution necessary to distinguish between plant species or communities using a greater variety of subtle spectral reflectance characteristics, potentially allowing for mapping of the invader and surrounding plant communities which cannot be accomplished using more conventional multi-spectral imagery.

This study tested the suitability of imaging spectrometer data for improved mapping of a native riparian plant community invaded by Arundo. The research included trials in mapping the major vegetation types in the riparian corridor: riparian woodland, scrub, and annual grasslands. The ability to monitor these vegetation types along with the invasive plant is important for tracking habitat required by endangered species being managed at Camp Pendleton. This work will be useful in future decisions about methods for mapping Arundo and associated riparian vegetation in other regions.

2. METHODS

2.1 Study Site

The Camp Pendleton Marine Corps Base is a 49,857 ha area in northern San Diego County, California, used for Marine Corps military maneuver training (Figure 1). The base contains the largest contiguous stretch of unbuilt coastal land in southern California (Steinitz, 1996). Despite sixty years in service as a ground-troops

[1] Center for Spatial Technologies and Remote Sensing (CSTARS) Department of Land, Air, and Water Resources, University of California, One Shields Ave., Davis, California 95616, USA. Corresponding author: dydipietro@ucdavis.edu

training and practice range, Camp Pendleton contains large areas of relatively intact native habitat. Biodiversity in this region is among the highest in the continental United States; vascular plant diversity on the base exceeds 650 species (Zedler et al., 1997). The Base's high biodiversity and location, abutting the San Mateo Wilderness Area and near the Santa Rosa Plateau Ecological Reserve, and that fact that it encompasses the lower reaches of five watersheds, make it a key component in conservation of the region's ecosystems.

The focal area for this study is the Santa Margarita River, the largest river on the base. The lower 16 of the river's 60 miles lie within the boundaries of Camp Pendleton. This stretch of river is one of the few relatively undisturbed riparian corridors remaining in southern California (Zembal, 1989) and is one of the last strongholds of the federal-listed endangered Least Bell's Vireo, a riparian obligate bird once common throughout California's Central and San Joaquin Valleys and Coast Ranges, and the Mojave Desert (Franzreb, 1989).

The Camp Pendleton Marine Corps Base presents several common problems land managers face in monitoring invasive species and improving habitat condition. The land is managed for multiple uses: military use as well as for the conservation of endangered species. Military training causes large scale and repeated disturbance to environmental conditions which in turn reduces the value of the landscape for future training activities and has consequences for natural systems. The types of mechanical disturbance that a military base experiences, from walking, camping, vehicles, wildfires, soil erosion, detonation of explosives, excavation, and the movement of troops and equipment to and from other parts of the world, provide opportunities for transport and establishment of invasive species.

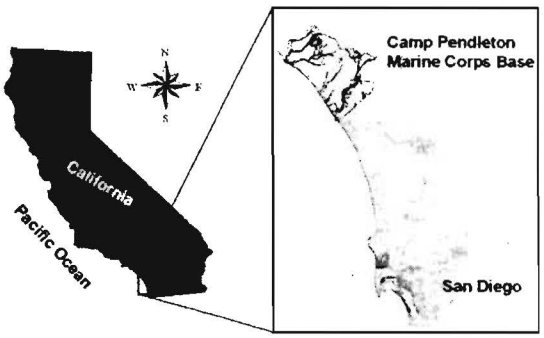

Fig. 1)

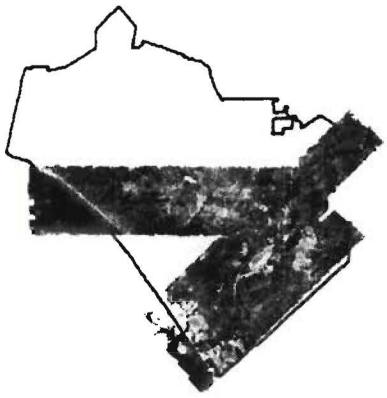

Fig. 2)

Figure 1. Location of Camp Pendleton Marine Corps Base on the southern coast of California.
Figure 2. September 2000 AVIRIS data coverage over Camp Pendleton

2.2 AVIRIS data acquisition and calibration

NASA's low-altitude, high spatial resolution (approximately 4 m x 4 m) Advanced Visible/Infrared Imaging Spectrometer (AVIRIS) data was acquired on 8 September 2000 over portions of Camp Pendleton Marine Base. Eight flightlines composed of 12-14 scenes each were collected (Figure 2) and geometrically corrected by the AVIRIS team at NASA JPL. At the time of the AVIRIS data collection in late summer, deciduous vegetation (such as willow and sycamore) was in full canopy and the giant cane, which becomes senescent during winter months, was near its peak of greenness and active growth. Water to support the riparian vegetation is provided by the baseflow of the Santa Margarita River, largely underground by this time of year, and so it is still in vigorous growth in September despite the late timing in California's summer dry season.

The AVIRIS data was calibrated to surface reflectance using the atmospheric correction program ACORN (Analytical Imaging & Geophysics, Boulder, Colorado) with field calibration spectra for reference. Image analyses were performed using ENVI software (Research Systems, Inc., Boulder, Colorado). The AVIRIS scenes were spectrally subset, georectified, and mosaicked for use in overlays with other geographic data. All analyses were performed on ungeorectified data to avoid error due to changes in pixel spectral properties from warping. A total of 59 noisy bands were removed and a mask was created to select for vegetated areas using a Normalized Difference Vegetation Index (NDVI) of greater than 0.2. The riparian zone was selected using a 100-year flood plain map for Camp Pendleton as the template for a mask. A Minimum Noise Fraction (MNF) transform was performed to

compress and reduce noise in the data and to order the transformed bands by the variability represented in the new bands (Green et al., 1988). MNF bands 1-20 containing 98% of the variance in the dataset were selected for use in the maximum likelihood supervised and spectral angle mapper classification. Reflectance data was also used in spectral angle mapper analysis and in analysis using the continuum removal technique.

2.3 Fieldwork and GPS data collection

This study combined AVIRIS data, aerial photos, field observations, and geographic information systems (GIS) data for the creation of training sets and accuracy assessment polygons. Ancillary data included 1999 1:3,000 aerial photos over selected areas, a riparian vegetation map created in 1997 by drawing field observations onto 1994 aerial photos, recent (2000, 2001) Arundo distribution maps for parts of the river created by the Base to track eradication efforts, and roads, coastline, and base boundary data from the San Diego Association of Governments (SANDAG) and Camp Pendleton's GIS operations office. The 16 aerial photographs provided by the Base were examined under magnification for determination of vegetation existing at the time of the photos.

Forty-four geolocations were recorded during two trips to the study site in September 2000 and September 2001 using a Trimble Pro-XRS (Trimble Navigation, Inc., Sunnyvale, California) global positional system (GPS) receiver providing sub-meter accuracy, and these were associated with notes and hand-drawn maps. Reflectance spectra of several dominant species, Arundo, and calibration targets were collected in the field coincident with the AVIRIS data collection overflight using a GER2600 Spectrometer (Geophysical & Environmental Research, Corp., Millbrook, New York) in continuous 2-11 nm bands across 325-2530 nm. Data were acquired near solar noon and calibrated to reflectance using a Spectralon reference panel (Labsphere, Inc., North Sutton, New Hampshire) for 13 canopy samples with 2-10 replicates each. Locations of the sampling sites were recorded with the GPS. Field spectral readings were compared with reflectance data from atmospherically-corrected AVIRIS data to evaluate the success of the calibration and the validity of the training sets selected (Figure 3). Preliminary classification maps were verified in September 2001 by loading the images onto an iPAQ (Compaq Computer Corp., Houston, Texas) handheld computer connected to the Trimble GPS for direct field validation.

2.4 Classification methods

A 7 km x 1.6 km subset of one flightline over the Santa Margarita River was chosen for its abundance of giant cane (referred to below as Image 1), and pre-processed as described above. Predominant spectral features were evaluated by viewing results from the unsupervised classifications and a display of MNF transform bands 2, 3, and 4. A pixel purity index found few pure pixels, and these were displayed to show spatial arrangement of potential classes in the scene. Seven vegetation types were chosen for classification: Arundo, scrub, riparian woodland, annual grassland, aquatic plants, green lawn, and tamarisk. The Arundo class consists of pure stands of Arundo, with polygons taken from areas of green Arundo as well as stands of more mature, senescent Arundo. The riparian woodland community in this reach of the Santa Margarita River consists primarily of tree willows (*Salix lasiolepis, S. laevigata, and S. gooddingii*), exotic Eucalyptus, and, to a lesser degree, cottonwoods (*Populus fremontii* and *P. balsamifera spp. trichocarpa*), and sycamore (*Platanus racemosa*). The scrub class includes two communities: riparian southern willow scrub dominated by mulefat (*Baccharis salicifolia*) and the shrub-willow *Salix exigua*, with scattered coyote brush (*Baccharis pilularis*), and Diegan coastal sage scrub comprised largely of California sagebrush (*Artemisia californica*) and white sage (*Salvia apiana*). The annual grass vegetation class consists of exotic annual grasses such as ripgut brome (*Bromus diandrus*), slender oat (*Avena barbata*), and wild barley (*Hordeum* spp.) (Hickman, 1993; Zedler et al., 1997). At the time of the image collection in September, annual grassland plants had completed their life cycles and were standing dead biomass. Tamarisk or salt cedar (*Tamarix* spp.) is another harmful invader in riparian areas, and so it was mapped when seen in the field so classifications could be included. The green lawn training set is an area of homogeneous green, irrigated lawn. The aquatic plant class polygons encompass stands of emergent sedges (*Carex* spp.) and rushes (*Juncus* spp.) and mats of microalgae. These last two were selected because they were observed to be confused with Arundo in preliminary, unsupervised classifications.

Regions of interest (ROIs) were created for use as training sets using a combination of field GPS data, field notes and hand-mapped polygons, and 1999 1:3000 aerial photos supplied by the Camp Pendleton Base. ROI polygons were created on an un-georeferenced true-color display of the image data using the GPS coordinates as reference by visually matching features in the un-georeferenced and georeferenced images. Spectral profiles of the vegetation classes, created by averaging values taken from the reflectance image data, are shown in Figure 4. It can

be seen from this comparison that the vegetation types have distinct response patterns across the region of the spectrum sampled by AVIRIS. The tamarisk spectral profile was very close to that of scrub, and was omitted from classifications due to poor results.

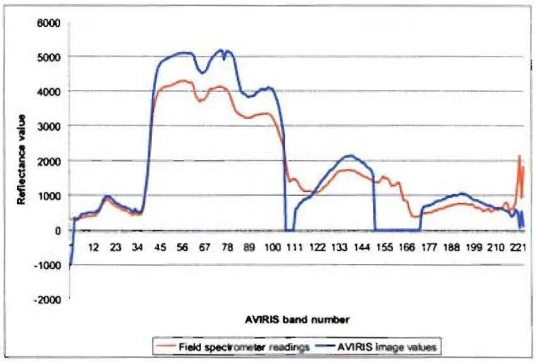

Fig 3)

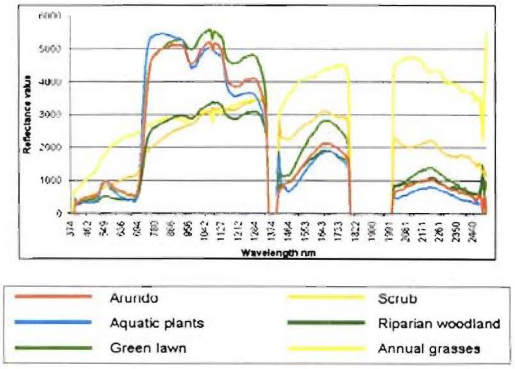

Fig 4)

Figure 3. Comparison of field spectrometer readings and AVIRIS image spectra (averaged values) for Arundo.

Figure 4. Spectral profiles from AVIRIS reflectance data for vegetation training sets (averages of values for all pixels).

Training set ROIs were analyzed for spectral distinctness using the ENVI image processing program's spectral separability calculation, which reports both the Jeffries-Matusita and Transformed Divergence separability measures (Richards, 1994). All were found to have high separability values (close to the highest value of 2.00). Upon examination using the ENVI n-dimensional visualization tool, however, it could be seen that the pixels from the ROIs were not completely unique with regard to the areas in the data space that they occupied. The classes were trimmed using the draw tool in the n-d visualizer, but the use of these spectrally trimmed ROIs did not improve upon classification results.

Polygons for use in validating classification results were digitized over a georectified true-color display of the AVIRIS imagery overlaid with the GPS points, and using the hand-drawn maps and notes from the field, ground photos, 1997 Camp Pendleton riparian vegetation map and 2001 Arundo eradication maps as reference. In total, 209 polygons were created for six vegetation types: Arundo, riparian woodland, scrub, annual grassland, aquatic plants, and tamarisk. The total area covered by these polygons was 68.3 ha, or approximately 15.4% of the 443.9 ha scene being classified. The true-color image, classification results, and validation polygons were co-registered using ground control points taken from a 1:100,000 roads coverage, and the confusion matrix function in ENVI used for quantitative comparison.

Several methods for classifying the image were compared: unsupervised classifications (Isodata and K-means); continuum removal using the water absorption feature at 970 nm with an unsupervised (Isodata) classification; supervised (maximum likelihood) classification using training sets from the image; and spectral angle mapper using training spectra from the image. Analyses were performed on MNF-transformed and reflectance data. Maximum likelihood and spectral angle mapper techniques were also applied to a second image (referred to below as Image 2) using spectra imported from the first image.

3. Results

3.1 Unsupervised classification

Results of unsupervised classifications using K-means and Isodata algorithms with several thresholds provided interesting insights into the spectral and spatial features of the dataset but did not yield results appropriate for use in mapping the desired vegetation types. The results were helpful in the selection of training set ROIs, but comparisons with ground data were too inaccurate to be considered further.

3.2 Continuum removal

The use of the water absorption feature at 970 nm to map the plants in the test image resulted in the identification of giant cane relatively well when it was applied to a scene with only Arundo and terrestrial riparian vegetation species. However, presence of other high water content plants in the image, such as the aquatic plants growing at the edges of the reservoir near the upper edge of the image, resulted in confusion and made this a less than optimal procedure for giant cane mapping (see Figure 5a).

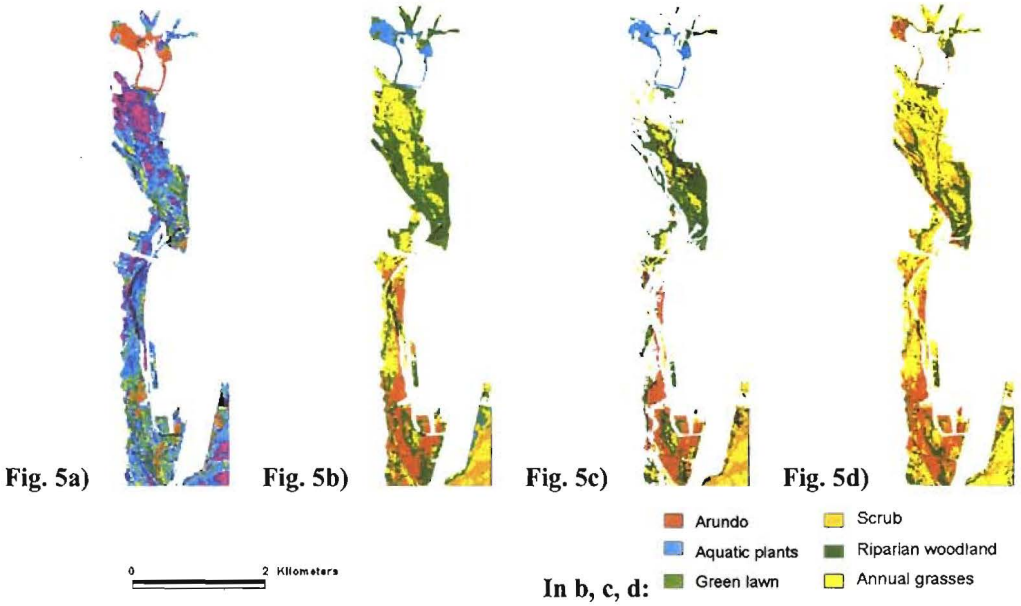

Figure 5. Results from selected classifications of Image 1.

a) continuum removal (5 classes assigned colors from red to blue red=plants with highest water content, blue=plants with lowest water content), b) maximum likelihood on MNF, c) spectral angle mapper on MNF, d) spectral angle mapper on reflectance data.

3.3 Maximum likelihood supervised classification

The maximum likelihood supervised classification performed on MNF transformed data using training sets taken from the same image was very successful in mapping Arundo, annual grasses, and riparian woodland, with less success in classifying the scrub vegetation type. Tamarisk results had a high rate of confusion with scrub, so the tamarisk training data was dropped from subsequent classifications. Figure 5b shows the best result, performed with no threshold. Arundo classified at a 95.27% overall accuracy rate, and annual grasses and aquatic plants classified correctly in 79.78% and 81.82% of the pixels, respectively. The high percentage of successful classification of Arundo, aquatic plants, and annual grassland is to be expected in the classification of the image from which the training sets were taken, as geometric characteristics of the data and the biophysical status of the monotypic Arundo, aquatic plant, and grassland stands are likely to be very similar to those in the training set polygons. The result for riparian woodland, 90.73% correct, however, is surprisingly good considering the range of species and canopy cover possible in that vegetation class. Scrub was confused in 45.01% of the pixels with riparian woodland, and 16.41% of the time with annual grass.

3.4 Spectral angle mapper using reference spectra from the same image

The spectral angle mapper technique, when used on calibrated reflectance data, is relatively insensitive to illumination and albedo effects (Kruse et al., 1993), and can be used with spectra imported from other images or stored in spectral libraries. For these reasons it was considered the most likely to provide repeatable results in different images, possibly both over the same spatial area taken in different years and over different spatial areas.

Spectral angle mapper was applied to both reflectance data (165 bands) and MNF transformed data, which yielded markedly different results. When applied to MNF transformed data (and the reference spectra extracted from the MNF data), an angle of 0.10 radians for all classes only classified a small fraction of the image. The classes began to have reasonable spatial distributions only at very large angles, and the best image was created using a 1.2 radian angle for all classes (Figure 5c). Results were as follows: Arundo mapped correctly in 84.89% of the pixels, and riparian woodland, annual grasses, and aquatic plants success rates were 79.76%, 48.02%, and 71.76%, respectively. Again, the classification of scrub yielded the lowest rate of success at 28.56%.

When reflectance data was used with the SAM method, and the reference spectra were extracted from the reflectance data, an angle of 0.10 radians for all vegetation types classified most of the image. In this case there was significant confusion in both directions between the Arundo and aquatic plant vegetation types. Removing the aquatic plant training set from the process increased confusion with the green lawn class. Figure 5d shows the most successful result, using four vegetation classes with angles of 0.15 radians for four classes: Arundo, scrub, riparian woodland, and annual grasses, and success rates of 70.91%, 42.56%, 64.37%, and 64.67%, respectively.

The MNF-transformed data was also rotated back to image space, and SAM performed using ROIs from the inverted MNF data and from the original reflectance data, and with a variety of angle settings for the different classes. Although the classes displayed good spatial patterns, none of these results classified the vegetation types as well as either SAM with the MNF transformed data or SAM with the reflectance data.

3.5 Maximum likelihood supervised classification of a second image, using imported spectra

The maximum likelihood classifier can accept imported spectral data for use as training sets with which to classify an image. Spectra for Arundo, riparian woodland, scrub, and annual grasses were imported from the first image classified and applied to a 500 m x 800 m section of an image (Image 2) over a lower reach of the Santa Margarita River, acquired in the same overflight but in a different flightline. Image 2 was pre-processed separately from Image 1 (from which the reference spectra were taken). For this classification, 165 bands were used, both from the original reflectance data and from the results of an MNF transform inverted back to image space. Training data from both the reflectance and MNF processed data were applied in various combinations and thresholds. Results were variable; none of the results were good for all classes in one image. In some cases, one or two classes looked reasonable and another completely spurious. In order to find a promising arrangement of training data and thresholds to use on the second image, the first image was classified with its own ROIs after MNF transformation and conversion back to image space. These results were also inconsistent (see discussion).

3.6 SAM classification of a second image using imported spectra

A SAM classification of Image 2 using vegetation spectra imported from reflectance data of Image 1 was performed for five classes: Arundo, riparian woodland, scrub, annual grasses, and aquatic plants. Both the reflectance data and the MNF result converted to image space were classified with the imported spectra. These results were evaluated qualitatively, using the 1997 riparian vegetation map and 1999 aerial photos in visual comparison. Figure 6 shows the resulting maps compared to the 1997 riparian vegetation for that area. A 0.15 radian angle was used in both cases for all classes. The technique applied to reflectance data appears to have worked well for riparian woodland and scrub, but the aquatic plants did not classify at the 0.15 radian angle, even though there are marshes in the floodplain within the image. Inspection of aerial photos from 1999 show that the image created from the reflectance data (Figure 6b) was more accurate for current giant cane distribution than the 1997 riparian vegetation map. The large area mapped as solid cane in the 1997 vegetation map (Figure 6a) appears as a 30-50% mosaic of cane and riparian woodland in the 1999 aerial photos. The cane-infested area along the river channel in the lower part of the image is approximately 50-75% Arundo mixed with riparian woodland in the 1999 aerial photo, and so reflects extensive new growth of the weed since the 1997 vegetation map was made. The result of the classification done with MNF transformed data looks more like the vegetation map (Figure 6c), but

comparison to the aerial photos indicates that it did not produce the best result. This method was also less effective at mapping the other vegetation classes.

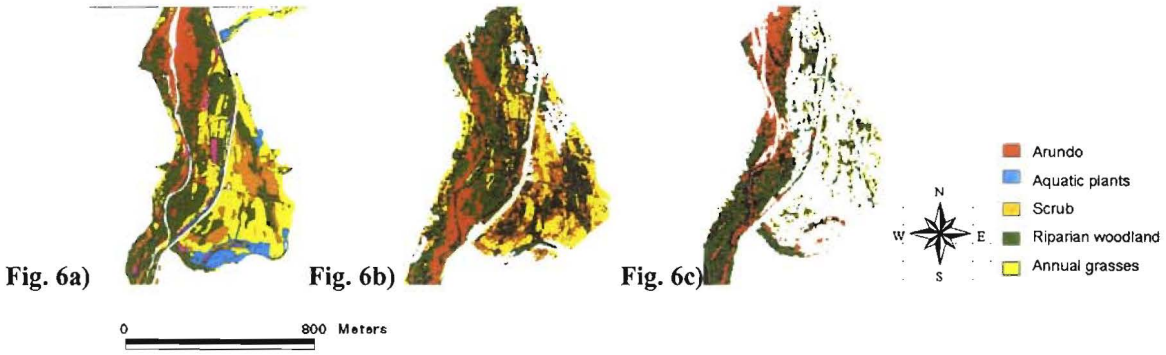

Figure 6. Results of classification of Image 2 using imported spectra.

a) 1997 riparian vegetation map, b) SAM classification of reflectance data using reference spectra of the vegetation types imported from a different image, c) SAM classification of MNF transformed data converted back to image space. The pink polygons in the 1997 riparian vegetation map at left represent tamarisk, but are classified as scrub in image b, as no training data for tamarisk was entered in this analysis.

Results are summarized in Table 1. For the mapping of a single image with training sets from the same image, the maximum likelihood supervised classification gave the best results for all classes. When reference data was applied from one image to the mapping of another, however, the SAM technique performed on reflectance data gave the best results.

Table 1. Summary of Results

IMAGE	METHOD	DATA	TRAINING SETS FROM	RESULTS
Image 1	Maximum Likelihood	MNF	Image 1 MNF	Good: Overall Accuracy= 75.7% Arundo Accuracy= 95.3% Kappa coefficient= 0.69
	SAM	MNF	Image 1 MNF	Good: Overall Accuracy= 61.5% Arundo Accuracy= 84.9% Kappa coefficient= 0.54
	SAM	Reflectance	Image 1 Reflectance	Good: Overall Accuracy=60.2% Arundo Accuracy= 70.9% Kappa coefficient= 0.48
	Maximum Likelihood and SAM	Reversed MNF	Image 1 Reflectance	Poor
Image 2	SAM	Reflectance	Image 1 Reflectance	Good
	SAM	Reversed MNF	Image 1 Reflectance	Poor
	Maximum Likelihood	Reflectance	Image 1 Reflectance	Poor
	Maximum Likelihood	Reversed MNF	Image 1 Reflectance	Poor

4. DISCUSSION

A maximum likelihood classification using training sets from the same image provides an excellent method for mapping vegetation classes, once training sets have been selected and all possible sources of confusion are included as ROIs. The limitation with this method, however, becomes apparent when a map for a larger region comprised of multiple images and flightlines is needed, or for images acquired in different years. The analyst is faced with either needing training sets from every scene or mosaicking the scenes together before any processing occurs. The first option is not likely to be feasible and even defeats the purpose of using a remote sensing approach. The other, that of mosaicking the images, was not practical due to large file sizes and the computing resources necessary to process them together as a single file. In many situations, available images are not contiguous or are collected at different times. A method is needed to classify multiple images for the same classes using training sets imported from one image, or using data from a spectral library. While this is a common practice for geological mapping, mapping vegetation presents challenges in that the spectral response is highly subjective to changes in environmental, climatic, and seasonal parameters.

The spectral angle mapper technique, although less successful than the maximum likelihood classification in mapping Image 1, looks more promising for use with imported reference spectra. The data must be in image space for the use of imported spectra. The use of the MNF transform is helpful for compressing the image data, but presents the challenge of transforming each image differently due to different ranges of variability in the images, thereby making the resulting MNF-transformed data impossible to compare with reference spectra from other images. Converting the data back to image space solves this problem, but there are apparently changes in the data that affect the clustering algorithms. Classifications performed directly on reflectance data provided better results than those performed on MNF transformed data that was converted to image space. This is possibly due to small but important differences in the average spectral responses of different vegetation classes being smoothed out of the data in the MNF noise reduction process, resulting in classes that are less distinct.

The scrub vegetation class presented a challenge with all methods, which confused it most often with riparian woodland. The greatest contributor to this error is probably the inherent variability within the classes in their species compositions and cover densities. It can be seen by examining the spectral response of class pixels using the n-dimensional visualizer that there is some overlap between riparian woodland and scrub, with the riparian woodland class having pixels that respond similarly to those of scrub. It may be possible to improve upon these results by refining the woodland class. Tamarisk classification was poor due to the fact that the canopy was green and neither senescent or flowering at the time of the image, and so failed to provide a significantly distinct enough spectral response to distinguish it as a separate class.

In order to gain insight into the factors contributing to variability in the dataset, statistical information from the MNF transform process was compared to the spectral properties of the vegetation classes to infer the physiochemical characteristics being used to distinguish the classes. During the MNF transform, original bands are first noise-whitened and then transformed to new bands by identifying the principal component vector (Green, 1988). The resulting eigenvectors are then ordered by their information content (i.e., proportion of variance represented) and the contribution of the original bands to these new bands is recorded as an eigenvalue number between 1 and -1 (Research Systems Inc., 1995). Contribution toward the variability in the transform bands is expressed in assigned weightings from zero in either the positive or negative direction. MNF band 1 showed weightings that were evenly distributed across the spectrum, which indicates a heavy contribution of albedo effects in the image rather than from differences in physical or chemical characteristics of the vegetation. MNF bands 2 and 3 are composed of information that is more heavily weighted in the 490-700 nm range than in any other region of the spectrum, indicating strong variability in the spectrally active areas of chlorophyll and other pigments. Also contributing to much of the variability in the data is the near-infrared region. Lower-order bands, such as band 5, show weightings more equally distributed across the spectrum, with contributions in the SWIR becoming more prominent. This is an intuitive result given the absorption properties of various plant and mineral constituents. Unlike broader-band, multispectral data, hyperspectral data provides the spectral resolution to take advantage of these characteristics.

5. CONCLUSIONS

This study shows that the invasive plant *Arundo donax* and associated riparian vegetation types can successfully be mapped using AVIRIS data and with standard imaging spectrometry techniques. However, adequate ground data for part of the area is necessary for development of training set and refinement of the mapping technique, which can then be applied to the larger region. Once selected and refined, training spectra from one image can then be applied to separate images in the same region and for the same year using the spectral angle mapper technique with the angles that gave good results in the original image. The use of the MNF transform may in some cases remove distinguishing features from spectral data and make classification of spectrally similar features less successful.

Despite the need for site-specific information, these techniques show promise as useful tools for evaluating the status of important habitats and the advance (or eradication) of an invasive weed. This is especially applicable in the management of riparian systems because constituent habitat types can change significantly in their spatial extents and distribution in just a few years. More work is needed to discover if spectra can be used in images from different years for the same region for development of a sequence of maps that would allow change analysis, since variations from year to year in the timing of plant phenological stages will certainly be a factor.

6. ACKNOWLEDGEMENTS

The authors would like to thank the following people for their assistance in the field and in the lab with various aspects of this project; without their contributions this project would not have been possible: George Scheer, Karen Olmstead, Mui Lay, and Pablo Zarco-Tejada of CSTARS, and Jason Giessow with the Santa Margarita and San Luis Rey Watersheds Weed Management Area. Funding was provided by the Department of Defense Strategic Environmental Research and Development Program (SERDP).

7. LITERATURE CITED

Avery, T. E. and Berlin, G. L., 1992. Fundamentals of Remote Sensing and Airphoto Interpretation. Macmillan Publishing Co., New York.

Barbour, M., Pavlik, B., Drysdale, F. and Lindstrom, S., 1993. California's Changing Landscapes. California Native Plant Society, Sacramento, California.

Bossard, C., Randall, J. M., Hoshovsky, M. C., 2000. Invasive Plants of California's Wildlands. University of California Press, Berkeley, California.

Franzreb, K. E., 1989. Ecology and Conservation of the Endangered Least Bell's Vireo. 1st edition. U.S. Fish and Wildlife Service, Sacramento, California.

Green, A. A., Berman, M., Switzer, P. and Craig, M. D., 1988. A transformation for ordering multispectral data in terms of image quality with implication for noise removal. IEEE Transactions on Geoscience and Remote Sensing, vol. 26, no. 1, pp. 65-74.

Hickman, J., ed., 1993. The Jepson Manual: Higher Plants of California. University of California Press, Berkeley, California.

Jackson, N. E., Frandsen, P., Douthit, S., (eds.), 1993. *Arundo donax* workshop proceedings. Ontario, California.

Kruse, F. A., Lefkoff, A. B., Boardman, A. B., Heidebracht, K. B., Shapiro, A. T., Barloon, P. J. and Goetz, A. F. H., 1993. The Spectral Image Processing System (SIPS) - interactive visualization and analysis of imaging spectrometer data. Remote Sensing of Environment, vol. 44, no. pp. 145-163.

Omori, G., 1996. Eradicating the giant reed (*Arundo donax*) in riparian areas of Marine Corps Base, Camp Pendleton. California. Agri Chemical & Supply, Inc., Oceanside, California.

Research Systems Inc., 1995. ENVI User's Guide, The Environment for Visualizing Images, Version 3.4. Research Systems, Inc., Boulder, Colorado.

Richards, J. A., 1994. Remote Sensing Digital Image Analysis. Springer-Verlag, Berlin.

Steinitz, C., (ed.), 1996. Biodiversity and Landscape Planning: Alternative Futures for the Region of Camp Pendleton, California. Cambridge.

Zedler, P., DeSimone, S., Giessow, J., Lawson, D., Else, J., Bliss, S., 1997. The Plant Communities of Camp Pendleton Marine Corps Base, California. San Diego State University, San Diego.

Zembal, R., 1989. Riparian Habitat and Breeding Birds Along the Santa Margarita and Santa Ana Rivers of Southern California. *In:* A.A. Schoenherr (ed.), Endangered Plant Communities of Southern California, 15th Annual Symposium, Schoenherr, pp. 98-114. Southern California Botanists, Special Publ. No. 3, Fullerton, California.

DETECTING SPIDER MITE DAMAGE IN COTTON THROUGH SPECTRAL MIXTURE ANALYSIS OF AVIRIS IMAGERY

Glenn J. Fitzgerald[1]
Steve J. Maas[2]
William R. DeTar[3]

Introduction

Few papers have addressed the issue of detection or identification of field-level features in agricultural field crops with hyperspectral remote sensing (Green et al., 1998; Gat et al., 1999). Multispectral images have been used to identify certain field stresses and anomalies such as diseases, weeds, and mites (Brown et al., 1994; Peñuelas et al., 1995; Summy, et al., 1997) but the limited spectral coverage may not allow unique identification, only that an anomaly is present. The large amount of information available for analysis in hyperspectral imagery permits the application of advanced image analysis techniques designed to extract unique data features from high dimensional data sets and reduce complexity to make the data more interpretable. Spectral Mixture Analysis (SMA) assumes that a small number of spectra representing the scene components of interest (endmembers) can describe most of the spectral variation in a scene and be used to "unmix" the pixels and determine the relative fractional abundance of each component on a per-pixel basis. This approach could allow discrimination of one plant stress from another through identification of unique spectral features or differences in the shapes of the spectral curves. The abundance maps produced could indicate both the spatial extent and severity of stresses. This would permit a farm manager or scout to locate precisely the identified stress in a field, providing for guided field scouting and precision application of appropriate control measures such as pesticides or biological control agents. This procedure has been well documented in geological and ecological studies (Adams et al., 1995; Adams and Smith, 1986; Elmore et al., 2000; Mustard, 1993; Okin et al., 2001; Roberts et al., 1993; Roberts et al., 1998; Smith et al., 1990) but has had little to no application in precision agriculture.

The strawberry spider mite, *Tetranychus turkestani* causes severe damage to cotton in the San Joaquin Valley in California. These mites feed on plants causing leaf puckering and reddish discoloration in early stages of infestation and leaf drop later (Anonymous, 1996). Because of the leaf color change, and perhaps physiological changes not visible to the naked eye it was hypothesized that the spectral signature of mite-damaged leaves might provide a method to detect the pest. The objective of this paper was to develop ground-based reference spectral signatures of various scene components (endmembers) in field-grown cotton in order to unmix AVIRIS imagery using spectral mixture analysis and determine if the fraction maps could accurately discriminate between a field of healthy cotton and an adjacent field of mite-damaged cotton. Additionally, it was expected that the SMA procedure would provide endmember abundance fraction maps delivering spatially explicit maps of mite damage severity.

Materials and Methods

An experiment was established on two, 2.8 ha research fields at the USDA-ARS research station in Shafter, CA (35.5° N, 119.3° E., 120 meters above sea level). Each field was planted to cotton (*Gossypium hirsutum* L. variety "Maxxa") on May 4, 1999. Both were managed according to standard cultural practices for cotton in the area except that one (field 41) was sprayed once with a wide spectrum pesticide about eight weeks after planting, virtually eliminating mites as well as beneficial arthropods which normally keep mite populations in check. The other (field 42) was treated with appropriate pesticides several times during the growing season to control spider mite infestations. For reference, Figure 1 shows near-infrared images of fields 41 and 42 acquired from a high resolution multispectral system (Fitzgerald et al., 1999b) and one band from AVIRIS. Weekly mite counts were performed to monitor their temporal and spatial distribution within each of the fields (Anonymous, 1996). Visual

[1] USDA-ARS, U.S. Water Conservation Laboratory, Phoenix, Arizona gfitzgerald@uswcl.ars.ag.gov
[2] Dept. of Plant & Soil Science, Texas Tech University, Lubbock, Texas
[3] USDA-ARS, Western Integrated Cropping Systems Research Unit, Shafter, California

records were kept noting areas of obvious mite damage throughout the season. Both fields were irrigated with sub-surface drip irrigation leaving the soil surface dry all season.

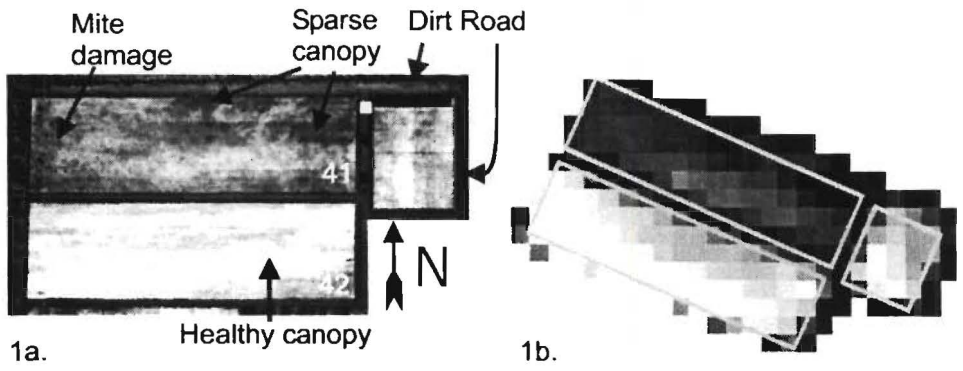

Figure 1a. High resolution (0.65 m) near-infrared image (850 nm) of cotton research fields 41 and 42 acquired on 25 Aug 1999. In field 41, mites were allowed to damage the cotton while in field 42 mites were controlled. Fields 41 and 42 each had dimensions of 100m X 300m. **Figure 1b.** AVIRIS image (band 41, 845 nm, 18 m pixel resolution) of the same fields acquired 28 Aug 1999.

A digital camera system consisting of visible and near-infrared "Varispec" liquid crystal tunable filters (LCTF) from Cambridge Research Instrumentation, Inc., Woburn, MA and a digital camera from PixelVision (Pluto model, 14-bit, cooled, 512 X 512 pixels) were mounted on a high clearance vehicle capable of entering cotton fields with the operator aboard a platform mounted on top. The liquid crystal filters are tuned electronically to allow narrow band wavelengths of light to pass through to the digital camera. The camera shutter and filter are synchronized so that an image is acquired when the filter switches to a new waveband. This system recorded images in 10 nm increments from 400 to 1050 nm. At a height of three meters above the soil, pixel resolution was about one mm. Images were calibrated to reflectance using a 99% "Spectralon" calibration panel which was placed in the field of view before and after image acquisition.

Imagery from AVIRIS was acquired for the research fields on four separate dates in 1999. Flight dates, local times, and solar zenith angle are shown in Table 1. The hyperspectral data cube from AVIRIS was composed of 224 images acquired contiguously from 400-2500 nm in approximately 10 nm bands. The AVIRIS data sets were atmospherically corrected and converted to reflectance using ATREM and EFFORT algorithms. Ground pixel resolution was 18 m.

Table 1. AVIRIS overflight dates, local times (PDT), and solar zenith angles.

Overflight Date	Local Time (PDT)	Solar Zenith
13 Jun 1999	11:29 am	22.7°
28 Aug 1999	12.09 pm	27.9°
1 Sep 1999	10:07 am	49.3°
24 Sep 1999	11:43 am	38.9°

Images acquired from the LCTF system were used to build a spectral library containing representative spectra (endmembers) that included sunlit healthy leaves (H), sunlit mite-damaged leaves (M), sunlit tilled soil (S), shaded tilled soil (Sh), and sunlit dead leaf (D). Pixels from each waveband representing the particular endmember (Fig. 2) were selected to build the spectral library (Fig. 3).

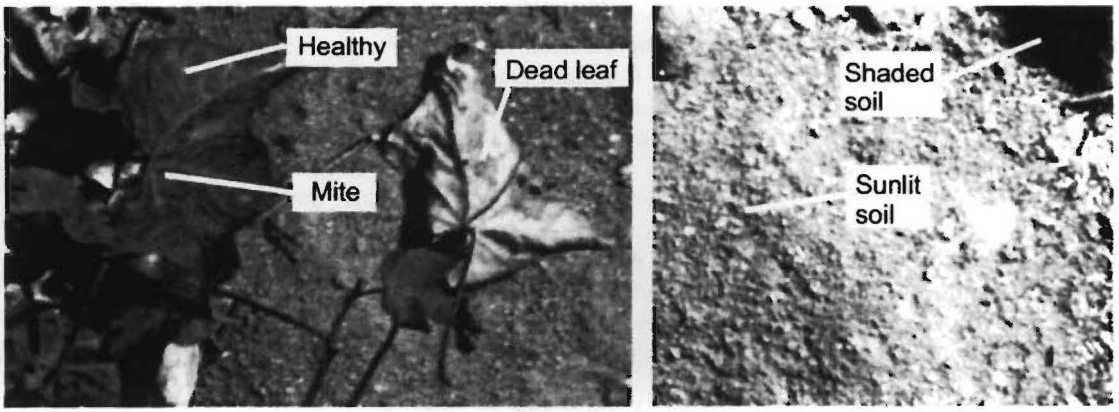

Figure 2. Liquid crystal tunable filter images showing scene components (endmembers). Each image represents about 0.15 m^2 (1.5 ft^2).

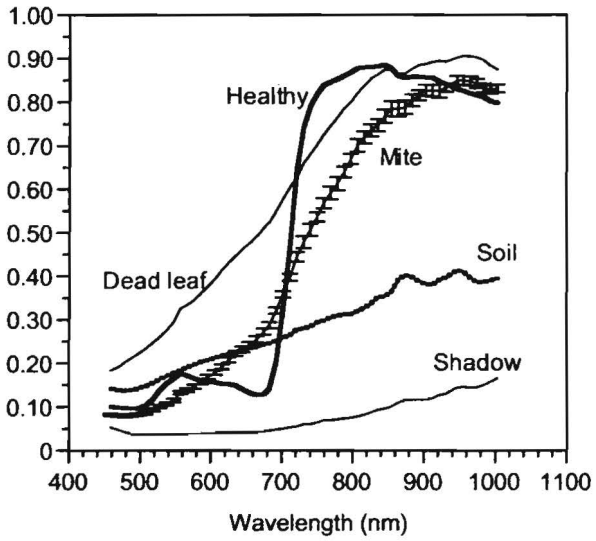

Figure 3. Spectral library endmembers derived from selected regions in the liquid crystal tunable filter imagery (see Figure 2). The error bars on the M endmember line represent ±1 standard error. Standard errors for the other curves were too small to show clearly.

The AVIRIS image cubes were masked to include only the fields of interest and then spectrally resampled to match the wavelengths of the LCTF spectral library. This resulted in 57 wavebands in 9.5 nm increments from 459 to 1002 nm. Spectral mixture analysis was then performed on the four AVIRIS images using the built-in linear spectral unmixing (LSU) routine in the ENVI software package (Better Solutions Consulting, Inc., Lafayette, CO). Analysis parameters were set to constrained unmixing with a weight of 10 which constrained the endmember fractions within each pixel to sum to unity. If the proper endmembers have been chosen for each pixel then the abundance fractions should be positive, the sum of all the abundance fractions (excluding the RMSE image) should equal unity, and the pixels should have a low RMSE (Smith et al., 1990; Roberts et al., 1998).

It was noticed in the fraction images that negative values occurred whenever a pixel contained an endmember that was not present at the time of image acquisition, e.g., pixels chosen over areas of known dense

canopy showed negative soil fractions or pixels from healthy vegetation (field 42) had negative M endmember fractions). Thus, a procedure was developed to assign variable numbers of endmember to the pixels. The criteria for assigning valid endmembers to each pixel was, 1) endmember sign (positive values retained, negative values assigned zero values), and 2) RMSE (whenever models of equal value occurred, the one with the lowest RMSE was selected). The number of potential endmembers was limited because the fields were not as heterogeneous as, say a regional image containing roads, lakes, urban features, etc. as discussed in Roberts et al. (1998). Thus, based on knowledge of the field and the fact that the objective of the study was to identify mite areas only, the five endmembers in Figure 3 were chosen as those representing the bulk of the variance in the fields. The iterative process to choose variable number of endmembers per pixel began with the five endmembers and flagged pixels with negative endmembers. The flagged pixels were re-analyzed with four endmembers, followed by three and two endmember models, consecutively. At each stage, if a set of endmembers was equally valid (e.g., two, three-endmember models contained positive values) then the one with the lowest RMSE was selected. This continued until all pixels were assigned endmembers.

Results

The combination of endmembers that consistently had the lowest RMSE, summed to unity, and correctly located known areas of mite damage, healthy plants, and soil was the combination that included the S, M, H, and Sh endmembers, except for the 13 Jun image that did not include the Mite endmember because mites were not present. Whenever Sh was excluded from the unmixing analysis, the sum of endmember abundances ranged from 0.60 to 0.92. When Sh was included, all pixel abundances summed from 0.99 to 1.00. A spectrum representing dead leaves was initially included in the unmixing procedure to account for non-photosynthesizing vegetation (NPV) but fraction values were always negative so they were excluded from further analysis.

Pixels forming Regions of Interest (ROI) were visually selected for field 41, field 42, and the dirt road around the fields. These represented the mite-damaged canopy, healthy canopy, and soil/dirt road areas, respectively. Table 2 shows the mean values of these regions and Figure 4 shows the abundance image maps indicating the spatial distribution and intensity of these endmembers (bright pixels indicate high abundance fraction values and black pixels equal zero).

Table 2. Fractional abundance means by endmembers for Regions of Interest selected within fields 41, 42, and the dirt roads surrounding the cotton fields. Zero values indicate absence of endmembers.

Field 41	13 Jun 99	28 Aug 99	1 Sep 99	24 Sep 99
Soil	0.650	0.012	0	0.027
Mite	0	0.092	0.010	0.044
Healthy	0.043	0.344	0.240	0.280
Shade	0.307	0.552	0.750	0.649
RMSE	0.018	0.021	0.016	0.015
Field 42				
Soil	0.650	0	0	0
Mite	0	0	0	0.020
Healthy	0.046	0.630	0.400	0.401
Shade	0.304	0.370	0.600	0.579
RMSE	0.019	0.053	0.042	0.027
Road				
Soil	0.882	0.715	0.464	0.576
Mite	0	0	0	0
Healthy	0	0.073	0.049	0.070
Shade	0.117	0.212	0.486	0.354
RMSE	0.027	0.018	0.019	0.015

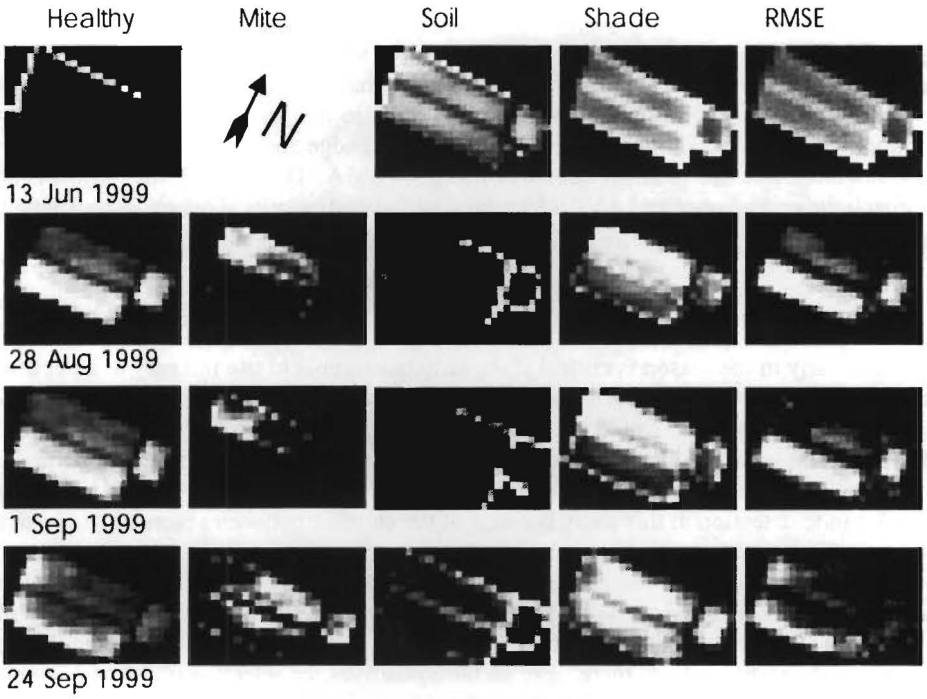

Figure 4. Fractional abundance image maps produced from spectral unmixing of the four AVIRIS image cubes. Highest to lowest values are represented by brightest to darkest pixels. Black pixels have zero value. All values were zero for the M endmember abundance map on 13 Jun 1999.

On 13 Jun 1999, the mean values from the two fields for the four endmembers and RMSE were essentially the same (Table 2). This was expected since mite damage had not yet occurred and all other factors were equal (irrigation, planting date, cultural practices, etc.). By 28 Aug 1999, mites had been present for seven weeks and the unmixing procedure correctly showed that field 41 had mite-damaged cotton plants whereas field 42 did not. Since the 1 Sep 1999 overflight occurred only four days later, little difference should be expected between the two in terms of relative endmember fractions. The differences in endmember fractions noted in Table 2 between the two dates can be attributed to the amount of Sh fraction. The solar zenith angle was much greater for 1 Sep than 28 Aug (Table 1) resulting in a greater Sh component and consequently lower fraction values for the other endmembers. The relative differences however were maintained (H > M > S). Pixels with greater M fraction values were located in the same areas in field 41 on both dates (Fig. 4) showing a consistent pattern.

By 24 Sep 1999, a few weeks before harvest, senescence became a dominant feature. Some pixels in Figure 4 are brighter for the M endmember and darker for the H endmember in field 42. Also, the location of bright pixels for the M images in field 41 (Fig. 4) changed from the previous two dates. When cotton senesces, it tends to form red spots on its leaves. The spectral signature from the reddish senescent vegetation undoubtedly resembled that of the M endmember (Fig. 3).

The S fraction was always greatest for the Road region and non-existent in field 42 once full canopy was established (Table 2). The dirt roads around the fields are clearly identified in the S fractions in Figure 4. Some vegetation was present in the pixels selected for the Road ROI as evidenced by small positive H endmember values in Table 2. This is reasonable since the 18m pixels would have encompassed edges of the fields as well as road.

The Sh endmember pixels were brightest where there was more canopy variability along the edges of the fields and in the mite infested and sparse canopy regions where there was a mix of canopy and soil (Fig. 4). The mean Sh fraction values were always greatest in field 41 and lowest in the Road ROI within a given date (Table 2). This seems to indicate there was more shade in more heterogeneous parts of the scene, a reasonable outcome.

The highest RMSE values occurred for healthy vegetation, for example in field 42 (Table 2, Fig. 4) probably due to calibration errors between the LCTF and AVIRIS imagery. The H endmember spectrum differed somewhat from the healthy canopy spectrum derived from the AVIRIS imagery (not shown). However, shapes of the curves were fundamentally similar showing the characteristic red edge and green peaks. It is likely the greater RMSE for the H endmember was due to imperfect curve fitting by SMA. Despite this, the routine is obviously robust enough to match the endmember and AVIRIS spectra, and overall results show good correlations to known ground conditions.

Discussion

Mite detection early in the season is critical if the farm manager is to use imagery as a decision aid for control. In this respect, these AVIRIS images are not useful since the acquisition times did not correspond to early mite infestations and the large pixel size would not allow early identification of a few mite-infested plants occupying a minute percentage of a pixel, even using SMA techniques. Additionally, under normal farming practices, mite damage would never be allowed to progress to the degree of damage present in field 41. However, these conditions were advantageous for mite detection in this study because of the contrast between severe and light or non-existent mite damage in the two fields and the spatially extensive damage within field 41.

There are several measures of success for the unmixing procedure in this analysis. One, the plant and soil conditions in field 41 and 42 were essentially the same on 13 Jun so it is encouraging to find the mean fraction values for these fields are so similar. Two, there were no false positives for selection of the M endmember in field 42. All M endmembers were selected in field 41. Three, the S fraction consistently was greatest over the dirt road and showed low values in field 41 but was not present in field 42 once full canopy was established. Four, the relative brightness and locations of abundance fractions from 28 Aug and 1 Sep, which were acquired only four days apart, are similar (Fig. 4). However, because the solar zenith angles are different, the abundance fractions are not the same (Table 2). It appears that it can be difficult to compare the abundance fractions across dates. There may be a temporal or non-linear component tied to the shade endmember since this changed with zenith angle and the Sh fraction differed on each date. Perhaps other shade endmembers should have been included in the analysis, such as shaded healthy leaves and shaded mite-damaged leaves.

The LSU procedure in the ENVI software outputs images with the same number of endmembers for every pixel. This is not realistic since there is spatial variability across images not just in terms of quantity (endmember abundance) but also in quality (which endmembers are present). Removing unrealistic (negative) endmembers resulted in pixels with varying numbers of endmembers (2-4) and is similar conceptually to the multiple endmember selection method presented by Roberts et al. (1998). The result shows abundance images that match known ground conditions. This procedure therefore incorporated both spectral and spatial variability. The comparison across four dates allowed a measure of temporal change to be incorporated into the analysis which is critical for agriculture. The resulting images showed both consistent features and explainable changes in the crop (Fig. 4).

In the near future, high spatial resolution hyperspectral imagery will be available that can pinpoint with greater accuracy the locations of stressed plants. Frequent image acquisition would allow temporal changes to be monitored, and early signs of problems could be detected. The utility of hyperspectral remote sensing for precision agriculture comes, in part, from the potential to identify stressed areas in fields early enough for the farm manager to make timely decisions. However, it remains to be seen whether early detection can be accomplished and is, therefore, a fertile area for research.

Disclaimer and Acknowledgments

Mention of specific suppliers of hardware and software in this manuscript is for informative purposes only and does not imply endorsement by the United States Department of Agriculture. Thanks to Nahum Gat at Opto-Knowledge Systems, Inc. for calibrating AVIRIS data, supplying the liquid crystal tunable filter camera system, and technical support.

This research was supported, in part, through the NASA SSC Hyperspectral EOCAP project and a grant from Cotton, Incorporated. AVIRIS flights were provided by the Jet Propulsion Laboratory, Pasadena, California.

Literature Cited

Adams, J.B., and Smith, M.O. (1986), Spectral mixture modeling: A new analysis of rock and soil types at the Viking Lander 1 Site, *J. Geophys. Res.* 91:8098-8112.

Adams, J.B., Sabol, D.E., Kapos, V., Filho, R.A., Roberts, D.A., Smith, M.O., and Gillespie, A.R. (1995), Classification of multispectral images based on fractions of endmembers: Application to land-cover change in the Brazilian Amazon, *Remote. Sens. Environ.* 52:137-154.

Anonymous (1996), Integrated pest management for cotton in the western region of the United States, 2nd edition. University of California, Division of Agriculture and Natural Resources, 164 pgs.

Brown, R.B., Steckler, J.-P.G.A., Anderson, G.W. (1994), Remote sensing for identification of weeds in no-till corn, *Transaction of ASAE* 37:297-302.

Elmore, A.J., Mustard, J.F., Manning, S.J., and Lobell, D.B. (2000), Quantifying vegetation change in semiarid environments: Precision and accuracy of spectral mixture analysis and the normalized difference vegetation index, *Remote Sens. Environ.* 73:87-102.

Fitzgerald, G.J., Maas, S.J. and Detar, W.R. (1999b), Detection of spider mites in cotton using multispectral remote sensing, In *Proc. 17th Biennial Workshop on Color Photography and Ideography in Resource Assessment,* Reno, Nevada, 5-7 May, pp. 77-82.

Gat, N., Erives, H., Maas, S.J., and Fitzgerald, G.J. (1999), Application of low altitude AVIRIS imagery of agricultural fields I the San Joaquin Valley, CA to precision farming, In *Summaries of the 8th JPL Airborne Earth Science Workshop*, (R.O. Green, Ed.), Pasadena, California, 9-11 Feb., pp. 145-150.

Green, R.O., Pavri, B., Roberts, D., and Ustin, S. (1998), Mapping agricultural crops with AVIRIS spectra in Washington State, In *Summaries of the 7th JPL Airborne Earth Science Workshop*, (R.O. Green, Ed.), Pasadena, California, Jan. 12-16, pp. 213-220.

Mustard, J.F. (1993), Relationships of soil, grass, and bedrock over the Kaweah Serpentine Melange through spectral mixture analysis of AVIRIS data, *Remote Sens. Environ.* 44:293-308.

Okin, G.S., Roberts, D.A., Murray, B., and Okin, W.J. (2001), Practical limits on hyperspectral vegetation discrimination in arid and semiarid environments, *Remote Sens. Environ.* 77:212-225.

Peñuelas, J., Filella, I., Lloret, P., Munoz, F., and Vilajeliu, M. (1995), Reflectance assessment of mite effects on apple trees, *Int. J. Remote Sens.* 16(14):2727-2733.

Roberts, D.A., Smith, M.O., and Adams, J.B. (1993), Green vegetation, non-photosynthetic vegetation, and soils in AVIRIS data, *Remote Sens. Environ.* 44:255-269.

Roberts, D.A., Gardner, M., Church, R., Ustin, S., Scheer, G., and Green, R.O. (1998), Mapping Chaparral in the Santa Monica mountains using multiple endmember spectral mixture models, *Remote Sens. Environ.* 65:267-279.

Smith, M.O., Ustin, S.L., Adams, J.B., and Gillespie, A.R. (1990), Vegetation in deserts: I. A regional measure of abundance from multispectral images, *Remote Sens. Environ.* 31:1-26.

Summy, K.R., Everitt, J.H., Escobar, D.E., Alaniz, M.A., and Davis, M.R. (1997), Use of airborne digital video imagery to monitor damage caused by two honeydew-excreting insects on cotton, In Proc. *16th Biennial Workshop on Color Photography and Videography in Resource Assessment*, 29 Apr.-1 May, pp.238-244.

MAPPING FOREST COMPOSITION IN THE CENTRAL APPALACHIANS USING AVIRIS: EFFECTS OF TOPOGRAPHY AND PHENOLOGY

Jane R. Foster and Philip A. Townsend[1]

1. INTRODUCTION

Of the many promising applications of imaging spectroscopy in forest ecosystems is the possibility of mapping species composition and distribution with greater accuracy than is possible using standard multispectral data. In areas with complex forest composition, vegetation mapping with hyperspectral imagery requires methodological approaches that can handle the complex spectral and vegetation data sets. In addition, it requires the careful implementation of image preprocessing routines that reduce the effects of other surface properties that may confound the mapping of forest composition. In this paper, we outline an approach to mapping the distribution of three prominent species in the central Appalachian Mountains using AVIRIS imagery and classification/regression trees. In addition, we evaluate the influence of terrain characteristics on mapping results, and finally compare the utility of spring vs. summer AVIRIS imagery for forest mapping.

2. STUDY AREA AND METHODS

2.1 Study Area

The study area is the 15,700 ha Green Ridge State Forest (GRSF) in western Maryland (Figure 1). GRSF is located in the Ridge and Valley physiographic province of the central Appalachian Mountains, and is characterized by steep mountains with deep valleys. Elevation ranges from 200-700 m. The forests were largely cleared around the turn of the twentieth century, and are now mostly intact and mature. Some scattered clearcuts and selective cuts are located within the study area, but are limited in extent. A few burned areas are also present; however, the largest areas of uneven forest are located in places where gypsy moth defoliation over the last two decades has caused substantial tree mortality. Forests are comprised largely of deciduous oaks, with Virginia pine (*Pinus virginiana*) on some west-facing slopes and hemlock (*Tsuga canadensis*) in some valley bottoms. The key species include white oak (*Quercus alba*), especially on mesic slopes and at lower elevations, red oak (*Quercus rubra*), and chestnut oak (*Quercus prinus*) on ridge tops, high elevations and rocky slopes. The understory is largely open, although blueberry (*Vaccinium spp.*) and the evergreen mountain laurel (*Kalmia latifolia*) can be locally abundant.

Figure 1. Location of Green Ridge State Forest in western Maryland.

2.2 Field Data

Continuous Forest Inventory (CFI) data from the Maryland Department of Natural Resources was used to characterize forest composition. The CFI database includes 436 plots in GRSF, all of which were sampled in 2000 or 2001. Each CFI plot is a 0.2 acre (0.08 ha) circular area on which all trees > 12 cm diameter are identified and measured. The CFI plots are arrayed on a regular grid at approximately 550 m intervals, yielding a statistical sample of the population of forest properties within the study area. We processed the tree diameter data to determine total basal area (TBA) of each plot, as well as basal area by species (SBA) and relative basal area by species (RBA) for each plot. We use RBA as a measure of species abundance at a plot level. All plots were geographically referenced using a Trimble Pathfinder Pro GPS. For this research, we concentrate on the distribution of three of the most common species in the study area: white oak, chestnut oak, and Virginia pine.

[1] University of Maryland Center for Environmental Science, Appalachian Laboratory, Frostburg, Maryland 21532; jfoster@al.umces.edu

2.3 Image Data and Preprocessing

The research presented here uses two AVIRIS images, acquired on 14 May 2000 and 13 July 2001 from an altitude of ~19,900 m (Table 1). The images were atmospherically corrected using the ATmospheric REMoval program (ATREM) (Gao et al. 1993). The AVIRIS imagery exhibited a cross-track view-angle dependent brightness gradient. This gradient of increasing brightness on the west side of the images results from the AVIRIS scan angle and direction, flight path orientation and solar azimuth, and was corrected by fitting a first-order additive quadratic curve to the mean radiance by view angle (Kennedy et al. 1997). The images were georeferenced to UTM coordinates in ENVI using a triangulation method with > 70 GCPs per scene and nearest neighbor resampling. The images exhibited the effects of differential terrain illumination due to the presence of steep north-south trending mountain ridges in the study area. We applied an empirical correction method (Allen 2000, Meyer et al. 1993), which is described in detail elsewhere in this proceedings (Townsend and Foster 2002). One objective of the research presented here is to determine the consequences of terrain normalization on the capability to map forest composition. Mean spectra for a 3 by 3 pixel window around each plot was collected for all plots in the AVIRIS flight line. This resulted in a sample of 331 plots for the 5/14/2000 scene (Figure 2) and 175 plots for the 7/13/2001 scene.

Table 1. Image Characteristics

Sensor	Date	Time (UTC)	Solar Azimuth	Solar Elevation
AVIRIS	5/14/2000	15:42:46	133.8	62.62
AVIRIS	7/13/2001	15:47:47	134.94	66.72

2.4 Image Classification

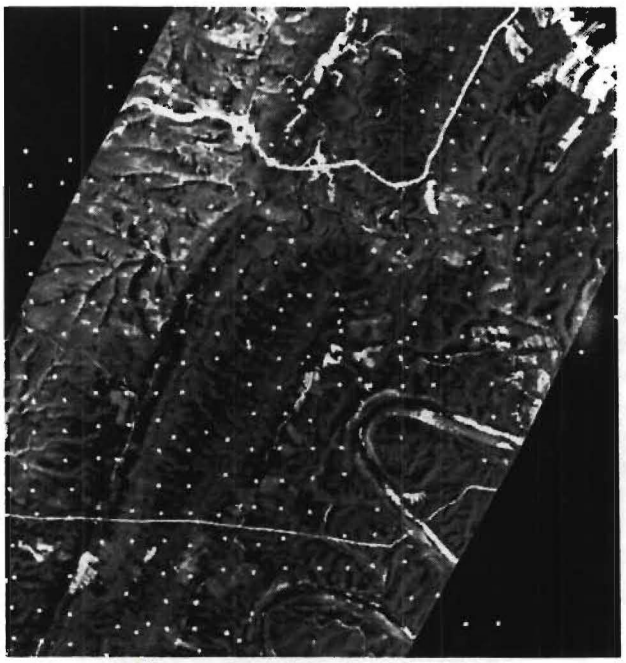

Figure 2. True color 14 May 2000 AVIRIS image of Green Ridge State Forest. White dots indicate locations of CFI plots.

The forests in GRSF exhibit a range of structure and density, with total basal area ranging from recently clear-cut (0) to 60 m^2ha^{-1}. The majority of the forests have BA values between 16-32 m^2ha^{-1}, which is typical for 100-year old forests in the region. However, because gross differences in vegetation structure influence overall reflectance from forested plots, we constrained our analyses to mature, fully stocked forests, i.e., those with TBA > 20 m^2ha^{-1}. This stratification required mapping TBA to delineate forests based on BA; for this, we used multiple stepwise regression (following Townsend 2002) to map TBA as a function of AVIRIS image bands. Following this, we used classification and regression trees (CART) to map composition of individual species. A variety of approaches have been used to map forest composition with hyperspectral data in mountainous landscapes (Martin et al. 1998) and with mixed forests (van Aardt and Wynne 2001), including discriminant analysis and maximum likelihood classifiers. CART is being used increasingly for mapping from remotely sensed imagery (Friedl and Brodley 1997, Friedl et al. 1999, Hess et al. 1995, Simard et al. 2000) and as such is only generally described here. Classification and regression trees (also known as decision trees) are fitted by binary recursive partitioning, in which data sets are consecutively divided into smaller subsets with increasing statistical homogeneity (Clark and Pregibon 1993). Classification trees are used with class data, while regression trees are used to predict continuous data. CART approaches are desirable because they are less sensitive to non-linearities in the input data than methods that require assumptions of Gaussian distributions (as do many image classification techniques) (Clark and Pregibon 1993, Venables and Ripley 1994). In addition, CART is an extremely valuable approach for data exploration when a potentially very large set of independent predictor variable are available, e.g. with hyperspectral data sets. CART can be used to determine the best set of bands for predicting cover characteristics and does not require data reduction, tests for normality or data transformations. One limitation

to CART is that its performance is most robust and repeatable with large data sets, such as the CFI vegetation database that we used. For this work, we used classification trees with relative basal area by species grouped into five categories (A = 0%; B = >0 – 10%; C = 10 – 30%; D = 30 – 50%; E = 50 – 100% RBA). These correspond to abundance levels of none, low, medium, moderate and high. The classification tree models were pruned to avoid overfitting the model to the training data using a cost complexity method designed to minimize misclassified results.

3. PRELIMINARY RESULTS

3.1 Total Plot Basal Area

Total Basal Area (TBA) was best modeled in the corrected 5/14/2000 image using a stepwise linear regression involving 13 image bands with an R^2 of 0.356 ($p < 0.03$). Although the R^2 was not as strong as desired, the relationship was deemed strong enough to subset the AVIRIS image for mapping species composition in mature forests (TBA ≥ 20) using CART. The bands employed in the TBA regression included three in the red portion of the spectrum, one on the red edge, and several in the far end of the near infrared. The regression equation was used to map TBA for the AVIRIS scene, and was then smoothed using a 5x5 median filter to assess the appropriateness of the spatial patterns of TBA created by the model (Figure 3). The map showed relatively low levels of plot BA in recently clear-cut areas throughout the forest, and predicted higher total basal area on mesic slopes grading into valley bottoms. This resulting map exhibits promise for mapping BA, especially because the overall histogram for the distribution of BA on the AVIRIS map matches that from the CFI sample (Figure 4). The prediction of BA from the 13 July image is not shown here. Regression using bands from the July image had an $R^2 < 0.2$. The July image was characterized by fully leafed out forests, which probably obscured some of the variation in TBA on that image.

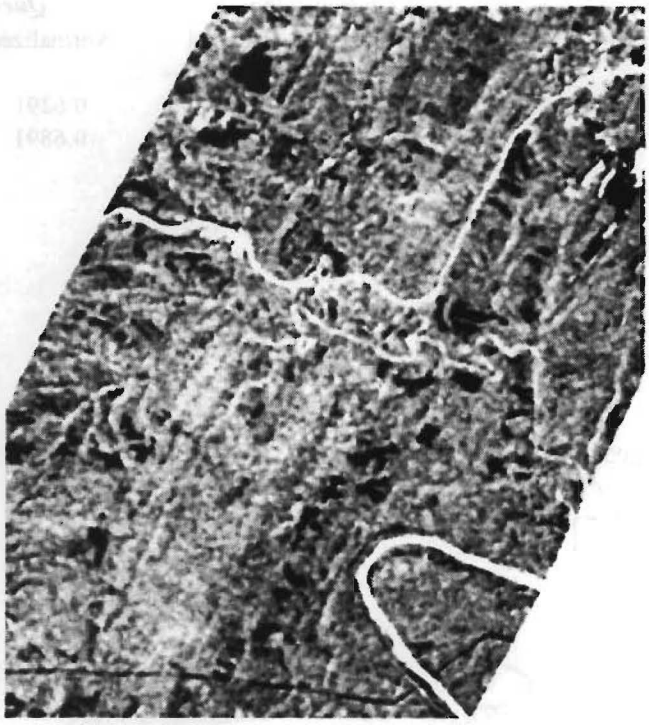

Figure 3. Predicted basal area for forests in Green Ridge State Forest. Gray scale ranges from 0 (black) to > 40 m^2ha^{-1} (white).

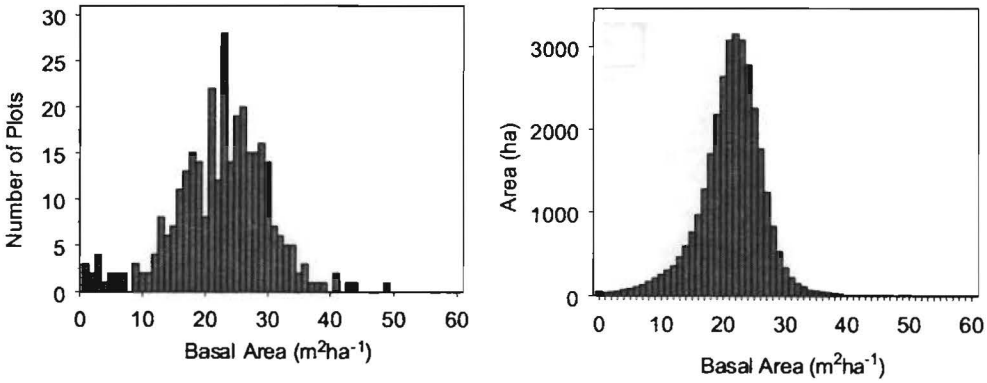

Figure 4. Comparison of the distribution of actual basal area (left) for the CFI plots with predicted BA for the entire study area (right).

3.2 Species Distributions

The results for predicting species abundance classes are listed in Table 2 for each date and for the normalized and non-normalized imagery. The best model for each species is highlighted. An example classification tree for Virginia pine is presented in Figure 5, with the resultant map in Figure 6. The bands used in all of the classification tree models are listed in Table 3.

Table 2. Classification tree results.

	Quercus alba		*Quercus prinus*		*Pinus virginiana*	
Image Date	Normalized	Original	Normalized	Original	Normalized	Original
14 May 2000	0.6009	0.6479	0.6291	0.6479	0.6901	0.6948
13 July 2001	0.6387	**0.6807**	**0.6891**	0.605	0.7479	**0.7563**

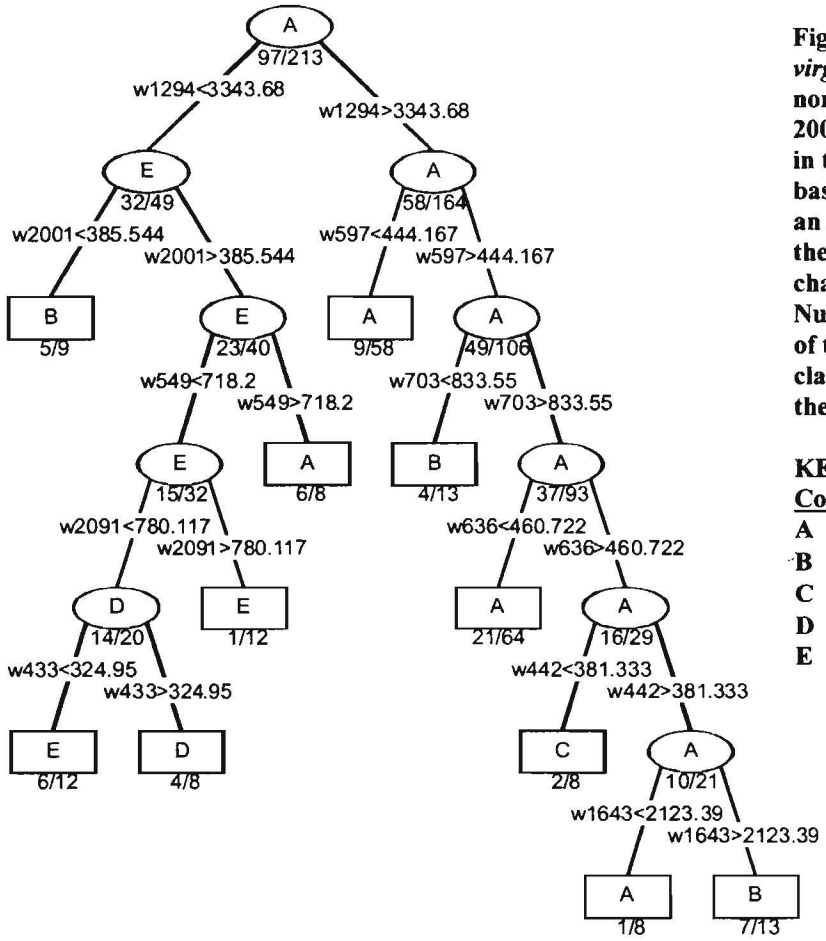

Figure 5. Classification tree for *Pinus virginiana*, generated from the normalized AVIRIS image of 14 May 2000. Each branch delineates a split in the dependent variable (relative basal area of *P. virginiana*) based on an AVIRIS image band (identified by the prefix w, e.g. w1294 = the AVIRIS channel centered on 1294 nm). Numbers below each box (node or leaf of the tree) indicate the mis-classification rate for that branch of the decision tree.

KEY

Code	Description
A	**RBA = 0%**
B	**0% < RBA ≤ 10%**
C	**10% < RBA ≤ 30%**
D	**30% < RBA ≤ 50%**
E	**RBA > 50%**

3.2.1 Effect of Image Date

The classification accuracies for species abundance (i.e., relative basal area) vary from 60-76%. In general, the summer image performed better for predicting the individual species. This probably results from the likelihood that not all of the deciduous trees in the region (including white oak and chestnut oak) were fully leafed out on 14 May 2000, making their detection somewhat problematic. The fact that classification accuracy for Virginia pine was relatively high for both the spring and summer images points to its ease of detection as an evergreen conifer. Note that even though the misclassification rates are high, our classification categories are very specific (*relative*

abundances by species). We consider these results to be very promising for mapping individual species patterns using decision trees. The logical next step to this research is to employ a multitemporal classification to take advantage of the differing reflectance characteristics of each species across seasons.

3.2.2 Topographic Effects

The comparison of models that used terrain normalized imagery versus the uncorrected original imagery yielded mixed results. For chestnut oak, which is typically located along steep slopes and ridge tops, the terrain-normalized imagery produced the best classification of species distribution. This is no surprise, as chestnut oak is typically located on the east and west slopes of the ridges in GRSF. The normalization would therefore be expected to improve the classification of this species by reducing differences in reflectance between illuminated and shadowed slopes. For Virginia pine, there was very little difference between the accuracy of models using normalized imagery and uncorrected imagery. This is likely due to the very distinct reflectance characteristics of Virginia pine, making it easily identifiable regardless of illumination effects. Finally, white oak was best predicted using the uncorrected imagery. This was somewhat of a surprise. However, because white oak generally occurs on gentle slopes, lower slopes and in flat areas, it is possible that the terrain normalization had very little impact on areas where white oak is found, and perhaps introduced some confusion in areas where white oak mixes with other deciduous oaks. Although these results do not provide

Figure 6. Prediction of relative basal area for *P. virginiana*, ranging from 0% (black areas) to > 50% (white). Virginia pine is especially prominent along west-facing slopes of ridges.

Table 3. Bands used in the classification tree models.

5/14/2000 Normalized			5/14/2000 Original			7/13/2001 Normalized			7/13/2001 Original		
QUAL	QUPR	PIVU	QUAL	QUPR	PIVU	QUAL	QUPR	PIVU	QUAL	QUPR	PIVU
452	491	433	433	452	423	451	422	471	432	442	422
529	510	442	510	578	500	461	432	490	451	538	693
655	520	539	549	607	655	741	471	538	529	2010	769
665	529	597	703	694	713	807	558	558	731	2060	1117
703	549	636	713	1155	799	1079	664	567	798	2379	1154
1193	568	703	741	1165	1474	1293	702	674	1135		1254
1444	587	1294	1174	1334	1494	1533	865	1333	1572		2010
1484	703	1643	1454	2001	1514	2020	2180	2020	1632		2060
1623	1334	2001	1533	2011	2001	2389	2270	2349	1772		2379
1792	1444	2091	1633	2021	2330	2438		2419	1782		2419
2041	1494		1703	2031					2309		2438
2211	1524		2011	2151					2438		
2420	2011		2031	2380							
	2191		2231								
	2410										
	2430										

QUAL = *Quercus alba* (white oak)
QUPR = *Quercus prinus* (chestnut oak)
PIVU = *Pinus virginiana* (Virginia pine)

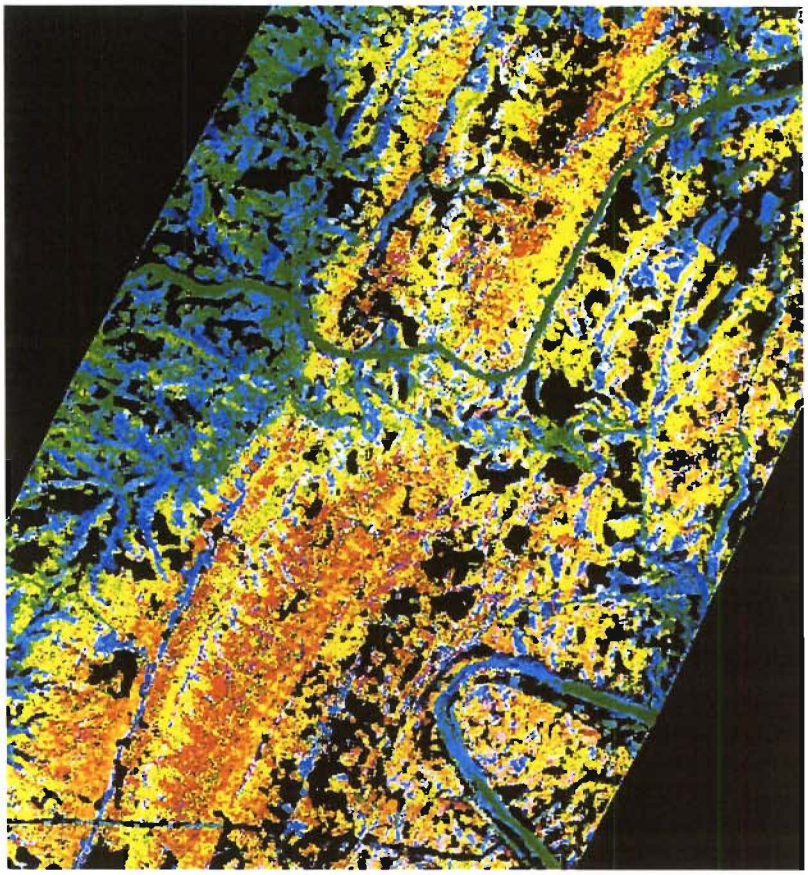

Figure 7. Composite prediction of the distributions of Virginia pine (projected in the blue channel), white oak (green channel), and chestnut oak (red channel). Black areas have TBA < 20 m^2ha^{-1}; the river and interstate are not masked out on this image. Red areas represent ridges and steep slopes dominated by chestnut oak; blue areas are west-facing slopes dominated by pines (and other conifers); green areas are mesic slopes dominated by white oak. Other colors represent mixes.

unequivocal support for the need to implement topographic normalizations, our results do suggest that more research is needed to determine the relative value of terrain normalization for species mapping.

4. CONCLUSIONS

A composite map of species distributions generated from the classification trees yields a map (Figure 7) that closely resembles the actual distributions and dominance of the three species described in this paper. These results represent a promising first step towards the application of AVIRIS imagery for detailed species mapping in rugged terrain. The results were mixed regarding the value of the terrain normalization; however, we expect that a multi-temporal analysis of the normalized AVIRIS imagery will result in improved classification results for all species. Finally, decision trees represent a promising technique for mapping using complex data sets (such as the CFI field data and AVIRIS hyperspectral data), reducing the need for data reduction or data transformation.

5. ACKNOWLEDGMENTS

This research was supported by NASA EO-1 Science Validation Team grant NCC5-493. Thanks to Robert Chastain and Brian Sturtevant for their contributions to this work, and to Chris McCann and the Maryland DNR CFI program for contributing forest data. This paper is Scientific Series Contribution Number 3551-AL, University of Maryland Center for Environmental Science.

6. REFERENCES CITED

Allen, T. R. 2000. Topographic normalization of Landsat Thematic Mapper data in three mountain environments. *Geocarto International* 15: 13-19.

Clark, L. A., and D. Pregibon. 1993. Tree-based models. Pages 377-419 in J. M. Chambers and T. J. Hastie, eds., *Statistical Models in S*. Chapman and Hall, New York.

Friedl, M. A., and C. E. Brodley. 1997. Decision tree classification of land cover from remotely sensed data. *Remote Sensing of Environment* 61: 399-409.

Friedl, M. A., C. E. Brodley, and A. H. Strahler. 1999. Maximizing land cover classification accuracies produced by decision trees at continental to global scales. *IEEE Transactions on Geoscience and Remote Sensing* 37: 969-977.

Gao, B. C., K. B. Heidebrecht, and A. F. H. Goetz. 1993. Derivation of scaled surface reflectances from AVIRIS data. *Remote Sensing of Environment* 44: 165-178.

Hess, L. L., J. M. Melack, S. Filoso, and Y. Wang. 1995. Delineation of inundated area and vegetation along the Amazon floodplain with the SIR-C synthetic aperture radar. *IEEE Transactions on Geoscience and Remote Sensing* 33: 896-904.

Kennedy, R. E., W. B. Cohen, and G. Takao. 1997. Empirical methods to compensate for a view-angle-dependent brightness gradient in AVIRIS imagery. *Remote Sensing of Environment* 62: 277-291.

Martin, M. E., S. D. Newman, J. D. Aber, and R. G. Congalton. 1998. Determining forest species composition using high spectral resolution remote sensing data. *Remote Sensing of Environment* 65: 249-254.

Meyer, P., K. I. Itten, T. Kellenberger, S. Sandmeier, and R. Sandmeier. 1993. Radiometric corrections of topographically induced effects on Landsat TM data in an Alpine environment. *ISPRS Journal of Photogrammetry and Remote Sensing* 48: 17-28.

Simard, M., S. S. Saatchi, and G. De Grandi. 2000. The use of decision tree and multiscale texture for classification of JERS-1 SAR data over tropical forest. *IEEE Transactions on Geoscience and Remote Sensing* 38: 2310-2321.

Townsend, P. A. 2002. Estimating forest structure in wetlands using multi-temporal SAR. *Remote Sensing of Environment* 79: 288-304.

Townsend, P. A., and J. R. Foster. 2002. Terrain normalization of AVIRIS and Hyperion imagery in forested landscapes. In R. O. Green, ed., *Proceedings of the Eleventh JPL Airborne Earth Science Workshop*. JPL, Pasadena, California.

van Aardt, J. A. N., and R. H. Wynne. 2001. Spectral separability among six southern tree species. *Photogrammetric Engineering and Remote Sensing* 67: 1367-1375.

Venables, W. N., and B. D. Ripley. 1994. *Modern Applied Statistics with S-Plus*. Springer-Verlag, New York.

ECOSYSTEM CARBON FLUX IN A DISTURBED, FRAGMENTED SOUTHERN CALIFORNIA LANDSCAPE

John Gamon,[1,2] D. Fuentes,[3] D. Sims,[1,2] S. Houston,[2] A. Moyes,[1,2] H.-L. Qiu,[1,3] W. Oechel[4]

1. BACKGROUND

Humans are altering biogeochemical cycles in many ways. Our activities, through land use change and altered fire frequency, have measurable impacts on biogeochemical cycles, including the photosynthetic and respiratory components of the carbon cycle. Recent policy discussions concerning carbon management (e.g. Kyoto protocol) require that we develop a quantitative understanding of terrestrial carbon fluxes (i.e. the photosynthetic and respiration rates of natural landscapes).

In southern California, activities resulting from human population pressures, including land use change (e.g. urban and suburban development) and altered fire regimes (e.g. arson and fire suppression) are likely to have significant impacts on resource use and carbon flux (photosynthetic and respiratory activity) of terrestrial ecosystems. Assessing human impacts on terrestrial carbon flux is particularly problematic in this region due to fragmented land use patterns, and complex terrain. The typical measurements for directly assessing landscape-scale carbon flux (e.g. eddy covariance) require large, relatively flat and unobstructed regions to work well (Moncreiff et al., 1996). Such methods are difficult or impossible to apply in the fragmented and topographically complex terrain that characterizes much of southern California today.

An alternate method of assessing photosynthetic and respiratory carbon flux is through models derived from remote sensing. For example, a light-use efficiency model is commonly used for assessing photosynthetic carbon uptake by vegetation. Originally presented by Monteith (1977), the typical light use efficiency model expresses net primary production (NPP), or the annual accumulation of carbon via photosynthesis, as the product of two terms, absorbed photosynthetically active radiation (APAR) and the efficiency (ε) with which absorbed radiation is converted to fixed carbon:

$$NPP = \varepsilon \times APAR \qquad \text{(eq. 1)}$$

In this case, efficiency is sometimes treated as a constant for a given biome and is derived from literature values (e.g. Ruimy, 1996). However, many recent studies have demonstrated that light-use efficiency can be quite variable, particularly over the short term (days to months) and for vegetation types exposed to temperature extremes or drought stress, (Running and Nemani, 1988; Gamon et al., 1995). This view of a dynamic light-use efficiency has prompted the exploration of alternate expressions of the light-use efficiency model that are capable of defining photosynthetic activity over a finer range of temporal and spatial scales.

Alternate versions of the light-use efficiency model express instantaneous photosynthetic rate (PS) as a product of absorbed photosynthetically active radiation (APAR) and radiation-use efficiency (ε):

$$PS = \varepsilon \times APAR \qquad \text{(eq. 2)}$$

---

[1] Center for Environmental Analysis (CEA-CREST), California State University, Los Angeles, California 90032 (jgamon@calstatela.edu)
[2] Department of Biological Sciences, California State University, Los Angeles, California 90032
[3] Department of Geography and Urban Analysis, California State University, Los Angeles, California 90032
[4] Global Change Research Group, San Diego State University, San Diego, California 92182

APAR can be further defined as the product of incident light intensity (PAR) and the fraction of incident light that is absorbed by vegetation that is potentially available for photosynthesis (f_{APAR}).

$$APAR = PAR \times f_{APAR} \qquad \text{(eq. 3)}$$

Typically, f_{APAR} is derived from remote sensing using a vegetation index such as the normalized difference vegetation index (NDVI), which is readily available from a wide range of satellite and aircraft instruments (Gamon et al., 1995; Gamon and Qiu, 1999). Incident light intensity (PAR) can be easily obtained from meteorological stations or remote sensing. Thus, evaluation of the APAR term for large landscapes is fairly straightforward. However, evaluation of the efficiency (ε) term in equation 2 is more problematic, and is usually not possible with remote sensing. However, with hyperspectral data, it is often possible to derive ε from narrow-band indices. For example, numerous studies have shown that the photochemical reflectance index (PRI), derived from reflectance at 531 nm and 570 nm can serve as an index of light-use efficiency at leaf and canopy scales (Gamon et al, 1992; Penuelas et al., 1995; Gamon et al., 2001; Stylinski et al., 2002). Recent applications of this index using aircraft remote sensing in the boreal forest have shown some promise for deriving light-use efficiency and photosynthetic rates for whole vegetation stands (Nichol et al., 2000; Rahman et al., 2001). If this approach can be extended to a larger variety of landscapes and vegetation types, including disturbed landscapes, then it could provide a powerful tool for assessing spatial and temporal patterns of photosynthetic activity across different landscapes.

The purpose of this study was to assess patterns of carbon flux in a fragmented southern Californian landscape exhibiting various degrees and types of human disturbance. To do this, we applied a light-use efficiency model to AVIRIS imagery to generate a map of photosynthetic carbon uptake. The AVIRIS imagery was also used to derive a detailed cover-type map that, along with the photosynthesis map, was used to examine the relative productivity of different landscape regions. If this approach can be successfully validated in such a complex and disturbed region, then it could provide a way to improve our understanding of the impact of human land-use change on the carbon cycle.

2. METHODS

2.1 AVIRIS imagery

Low-altitude AVIRIS imagery of the Cheeseboro Canyon region (center longitude and latitude: 34° 9'56" N, 118° 43' 12" W) obtained on Sept 9, 2000, was used for this analysis, yielding a "pixel size" (instantaneous field of view) of approximately 4.3 meters. The images (3.5 AVIRIS scenes from flight # f000909t01p01_r05) were processed to surface reflectance using the commercial software (ACORN, Analytical Imaging and Geophysics LLC, Boulder, Colorado). This region was chosen in part because it contains large holdings of public land (allowing access for field validation) but also because it forms a critical wildlife corridor between the Santa Monica Mountains and the Santa Susana Mountains. Changing human land use in this region, which includes suburban development, roadways and a large landfill, provided the opportunity to examine the impact of diverse land-use patterns and cover types on photosynthetic productivity, expressed as net carbon uptake of different landscape regions.

2.2 Light-use efficiency model

The light use efficiency model was developed using independent measurements primarily collected in a mature chaparral stand at San Diego State University's Sky Oaks Reserve (San Diego County), where measurements of ecosystem photosynthesis, spectral reflectance, and stand structure are underway. At this site, spectral reflectance along a 100-m transect in the vicinity of the eddy covariance sampling was obtained using a field spectrometer (UniSpec DC, PP Systems, Haverhill Massachusetts). Reflectance data were used to model net photosynthesis according to equation 2.

NDVI (table 1) was used to derive f_{APAR} according to the following empirical calibration:

$$f_{APAR} = (NDVI \times 1.25) - 0.135 \qquad \text{(eq. 4)}$$

The values for f_{APAR} were then combined with midday light intensity (PAR, estimated to be 1740 umol m^{-2} s^{-1}) to derive APAR, according to equation 3.

Light use efficiency (ε) was derived from the photochemical reflectance index (PRI, table 1) by calibrating PRI measurements (sampled with spectral reflectance) against whole-ecosystem light-use efficiency (derived from eddy covariance measurements at midday), yielding the following equation:

$$\varepsilon = 0.034 + (PRI \times 0.447) \qquad \text{(eq. 5)}$$

The estimated LUE values were then combined with APAR estimates, as indicated in equation 2, to yield a modeled estimate of net CO_2 flux (i.e. net photosynthetic rate) for all AVIRIS scenes.

2.3 Deriving cover types

AVIRIS scenes were also used to derive a vegetation map for the region. First, a series of reflectance indices (table 1) were derived from the AVIRIS reflectance imagery. The precise bands employed in the index equations were obtained using the linear interpolation option included in ENVI 3.5 (Research Systems Inc., Boulder Colorado). The resulting index images were then combined and used in a maximum likelihood routine to map the distribution of land cover types. We used an existing vegetation map of this region, derived from a spring 1993 Landsat TM image and aerial orthophoto quadrangles (Franklin, 1997), provided by the National Park Service, to identify regions of uniform cover type to use as training sites in the maximum likelihood routine. The identity of these training sites were then confirmed by field visits. The resulting vegetation map was then used to analyze the relative flux rates of different cover classes, as shown in table 2.

Table 1 - Reflectance indices used in this study for vegetation mapping. Indices also used for deriving carbon flux are indicated with an asterisk (*).

Index	Formula	Purpose	Reference
Water Band Index	R_{900}/R_{970}	Vegetation water content	Peñuelas et al., 1993 & 1997
Chlorophyll index	$(R_{750}-R_{705})/(R_{750}+R_{705})$	Vegetation chlorophyll content	Gitelson & Merzlyak, 1994; Gamon & Surfus, 1999
Photochemical reflectance index*	$(R_{531}-R_{570})/(R_{530}+R_{570})$	Photosynthetic light use efficiency	Gamon et al., 1992; Peñuelas et al., 1995; Gamon et al., 2001; Stylinski et al., 2002
Normalized difference water index	$(R_{860}-R_{1240})/(R_{860}+R_{1240})$	Vegetation water content	Gao, 1996
Normalized difference vegetation index*	$(R_{800}-R_{680})/(R_{800}+R_{680})$	Fraction of light absorbed by green vegetation (F_{PAR}), potential photosynthesis	Bartlett et al., 1990; Gamon et al., 1995

3. RESULTS AND DISCUSSION

A comparison between the Landsat-derived map (Franklin, 1997) and the AVIRIS-derived vegetation map is provided in figure 1. Not surprisingly, the AVIRIS-derived map shows a much finer-grained classification due, in part, to the finer pixel size of the low-altitude AVIRIS imagery. Field surveys indicated that, in many locations, the AVIRIS imagery yielded a more accurate map. For example, the

Landsat-derived map indicated large areas of coastal sage scrub (dark green) that were often not present in the field. The AVIRIS imagery indicated that a large part of this region was actually a fairly continuous area of grassland (e.g. the north-south trending light green region in the central part of the AVIRIS-derived map in figure 1). Field surveys indicated that most of this region was indeed dominated by grassland rather than coastal sage scrub. Additionally, new regions of disturbance showed up in the AVIRIS scenes that were not visible in the Landsat-derived map produced a few years earlier. For example, the right side of the AVIRIS-derived map (figure 1) indicated a large region of disturbed land that subsequent field visits proved to be a new suburban construction site dominated by bare soil. Although a quantitative accuracy assessment has yet to be conducted, our qualitative assessment suggested that the AVIRIS map was probably an improvement over the original Landsat-derived map.

Combining information from the vegetation map (figure 1) with the carbon flux map (figure 2) allowed us to evaluate the relative photosynthetic activity of different land cover types (table 2). According to the model (figure 2), oak woodland along riparian corridors exhibited the highest net photosynthetic rate, with all other vegetation types (chaparral, coastal sage scrub, and annual grassland) exhibiting much lower rates (table 2). Lower rates for these vegetation types are consistent with previous studies, and are to be expected at the end of the summer dry season (Gamon et al., 1995). Suburban development, which consisted of a combination of houses, driveways, roads, and irrigated landscapes, exhibited a net photosynthetic rate that was approximately half (48.7%) that of the riparian oak woodland. By contrast, recently disturbed areas exhibited rates that were essentially zero or slightly negative (landfill, new development, and recently burned chaparral). If correct, negative rates would indicate that the land surface was actually a slight source of carbon to the atmosphere. In other words, respiratory activity (carbon loss to the atmosphere) was larger than photosynthetic activity (carbon gain from the atmosphere), leading to a negative *net* photosynthetic rate. However, it should be noted, that these modeled rates have not been validated yet. These relatively small percentage differences in modeled rates between landscape categories could be explained in a variety of ways, and could simply be due to errors inherent in the particular approach (e.g. errors in atmospheric correction or errors in the flux model itself).

Table 2 – relative photosynthetic activity, expressed as maximum midday photosynthetic rate, for selected cover types chosen from the AVIRIS-derived map in figure 1. Photosynthetic rates are derived from the flux image in figure 2, and are expressed as a percent of maximum rates exhibited by oak woodland in riparian corridors.

Landcover classification	**Relative photosynthetic rate (%)**
Riparian	100
Chaparral	16.6
Recently burned chaparral	-1.0
Coastal sage scrub	13.2
Grassland	-2.6
Suburban development	48.7
Disturbed (new development)	-4.9
Disturbed (landfill)	-0.6

This analysis allows us to draw several useful, if tentative, conclusions about the impact of human activity on photosynthetic productivity. Most notably, even in the best of circumstances (well-watered suburban landscapes), the photosynthetic activity of altered landscapes remains a fraction of that of riparian woodland, yet higher than other natural (unbuilt) landscapes. Presumably, surburban vegetation, which is typically heavily irrigated, has relatively high photosynthetic rates. On a leaf-area basis, these rates are most likely similar to those of riparian vegetation similarly exposed to abundant water. However, despite a presumably heavy input of water and fertilizer, the overall photosynthetic rates of suburban developments are only half that of riparian areas. Presumably, this effect is partly due to the large areas devoid of vegetation (e.g. paved areas, rooftops, and other constructed landscapes), in human-derived landscapes. Although not explicitly considered here, further analysis might attempt to examine the "resource-use efficiency" (e.g. water-use efficiency) of different landscape types. An analysis of resource-use efficiency

could take into account water and fertilizer usage in various human-derived landscapes and could compare these to nearby "natural" (unbuilt) landscapes. Such an analysis might be useful for developing strategies to maximize photosynthetic productivity of landscapes with a minimum of resource use.

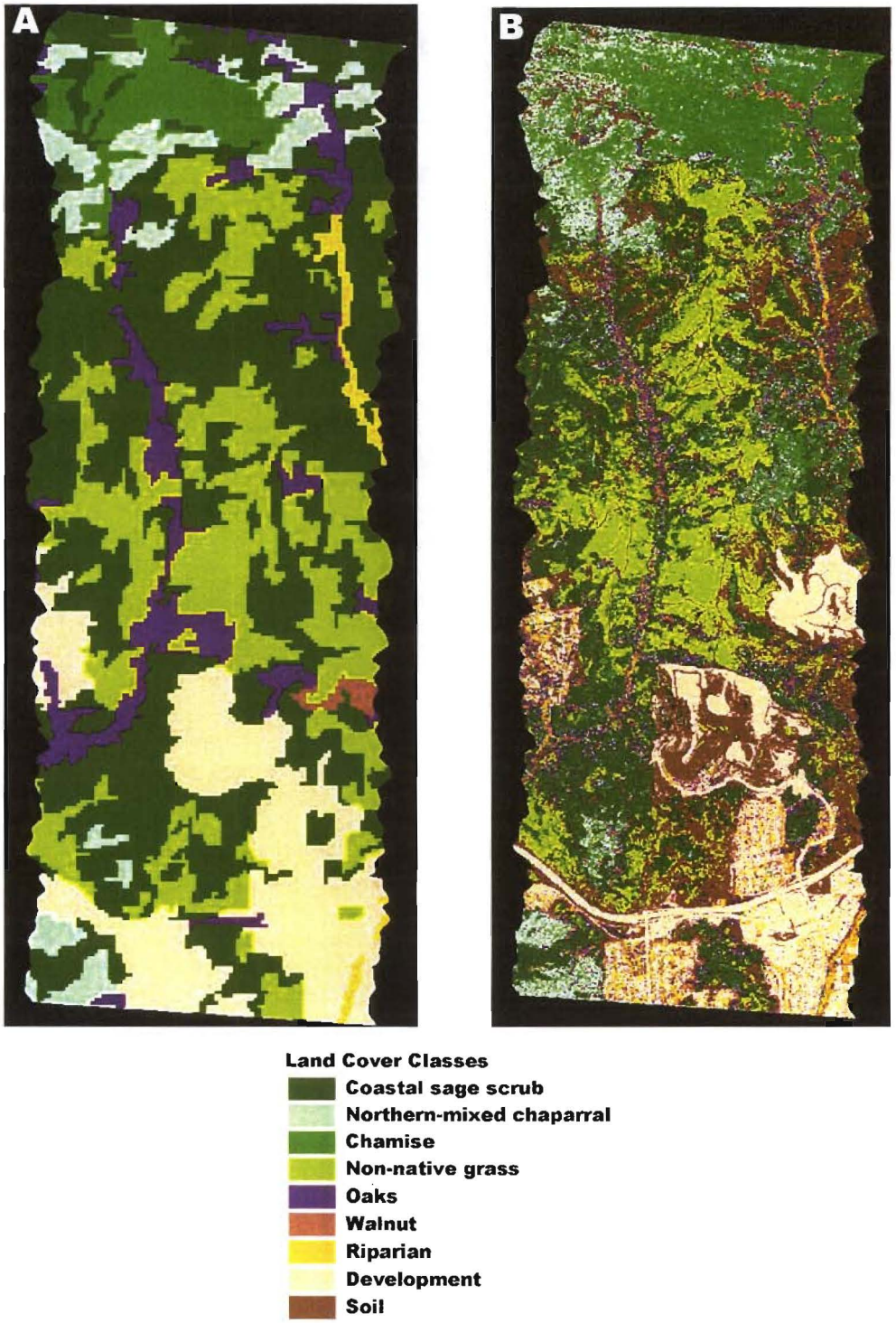

Figure 1 – Landsat-derived vegetation map (A) and AVIRIS-derived vegetation map (B) for Cheeseboro Canyon.

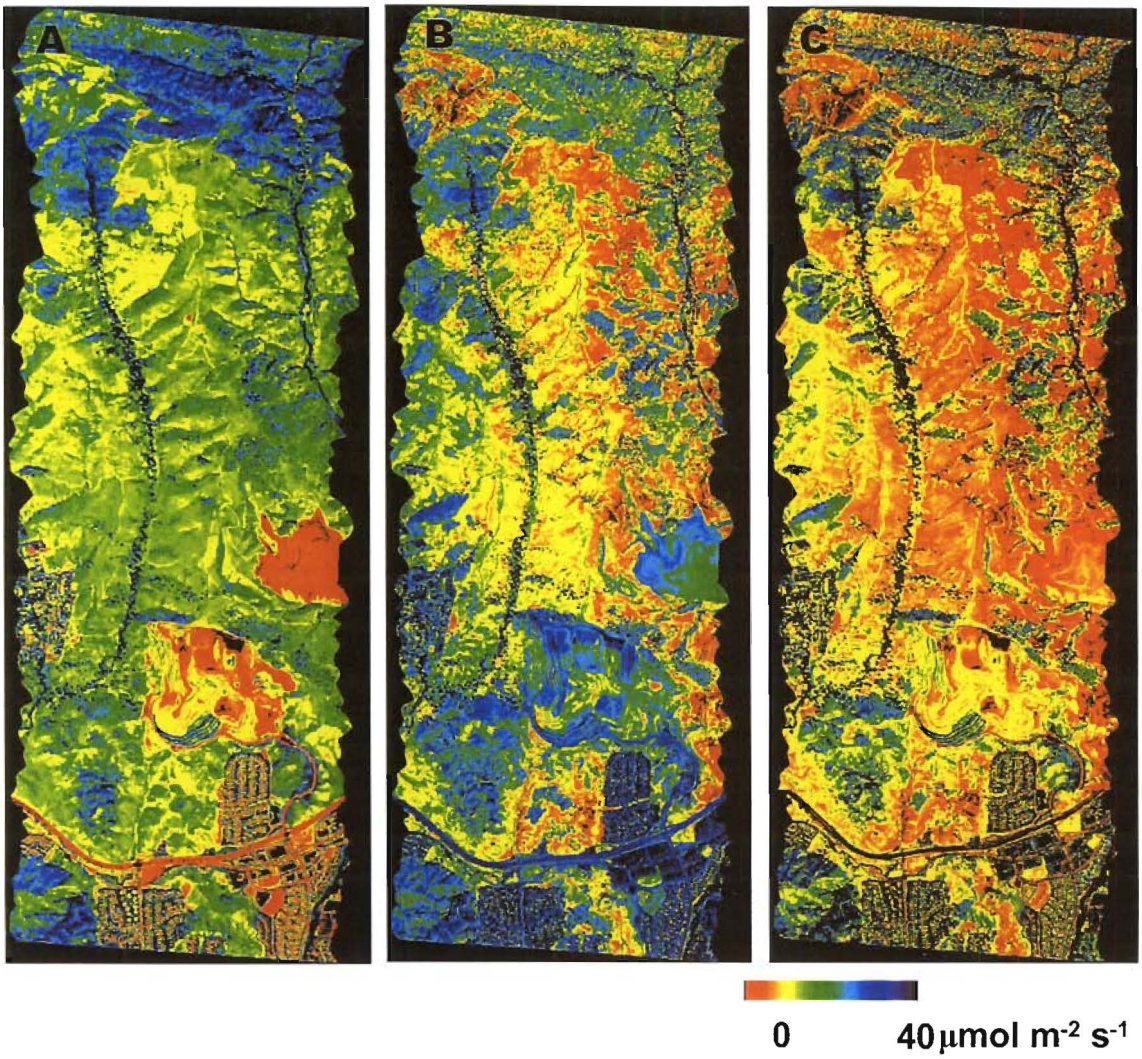

Figure 2 – Images of NDVI (A) and PRI (B) used to derive an image of midday net photosynthetic rate (C) according to the model in equation 2. In panels A and B, red indicates low values, and blue-black indicates high values (similar scale to panel C).

The analysis presented here also illustrates the value of riparian woodland. If our analysis is correct, these regions are far more productive on a land-area basis than all the built landscapes. It is well known that riparian regions also provide critical wildlife habitat, and important corridors for wildlife migration. In the case of this particular region, the riparian corridors provide a potentially critical connection between two large public land holdings, the Santa Monica Mountains, and the Santa Susana Mountains. Part of the attraction to wildlife is undoubtedly a result of its relatively high photosynthetic productivity, which provides food as well as protective cover.

It should be emphasized that the modeled photosynthetic rates reported here have not yet been validated by direct field measurements, and that a thorough validation (e.g. by direct flux measurements), would be difficult or impossible for much of this fragmented landscape, some of which is privately owned. Thus, the photosynthetic rates and conclusions presented here should be considered *hypotheses* to be tested with further study. More work is needed to develop methods of validating this approach in such a complex landscape.

4. CONCLUSIONS

The results presented here demonstrate a method for assessing cover type and photosynthetic productivity for a range of natural and human-disturbed landscapes in southern California, a region heavily impacted by human disturbance. The cover type with the highest photosynthetic productivity was riparian woodland, a cover type that also serves an important function as a wildlife corridor in this region. Suburban development exhibited the next highest photosynthetic productivity (approximately 50% of riparian woodland), but presumably at a large cost in terms of fertilizer and water usage. By contrast, recently disturbed sites (e.g. new developments, landfill, and recently burned chaparral) showed photosynthetic rates that were essentially zero or slightly negative, suggesting a possible source of carbon to the atmosphere. Future work will attempt to validate the methods and conclusions presented here, allowing us a quantitative assessment of human impacts on the carbon budget in this region.

5. ACKNOWLEDGEMENTS

We thank the staff of the Santa Monica Mountains National Recreation Area (National Park Service), for the provision of the Landsat-derived vegetation map and for logistical support in the field. We are grateful to the AVIRIS team for providing the low-altitude AVIRIS imagery. Funding for this work was provided by NSF's CREST program.

6. REFERENCES CITED

Bartlett, D.S., G.J. Whiting, J.M. Hartman, 1990, "Use of Vegetation Indices to Estimate Intercepted Solar Radiation and Net Carbon Dioxide Exchange of a Grass Canopy," Remote Sensing of Environment, vol. 10, pp. 115-128.

Franklin J. (1997) Forest Service Southern California Mapping Project. Task 11. Description and Results. Final Report. Santa Monica Mountains National Recreation Area, National Park Service.

Gamon J.A. and H-L.Qiu, 1999, "Ecological Applications of Remote Sensing at Multiple Scales, in: Handbook of Functional Plant Ecology, F.I. Pugnaire and F. Valladares editors, Marcel Dekker, Inc. New York, pp. 805-846.

Gamon J.A. and J.S. Surfus, 1999, "Assessing Leaf Pigment Content and Activity with a Reflectometer," New Phytologist, vol. 143, pp. 105-117.

Gamon J.A., C.B. Field, A.L. Fredeen, and S. Thayer, 2001, "Assessing photosynthetic downregulation in sunflower stands with an optically-based model," Photosynthesis Research, vol. 67, pp. 113-125.

Gamon J.A., C.B. Field, M. Goulden, K. Griffin, A. Hartley, G. Joel, J. Peñuelas, and R. Valentini, 1995, "Relationships between NDVI, canopy structure, and photosynthetic activity in three Californian vegetation types," Ecological Applications, vol. 5, no. 1, pp. 28-41.

Gamon J.A., J. Peñuelas, and C.B. Field, 1992, "A Narrow-Waveband Spectral Index that Tracks Diurnal Changes in Photosynthetic Efficiency," Remote Sens. of Environ., vol. 41, pp. 35-44.

Gao B.-C., 1996, "NDWI- A Normalized Difference Water Index for Remote Sensing of Vegetation Liquid Water from Space," Remote Sensing of Environment, vol. 58, pp. 257-266.

Gitelson A., and M.N. Merzlyak, 1994, "Spectral Reflectance Changes Associated with Autumn Senescence of *Aesculus hippocastanum* L. and *Acer platanoides* L. Leaves. Spectral Features and Relation to Chlorophyll Estimation," Journal of Plant Physiology, vol. 143, pp. 286-292.

Moncrieff JB, Y. Malhi Y, and R. Leuning, 1996, "The Propagation of Errors in Long-Term Measurements of Land-Atmosphere Fluxes of Carbon and Water," Global Change Biology, vol. 2, pp. 231-240.

Monteith, J.L., 1977, Climate and the Efficiency of Crop Production in Britain, Philosophical Transactions of the Royal Society of London, vol. 281, pp. 277-294.

Nichol C. J., K.F. Huemmrich, T.A. Black, P.G. Jarvis, C.L. Walthall, J. Grace, and F.G. Hall, 2000, "Remote Sensing of Photosynthetic Light Use Efficiency of Boreal Forest. Agric. Forest Meteorol., vol.101, pp. 131-142.

Peñuelas J, I. Filella and J.A. Gamon, 1995, "Assessment of Photosynthetic Radiation-use Efficiency with Spectral Reflectance," New Phytologist, vol. 131, pp. 291-296.

Peñuelas J, I. Filella, C. Biel, L. Serrano, and R. Savé, 1993, "The Reflectance at the 950-970 nm Region as an Indicator of Plant Water Status," International Journal of Remote Sensing, vol.14, pp. 1887-1905.

Peñuelas J, J. Piñol, R. Ogaya, and I. Filella, 1997, "Estimation of Plant Water Concentration by the Reflectance Water Index WI (R900/R970)," International Journal of Remote Sensing, vol. 18, pp. 2869-2875.

Rahman A.F., J.A. Gamon, D.A. Fuentes, D. Roberts and D. Prentiss, 2001, "Modeling Spatially Distributed Ecosystem Flux of Boreal Forests using Hyperspectral Indices from AVIRIS Imagery," J. Geophys. Res., vol. 106 (D24), pp. 33579-33591.

Ruimy A., G. Dedieu, B. Saugier, 1996, "TURC: a Diagnostic Model of Continental Gross Primary Productivity and Net Primary Productivity," Global Biogeochemical Cycles, vol. 10, pp. 269-285.

Running S.W. and R.R. Nemani, 1988, Relating Seasonal Patterns of the AVHRR Vegetation Index to Simulated Photosynthesis and Transpiration of Forests in Different Climates. Remote Sensing of Environment, vol. 24, pp. 347-367.

Stylinski, C.D., J.A. Gamon, and W.C. Oechel, 2002, "Seasonal Patterns of Reflectance Indices, Carotenoid Pigments and Photosynthesis of Evergreen Chaparral Species," Oecologia, vol. 131, pp. 366-374.

A CURVE-FITTING TECHNIQUE TO IMPROVE WAVELENGTH CALIBRATIONS OF IMAGING SPECTROMETER DATA

Bo-Cai Gao,* Marcos J. Montes,† and Curtiss O. Davis‡

1 INTRODUCTION

There are now growing interests in hyperspectral remote sensing for research and applications in a variety of fields, including geology, agriculture, forestry, coastal and inland water studies, environment hazards assessment, and urban studies (Mouroulis et al., 2000). The concept of imaging spectrometry, or hyperspectral imaging, was originated from geological communities in the early 1980s (Goetz et al., 1985), mainly for the purpose of mineral exploration. Imaging spectrometers acquire images in many contiguous narrow channels such that for each picture element (pixel) a complete reflectance or emittance spectrum can be derived from the wavelength region covered. Figure 1 shows an example of a spectrum acquired with the Airborne Visible Infrared Imaging Spectrometer (AVIRIS) (Vane et al., 1993; Green et al., 1998) from an ER-2 aircraft at 20 km altitude. The solar radiation on the Sun-surface-sensor path is subject to absorption and scattering by the atmosphere and the surface. Major atmospheric absorption bands, such as those of water vapor centered at approximately 0.94, 1.14, 1.38, and 1.88 μm, the oxygen band at 0.76 μm, the carbon dioxide bands near 2.01 and 2.06 μm, and a solar Fraunhofer line near 0.43 μm are clearly seen. In order to study surface properties using imaging spectrometer data, the atmospheric absorption and scattering effects must be removed. Several atmospheric correction algorithms (e.g., Gao et al., 1993; Gao and Davis; 1997; Adler-Golden et al., 1998; Qu et al., 2000) for deriving surface reflectances from imaging spectrometer data have been developed in the past decade.

For both the airborne and spaceborne imaging spectrometers, shifts in radiometric and spectral calibrations can occur. Calibration coefficients for all detectors obtained in a laboratory may need to be adjusted when applied to

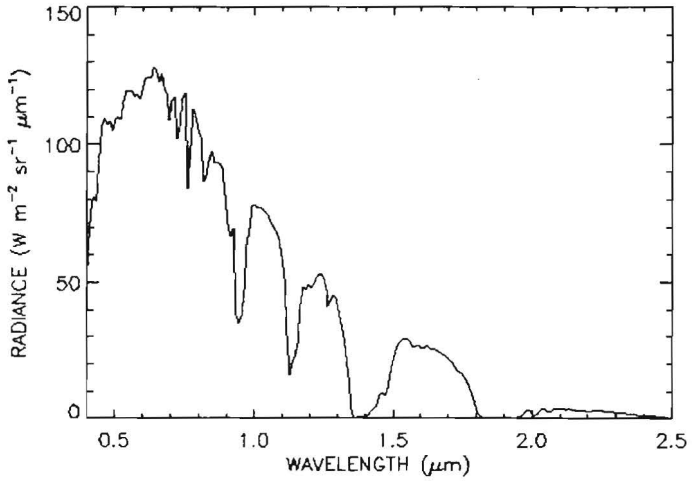

Figure 1: An AVIRIS spectrum showing typical features due to the solar spectrum and gaseous absorption by the terrestrial atmosphere.

* Remote Sensing Division, Code 7212, Naval Research Laboratory, Washington, D.C. 20375; Bo-Cai.Gao@NRL.Navy.mil

† Remote Sensing Division, Code 7212, Naval Research Laboratory, Washington, D.C. 20375; Marcos.Montes@NRL.Navy.mil

‡ Remote Sensing Division, Code 7203, Naval Research Laboratory, Washington, D.C. 20375; Curtiss.Davis@NRL.Navy.mil

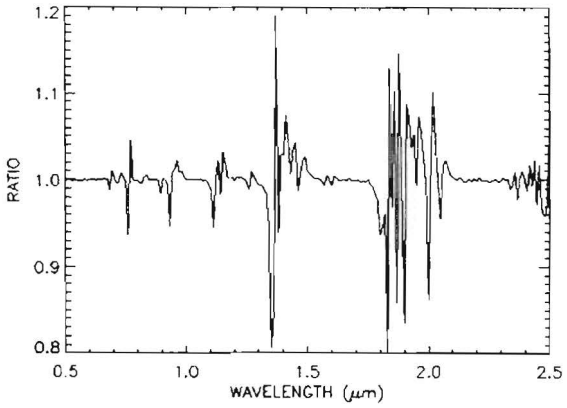

Figure 2: The ratio of two simulated transmission spectra with a spectral resolution of about 10 nm but with a relative wavelength shift of 1 nm between them. Over regions where there are absorption bands of atmospheric gases, the ratio values deviate significantly from 1.0.

data obtained from an aircraft or a satellite platform. Shifts in channel center wavelengths and changes in spectral resolution may occur when an instrument is airborne or spaceborne due to vibrations, and to changes in instrument temperature and pressure. In order to use radiative transfer-based approach to derive surface reflectances from hyperspectral imaging data for improved studies of surface properties, accurate radiometric and spectral calibration to the data must be made (Green, 1998).

Following calibrations, atmospheric correction algorithms are typically applied to imaging spectrometer data to remove the effects of atmospheric gas absorption, and Rayleigh and aerosol scattering (Gao et al., 1993). The atmospheric gas absorption features are very sharp and errors in wavelength calibrations can produce significant errors in the retrieved land or ocean surface reflectances around these features. For the purpose of illustrating the importance of wavelength calibrations, we calculated two spectra at the typical AVIRIS resolution of approximately 10 nm. One spectrum was calculated for the correct wavelengths, and the other with a 1 nm shift in wavelengths for all the channels. Figure 2 shows the ratio of the two spectra. Over regions where there are absorption bands of atmospheric gases, the ratio values deviate significantly from 1. Therefore, small errors in wavelength positions can introduce large errors in the derived reflectance spectra.

In this paper, we describe an algorithm for refining spectral calibrations of imaging spectrometer data. The algorithm is based on spectrum-matching of atmospheric water vapor, oxygen, and carbon dioxide bands, and solar Fraunhofer lines. We then present sample results from applications of the algorithm to data acquired with a few airborne and spaceborne hyperspectral imaging sensors.

2 METHOD

Spectrum-matching techniques (Chang and Shaw, 1977) were developed in the 1970s for retrieving positions and widths of atmospheric gases from laboratory-measured "ultra" spectra (in which individual lines within bands of atmospheric gases are resolved). Later on, a spectrum-matching technique was developed for deriving column atmospheric water vapor amounts (Gao and Goetz, 1990) from hyperspectral imaging data (in which major bands of atmospheric gases are resolved) acquired with the AVIRIS instrument. We have recently developed another spectrum-matching algorithm for refining wavelength calibrations of imaging spectrometer data. This algorithm is based on the matching between measured atmospheric water vapor, oxygen, carbon dioxide bands, and solar Fraunhofer lines with the corresponding calculated bands. The spectral calculations are performed using procedures described by Gao et al. (2000) and Gao and Davis (1997), which utilize high-resolution line-by-line atmosphere transmittance calculations based on the HITRAN 2000 database.[§]

In order to automate the wavelength calibrations of hyperspectral data based on atmospheric or solar Fraunhofer band matching, we assume that the wavelengths of the measured spectrum can shift from –5 nm to +5

[§] Rothman et al., 2001 private communication.

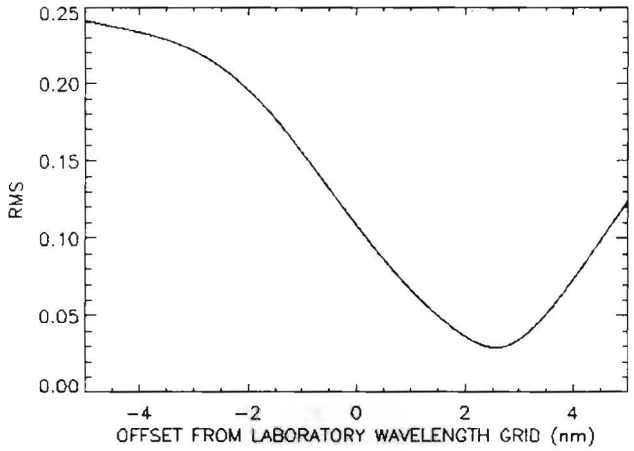

Figure 3: Standard deviation between the laboratory calibration spectra and the modeled spectra as a function of wavelength shift.

nm in steps of 0.01 nm. For each step, we calculate the standard deviation between the measured and the simulated spectrum. Figure 3 shows the standard deviation of matching for a PHILLS (Portable Hyperspecral Imager for Low Light Spectroscopy) spectrum in the vicinity of the 0.76 μm oxygen feature as a function of wavelength shift. A minimum occurs at a wavelength shift of 2.57 nm, so this is considered to be our best estimate of the wavelength shift.

In the case of hyperspectral images measured with sensors built with arrays of area detectors, each across track pixel may have a different wavelength calibration. The spectrum-matching technique described above needs to be applied to each cross track pixel of the data. In our practical applications, we average (in the along track direction) all the spectra of a scene for a particular cross track sample to improve signal-to-noise ratio, and apply the spectrum-matching technique to the averaged spectrum to obtain an estimate of wavelength shift for the column. The process is repeated for every cross track pixel in the imaging scene.

Through theoretical considerations and analysis of measured imaging spectrometer data, we have found that a number of atmospheric and solar bands in the 0.4 – 2.5 μm solar spectral region can be useful for wavelength calibrations using the spectrum-matching technique described above. Specifically, for instruments with a spectral resolution of approximately 10 nm, the atmospheric water vapor bands centered near 0.82, 0.94, 1.14 μm, the oxygen band near 0.76 μm, and the carbon dioxide bands near 1.58 and 2.06 μm can be used for wavelength calibrations. For instruments with a spectral resolution of about 5 nm, an additional solar Fraunhofer line near 0.43 μm becomes useful due to the increased resolving power of the instruments. For instruments having a spectral resolution of 2.5 nm or better, several more solar Fraunhofer lines centered near 0.516, 0.656, 0.854, and 0.863 μm, can be used for wavelength calibrations because of the further increased resolving powers.

3 RESULTS

Our spectrum-matching algorithm has been applied to hyperspectral data collected with several imaging spectrometers for refining wavelength calibrations. Sample results from applications to AVIRIS, PHILLS, and Hyperion data are described below.

3.1 *AVIRIS*

We typically average all the 512 spectra in one along track column of a scene to obtain a spectrum with signal to noise ratios well above 1000 before applying our spectrum-matching technique to AVIRIS data. The spectrum-matching technique is then applied to the averaged spectrum to estimate wavelength shift from the supplied laboratory AVIRIS calibrations. Sample wavelength shifts obtained from an AVIRIS data set are shown in Figure 4. The AVIRIS data used in this study was acquired over the Cuprite (30° 30'N and 117° 10' W) mining district in Nevada on 23 June 1995. The three curves in Fig. 4 are wavelength shifts as a function of sample number (cross track direction). These wavelength shifts are obtained through matching an atmospheric oxygen band near

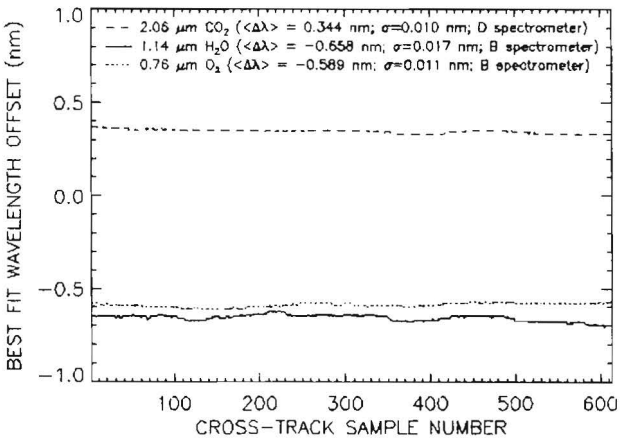

Figure 4. AVIRIS wavelength offsets derived through spectrum-matching of an oxygen band near 0.76 μm, a water vapor band near 1.14 μm, and a carbon dioxide band near 2.06 μm.

0.76 μm, a water vapor band near 1.14 μm, and a carbon dioxide band near 2.06 μm. Both the oxygen and the water vapor bands are located in the wavelength region covered by the Spectrometer B of AVIRIS. The carbon dioxide band is located in the wavelength range covered by the Spectrometer D. The mean of wavelength shifts from fitting the oxygen band for all the samples is –0.589 nm with a standard deviation of 0.011 nm. This mean shift is within the AVIRIS' laboratory wavelength calibration uncertainty of ±1 nm. Because AVIRIS is a scanning instrument, the shift is essentially the same across the scene. The mean shift can be considered to be the best estimate of AVIRIS' wavelength shift based on the oxygen-band-fitting. The standard deviation of 0.012 nm can be considered to be the accuracy using the spectrum-matching technique for wavelength calibrations. The mean wavelength shift obtained from fitting the 1.14-micron water vapor band is –0.658 nm with a standard deviation of 0.017 nm. This mean shift is consistent with the mean shift obtained from fitting the oxygen band. The mean shift derived from fitting the CO_2 band near 2.06 μm is +0.344 nm with a standard deviation of 0.010 nm. The wavelength shift for the Spectrometer D is positive while that for the Spectrometer B is negative. The amounts of shifts are all within the stated AVIRIS' laboratory calibration accuracy of ±1 nm.

3.2 *PHILLS*

Over the past few years the Naval Research Laboratory (NRL) has build a series of PHILLS instruments (Davis, et al., 1999; Davis et al., 2002). All the PHILLS instruments use area arrays in focal planes. The PHILLS instruments have spectral resolution of 1.13 nm per pixel and are typically binned by 4 to 4.52 nm. Data collections

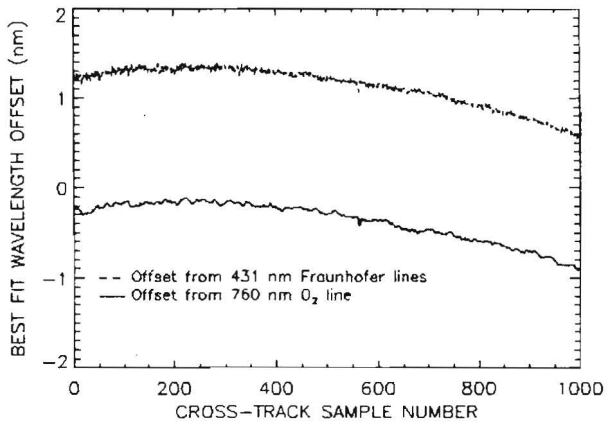

Figure 5: PHILLS wavelength offsets based on fitting an oxygen band near 0.76 μm and a solar band at 0.431 μm.

have been made from low altitude airplane platforms during several field experiments. The temperature and pressure around the PHILLS instruments have not been controlled during the data acquisitions. Our spectrum-matching technique has been applied to the column-averaged PHILLS spectra for estimating wavelength offsets. Sample results obtained from one PHILLS data set are shown in Figure 5. The PHILLS data with a spectral resolution of 4.52 nm were acquired over an area in New Jersey (39°20' N and 74°30' W) on 31 July 2001. The two curves in Fig. 5 are wavelength offsets (as a function of sample number in the cross track direction) derived through matching the oxygen band near 0.76 μm and a solar Fraunhofer line near 0.43 μm. The offset curve from the oxygen band matching shows a difference of about 0.7 nm from left side of the detector array to the right side of the array. This is the result of a combination of spectral smile of about 0.3 nm over 1000 pixels and a tilt of about 0.6 nm over 1000 pixels caused by misalignment between the spectrometer and the camera. The two curves in Fig. 5 have a vertical offset of approximately 1.3 nm, indicating a possible change in light dispersion property for the PHILLS instrument in the aircraft environment.

3.3 *Hyperion*

TRW Space, Defense and Information Systems in Los Angeles, CA built the Hyperion instrument. It is the first spaceborne imaging spectrometer flying on a NASA experimental satellite platform named Earth Observer-1 (EO-1) (Ungar, 1997). This instrument was launched into space in November 2000. It covers the 0.4 – 2.5 μm reflected solar spectral region with more than 220 narrow channels at a spectral sampling spacing of about 10 nm. It has a spatial resolution of 30 m on the ground, and a surface swath width of 7 km (Ungar, 1997). The dashed line in Figure 6 is the curve of center wavelength position for Band 41 as a function of sample number in the satellite cross track direction. The center wavelengths were obtained based on laboratory calibrations of the Hyperion sensor at TRW. Because the center wavelengths depend on the sample number, the "smile" effect is obviously present in the Hyperion sensor. The dotted line in Fig. 6 is a curve of our estimated center wavelength positions based on matching the 0.76 μm oxygen band from one set of Hyperion data acquired over the Cuprite mining district in Nevada on March 1, 2001. This curve is shifted upward by roughly 1 nm in comparison with the laboratory calibration curve. Actually, the amount of shifts depends slightly on the sample number. The solid line in Fig. 6 is our estimates of center wavelengths for Band 41 from another Hyperion data set acquired over the heavily vegetated Coleambally Irrigation Area (39°48' S, 145°39' E) in Australia on March 6, 2001. The shape of this curve is very similar to that of the Cuprite curve. The similarity of the two curves (one from a heavily vegetated area, one from a much less vegetated area) provides evidence that we are correctly accounting for the differing backgrounds in the vicinity of the 0.76 μm feature.

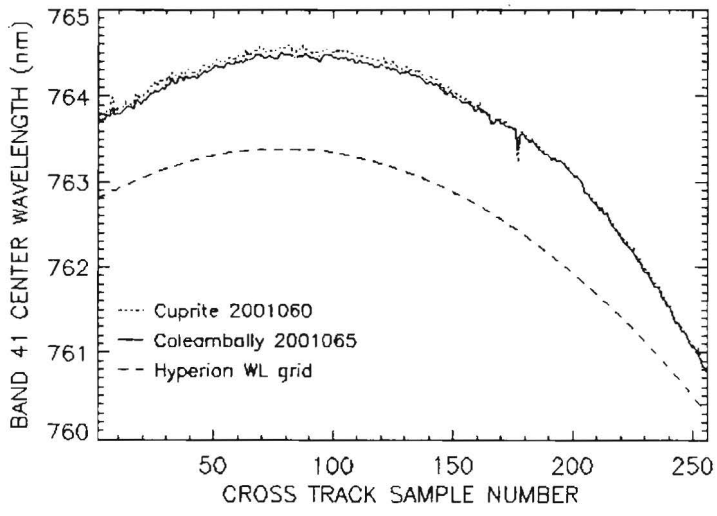

Figure 6: Center wavelengths as a function of sample number in the cross track direction for Channel 41 of the Hyperion instrument obtained from laboratory calibration (dashed line) and retrieved from the Cuprite Hyperion data set (dotted line) and from the Coleambally Hyperion data set (solid line) based on spectrum-matching of the oxygen band near 0.76 μm.

4 DISCUSSIONS

The application of our algorithm to AVIRIS data has demonstrated that the channel positions can be estimated with an accuracy of 0.017 nm or better using our spectrum-matching technique, while the AVIRIS' laboratory calibration uncertainty is about ± 1 nm. Therefore, improved wavelength calibrations can be obtained using the spectrum-matching technique. After adjusting the standard AVIRIS wavelength table based on our results, errors in derived surface reflectance spectra using atmospheric correction algorithms will be decreased significantly, particularly over spectral regions where the atmospheric gas absorption features are strong.

For array spectrometers, the spectral calibration may vary across the scene as a result of spectral smile or misalignment. The applications of our spectrum-matching algorithm to the PHILLS data and Hyperion data have shown that our algorithm is sufficiently accurate to allow the measure of these artifacts. Corrections of these artifacts, in particular the misalignment, are possible for airborne imaging spectrometers.

5 SUMMARY

We have developed a spectrum-matching algorithm for refining the wavelength calibrations of imaging spectrometer data. Atmospheric water vapor, carbon dioxide, oxygen bands, and solar Fraunhofer lines are used for the spectrum matching. The algorithm has been applied to data acquired with the AVIRIS, PHILLS, and Hyperion instruments onboard aircraft or satellite platforms. After the refinement in wavelength calibrations, improved derivation of surface reflectance spectra from hyperspectral imaging data based on radiative transfer modeling can be obtained. Subsequently, better studies of surface properties using the derived surface reflectance spectra can be conducted.

6 ACKNOWLEDGEMENTS

The authors gratefully acknowledge the support of the U.S. Office of Naval Research for this research.

7 REFERENCES

Adler-Golden, S., A. Berk, L. S. Bernstein, S. Richtsmeier, P. K. Acharya, M. W. Matthew, G. P. Anderson, C. L. Allred, L. S. Jeong, and J. H. Chetwynd, 1998, "FLAASH, A MODTRAN4 atmospheric correction package for hyperspectral data retrievals and simulations", *in Proceedings of the Seventh JPL Airborne Earth Science Workshop, Jan. 12 - 16 (Editor: R. O. Green),* JPL Publication 98-21, 1, 9-14, Jet Propul. Lab., Pasadena, CA.

Chang, Y. S., and J. H. Shaw, 1977, "A nonlinear least squares method of determining line intensities and half-widths", Appl. Spectroscopy, 31, 213-220.

Davis, C. O., M. Kappus, J. Bowles, J. Fisher, J. Antoniades, and M. Carney, 1999, "Calibration, characterization and first results with the ocean PHILLS hyperspectral imager", SPIE, 3753, 160-167.

Davis, C. O., J. Bowles, R. A. Leathers, D. Korwan, T. V. Downes, W. A. Snyder, W. J. Rhea, W. Chen, J. Fisher, W. P. Bissett, and R. A. Reisse, 2002, "Ocean PHILLS hyperspectral imager: design, characterization, and calibration", *Optics Express*, 10, 210-221.

Gao, B.-C., and A. F. H. Goetz, 1990, "Column atmospheric water vapor and vegetation liquid water retrievals from airborne imaging spectrometer data", *J. Geophys. Res., 95*, 3549-3564.

Gao, B.-C., K. H. Heidebrecht, and A. F. H. Goetz, 1993, "Derivation of scaled surface reflectances from AVIRIS data," *Remote Sens. Env.*, 44, 165-178.

Gao, B.-C., and C. O. Davis, 1997, "Development of a line-by-line-based atmosphere removal algorithm for airborne and spaceborne imaging spectrometers", in *SPIE Proceedings, Vol. 3118*, 132-141.

Gao, B.-C., M. J. Montes, Z. Ahmad, and C. O. Davis, 2000, "Atmospheric correction algorithm for hyperspectral remote sensing of ocean color from space", Appl. Opt., 39, 887-896.

Goetz, A. F. H., G. Vane, J. Solomon, and B. N. Rock, 1985, "Imaging spectrometry for earth remote sensing," *Science, 228*, 1147-1153.

Green, R. O., M. L. Eastwood, C. M. Sarture, T. G. Chrien, M. Aronsson, B. J. Chippendale, J. A. Faust, B. E. Parvi, C. J. Chovit, M. Solis, M. R. Olah, and O. Williams, 1998, "Imaging spectrometry and the Airborne Visible/Infrared Imaging Spectrometer (AVIRIS)", Remote Sens. Env., 65, 227-248.

Green, R. O. , 1998, "Spectral calibration requirement for Earth-looking imaging spectrometers in the solar-reflected spectrum", Appl. Opt., 683-690.

Mouroulis, P., R. O. Green, and T. G. Chrien, 2000, "Design of pushbroom imaging spectrometers for optimum recovery of spectroscopic and spatial information", Appl. Opt., 39, 2210-2220.

Qu, Z., A. F. H. Goetz, and K. B. Heidebrecht, 2000, "High accuracy atmospheric correction for hyperspectral data (HATCH)", in Proceedings of the *Ninth JPL Airborne Earth Science Workshop, Feb. 23 - 25 (Editor: R. O. Green),* JPL Publication 00-18, 1, 373-380, Jet Propul. Lab., Pasadena, CA.

Ungar, S. G. , 1997, "Technologies for future Landsat missions", Photogarm. Eng. & Remote Sens., 63, 901-905.

Vane, G., R. O. Green, T. G. Chrien, H. T. Enmark, E. G. Hansen, and W. M. Porter, 1993, "The Airborne Visible/Infrared Imaging Spectrometer," *Remote Sens. Env., 44*, 127-143.

ACQUISITION OF UNDERWATER REFLECTANCE MEASUREMENTS AS GROUND TRUTH

James A. Goodman[1] and Susan L. Ustin

1. INTRODUCTION

Work is being performed to establish effective quantitative methods for the mapping, monitoring and assessment of coral reef ecosystems using hyperspectral remote sensing. Specifically, imagery acquired over the Hawaiian Islands by NASA's Airborne Visible InfraRed Imaging Spectrometer (AVIRIS) is being used to develop, apply and evaluate algorithms for analyzing coral reefs using airborne hyperspectral data. The imagery was obtained during two separate AVIRIS deployments to Hawaii, one in April 2000 and another in October 2001. The coral ecosystems covered in these deployments exhibit conditions ranging from significantly human impacted reefs in the Main Hawaiian Islands to the relatively pristine coral environments of the Northwestern Islands. In addition to this significant spatial coverage, the deployments also provide temporal coverage through repeat acquisition of select study areas. Of these locations, the primary study area being used for this research is Kaneohe Bay on the windward shore of Oahu (Figure 1). This area provides many advantages as a model system for developing algorithms, including ease of accessibility for fieldwork, a wealth of supporting research literature and limited species diversity. The bay also exhibits a significant range in habitat health, from coral-dominated to algae-dominated, thereby allowing evaluations of algorithm effectiveness in identifying such differences.

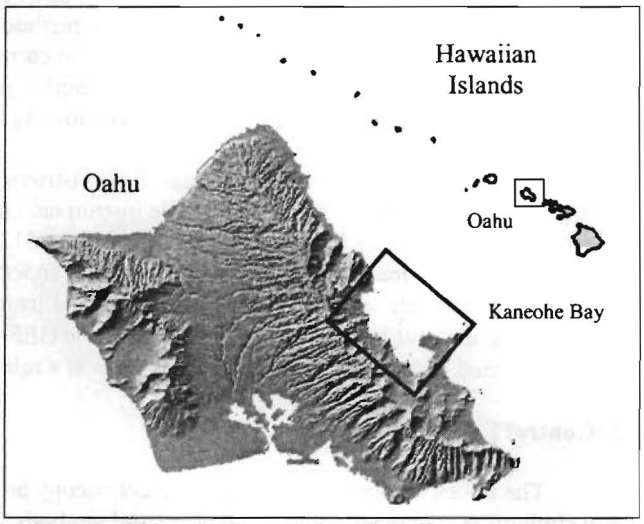

Figure 1. Kaneohe Bay, Oahu, Hawaii.

As an evolving field in remote sensing, hyperspectral analysis of benthic environments still requires many technical developments prior to reaching a comprehensive level of image classification and analysis. The confounding influences of varying water column properties and the complex mosaics of coral species create many technical challenges and physical limitations for applications of remote sensing in benthic habitats (Dustan et al., 2000; Holden and LeDrew, 1998; Lubin et al., 2001). Furthermore, there is an observed deficiency in accepted standard methods for acquiring field spectral measurements. As such, an early focus of this research project has been to examine traditional terrestrial hyperspectral techniques, particularly acquisition of field reflectance measurements, and adapt those methods for application in an underwater environment. Presented below is a description of the field instrument selected for this task, a summary of the field methods developed using a set of control experiments, and an illustration of reflectance results obtained in Kaneohe Bay for coral, algae and benthic calibration targets.

2. METHODS

As support for hyperspectral analysis, field spectroscopy plays an important role in characterizing the reflectance properties of the individual components comprising an image. The *in situ* data supplied by these field measurements provide valuable information with which to compare, calibrate, and analyze data obtained by the sensor. Field-portable spectroradiometers are commonly used in terrestrial hyperspectral analysis to measure the reflectance of target areas for use in image calibration, develop spectral libraries for image analysis, and identify suitable endmembers for use in classification algorithms (Milton, 1987; Salisbury, 1998). Similar methods are being used in the underwater environment; however, as of yet, no standard has been developed.

[1] Center for Spatial Technologies and Remote Sensing (CSTARS), Department of Land, Air and Water Resources, University of California, Davis (jagoodman@ucdavis.edu).

2.1 Instrument

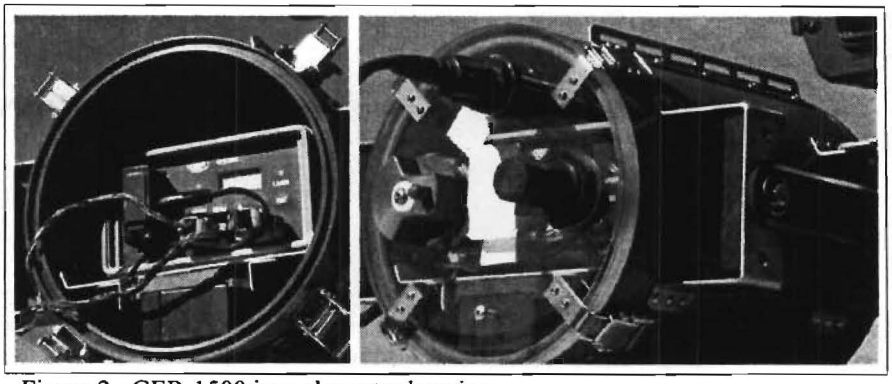

Figure 2. GER-1500 in underwater housing.

The fundamental starting point for acquiring underwater spectral measurements was to select a suitable instrument for the task. Although subsurface spectra are acquired for a variety of scientific purposes and appropriate instruments have been developed for these investigations, diver-portable spectroradiometers are less common. In the interest of cost and instrument availability, it was decided to modify a field-portable GER-1500 spectroradiometer for use in the underwater environment. Selecting this instrument, as opposed to a specifically designed underwater unit, has the advantage of maintaining the ability to use the instrument outside of its housing for acquiring measurements of terrestrial targets. While one option is to leave the instrument on the surface (typically in a small boat) and simply utilize the fiber optic cable underwater (Hochberg and Atkinson, 2000; Holden and LeDrew, 1998; Holden and LeDrew, 2001), this method has the disadvantages of a limited range and depth in which spectra can be acquired, as well as difficulties in communication between the diver and the instrument operator located on the surface. Thus, the design selection used here was to completely enclose the GER-1500 in a custom underwater housing with external controls allowing full operation of the instrument by a diver (Figure 2).

The GER-1500 is a reasonably small field instrument with the ability to function in a stand-alone mode of operation. This mode allows full access to the instrument controls, as well as an internal memory capacity for storing field data. It has a silicon diode array measuring 512 spectral bands in the region from 350 to 1050 nm with a resolution of approximately 1.5 nm. Aside from the underwater housing itself, modifications included a larger capacity battery for extended life between charging and instrument adjustments to allow operation from external controls on the underwater housing. In addition to the GER-1500, a 10 inch Spectralon® 99% diffuse reflectance panel was carried underwater with the diver for use as a reference standard.

2.2 Control Experiments

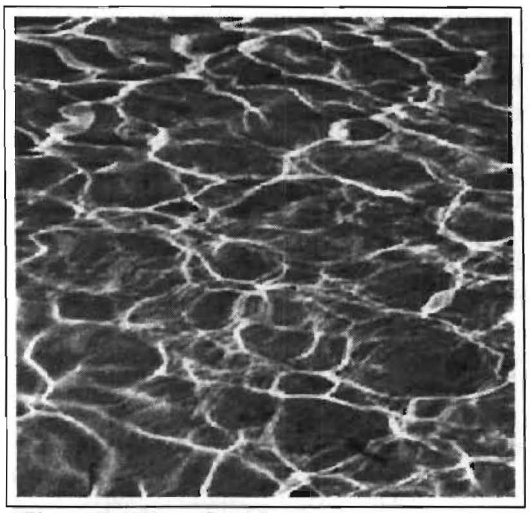

Figure 3. Wave-focusing.

The issues involved in underwater spectroscopy have many similarities to already established terrestrial methods, but there are a few important differences. Unlike terrestrial conditions, the presence of a water column, which separates both the airborne sensor and field instrument from the features being measured, introduces significant variations in the light field that must be brought into consideration. Of most importance was the effect of wave-focusing (Figure 3), which is a function of the sea surface state and manifests itself as a rapidly fluctuating underwater light field. Surface waves also inherently exhibit differing heights and orientations, which result in changing path lengths for downwelling irradiance as well as varying illumination angles due to refraction. Thus, the presence of surface waves, which occurs on all but the rarest of windless days in the field, greatly complicates the ability to achieve uniform illumination conditions for both reference and target measurements. A set of control experiments were performed using the above described underwater field spectroradiometer to develop a field methodology to account for these illumination issues and thereby minimize errors introduced by environmental fluctuations (Goodman and Ustin, 2002). Different lighting conditions and instrument settings were used to establish the reliability of obtaining field spectra under variable situations. Experiments were performed in a controlled pool environment at the Bodega Marine Laboratory of the University of California, Davis. Results from these experiments indicated the utility of acquiring field reflectance

measurements by creating diffuse lighting conditions (achieved by shading the target of interest) during both measurement of the reference standard and the target surface.

Figure 4. Underwater measurement.

2.3 Field Measurements

Results obtained from the control experiments were utilized to develop a measurement protocol for acquiring underwater field reflectance data. The diver making the spectral measurements floats over the bottom target or reference panel to produce shaded conditions during data acquisition (Figure 4). For consistency, all measurements are acquired from a distance of 30 cm from the subject. Additionally, the spectroradiometer is set to average three measurements per reading and each reference reading is quickly followed by five readings of the selected target. This protocol was applied during two separate visits to Kaneohe Bay to obtain *in situ* measurements of sand, rubble, coral and algae. Supporting data obtained in the field included time of measurement, water depth, photographic record and WAAS-corrected GPS location. The first visit corresponded with the October 2001 AVIRIS deployment to Hawaii and was undertaken with the express purpose of acquiring field data coincident with the AVIRIS overflight of Kaneohe Bay. The second visit was completed in April of 2002 in order to obtain field data at the same time of year as the earlier acquired AVIRIS imagery in 2000. This data is being used to investigate potential seasonal differences in the reflectance data (e.g., physical and physiological differences in the targets and as a function of seasonal differences in illumination characteristics), as well as expand on the spatial coverage of the field data.

3. RESULTS

3.1 Coral and Algae

The methods employed in the field data collection were designed to minimize errors in underwater reflectance measurements resulting from the inherent variability of lighting conditions. Thus, it can be inferred that the resulting spectral characteristics of each target can be attributed primarily to its biological and physical properties and not to products of environmental variations. Accordingly, because individual measurements were acquired from numerous locations and depths, results are presented not just in terms of averages but also with an indication of species variation (e.g., through the standard deviation). Results from the 2001 data collection in Kaneohe Bay for two species (one coral and one algae) are presented in Figure 5.

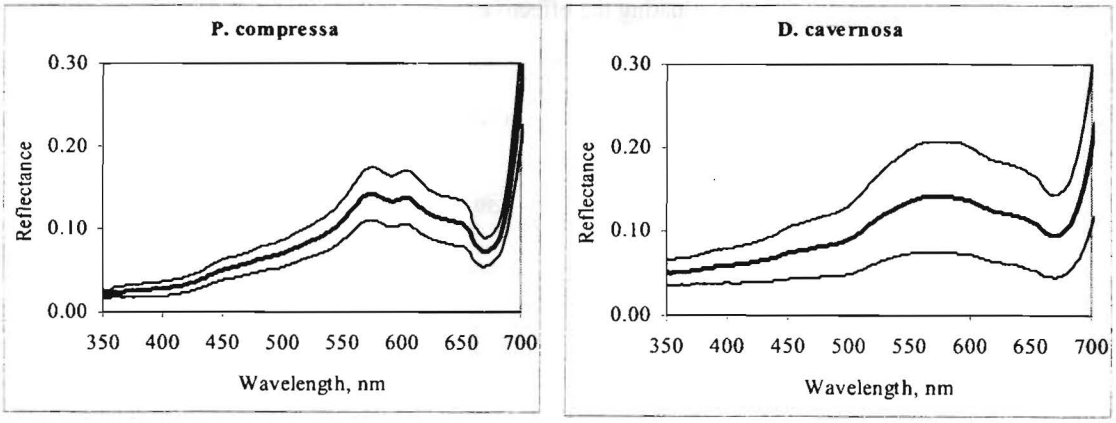

Figure 5. Reflectance of *Porites compressa* (coral, n = 51) and *Dictyosphaeria cavernosa* (algae, n = 34); average and +/- 1 standard deviation.

The reflectance characteristics observed in Figure 5 are similar to averages presented in other coral reflectance investigations. The difference here is the inclusion of the standard deviation of measured spectra for each species. This provides a valuable indication of the variation within and between each species, which aside from a few limited publications (Andrefouet et al., 2001; Hochberg and Atkinson, 2000; Holden and LeDrew, 2001) is typically not reported. Such variation is a significant factor to consider in spectral analysis, particularly for investigations focused on examining the spectral separability between and among species (and between other bottom materials such as sand, rubble and mud). Furthermore, it is important that the measure of variation is indicative of actual differences between species and not to fluctuating environmental conditions. The field protocol used here has been shown to minimize such unwanted errors in underwater reflectance measurements (Goodman and Ustin, 2002). Therefore, by using this protocol, the measured differences and similarities in reflectance characteristics indicated by this data can be confidently attributed to the actual differences in reflectance properties of each individual species.

3.2 Calibration Targets

In addition to obtaining measurements of individual coral and algae species, reflectance characteristics of five natural calibration targets were also acquired during the two field visits. These targets are similar to terrestrial calibration areas whose spectral information is used to assist in calibrating hyperspectral imagery to reflectance. For image analysis of coral reef and other shallow benthic habitats, the calibration procedure necessitates both atmospheric and water column corrections. Accordingly, underwater calibration targets needed to be identified and measured for use in calibrating images. The targets selected for Kaneohe Bay (Figure 6) are distributed at different locations and at different water depths throughout the study area. Each individual target consists of a large homogeneous sand area of uniform depth and was characterized by collecting a random sampling of 40 to 60 individual reflectance measurements. Results for two of the areas acquired in 2001 are presented in Figure 7. It is apparent that these areas exhibit a much greater variation in reflectance than the individual coral and algae species. Also evident in these graphs (and for all the target areas measured within Kaneohe Bay) is the characteristic chlorophyll-a absorption feature around 680 nm. This feature has been reported in other investigations and results from the presence of benthic microalgae within the sand, which can contribute significantly to overall primary productivity (Roelfsema et al., 2002). As with the coral and algae measurements, the field method used in this research produces an indication of the natural differences between targets. Among other functionality, this allows the target measurements to more confidently serve as ground truth for use in evaluating the effectiveness of water column correction algorithms.

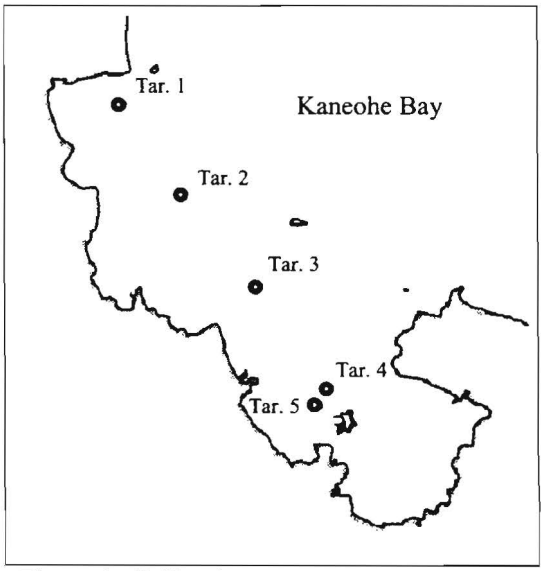

Figure 6. Calibration targets.

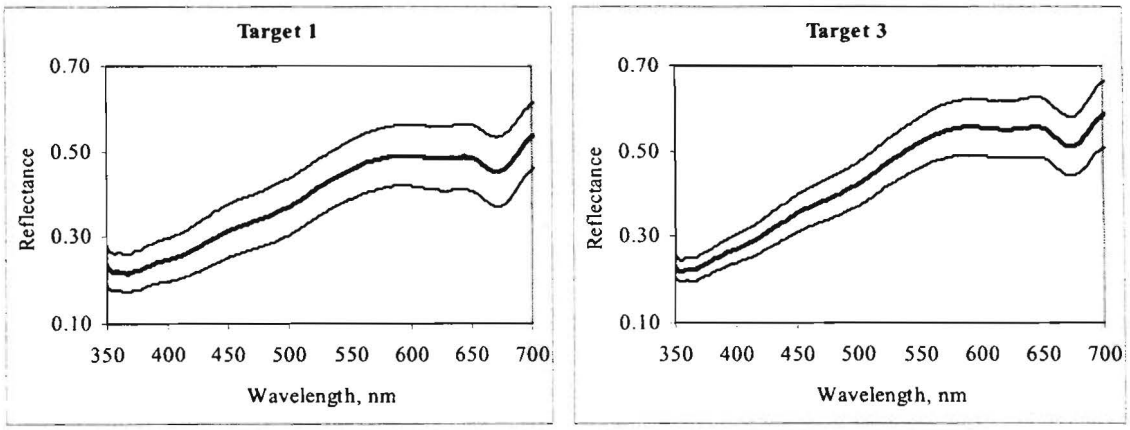

Figure 7. Reflectance of targets 1 (n = 50) and 3 (n = 45); average and +/- 1 standard deviation.

4. CONCLUSION

The physical limitations and technical difficulties associated with the water column present a challenging environment for remote sensing investigations. The energy interactions occurring at the air-water interface and within the water column alter many of the basic assumptions used in traditional terrestrial investigations. This is particularly evident when making *in situ* underwater reflectance measurements. Surface waves produce wave-focusing, changing wave height and varying refraction geometries. Absorption and scattering properties are also affected by varying constituents within the water column. Together, these factors result in highly variable underwater illumination conditions, both spatially and temporally. Control experiments were employed to address these issues and produce a field methodology that minimizes errors associated with environmental fluctuations. The methodology was then used to acquire reflectance measurements of coral, algae and sand within Kaneohe Bay. Data acquired from these field investigations is an important component of the ongoing research to develop hyperspectral image analysis techniques for coral reefs. Specifically, this includes utilizing the natural underwater calibration targets for empirical image calibration, applying a semi-analytical model for water column correction, developing algorithms for benthic habitat mapping, identifying large-scale coral community composition and examining causal relationships associated with environmental stress and global change.

5. ACKNOWLEDGEMENTS

This work was supported by NASA Headquarters under the Earth System Science Fellowship Grant NGT5-ESS/01-0000-0208. It is has been made possible by the Department of Land, Air and Water Resources and the Center for Spatial Technologies and Remote Sensing at the University of California, Davis. Additional support was also provided by the University of California Pacific Rim Research Program, the California Space Institute Graduate Student Fellowship Program, the Canon National Park Science Scholars Program and NASA's Jet Propulsion Laboratory. Furthermore, the authors would like to thank the Hawaiian Institute of Marine Biology for their assistance and Paul Sjordal for his untiring efforts in the field.

6. REFERENCES

Andrefouet, S, F.E. Muller-Karger, E.J. Hochberg, C. Hu and K.L. Carder, 2001, "Change Detection in Shallow Coral Reef Environments Using Landsat 7 ETM+ Data," Remote Sensing of Environment, vol. 79, pp. 1-13.

Dustan, P., S. Chakrabarti and A. Alling, 2000, "Mapping and Monitoring the Health and Vitality of Coral Reefs From Satellite: A Biospheric Approach," Life Support & Biosphere Science, vol. 7, pp. 149-159.

Goodman, J. and S. Ustin, 2002, "Underwater Spectroscopy: Methods and Applications in a Coral Reef Environment," 7th International Conference on Remote Sensing for Marine and Coastal Environments, Miami, Florida, May 19 – 22.

Hochberg, E.J. and M.J. Atkinson, 2000, "Spectral Discrimination of Coral Reef Benthic Communities," Coral Reefs, vol. 19, pp. 164-171.

Holden, H. and E. LeDrew, 1998, "Spectral Discrimination of Healthy and Non-Healthy Corals Based on Cluster Analysis, Principal Components Analysis, and Derivative Spectroscopy," Remote Sensing of the Environment, vol. 65, pp. 217-224.

Holden, H. and E. LeDrew, 2001, "Hyperspectral Discrimination of Healthy Versus Stressed Corals Using In Situ Reflectance," Journal of Coastal Research, vol. 17, no. 4, pp. 850-858.

Lubin, D., W. Li, P. Dustan, C.H. Mazel and K. Stamnes, 2001, "Spectral Signatures of Coral Reefs Features From Space," Remote Sensing of Environment, vol. 75, no. 1, pp. 127-137.

Milton, E.J., 1987, "Principles of Field Spectroscopy," International Journal of Remote Sensing, vol. 8, no. 12, pp. 1807-1827.

Roelfsema, C.M., S.R. Phinn and W.C. Dennison, 2002, "Spatial Distribution of Benthic Microalgae on Coral Reefs Determined by Remote Sensing," Coral Reefs, vol. 21, pp. 264-274.

Salisbury, J.W., 1998, "Spectral Measurements Field Guide," Defense Technology Information Center, Report No. ADA362372.

Initial Estimates from AVIRIS of the Temperature and Fractional Areas of Fires at the World Trade Center Disaster

Robert O. Green,[1] Roger N. Clark,[2] Joseph Boardman,[3] Betina Pavri,[1] Chuck Sarture[1]
[1]Jet Propulsion Laboratory, California Institute of Technology
Pasadena, California 91109
[2]U.S. Geological Survey
[3]Applied Imaging and Geophysics LLC

1.0 INTRODUCTION

On the 14th of September 2001, in the wake of the destruction of the World Trade Center, the question of using AVIRIS (Vane et al., 1993; Green et al., 1998) to detect possible asbestos contamination was raised. AVRIS measures the spectral range from 370 to 2510 nm, with 10 nm sampling and high precision. This spectral range, spectral resolution, and precision, supported the use of AVIRIS to measure the 2300-nm absorption features of the principal asbestos minerals. Based on this potential contribution, approval was given for AVIRIS to acquire data over the disaster site.

At the time, AVIRIS was installed on the Twin Otter aircraft and grounded at the Atlanta, Georgia, airport. With careful and persistent effort in the challenging environment following September 11th, permission was given to fly AVIRIS at low altitude over the disaster site. AVIRIS data were acquired of the site and surrounding area on the 16th of September 2001. Rapid examination of these data in the following 24 hours unexpectedly revealed the presence of multiple hot fires still burning in the debris. Subsequently, rapid characterization and reporting of the hot-fire properties in the debris area were added to the analysis objective for the AVIRIS data.

A Planck-function-based spectral-fitting fire temperature and fractional area algorithm (Green, 1996; Green, 2001) was applied to the AVIRIS-measured hot-fire spectra. A precise georectification of these AVIRIS data was performed to locate the geographic position of the hot fires (Boardman, 1999). The locations and derived fire temperatures and fractional areas were reported to the rescue teams on the ground on the 17th of September. Based on these initial results additional AVIRIS overflights of the disaster site were made on the 18th, 22nd, and 23rd. This paper reports the measurements, algorithms, analyses, and results of the fire temperature and fractional area determinations with AVIRIS calibrated spectra at the World Trade Center site in September 2001. Additional results relating to the detection of asbestos and other materials are reported elsewhere (Clark et al., 2002).

2.0 MEASUREMENTS

AVIRIS spectral image measurements were acquired over the World Trade Center disaster site in the period from 14:51 to 17:07 UTC on the 16th of September 2001. They were returned to JPL early in the morning of the 17th for analysis. Figure 1 shows an AVIRIS image cube rendition of a portion of one of the AVIRIS flight lines, with the disaster site in the left center of the image. The edge panels of the image cube rendition depict the spectral dimension of the AVIRIS data.

These data were acquired from an altitude of 1500 m, which gives a corresponding spatial resolution of 1.5 m, based on the 1 milliradian instantaneous field-of-view of the AVIRIS instrument. Early examination of the AVIRIS image data at 2300 nm on the morning of the 17th revealed a number of high-intensity radiance targets. Figure 2 shows the AVIRIS image from the 2300-nm spectral region, with numerous bright targets evident in the area of the World Trade Center. Additional bright targets at this wavelength are also evident towards the right of the image at some distance from the disaster site. Detailed examination of the spectra from high-intensity targets at the World Trade Center disaster site revealed spectral signatures of hot fires. The bright spectra to the right of the image in Figure 2 were shown to be the result of sun glint from reflective roof surfaces. AVIRIS spectra from surface

background material, a burning fire at the disaster site, and sun glint from a building roof are shown in Figure 3. The background material spectrum has the form of solar-reflected radiance from a surface, of moderate uniform spectral reflectance across the AVIRIS range. The hot-fire spectrum exhibits the reflectance of a dark material in the range from 400 to 1000 nm. At wavelengths longer than 1000 nm, the hot fire spectrum radiance intensity increases until reaching the AVIRIS instrument saturation level in the 2000–2500-nm spectral range. This increase in radiance to longer wavelengths is consistent with surface sourced radiance emitted by a hot fire. In contrast, the sun glint spectrum shows a high spectral radiance that conforms to the shape of the solar spectral irradiance source convolved with the two-way transmittance of the atmosphere. In this spectrum, minor AVIRIS instrument saturation occurs near the 1000 nm wavelength region. AVIRIS instrument radiance saturation levels are set to preserve measurement precision for materials in the range from 0 to that of a 1.0 reflectance Lambertian surface with the sun directly overhead. Both the burning fire and sun glint spectra exceed this saturation level in limited portions of the spectrum. However, measurement of the spectral shape by AVIRIS in the nonsaturated portions of the spectrum provides a basis to identify the properties of these targets. In the case of the burning fire, the spectral shape and intensity may be used to derive estimates of both the temperature and fractional area of the hot source.

Figure 1. AVIRIS image cube of World Trade Center disaster site acquired on the 16th of September 2001.

Figure 2. AVIRIS 2300-nm wavelength image of the World Trade Center disaster site. The bright signal to right side of the image is sun glint from a reflective roof surface.

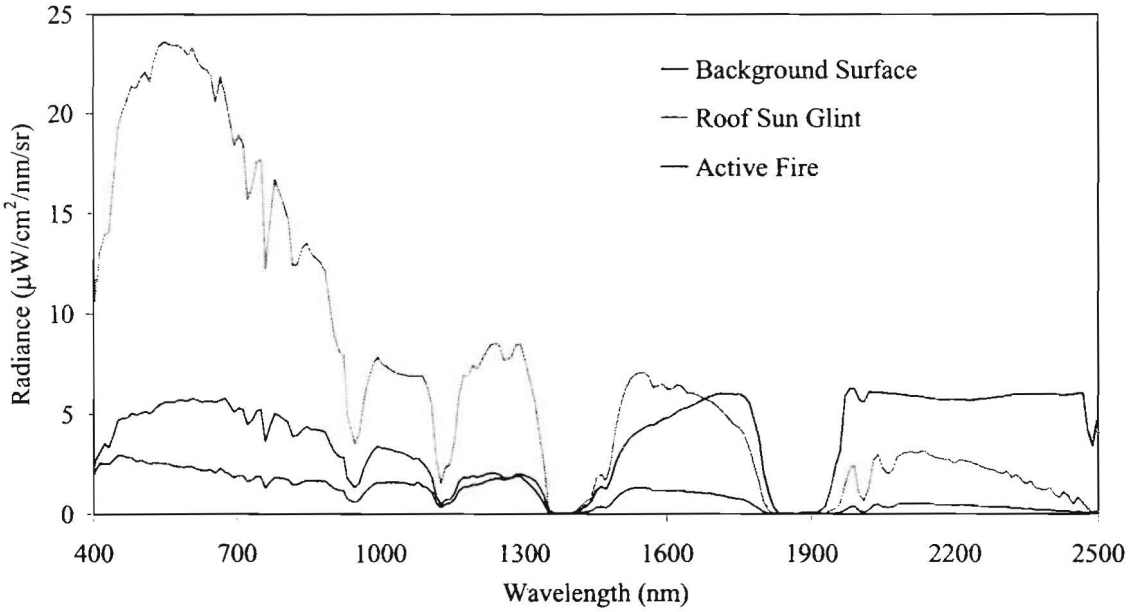

Figure 3. AVIRIS spectra for the World Trade Center disaster site. Background, active fire, and roof sun glint spectra are shown. The active fire exhibits exceptionally high radiance in the 2000–2500-nm wavelengths emitted from the fire and comparatively low radiance in the 400 –1000-nm spectral region.

3.0 PHYSICAL MODEL AND ALGORITHM APPROACH

The electromagnetic energy emitted by matter is a function of spectral emissivity that is related to composition and of the material temperature. The well-known Plank function (Liou, 1980) describes the radiance emitted by a target with emissivity of 1.0 as a function of temperature. Figure 4 shows the calculated Planck-function curves for a series of targets of temperature 600, 800, 1000, and 1200 Kelvin. In addition, the solar-reflected radiance for a 1.0 reflectance Lambertian target is also shown. For the Planck-function-modeled spectra, the radiance emitted increases as a strong function of temperature. Just as importantly, the slope and position of the Planck-function spectrum increases and shifts to shorter wavelengths as the temperature increases. This change in slope and wavelength position provides a basis for use of spectral measurement to determine the temperature of hot fires.

Because hot fires almost never uniformly fill the field of view of a spectral measurement, the fractional area of the hot source must be accounted for as well as the temperature. Equation 1 gives a simple relationship between the measured radiance at a given wavelength ($L\lambda$) and a Planck function ($B\lambda$) at a given temperature (T) and fractional area (A) for a 1.0 emissivity target.

$$L\lambda = A^* B\lambda(T) \quad (1)$$

For daytime measurements by AVIRIS in regions of the spectrum where the atmospheric transmittance in approximately 1.0, an additional term is needed to account for the solar-reflected radiance ($L\lambda s$) and is included in Equation 2. This equation provides a simple model of the radiance measured by AVIRIS over a hot target in the highly transparent regions of the atmosphere

$$L\lambda = A^* B\lambda(T) + L\lambda s \quad (2)$$

With this equation, a spectral-fitting algorithm has been implemented, where the fractional area and temperature parameters of the model are adjusted until optimal agreement is reached with the AVIRIS-

measured radiance for the hot-target spectrum. The best fit resulting temperature and fractional area are then reported for each analyzed spectrum. For this approach, the solar-reflected radiance may be estimated from adjacent measured spectra that are not hot, or with a radiative transfer model such as MODTRAN (Berk et al., 1989; Anderson et al., 1995; Anderson et al., 2000). Planck-function spectral-fitting algorithms have been previously used with AVIRIS measurement of hot volcanic lava and hot burning fires (Oppenheimer et al., 1993; Green, 1996; Green; 2001).

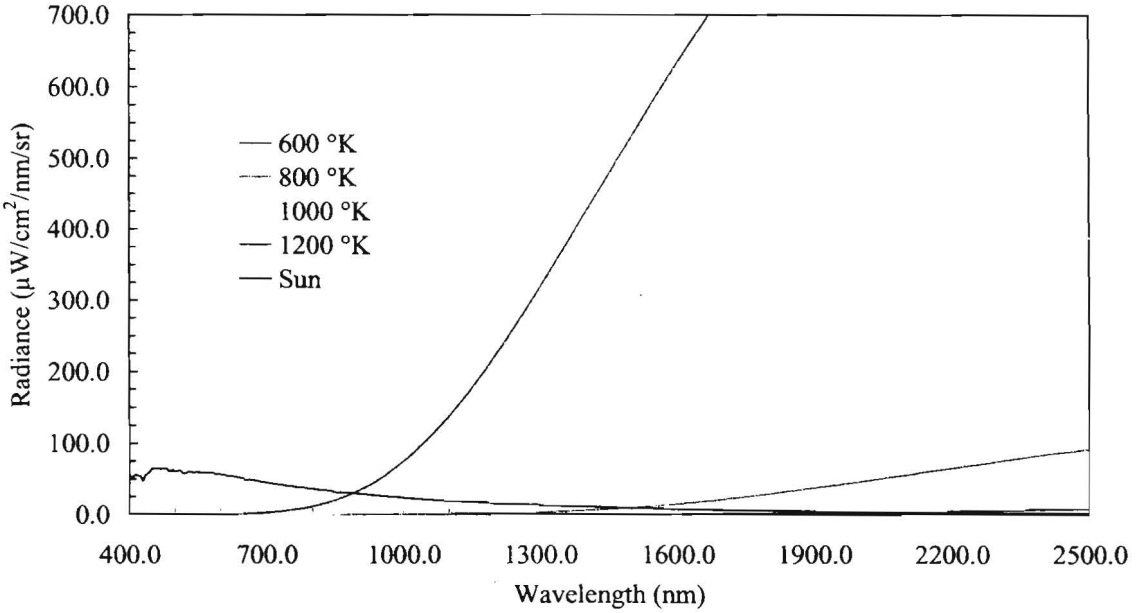

Figure 4. Planck-function calculated radiance for targets at different temperatures. The radiance of a 1.0 Lambertian target illuminated with the Sun at the zenith is also shown.

4.0 ANALYSIS

Hot-fire AVIRIS spectra from the World Trade Center data set were analyzed with this Planck-function spectral-fitting algorithm for derivation of temperature and fractional area. Areas with active fires were identified in the AVIRIS image from the 2300-nm wavelength region of the spectrum. For the 16th of September AVIRIS data set, the brightest spectra from eight different areas with active fires in the World Trade Center site were analyzed. These spectra were labeled A to H. Figure 5 shows a hot-fire spectrum and an adjacent solar-reflected spectrum as well as the difference spectrum. Apart from the regions of strong atmospheric absorption near 1400, 1900, and 2500 nm, the spectral shape of the difference spectrum is dominated by the fire-emitted radiance.

The fire temperature and fractional area estimation analysis proceeds by determining the best fit between the AVIRIS spectrum with solar reflected component subtracted and the Planck function model. Figure 6 shows the best spectral fit between the hot fire spectrum and the Plank function model for the spectrum from area G in the 16th of September AVIRIS data set. No portion of this spectrum is saturated in the AVIRIS measurement. The fit was optimized in the spectral regions with minimal atmospheric absorption. A temperature of 984 K and fractional area of 1.48% was derived for this spectrum. This is expected to be a low estimate for the temperature because the emissivity of the hot target was assumed to be 1.0. If the emissivity were lower than 1.0 the temperature would be higher to generate the intensity of measured radiance.

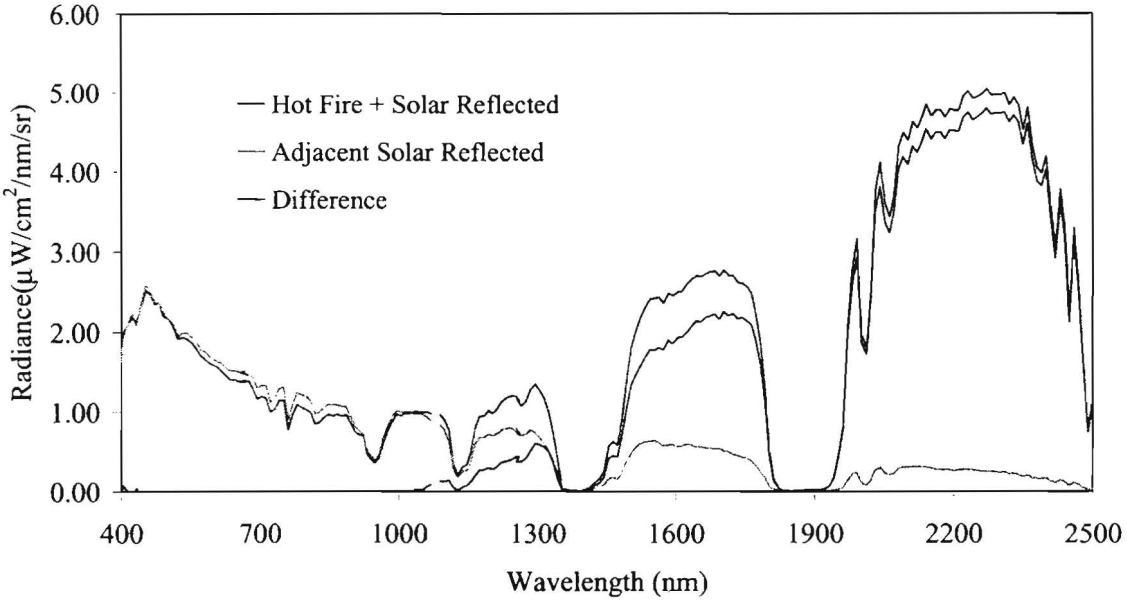

Figure 5. Hot-fire spectrum, adjacent solar-reflected spectrum, and difference spectrum for area G in the World Trade Center AVIRIS data set.

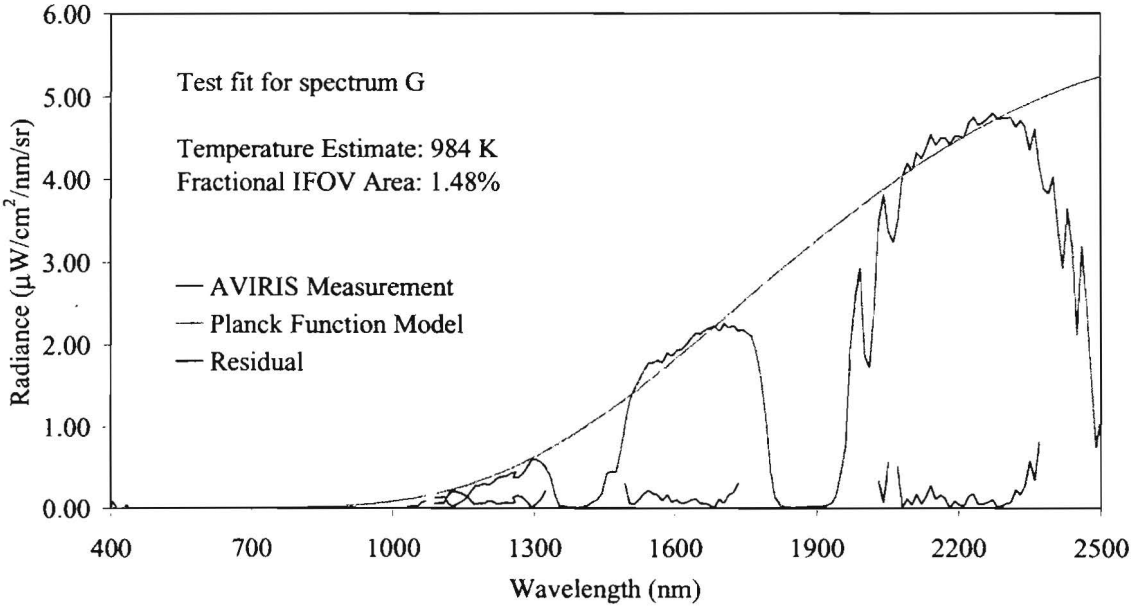

Figure 6. Spectral fit result in continuum regions between AVIRIS spectrum with solar-reflected background radiance subtracted and Planck-function model.

An additional example of the temperature and fractional area estimation algorithm for the highest intensity spectrum from area A of the 16th of September data set is shown in Figure 7. For this spectrum a temperature of 928 K with a fractional area of 6% was derived. As with all analyses, the solar-reflected component of the radiance was estimated and subtracted using an adjacent solar-reflected dominated spectrum. For this spectrum from area A, the temperature and fractional area of the fire measured were sufficient to cause instrument saturation in the 2000- to 2500-nm region of the AVIRIS spectral range.

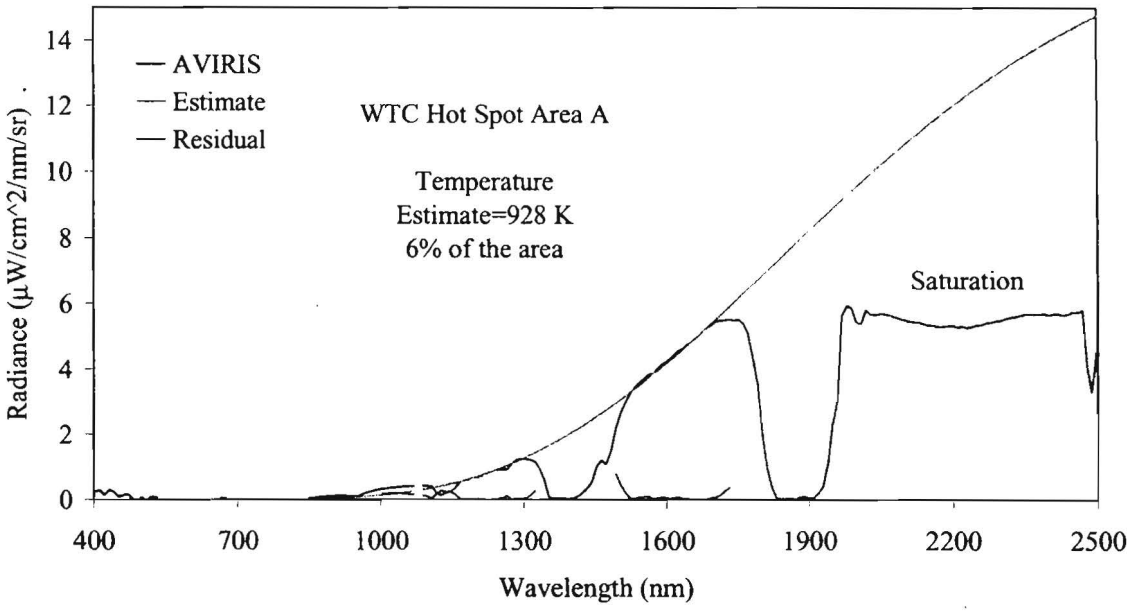

Figure 7. Temperature and area estimate for spectrum A acquired on the 16th of September 2001.

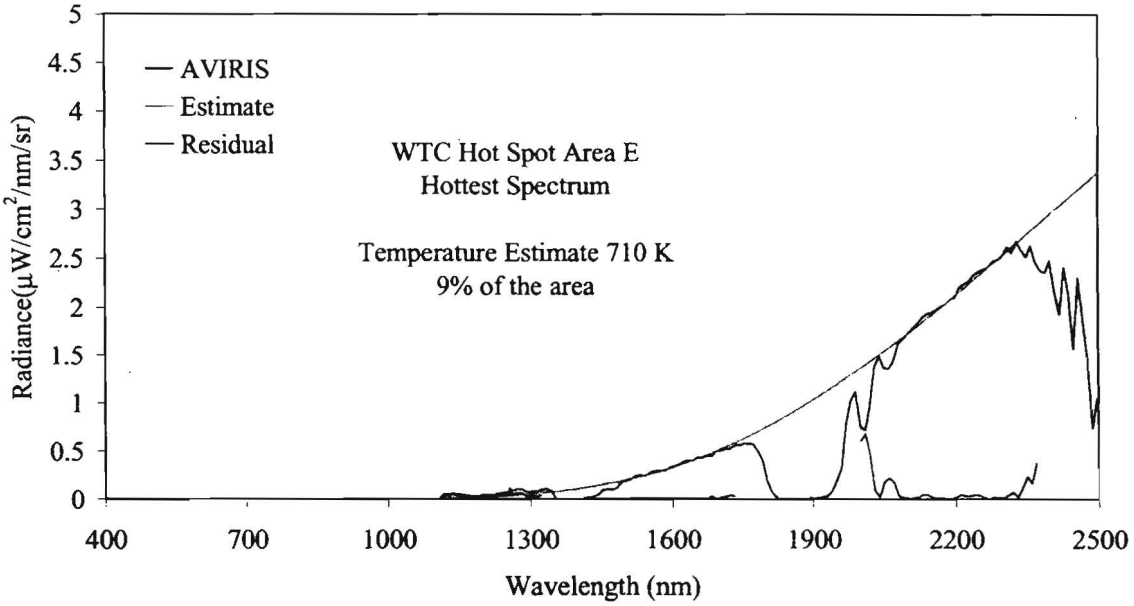

Figure 8. Spectral fit result for World Trade Center spectrum E.

However, even with saturation over part of the AVIRIS spectral range, the measured spectral shape and intensity in the 1000- to 1800-nm spectral range provide sufficient leverage for the algorithm to derive a temperature and fractional area for this spectrum.

A further example of the temperature and fractional area analyses is shown in Figure 8 for the spectrum from area E of the 16th of September AVIRIS World Trade Center data set. The AVIRIS-measured spectrum with solar-reflected component subtracted, the Planck-function model fit, and residual difference are shown. For this spectrum, a temperature of 710 K and fractional area of 9% was derived. This spectrum was best modeled with a lower derived temperature and higher fractional area than the

previous examples. This result is consistent with the shallower spectral slope of this spectrum and the shift of intensity rise to longer wavelengths.

To present and demonstrate the algorithm and analyses for estimation of fire temperature and fractional area from the 16th of September AVIRIS World Trade Center data set, selected examples have been shown. Temperature and fractional area parameters were derived even in the presence of AVIRIS instrument saturation over a portion of the spectrum. As expected, a range of temperatures and fractional areas were derived from spectra with distinctly different spectral forms. For these examples, the spectral fits between AVIRIS measured spectra and the Planck-function-based modeled spectra were in good agreement in the regions of high atmospheric transmittance. These spectrally derived values of temperature and fraction area are consistent with the expected emitted radiance from the hot fires burning an extended period in the surface debris of the World Trade Center disaster site.

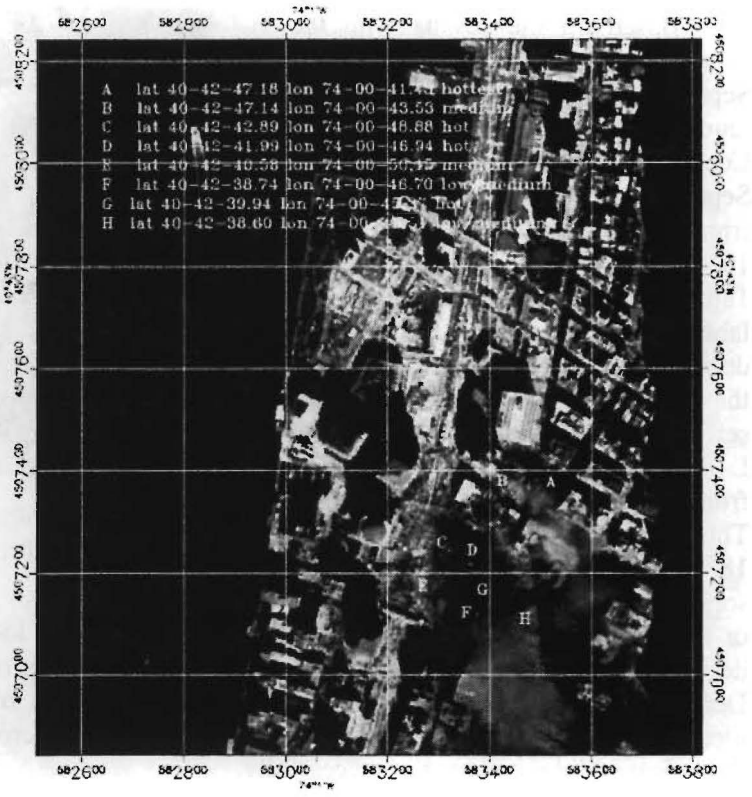

Figure 9. AVIRIS image acquired on the 16th of September 2001 with hot spots labeled.

5.0 RESULTS

The algorithm was applied to the highest intensity spectrum from each of the eight hot-fire areas identified. Figure 9 shows a portion of an AVIRIS image of the World Trade Center disaster site acquired on the 16th of September. The eight hot-fire areas identified are labeled A to H. Table 1 shows the corresponding locations of the hot-fire areas and the derived temperature and fractional area for the analyzed spectra. Temperatures range from 700 to 984 K, and fractional areas range from 1.5 to 18 % for the 16th of September data sets. These results were reported to the teams on the ground at the disaster site.

Table 1. Location, temperature, and fractional area determined for the highest intensity spectrum in the eight hot target areas identified.

Spectrum	Latitude	Longitude	Temp (K)	Area (%)
A	40 42 47.18	74 00-41.43	928	6
B	40 42 47.14	74 00-43.53	827	2
C	40 42 42.89	74 00-48.88	921	3.3
D	40 42 41.99	74 00-46.94	791	18
E	40 42 40.58	74 00-50.15	710	9
F	40 42 38.74	74 00-46.70	700	8
G	40 42 39.94	74 00-45.37	984	1.5
H	40 42 38.60	74 00-43.51	817	1.8

Based on the results with the data measured on the 16th of September 2001, AVIRIS was requested to over fly the World Trade Center disaster site on the 18th of September. A subset of an image from that overflight is shown in Figure 10. In this data set acquired on the 18th, hot-fire areas were identified and labeled from A to L. The A to H designations were selected to match the areas of the 16th of September data set. The additional hot areas—J to L—were not identified in the data set from the 16th September overflight. This increase in hot-fire areas on the 18th may be due to increased sophistication in identifying hot areas or to the occurrence of new hot areas.

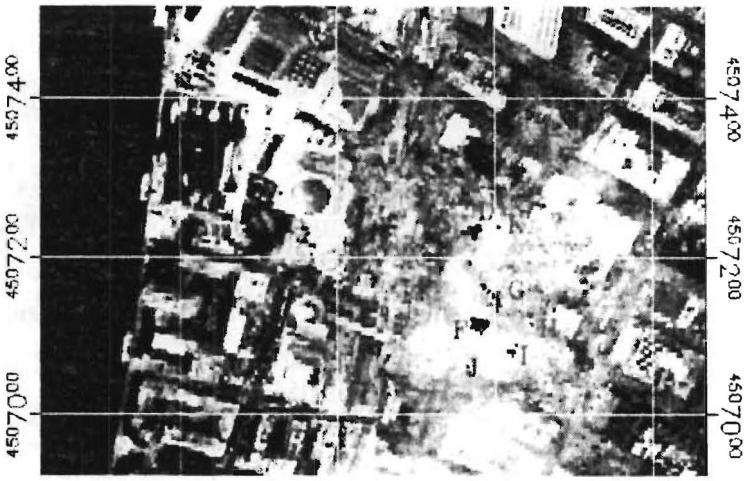

Figure 10. AVIRIS image from the 18th of September 2001 with identified hot zones labeled.

Table 2 gives the locations, temperatures and fractional areas derived for the highest intensity spectra in the hot-fire areas of the 18th of September AVIRIS data set. Derived temperatures range from 471 to 952 K and areas from 0.5 to 36 %. In the case of area E identified in the 16th of September data set no hot spectra were found on the 18th. For area J the spectral fit algorithm did not converge successfully.

Table 2. Location, temperature, and fractional area determined for the 18th of September data set.

Hot Spectrum	Latitude	Longitude	Temp (K)	Area (%)
A	40-42-46.96	74-00-41.21	952	2.2
B	40-42-47.31	74-00-43.31	790	36
C	40-42-43.38	74-00-48.15	500	22
D	40-42-42.48	74-00-46.64	700	5
E			not seen	
F	40-42-38.62	74-00-46.41	725	7
G	40-42-39.77	74-00-45.45	932	2
H	40-42-39.04	74-00-43.65	471	4
I	40-42-36.97	74-00-44.54	762	35
J	40-42-36.97	74-00-47.01	no fit	
K	40-42-42.69	74-00-45.26	538	7
L	40-42-44.14	74-00-46.98	805	0.5

These results from the 16th and 18th September AVIRIS World Trade Center measurements show the estimation of fire temperatures and fractional areas for the highest intensity spectra in each of the hot areas identified. The spectral-fitting algorithm used is based on the physics of the Planck function and a simple model of the effects of solar-reflected energy and fractional filling of the spectral measurement spatial sample. Temperatures and fractional area were derived from the AVIRIS calibrated spectra that were consistent with the conditions at the World Trade Center disaster site in this period of September 2001.

6.0 TEST OF THE FRACTIONAL AREA COMPONENT OF THE MODEL

Following initial analysis and reporting of hot-fire location, temperature, and fractional area results from the AVIRIS World Trade Center data sets, a test of the fractional area component of the Planck-function model was performed. The high-intensity spectrum from site G on the 16th of September was used. This spectrum was averaged with an adjacent spectrum that did not exhibit a hot-fire signature. Spectrum G, the adjacent spectrum, and the average are shown in Figure 11. Based on the simple temperature and fractional area model, the effect of the averaging should be to reduce the fractional area by a factor of 2. However, the derived temperature should remain unchanged because the spectral shape of the emitted energy is preserved across the spectrum.

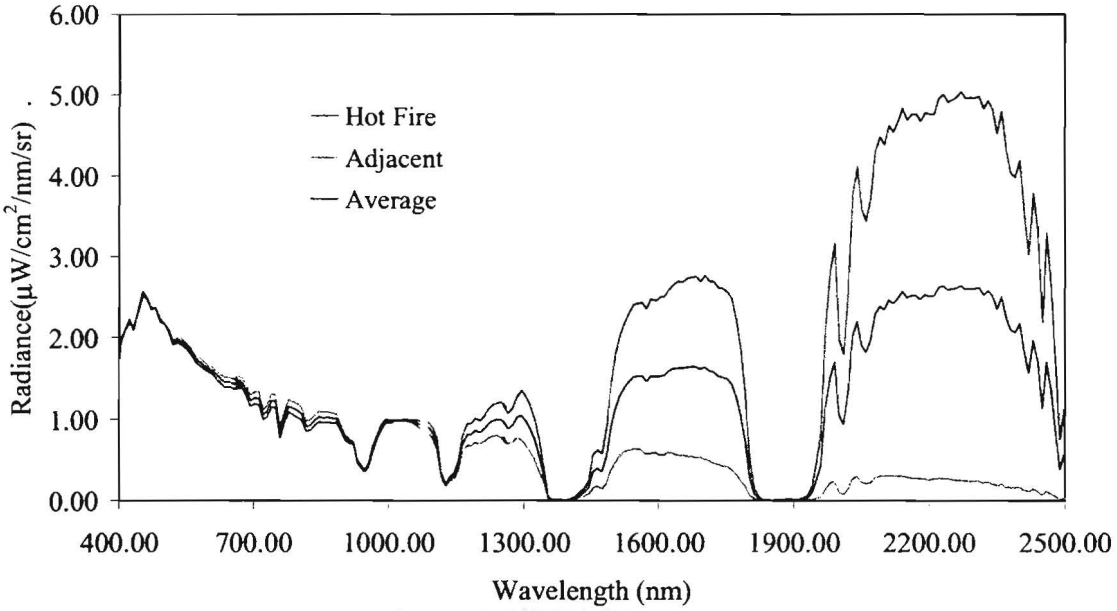

Figure 11. Dilution of the hot-fire component of spectrum G from the AVIRIS measurements on the 16th of September 2001 at the World Trade Center disaster site.

To test the validity of the fractional area component of the model, the diluted spectrum was analyzed with the full Planck-function algorithm. Figure 12 shows the spectral-fitting results from this test. As expected, the derived fractional area was half that derived for the undiluted spectrum G shown in Figure 6, and the derived temperature was the same. An additional test was performed with dilution of spectrum G by 3 adjacent nonburning spectra. A similar conservation of temperature estimate was achieved with a reduction of fraction area to one fourth of the original. These simple tests support the validity of the fractional area estimation component of the Planck-function-based hot-target model used in these analyses of the AVIRIS World Trade Center data.

7.0 CONCLUSION

On the 14th of September 2001, a request was made for AVIRIS to acquire spectral measurements over the World Trade Center disaster site for detection of asbestos contamination in the debris. AVIRIS measurements were acquired on the 16th of September. Rapid examination of the data showed spectral expression of hot fires in the World Trade Center debris. A simple Planck-function-based spectral-fitting algorithm was applied to the AVIRIS-calibrated radiance spectra to estimate the temperature and fractional area of the highest-intensity AVIRIS spectrum in each identified area of hot fires. The location, temperature, and fractional area derived for the eight zones identified in the 16th of September data set

were delivered to the teams on the ground. Based on these rapid results, AVIRIS was requested to acquire additional data on the 18th of September. A similar analysis was performed estimating the temperature and fractional areas of the highest intensity spectra of the identified area of hot fires for this data set. Overall, the derived temperatures of the analyzed spectra from each of the hot zones decreased from the 16th to the 18th. In one case, no hot spectrum was identified on the second date. As with the results from the 16th, the hot-fire location, temperature, and fractional area derivations were provided to the ground teams to help understand and mitigate risk.

AVIRIS measurements in the solar-reflected spectrum offer an important approach to estimate the temperature and fractional area of hot targets. The estimation of temperature and area is based on the spectral slope, position, and intensity of the emitted radiation. This approach may be extended to a range of applications such as disaster response, controlled burn and wild fire research as well as volcanic lava flow temperature investigation. Additional research is needed to further validate the derived temperatures from this approach and to understand the sensitivity of the results to the assumption in the inversion model.

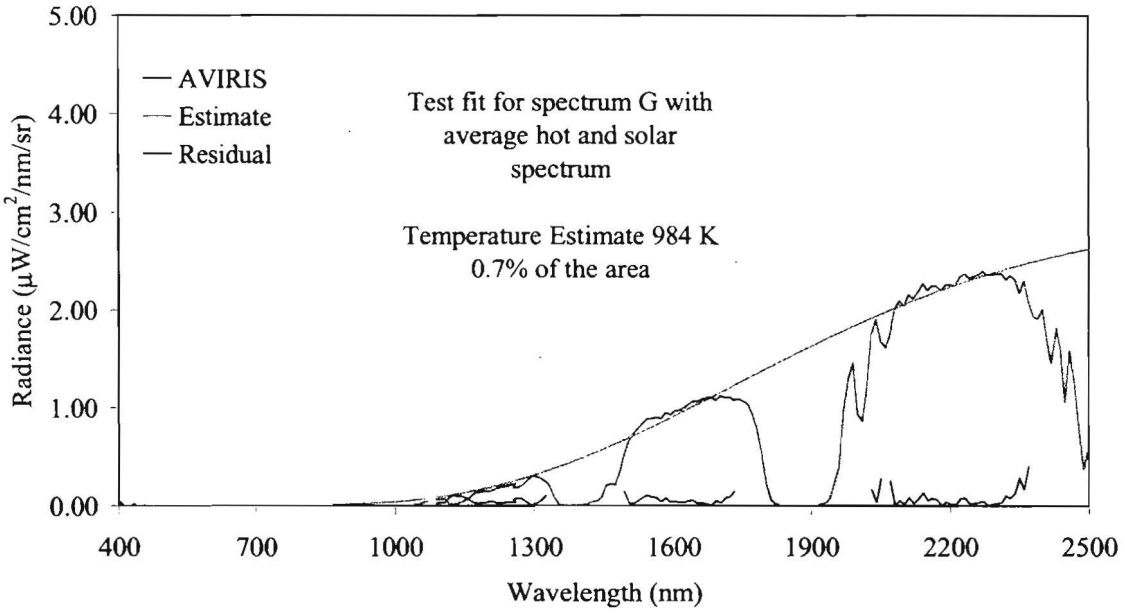

Figure 12. Derived temperature and fractional area from the diluted spectrum G. The derived temperature was unaffected by dilution of the original spectrum from an adjacent non burning spectrum.

8.0 REFERENCES

Anderson, G.P. et al., "MODTRAN3: An update and recent validations against airborne high resolution interferometer measurements," *Summaries of the Fifth Annual JPL Airborne Earth Science Workshop*, JPL Publication 95-1, Vol. 1, pp. 5-8, Jet Propulsion Laboratory, Pasadena, California, 1995.

Anderson, G.P., M. L. Hoke, J. H. Chetwynd, Jr., A. J. Ratkowski, L. S. Jeong, A. Berk, L. S. Bernstein, S. M. Adler-Golden, et al., "MODTRAN4 Radiative Transfer modeling for remote sensing," *SPIE, 4049*, pp. 176–183, 2000.

Berk, A., et al., "MODTRAN: A moderate resolution model for LOWTRAN 7," Final Report, GL-TR-0122, Air Force Geophys. Laboratory, Hanscom AFB, Massachusetts, 42 pp., 1989.

Boardman, J. W., "Precision Geocoding of Low-Altitude AVIRIS Data: Lessons Learned in 1998," *Proc. Eighth Airborne Earth Science Workshop*, JPL Publication 99-17, Vol. 1, Jet Propulsion Laboratory, Pasadena, California, 1999.

Clark, R. N., R. O. Green, G. A. Swayze, G. Meeker, S. Sutley, T. M. Hoefen, K. E. Livo, G. Plumlee, B. Pavri, C. Sarture, S. Wilson, P. Hageman, P. Lamothe, J. S. Vance, J. Boardman I. Brownfield, C. Gent, L. C. Morath,

J. Taggart, P. M. Theodorakos, and M. Adams, "Environmental studies of the World Trade Center area after the September 11, 2001 attack," U. S. Geological Survey, Open File Report OFR-01-0429, http://speclab.cr.usgs.gov/wtc/, 2002.

Green, R. O., "Estimation of Biomass Fire Temperature and Areal Extent from Calibrated AVIRIS Spectra," *Proc. Sixth Annual Airborne Earth Science Workshop*, JPL Publication 96-4, Vol. 1, Jet Propulsion Laboratory, Pasadena, California, March 3–5, 1996.

Green, R. O., M. L. Eastwood, and C. M. Sarture, "Imaging spectroscopy and the Airborne Visible Infrared Imaging Spectrometer (AVIRIS)," *Remote Sens. Environ.* 65: (3) 227–248, September 1998.

Green, R. O., "Estimating the Expressed Temperature and Fractional Area of Hot Lava at the Kilauea Vent with AVIRIS Spectral Measurements," *Proc. Tenth JPL Airborne Earth Science Workshop*, JPL Publication 02-1, Jet Propulsion Laboratory, Pasadena, California, 2001.

Liou, K. N., *An Introduction to Atmospheric Radiation*, Academic Press, Inc., New York, 392 pp., 1980.

Oppenheimer, C., D. A. Rothery, D. C. Pieri, M. J. Abrams, V. Carrere, "Analysis Of Airborne Visible/Infrared Imaging Spectrometer (AVIRIS) Data of Volcanic Hot-Spots," Open Univ., Dept. Earth Sci./Milton Keynes/MK7 6AA/Bucks./England/*International Journal of Remote Sensing*, 14, (16), 2919–2934, 1993.

Vane, G., R. O. Green, T. G. Chrien, H. T. Enmark, E. G. Hansen, and W. M. Porter, "The Airborne Visible Infrared Imaging Spectrometer (AVIRIS)," *Remote Sens. Environ.*, *44* (2-3), 127–143, 1993.

9.0 ACKNOWLEDGMENTS

This research was carried out at the Jet Propulsion Laboratory, California Institute of Technology, Pasadena, California, under contract with the National Aeronautics and Space Administration.

AVIRIS Inflight Calibration Experiment Results for 2001

Robert O. Green and Betina Pavri
Jet Propulsion Laboratory, California Institute of Technology
Pasadena, California 91109

1.0 INTRODUCTION

The Airborne Visible/Infrared Imaging Spectrometer (AVIRIS) (1998a) is calibrated each year in the laboratory (Chrien et al. 1990, 1995, 1996, 2000). To assess the validity of the laboratory calibration in the flight environment, an inflight calibration experiment is conducted (Conel 1988, Green et al. 1990, 1992, 1993a, 1995, 1996, 1998b, 1999, 2000, 2001). For the inflight calibration experiment, a homogeneous surface calibration target is designated where the surface spectral reflectance, atmospheric aerosol and water vapor properties are measured. These measurements are used to predict the upwelling radiance incident at the AVIRIS instrument aperture with radiative transfer model calculations. The predicted radiance is compared and analyzed with respect to the AVIRIS measured radiance to understand the state of the AVIRIS calibration in the flight environment. AVIRIS airborne data calibration is traced to the laboratory measurements using the signal of the onboard calibrator (Green et al. 1993b). In 2001 the principal inflight calibration experiments occurred on February 7 at Salar de Arizaro, Argentina and on June 6 at Rogers Dry Lake, California. The measurements and results of these inflight calibration experiments in 2001 are described in this paper.

2.0 ARGENTINA EXPERIMENT

AVIRIS was deployed on the Twin Otter aircraft platform to Argentina in January and February 2001 as part of science validation effort for the Hyperion spaceborne imaging spectrometer onboard the NASA New Millennium EO-1 spacecraft. For inflight calibration validation of both Hyperion and AVIRIS, the Salar de Arizaro, a high altitude dry salt lakebed, was selected. Salar de Arizaro is located 24 degrees south latitude and 67 degrees west longitude at an elevation of 3700 m in the Andes of northwestern Argentina. Figure 1 shows a Landsat Thematic Mapper image of Salar de Arizaro with the general location of the calibration site indicted. Figure 2 shows a picture taken from the surface Salar de Arizaro on February 6, 2001. The surface is bright and uniform at the meter scale and greater; however, there is considerable microtopography reflectance variability at the 0.3-meter scale and finer.

Figure 1. Landsat image of Salar de Arizaro Argentina with the AVIRIS inflight calibration site indicated.

Figure 2. A picture of the surface of Salar de Arizaro on February 6, 2001.

2.1 Surface Measurements

At the Salar de Arizaro calibration site, both surface and atmospheric measurements were acquired. A calibration target was established with dimensions of 300 by 60 m on the dry salt lake surface. At each end of the calibration target, demarcation tarps were placed to allow unambiguous location of the target in the AVIRIS image data. Surface reflectance measurements were acquired with a field spectrometer (Analytical Spectral Devices Inc., Full Range Spectrometer) in the period from 40 minutes before to 40 minutes after the AVIRIS overflight of the calibration target. A spectralon (Labsphere Inc.) reflectance standard was measured at the beginning, middle, and end of each transect down the length of the calibration target. The measured data were calibrated to reflectance using the spectralon target and a bidirectional reflectance correction factor for the 35-degree solar zenith angle at the time of the data acquisition. Figure 3 shows the average spectrum and the standard deviation and the standard deviation of the average of the 1824 spectra measured. The spectral reflectance of the Salar de Arizaro calibration target is exceptionally bright over the entire spectral range, however the microtopography induces large spectrum-to-spectrum reflectance differences. Figure 4 shows the reflectance value at 900 nm for all measured spectra and reveals the extreme spectrum-to-spectrum variability of the surface. To assess the effect of this variability, an average spectrum was calculated from all the odd spectra and all the even spectra. These two average spectra agreed at the 0.002 reflectance level, indicating enough spectra were measured for the average spectrum to accurately represent the reflectance of the calibration target. This agreement is also consistent with the calculation of the standard deviation of average for the measured spectra (Taylor 1982) and shows a knowledge of the average reflectance of the calibration target at the 0.002 reflectance level.

In addition to the surface reflectance, the atmospheric characteristics were measured with a sun tracking solar radiometer (Professor John Reagan, University of Arizona). The solar intensity was measured from sunrise through local solar noon in the 10 wavelength of the radiometer (370, 400, 440, 520, 620, 670, 780, 870, 940, 1030 nm). Figure 5 shows the measurements from this instrument at the calibration target on Salar de Arizaro. These data were used to calculate the instantaneous optical depths on February 7, 2001. Figure 6 shows the derived instantaneous optical depths for the 9 non water vapor wavelength measurements. The measurement from 940 nm was used to estimate the water vapor (Bruege et al. 1992, Reagan et al. 1987).

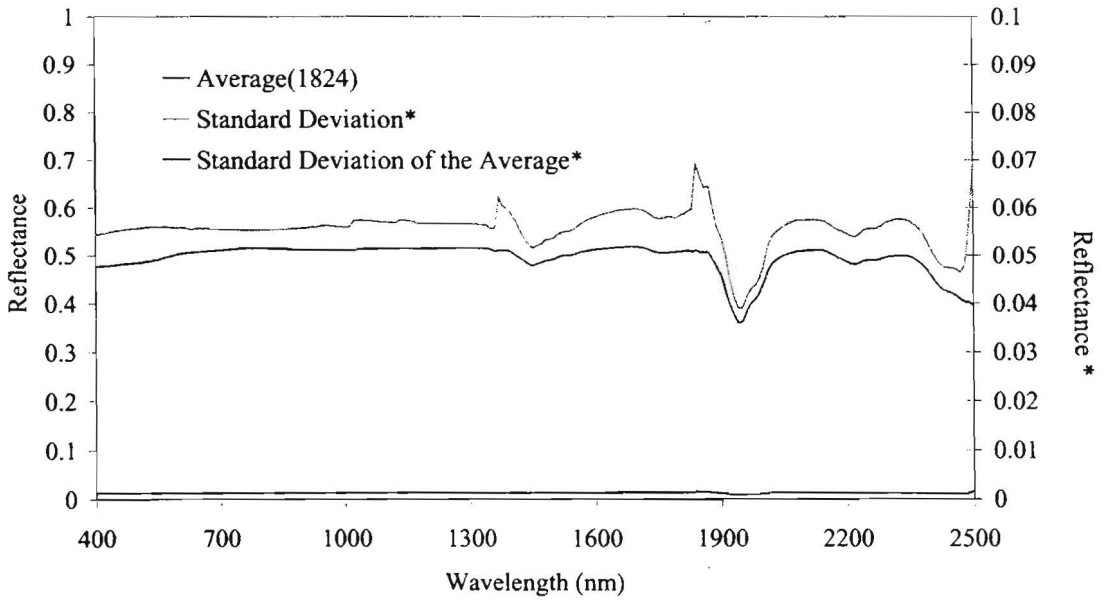

Figure 3. Average reflectance spectrum for Salar de Arizaro on February 7, 2001. The standard deviation and standard deviation of the average are shown as well.

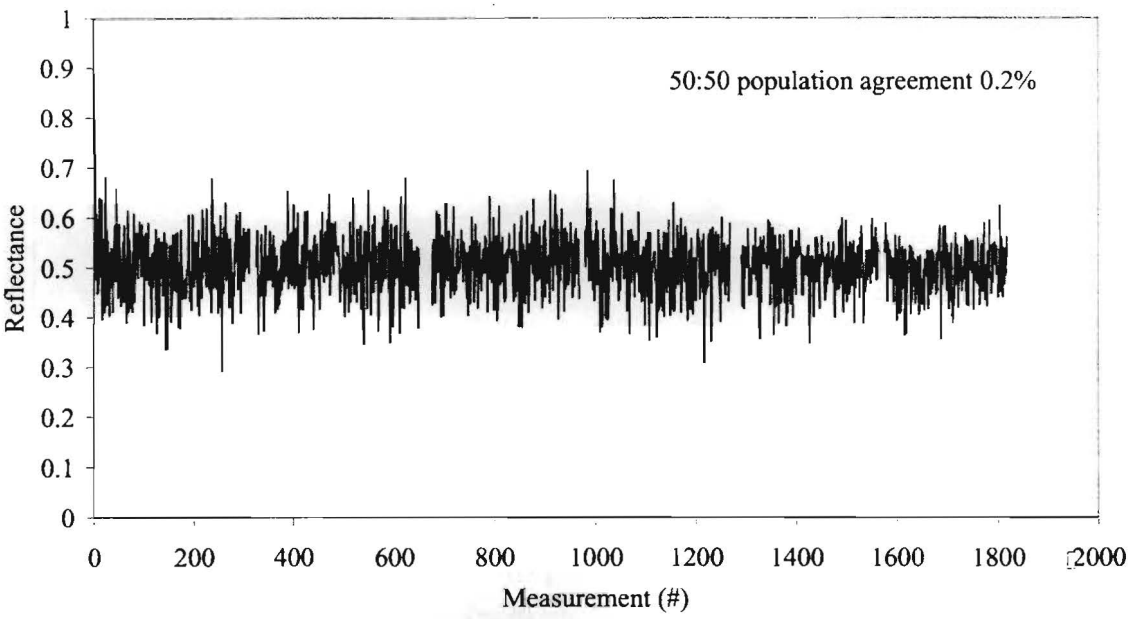

Figure 4. Reflectance at 900 nm for all 1824 measurements of the calibration target on Salar de Arizaro. The surface microtopography causes large spectrum-to-spectrum variability.

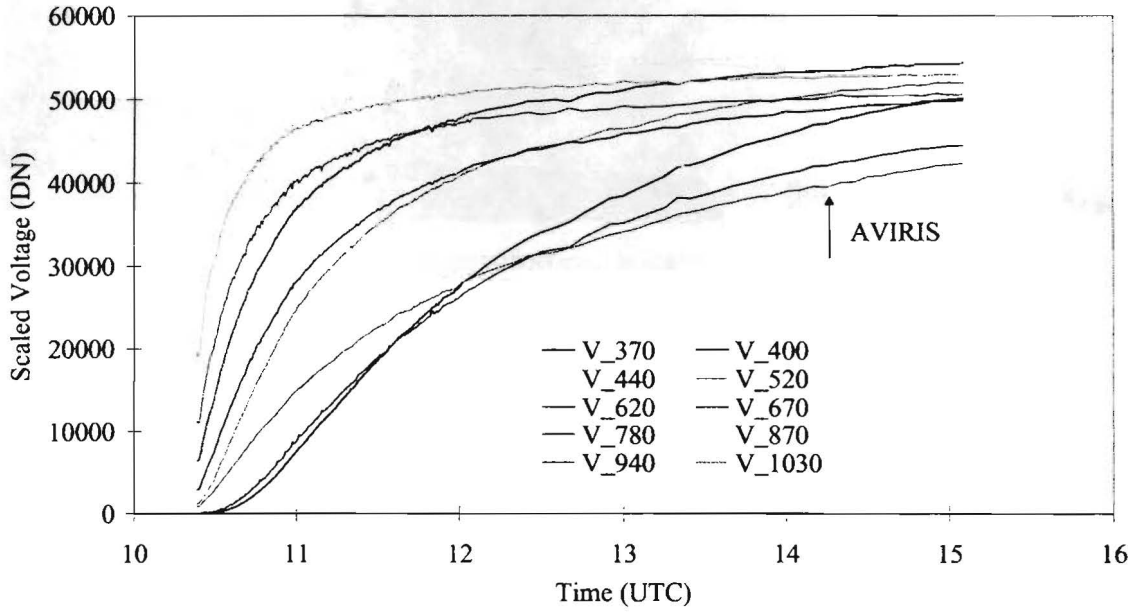

Figure 5. Measurements from the sun tracking solar radiometer at Salar de Arizaro on February 7, 2001.

2.2 AVIRIS Measurements

On February 7, 2001 at 14:22 UTC, AVIRIS acquired data over the calibration target on the Salar de Arizaro. Figure 7 shows a georectified AVIRIS image that includes the calibration target. One of demarcation tarps is evident immediately adjacent to the east-west road and the other south of the road. From the AVIRIS measured data, the average calibrated radiance spectrum was extracted for the Salar de Arizaro calibration target and is shown in Figure 8.

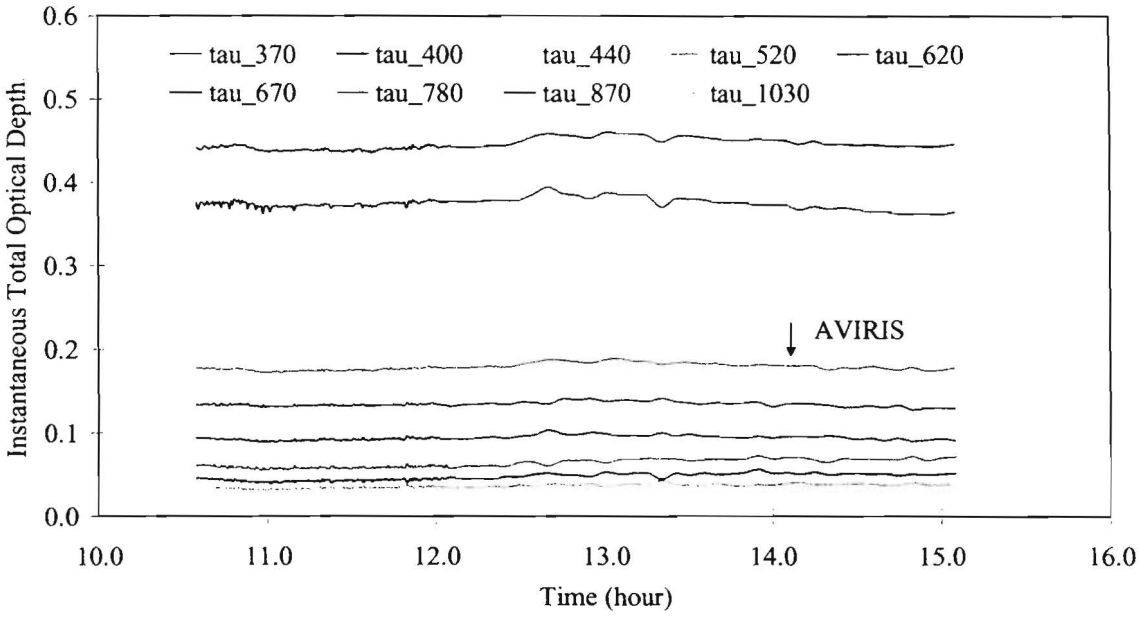

Figure 6. Calculated instantaneous total optical depths for February 7, 2001 at Salar de Arizaro.

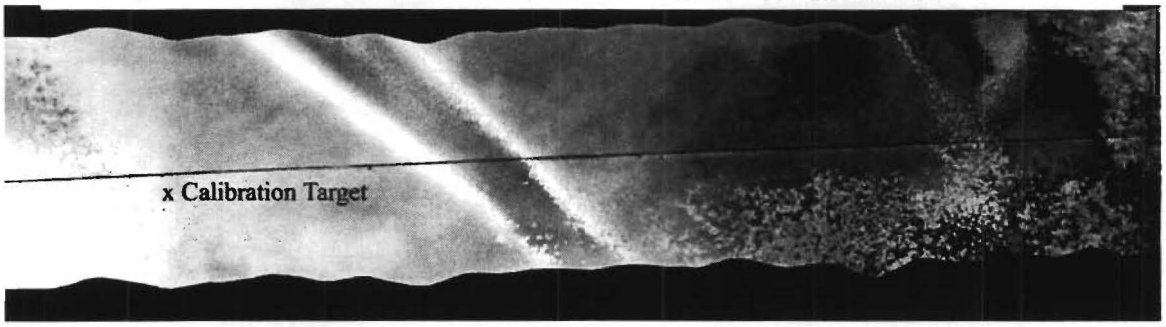

Figure 7. AVIRIS image of calibration target on Salar de Arizaro.

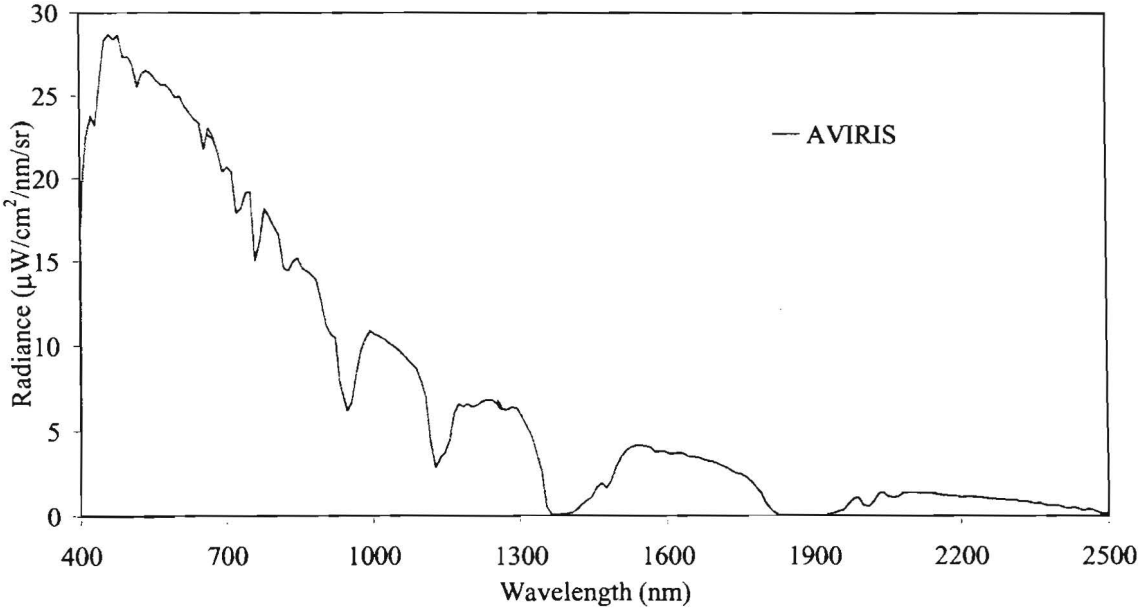

Figure 8. Average radiance spectrum measured by AVIRIS for the calibration target on Salar de Arizaro.

2.3 Modeled Radiance

To predict the radiance incident at AVIRIS over the calibration target, the MODTRAN radiative transfer code (Berk et al. 1989, Anderson et al. 1995) was used. MODTRAN was constrained by the latitude, longitude, elevation, and time as well as the surface spectral reflectance, optical depths, and water vapor derived from the solar radiometer measurements. The MODTRAN mid-latitude summer atmospheric model was used with visibility scaled to 100 km. This visibility gave the best agreement between the measured total optical depths and the corresponding MODTRAN calculated total optical depths. A water vapor amount of 8.13 precipitable mm was used based upon the solar radiometer measurements at 940 nm wavelength. Carbon dioxide was constrained to a mixing ratio of 371 ppm by the Mauna Loa values for February 2001 (Keeling and Whorf 2001). Ozone was constrained to 263 dobsin units by the Total Ozone Mapping Spectrometer (TOMS) satellite instrument measurements (McPeters 2001). Figure 9 shows the MODTRAN modeled radiance for AVIRIS over the calibration target on February 7, 2001.

2.4 Results

To assess the inflight calibration of AVIRIS, the AVIRIS measured spectrum for the calibration target was compared to the MODTRAN predicted spectrum. The comparison is shown in Figure 10. In general, there is good agreement across the spectral ranges. This figure also shows a ratio of the AVIRIS spectrum to the MODTRAN spectrum. The features in the ratio result from a combination of uncertainties that include: AVIRIS laboratory calibration, change in AVIRIS calibration in the flight environment, the MODTRAN model, and the atmospheric and solar parameters internal to the MODTRAN code. Overall, the average absolute agreement between the MODTRAN and AVIRIS spectra of the calibration target is 96 % excluding the regions of strong atmospheric absorption.

In addition to inflight radiometric calibration, the inflight radiometric precision of AVIRIS was assessed. Radiometric precision was calculated as the noise equivalent delta radiance (NEdL) for AVIRIS on the Salar de Arizaro flight. The NEdL is calculated as the standard deviation of the AVIRIS dark signal in units of radiance. For the Arizaro calibration target data (and all AVIRIS data), the dark signal was automatically measured immediately before and after the flight line data acquisition. Figure 11 shows the calculated AVIRIS NEdL for the Salar de Arizaro data set. The NEdL may be viewed as the precision error bars in radiance due to the AVIRIS instrument for any measured radiance spectrum.

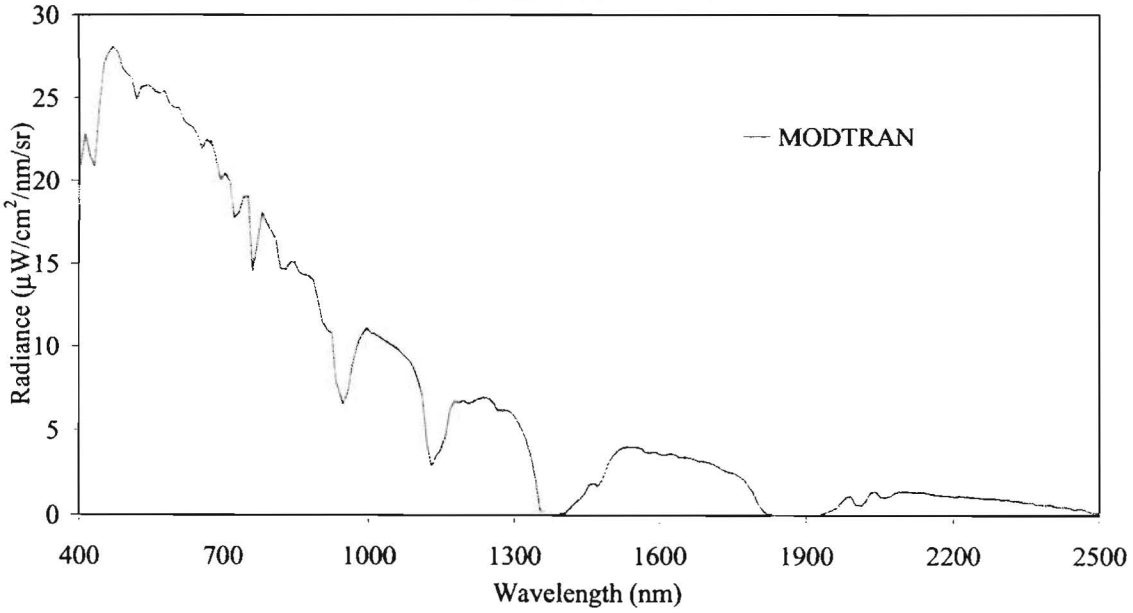

Figure 9. MODTRAN modeled radiance for the Salar de Arizaro calibration target on February 7, 2001.

For bright signal targets, the NEdL increased due to the photon noise contributions to the uncertainty in the measurement.

3.0 CALIFORNIA EXPERIMENT

On June 6, 2001, an AVIRIS inflight calibration experiment was conducted at a site on Rogers Dry Lake, California. Rogers Dry Lake is a large silt composition playa located 35 degrees north latitude and 117.8 degrees west longitude—about 2 hours drive north of Los Angeles. Figure 12 shows an AVIRIS

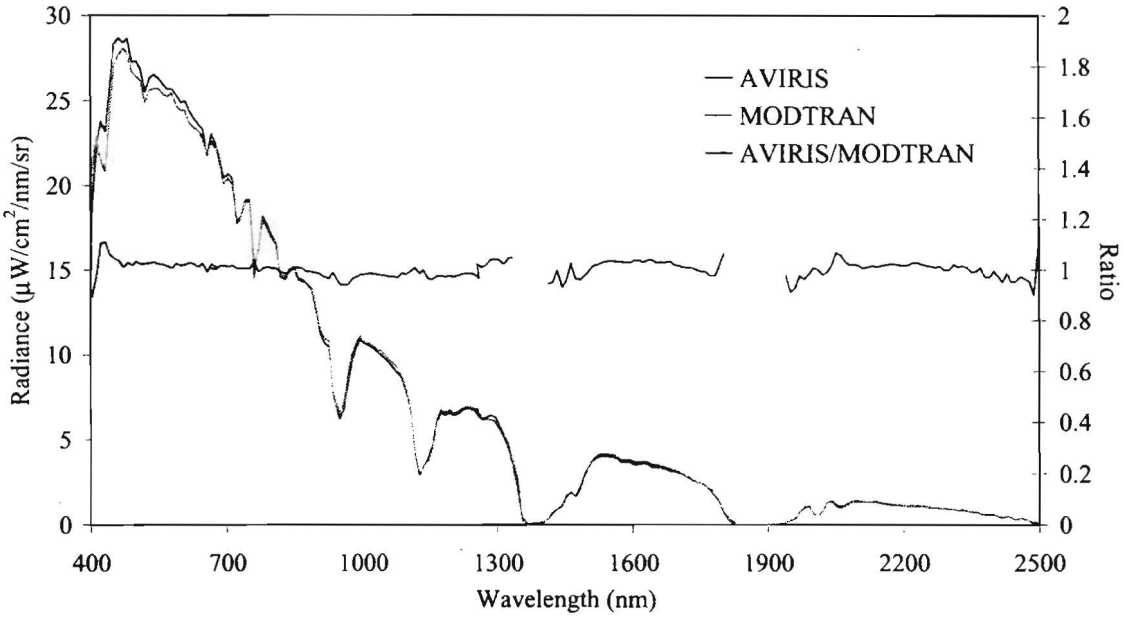

Figure 10. AVIRIS measured and MODTRAN modeled radiance spectra for the calibration target on Salar de Arizaro, Argentina.

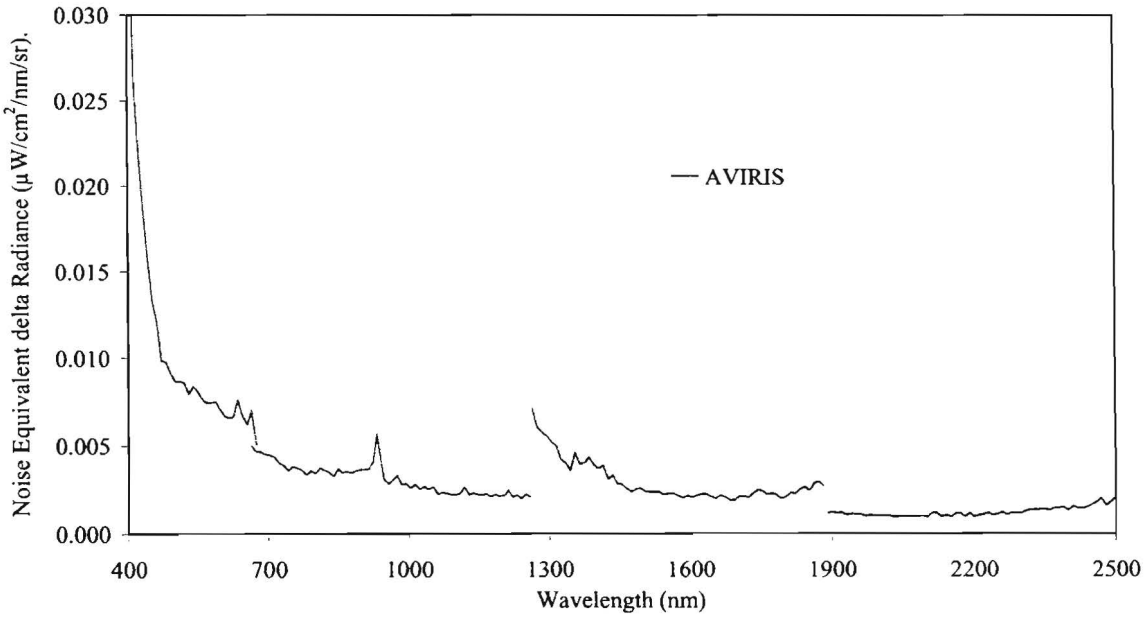

Figure 11. Calculated NEdL for AVIRIS in the flight environment over the calibration target of Salar de Arizaro.

image of the northern portion of Rogers Dry Lake, California. The location of the surface calibration target for the inflight calibration experiment is also shown.

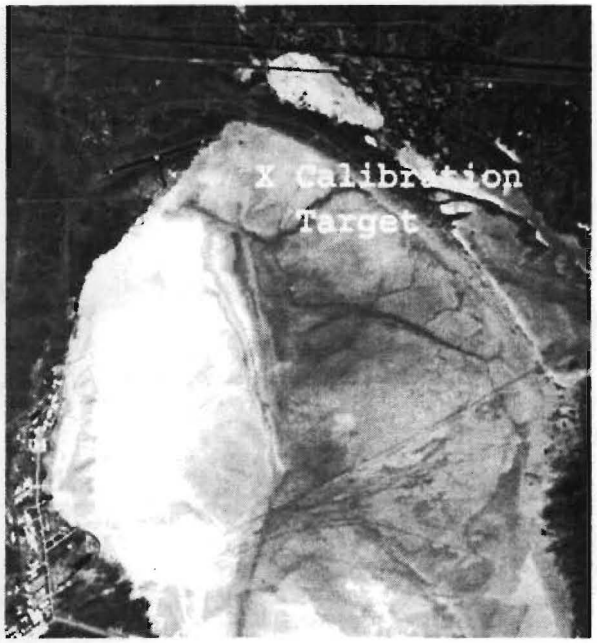

Figure 12. AVIRIS image of the northern portion Rogers Dry Lake, California acquired on June 6, 2001 with the calibration target area indicated.

3.1 Surface Measurements

A calibration target was designated on the surface of Rogers Dry Lake. The dimensions were 240 by 40 m with blue demarcation tarps placed on the surface 20 m beyond each end of the long axis of the target. Surface measurements of the calibration target were acquired with field spectrometer (Analytical Spectral Devices Inc., Full Range Spectrometer). These measurements were acquired in the period 30 minutes before and after the AVIRIS overflight of the calibration target. A spectral reflectance standard (Spectralon, Labsphere Inc.) was measured at the beginning, middle, and end of each transect of the calibration target. The data were reduced to surface reflectance with the spectral reflectance standard and accommodation for the bidirectional reflectance of the reflectance standard for the 43-degree solar illumination zenith angle. Figure 13 shows the average reflectance of the calibration target. Also shown are the standard deviation and the standard deviation of the average for the 1029 measurements of the calibration target. The standard deviation of the average is below 0.001 reflectance over the almost the entire spectral range. This indicates excellent knowledge of the average reflectance of the calibration target. Figure 14 shows the reflectance value for each spectrum at wavelengths of 500, 1000, 1500, and 2000 nm for all 1029 measurements. The spectrum-to-spectrum variation is small and consistent with the standard deviation of the set of calibration target reflectance measurements.

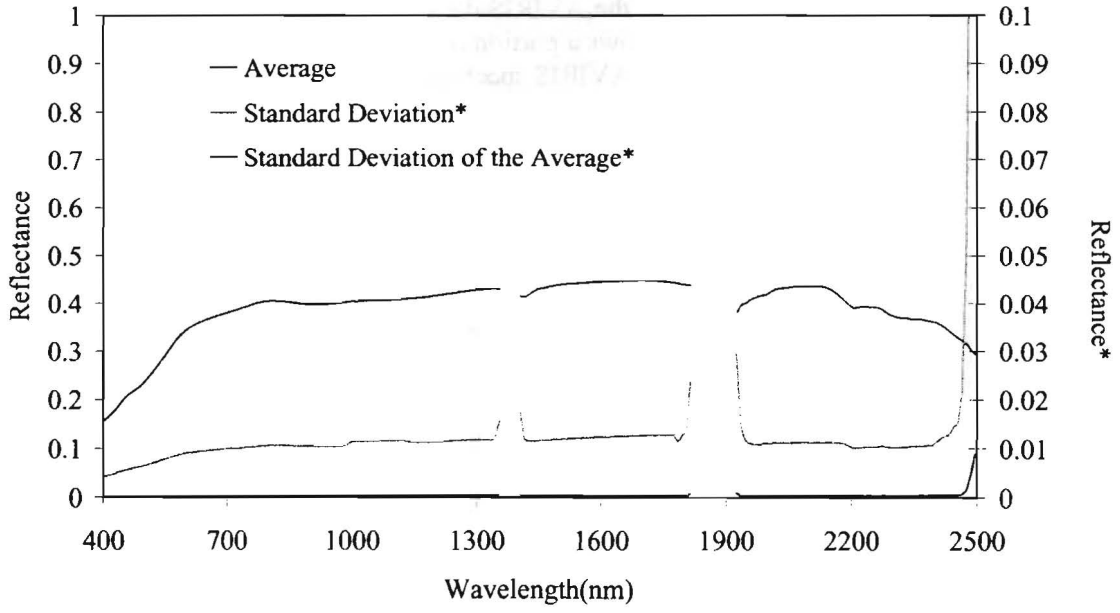

Figure 13. Average reflectance of the Rogers Dry Lake calibration target measured on June 6, 2001. The standard deviation and standard deviation of the average are shown for the 1029 measurements acquired as well.

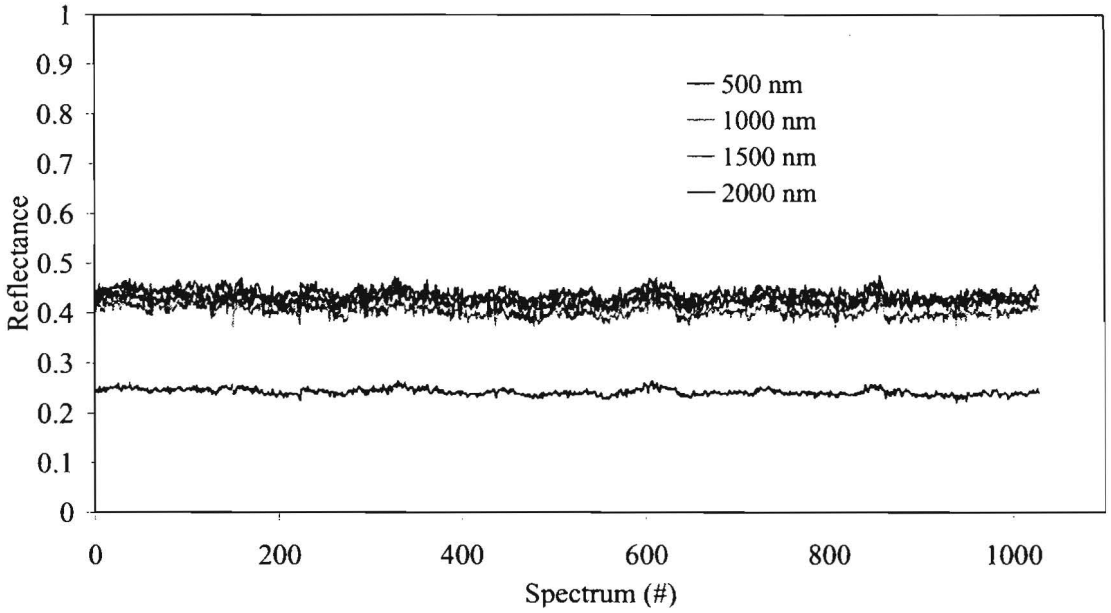

Figure 14. Reflectance values at wavelengths 500, 1000, 1500, and 2000 nm for the 1029 measurements of the calibration target. Only small spectrum to spectrum variation is present confirming the homogeneity of the site.

In addition to the surface reflectance, a sun tracking solar radiometer was set up adjacent to the calibration target to measure the atmospheric aerosol properties and atmospheric water vapor. On June 6, 2001 this instrument failed. As a fallback, measurements from the Aeronet (Holben et al. 1998) site at the NASA Dryden Research Center on the western side of Rogers Dry Lake were used. Table 1 shows the Aeronet aerosol optical depths and the calculated Rayleigh and total optical depths. A water vapor value of 15.1 precipitable mm was also derived for the time of the AVIRIS overflight.

3.2 AVIRIS Measurements

AVIRIS acquired data over the calibration target on Rogers Dry Lake at 16:38:17 UTC on June 6, 2001. The demarcation tarps were identified in the AVIRIS data and the average radiance spectrum was extracted for the calibration target. Figure 15 shows a portion of the AVIRIS image with the demarcation tarps in the center. Figure 16 shows the average AVIRIS spectrum for the calibration target.

Table 1. Optical depths for June 6, 2001 at Rogers Dry Lake, California

	Optical Depth		
Wavelength (nm)	Aerosol	Rayleigh	Total
340	0.105	0.64	0.74
380	0.078	0.40	0.48
440	0.051	0.22	0.27
500	0.047	0.13	0.17
670	0.033	0.039	0.073
870	0.026	0.013	0.040
1020	0.032	0.0073	0.039

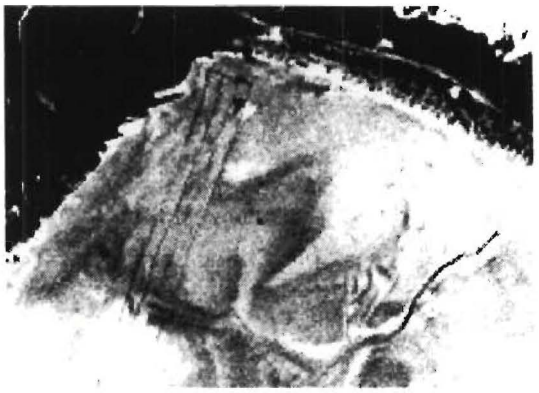

Figure 15. A subset of the AVIRIS measured image that shows the calibration target on the surface of Rogers Dry Lake. The demarcation tarps are evident one above the other in the center of the subset image.

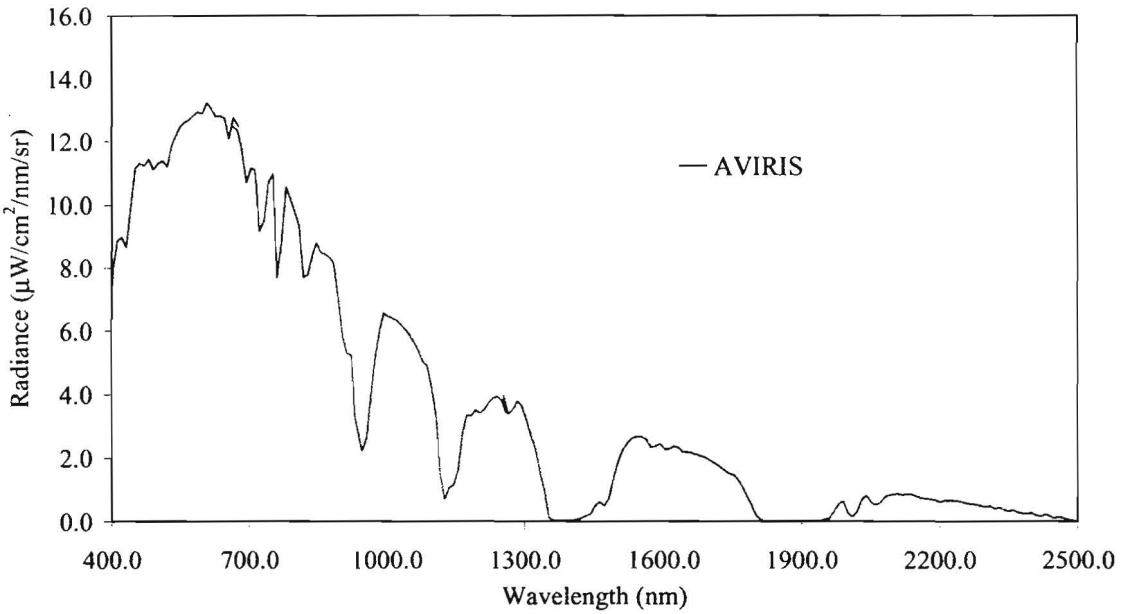

Figure 16. Average AVIRIS spectrum measured for the calibration target on Rogers Dry Lake, California, on June 6, 2001.

3.3 Modeled Radiance

The MODTRAN radiative transfer code was used to model the upwelling radiance incident at AVIRIS over the Rogers Dry Lake calibration target. MODTRAN was constrained by the latitude, longitude, elevation, and time as well as the measured surface reflectance, the optical depths and water vapor determinations. A MODTRAN visibility of 150 km with the mid latitude summer atmospheric model gave a good match with the in situ measured optical depths. Atmospheric carbon dioxide was constrained to a mixing ratio of 371 ppm consistent with the Mauna Loa values for June 2001 (Keeling and Whorf 2001). Ozone was constrained to 313 dobsin units by the TOMS satellite instrument measurements (McPeters 2001). Figure 17 shows the modeled upwelling radiance.

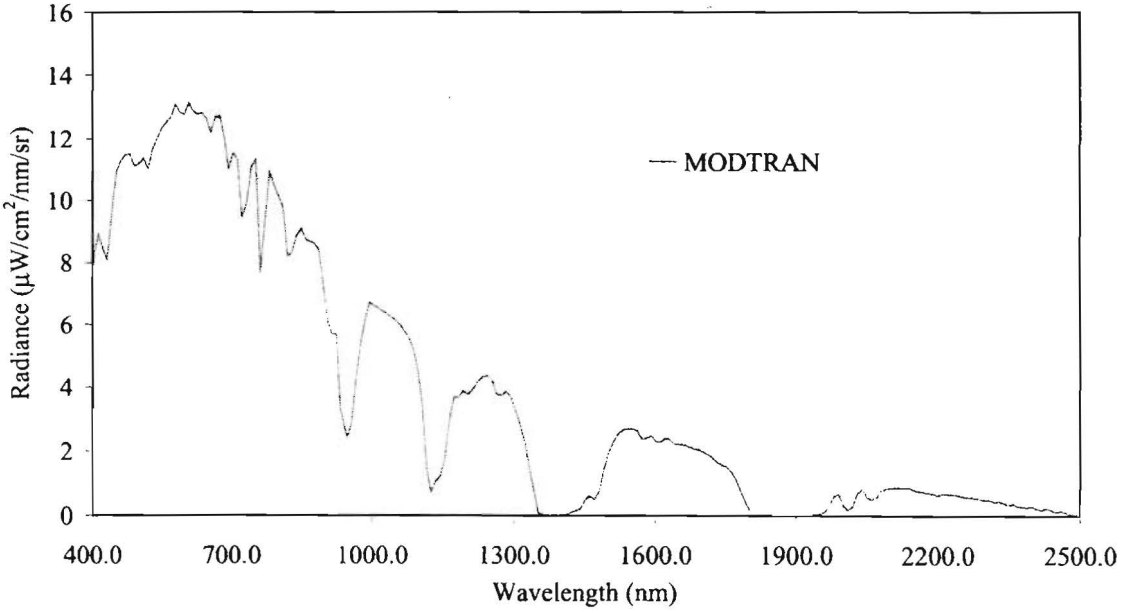

Figure 17. MODTRAN modeled radiance for the AVIRIS inflight calibration experiment on Rogers Dry Lake, California, on June 6, 2001.

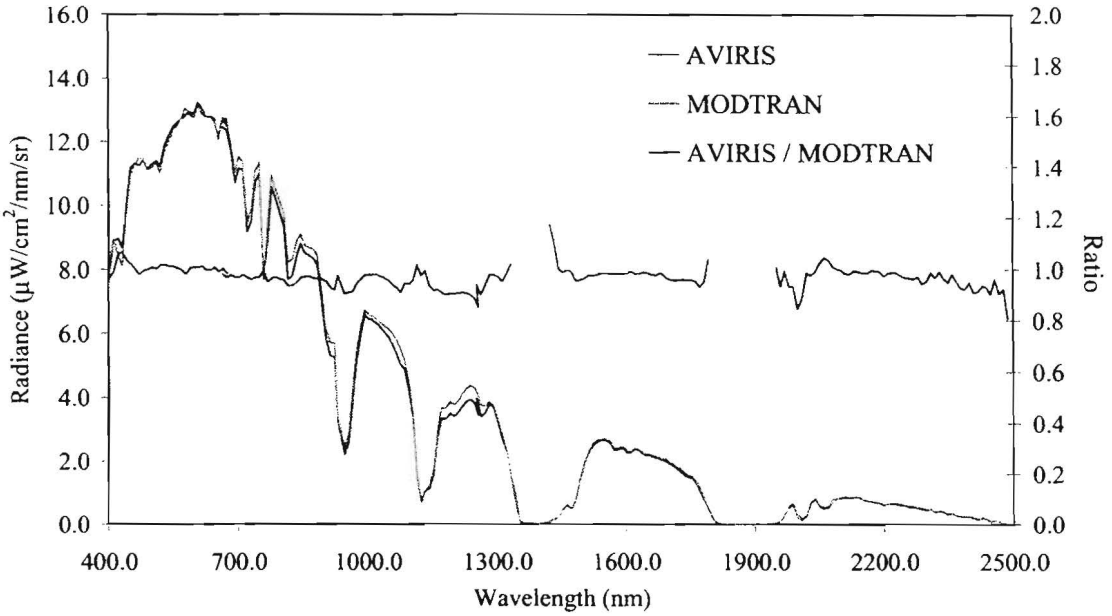

Figure 18. Comparison of the AVIRIS measured and MODTRAN modeled radiance spectra for the calibration target on Rogers Dry Lake, California, on June 6, 2001.

3.4 Results

To assess the inflight calibration of AVIRIS the measured radiance is compared to the modeled radiance. Figure 18 shows this comparison and a ratio of the AVIRIS measured to the MODTRAN modeled spectrum. Exclusive of the strong water vapor absorption regions of the spectrum the average absolute agreement is better than 96%.

The inflight radiometric precision of AVIRIS was assessed for June 6, 2001 inflight calibration experiment. The NEdL was calculated as the standard deviation of the AVIRIS dark signal in units of radiance. Figure 19 shows the calculated AVIRIS NEdL for this Rogers Dry Lake calibration experiment.

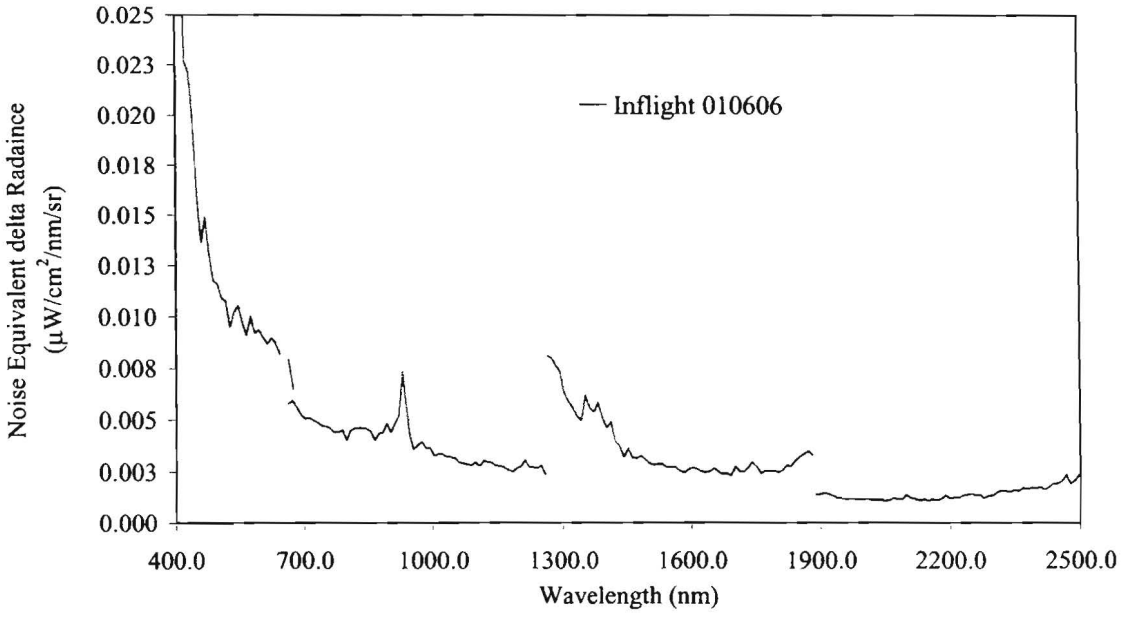

Figure 19. Calculated inflight dark signal NEdL for the June 6, 2001 calibration experiment.

4.0 CONCLUSION

The measurements, analyses, and results from two AVIRIS inflight calibration experiments of 2001 have been presented. The first experiment was conducted at 3700 m on the dry salt lake of Salar de Arizaro, Argentina on February 7, 2001. This was the first ever calibration experiment at a site of this altitude. In general, simpler atmospheres are expected at higher altitudes. The surface reflectance of Arizaro was also unusual with very high reflectance across the AVIRIS spectral range specifically including the blue portion of the spectrum. At the Arizaro calibration target, measurements of surface reflectance, atmospheric optical depths, and water vapor were acquired. These measurements were used to constrain the MODTRAN radiative transfer code and predict the radiance incident at AVIRIS at the time of the AVIRIS overflight. Comparison of the AVIRIS measured and MODTRAN predicted radiance showed an average absolute agreement of better than 96 percent exclusive of the strong atmospheric water absorption bands. AVIRIS inflight precision was also assessed through calculation of the dark signal noise equivalent delta radiance. Noise equivalent delta radiance is the radiance uncertainty due to the AVIRIS instrument.

A second AVIRIS inflight calibration experiment was conducted at Rogers Dry Lake, California on June 6, 2001. Surface measurements were acquired of the reflectance at atmospheric properties and used to constrain the MODTRAN radiative transfer code and predict the radiance at AVIRIS. Comparison of the AVIRIS measured to the MODTRAN predicted showed an average absolute agreement of better than 96 percent exclusive of the spectral regions of strong atmospheric water vapor absorption. The AVIRIS inflight instrument precision uncertainty was calculated as the noise equivalent delta radiance.

The results from these two AVIRIS inflight calibration experiments are consistent with the corresponding results of the past few years. There are a combination of factors that currently inhibit matches between AVIRIS measurements and MODTRAN prediction much better than 96 percent. These factors include: AVIRIS laboratory calibration, change in AVIRIS calibration in the flight environment, uncertainty in the surface measurements, assumptions in the MODTRAN radiative transfer calculations, and uncertainty in the solar and atmospheric parameters used within MODTRAN. It is hoped with improvements to the AVIRIS onboard calibrator and improvements to the MODTRAN constraining atmospheric and solar parameters, the level of agreement will improve.

5.0 REFERENCES

Anderson, G. P., J. Wang, and J. Chetwynd, "An Update and Recent Validations Against Airborne High Resolution Interferometer Measurements," *Summaries of the Fifth Annual JPL Airborne Earth Science Workshop*, JPL Publication 95-1, Vol. 1, AVIRIS Workshop, Jet Propulsion Laboratory, Pasadena, California, January 23–26, 1995.

Berk, A., L. S. Bernstein, and D. C. Robertson, "MODTRAN: A Moderate Resolution Model for LOWTRAN 7," Final Report, GL-TR-0122, AFGL, Hanscomb AFB, MAassachusetts, 42 pp., 1989.

Bruegge C. J., J. E. Conel, R. O. Green, J. S. Margolis, R. G. Holm et al., "Water vapor column abundance retrievals during fire," *Journal of Geophysical Research Atmospheres*, 97(D17) 18759–18768, 1992.

Chrien, T. G., R. O. Green, and M. Eastwood, "Laboratory spectral and radiometric calibration of the Airborne Visible/Infrared Imaging Spectrometer (AVIRIS)," *SPIE,* Vol. 1298, *Imaging Spectroscopy of the Terrestrial Environment*, 1990.

Chrien, T. G., R. O. Green, C. Chovit, M. Eastwood, J. Faust, P. Hajek, H. Johnson, H. I. Novack, and C. Sarture, "New Calibration Techniques for the Airborne Visible/Infrared Imaging Spectrometer (AVIRIS), 1995," *Proc. Fifth Annual Airborne Earth Science Workshop*, JPL Publication 95-1, Jet Propulsion Laboratory, Pasadena, California, 1995.

Chrien, T. G., R. O. Green, C. J. Chovit, M. L. Eastwood, and C. M. Sarture, "Calibration of the Airborne Visible/Infrared Imaging Spectrometer in the Laboratory," *Proc. Sixth Annual Airborne Earth Science Workshop*, JPL Publication 96-4, Vol. 1, Jet Propulsion Laboratory, Pasadena, California, March 3–5, 1996.

Chrien, T. G., R. O. Green, D. Cohen, B. Pavri, J. Wall, and C. Sarture, "Predicted Accuracy and validation of the AVIRIS Radiometric Calibration Standard," *Proc. Ninth Airborne Earth Science Workshop*, JPL Publication 00-18, Jet Propulsion Laboratory, Pasadena, California, 2000.

Conel, J. E., R. O. Green, R. E. Alley, C. J. Bruegge, V. Carrere, J. S. Margolis, G. Vane, T. G. Chrien, P. N. Slater, S. F. Biggar, P. M. Teillet, R. D. Jackson, and M. S. Moran, "In-Flight Radiometric Calibration of the Airborne Visible/Infrared Imaging Spectrometer (AVIRIS)," *SPIE,* Vol. 924, *Recent advances in sensors, radiometry and data processing for remote sensing*, 1988.

Green, R. O., J. E. Conel, V. Carrere, C. J. Bruegge, J. S. Margolis, M. Rast, and G. Hoover, "In-flight Validation and Calibration of the Spectral and Radiometric Characteristics of the Airborne Visible/Infrared Imaging Spectrometer (AVIRIS)," *Proc. SPIE Conference on Aerospace Sensing, Imaging Spectroscopy of the Terrestrial Environment*, Orlando, Florida, April 16–20, 1990.

Green, R. O., J. E. Conel, C. J. Bruegge, J. S. Margolis, V. Carrere, G. Vane, and G. Hoover, "In-flight Calibration of the Spectral and Radiometric Characteristics of AVIRIS in 1991," *Summaries of the Third Annual JPL Airborne Geoscience Workshop*, JPL Publication 92-14, Vol. 1, pp. 1–4, Jet Propulsion Laboratory, Pasadena, California, 1992.

Green, R. O., J. E. Conel, M. Helminger, J. van den Bosch, C. Chovit, and T. Chrien, "Inflight Calibration of AVIRIS in 1992 and 1993," *Summaries of the Fourth Annual JPL Airborne Geoscience Workshop*, JPL Publication 93-26, Vol. 1, Jet Propulsion Laboratory, Pasadena, California, October 25, 1993a.

Green, R. O., "Use of Data from the AVIRIS Onboard Calibrator," *Summaries of the Fourth Annual JPL Airborne Geoscience Workshop*, JPL Publication 93-26, Vol. 1, Jet Propulsion Laboratory, Pasadena, California, October 25, 1993b.

Green, R. O., J. E. Conel, M. Helmlinger, J. van den Bosch, and P. Hajek, "In-Flight Radiometric Calibration of AVIRIS in 1994," *Proc. of the Fifth Annual JPL Airborne Earth Science Workshop*, JPL Publication 95-1, Jet Propulsion Laboratory, Pasadena, California, January 23–26, 1995.

Green, R. O., Conel, J. E., Margolis, C. Chovit, and J. Faust, "In-Flight Calibration and Validation of the Airborne Visible/Infrared Imaging Spectrometer (AVIRIS)," *Proc. Sixth Annual Airborne Earth Science Workshop*, JPL Pub. 96-4, Vol. 1, Jet Propulsion Laboratory, Pasadena, California, March 3–5, 1996.

Green R. O., B. Pavri, J. Faust, O. Williams, and C. Chovit, "Inflight Validation of AVIRIS Calibration in 1996 and 1997," *Proc. Seventh Airborne Earth Science Workshop*, JPL Pub. 97-21, Vol. 1, pp. 193–205, Jet Propulsion Laboratory, Pasadena, California, 1998a.

Green, R. O., M. L. Eastwood, and C. M. Sarture, "Imaging Spectroscopy and the Airborne Visible Infrared Imaging Spectrometer (AVIRIS)," *Remote Sens Environ* 65: (3) 227–248 SEP 1998b.

Green, R. O., B. Pavri, J. Faust, C. Chovit, and O. Williams, "AVIRIS In-Fight Radiometric Calibration Results for 1998," *Proc. Eighth Airborne Earth Science Workshop*, JPL Publication 99-17, Vol. 1, pp. 161–175, Jet Propulsion Laboratory, Pasadena, California, 1999.

Green, R. O., and B. Pavri, "AVIRIS Inflight Calibration Experiment, Measurements, Analyses and Results, Sensitivity Analysis and Intraflight Stablity," *Proc. Ninth Airborne Earth Science Workshop*, JPL Publication 00-18, pp. 207–222, Jet Propulsion Laboratory, Pasadena, California, 2000.

Green, R. O., and B. Pavri, "AVIRIS Inflight Calibration Experiment Measurements, Analyses and Results," *Proc. Tenth Airborne Earth Science Workshop*, JPL Publication 02-01, pp. 205–219, Jet Propulsion Laboratory, Pasadena, California, 2001.

Holben B. N., T. F. Eck, I. Slutsker, D. Tanre, J. P. Buis, A. Setzer, E. Vermote, J. A. Reagan, Y. Kaufman, T. Nakajima, F. Lavenu, I. Jankoviak, and A. Smirnov, "AERONET-A Federated Instrument Network and Data Archive for Aerosol Characterization," *RSE*, 66, 1–16, 1998.

Keeling, C. D., and T. P. Whorf, 2001, "Atmospheric CO^2 concentrations (ppmv) derived from in-situ air samples collected at Mauna Loa Observatory, Hawaii," Scripps Institution of Oceanography (SIO), University of California, La Jolla, California USA 92093-0244, http://cdiac.esd.ornl.gov/ftp/maunaloa-co2/maunaloa.co2

McPeters, R. D., 2001, EarthProbe/TOMS data set, NASA/GSFC TOMS Ozone Processing Team (OPT), Code 916, NASA Goddard Space Flight Center, Greenbelt, Maryland 20771, ftp://toms.gsfc.nasa.gov/pub/eptoms/images/global/y2001/et010207.gif and ftp://toms.gsfc.nasa.gov/pub/eptoms/images/global/y2001/et010606.gif, 2001.

Reagan, J. A., K. Thome, B. Herman, and R. Gall, "Water Vapor Measurements in the 0.94 Micron Absorption Band: Calibration, Measurements and Data Applications," *Proc. IGARSS*, Ann Arbor, Michigan, May 18–21, 1987.

Taylor, J. R., *An Introduction to Error Analysis*, Oxford University Press, p. 270, 1982.

6.0 ACKNOWLEDGMENTS

The research for this paper was carried out at the Jet Propulsion Laboratory, California Institute of Technology, Pasadena, California, under a contract with the National Aeronautics and Space Administration. The Aeronet measurements were provided from the Dryden Research Center research site, which operates under the leadership of Jeannette van den Bosch.

Hierarchical Segmentation of Hyperspectral Data

J. Anthony Gualtieri
Code 935 and Global Sciences and Technology
NASA/GSFC
Greenbelt, MD 20771
John.A.Gualtieri.1@gsfc.nasa.gov

James C. Tilton
Code 935
NASA/GSFC
Greenbelt, MD 20771
James.C.Tilton@nasa.gov

1 Introduction

We present a new algorithm for unsupervised classification which we apply here to AVIRIS hyperspectral data. The algorithm is based on the notion of region growing in a hierarchical setting and involves both spectral clustering and spatial clustering. This is in contrast to the standard approach to performing unsupervised classification of hyperspectral data wherein pixels are clustered (segmented) into regions based only on the *similarity* of their spectra without consideration of their spatial positions. Thus an important source of information about segmentation, contiguity of spatial neighbors, is ignored. And notice that spectral clustering will yield the same clusters for a data cube, and for the same data cube where the spatial positions have been randomly permuted.

Hierarchical segmentation normally begins by assuming every pixel in the hyperspectral data cube is a separate region (however, provision is made for initialization with a per-segmentation). Then, a dissimilarity criterion is computed between spectra in neighboring regions, the minimum dissimilarity criterion is found over all pairs of neighboring regions, and all pairs of neighboring regions with this minimum dissimilarity criterion value are merged. Optionally, this spatial clustering step is followed by a spectral clustering step in which a dissimilarity criterion is computed between spectra of all spatially non-adjacent regions, and all pairs of such regions with dissimilarity less than or equal to the minimum dissimilarity value found in the spatial clustering step are merged. After sufficient iterations of this procedure are completed so that a potentially meaningful segmentation is produced, the segmentation process is checked for convergences. A convergence is signified by a jump in a global dissimilarity criterion calculated between the region mean image and the original image data values. When a convergence is detected, the image segmentation from the previous iteration is saved. The region growing process (spatial clustering plus the optional spectral clustering) is continued until there are only two regions remaining, and this two region segmentation is also saved. The outcome is a hierarchical stack of segmentations at different levels of segmentation detail in the form of a tree structure with two regions at the top which come from merges of multiple regions at the next level down, and so on, to the highest level of segmentation detail from the first detected convergence.

Clearly this process is compute intensive. However the advent of cluster computing by

Beowulf class machines [1], in which tens of commodity Intel processors running Linux are interconnected with a high speed network, allows methods requiring large computational resources to be explored. For example on a 64 processor Beowulf machine with a Myrinet network linking the processors, it is possible to perform hierarchical segmentation on a data cube of size [lines, samples, bands] = [464, 595, 182] in 16 minutes, and on a data cube of size [lines, samples, bands] = [128, 128, 182] in 129 sec.

Below we describe the hierarchical segmentations algorithm and demonstrate its use on a hyperspectral data cube taken by AVIRIS at the Patuxent Wildlife Research Center in Laurel Maryland.

2 Hierarchical Segmentation

Image segmentation is a partitioning of an image into sections or regions. These regions may be later associated with a ground cover type or land use type, but the segmentation process simply gives generic labels (region 1, region 2, etc.) to each region. The regions consist of groupings of hyperspectral image pixels that have similar data feature values. These data feature values may be the hyperspectral data values themselves, and/or they may be derived features such as band ratios [2] or textural features [3]. Image segmentation is a key first step in a number of approaches to image analysis. In image analysis, the group of pixels contained in each region provides a good statistical sampling of data values for more reliable labeling based on multi-spectral or hyperspectral feature values. In addition, the region shape can be analyzed as an additional clue for the appropriate labeling of the region. Most image segmentation approaches can be placed in one of three classes [4]: 1. Characteristic feature thresholding or clustering, 2. Boundary detection, 3. Region growing.

Characteristic feature thresholding or clustering is often ineffective because it does not exploit spatial information. Boundary detection does exploit spatial information through examining local edges found throughout the image. For simple noise-free images, detection of edges results in straightforward boundary delineation. However, edge detection on noisy, complex images often produces missing edges and extra edges producing region boundaries that do not necessarily form a set of closed connected curves that surround connected regions. We prefer region growing because it exploits spatial information and guarantees the formation of closed connected regions. However, region growing is not without its problems. With region growing, spectrally similar but spatially disjoint regions are never associated together, and it is often not clear at what point the region growing process should be terminated. Also, region growing tends to be a computationally intensive process.

Tilton has developed a hybrid region growing and spectral clustering approach (first described in [5]) that largely overcomes these problems. The hybridization with spectral clustering allows association of spectrally similar but spatially disjoint regions. The approach also includes the detection of natural convergence points to assist in determining at what point the region growing process should terminate. Finally, the recursive version of this

approach is very effectively implemented on MIMD (Multiple Instruction, Multiple Data stream) parallel computers, which greatly reduces the amount of time required to segment large images with this approach. Next we give a description of the segmentation approach. The actual implementation is on Beowulf class cluster machine at Code 935, NASA/GSFC [6].

2.1 Hybrid of Region Growing and Spectral Clustering

We begin by defining the global criterion that will control how the algorithm will decide when to merge regions of similar clusters, and how the algorithm will decide that the particular level reached in the merging process is a natural convergence point and should be saved. Then we describe a high-level outline of the hybrid image segmentation (HSEG) approach.

2.1.1 Dissimilarity Criterion

Selection of an appropriate dissimilarity criterion is generally dependent on the application the resulting segmentations will be used for, and on the characteristics of the image data. However in earlier studies, Tilton [7] found the *Euclidean Spectral Distance* to be a useful criterion.

Let two regions (which may be individual pixels or regions of contiguous or non-contiguous pixels that are spectrally similar), be labeled by ω, ψ. For these regions we can compute mean spectral vectors $\bar{\mathbf{x}}_\omega = (\bar{x}_{\omega 1}, \bar{x}_{\omega 2}, \ldots, \bar{x}_{\omega n_b})$ and $\bar{\mathbf{x}}_\psi = (\bar{x}_{\psi 1}, \bar{x}_{\psi 2}, \ldots, \bar{x}_{\psi n_b})$, where $\bar{x}_{\omega q} = \sum_{i \in \omega_q} x_{iq} / \sum_{i \in \omega_q} 1$ and similarly for $\bar{x}_{\psi q}$, and where q $(1 \leq q \leq n_b)$ is the index of the spectral band and n_b is the total number of bands per pixel.

From these a Euclidean spectral distance defines the dissimilarity criterion,

$$\mu_{\omega\psi} = \frac{\left[\sum_{q=1}^{n_b} (\bar{x}_{\omega q} - \bar{x}_{\psi q})^2\right]^{\frac{1}{2}}}{n_b}.$$

2.1.2 Global Criterion

The global criterion is used to identify significant changes in the segmentation results from one iteration to the next. This criterion is defined like the dissimilarity criterion, except that it compares the original image data with the region mean image from the current segmentation. The value of this criterion is calculated at each image point, and averaged over the entire image. Thus we define the global criterion as,

$$\mu_{glbl} = \frac{\sum_{\omega \in \{\alpha, \beta, \ldots\}} \sum_{i \in \omega} \left[\sum_{q=1}^{n_b} (x_{\omega q} - x_{iq})^2\right]^{\frac{1}{2}}}{n_s n_l n_b}$$

where i indexes an image pixel, ω indexes over regions of spectrally similar pixels given by the current segmentation $\{\alpha, \beta, \ldots\}$, q indexes over the all the spectral channels $1 \ldots n_b$ for each pixel or region, and n_s and n_l are the number of samples (columns) and lines (rows) in the image.

Next we give in pseudo code the Hierarchical Segmentation Algorithm. This is the basic algorithm, but in order to render it computationally on any but small hyperspectral cubes it will need to be embedded in a recursive hierarchical segmentation algorithm which is given in the sequel. We will show two ways it can be used depending on the value of the parameter N_{chk}:

$$N_{chk} \begin{cases} = 0 & \text{suppresses convergence checking} \\ > 0 & \text{uses convergence checking} \end{cases}$$

2.1.3 The Hierarchical Segmentation Algorithm

seg = **HSEG(** $cube, N_{min}, N_{chk}, \phi_{thresh}, seg^{init}$**)**

% $cube$ hyperspectral cube of size r, s, n_b
% N_{min} number of regions threshold. When called by **recur_hseg** with $n_{rec} > 0$, set $\gg 2$, else 2
% N_{chk} number of regions threshold when level 0 has converged.
% ϕ_{thresh} threshold for natural global convegence test
% seg^{init} initial hyperspectral cube segmentation
%Define: k the heirarchical level index
% $N^{(k)}$ number of regions in level k
% τ_{loop} control output

$k = 0$, $N^{(0)} = r \times s$, $seg = seg^{init}$, $\mu_{glbl}^{(pre)} = 0$, τ_{loop} =**true** % initialization

while($N^{(k)} > N_{min}$ **)** % outer loop with end criterion
while(τ_{loop} == **true** & $N_{chk} > N_{min}$**)** % inner loop with natural convergence criterion
compute $\mu_{\omega\psi}$ between all pairs of % region growing
spatially adjacent regions, $\omega\psi$,
find smallest $\mu_{adj}^{(min)}$ over all spatially % region growing
adjacent regions
$seg \leftarrow$**merge(**seg, all pairs of spatially adjacent regions
ϵ and ν where $\mu_{\epsilon\nu} = \mu_{adj}^{(min)}$ **)** % region growing
$N^{(k)} \leftarrow$ new number of regions
compute $\mu_{\sigma\tau}$ where σ and τ index over % spectral clustering
all pairs of non-spatially adjacent regions.
$seg \leftarrow$**merge(** seg, all pairs of non-spatially adjacent
regions λ and ξ where $\mu_{\lambda\xi} \leq \mu_{adj}^{(min)}$ **)** % spectral clustering
$N^{(k)} \leftarrow$ new number of regions
if ($N^{(k)} \leq N_{chk}$ **)** % natural convergence test begins at N_{chk}
compute $\mu_{glbl}^{(curr)}$.
if ($\mu_{glbl}^{(pre)} > 0$**)** $\phi = \mu_{glbl}^{(curr)} / \mu_{glbl}^{(pre)}$ % compute ϕ only when defined
else $\phi = \phi_{thresh}$
$\mu_{glbl}^{(pre)} = \mu_{glbl}^{(curr)}$
if($\phi \geq \phi_{thresh}$ **)** $\tau_{loop} \leftarrow$ **false**
end if
end while
if (τ_{loop} ==**false** **)**
save region label map from the iteration k
as the segmentation result for level k.
$\tau_{loop} \leftarrow$**true**
$k \leftarrow k + 1$
endif
end while
if($N_{chk} > 0$ **)**
save region label map from the current iteration as the
coarsest instance of the final hierarchical segmentation result.
stop
end if
end

2.1.4 Implementation Overview

A practical implementation of the hierarchical segmentation algorithm for all but the smallest hyperspectral cubes requires that the combinatorial growth in inter-region comparisons in the spectral clustering steps be addressed. Tilton's solution, is to recursively subdivide the image data into smaller and smaller sections until an image size is reached in which the required number of inter-region comparisons is sufficiently constrained that the **HSEG** algorithm can be applied without the global criterion, and run until a pre chosen number of regions, N_{min} has been found. At this point the segmentation so found is passed to the **HSEG** algorithm *with* the global criterion, which then produces the stack of region labeled segmentations. The number in the stack is dependent on the global criterion ϕ_{thresh} and the number of regions that initializes the **HSEG** computation [8]. Additional processing speed can be obtained through a parallel implementation of the recursive hierarchical segmentation algorithm [9]. However, the recursive decomposition and subsequent recombination of results can easily impart processing window artifacts in the segmentation results so obtained unless steps are taken to remove the artifacts. Effective and efficient methods for removing these artifacts have been devised [10]. This is called the **RHSEG** algorithm and is given in the sequel.

2.1.5 Implementation Details

For recursion, the original hyperspectral cube is subdivided along the spatial coordinates into 4 equal sized cubes rectangular in the spatial coordinates, each of which is itself subdivided into 4 equal rectangles and so on n_{rec} times until each of the $4^{n_{rec}}$ cubes resulting are small enough to directly apply **HSEG** to. Typically we choose n_{rec} such that the number of pixels in the smallest cube, $n_l/2^{n_{rec}} \times n_s/2^{n_{rec}}$, is in the range 500...2000. In order for the number of pixels in the two spatial directions be integers at level n_{rec} we pad out the original cube to $n_l^{(pad)}$ and $n_s^{(pad)}$ with spectra of all 0's so that $n_l^{(pad)}/2^{n_{rec}}$ and $n_s^{(pad)}/2^{n_{rec}}$ are both integers. The recursive algorithm, called **RHSEG**, first establishes the number of recursions and then calls recursively calls **recur_hseg** until the resulting subdivided hyperspectral cubes can be processed, without the global criterion, by **HSEG**. The resulting subdivided segmentation are then reassembled in **recur_hseg** until a segmentation at the top level of the recursion is obtained. This then initializes a final call of **HSEG** with the global criterion, and produces the output stack of region labeled segmentations.

$seg(n_l, n_s)$ = **RHSEG** $(cube(n_l, n_s, n_b), N_{min}, N_{chk}, \phi_{thresh}, seg^{init})$
% $(cube(n_l, n_s, n_b)$ initial data cube
% N_{min} number of regions threshold.
% N_{chk} number of regions threshold when level 0 has converged.
% ϕ_{thresh} threshold for natural global convegence test
% seg^{init} optional initial hyperspectral cube segmentation
% Define: n_{rec} number of recursive calls
% l_{rec} recursion level
% $n_l^{(pad)}$, $n_s^{(pad)}$ padded sizes

compute n_{rec} as an integer such that $\frac{1}{2}\log_2[n_l n_s/2000] \leq n_{rec} \leq \frac{1}{2}\log_2[n_l n_s/500]$
$n_l^{(pad)} = 2^{n_{rec}}\lceil n_l/2^{n_{rec}}\rceil$
$n_s^{(pad)} = 2^{n_{rec}}\lceil n_s/2^{n_{rec}}\rceil$
$cube(n_l^{(pad)}, n_s^{(pad)}, n_b)$ = **pad(** $cube(n_l, n_s, n_b)$ **)** % pad out with 0 spectra
$l_{rec} = 0$
seg = **recur_hseg(** $cube(n_l^{(pad)}, n_s^{(pad)}, n_b), N_{min}, N_{chk}, \phi_{thresh}, n_{rec}, l_{rec}, seg^{init}$ **)**
end

seg = **recur_hseg(** $cube(r, s, n_b), N_{min}, N_{chk}, \phi_{thresh}, n_{rec}, l_{rec}, seg^{init}$ **)**
% $cube(r, s, n_b)$ sub-cube of size $r \times s \times n_b$
% N_{min} minimum number of regions for stopping criterionn
% N_{chk} number of regions threshold when level 0 has converged.
% ϕ_{thresh} threshold for natural global convegence test
% n_{rec} number of recursive calls desired
% l_{rec} recursion level
% seg^{init} optional initial hyperspectral cube segmentation
%Define i index $\in 1, 2, 3, 4$ naming i'th sub-cube in recursion
if($l_{rec} < n_{rec}$ **true)**
for i=1,4 **do**
$cube_i(r/2, s/2, n_b)$ = **split4(**$i, cube(r, s, n_b)$ **)**
$seg_i^{init}(r/2, s/2, n_b)$ = **split4(**$i, seg^{init}(r, s, n_b)$ **)**
$seg_i(r/2, s/2, n_b)$ = **recur_hseg(** $cube_i(r/2, s/2, n_b), N_{min}, N_{chk}, \phi_{thresh}, n_{rec}, l_{rec}+1, seg_i^{init}(r/2, s/2, n_b)$ **)** % Incremented l_{rec}
end do
$seg^{init}(r, s, n_b)$ = **concatenate(** $seg_1, seg_2, seg_3, seg_4$ **)**
end if
if($l_{rec} == 0$ & $N_{chk} > N_{min}$ **)** $N_{min} = N_{chk}$
seg^{temp} = **HSEG(** $cube, N_{min}, 0, \phi_{thresh}, seg^{init}$**)** % Note, set $N_{chk} = 0$
seg^{init} = **eliminate_artifacts(** seg^{temp} **)**
if($l_{rec} == 0$ **)**
$N_{min} = 2$
seg = **HSEG(** $cube, N_{min}, N_{chk}, \phi_{thresh}, seg^{init}$**)**
end if
return
end

As described above, the **RHSEG** algorithm is prone to producing processing window artifacts in its segmentation results. These processing window artifacts are eliminated by examining the segmentation results after the completion of the call to **HSEG** in **recur_hseg**, and changing the region membership of pixels that are more similar to a region other than

the region the pixels are currently assigned to. How this process is efficiently implemented is described in [10].

2.1.6 Parameter Settings and Program Refinements

As described in sections 2.1.3 and 2.1.4 above, the **HSEG** and **RHSEG** algorithms with the Euclidean spectral distance dissimilarity criterion tend to produce segmentations with a large number of small regions. Since these small regions are generally of little use in the ultimate analysis of the segmentation results, an option has been added to the **HSEG** and **RHSEG** algorithms to encourage these small regions to merge into other regions. When this option is selected, the dissimilarity function is multiplied by the factor

$$1 - \left[\frac{P_m - P_S}{P_m}\right],$$

where P_m is a user supplied parameter, and P_s is the number of pixels in the smaller of the two regions being compared. This bias factor is applied only when $P_s < P_m$. In this paper we have used $P_m = 16$, $N_{min} = 256$, $N_{chk} = 64$, and $\phi = 1.01$.

3 Results for Patuxent Wildlife Research Center

On August 1, 2001 a series of AVIRIS scenes along a single flight line which included the Patuxent Wildlife Research Center (PWRC) in Laurel, Maryland was acquired. PWRC is a research facility of the U.S Fish and Wildlife Services and is roughly 50 square km and comprises mostly forest with some meadows, lakes, ponds, wetlands, and the Patuxent River. The data was radio-metrically corrected and geo-registered with a pixel size of 12.1 m. Scene 3 of flight-line, f010801t01p03_r08, was corrected for cross track illumination variation, due to the flight-line being flown at +60 deg from true north, and the bands were subset from 224 to 182 by removing bands with negative values due to water absorption and noise. To demonstrate the algorithm, a square subset of size 128 × 128 was subset out [11]. A preliminary use of recursive hierarchical segmentation **RHSEG** was performed to create masks for the clouds and cloud shadows in the scene. In this case 17 levels were found as shown in Fig. 1.

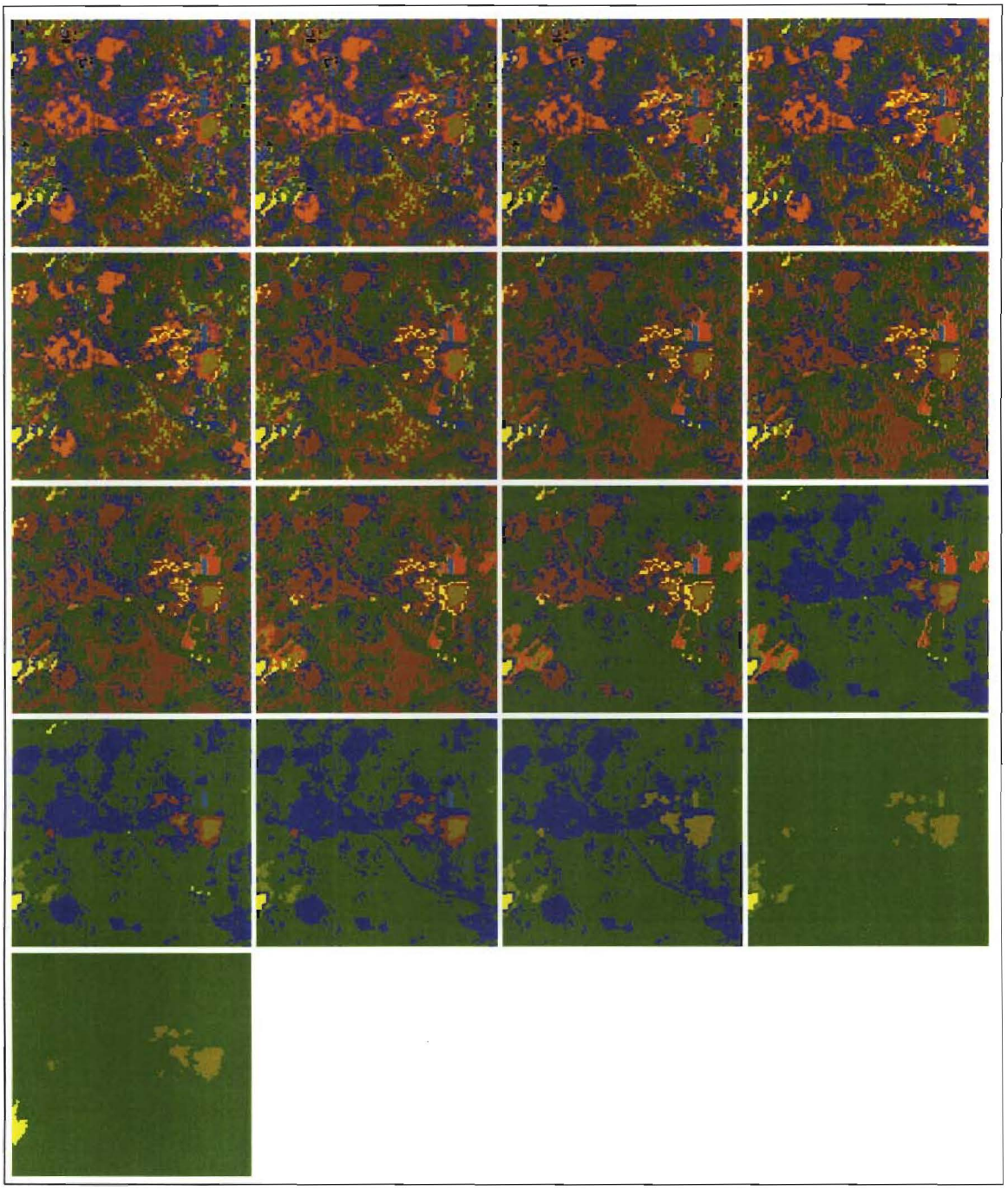

Fig. 1: The 17 levels of the hierarchical segmentation with an arbitrary color map that is the same for each level. Level 1 is the top left and follows left to right and then down. Note that there are 64 different colors in level 1, but they cannot all be resolved. At level 17 there are only 3.

This involves the use of the region labeling tool developed by Tilton [12]. The tool provides a Gui, typically with two windows, one showing a reference image such as an approximate true color image, and a second window in which the user can move up and down the segmentation hierarchy. The mouse is used as a pointing tool to track and show

the same spatial location in both windows, and the mouse buttons allow the user to select a single region at any level in the hierarchy window and then track that region up and down, as it either remains the same or coalesces with other regions going up or remains the same or splits into sub-regions going down the hierarchy.

Thus a feature in the reference image is used to select regions in the hierarchy. If, in tracking that region of the hierarchy, it is found to be stable over several levels, then it is taken to mean it is a region in the final segmentation. The user then can select a color from a palette, and a label for the region. For example in Fig. 1 at level 16 the yellow, brown, and tan regions match the clouds and cloud shadows, and these regions persist, though resolving to additional colors with the same external boundary down to level 10, The region labeling tools allows the selection of those three regions at level 17 to then be tracked down to lower levels to see how those regions break up into sub regions. To the extent that they maintain the same shape over several levels is an indication of their describing a real region feature in the scene. The analyst can also use the region labeling tool to select regions of interest by enclosing them with drawn closed loops in order to add pixels to a region in an existing segmentation.

In this way a cloud/cloud shadow mask was derived. Then the mask was applied to the original hyperspectral cube and **RHSEG** was applied to the masked hyperspectral cube. That resulted in the segmentation shown in Fig. 2, for which 18 levels occurred.

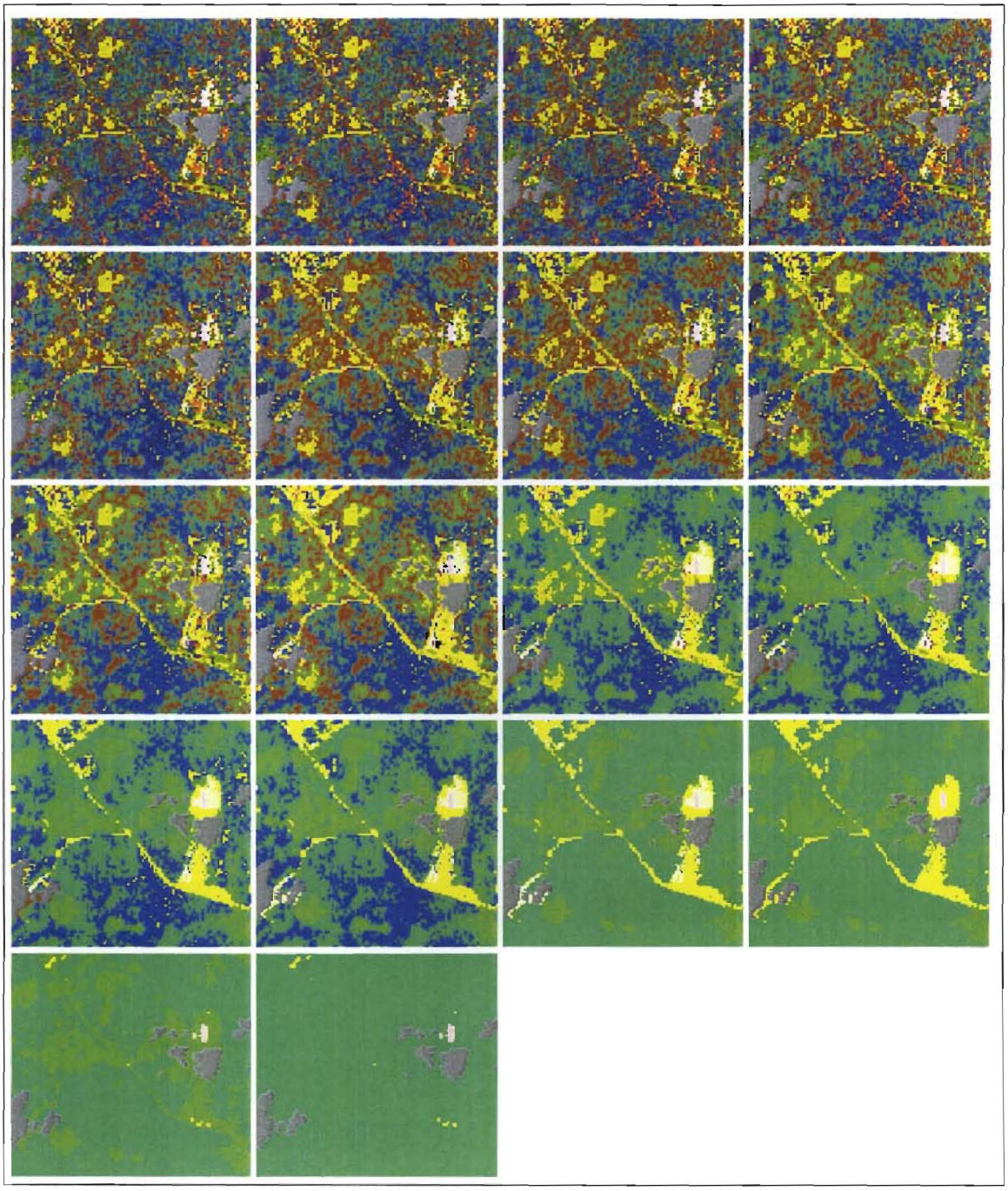

Fig. 2: The 18 levels of the hierarchical segmentation with a cloud mask, in grey, where the arbitrary color map as used in Fig. 1 has been changed so that the colors agree with color choices used in the right part of Fig. 3. This was done after the user manually selected the colors for the classification in the right part of Fig. 3 using the region labeling tool. Then the default color map was modified to substitute these colors for the original colors in this segmentation to make it easier to see the relationship of this segmentation to the result in the right of Fig. 3.

A second application of the region labeling tool to the segmentation in Fig. 2 was then used to obtain the result shown in the right of Fig. 3. The approximate true color image is shown in the left of Fig. 3. Note that segmentation result in the right of Fig. 3. is close, but not identical to level 15 in Fig. 2. For example the road features (in yellow) are continuous in our final segmentation, are broken in level 15, but are seen to be continuous in levels 11 down to 6 in Fig. 2.

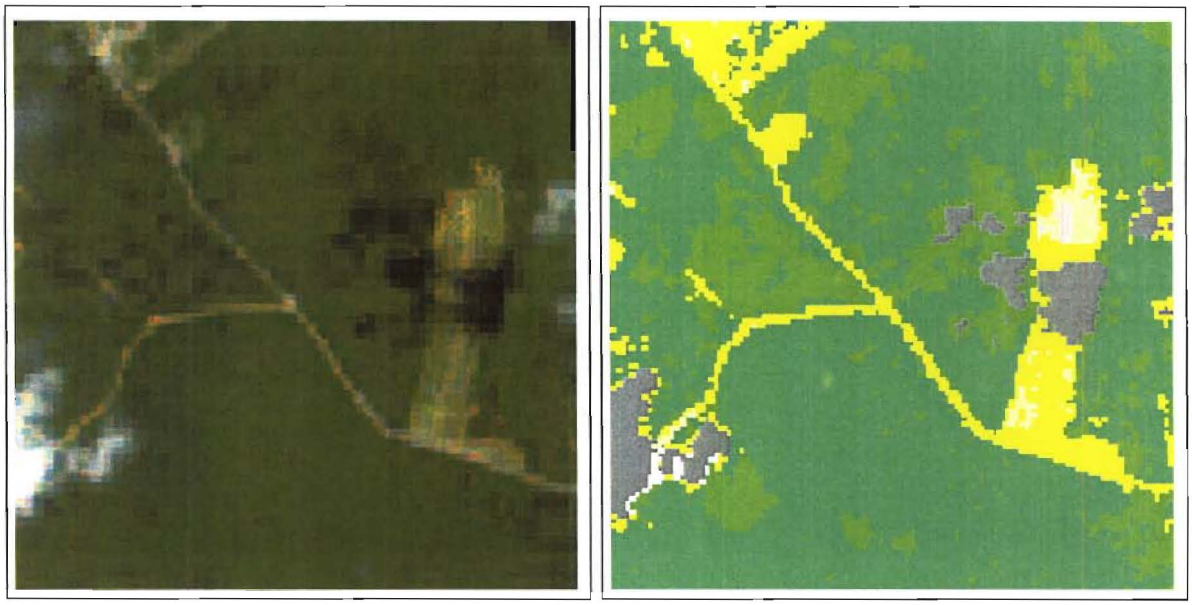

Fig. 3: On the left the approximate true color image, and on the right a classification based on cloud/cloud shadow masking followed by hierarchical segmentation and subsequent use of the region labeling tool. Here gray represents the cloud/cloud shadow mask. Note it is similar, but not identical to level 15 in Fig. 2

4 Conclusion

The hierarchical segmentation algorithm has been described together with its implementation on a Beowulf computer using a recursive approach. The algorithm performs both spatial region growing and spectral clustering, thereby using both spectral and spatial information in the hyperspectral cube. It yields a new representation of hyperspectral imagery as a hierarchy of images that show how regions coalesce as one ascends the hierarchy. By examining the stability of regions across levels in the hierarchy, a segmentation can be found that can form the basis for unsupervised classification. To help in this examination across levels, the region labeling tool is introduced to assist an analyst in extracting these stable features. We have demonstrated the algorithm and the region labeling tool on a small AVIRIS hyperspectral cube, and obtained a reasonable segmentation into recognizable features. While this is a preliminary result, and it does involve the analyst interpreting the scene, the hierarchical segmentation together with the region labeling tool provides a new method to analyze hyperspectral data. In the future we plan to further automate this process by taking advantage

of the rich representation of the data that the hierarchical segmentation provides.

Acknowledgment

J. A. Gualtieri would like to thank Prof. Shunlin Liang of the Department of Geography at the University of Maryland, College Park for adding the low altitude flight line over PWRC used in this work to his AVIRIS flight request in 2001.

References

[1] T. Sterling, D. Savarese, D. J. Becker, J. E. Dorband, U. A. Ranawake, and C. V. Packer. BEOWULF: A parallel workstation for scientific computation. In *Proceedings of the 24th International Conference on Parallel Processing*, volume I, Architecture, pages I:11–14, Boca Raton, FL, August 1995. CRC Press.

[2] R. A. Schowengerdt. *Remote Sensing, Models and Methods for Image Processing*, chapter 5. Academic Press, Chestnut Hill, MA, 2nd ed. edition, 1997.

[3] R. M. Haralick. Statistical and structural approaches to texture. *Proceedings of the IEEE*, 67:786–804, 1979.

[4] K. S. Fu and J. K. Mui. A survey on image segmentation. *Pattern Recognition*, 13:3–16, 1981.

[5] J. C. Tilton. Image segmentation by region growing and spectral clustering with a natural convergence criterion. In *Proc. of the 1998 International Geoscience and Remote Sensing Symposium*, July 1998.

[6] This is a Beowulf class cluster machine consisting of 66 nodes each a Pentium PRO PC with 2 CPU's where 64 nodes are for computation and 2 are for control. See `http://newton.gsfc.nasa.gov/thehive`.

[7] J. C. Tilton. A recursive pvm implementation of an image segmentation algorithm with performance results comparing hive and the cray t3e. In *Proceeding of the 7th Symposium on Massively Parallel Computation*, pages 146–153, Feb. 1999.

[8] J. C. Tilton. Method for recursive hierarchical segmentation by region growing and spectral clustering with a natural convergence criterion, Feb 2000. Disclosure of Invention and New Technology (Including Software): NASA Case No. GSC 14,328-1, NASA's Goddard Space Flight Center.

[9] J. C. Tilton. Method for implementation of recursive hierarchical segmentation on parallel computers, Feb. 2000. Disclosure of Invention and New Technology (Including Software): NASA Case No. GSC 14,305-1, NASA's Goddard Space Flight Center.

[10] J. C. Tilton. A method for recursive hierarchical segmentation which eliminates processing window artifacts, Oct. 2002. Disclosure of Invention and New Technology (Including Software): NASA Case No. GSC 14,681-1, NASA's Goddar Space Flight Center.

[11] The subset was obtained by first subsetting [lines, samples] = [650:1113, 54:648] from scenes 2 of AVIRIS flightline f010801t01p03_r08 taking [1,1] as the upper left hand cornet. From this a subset of size 128 by 128 was taken. The original 224 bands were subsetted to 182 by removing bands [4, 77, 107-115, 153-169, 209, 211-212, 214-224] which were found to have negative values, indicating noise or water absorption. An approximate true color image can be obtained by selecting bands [r, g, b] = [34, 19, 11] from the 182 band data cube.

[12] J. C. Tilton. A region labeling tool for use with hierarchical segmentation, Feb. 2000. Disclosure of Invention and New Technology (Including Software): NASA Case No. GSC 14,331-1, NASA's Goddard Space Flight Center, February 29, 2000.

CHARACTERIZATION OF LAND DEGRADATION AT THE ÑACUÑÁN BIOSPHERE RESERVE IN ARGENTINA WITH AVIRIS DATA

Alfredo Huete,[1] Tomoaki Miura,[1] Xiang Gao,[1] Carlos Borghi,[2] and Ricardo Ojeda[2]
[1]Department of Soil, Water and Environmental Science, University of Arizona, Tucson, Arizona 85721, USA
ahuete@ag.arizona.edu; tomoaki@ag.arizona.edu; xgao@ag.arizona.edu
[2]Instituto Argentino de Investigaciónes de las Zonas Áridas (IADIZA), Mendoza, Argentina

I. INTRODUCTION

Land degradation impacts on several critical environmental issues such as food security, diminishing quality and quantity of fresh water resources, preservation of natural resources, loss of biodiversity, and global climate change. Land degradation is responsible for soil erosion and can eventually lead to desertification. The International Convention to Combat Desertification (CCD) defines desertification as "land degradation in arid, semi-arid, and dry sub-humid areas resulting from various factors, including climate variations and human activity". The resulting loss of soil cover, the loss of genetic diversity, the physical and chemical degradation of soils, and sedimentation of river basins and dams creates major environmental constraints for sustainable development.

General information and data regarding the degree and extent of land degradation are lacking and effective monitoring and detection programs are hampered by the lack of a comprehensive set of guidelines for survey, assessment, and monitoring of land degradation, including early warning indicators. Remote sensing offers a quantifiable and replicable technique to assess desertification under a unified methodology at regional and global scales. To manage or reverse land degradation, one needs early warning signals, given the high costs for remediation. There are many indicators of land degradation and desertification, many of which lend themselves to remote sensing- based monitoring. These include (1) loss of vegetative cover; (2) changes in vegetation composition; (3) landscape instability due to wind and water erosion; (4) soil salinization; (5) soil structure deterioration; (6) less soil moisture; (7) increases in albedo; and (8) higher land surface temperatures.

Aguiar et al. (1988) produced maps of desertification in Patagonia with NOAA-AVHRR and Landsat MSS. Their methodology included recording data on degradation of vegetative cover and of soil water erosion, wind erosion, soil crusting and compaction, and salinization/alkalinization. Pickup and Nelson (1984) showed that changes in the variance of pixel subareas in Australia could be the most sensitive indicator of landscape instability, with an increase in variance indicating erosion and a decrease in variance indicating the possibility of deposition. In a study on the Jornada Experimental Range in New Mexico, an increase in the spatial and temporal heterogeneity of water, nutrients, and other soil resources has favored the invasion of desert shrubs (Schlesinger et al., 1990). Archer et al, (1995) have coupled shrub invasion mechanisms with climate and land use activities. Indicators of soil erosion and land degradation were the loss of vegetative cover and spatial variation of soil spectral properties owing to the loss of topsoil and exposure of subsoil layers. As erosion proceeds, more of the parent material mineralogies and spectral properties become evident while the optical properties of the organic rich upper layers become less pronounced. The undisturbed, well-developed soil and the underlying parent material represent the two endpoints from which the various degrees of soil erosion and land degradation can be assessed. These characteristics can be monitored with satellite imagery, using spectral indices and mixture models (Tucker and Nicholson, 1999).

Hyperspectral remote sensing has improved the feasibility of unambiguously identifying numerous soil and vegetation absorption features, related to mineralogy, liquid water, chlorophyll, cellulose, and lignin contents (Smith et al., 1990; Gao and Goetz, 1994; Asner and Green, 2002). This is potentially useful in the analysis of land degradation in semiarid regions which often entail simultaneous changes in both soil and vegetation biophysical and optical properties. In this study we attempt to fully characterize a set of natural and altered land cover sites in order

to determine the potential of hyperspectral imagery for characterization of land degradation. Here, we specifically report on the use of spectral mixture analysis and multi-component fraction extracts for assessments of land health.

2. STUDY SITES AND METHODS

The Ñacuñán Biosphere Reserve comprises and area of 12,271 ha at a mean altitude of 540 m and is located in a warm semi-desert shrub land ecosystem in the province of Mendoza (34°02'S; 67°54'W). With an average annual temperature of 15.8 C and 200 mm annual precipitation, the site is characterized by open forests of mesquite (*Prosopis spp.*) and creosote bush (*Larrea divaricata and L. cuneifolia*), locally known as algarrobal and jarillal communities, respectively (Ojeda et al., 1998). These open forest communities were totally cut down between the years 1907 and 1937 and are now protected under a restoration and protection plan. The algarrobal community of mixed mesquite-creosote bush is the main cover type inside the reserve followed by the jarillal (creosote bush) community. The dark green leaves of the creosote bush render this community very dark in appearance in satellite imagery relative to the algarrobal vegetated areas (Fig. 1). There are two additional vegetation formations resulting from previous and current phases of land degradation, including a 'medanal' community consisting of both mesquite and creosote bush species and characterized by sand dune formations and a 'peladal' community which is severely degraded, has stunted creosote bush, and appears very bright (Fig. 1). These degraded vegetation communities are present inside the reserve but are much more prominent outside the reserve, particularly to the north (Fig. 1a).

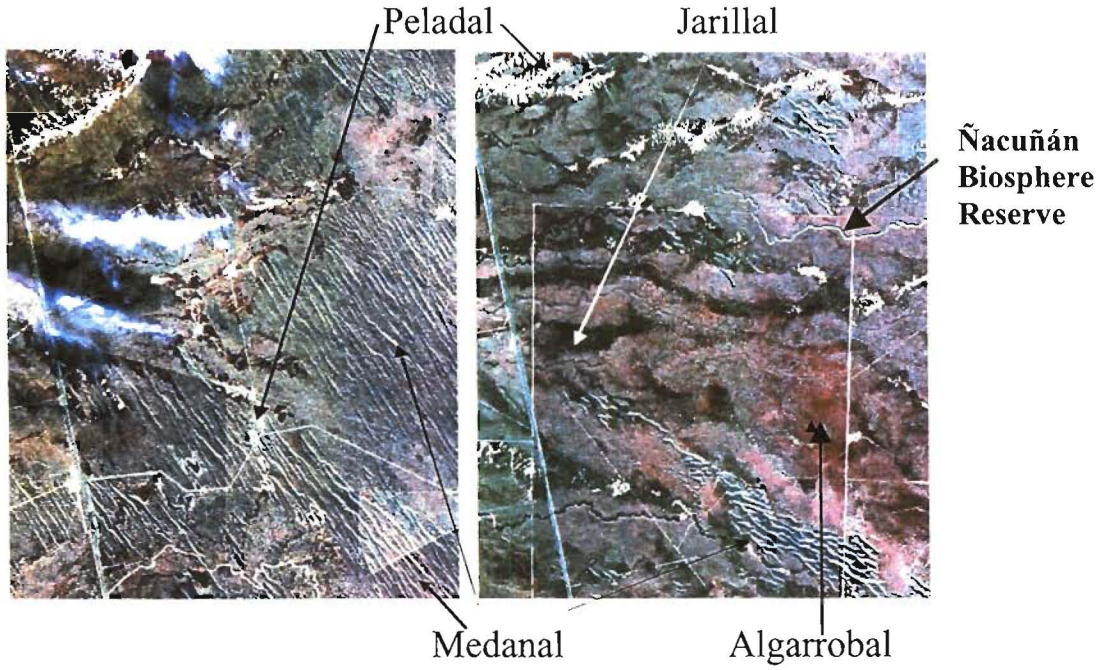

Figure 1. Ikonos image depicting the vegetation communities at the Ñacuñán Biosphere Reserve, Argentina (right) and the extensive degraded areas found north of the Reserve (left).

Field optical and biophysical measurements were conducted from January 28 through February 6, 2001. An ASD FieldSpec radiometer with a spectral range from 370 nm to 1050 nm, and GPS unit were mounted on a yoke device 2 m above the surface and used over 100-m transects for canopy optical characterization. The 100-m transect measurements were only made through the medanal and peladal canopies as the vegetation was too tall for transect measurements in the algarrobal and jarillal communities. In addition, we conducted 50-m transects through two bare soil playas, denuded of vegetation. All ASD spectra were collected between 10am and noon and converted to reflectance values with the use of a standard reference, Spectralon panel. We also made simultaneous measurements of leaf area index (LAI) and fractional component covers (green vegetation (GV), non-photosynthetic vegetation (NPV), litter and soil) along the 100 m transects using the line intercept method with a spacing of 20 cm, yielding 500 cover points per transect.

Low level Airborne Visible/ Infrared Imaging Spectrometer (AVIRIS) flights were made at the Ñacuñan Reserve on February 15, 2001. The AVIRIS imaging spectrometer operates in the 400 to 2450 nm region collecting 224 spectral bands with a nominal 10 nm spectral response function. AVIRIS flew at an altitude of 4 km yielding 4 m pixels. The hyperspectral imagery was corrected for atmosphere and converted to surface reflectances with the aid of an atmosphere correction program, ATREM, constrained with field ASD radiometric measurements. With the aid of GPS data and Ikonos images, we co-registered the averaged ASD field spectra over the denuded playas and peladal areas to serve as the calibration ground control points.

We performed a basic, linear spectral mixture analyses to decompose the AVIRIS data into its fractional components, including a soil component, a non-photosynthetic vegetation (NPV) signal (wood/litter), and a green vegetation (GV) sensitive measure. The basis of the mixture model is that the measured spectral response of a pixel is equal to the weighted sum of multiple reflecting surface features,

$$d_{ik} = \sum_{j=1}^{n} r_{ij}\, c_{jk} + e \qquad (1)$$

where d_{ik} is the measured spectral response of the spectral mixture k in waveband i, n is the number of independent reflecting components in the mixture, r_{ij} is the response of component j in waveband i, c_{jk} is the relative contribution of component j in spectral mixture k, and e is the residual error. In matrix notation, Eq. (1) is expressed as

$$[D] = [R]\ [C] + [e] \qquad (2)$$

where [D] is the spectral data matrix, [R] is the response matrix of the independent reflecting materials or 'endmembers', [C] is the fractional component contributions or 'loadings' matrix, and [e] are the residual errors. The dimensionality, n, represents the number of unique reflecting materials in the mixture data set and is determined with the aid of principal components analysis (PCA), which decomposes the spectral data matrix [D] into an abstract feature matrix $[R]_A$ and an eigenvector matrix $[C]_A$ such that $[D] = [R]_A\ [C]_A$. The abstract-based principal components analysis results were then converted (rotated) into physical-based results through the use of 'endmembers'. We used pure pixel endmembers for the green vegetation and soil endmembers, field-based spectra for the NPV endmember, and a shade endmember was created using a signature of zero reflectances.

3. RESULTS

The averaged spectral signatures (n~100) from the AVIRIS derived reflectances across normal and degraded vegetation communities are depicted in Fig. 2. Most of the transect spectra contain very weak vegetation signals and resemble soil spectra. The two peladal sites consisted of sparse creosote bush with different soil backgrounds, one being darker and more clayey with large dry, cracks on the surface. The moderately degraded medanal site had lower reflectances with a weak, red absorption feature in its signature (Fig. 2). This was nearly equivalent to the spectral signatures of the algarrobal sites. The jarillal vegetation community had the lowest spectral reflectance signature. In the shortwave-infrared (SWIR) region, all the vegetation communities, with the exception of the peladal sites, showed lignin absorption features, allowing for spectral separation of soil from NPV and GV (Asner and Lobell, 2000).

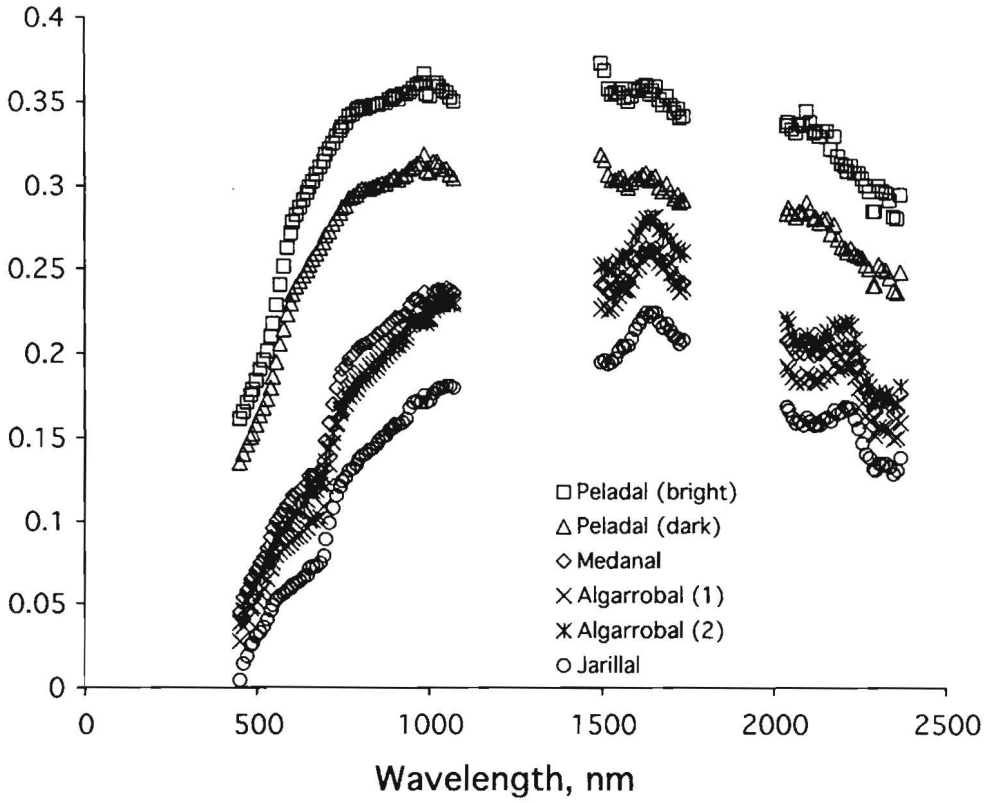

Figure 2. Averaged AV IRIS spectra of the main vegetation communities within and outside the Ñacuñán Biosphere Reserve.

An eigenanalysis of the AVIRIS hyperspectral data revealed a data dimensionality of 4 with 99.86% of the variance accounted for. The first 4 eigenvectors reveal the important spectral structure and signature curve shapes of the AVIRIS image (Fig. 3). The first eigenvector is equivalent to the mean spectral signature for the entire image and provides a brightness measure. The second eigenvector resembles green vegetation spectra. The 3rd and 4th eigenvectors resemble the non-photosynthetically active vegetation (NPV) spectral absorption features in the SWIR with unique absorption features relevant to the separation of NPV from soil and green vegetation (2080, 2210, and 2270 nm). The 4th eigenvector also show increasing secondary variations related to instrument noise but was retained for the information it contained in the SWIR.

Spectral mixture analysis was conducted by supplying 'pure' reference endmembers of known biophysical properties to transform and rotate the abstract PCA solution into a set of physically useful, fractional component images. The resulting fractional component images show very little difference in green vegetation (GV) between the inside and outside portions of the Ñacuñán reserve and there was no clear, discernable pattern of GV fractional values among the algarrobal, jarillal, and medanal communities inside the reserve (Fig. 4). The green vegetation fraction was lowest in the severely degraded peladal and moderately degraded medanal areas in the northern portion of the image. Green vegetation fractional amounts were also most variable in the peladal areas exhibiting minimal values in the severely degraded areas with adjacent high values due to clusters of cottonwood trees and mesquite growing at the edges of the denuded playas. These playas are used to harvest and store water, which sustain the cottonwood trees.

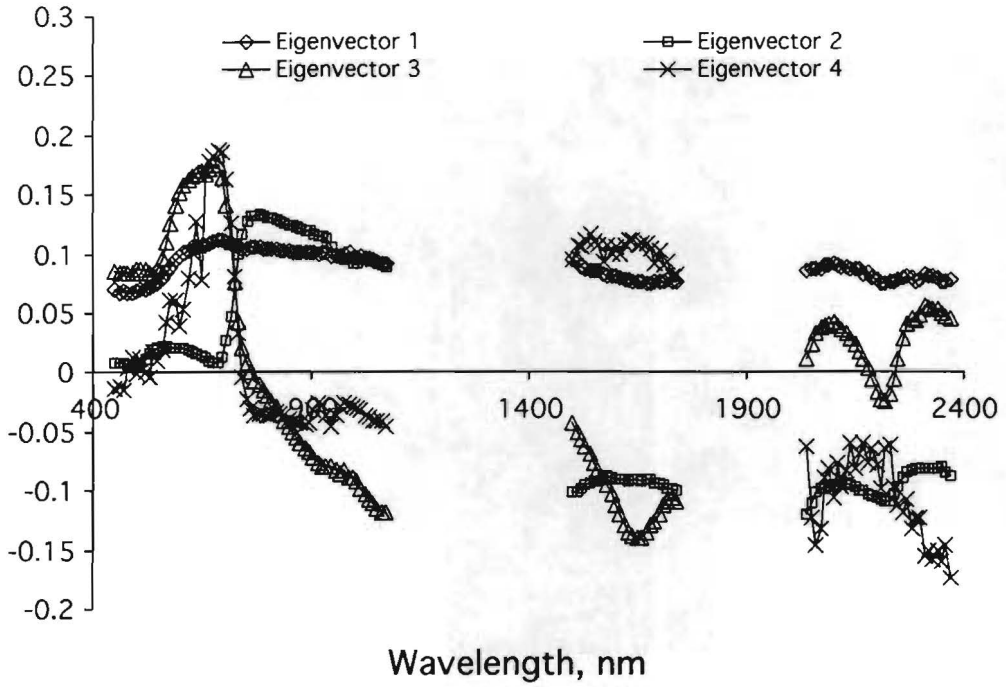

Figure 3. The first 4 primary eigenvectors derived from a principal components analysis of the AVIRIS image acquired over the Ñacuñán Biosphere Reserve.

The NPV signal was generally lower in the degraded northern part of the image consisting of medanal communities and was extremely low over the peladal areas (Fig. 4). As with the GV fraction, there were no discernable patterns of NPV among the vegetation formations within the reserve as well as in the immediate adjacent portions outside the reserve. There were larger differences in the soil fraction with darker soil values inside the reserve (Fig. 4). The soil fractional values were lowest in the jarillal communities (creosote bush) and highest in the degraded peladal communities outside and north of the reserve. The medanal site was of intermediate brightness and the algarrobal communities were slightly lower. The soil fraction for the algarrobal communities also appeared slightly darker inside the reserve compared with outside (Fig. 4). Fractional shade amounts also exhibited strong variability in the degraded peladal areas as a result of the dense trees casting shadows, surrounded by bare playas nearly devoid of vegetation canopy shade. Some of the clay playas, however, were extremely dry and cracked with crevices 20 – 30 cm wide and 10 – 20 cm deep, creating significant amounts of shade.

A scatterplot of the green vegetation fraction (GV) plotted against the NPV vegetation fraction for the range of sites, shows a general positive relationship in which increasing greenness is associated with higher values of NPV (Fig. 5). Both GV and NPV increase as the amount of vegetation increases, from the severely degraded peladal sites to the moderately degraded medanal (sand-dune) sites, and finally the healthy jarillal (creosote bush) and algarrobal (mesquite) communities. This formed a primary axis of total vegetation cover (GV + NPV) that enabled the separation of the various land degradation classes. A second axis of variation can also be seen whereby, within a given vegetation community, there is an inverse relationship between NPV and GV. This basically depicts the vegetation cover as either foliated (green leaves) or defoliated exposing the woody, NPV signal. For a given level of total plant cover, the proportions of GV and NPV will vary inversely, depending on environmental variables (soil moisture, meteorology) and phenology (dry season to wet season).

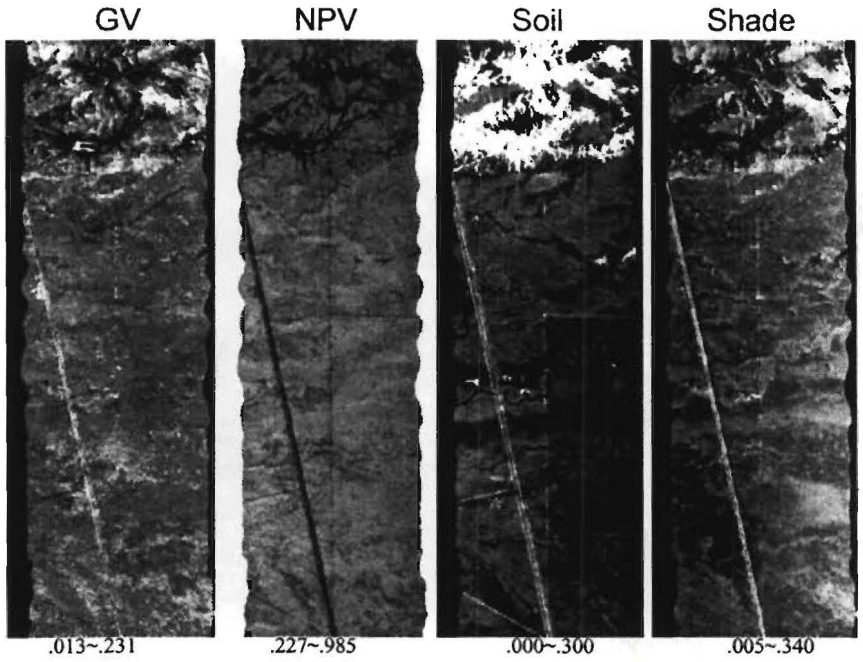

Figure 4. Fractional component images of the AVIRIS image data set over the Ñacuñán Biosphere Reserve, (a) GV, (b) NPV, (c) Soil, and (d) Shade images.

The two algarrobal sites represent sparse and dense 'green' vegetation, respectively. Note that the GV axis does not differentiate between the algarrobal and jarillal communities. The medanal site decreased in both GV and NPV, while the peladal areas were discriminable through either the GV or NPV fraction. Figure 5 depicts quite well the need for multiple landscape parameters for characterization and monitoring of land degradation. Neither greenness (GV) nor NPV components alone can discriminate the various vegetation communities and stages of land degradation due to the large overlap in vegetation properties. With these ambiguous signals, it would take much longer to reliably assess if land degradation is actually occurring. However, when GV and NPV are combined, one can note distinct clusters among the degradation classes and the trend of decreasing PV and NPV in shifting towards the origin with increasing degradation. A shift towards the origin indicates less total vegetation cover, which may be used as one reliable measure of land degradation.

The discrimination of the land degradation classes can also be observed in a plot of GV against the soil brightness signal (Fig. 6). There is an overall inverse relationship whereby as the vegetation fraction decreases as the soil component increases. However, the soil component not only increases in response to the greater proportion of exposed soil but also due to the 'brighter' soils found in the degraded areas (lower organic matter). This caused a shift toward higher soil values for a given amount of vegetation cover over the severely degraded peladal areas (Fig. 6). The soil component may thus be useful as a third landscape parameter for land degradation studies. As an example, the GV values of the medanal community were similar to those of the algarrobal community but were separable through the 'brighter' soil signal found in the degraded medanal site. Thus, the addition of the soil component information provided a means for further discrimination and landscape degradation analysis.

Similarly, Fig. 7 shows the much higher content of variance and information present in the fractional images of NPV, soil, and shade compared with green vegetation (GV) for the highly degraded areas north of the Reserve. Fence line boundaries with differing grazing patterns and management schemes are readily seen in the NPV, soil, and shade images but are nearly absent in the green vegetation fraction image.

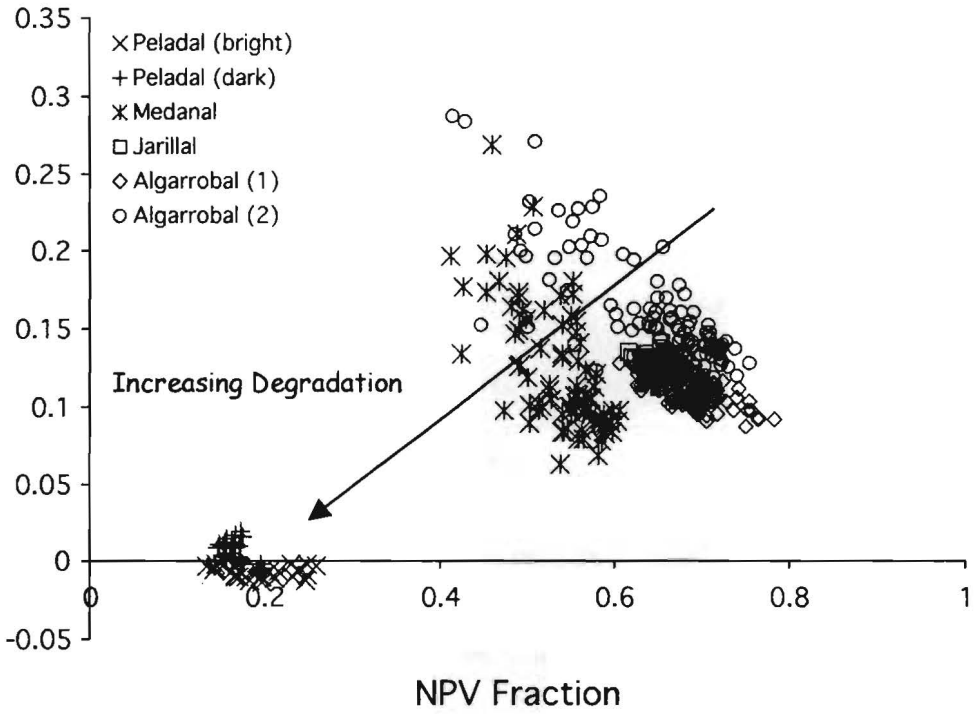

Figure 5. The green vegetation fractional component (GV) plotted against the NPV component for the major vegetation communities inside and outside the Ñacuñán Biosphere Reserve.

4. CONCLUSIONS AND DISCUSSION

The results of this study showed that simple 'greenness' measures, such spectral vegetation indices and GV fraction components, were not well adapted to the assessment of land degradation and desertification at the Ñacuñán Biosphere Reserve in Argentina. Land degradation in semiarid regions result in simultaneous changes in soil and vegetation optical properties involving the amount and composition/ structure of vegetation, the proportion of green (GV) and non-green (NPV), and the soil background. Spectral vegetation indices are limited in their ability to characterize such complex environments and may lead to ambiguous conclusions concerning land degradation. Greenness by itself will decrease with land degradation but will also shift greatly in response to seasonal variations as well as plant community composition changes with different proportions of GV and NPV (e.g., shifts from herbaceous to woody vegetation or shifts from perennial to annual vegetation).

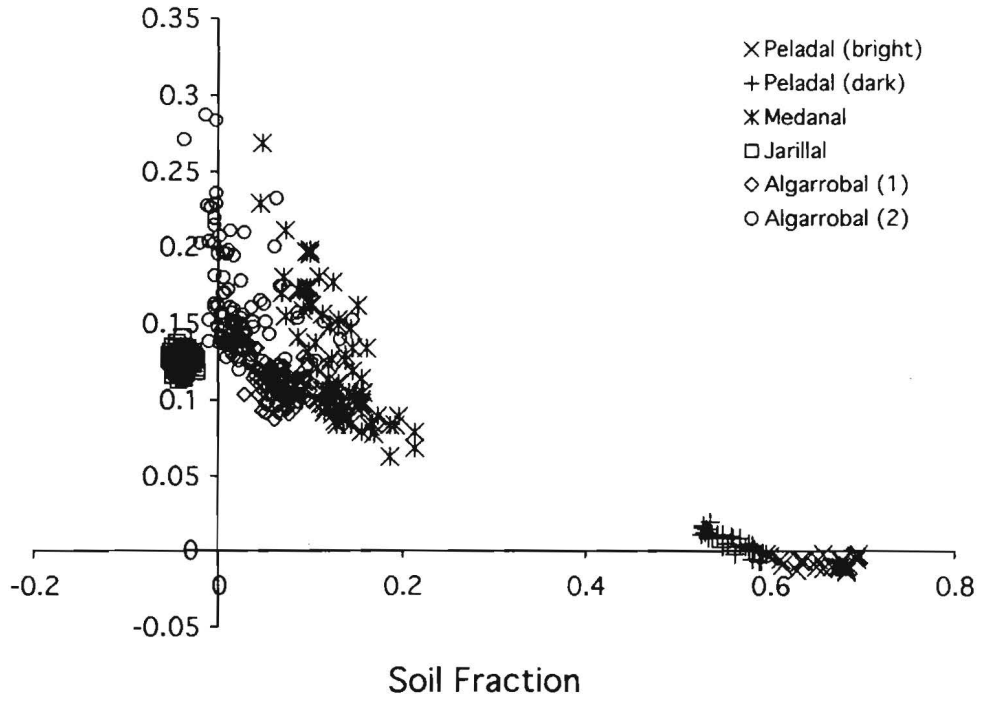

Figure 6. The green vegetation fractional component (GV) plotted against the soil component for the major vegetation communities inside and outside the Ñacuñán Biosphere Reserve.

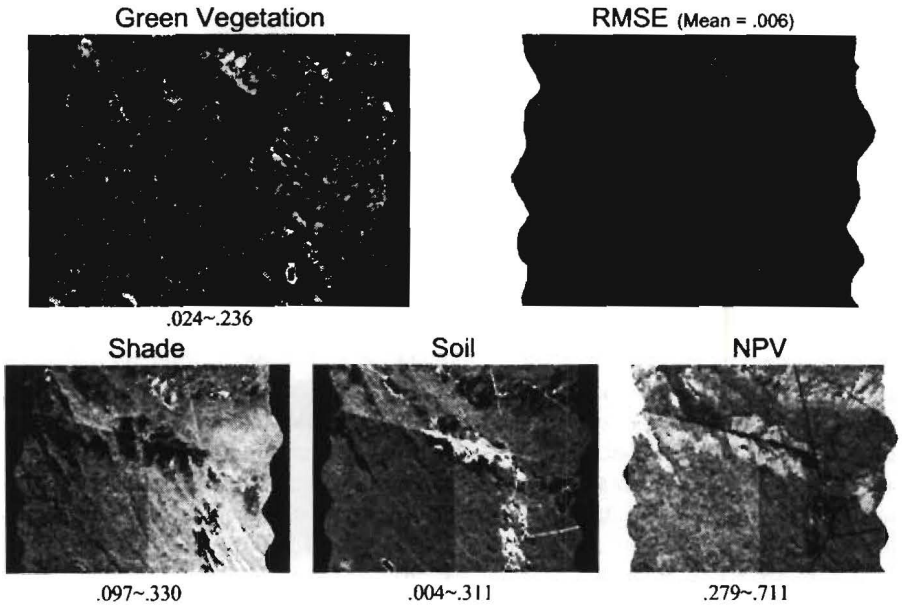

Figure 7. Fractional component images of the AVIRIS image data set in the degraded areas north of the Ñacuñán Biosphere Reserve, (a) GV, (b) RMSE, (c) Shade, (d) Soil, and (e) NPV images.

We found that land degradation was significantly improved with the inclusion of fractional NPV component information derived from spectral mixture analysis. The combination of NPV with PV enabled a more efficient and accurate characterization of the landscape with respect to natural vegetation communities and various stages of degradation. Whereas the separate GV and NPV fractional components could not differentiate many of the land degradation classes, they were able to do so in combination. The GV and NPV fractions enabled the assessment of total vegetation cover and allowed one to decouple differences in green vegetation resulting from phenology and vegetation composition across the landscape.

The soil fraction component also added useful information for better interpretations of land degradation. The soil background component is especially relevant for the monitoring of land degradation since the soil signal is generally dominant, highly variable, and vulnerable to large changes in areas undergoing degradation. Soil changes associated with land degradation are due to surface erosion, subsoil exposure, loss of soil carbon and moisture, and soil spatial heterogeneity. Land degradation invariably results in a stronger soil signal component to measured spectra and the spatial and temporal variations associated with the soil background must be decoupled from variations associated with vegetation in order to better interpret land degradation.

The extracted soil component from the mixture analysis was determined by two factors that created a certain degree of ambiguity to the interpretation of the mixture model results. The strength of the soil signal varied with the fractional amount of soil exposed as well as the inherent brightness of the soil. Thus, increases in the soil signal were the result of less vegetation cover (GV and NPV) as well as higher soil reflectances associated with degradation (crusting, less moisture, less organic carbon, erosion). There are more advanced methods of spectral mixture analysis that aim to extract the soil reflectance signal independent of exposed soil fraction and vegetation influences (Okin et al., 2001; Palacios-Orueta et al., 1999).

The use of satellite observations to monitor land degradation processes has a promising future, particularly with the use of hyperspectral sensor systems that offer the potential of extracting soil and vegetation biogeophysical component information for a more complete land surface characterization. When these multiple optical parameters are combined with GIS, process models, and moderate resolution sensors for phenology determinations, then desertification can be more quantitatively evaluated and monitored and the different processes that contribute to desertification (erosion, salinization, denuding of soil, overgrazing, water resources) can be assessed. The Earth Orbiter 1 (EO-1), launched in November 2000 as part of NASA's New Millennium program, includes a hyperspectral imager, Hyperion. The Hyperion hyperspectral imager is a pushbroom sensor providing 220, 10 nm bands covering the spectrum from 400 to 2500 nm. A space-based hyperspectral sensor with consistent and repeat observation capabilities will greatly improve land degradation monitoring and provide early warning detection capabilities.

5. ACKNOWLEDGMENTS

Greg Asner and Kathy Heidebrecht also provided help in site locations and provided calibration spectra and photos to help with our analyses. This work was supported by the NASA EO-1 grant NCC5-478 (A.R. Huete).

6. REFERENCES

Aguiar, M.R., Paruelo, J.M., Golluscio, R.A., León, R.J.C., Burkart, S.E., and Pujol, G., 1988, "The heterogeneity of the vegetation in arid and semiarid Patagonia: an analysis using AVHRR/NOAA satellite imagery," *Annali di Botanica,* 46:103-114.

Archer, S., Schimel, D., and Holland, E., 1995, "Mechanisms of shrubland expansion: land use, climate, or CO_2?," *Climatic Change,* 29:91-99.

Asner, G.P., and Green, R.O., 2002, "Imaging spectroscopy measures desertification in United States and Argentina," *EOS Trans.* 82 (49):601.

Asner, G.P. and Lobell, D.B., 2000, "A biogeophysical approach for automated SWIR unmixing of soils and vegetation," *Remote Sensing of Environment,* 74:99-112.

Gao, B.C. and Goetz, A.F.H., 1994, "Extraction of dry leaf spectral features from reflectance spectra of green vegetation," *Remote Sensing of Environment,* 47:369-374.

Ojeda, R.A., Campos, C.M., Gonnet, J.M., Borghi, C.E., and Roig, V.G., 1998, "The MaB reserve of Ñacuñan, Argentina: its role in understanding the Monte Desert biome," *J. Arid Environ.,* 39:299-313.

Okin, G.S., Roberts, D., Murray, B., and Okin, W.J., 2001, "Practical limits on hyperspectral vegetation discrimination in arid and semiarid environments," *Remote Sensing of Environment,* 77:212-225.

Palacios-Orueta, A., Pinzón, Ustin, S.L., and Roberts, D.A., 1999, "Remote sensing of soils in the Santa Monica Mountains: II. Hierarchical foreground and background analysis," *Remote Sensing of Environment,* 68:138-151.

Pickup, G., and Nelson, J., 1984, "Use of Landsat radiance parameters to distinguish soil erosion, stability and deposition in arid central Australia," *Remote Sens. Environ.*, 16:195-204.

Schlesinger, W.H., Reynolds, J.F., Cunningham, G.L., et al., 1990, "Biological feedback in global desertification," *Science,* 247:1043-1048.

Smith, M.O., Ustin, S.L., Adams, J.B., and Gillespie, A.R., 1990, "Vegetation in deserts: 1. A regional measure of abundance from multispectral images," *Remote Sens. Environ.* 31:1-26.

Tucker, C.J. and Nicholson, S.E., 1999, "Variations in the size of the Sahara Desert from 1980 to 1997," *Ambio,* 28:587-591.

LEAF AREA INDEX AND COVER OF SHORTGRASS STEPPE USING AVIRIS IMAGERY

E. Raymond Hunt, Jr.*
Hydrology and Remote Sensing Laboratory
USDA Agricultural Research Service
Beltsville, Maryland

1. INTRODUCTION

Management of rangelands in the western United States requires data on vegetation community type, vegetation cover and productivity, and erosion potential in order to assess the sustainability of livestock grazing for food production. Remotely sensed imagery can provide attributes related to these data requirements over large areas. The Wyoming Hyperspectral Imagery Pilot Project was initiated in 1995 to determine the relationships between remotely sensed attributes and management data requirements using the best NASA sensor (at the time), the Airborne Visible Infrared Imaging Spectrometer (AVIRIS) from the Jet Propulsion Laboratory (Green et al., 1998). The radiometric, spectral, and spatial characteristics of AVIRIS allow image degradation to simulate operational sensors such as the Landsat Thematic Mapper and Advanced Very High Resolution Radiometer.

Bare soil cover, which is related to erosion potential, and vegetation cover can be determined from hyperspectral imagery using the method of spectral endmember unmixing (Roberts et al., 1998). Endmembers must be spectrally distinct. Unfortunately most semi-arid vegetation have similar spectral signatures so determination of the cover fraction contributed by each species to the community composition is probably not feasible, except for some species (McGwire et al., 2000; Parker Williams and Hunt, 2001). However, green vegetation cover, non-green vegetation cover (litter), and bare soil are important community attributes directly applicable for rangeland management.

Vegetation productivity and leaf area index (LAI) are usually estimated using remotely sensed vegetation indices, particularly the Normalized Difference Vegetation Index (NDVI):

$$NDVI = (R_{NIR} - R_{Red})/(R_{NIR} + R_{Red}) \quad (1)$$

where R_{NIR} is the reflectance in the near infrared and R_{Red} is the reflectance of red wavelengths. Preliminary analyses of AVIRIS data over the Agricultural Research Service's (ARS) Central Plains Experimental Range (CPER), a shortgrass steppe community near Nunn, Colorado, showed that NDVI were equal over a large range of biomass maintained by grazing intensity (Hunt, 2000). Various models of canopy reflectance show that fractional vegetation cover is an important variable determining NDVI (Carlson and Ripley, 1997; Myneni and Williams, 1994; Rondeaux et al., 1996). In particular, the SAIL model (Verhoef, 1984) has been used extensively to examine the responses of vegetation indices such as the NDVI to different variables (Baret and Guyot, 1991; Rondeaux et al., 1996). In addition to the SAIL model, reflectances of stacked leaves provide an empirical method to approximate changes of reflectance with increasing LAI, and when included in a two-component mixture model, could help elucidate the interactions between cover and LAI affecting NDVI.

2. METHODS

AVIRIS data were obtained over the CPER on two dates, 25 July 1995 and 6 August 1998. The first year had abnormally high amounts of summer precipitation, whereas the second year had normal amounts of summer rain. The vegetation of CPER is shortgrass steppe, which is dominated by blue grama grass (*Bouteloua gracilis*). There is a long-term grazing intensity experiment (Figure 1) with three stocking levels (high, medium, and light) in 0.5 mile^2 pastures, which strongly determine the amount of standing biomass (Hart and Ashby, 1997). The heavy-grazed pasture has a permanent water hole; all data surrounding this water hole were excluded from data analyses by defining regions of interest and using the statistics from only these areas. Furthermore, all dirt roads in each pasture were excluded from the regions of interest. The final treatment is the large number of permanent plots where cattle

* Building 007 Room 104, 10300 Baltimore Ave., Beltsville, Maryland 20705 (email: erhunt@hydrolab.arsusda.gov)

grazing has been excluded. Species composition, biomass and cover data of these four areas are routinely collected; LAI was calculated from biomass using a specific leaf area of 9 m^2 kg^{-1}.

The flightline of the ER2 aircraft was east to west in 1995 and south-east to north-west in 1998; these flightlines resulted in a brighter northern edge of the image resulting from the sun-ground-sensor geometry and the vegetation bidirectional reflectance distribution functions. Fortunately, all the grazing experiments were near nadir in both flightlines. The atmospheric correction program, ATREM version 3.1 (Gao et al., 1993), was used to calculate surface reflectances from the calibrated AVIRIS radiances. Then an empirical line correction was applied to the data using a dark target (US Highway 85) and a bright target (a gravelly dry bare stream bed of Owl Creek, near the CPER Headquarters). The ground reflectances of these targets were acquired on 21 June 2000 using an Analytical Spectral Devices Inc. (ASD) FieldSpec Pro spectroradiometer (350 to 2500 nm), and averaged into the 224 AVIRIS bands using the calibrated wavelength files for each year. NDVI was calculated from the final reflectances using AVIRIS bands 53 (846 nm center wavelength) and 33 (664 nm center wavelength).

Four endmembers were used for spectral unmixing: bare soil, leaf litter, green vegetation, and shadow (Roberts et al., 1998). In both images, there were areas of plowed fields and recently harvested grain crops for the soil and litter endmembers, respectively. The vegetation endmember was obtained from the AVIRIS data in riparian areas with lush vegetation and deep soils. Finally the shadow endmember was assumed to be 1% reflectance for all wavelengths.

On 21 June 2000, transmittances and reflectances of stacked sunflower (*Helianthus annuus*) leaves were measured using the ASD FieldSpec Pro spectroradiometer. Because the spectral characteristics change rapidly when leaves are removed from the plant, fresh leaves were used for each new series of stacked leaves. Reflectances of the soil background were also measured, and the results were used in the SAIL model (Verhoef, 1984; M. Kim, personal communication). The leaf angle distribution was set to be entirely planophile. NDVI were also calculated for specific mixtures of LAI (from the stacked reflectances) and plant-soil cover. For total reflectance at either the 660 and 850 nm wavelengths (R_8):

$$R_8 = (1 - f)\, R_{soil} + f\, R_{LAI} \qquad (2)$$

where f is the fraction covered by green leaves, R_{soil} is the soil reflectance, and R_{LAI} is the reflectance of the leaf stack where LAI equals the number of stacked leaves. The fraction f was varied from 0 to 1 in increments of 0.1; NDVI was then calculated from Eq. 1.

3. RESULTS AND DISCUSSION

The average green vegetation cover was not significantly different among treatments for either year, with the average cover for 62% in 1995 and 55% in 1998. In 1995, measured aboveground biomass were 86.4, 106.7 and 175.3 g dwt m^{-2}, and in 1998, measured biomass were 129.8, 130.7, and 159.8 g dwt m^{-2} for the heavy, medium and light grazed pastures, respectively. This translates to LAI from 0.8 to 1.5 m^2 m^{-2} for the lowest to highest aboveground biomass. The non-grazed permanent plots had an LAI of 1.8 m^2 m^{-2} for 1995, which was assumed to be the LAI in 1998.

The AVIRIS average reflectance spectrum for heavy-grazed pasture was highest at almost all wavelengths and the average reflectance spectrum for the non-grazed permanent plots was lowest at the visible and near-infrared wavelengths (Figure 2). The fraction of green vegetation cover from the endmember unmixing was approximately equal to the actual vegetation cover. The differences between the AVIRIS spectra in Figure 2 were from differences in the shadow endmember fraction. The amount of shadow followed one-to-one the amount of shrub cover on the plots (Figure 3).

NDVI were not correlated with LAI (Figure 4), and NDVI were weakly correlated with cover (data not shown). SAIL model predictions of NDVI for a grassland canopy are also shown on Figure 4, indicating that the range of LAI from 0.8 to 1.8 m^2 m^{-2} should have a large increase in NDVI. The weak correlation between NDVI and cover may simply be the result from the small variation of the independent variable, because when the data from other pastures during 1995 are included (no biomass/LAI data are available for these pastures), the correlation increases with an R^2 of 0.72.

For stacked sunflower leaves, reflectances at visible wavelengths decreased and the reflectances at NIR wavelengths increased as the number of leaves increased from one to four (Figure 5). Reflectances at 660 nm and

850 nm were used to calculate NDVI. For a planophile canopy, NDVI predicted for LAI of 1, 2, 3, and 4 m^2 m^{-2} by the SAIL model were similar to the NDVI for stacks of one, two, three and four leaves, respectively (Figure 6). From the SAIL model, fractional LAI from 0 to 1 m^2 m^{-2} was also similar to the reflectance of a single leaf mixed with soil background reflectance. However, the NDVI for two stacked leaves that covered only one-half of the area (LAI = 1 m^2 m^{-2}) was only 75% of the NDVI of one leaf spread over the entire area (LAI also = 1 m^2 m^{-2}). Four stacked leaves covering only 25% of the area (LAI = 1 m^2 m^{-2}) is about half the NDVI of the one leaf spread over the entire area and that predicted by the SAIL model (Figure 6).

4. CONCLUSIONS

These results demonstrate that NDVI are more strongly related to vegetation cover and less strongly related to LAI. At continuous canopy cover, both with the SAIL model predictions and stacked leaf reflectances, changes in LAI from 1 to 2 m^2 m^{-2} were less important than changes in cover from 50% to 100%. Whereas these simulations were done for an planophile canopy rather than an erectophile grass canopy (because it is easier to stack sunflower leaves), these simulations were done to test hypotheses on NDVI/LAI suggested by the AVIRIS analyses for shortgrass steppe at CPER.

With vegetation cover, and by estimate bare soil cover, being determined using vegetation indices, then a key data requirement for rangeland management can be provided by remotely sensed data. Continuity of record from the Landsat Thematic Mapper provided with Landsat 7 will provide managers with some estimates of long-term rangeland sustainability. One the other hand, more work needs to be done in explaining how changes in cover over a growing season are related to primary production through changes in the fraction of absorbed photosynthetically active radiation.

5. ACKNOWLEDGMENTS

First, Mr. Jim Foreman, a rancher from Ten Sleep, Wyoming, is thanked for starting the Wyoming Hyperspectral Imagery Pilot Project and providing continued leadership. Dr. Diane E. Wickland of NASA Headquarters supported the AVIRIS data acquisitions, and other financial support was provided to the University of Wyoming from the Wyoming Department of Agriculture, United States Forest Service, and the Upper Midwest Aerospace Consortium. Ms. Michele M. Barlow performed the initial image analyses, and Ms. Heidi Gurstung assisted with spectrometer data collection. Dr. Richard Hart (ARS, Cheyenne, Wyoming) and Dr. Mary Ashby (ARS, Fort Collins, Colorado) provided biomass and cover data at CPER.

6. REFERENCES

Baret, F. and G. Guyot, 1991, "Potentials and limits of vegetation indices for LAI and APAR assessment," Remote Sensing of Environment, vol. 35, pp. 161-173.

Carlson, T. N. and D. A. Ripley, 1997, "On the relation between NDVI, fractional vegetation cover, and leaf area index," Remote Sensing of Environment, vol. 62, pp. 241-252.

Gao, B.-C., K. B. Heidebrecht, and A. F. H. Goetz, 1993, "Derivation of scaled surface reflectances from AVIRIS data," Remote Sensing of Environment, vol. 44, pp. 145-163.

Green, R. O., M. L. Eastwood, and O. Williams, 1998, "Imaging Spectroscopy and the Airborne Visible Infrared Imaging Spectrometer (AVIRIS)," Remote Sensing of Environment, vol. 65, pp. 227-248.

Hart, R. H. and M. M. Ashby, 1998, "Grazing intensities, vegetation, and heifer gains: 55 years on shortgrass," Journal of Range Management, vol. 51, pp. 392-398.

Hunt, E. R., Jr., 2000, "Analysis of hyperspectral imagery for assessment of Wyoming Rangelands," In: Proceedings of the Second International Conference on Geospatial Information in Agriculture and Forestry, Lake Buena Vista, Florida, 10-12 January 2000, ERIM, Ann Arbor.

McGwire, K., T. Minor, and L. Fenstermaker, 2000, "Hyperspectral mixture modeling for quantifying sparse vegetation cover in arid environments," Remote Sensing of Environment, vol. 725, pp. 360-374.

Myneni, R. B. and D. L. Williams, 1994, "On the relationship between FAPAR and NDVI," Remote Sensing of Environment, vol. 49, pp. 200-211.

Parker Williams, A. and E. R. Hunt, Jr., 2001, "Using hyperspectral remote sensing to map invasive plants on rangelands." In: Proceedings of the Third International Conference on Geospatial Information in Agriculture and Forestry, Denver, Colorado, 5-7 November 2001, ERIM, Ann Arbor.

Roberts, D. A., M. Gardner, R. Church, S. Ustin, G. Scheer, and R. O. Green, 1998, "Mapping chaparral in the Santa Monica mountains using multiple endmember spectral models," Remote Sensing of Environment, vol. 65, pp. 267-279.

Rondeaux, G., M. Steven, and F. Baret, 1996, "Optimization of soil-adjusted vegetation indices," Remote Sensing of Environment, vol. 55, pp. 95-107.

Verhoef, W., 1984, "Light scattering by leaf layers with application to canopy reflectance modelling: the SAIL model," Remote Sensing of Environment, vol. 16, pp. 125-141.

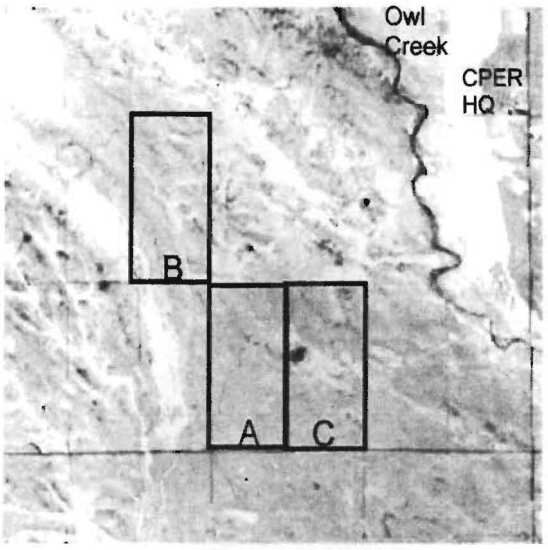

Figure 1. Grayscale NDVI image of the Central Plains Experimental Range from the 1995 AVIRIS data. The treatments are (A) light grazing, (B) medium grazing, and (C) heavy grazing. Un-grazed permanent plots are scattered over CPER.

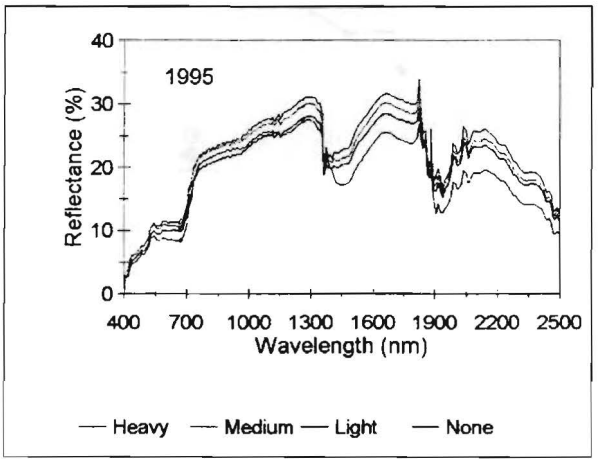

Figure 2. Average reflectance spectra for the four grazing treatments at CPER.

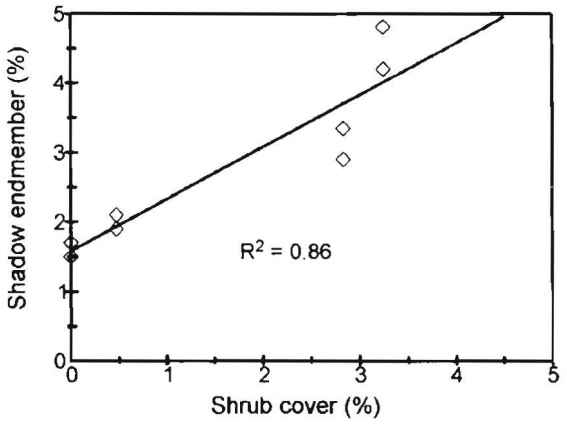

Figure 3. Relationship between the fraction of the shadow endmember and shrub cover from 1995 and 1998 AVIRIS data for the four grazing treatments.

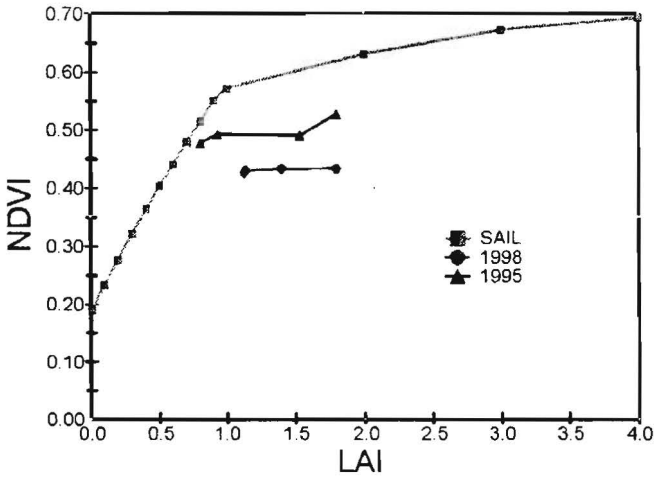

Figure 4. Relationship between NDVI and LAI for the four grazing treatments and simulations for an erectophile grass canopy using the SAIL model.

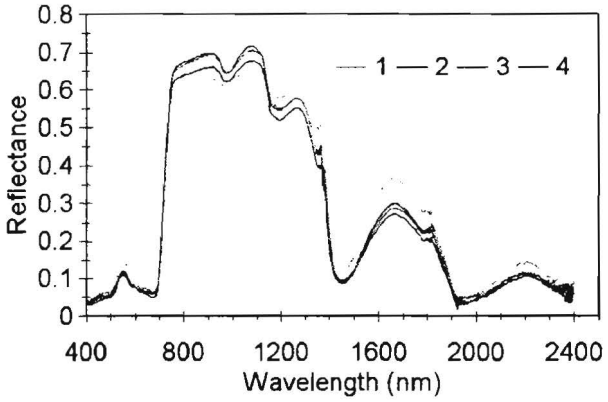

Figure 5. Reflectances of stacked *Helianthus annuus* (sunflower) leaves. Each reflectance is the average of 5 spectra.

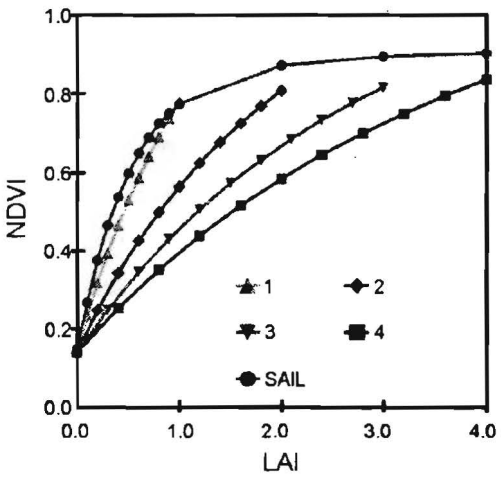

Figure 6. Relationships between NDVI and LAI for stacked *Helianthus annuus* leaves using a mixture model approach. Circles shows SAIL model predictions for *H. annuus* leaf reflectance and transmittance. Triangles show the NDVI of one leaf mixed at different proportions with bare soil. Diamonds show the NDVI of two stacked leaves mixed at different proportions with bare soil. Inverted triangles show the NDVI of three stacked leaves mixed at different proportions with bare soil. Squares show the NDVI of four stacked leaves mixed at different proportions with bare soil. NDVI for stacked leaves was calculated from the reflectances in Figure 5.

Comparison between AVIRIS and Hyperion for Hyperspectral Mineral Mapping

Fred A. Kruse[1]

1.0 Introduction

The 0.4 to 2.5 μm spectral range provides abundant information about many important Earth-surface minerals (Clark et al., 1990). In particular, the 2.0 to 2.5 μm spectral range covers spectral features of hydroxyl-bearing minerals, sulfates, and carbonates common to many geologic units and hydrothermal alteration assemblages. Imaging Spectrometers, or "Hyperspectral" sensors provide the unique combination of both spatially contiguous spectra and spectrally contiguous images of the Earth's surface that allows spatial mapping of these minerals (Goetz et al., 1985). Airborne hyperspectral data have been available to researchers since the early 1980s and their use for mineral mapping is well established (Goetz et al., 1985; Kruse and Lefkoff, 1993; Boardman and Kruse, 1994; Boardman et al., 1995; Kruse, et al., 1999). Current airborne sensors provide high-spatial resolution (2–20 m), high-spectral resolution (10–20 nm), and high SNR (>500:1) data for a variety of scientific disciplines (Green et al., 2001; Kruse et al., 2000).

NASA's EO-1 Hyperion sensor, launched in November 2000, is a test bed instrument designed to demonstrate hyperspectral imaging from space (Pearlman et al., 1999). Science validation efforts are in progress and selected AIG/CSIRO Hyperion results demonstrating mineral mapping have previously been presented and published (Kruse et al., 2001, 2002). New details and accuracy assessment compared to AVIRIS data are presented here.

2.0 Comparison of AVIRIS And Hyperion Specifications

The Airborne Visible/Infrared Imaging Spectrometer (AVIRIS) represents the current state of the art airborne hyperspectral system (Porter and Enmark, 1987; Green et al., 2001). AVIRIS, flown by NASA/Jet Propulsion Laboratory (JPL) is a 224-channel imaging spectrometer with approximately 10-nm spectral resolution covering the 0.4–2.5-μm spectral range. The sensor is a whiskbroom system utilizing scanning foreoptics to acquire cross-track data. The IFOV is 1 milliradian. Four off-axis double-pass Schmidt spectrometers receive incoming illumination from the foreoptics using optical fibers. Four linear arrays, one for each spectrometer, provide high sensitivity in the 0.4 to 0.7 μm, 0.7 to 1.2 μm, 1.2 to 1.8 μm, and 1.8 to 2.5 μm regions respectively. AVIRIS is flown as a research instrument on the NASA ER-2 aircraft at an altitude of approximately 20 km, resulting in approximately 20-m pixels and a 10.5-km swath width. Since 1998, it has also been flown on a Twin Otter aircraft at low altitude, yielding 2–4 m spatial resolution.

The launch of NASA's EO-1 Hyperion sensor in November 2000 marked the establishment of spaceborne hyperspectral mineral mapping capabilities. Hyperion is a satellite hyperspectral sensor covering the 0.4 to 2.5 μm spectral range with 242 spectral bands at approximately 10 nm spectral resolution and 30 m spatial resolution from a 705-km orbit (Pearlman et al., 1999). Hyperion is a pushbroom instrument, capturing 256 spectra over a 7.5-km-wide swath perpendicular to the satellite motion. The system has two grating spectrometers; one visible/near infrared (VNIR) spectrometer (approximately 0.4–1.0 μm) and one short-wave infrared (SWIR) spectrometer (approximately 0.9–2.5 μm). Data are calibrated to radiance using both pre-mission and on-orbit measurements. Table 1 shows a comparison of key AVIRIS and Hyperion characteristics.

Table 1: AVIRIS/Hyperion Sensor Characteristics Comparison

HSI Sensor	Spectral Resolution	Spatial Resolution	Swath Width	SWIR SNR
AVIRIS-High Altitude	10 nm	20 m	12 km	~500:1
Hyperion	10 nm	30 m	7.5 km	~50:1

[1] Analytical Imaging and Geophysics LLC, Boulder, Colorado, USA, E-mail: kruse@aigllc.com

3.0 Basic Hyperspectral Mineral mapping – Cuprite, Nevada

3.1 Site Description

Cuprite, Nevada, located approximately 200 km northwest of Las Vegas (Figure 1) is a relatively undisturbed acid-sulfate hydrothermal system exhibiting well exposed alteration mineralogy consisting principally of kaolinite, alunite, and hydrothermal silica. The geology and alteration were previously mapped in detail (Abrams et al., 1977; Ashley and Abrams, 1980). Swayze (1997) includes a good geologic summary, a generalized geologic map, and detailed mineral maps derived from 1990 and 1994 AVIRIS data. Cuprite, has been used as a geologic remote sensing test site since the early 1980s and many studies have been published (Goetz et al., 1985; Ashley and Abrams, 1980; Goetz and Strivastava, 1985; Swayze, 1997; Shipman and Adams, 1987; Kruse et al., 1990; Hook, 1990; Swayze et al., 1992; Goetz and Kindel, 1996; Kruse et al., 2002)

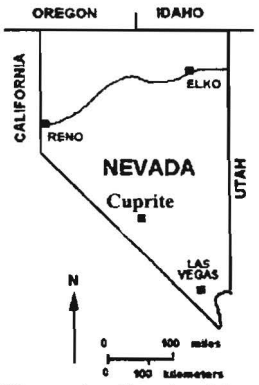

Figure 1: Cuprite, Nevada, Location map.

This study compares mineral mapping results from AVIRIS data acquired 19 June 1997 to Hyperion data collected 1 March 2001. Figure 2 shows reference images for the AVIRIS and Hyperion data.

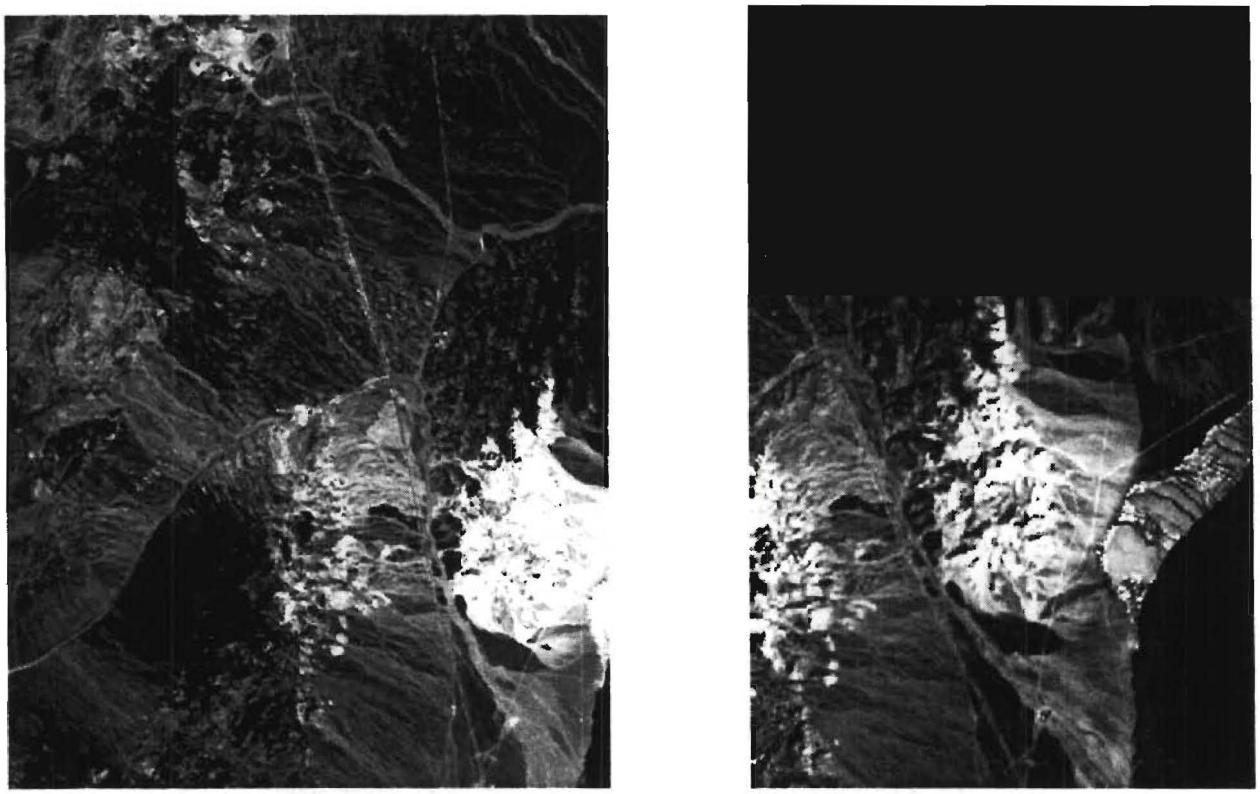

Figure 2: Reference images showing the AVIRIS (left) and Hyperion (right) coverage of the Cuprite, Nevada, site. The site is typically described as consisting of two hydrothermal centers (Swayze, 1997). These can be seen in the images as bright areas to the right and left of the road running from NW to SE across the scenes.

3.2 Methods

AIG has developed standardized methods for analysis of hyperspectral data (Figure 3) (Kruse et al., 1996; Kruse and Boardman, 2000). Both the AVIRIS and Hyperion data were processed to geologic products using these AIG-developed approaches for extraction of mineralogic and geologic information. This hyperspectral analysis methodology includes 1) data pre-processing (as required), 2) correction of data to apparent reflectance using the ACORN™ atmospheric correction software, 3) linear transformation of the reflectance data to minimize noise and determine data dimensionality, 4) location of the most spectrally pure pixels, 5) extraction and automated identification of endmember spectra, and 6) spatial mapping and abundance estimates for specific image endmembers. A key point of this methodology is the reduction of data in both the spectral and spatial dimensions to locate, characterize, and identify a few key endmember spectra that can be used to explain the rest of the hyperspectral dataset. Once these endmembers are selected, then their location and abundances can be mapped from the original data. These methods derive the maximum information from the hyperspectral data themselves, minimizing the reliance on *a priori* or outside information.

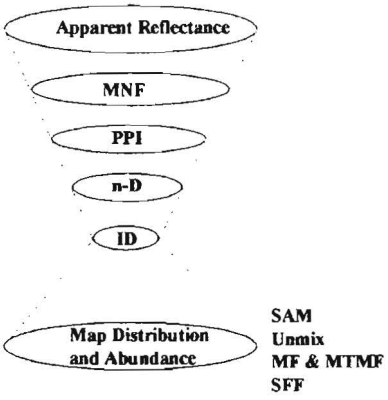

Figure 3: AIG Standardized Processing methods for hyperspectral data analysis.

3.2.1 Destriping for Hyperion area array data

If required, preprocessing/data clean-up may be applied to the data prior to atmospheric correction. In the case of Hyperion data, though radiometric corrections were applied prior to data delivery to AIG, there was still a pronounced vertical striping pattern in the data (visible in individual bands, but more pronounced when using the linearly transformed data). Such striping is apparently caused by dark current imbalances (DC Bias) of the detectors across the pixel direction of the detector (Dykstra and Segal, 1985). This is often seen in data acquired using push-broom (area array) technology (e.g., AIS, Hyperion). Destriping was accomplished using custom software (following the model of software written for the original pushbroom imaging spectrometer AIS) (Dykstra and Segal, 1985; Kruse, 1988). This approach adjusts each image column brightness (in all bands) based on a calculated offset relative to the scene average detector response. Assumptions made were that individual detectors were reasonably well behaved (stable) and that over the course of a data collect ("flightline"), that each of the cross-track detectors has covered, on the average, very similar surface materials. Implementation consisted of calculation of an average spectrum for each of the 256 Hyperion detectors followed by determination of a global scene average spectrum. Each column spectrum was then subtracted from the global spectrum to determine offsets to be added to each pixel in the corresponding column. Each pixel in each column of the radiance data was then adjusted accordingly using the calculated offset. Destriping is only required for correcting the pushbroom Hyperion data and thus no destriping was applied to the AVIRIS data.

3.2.2 Atmospheric Correction

The AIG analysis methods are generally applicable to both airborne and satellite data. The methodology requires processing radiance-calibrated data to apparent reflectance. ACORN, currently used by AIG for correction of both airborne and satellite hyperspectral data (AIG, 2001), is a commercially-available, enhanced atmospheric model-based software that uses licensed MODTRAN4 technology to produce high quality surface reflectance without ground measurements. The Cuprite AVIRIS and Hyperion data were both converted to apparent reflectance using ACORN. Appropriate model parameters for each instrument and collection date were used, otherwise, all other parameters were identical for both datasets.

3.2.3 Standardized AIG Hyperspectral Analysis

Standardized AIG hyperspectral analysis methods used for both the airborne sensors and Hyperion data (implemented in the ENVI™ image analysis software) include spectral polishing using "EFFORT" (Boardman, 1998a), spectral data reduction using the Minimum Noise Fraction (MNF) transformation (Green et al., 1988; Boardman, 1993), spatial data reduction using the Pixel Purity Index™ (PPI) (Boardman, 1993), an n-Dimensional Visualizer™ to determine image endmembers (Boardman, 1993), identification of endmembers using their reflectance spectra (Kruse et al., 1993a) in the Spectral Analyst™, and mineral mapping using both the Spectral Angle Mapper (SAM) (Kruse et al., 1993b) and Mixture-Tuned-Matched Filtering (MTMF™) (Boardman, 1998b). This approach is shown in Figure 1 below and also outlined in Kruse et al. (1996) and Kruse and Boardman (2000).

3.2.4 Geometric Corrections

The final step in the analysis is usually to present the results on a map base. In this case, to facilitate comparison of the Hyperion data to AVIRIS mineral mapping results and minimize resampling artifacts, the AVIRIS data were used as the base rather than a map. The Hyperion data were geometrically corrected to match the AVIRIS data by picking ground control points (GCP) and using a 1st degree polynomial warp with nearest neighbor resampling. Approximately 20 GCPs were used and the residual errors were on the order of 2 pixels. Hyperion image-maps (not the full data cube!) were geocorrected to match the AVIRIS data.

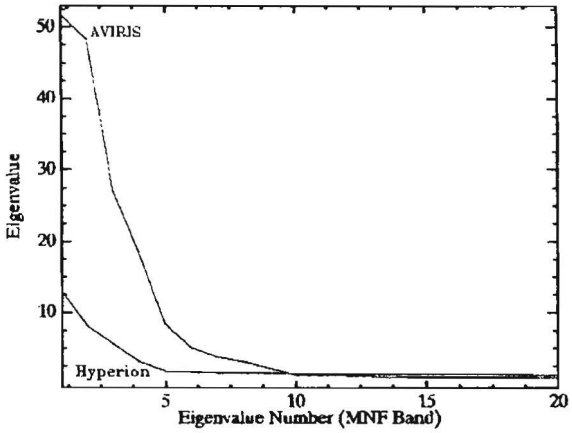

Figure 4: MNF eigenvalue plots for the Cuprite, Nevada, AVIRIS and Hyperion data

3.3 Results

Operationally, spectral bands covering the short wave infrared (SWIR) spectral range (2.0 – 2.5 μm for AVIRIS and 2.0 – 2.4 μm for Hyperion) were selected and these bands were linearly transformed using the MNF transformation. Figure 4 shows a plot of the MNF eigenvalues for both datasets. Higher eigenvalues generally indicate higher information content. The MNF results indicate that the AVIRIS data contain significantly more information than the Hyperion data covering approximately the same spatial area and spectral range. The actual data dimensionality is usually determined by comparing both the eigenvalue plots and the MNF images for each dataset (Figures 4, 5, and 6). In the case of AVIRIS, the MNF analysis indicates a dimensionality of approximately 20. The Hyperion data exhibits dimensionality of approximately 6.

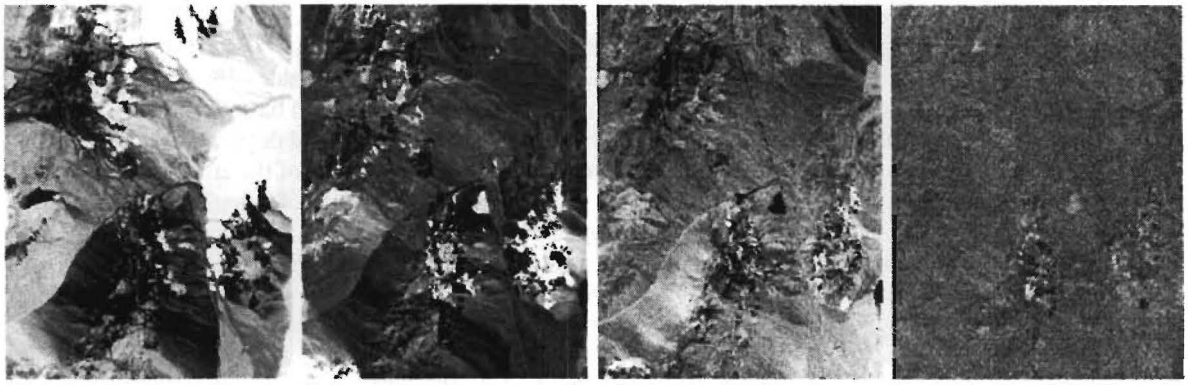

Figure 5. MNF images for the AVIRIS SWIR data. Images from left to right, MNF band 1, MNF band 5, MNF band 10, MNF band 20.

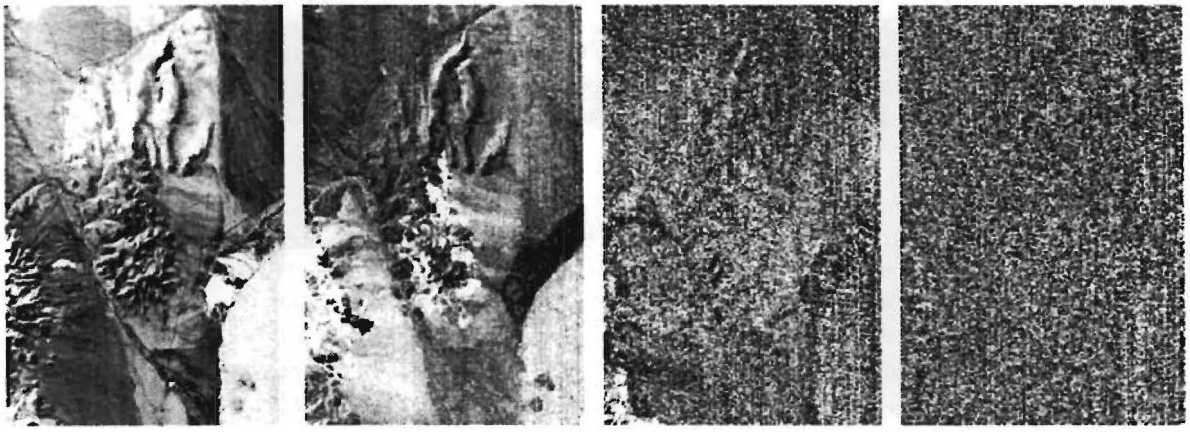

Figure 6. MNF images for the Hyperion SWIR data. Images from left to right, MNF band 1, MNF band 2, MNF band 5, MNF band 10.

The top MNF bands for each data set (20 for AVIRIS, 6 for Hyperion), which contain most of the spectral information (Green et al., 1988), were used to determine the most likely endmembers using the PPI procedure. These potential endmember spectra were loaded into an n-dimensional scatterplot and rotated in real time on the computer screen until "points" or extremities on the scatterplot were exposed (Boardman, 1993). These projections were "painted" using region-of-interest (ROI) definition procedures and then rotated again in 3 or more dimensions (3 or more MNF bands) to determine if their signatures were unique in the MNF data. Once a set of unique pixels were defined, then each separate projection on the scatterplot (corresponding to a pure endmember) was exported to a ROI in the image. Mean spectra were then extracted for each ROI from the apparent reflectance data to act as endmembers for spectral mapping (Figure 7). These endmembers or a subset of these endmembers (in the case of AVIRIS) were used for subsequent classification and other processing. Mixture-Tuned-Matched Filtering (MTMF), a spectral matching method (Boardman, 1998b), was used to produce image-maps showing the distribution and abundance of selected minerals. (Note: MNF endmember spectra, not reflectance spectra are used in the MTMF). The results are generally presented as gray-scale images (not shown) with values from 0 to 1.0, which provide a means of estimating mineral abundance. Brighter pixels in the images represent higher mineral abundances. Results images for both AVIRIS and Hyperion were produced by correcting the Hyperion data to match the AVIRIS spatial scale and orientation as described above. Selected results were combined as color-coded images to show the distribution of the principal (spectrally predominant) minerals (Figure 8).

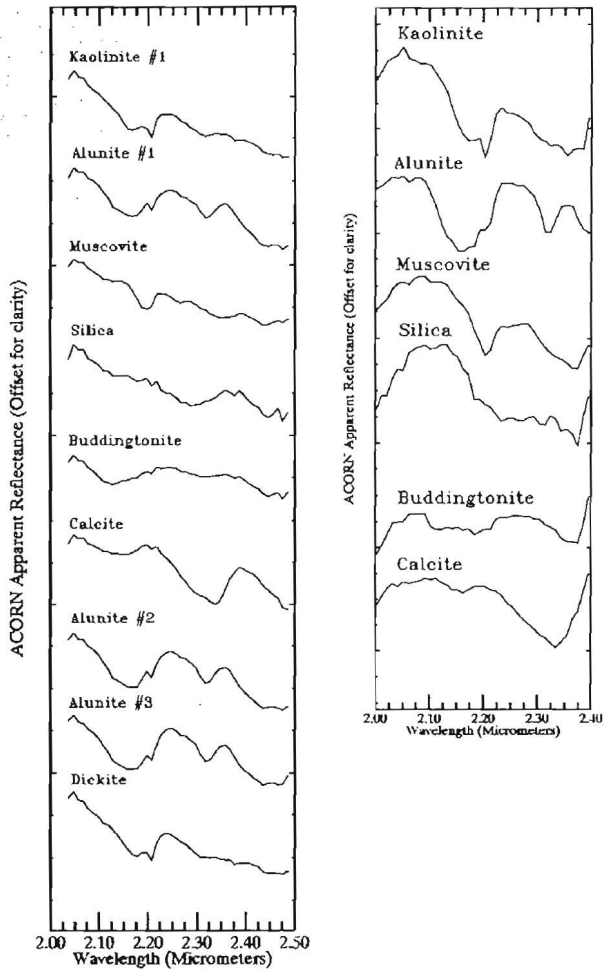

Figure 7: Comparison of selected AVIRIS endmember spectra (left) and Hyperion endmember spectra (right). Note that AVIRIS detected several varieties of alunite plus an additional kaolinite-group mineral (dickite) that were not detectable using the Hyperion data. Other AVIRIS minerals and vegetation not shown.

Visual comparison of the two classified datasets shows that Hyperion identifies similar minerals and produces similar mineral mapping results to AVIRIS. In this case, the difference in pixel size is generally inconsequential (causing only slight loss of spatial detail in Hyperion results). It seems likely that the lower SNR of the Hyperion data (specified at approximately 50:1 vs >500:1 for AVIRIS) does affect the ability to extract characteristic spectra and identify individual minerals. (See the Hyperion buddingtonite spectrum in Figure 7 above, which does not clearly show the characteristic buddingtonite spectral feature shape near 2.11 μm, which is well resolved in AVIRIS [Figure 7] and other hyperspectral aircraft data) (Kruse et al., 1990, 2000; Swayze, 1997; Green et al., 2001). This spectrum could also, however, be an effect of the pixel size causing greater mixing in the Hyperion data for relatively small buddingtonite occurrences. Additionally, bear in mind that Figure 8 shows a basic AVIRIS mineral map. It is possible to extract more detailed mineralogic information from the AVIRIS data (Swayze, 1997; Green et al., 2001; Kruse et al., 2001, 2002;) as well as abundance information (Boardman and Kruse, 1994; Boardman et al., 1995, Kruse et al, 1999). Determination of abundances for minerals identified by Hyperion is possible, but not illustrated here. Our analysis also indicates that the Cuprite Hyperion data do not allow extraction of the same level of detailed mineralogic information as AVIRIS (eg: within-species separation of micas and temperature mapping of Alunites) (Swayze, 1997; Swayze et al., 1992). Actually though, Hyperion performs surprisingly well considering the overall SWIR SNR.

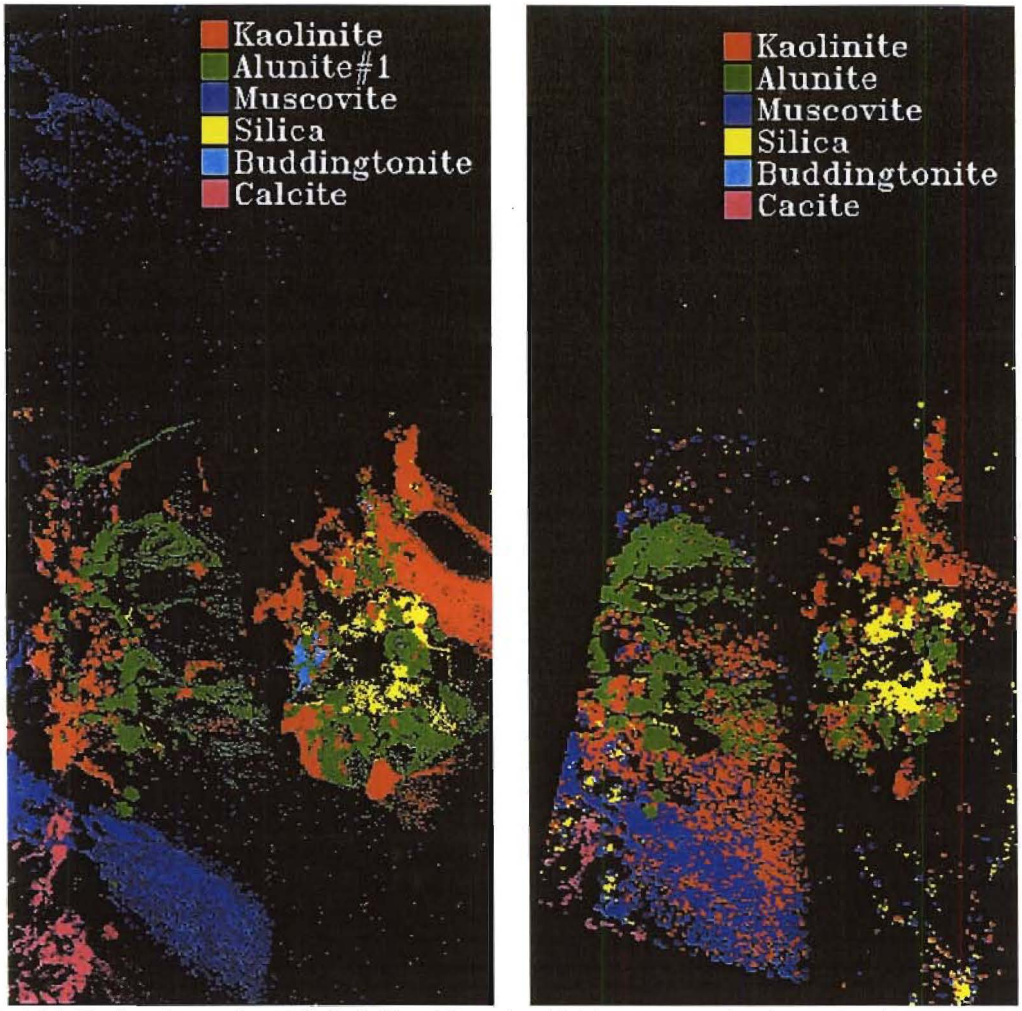

Figure 8: MTMF mineral maps for AVIRIS (left) and Hyperion (right) produced using the endmember spectra in Figure 7.

3.4 Accuracy Assessment and Error Analysis

Visual comparison of the Hyperion and AVIRIS MTMF image maps in Figure 8 using the AVIRIS data as the "Ground Truth" indicates that in general, using these mapping methods, the two datasets produce similar mapping results. Figure 9 shows a comparison of MTMF results for the minerals kaolinite and alunite, presented as binary images covering the data's overlapping area (white is a specific mineral, black is unclassified), and it can be seen that these have similar patterns of classified pixels for the selected minerals.

Detailed direct comparison of the mapping results demonstrates, however, that the correspondence is not as great as may be thought from visual comparison. Comparison of the MTMF spectral mapping results using a confusion matrix approach shows that many pixels classified using AVIRIS are unclassified on Hyperion (up to 60%, but variable by mineral). These are errors of omission. This is probably explained by the differences in SNR between the two datasets. Some spectral features are simply below the level of detection on the Hyperion data (This issue is explored further in a later section). The same analysis, but excluding the unclassified areas, yields approximately 75% overall agreement of Hyperion to AVIRIS, with a Kappa Coefficient of 0.66 (Table 2) (Richards, 1994). This highlights errors of commission (where pixels mapped as one mineral by AVIRIS are mapped as another mineral by Hyperion). First, some pixels unclassified using AVIRIS are misclassified as a specific mineral on Hyperion (around 5% commission error). Additionally, some pixels classified by AVIRIS as specific minerals are misclassified as different minerals on Hyperion (~25% commission error). Specifically, there is minor classification error between: Kaolinite mapped by Hyperion as Muscovite (7%), Kaolinite and Silica (4%), Muscovite and Calcite (2%), Silica and Alunite (6%), Silica and Muscovite (3%), Silica and Calcite (1%), Buddingtonite and Kaolinite (7%), Calcite and Muscovite (5%), and Calcite and Silica (4%). Moderate errors occur between:, Kaolinite mapped

by Hyperion as Alunite (15%), Alunite and Kaolinite (16%), and Silica and Kaolinite (13%). The highest errors occur between: Buddingtonite mapped by Hyperion as Alunite (58%), and Muscovite mapped by Hyperion as Kaolinite (25%). Table 2 summarizes the error relationships between minerals.

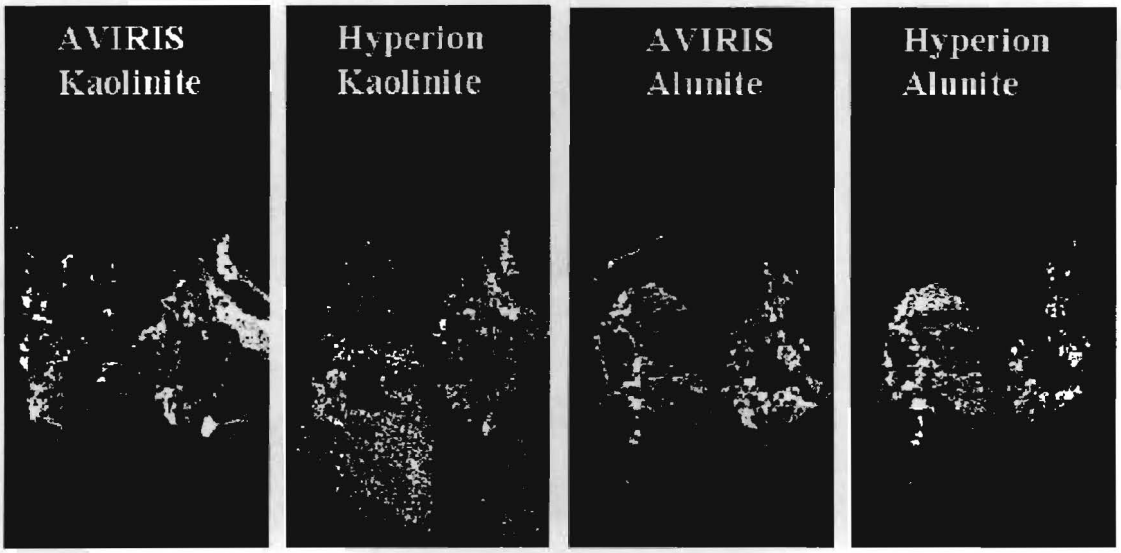

Figure 9: Comparison of MTMF mineral mapping results for kaolinite and alunite. White pixels indicate successful classification.

Table 2: Confusion matrix comparing Hyperion MTMF mapping results to AVIRIS "Ground Truth" MTMF results.

	AVIRIS "Ground Truth" Class (Percent)						
Hyperion	Kaolinite %	Muscovite %	Silica %	Buddingtonite %	Alunite%	Calcite %	Total %
Kaolinite	73.13	25.09	12.87	7.02	16.39	2.66	36.20
Muscovite	7.14	72.58	2.52	0.00	0.88	4.56	20.63
Silica	4.33	0.79	76.96	0.00	2.23	4.18	8.70
Buddingtonite	0.02	0.00	0.00	35.09	0.49	0.00	0.61
Alunite	14.83	0.00	6.39	57.89	79.68	0.00	31.38
Calcite	0.55	1.54	1.26	0.00	0.33	88.59	2.48
Total	100.00	100.00	100.00	100.00	100.00	100.00	100.00

While this comparison serves to highlight the accuracy and overall performance of the Hyperion dataset compared to AVIRIS, several other issues may affect the accuracy assessment. These include: 1) the data coverage (spatial extent) of the two datasets – they cover substantially the same ground, but not exactly (affects unclassified class), 2) the data pixel size (AVIRIS is 20m, Hyperion 30m), 3) Image acquisition differences (date/time, atmospheric conditions, SNR), 4) slightly different spectral characteristics (2.0 – 2.5 μm for AVIRIS vs 2.0 – 2.4 μm for Hyperion; varying band centers and spectral resolution), 5) different image-based endmembers spectra used for MTMF (endmember spectra not identical), 6) MTMF threshold consistency and class combining (AVIRIS), and 7) Hyperion to AVIRIS image registration accuracy.

4.0 SNR COMPARISONS – EFFECT ON MINERAL MAPPING

Previous Hyperion investigations show that there is a strong relationship between the acquisition time of year and the signal-to-noise ratio (SNR) of the Hyperion data (Kruse et al., 2001, 2002). SNR for the same targets are higher in the summer and lowest in the winter. This has a direct effect on spectral mineral mapping, with lower SNR resulting in extraction of less detail (also see AVIRIS vs Hyperion MNF comparison above). Calculation of data SNR using a Mean/Standard Deviation method for a homogeneous target (Stonewall Playa) produces the results shown in Figure 10 for the Cuprite AVIRIS (June 1997) and Hyperion (March 2001). While these SNR are representative of those that can be extracted directly from the data, slightly higher SNR could probably be obtained through analysis of the data dark current signal. Figure 10 also shows calculated SNR for Hyperion data collected

during July 2001 (northern hemisphere summer) for a site in northern Death Valley, California. All SNR are normalized to 50% reflectance. Note that the SWIR SNR is significantly higher than the calculated Cuprite SWIR SNR for the March 2001 data (SWIR SNR ~50:1 vs 25:1). The implications of the decreased Hyperion winter SNR are evident in endmember spectra extracted from both the Cuprite AVIRIS and Hyperion (Figure 7) and the northern Death Valley Hyperion data (Figure 11).

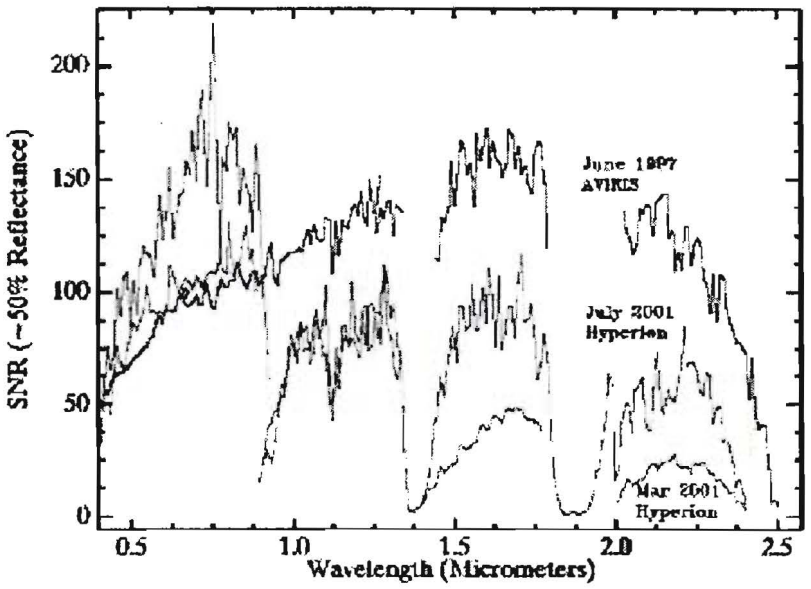

Figure 10: SNR Comparisons for June 1997 AVIRIS, July 2001 Hyperion, and March 2001 Hyperion.

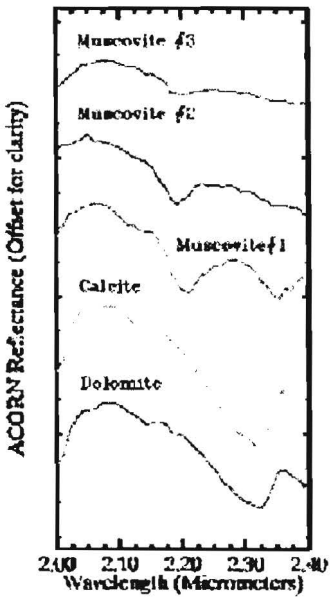

Figure 11: Northern Death Valley Hyperion Spectral Endmembers

While the Cuprite Hyperion data allow basic mineral identification, more detail (additional endmembers) are detected and mapped using the higher SNR AVIRIS and Hyperion data. This is also important for geologic/mineral mapping, because higher SNR allows separation of similar endmembers such as calcite from dolomite (Figure 11) and within-species variability such as kaolinite vs dickite (Figure 7). In the northern Death Valley case, the high SNR allows detection of 3 different mica endmembers with different aluminum substitution (Kruse et al., 1999). Previous investigations have indicated that SNR is critical for this determination (Kruse et al., 1999, 2001, 2002).

5.0 Conclusions

Analysis of Hyperion data for Cuprite, Nevada, which has established ground truth and years of airborne hyperspectral data, show that Hyperion is performing to specifications and data from the short wave infrared (SWIR) spectrometer can be used to produce useful geologic (mineralogic) information. Airborne Visible/Infrared Imaging Spectrometer (AVIRIS) data collected during June 1997 served as the "ground truth" for this investigation. Comparison of Hyperion results to the known mineralogy derived from AVIRIS data generally validate on-orbit mineral mapping and Hyperion performance. Minerals mapped at Cuprite using Hyperion include kaolinite, alunite, buddingtonite, calcite, muscovite, and hydrothermal silica. This case history demonstrates the analysis methodologies and level of information available from these Hyperion data. It also demonstrates the importance of high signal-to-noise performance for hyperspectral sensors. The Cuprite Hyperion data represent an "early" Hyperion acquisition for the northern hemisphere (a winter scene); thus the SWIR signal-to-noise ratio (SNR) (Mean/Standard Deviation method on Stonewall Playa) is approximately 25:1. Other Hyperion scenes collected under optimum (summer) conditions exhibit SWIR SNR as high as approximately 50:1. The level of mineralogic information available from the data is directly tied to the SNR.

Standardized hyperspectral data processing methods applied to the Cuprite Hyperion data lead to definition of specific key minerals, however, it is more difficult (than for AVIRIS) to extract the information because of the Hyperion data's lower SNR. The effect of this reduced response compared to AVIRIS is lower data dimensionality,

thus fewer endmembers can be identified and mapped than with AVIRIS. Accuracy assessment and error analysis indicates that with these Cuprite Hyperion data that, in many cases, mineral identification is not possible where specific minerals are known to exist. Detailed direct comparison of mixture-tuned-matched-filtering (MTMF) spectral mapping results using a confusion matrix approach shows that many pixels classified using AVIRIS are unclassified on Hyperion (up to 60%, but variable by mineral). These are errors of omission. This is probably explained by the differences in SNR between the two datasets. Some spectral features are simply below the level of detection on the Hyperion data. The same analysis, but excluding the unclassified areas, yields approximately 75% overall agreement of Hyperion to AVIRIS, with a Kappa Coefficient =0.66. This highlights errors of commission (where pixels mapped as one mineral by AVIRIS are mapped as another mineral by Hyperion). First, some pixels unclassified using AVIRIS are misclassified as a specific mineral on Hyperion (around 5% commission error). Additionally, some pixels classified by AVIRIS as specific minerals are misclassified as different minerals on Hyperion (~25% commission error). The highest errors occur between: Buddingtonite mapped by Hyperion as Alunite (58%), and Muscovite mapped by Hyperion as Kaolinite (25%).

As a technology demonstration, Hyperion performs surprisingly well for mineral identification and mapping. We expect (and have demonstrated) improved mineral identification and mapping results from "summer" season Hyperion acquisitions with higher SNR than the Cuprite data. These improvements principally take the form of mapping of subtle distinctions such as determining the difference between calcite and dolomite and mapping within-species variability caused by molecular substitution (eg: aluminum substitution in micas). Unfortunately, Hyperion data collected under less than optimum conditions (winter season, dark targets) have marginal SWIR SNR and allow mapping of only the most basic mineral occurrences and mineral differences (Kruse et al., 2001, 2002). This results in a recommendation that future HSI satellite sensors have significantly higher SNR performance specifications than Hyperion for the SWIR (at least 100:1 based on dark current measurements).

6.0 Acknowledgments

This research was partially funded by NASA under grant NCC5-495. Additional financial support was provided by Analytical Imaging and Geophysics LLC internal research and development funds. AVIRIS data were provided by JPL. ACORN is a trademark of ImSpec Associates, LLC. ENVI is a registered trademark of Research Systems Inc., Boulder, Colorado. Pixel Purity Index (PPI), n-Dimensional Visualizer, Spectral Analyst, and Mixture-Tuned Matched Filter (MTMF) are all trademarks of Research Systems Inc.

7.0 References

Abrams, M. J., Ashley, R. P., Rowan, L. C., Goetz, A. F. H., and Kahle, A. B., 1977, Mapping of hydrothermal alteration in the Cuprite mining district, Nevada, using aircraft scanner images for the spectral region 0.46 – 2.36 μm, *Geology*, v. 5, p. 713-718.

AIG, 2001, *ACORN User's Guide, Stand Alone Version: Analytical Imaging and Geophysics LLC*, 64 p.

Ashley, R. P., and Abrams, M. J., 1980, Alteration mapping using multispectral images-Cuprite Mining District, Esmeralda County, Nevada: *U.S. Geological Survey Open File Report 80-367*, 17 p.

Boardman, J. W., 1993, Automated spectral unmixing of AVIRIS data using convex geometry concepts: in *Summaries, Fourth JPL Airborne Geoscience Workshop, JPL Publication 93-26*, v. 1, p. 11-14

Boardman J. W., and Kruse, F. A., 1994, Automated spectral analysis: A geologic example using AVIRIS data, north Grapevine Mountains, Nevada: in *Proceedings, Tenth Thematic Conference on Geologic Remote Sensing,* Environmental Research Institute of Michigan, Ann Arbor, MI, p. I-407 - I-418.

Boardman, J. W., Kruse, F. A., and Green, R. O., 1995, Mapping target signatures via partial unmixing of AVIRIS data: in *Summaries, Fifth JPL Airborne Earth Science Workshop, JPL Publication 95-1*, v. 1, p. 23-26.

Boardman, J. W., 1998a, Post-ATREM polishing of AVIRIS apparent reflectance data using EFFORT: a lesson in accuracy versus precision, in *Summaries of the Seventh JPL Airborne Earth Science Workshop*, v. 1, p. 53.

Boardman, J. W., 1998b, Leveraging the high dimensionality of AVIRIS data for improved sub-pixel target unmixing and rejection of false positives: mixture tuned matched filtering, in: *Summaries of the Seventh Annual JPL Airborne Geoscience Workshop*, Pasadena, CA, p. 55.

Clark, R. N., King, T. V. V., Klejwa, M., and Swayze, G. A., 1990, High spectral resolution spectroscopy of minerals: *Journal of Geophysical Research*, v. 95, no. B8, p. 12653-12680.

Dykstra, J. D., and Segal, D. B., 1985, Analysis of AIS data of the Recluse Oil Field, Recluse, Wyoming: *in Proceedings, AIS workshop, 8-10 April, 1985, JPL Publication 85-41*, Jet Propulsion Laboratory, Pasadena, California, p. 86-91.

Goetz, A. F. H., and Strivastava, V., 1985, Mineralogical mapping in the Cuprite Mining District: In *Proceedings of the Airborne Imaging Spectrometer (AIS) Data Analysis Workshop, JPL Publication 85-41*, p. 22-29.

Goetz, A. F. H., G. Vane, J. E. Solomon, and B. N. Rock, 1985. Imaging spectrometry for earth remote sensing, *Science*, v. 228, p. 1147 - 1153.

Goetz, A. F. H., and Kindel, B., 1996, Understanding unmixed AVIRIS images in Cuprite, NV using coincident HYDICE data: in *Proceedings, 6th JPL Airborne Earth Science Workshop: Jet Propulsion Laboratory Publication 96-4*, v. 1.

Green, A. A., Berman, M., Switzer, B., and Craig, M. D., 1988, A transformation for ordering multispectral data in terms of image quality with implications for noise removal: *IEEE Transactions on Geoscience and Remote Sensing*, v. 26, no. 1, p. 65 - 74.

Green, R.O., B.J. Chippendale, C. Chovit, T. Chrien, S. Dilanchian,, M. Eastwood, J. Faust, V. Grigoryan, J. Holbrook, F. Loaiza, S. Lundeen, I. McCubbing, B. Pavri, J. Raney, C. Sarture, M. Solis, 2001, Overview of the AVIRIS 2000 Flight Season: in *Proceedings of the 10th JPL Airborne Earth Science Workshop: Jet Propulsion Laboratory Publication*, (in press).

Hook, S. J., 1990; The combined use of multispectral remotely sensed data from the short wave infrared (SWIR) and thermal infrared (TIR) for lithological mapping and mineral exploration: in *Proceedings, Fifth Australasian Remote Sensing Conference, Perth, Western Australia*, v. 1, p. 371 – 380.

Kruse, F. A., 1988, Use of Airborne Imaging Spectrometer data to map minerals associated with hydrothermally altered rocks in the northern Grapevine Mountains, Nevada and California: *Remote Sensing of Environment*, v. 24, no. 1, pp. 31-51.

Kruse, F. A., Kierein-Young, K. S., and Boardman, J. W., 1990, Mineral mapping at Cuprite, Nevada with a 63 channel imaging spectrometer: *Photogrammetric Engineering and Remote Sensing*, v. 56, no. 1, p. 83-92.

Kruse, F. A., and Lefkoff, A. B., 1993, Knowledge-based geologic mapping with imaging spectrometers: *Remote Sensing Reviews*, Special Issue on NASA Innovative Research Program (IRP) results, v. 8, p. 3 - 28.

Kruse, F. A., Lefkoff, A. B., and Dietz, J. B., 1993a, Expert System-Based Mineral Mapping in northern Death Valley, California/Nevada using the Airborne Visible/Infrared Imaging Spectrometer (AVIRIS): *Remote Sensing of Environment, Special issue on AVIRIS, May-June 1993*, v. 44, p. 309 - 336.

Kruse, F. A., Lefkoff, A. B., Boardman, J. B., Heidebrecht, K. B., Shapiro, A. T., Barloon, P. J., and Goetz, A. F. H., 1993b, The Spectral Image Processing System (SIPS) - Interactive Visualization and Analysis of Imaging Spectrometer Data: *Remote Sensing of Environment, Special issue on AVIRIS, May-June 1993*, v. 44, p. 145 - 163.

Kruse, F. A., Huntington, J. H., and Green, R. O, 1996, Results from the 1995 AVIRIS Geology Group Shoot: in *Proceedings, 2nd International Airborne Remote Sensing Conference and Exhibition*: Environmental Research Institute of Michigan (ERIM), Ann Arbor, v. I, p. I-211 - I-220.

Kruse, F. A., Boardman, J. W., and Huntington, J. F., 1999, Fifteen Years of Hyperspectral Data: northern Grapevine Mountains, Nevada: in Proceedings of the 8th JPL Airborne Earth Science Workshop: Jet Propulsion Laboratory Publication, *JPL Publication 99-17*, p. 247 - 258.

Kruse, F. A., and Boardman, J. W., 2000, Characterization and Mapping of Kimberlites and Related Diatremes Using Hyperspectral Remote Sensing: in Proceedings, 2000 IEEE AeroSpace Conference, 18 – 24 March 2000, Big Sky, Montana.

Kruse, F. A., Boardman, J. W., Lefkoff, A. B., Young, J. M., Kierein-Young, K. S., Cocks, T. D., Jenssen, R., and Cocks, P. A., 2000, The AIG/HyVista 1999 USA HyMap Group Shoot: Overview and Analysis Examples: in *Proceedings IGARSS 2000, 24 – 28 July, 2000, Honolulu, Hawaii*, IEEE, Catalog Number 00CH37120C, ISBN 0-7803-6362-0, published on CD-ROM.

Kruse, F. A., Boardman, J. W., and Huntington, J. F., 2001, Progress Report: Geologic Validation of EO-1 Hyperion: in *Proceedings of the 10th JPL Airborne Earth Science Workshop: Jet Propulsion Laboratory Publication*. (in-press).

Kruse, F. A., Boardman, J. W., and Huntington, J. F., 2002, Comparison of EO-1 Hyperion and Airborne Hyperspectral Remote Sensing Data for Geologic Applications: in *Proceedings, SPIE Aerospace Conference, 9-16 March 2002, Big Sky, Montana* (in press).

Pearlman, J, Stephen Carman, Paul Lee, Lushalan Liao and Carol Segal, 1999, Hyperion Imaging Spectrometer on the New Millennium Program Earth Orbiter-1 System: In *Proceedings, International Symposium on Spectral Sensing Research (ISSSR), Systems and Sensors for the New Millennium, published on CD-ROM, International Society for Photogrammetry and Remote Sensing (ISPRS)*.

Porter, W. M., and Enmark, H. E., 1987, System overview of the Airborne Visible/Infrared Imaging Spectrometer (AVIRIS), in *Proceedings, Society of Photo-Optical Instrumentation Engineers (SPIE)*, v. 834, p. 22-31.

Richards, J.A., 1994, *Remote Sensing Digital Image Analysis, An Introduction*, Springer-Verlag, New York, pp. 271 – 275.

Shipman, H. and Adams, J. B., 1987, Detectability of minerals on desert alluvial fans using reflectance spectra, *Journal of Geophysical Research*, v. 92, no. B10, p. 10391-10402.

Swayze, G. A., 1997, The hydrothermal and structural history of the Cuprite Mining District, southwestern Nevada: An integrated geological and geophysical approach: *Unpublished Ph. D. thesis, University of Colorado, Boulder*, 341 p.

Swayze, G. A., Clark, R. L., Sutley, S. and Gallagher, A. J., 1992, Ground-truthing AVIRIS mineral mapping at Cuprite, Nevada: in *Summaries of the Third Annual JPL Airborne Geosciences Workshop, V 1., AVIRIS Workshop, JPL Publication 92-14*, p. 47 – 49.

Integrated Multispectral and Hyperspectral Mineral Mapping, Los Menucos, Rio Negro, Argentina, Part I: Landsat TM Reconnaissance and AVIRIS Prospect Mapping

Fred A. Kruse,[1] Sandra L. Perry,[2] and Alejandro Caballero[3]

1. 0 Introduction

The Los Menucos gold district was discovered in 1998 by Arminex, S.A. using regional exploration methods employing Landsat Thematic Mapper (TM) satellite imagery and field investigation (Franco et al., 2000; Gemuts and Perry, 2000; Perry and Gemuts, 2000). This district has the largest significant concentration of advanced argillic, altered Permian ignimbrite and rhyolite assemblages in Argentina. Alteration is related to the intrusion of Triassic-age (?) rhyolite dome complexes below thick Permian-age felsic volcanic rocks. Associated with dome fields are large areas of phreatic breccias and hematite-rich altered oxidized zones. Alteration is characterized by vuggy silica, quartz stockwork, kaolin, and alunite. The region has potential for low-sulfidation style gold mineralization. The Los Menucos region was submitted and selected as a NASA E0-1 collection site during 2000 to evaluate other earth observation sensors, including hyperspectral (airborne AVIRIS and satellite EO-1 Hyperion) as well as multispectral data sets (Landsat 7 Enhanced Thematic Mapper and ASTER imagery). The results of the TM reconnaissance and AVIRIS analysis are presented here. The Hyperion, ETM and ASTER results are presented in a companion paper (Kruse et al., 2002a).

2.0 Landsat TM Reconnaissance

Over 100 sites were predicted as alteration anomalies resulting from digital enhancement of Landsat TM imagery analyzed by Perry Remote Sensing LLC (PRS). These results were used to drive field exploration, and in less than one year, a field crew of six geologists systematically visited and sampled all of these anomalies. Eighty percent of the areas visited exhibited epithermal-style alteration, and five percent were mineralized. The exploration effort led Arminex to assemble 80,000 hectares near the village of Los Menucos and established the area as the first gold district in Rio Negro province. Early in 2000, Rio Tinto Mining & Exploration (RTZ) took an option on the Arminex property and agreed to continue drilling and testing at key prospect areas.

3.0 Airborne Visible/Infrared Imaging Spectrometer (AVIRIS)

The Airborne Visible/Infrared Imaging Spectrometer (AVIRIS), flown by NASA/Jet Propulsion Laboratory (JPL) is a 224-channel imaging spectrometer with approximately 10 nm spectral resolution covering the 0.4 – 2.5-μm spectral range. It was flown for the Los Menucos site, Argentina on a Twin Otter aircraft at low altitude on 14-15 February 2001. The AVIRIS dataset consists of 6 overlapping, approximately 2.7km x 30km north-south flightlines, at 3.5m spatial resolution. Each flightline was processed and analyzed separately in reconnaissance mode

[1] Analytical Imaging and Geophysics LLC, Boulder, Colorado, USA, E-mail: kruse@aigllc.com
[2] Perry Remote Sensing LLC, Englewood, Colorado, USA
[3] Rio Tinto Mining & Exploration Ltd., Santiago, Chile

(optimized for the entire dataset, not individual sites). Two spectral ranges were analyzed; 1) 0.4–1.3 μm (iron oxides), and 2) 2.0–2.5 μm (clays, carbonates, etc). Processing consisted of standardized hyperspectral analysis developed by AIG (Boardman and Kruse, 1994; Boardman et al., 1995; Kruse et al., 1996; Kruse et al., 2002b, 2002c; Kruse, 2002) to allow identification and mapping of key alteration minerals. This hyperspectral analysis methodology includes 1) correction of data to apparent reflectance using the ACORN atmospheric correction software (AIG, 2001), 2) linear transformation of the reflectance data to minimize noise and determine data dimensionality, 3) location of the most spectrally pure pixels, 4) extraction and automated identification of endmember spectra, and 5) spatial mapping and abundance estimates for specific image endmembers. A key point of this methodology is the reduction of data in both the spectral and spatial dimensions to locate, characterize, and identify a few key endmember spectra that can be used to explain the rest of the hyperspectral dataset. Once these endmembers are selected, then their location and abundances can be mapped from the original data. These methods derive the maximum information from the hyperspectral data themselves, minimizing the reliance on a priori or outside information. The results were map-corrected and combined into an image mosaic covering an approximately 10km x 30km area covering several key mineral prospects.

The high spatial resolution AVIRIS data allowed identification and mapping of common alteration minerals such as hematite, goethite, kaolinite, dickite, alunite, pyrophyllite, muscovite/sericite, montmorillonite, and calcite. Distinguishing between similar minerals such as kaolinite and dickite was possible because of the high signal-to-noise (SNR) of the AVIRIS sensor. The AVIRIS data pointed out minerals and mineral assemblages that would not have been readily apparent utilizing conventional field mapping methods. In particular, a large zoned hydrothermal system, dominated by several different muscovite species was mapped, and in addition, several previously unknown pyrophyllite occurrences cross-cutting predominant structural trends were detected and mapped.

4.0 Field Verification

AVIRIS mineral maps were used along with the Landsat TM mapping as base maps for field verification. Field reconnaissance was conducted during April 2001 with the assistance of RTZ geologists. Several prospects and other mineralogically interesting areas shown by the AVIRIS mineral maps were visited, the rocks and alteration were examined, and samples were collected utilizing real-time GPS positioning. Over 160 field-spectrometer readings were compiled to generate spectral libraries of key alteration minerals throughout the district. The field reconnaissance and spectral measurements verified the accuracy of the AVIRIS mapping. Known mineralized areas were accurately characterized and several new prospects identified (Kruse et al., 2002c). Spectral libraries were later used to refine AVIRIS results and to apply to EO-1 Hyperion and Landsat/ASTER multispectral evaluation.

5.0 Conclusions

The Los Menucos district provides an excellent case history of a complex epithermal gold system initially identified using satellite imagery and further mapped and explored using hyperspectral imaging systems. The district offers a host of argillic and advanced argillic alteration minerals at the surface, including many which are difficult to visually identify, thus it has proved to be an excellent test area for hyperspectral mapping. The combination of Landsat

TM reconnaissance with detailed AVIRIS mineral mapping provides powerful exploration tools. In the span of three field seasons, the district was explored, mapped, and further refined for sampling and drilling, using remote sensing technology to optimize man-hours in the field.

6.0 Acknowledgments

This research was partially funded by NASA under grant NCC5-495. Additional financial support was provided by Analytical Imaging and Geophysics LLC and Perry Remote Sensing LLC internal research and development funds and by RTZ for field verification in Argentina. AVIRIS and field spectrometer data were provided by JPL. ACORN is a trademark of ImSpec Associates, LLC. This project was suggested by Perry Remote Sensing LLC, Englewood, Colorado, as a cooperative effort. Special thanks are due to Sandra Perry for her support.

7.0 References

AIG, 2001, ACORN User's Guide, Stand Alone Version: *Analytical Imaging and Geophysics LLC*, 64 p.

Boardman, J. W., and Kruse, F. A., 1994, Automated spectral analysis: A geological example using AVIRIS data, northern Grapevine Mountains, Nevada: in *Proceedings, Tenth Thematic Conference, Geologic Remote Sensing*, Environmental Research Institute of Michigan, 9-12 May 1994, San Antonio, Texas, p. I-407 - I-418.

Boardman, J. W., Kruse, F. A., and Green, R. O., 1995, Mapping target signatures via partial unmixing of AVIRIS data: in *Summaries, Fifth JPL Airborne Earth Science Workshop, JPL Publication 95-1*, v. 1, p. 23-26.

Franco, S., Puente, N., Varela, C., Gemuts, I., 2000, Mineralizacion Aurifera en El Distrito Los Menucos, Provincia de Rio Negro, Argentina: in *Proceedings, Argentina Mining 2000*, Mendoza, Argentina, August 22 - 25, 2000, p. 112 - 126.

Gemuts, I., and Perry, S., 2000, Los Menucos Au District, Rio Negro Province, Argentina: *Abstract and Presentation, Northwest Mining Association, Spokane, Washington*, December 7 - 10, 2000.

Kruse, F. A., Huntington, J. H., and Green, R. O, 1996, "Results from the 1995 AVIRIS Geology Group Shoot." In *Proceedings, 2nd International Airborne Remote Sensing Conference and Exhibition*, Environmental Research Institute of Michigan, v. I: p. I-211 - I-220.

Kruse F. A., Perry, S. L., and Caballero, A., 2002a, Integrated Multispectral and Hyperspectral Mineral Mapping, Los Menucos, Rio Negro, Argentina, Part II: EO-1 Hyperion/AVIRIS Comparisons and Landsat TM/ASTER Extensions: In *Proceedings 11th JPL Airborne Geoscience Workshop, Jet Propulsion Laboratory*, 4-8 March 2002 (This Volume)

Kruse, F. A., Boardman, J. W., and Huntington, J. F., 2002b, Comparison of Airborne and Satellite Hyperspectral Data for Geologic Mapping: in *Proceedings, SPIE International Symposium on AeroSense*, 1-5 April 2002, Orlando, FL (in press).

Kruse, F. A., Boardman, J. W., and Huntington, J. F., 2002c, Comparison of EO-1 Hyperion and Airborne Hyperspectral Remote Sensing Data for Geologic Applications: in *Proceedings, SPIE Aerospace Conference*, 9-16 March 2002, Big Sky, Montana (in press).

Kruse, F. A., Comparison of AVIRIS and Hyperion for Hyperspectral Mineral Mapping, 2002, In proceedings *11th JPL Airborne Geoscience Workshop, Jet Propulsion Laboratory, 4-8 March 2002* (This Volume)

Perry, S., and Gemuts, I., 2000, New High Sulfidation Gold District: Los Menucos, rio Negro Province, Argentina - A Landsat Discovery: *Presented at Fourteenth International Conference, Applied Geologic Remote Sensing, November 6 - 8, 2000, Las Vegas, Nevada*, Veridian ERIM International.

Integrated Multispectral and Hyperspectral Mineral Mapping, Los Menucos, Rio Negro, Argentina, Part II: EO-1 Hyperion/AVIRIS Comparisons and Landsat TM/ASTER Extensions

Fred A. Kruse,[1] Sandra L. Perry,[2] and Alejandro Caballero[3]

1.0 Introduction

The Los Menucos gold district was discovered in 1998 by Arminex, S.A. using regional exploration methods employing Landsat Thematic Mapper (TM) satellite imagery and field investigation (Franco et al., 2000; Gemuts and Perry, 2000; Perry and Gemuts, 2000). This district has the largest significant concentration of advanced argillic, altered Permian ignimbrite and rhyolite assemblages in Argentina. Alteration is related to the intrusion of Triassic-age (?) rhyolite dome complexes below thick Permian-age felsic volcanic rocks. Associated with dome fields are large areas of phreatic breccias and hematite-rich altered oxidized zones. Alteration is characterized by vuggy silica, quartz stockwork, kaolin, and alunite. The region has potential for low-sulfidation style gold mineralization. The Los Menucos region was submitted and selected as a NASA E0-1 collection site during 2000 to evaluate other earth observation sensors, including hyperspectral (airborne AVIRIS and satellite EO-1 Hyperion) as well as multispectral data sets (Landsat 7 Enhanced Thematic Mapper and ASTER imagery). The results of the TM reconnaissance and AVIRIS analysis are presented in a companion paper (Kruse et al., 2002a). The Hyperion, ETM and ASTER results are presented here.

2.0 Landsat TM Reconnaissance and AVIRIS Verification

Over 100 sites were predicted as alteration anomalies resulting from digital enhancement of Landsat TM imagery analyzed by Perry Remote Sensing LLC (PRS). These results were used to drive field exploration, and in less than one year, a field crew of six geologists systematically visited and sampled all of these anomalies. Eighty percent of the areas visited exhibited epithermal-style alteration, and five percent were mineralized. The exploration effort led Arminex to assemble 80,000 hectares near the village of Los Menucos and established the area as the first gold district in Rio Negro province. Early in 2000, Rio Tinto Mining & Exploration (RTZ) took an option on the Arminex property and agreed to continue drilling and testing at key prospect areas.

Since the district was initially identified by field testing Landsat, and hosts an array of alteration minerals, the location was also submitted and selected as a NASA E0-1 site to evaluate the EO-1 Hyperion sensor as well as multispectral data sets (Landsat 7 Enhanced Thematic Mapper and ASTER imagery). Airborne Visible/Infrared Imaging Spectrometer (AVIRIS) data were flown by NASA/Jet Propulsion Laboratory (JPL) in support of Hyperion during February 2001. AVIRIS is a 224-channel imaging spectrometer with approximately 10 nm spectral resolution covering the 0.4 – 2-μm spectral range. Six overlapping flightlines at 3.5m spatial resolution were analyzed and used to identify and map common alteration minerals at the Los Menucos site

[1] Analytical Imaging and Geophysics LLC, Boulder, Colorado, USA, E-mail: kruse@aigllc.com
[2] Perry Remote Sensing LLC, Englewood, Colorado, USA
[3] Rio Tinto Mining & Exploration Ltd., Santiago, Chile

(Kruse et al., 2002b). These detailed mineral maps were compiled as "ground-truth" for the Hyperion analysis and were used along with the Landsat TM and field reconnaissance conducted during April 2001 to validate the Hyperion data.

3.0 EO-1 Hyperion

Hyperion, launched in November 2000, is a new satellite hyperspectral sensor covering the 0.4- to 2.5-μm spectral range with 242 spectral bands at approximately 10-nm spectral resolution and 30-m spatial resolution from a 705km orbit. A typical dataset covers an approximately 7.5-km-wide swath 165 km long. Hyperion data for the Los Menucos, Argentina, site were first acquired on 25 February 2001, close to the 14-15 February AVIRIS acquisition date. Unfortunately, the Hyperion data were predominantly cloudy, however, several RTZ prospects were mostly clear on the 25 February date. Additional datasets were acquired on 30 April (mostly cloudy), 16 May (cloudy), 1 June (mostly cloudy), 17 June (clear – but low signal-to-noise), 3 July (cloudy), and 19 July (cloudy).

The 25 February Hyperionion data were processed to geologic products using AIG-developed approaches for extraction of mineralogic and geologic information (Boardman and Kruse, 1994; Boardman et al., 1995; Kruse et al., 1996; Kruse et al., 2002c; Kruse, 2002). This hyperspectral analysis methodology includes 1) data pre-processing (pushbroom data destriping), 2) correction of data to apparent reflectance using the ACORN atmospheric correction software (AIG, 2001), 3) linear transformation of the reflectance data to minimize noise and determine data dimensionality, 4) location of the most spectrally pure pixels, 5) extraction and automated identification of endmember spectra, and 6) spatial mapping and abundance estimates for specific image endmembers. A key point of this methodology is the reduction of data in both the spectral and spatial dimensions to locate, characterize, and identify a few key endmember spectra that can be used to explain the rest of the hyperspectral dataset. Once these endmembers are selected, then their location and abundances can be mapped from the original data. These methods derive the maximum information from the hyperspectral data themselves, minimizing the reliance on a priori or outside information.

Several characteristic mineral spectra (silica, kaolinite, muscovite) were extracted from the Los Menucos Hyperion data. Mineral maps were produced and compared to those derived from the AVIRIS data. Comparison of the two datasets shows that Hyperion identifies similar minerals and produces grossly similar mineral mapping results as AVIRIS, however, it doesn't produce the level of detail available from the AVIRIS data. Some minerals are missed, and others are confused (dickite/kaolinite). This is largely the effect of reduced Hyperion signal-to-noise-performance compared to the AVIRIS (~50:1 and less for Hyperion, compared to >500:1 for AVIRIS) (Kruse, 2002). The Hyperion data are most useful for small-scale reconnaissance mapping and are attractive because world-wide acquisitions are possible. In the Los Menucos case, however, the problem was that no cloud-free data were acquired during the southern hemisphere summer – this would have maximized the SNR.

4.0 Extending Mineral Mapping using Landsat ETM+

Multispectral image analyses were also conducted to extend fieldwork to adjacent regions, based on known mineral locations and hyperspectral results. This approach is worth testing because it could vastly aid regional exploration for areas lacking ground truth or hyperspectral coverage.

Landsat 7 was launched by NASA in 1999 and carries the Enhanced Thematic Mapper (ETM) sensor, offering 8 spectral bands (3 visible, 1 near IR and 2 shortwave IR bands at 30 meter spatial resolution, plus 1 thermal IR band at 60 meters, and 1 panchromatic band at 15 meters). In evaluating ETM, known mineral locations were outlined as training sites followed by minimum distance (MD) image classification on decorrelated reflectance bands (PCs). Landsat results proved helpful in predicting mineral mixtures and general mineral groups, such as iron oxides (FeOx) and alteration-clay minerals. The broad bandwidth of Landsat 7, however, was not capable of segmenting specific clays, carbonates, or Fe minerals. Nonetheless, Landsat classes were distinct for kaolinite/muscovite and alunite/kaolinite mixtures, as documented at three known mineralized sites inside the project area. In addition, Landsat analysis appeared to spectrally differentiate soil caliche (carbonates) associated with altered alunite locations. Nine exploration targets were identified outside the exploration block for further field investigation based on ETM evaluation.

5.0 ASTER Data Analysis

The ASTER system is on-board the NASA "Terra" satellite, launched late in 1999. ASTER is composed of three Japanese sensors offering a total of 14 spectral bands (3 visible and near IR, 6 shortwave IR, and 5 thermal IR) at spatial resolutions ranging from 15 to 90 meters. ASTER imagery offers better spectral resolution as compared to Landsat ETM, especially in the shortwave IR spectral region. For evaluating ASTER imagery, minerals from Los Menucos spectral libraries (compiled in the field) were selected as endmembers in a Spectral Angle Mapper (SAM) image classification on atmospherically-corrected ASTER bands. Minerals used included alunite, kaolinite, illite, dickite, geothite, hematite, jarosite, and pyrophyllite. ASTER results correlated well with known kaolinite and alunite locations but were less useful in predicting pyropyllite and illite, as well as FeOx minerals (as compared to Landsat ETM). Results suggest that ASTER can be useful in predicting mineral suites, although its bandwidth does not appear capable of differentiating slight spectral differences, such as those needed to identify dickite versus kaolinite or pyrophyllite versus alunite. Nonetheless, ASTER results did coincide with known field locations of alunite and kaolinite inside the project area and also identified twelve areas outside the exploration block.

6.0 Conclusions

The Los Menucos district provides an excellent case history of a complex epithermal gold system initially identified using satellite imagery and further mapped and explored using hyperspectral imaging systems. The district offers a host of argillic and advanced argillic alteration minerals at the surface, including many of which are difficult to visually identify, and therefore is an excellent area to test and gauge spectral sensors. Hyperion provides basic mineralogic information, however, reduced SNR performance with respect to AVIRIS and persistent cloud cover during Hyperion data collection efforts have limited its effectiveness. The combination of detailed AVIRIS mineral mapping with multispectral data produced promising results that may allow extended mapping utilizing multispectral sensors such as Landsat and ASTER.

7.0 Acknowledgments

This research was partially funded by NASA under grant NCC5-495. Additional financial support was provided by Analytical Imaging and Geophysics LLC and Perry Remote Sensing

LLC internal research and development funds and by RTZ for field verification in Argentina. AVIRIS data and the field spectrometer were provided by JPL. ACORN is a trademark of ImSpec Associates, LLC. This project was suggested by Perry Remote Sensing LLC, Englewood, Colorado, as a cooperative effort. Special thanks are due to Sandra Perry for her support.

8.0 References

AIG, 2001, ACORN User's Guide, Stand Alone Version: *Analytical Imaging and Geophysics LLC*, 64 p.

Boardman, J. W., and Kruse, F. A., 1994, Automated spectral analysis: A geological example using AVIRIS data, northern Grapevine Mountains, Nevada: in *Proceedings, Tenth Thematic Conference, Geologic Remote Sensing*, Environmental Research Institute of Michigan, 9-12 May 1994, San Antonio, Texas, p. I-407 - I-418.

Boardman, J. W., Kruse, F. A., and Green, R. O., 1995, Mapping target signatures via partial unmixing of AVIRIS data: in *Summaries, Fifth JPL Airborne Earth Science Workshop, JPL Publication 95-1*, v. 1, p. 23-26.

Franco, S., Puente, N., Varela, C., Gemuts, I., 2000, Mineralizacion Aurifera en El Distrito Los Menucos, Provincia de Rio Negro, Argentina: *Proceedings, Argentina Mining 2000, Mendoza, Argentina*, August 22 - 25, 2000, p. 112 - 126.

Gemuts, I., and Perry, S., 2000, Los Menucos Au District, Rio Negro Province, Argentina: *Abstract and Presentation, Northwest Mining Association, Spokane, Washington*, December 7 - 10, 2000.

Kruse, F. A., Huntington, J. H., and Green, R. O, 1996, "Results from the 1995 AVIRIS Geology Group Shoot." In *Proceedings, 2nd International Airborne Remote Sensing Conference and Exhibition*, Environmental Research Institute of Michigan, v. I: p. I-211 - I-220.

Kruse F. A., Perry, S. L., and Caballero, A., 2002a, Integrated Multispectral and Hyperspectral Mineral Mapping, Los Menucos, Rio Negro, Argentina, Part I: Landsat TM Reconnaissance and AVIRIS Prospect Mapping: In *Poceedings 11th JPL Airborne Geoscience Workshop, Jet Propulsion Laboratory*, 4-8 March 2002 (This Volume)

Kruse, F. A., Boardman, J. W., and Huntington, J. F., 2002b Comparison of EO-1 Hyperion and Airborne Hyperspectral Remote Sensing Data for Geologic Applications: in *Proceedings, SPIE Aerospace Conference*, 9-16 March 2002, Big Sky, Montana (in press).

Kruse, F. A., Boardman, J. W., and Huntington, J. F., 2002c Comparison of Airborne and Satellite Hyperspectral Data for Geologic Mapping: in *Proceedings, SPIE International Symposium on AeroSense*, 1-5 April 2002, Orlando, FL (in press).

Kruse, F. A., Comparison of AVIRIS and Hyperion for Hyperspectral Mineral Mapping, 2002, In *Proceedings 11th JPL Airborne Geoscience Workshop, Jet Propulsion Laboratory, 4-8 March 2002* (This Volume)

Perry, S., and Gemuts, I., 2000, New High Sulfidation Gold District: Los Menucos, rio Negro Province, Argentina - A Landsat Discovery: *Presented at Fourteenth International Conference, Applied Geologic Remote Sensing, November 6 - 8, 2000, Las Vegas, Nevada*, Veridian ERIM International.

COMPARISON OF AVIRIS AND LANDSAT ETM+ FOR THE ESTIMATION OF LEAF AREA INDEX

Kyu-Sung Lee[1, 2] and Warren B. Cohen[2]

1. INTRODUCTION

Although there are several parameters of interest in the quantitative aspects of vegetative remote sensing, leaf area index (LAI) has been one of the most useful and important parameters to characterize the vegetation activities from local to global scales. LAI, defined as the sum of the leaf area per unit ground area, can be used to measure the activities (photosynthesis, transpiration, and evapotranspiration) and the production of plant ecosystems (Pierce and Running, 1988; Bonan, 1993). The measurement of LAI on the ground is very difficult and requires a great amount of labor and cost (Gower et al., 1999). Since the plant canopy is composed of leaves, which is a direct source of the energy-matter interactions in most earth-observing remote sensing systems, LAI has been an attractive variable of interest in vegetative remote sensing.

There have been many attempts to estimate LAI using various types of remote sensor data since the early stage of space remote sensing (Badhwar et al., 1986; Peterson et al., 1987; Turner et al., 1999). Remote sensing estimation of LAI has been primarily based on the empirical relationship between the ground measured leaf area index and sensor observed spectral responses (Curran et al., 1992; Peddle et al., 1999). Beside such empirical approaches, there have been a few studies to estimate LAI by the inversion of canopy reflectance models (Smith, 1993; Jacquemoud et al., 1995; Kuusk, 1998). However, these studies were mostly based on broadband multi-spectral data, such as Landsat TM and SPOT images. Recent development of imaging spectrometry technology has brought a new form of remote sensor data, which has shown great potential for many applications. In particular, the Airborne Visible/Infrared Imaging Spectrometer (AVIRIS) data, which have been provided since the late 1980s, were used to study specific features of vegetation targets. The 224 continuous spectral band data demonstrated the capability to depict certain characteristics of vegetation canopy, such as biochemical constituent (Wessman et al., 1988; Johnson et al., 1994). There have been a few studies using hyperspectral data in relation to leaf area index. In recent years, hyperspectral data has been used to estimate LAI by the inversion of radiative transfer models, which simulate the mechanics of canopy reflectance (Asner et al., 2000).

The objective of this study is to evaluate the capability of narrowband hyperspectral data for estimating leaf area index by comparing them with those of broadband multispectral instruments. Although there were many studies dealing with the remote sensing estimation of LAI by various types of image data, it has been rare to find the advantage of using the narrowband hyperspectral data over the broadband multispectral data. The lack of comparative studies might be explained by the shortage of both hyperspectral and broadband data sets available at the same location. Even though it was a simulated form of hyperspectral data, the hyperspectral-based vegetation indices did not provide better results than broadband data for estimating LAI (Jacquemoud et al., 1995; Broge and Leblanc, 2000). Lefsky et al. (2001) have compared several data types, including Landsat TM, high spatial data, AVIRIS, and scanning lidar data, for estimating forest stand structures and found that AVIRIS data were not better than other data types for relating stem diameter, biomass, and basal area. Some studies have compared vegetation indices derived from both narrowband and broadband data to relate them for discriminating different vegetation groups or cover types (Teillet et al., 1997; Galvao et al., 2000). Hyperspectral data may or may not be better than broadband data to estimate LAI. The empirical approach is often very useful for analyzing and comparing different types of remote sensing data by relating them to the ground-measured biophysical variables. This study attempts to compare AVIRIS and Landsat ETM+ data by relating them to LAI over the two study sites of tall-grass prairie and mixed forest, which have well-established ground measurement plots.

[1] Inha University, Department of Geoinformatic Engineering, Inchon, Korea (ksung@inha.ac.kr)
[2] USDA Pacific Northwest Research Station, Forestry Sciences Laboratory, Corvallis, Oregon

2. DATA AND METHODS

2.1 Study Sites and Data

This study was conducted in collaboration with the BigFoot project, which was designed to provide local validation of global estimates of biophysical variables and processes using MODIS data (Cohen and Justice, 1999). Study areas include two sites of mixed forest and grass prairie. These areas are also the sites of the long-term ecological research plots and a rich source of ground information. The Harvard Forest (HARV) site has a 5 x 5 km^2 area located about 50 km northwest of Worcester, Massachusetts. The forest has mixed species of eastern hemlock, red pine, and eastern hardwood. The Konza Prairie (KONZ) site is located approximately 10 km southwest of Manhattan, Kansas, and mostly covered by grass and shrub.

At each site there were one hundred, 25 x 25 m^2 plots where land cover, LAI, absorbed radiation, and net primary production were measured/observed. Each plot has four to nine subplots. Subplot measurements were averaged to provide a single value for each measured variable at each plot. Plot locations were determined using a real-time differential GPS. The accuracy of the system was <0.3 m in both the x and y dimensions. At the HARV site, LAI was measured at two time periods (June and August) during the growing season in 2000. Due to unexpected problems during the field measurements, only 73 of the 100 plots were measured. At the KONZ site, LAI measurements were made in all the 100 plots in June 2000.

Considering the phenological variation of vegetation target, both AVIRIS and Landsat ETM+ data were obtained as close to the ground data collection as possible (Table 1). For the KONZ study site, the data acquisition date was close in time to the ground measurements. The HARV study site, however, shows some discrepancy between image acquisition and ground measurement. We used two sets of LAI measurements separately for analyzing AVIRIS and ETM+ data. AVIRIS data were analyzed with the field LAI data of June while ETM+ data were analyzed with the LAI measurement of June.

Table 1. Date of data acquisition for AVIRIS and TM image data and ground measurements of LAI.

Harvard Forest (HARV), Massachusetts	May 16, 2000		June 18, 2000
		August 31, 1999	August 4, 2000
Konza Prairie (KONZ), Kansas	June 22, 2000	June 7, 2000	June 6, 2000

2.2 Preprocessing of Image Data

Both AVIRIS and ETM+ images were georeferenced, radiometrically calibrated, and converted to surface reflectance value. Initially, Landsat ETM+ data were georeferenced to UTM coordinates by using USGS digital orthophoto quadrangles. The AVIRIS data were then georectified into the ETM+ image by image-to-image registration. The average positional accuracy of the geometric correction was less than 0.5 pixels.

In quantitative analysis of remote sensing images, atmospheric correction is a critical step to convert the digital number (DN) value to a more absolute magnitude of surface reflectance. Due to the carefully designed experimental sensor system, AVIRIS data have relatively well-developed atmospheric correction algorithms. Atmospheric water-vapor absorption is the most influential factor in the atmospheric correction of remote sensing data. The atmospheric correction of hyperspectral data has a clear advantage over multispectral data since the magnitude of water-vapor effects can be directly assessed from certain spectral channels of their own data sets. AVIRIS data used in this study were atmospherically corrected by using the ATREM program (Gao et al., 1993), which is based on a radiative transfer model. ATREM uses two water absorption spectra (around 940 nm and 1140 nm) channels in the AVIRIS channels to estimate the amount of water vapor at the time of data acquisition.

Although there have been several studies dealing with the atmospheric correction of Landsat TM and ETM+ data, all of them have certain limitations to calculate the absolute magnitude of waver vapor absorption. For our study, we used the COST radiometric correction model of Chavez (1996), which is an empirical model based upon 'dark' objects. Radiometrically 'dark' objects were assumed to have 2 % reflectance across all bands. Excluding the thermal infrared band, the six reflective bands of ETM+ data were converted to surface reflectance.

2.3 AVIRIS Data Manipulation

From the aspect of the number of spectral bands and the range of spectrum involved, the relative amount of information content of AVIRIS may be far more than that of Landsat ETM+. Therefore, any absolute comparisons between these two data types may not be reasonable. Also, the comparison between ETM+ and AVIRIS can be subjective, depending on the method applied. In this study, we generated four sets of AVIRIS data to be compared with the six reflective bands of Landsat ETM+. These AVIRIS data sets were mostly out of 89 channels covering the wavelength range of six ETM+ bands, with the exception of the data set obtained by principal component analysis, which used all AVIRIS channels excluding the water-absorption and high-noise channels. Table 2 shows the list of AVIRIS data sets generated for the comparison with ETM+ data.

Table 2. Sets of AVIRIS data to be compared with Landsat ETM+ data.

	Number of AVIRIS channels used	
Simulated ETM+ (sim_TM)	89 channels covering the spectrum of six ETM+ bands	• Weighted average of TM corresponding channels • Weighting factors were determined to represent spectral responsivities of each ETM+ band
Center wavelength of TM (cen_TM)	6 channels matching with the center wavelength of each ETM+ band	• ch 12 (481nm) for ETM+ band 1 • ch 21 (568nm) for ETM+ band 2 • ch 31 (665nm) for ETM+ band 3 • ch 52 (837nm) for ETM+ band 4 • ch 137 (1653nm) for ETM+ band 5 • ch 195 (2220nm) for ETM+ band 7
Selected combination (sel_AVIRIS)	7 channels (HARV) 14 channels (KONZ)	Selection by multiple stepwise regression using 89 channels covering ETM+ spectrum
Principal component (pc_AVIRIS)	187 channels	Principal component transformation of all 187 channels (excluding water-absorption and noise channels from original 224 channels)

2.4 Multiple Regression and Canonical Correlations Analysis

At first, we extracted surface reflectance values from the all sets of AVIRIS and Landsat ETM+ data for the location of every ground plot for each study site. Field-measured LAI was then related to spectral reflectance values extracted from the image data by using the multiple regression method. The coefficient of determination (R^2) of each regression equation is used as a simple measure of predicting LAI by the image data. The 89 AVIRIS channels would have too many independent variables for relating LAI by the multiple regression method. We used the stepwise selection method to select the best sets of AVIRIS channels.

Another way of looking at the closeness between LAI and image-extracted spectral reflectance was canonical correlation analysis (CCA). Canonical correlation analysis is a multivariate statistical method to look at the relationships between two sets of variables (multiple *X*s and multiple *Y*s) (Tabachnick and Fidell, 1989). CCA maximizes the correlation between a composite of variables from one set with a composite of variables from another set. When there is only one *X* (such as the LAI in this study), CCA provides a set of coefficients to transform the *Y*s (selected image bands) such that they have the maximum correlation with *X*. The canonical correlation coefficients were used as a single measure of relationship between LAI and a set of multiple image bands selected for each data

set. Since CCA is a generalized form of multiple regression, canonical correlation coefficient (r) is basically the same as the square root of the coefficient of determination (R^2) of the multiple regression model.

3. RESULTS

As an initial effort to examine the relationship between the field-measured LAI and AVIRIS spectral reflectance, correlation coefficients were calculated. As can be observed in Figure 1, two study sites show a rather different pattern of correlation along the wavelength. In the HARV study site, where the variation of LAI and species composition is relatively large, relatively high correlations were found in visible and middle infrared spectra. The statistical significance level is proportional to the absolute value of correlation coefficients (r), and the confidence limit is less than 95% when $|r|$ is below 0.15. It turned out that the near infrared spectrum (730–1300 nm) showed no significant correlation with LAI. The weak correlations in the near infrared spectrum might be explained by the saturated spectral reflectance at the high LAI (around 5 on average) of the HARV study site. The strongest correlations were found at the red-edge position (around 720 nm) and the middle infrared spectrum (2070–2400 nm). In the KONZ study site, where the range of LAI is rather narrow and cover type is relatively homogeneous grass prairie, relatively high correlation coefficients with the field-measured LAI were found at the near infrared spectrum (730–1300 nm). The field-measured LAI in this study area were relatively small (less than 2 on average), and they were relatively sensitive in the near infrared spectrum. Unlike the HARV study site, no significant correlations were found at the visible spectrum. In the middle infrared spectrum, significant correlations were only found in the wavelengths longer than 2100 nm. Such high correlations in the middle infrared spectrum have not been well explained and probably need further analysis. Again, the strongest correlation with the field-measured LAI was found at the red-edge position around 730 nm, which has been reported by several previous studies (Danson, 1996).

For the comparison, the similar correlation coefficients were also obtained by using the ETM+ reflectance for each study site (Figure 2). Unlike with the AVIRIS reflectance, no significant correlations were found at the visible and near infrared spectra. The only statistically significant correlations were found in the second middle infrared band (ETM+ band 7), which has a spectrum range between 2090 and 2350 nm.

Comparing the two correlation plots in Figures 1 and 2, we might anticipate the outcome of the multiple regression models using AVIRIS and ETM+ data. Due to the relatively weak correlations along the entire range of wavelength spectra in both AVIRIS and ETM+, the coefficients of determination (R^2) of the regression models were relative low. Overall, most AVIRIS data sets did not show any striking improvements of R^2 values over the ETM+ data although certain combinations of AVIRIS channels showed some improvement to explain the LAI (Table 3). The simulated ETM+ data or the six AVIRIS channels matching the center wavelength of ETM+ bands was not much different from the ETM+ data in predicting the LAI for both sites. From the viewpoint of the sensor dynamic range, pixel gray level, and atmospheric correction procedure, AVIRIS can be said to have better radiometric resolution than ETM+ data. The simulated ETM+ data have exactly the same spectral range as the ETM+ and probably have improved radiometric quality than ETM+. However, the high radiometric resolution of AVIRIS does not help to explain the LAI as compared to the ETM+.

Table 3. Coefficients of determination (R^2) of multiple regression models to relate the field measured LAI.

Data set used	Harvard Forest	Konza Prairie
ETM+ 6 bands	0.1729	0.2815
AVIRIS (simulated ETM+)	0.3348	0.1986
AVIRIS (6 channels of ETM+ center wavelength)	0.3336	0.2557
AVIRIS (best subset channels)	0.5138	0.5571
AVIRIS (first 15 principal components)	0.4376	0.3486

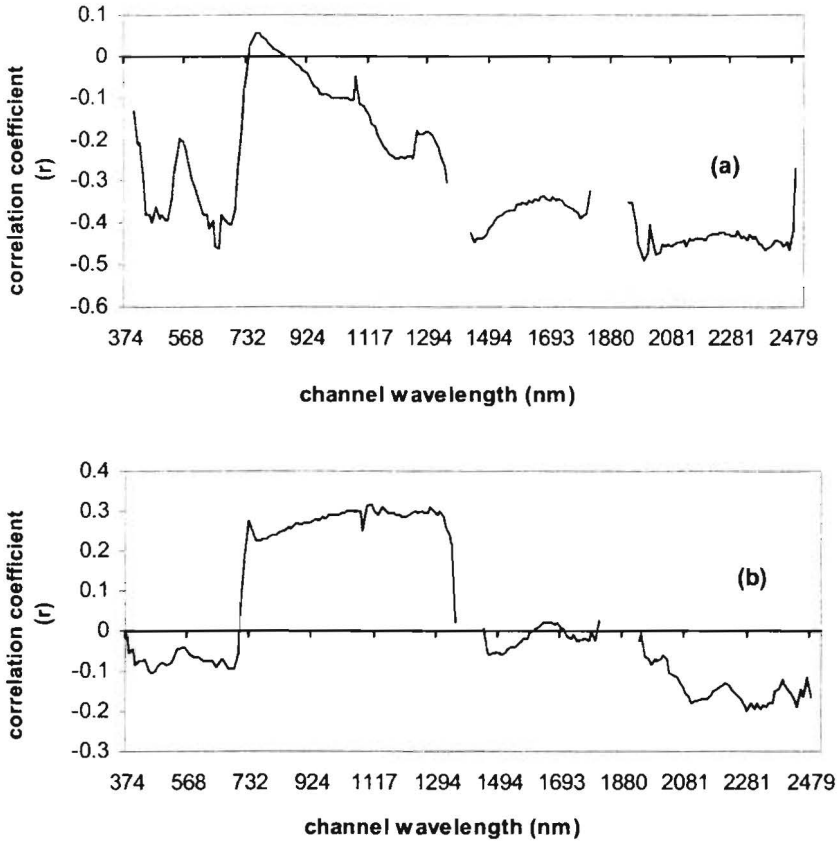

Figure 1. Correlation coefficients between the field-measured leaf area index (LAI) and reflectance along the AVIRIS spectral channels for Harvard Forest (a) and Konza Prairie (b). Statistical significance level is proportional to the absolute value of r (less than 95% confidence limits when $|r| < 0.15$).

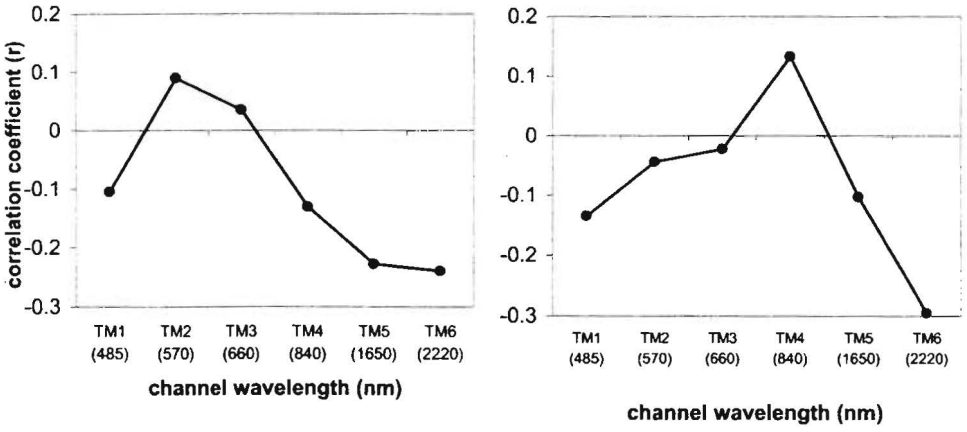

Figure 2. Correlation coefficients between the field-measured leaf area index (LAI) and reflectance along the ETM six bands for the Harvard Forest (left) and Konza Prairie (right). Statistically significant correlations were not found in visible and near infrared spectra.

Principal component analysis (PCA) has been frequently used in dealing with multi-dimensional remote sensing data. In particular, with the capacity of assembling total variation of whole data into a reduced number of bands, the principal component transformation is often used in analyzing hyperspectral data. In our study, we applied PCA to the 187 AVIRIS channels after excluding those water-absorption and high-noise channels from the original 224 channels. The first 15 principal components include 99.9% of total variations of the 187 channels AVIRIS data used. Even though the 15 bands of PCA transformed data have the most information content, they were not very helpful for explaining the LAI. The R^2 value of the regression model using PCA transformed data shows only a slight improvement.

In both study sites, the best-fit regression model was achieved when we used only a few selected channels of AVIRIS data. The coefficients of determination (R^2) were higher than the ETM and other subsets of AVIRIS data. The best channel selection was performed by the stepwise multiple regression method. Table 4 shows the final results of the stepwise multiple regression to select the best AVIRIS channels to explain LAI. Although we could protect against including any channels that do not contribute to the predictive power of the regression model by specifying small significance level (i.e., 5 percent), we tried to include more channels that could contribute to predicting LAI by increasing the significance level up to 15 percent (SAS, 1988). Only 7 AVIRIS channels were selected in the HARV study site while 14 channels were selected for the KONZ study site. These selected AVIRIS channels do not correspond exactly for the two study sites except for the one middle infrared channel (2310 nm).

Table 4. The result of stepwise multiple regression analysis to select the best AVIRIS channels to explain the field measured LAI for each study site.

	Harvard Forest		**Konza Prairie**	
	channel entered (nm)	**R^2**	**channel entered (nm)**	**R^2**
1	Ch 11 (471)	0.2914	Ch 56 (876)	0.0731
2	Ch 53 (847)	0.3225	Ch 54 (856)	0.2141
3	Ch 204 (2310)	0.3628	Ch 201 (2281)	0.2781
4	Ch 24 (597)	0.4059	Ch 186 (2131)	0.3358
5	Ch 49 (808)	0.4523	Ch 59 (904)	0.3603
6	Ch 15 (510)	0.4869	Ch 208 (2350)	0.3809
7	Ch 58 (894)	0.5138	Ch 31 (665)	0.4025
8			Ch 185 (2121)	0.4423
9			Ch 204 (2310)	0.4663
10			Ch 205 (2320)	0.4867
11			Ch 192 (2191)	0.5100
12			Ch 196 (2231)	0.5274
13			Ch 199 (2261)	0.5447
14			Ch 206 (2330)	0.5571

Although the magnitude of R^2 for each regression model is the same as the squared value of the canonical correlation coefficient, the scatter plot between the canonical variable and LAI shows effectively the interrelationships (Figures 3 and 4). In both study sites, there was not much differences among the three scatter plots (on the left side) for the canonical variable of ETM+, simulate ETM and 6 ETM center channels although the canonical correlation coefficients were slightly different. As indicated by the R^2 value of the regression model, the highest canonical correlation was found for the canonical variable of the best subset of AVIRIS channels.

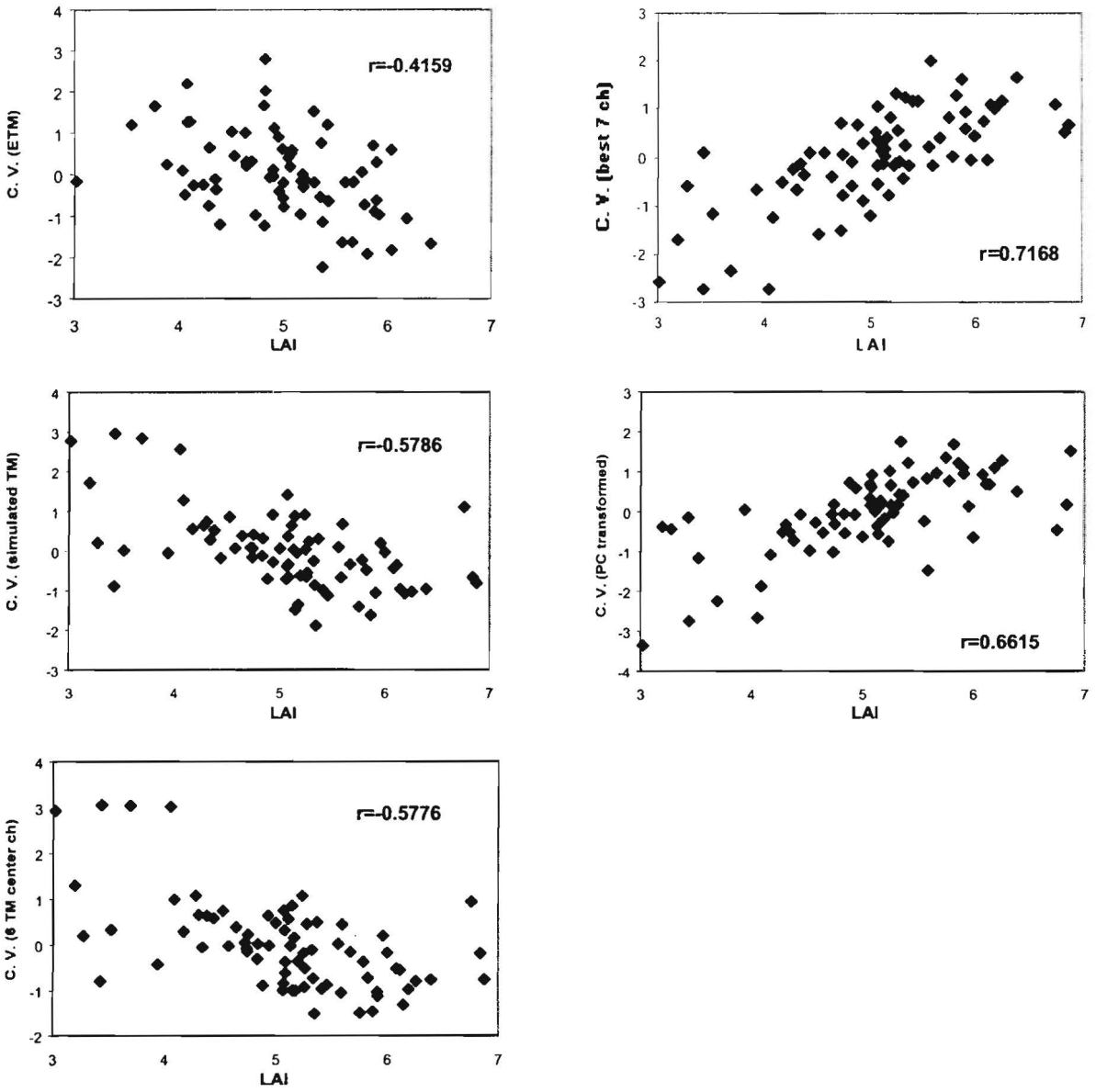

Figure 3. Canonical correlations of ETM and selected sets of AVIRIS data aligned with the leaf area index for the Harvard Forest study site.

4. CONCLUSIONS

It has been more than ten years since hyperspectral images were introduced. There are several airborne imaging spectrometer systems around the world. Further, we have already seen the spaceborne imaging spectrometers and are expecting more hyperspectral sensor systems in the near future. Although hyperspectral image data are known to have great potential in many applications of vegetative remote sensing, there have been very few studies that actually show the advantages of narrowband hyperspectral data over the traditional broadband multispectral data.

In an attempt to compare the predictive power of AVIRIS and ETM+ data, several subsets of AVIRIS data were analyzed in relation to the field-measured LAI for the two study sites of mixed forest and grassland. Among the four subsets of AVIRIS data, the best combination of selected AVIRIS channels was better than ETM+ or other

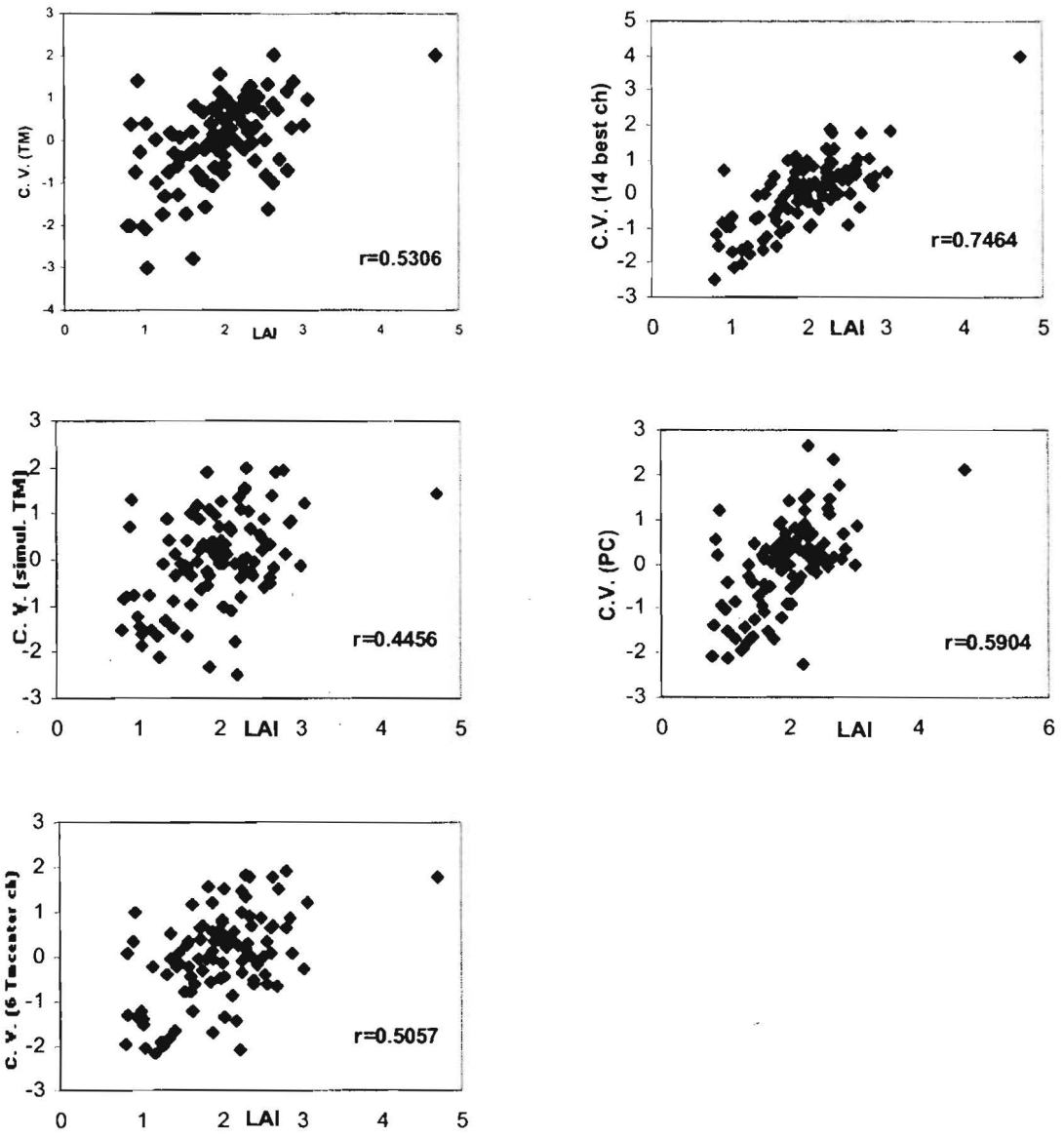

Figure 4. Canonical correlations of ETM and selected sets of AVIRIS data aligned with the leaf area index for the Konza Prairie study site.

subsets of AVIRIS in predicting LAI. There was no difference between the ETM-like subsets (simulated ETM+ and the six channels corresponding to the center wavelength ETM+ bands) and the actual ETM+. Although principal component analysis has been frequently used in hyperspectral data analysis, the transformed principal components were not necessarily aligned to predict the LAI.

In many applications of hyperspectral data, it may be rare to use all the spectral channels of the original hyperspectral image. As seen in this study, the 7 to 14 selected channels worked better to predict LAI than the principal component transformed data set. This empirical study demonstrated that narrowband hyperspectral data could be better than the broadband ETM+ data in estimating LAI. Our next question would be how we can select those best channels to use for certain applications. We believe that channel selection should be based on the integrated approach of theories, effective data processing, and empirical validation.

5. REFERENCES

Asner, G.P., R.N. Treuhaft, B. E. Law, 2000. A hyperspectral photon transport system to simulate imaging spectrometer observations of terrestrial ecosystems, Proc. of 2000 JPL AVIRIS Workshop.

Badhwar, G.D., R.B. MacDonald, and N.C. Mehta, 1986. Satellite-derived leaf area index and vegetation maps as input to global carbon cycle models—a hierarchical approach, *International Journal of Remote Sensing,* 7(2):265–281.

Bonan, G., 1993. Importance of leaf area index and forest type when estimating photosynthesis in boreal forests, *Remote Sensing of Environment,* 43:303–314.

Broge, N.H. and E. Leblanc, 2000. Comparing prediction power and stability of broadband and hyperspectral vegetation indices for estimation of green leaf area index and canopy chlorophyll density, *Remote Sensing of Environment,* 76:156–172.

Chavez Jr., P., 1996. Image-based atmospheric corrections—revised and improved, *Photogrammetric Engineering & Remote Sensing,* 62:1025–1036.

Cohen, W. and C. Justice, 1999. Validating MODIS terrestrial ecology products: linking in situ and satellite measurements, *Remote Sensing of Environment,* 70:1–3.

Curran, P.J., J. Dungan, and H.L. Gholz, 1992. Seasonal LAI measurements in slash pine using Landsat TM. *Remote Sensing of Environment,* 39:3–13.

Danson, F.M., 1996. Developments in the Remote Sensing of Forest Canopy Structure, in Advances in Environmental Remote Sensing, edt. by Danson and Plummer, John Wiley & Sons, New York, USA, 53–69.

Galvao, L.S., I. Vitorello, and M.A. Pizarro, 2000. An adequate band positioning to enhance NDVI contrasts among green vegetation, senescent biomass, and tropical soils, *International Journal of Remote Sensing,* 21(9):1953–1960.

Gao, B.C., Hedebrecht, K., and Goetz, A.F.H., 1993. Derivation of scaled surface reflectances from AVIRIS data, *Remote Sens. Environ.,* 44:165–178.

Gower, S., C. Kucharik, and J. Norman, 1999. Direct and indirect estimation of leaf area index, fAPAR, and net primary production of terrestrial ecosystems, *Remote Sensing of Environment,* 70:29–51.

Jacquemond, S., F. Baret, B. Andrieu, F. M. Danson, and K. Jaggard, 1995. Extraction of vegetation biophysical parameters by inversion of the PROSPECT + SAIL models on sugar beet canopy reflectance data. Application to the TM and AVIRIS sensors, *Remote Sensing of Environment,* 52:163–172.

Johnson, L.F., C.A. Hlavka, and D.L. Peterson, 1994. Multivariate analysis of AVIRIS data for canopy biochemical estimation along the Oregon transect, *Remote Sensing of Environment,* 47: 216–230.

Kuusk, A., 1998. Monitoring of vegetation parameters on large areas by the inversion of a canopy reflectance model, *Inter. J. Remote Sensing.,* 19(15):2893–2905.

Lefsky, M., W. Cohen, and T. Spies, 2001. An evaluation of alternative remote sensing products for forest inventory, monitoring, and mapping of Douglas-fir forests in western Oregon, *Canadian Journal of Forest Research,* 31:78–87.

Peddle, D.R., F.R. Hall, and E.F. LeDrew, 1999. Spectral mixture analysis and geometric-optical reflectance modeling of boreal forest biophysical structure, *Remote Sensing of Environment,* 67:288–297.

Peterson, D.L., M.A. Spanner, S.W. Running, and K. Teuber, 1987. Relationship of Thematic Mapper data to leaf area index of temperate coniferous forests, *Remote Sensing of Environment,* 22:323–341.

Pierce, L.L and S.W. Running, 1988. Rapid estimation of coniferous forest leaf area index using a portable integrating radiometer, *Ecology,* 69:1762–1767.

SAS, 1988. SAS/STAT User's Guide, Release 6.03 Edition, SAS Institute Inc., Cary, NC, USA

Smith, J.A., 1993. LAI Inversion using a back-propagation neural network trained with a multiple scattering model, *IEEE Trans. Geoscience and Remote Sensing,* 31(5):1102–1106.

Tabachnick, B., and L. Fidell, 1989. *Using Multivariate Statistics, 2nd Edition.* 1989. Harper Collins Publishers, Inc., United Kingdom.

Teillet, P.M., K. Staenz, and D.J. Williams, 1997. Effects of spectral, spatial, and radiometric characteristics on remote sensing vegetation indices of forested regions, *Remote Sensing of Environment,* 61:139–149.

Turner, D., W. Cohen, R. Kennedy, K. Fassnacht, and J. Briggs, 1999. Relationships between leaf area index and Landsat TM spectral vegetation indices across three temperate zone sites, *Remote Sensing of Environment,* 70:52–68.

Wessman, C.A., J.D. Aber, D.L. Peterson, and J.M. Melilo, 1988. Remote sensing of canopy chemistry and nitrogen cycling in temperature forest ecosystems, *Nature,* 335:154–156.

Characterizing Mineral Alteration Using Airborne Visible-Infrared Imaging Spectrometer Data at Questa, New Mexico

K. Eric Livo and Roger N. Clark

U. S. Geological Survey, Mail Stop 973, Box 25046 Federal Center, Lakewood, Colorado 80225

Introduction

A baseline and pre-mining ground-water quality study of the Red River Basin in New Mexico is being undertaken by the U.S. Geological Survey. As part of this study, Airborne Visible-Infrared Imaging Spectrometer (AVIRIS) data were analyzed to characterize mined and non-mined ground along the Red River between the towns of Questa and Red River, New Mexico. This area has zones of intensely mineralized and altered ground that effect the water quality of Red River. Analysis of the reflectance data has identified mineral assemblages that can affect water quality by lowering the pH and introducing metals, salts, and sediments.

Data

The AVIRIS data (Green et al., 1998) were acquired by a single west to east NASA/JPL overflight on June 30, 1999. The flightline trends parallel to the Red River (that flows westward into the Rio Grande), starting at the town of Questa and ending east of the town of Red River imaging both sides of the river. The line starts at the west-bounding fault of the Taos Range with the Rio Grande Valley, and continues eastward following the deeply incised Red River valley.

Methods

NASA/JPL AVIRIS data were calibrated to ground reflectance, and analyzed using custom U.S. Geological Survey software and spectral mineral library (Clark et al., 1993a, 1993b, 1993c). Field examination was used to verify these results. This analytical approach has been developed and used over the past 13 years to map a range of geologic terrain, including porphyry systems and other hydrothermally altered ground. Identifiable minerals include a variety of iron hydroxides, sulfates, clays, micas, and carbonates.

A two stage process was used to calibrate the airborne radiance data to surface reflectance. An atmospheric model was first applied to remove atmospheric gas effects and convert the radiance data to estimated ground reflectance. The data was converted using the Atmosphere REMoval (ATREM) Program (Gao et al., 1997). Second, this estimated reflectance data was then calibrated to apparent ground reflectance using field spectra from a ground calibration site, to remove residuals from the ATREM processed data. Soil from this site was measured using an Analytical Spectral Devices (ASD) FR field spectrometer, then a multiplier and offset were derived using the ASD field spectra, the AVIRIS calibration site spectra, and AVIRIS spectra collected nearby in shadowed-heavily vegetated terrain (Clark et al., 2002a, this vol.).

During analysis of AVIRIS data, the U.S. Geological Survey's Tetracorder version 3.7a program (Clark et al., 2002b) was used to spectrally test the data against the U.S. Geological Survey's spectral library. Pixel spectra from AVIRIS were tested against several hundred mineral and mineral mixture library spectra using a goodness-of-fit algorithm. The fit value for the continuum removed absorption features between the pixel spectrum and each mineral library spectrum was used to indicate the likelihood of mineral identification. Further tests by the Tetracorder program used absorption band depth, continuum slope, and mineral exclusion rules to guide mineral identification. Mineral identification was completed through interactive analysis of the spectral data and output images and verified using selected sites in the field.

Spectral analysis identified and mapped a variety of minerals that were then associated with mineral assemblages. As an example, spectral features of one mineral assemblage (quartz-sericite-pyrite) are seen in the middle spectrum in figure 1, with the absorption features of sericite seen at 2.2 microns and jarosite (after pyrite) seen at 0.42, 0.50, 0.92, and 2.27 microns. Occurrence of sericite and jarosite are diagnostic in associating areas with the quartz-sericite-pyrite assemblage. The other spectra in figure 1 show representative absorption features for supergene kaolinite (2.17 & 2.22 microns) and geothite (0.50 and 0.92 microns). These two minerals are common throughout the district.

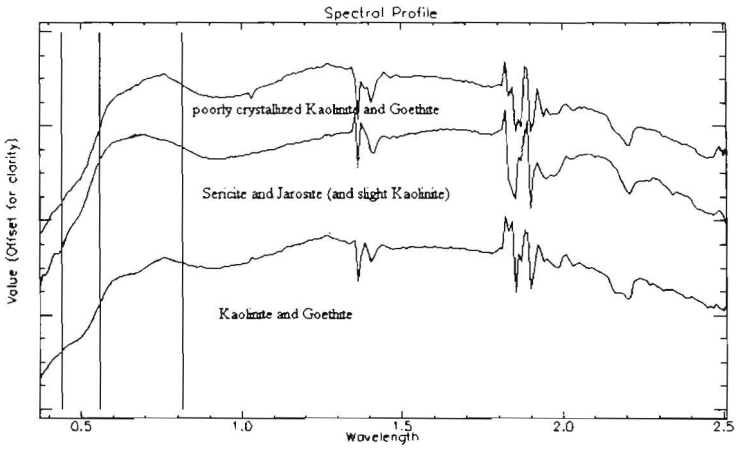

Figure 1. Single pixel spectra extracted from the Questa AVIRIS data showing absorption features of: Kaolinite (2.17 & 2.20), Sericite (2.2 & 3.5), Goethite (0.50 & 0.92), and Jarosite (0.42, 0.92, & 2.27 microns)

Constraints on mineral mapping at Questa were the lack of spectral character and low abundance of several important alteration, ore forming, and rock forming minerals, such as quartz, feldspar, pyrite, topaz, and biotite. Most quartz and feldspar do not have spectral responses in the AVIRIS wavelengths suitable for identification, while topaz and biotite are in low abundance. Abundant vegetation, especially on north slopes, covered rock and soil in many areas, preventing mineral identification.

Geologic History

The Red River flows westward from the Taos Range into the Rio Grande River, cutting through Precambrian rocks overlain in part by Tertiary volcanic rocks of the Latir volcanic field, along the southern edge of the 26-MA Questa caldera (Bethke and Lipman, 1989). The cogenetic volcanic and plutonic rocks host the alteration mineral assemblages and molybdenum mineralization in zones that trend east-west along the southern boundary of the caldera. The silicic alkalic rhyolite tuff ash-flow sheet that initially ponded within the caldera was subsequently fault tilted and brecciated, then intruded by batholithic granite rocks which set up the hydrothermal systems that altered and mineralized the country rock. Later faulting and deformation related to the Rio Grande Rift mechanically and chemically prepared the contact between the Tertiary granite stocks and the overlying tuff, allowing mineralizing fluids to form sheet vein and disseminated molybdenum ore bodies (Meyer and Foland, 1991).

Altered Mineral Assemblages

Igneous activity at Questa created hydrothermal (hot water) systems that episodically altered minerals within the country rock resulting in the formation of new minerals stable under the thermal, chemical, and pressure conditions of the hydrothermal cells. These altered minerals formed discrete assemblages that reflect or represent changes in chemistry and temperature of the hydrothermal system. The driving force for the system was the thermal energy derived from the cooling granite stocks, releasing hot magmatic solutions and heating ground waters. These hydrothermal fluids were driven upward, away from the granites, exchanging ions with the surrounding wallrock. A particular mineral assemblage is a function of its place in the hydrothermal system and the chemistry of the fluids at that point. Alteration assemblages recognized in the Questa AVIRIS data are:

Propylitic assemblage: an acid buffering assemblage of minerals including calcite, chlorite, and epidote, that are spectrally identified in the AVIRIS data. In particular, calcite is useful in buffering acid-water to more neutral pHs and precipitating metals held in solution. Propylitic alteration generally forms as a

regional early stage alteration, distal to the mineralizing center and can be locally replaced by later more intense alterations. The assemblage can also form also as a retrograde late stage product in the hydrothermal system.

Quartz-sericite-pyrite (QSP) assemblage: a suite of minerals whose sulfide content is potentially acid-generating. Sericite can be spectrally identified directly, while pyrite is inferred through the spectral identification of jarosite, an iron sulfate formed through the weathering of pyrite and other sulfide minerals. QSP alteration commonly is a moderately intense alteration assemblage that can be wide spread, altering the country rock into material that may have high acid-water generation potential and high leachable metal content, that formed later in the alteration process. Sericite, as used in this manuscript, refers to various grain-sizes of muscovite, and the clay illite, which have similar spectroscopic features.

Advanced argillic assemblage: an assemblage that indicates higher formation temperatures with associated sulfur, such as found in local hydrothermal feeder systems and pipes. Kaolinite, pyrophyllite, and alunite, common minerals associated with advanced argillic alteration, have been spectrally identified in peripheral zones at Questa. These minerals are also created through supergene weathering at Questa.

In addition to altered mineral assemblages, later supergene weathering has formed altered minerals that have potential for effecting the environment. In the moist, oxygenated near neutral pH surface environment, iron-rich minerals have been converted to goethite; in a lower pH setting, pyrite and other sulfides have been converted to jarosite, gypsum, and alunite while feldspar is altered to kaolinite. Occurrence of jarosite, gypsum, alunite, and kaolinite suggest acidic conditions with sulfur content in the country rock (Meyer and Leonardson, 1990; Titley, 1994). Further weathering and neutralization will convert jarosite into goethite.

Mineral Maps

The iron-bearing mineral map (fig. 2) shows the supergene weathering minerals jarosite (after pyrite) and goethite (after iron-rich minerals). Jarosite indicates areas of potential acid-water generation

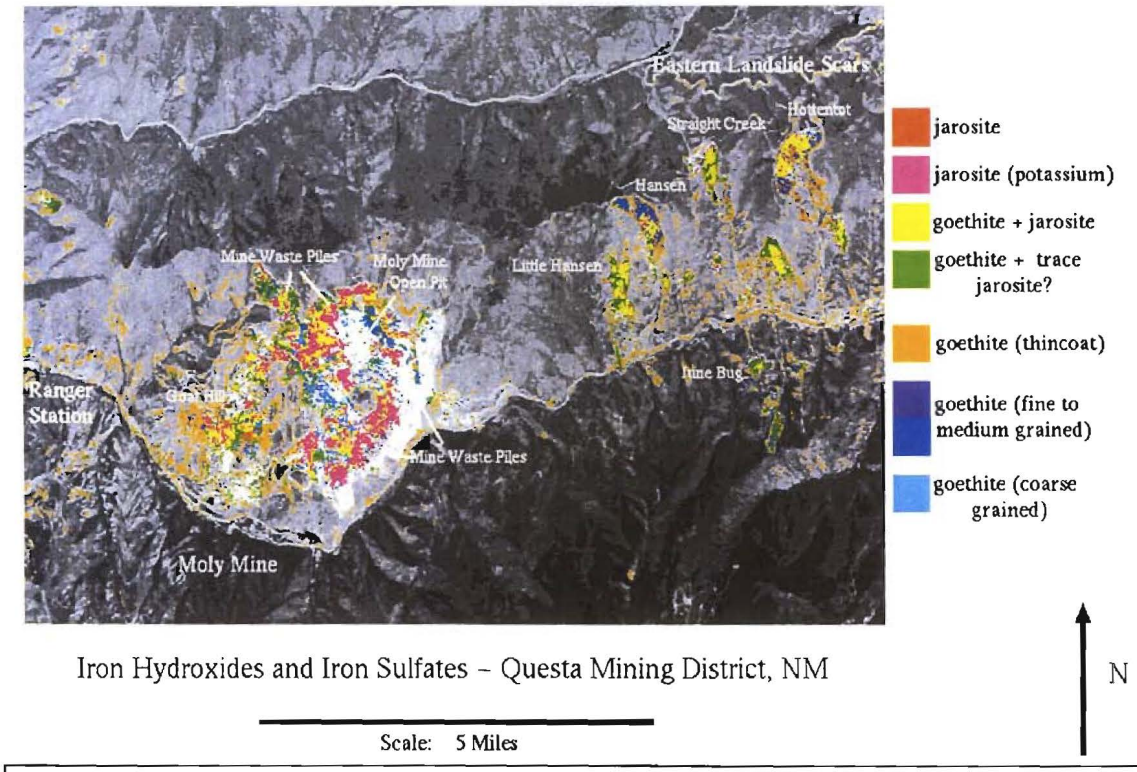

Figure 2. Iron bearing altered minerals; with the Landslide 'Scar' areas on the east and the Moly Mine complex on the west-center.

created by the breakdown of pyrite and other sulfides that form sulfuric acid. Jarosite is not stable under surface conditions and will break down into iron-oxides as its environment becomes neutralized (Bigham et al., 1992). Goethite indicates less acidic regions, where ferric iron is released by mafic minerals, or where neutralization of sulfide rich ground converts jarosite to goethite (Swayze et al., 2000). Note, the map indicates, and field examination confirms, little if any, hematite in contrast to acid-sulfate systems like Cuprite, Nevada.

The clays, micas, and sulfates mineral map (fig. 3) show the main alteration minerals due to ore forming processes. Most importantly, the quartz-sericite-pyrite assemblage is expressed by the wide occurrence of sericite at the Moly Mine site and also at the eastern landslide 'scar' areas. Kaolinite, some of which could be primary, is most commonly a secondary mineral due to supergene weathering and is associated with sericite. Other supergene minerals are gypsum and jarosite. The presence of these minerals suggest strong acid-water generation potential.

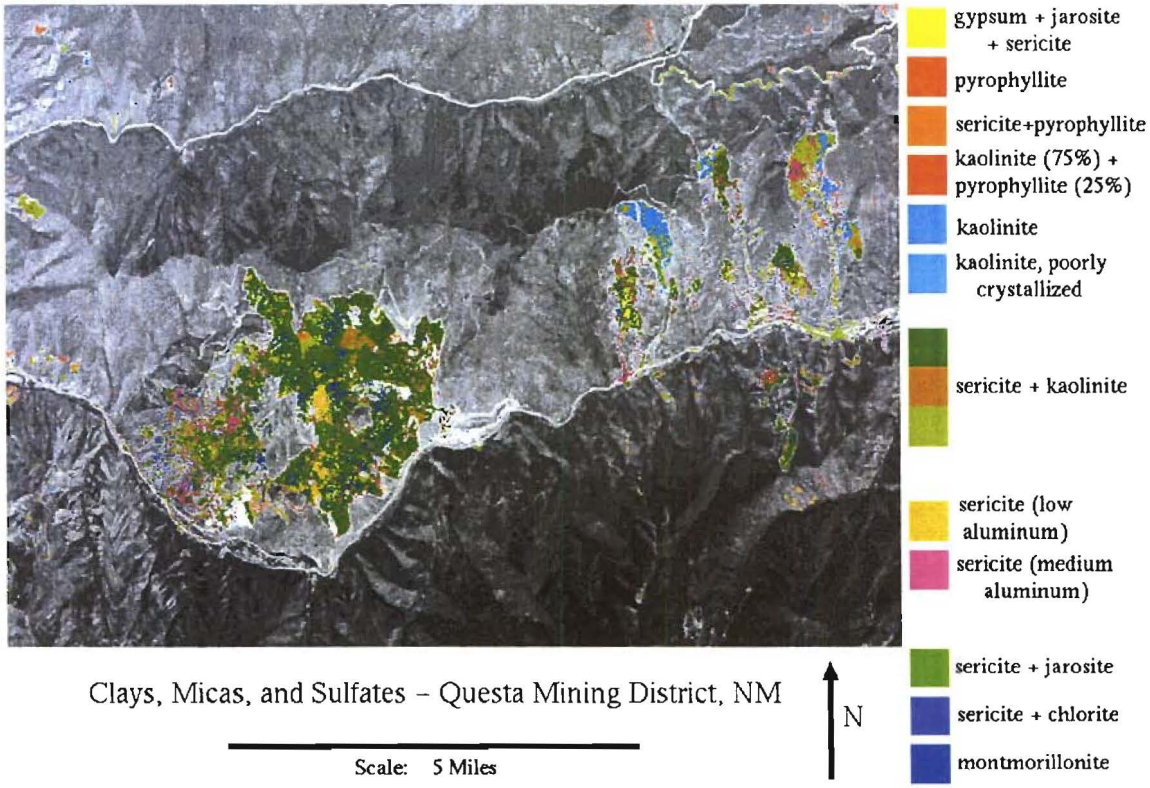

Figure 3. Clay, Mica, and Sulfate altered minerals.

The carbonates, alunite, and epidote mineral map (fig. 4) show regions potentially buffered by the propylitic assemblage minerals calcite and epidote, and includes chlorite (fig. 3). Calcite an important neutralizer of acid-water, occurs down gradient from the altered areas, and may serve to naturally buffer the groundwater. The extensive propylitic zone forms distal halos surrounding the more intensely altered centers seen in figure 2 and 3.

(For digital copies of these mineral maps, see: Livo and Clark, 2002)

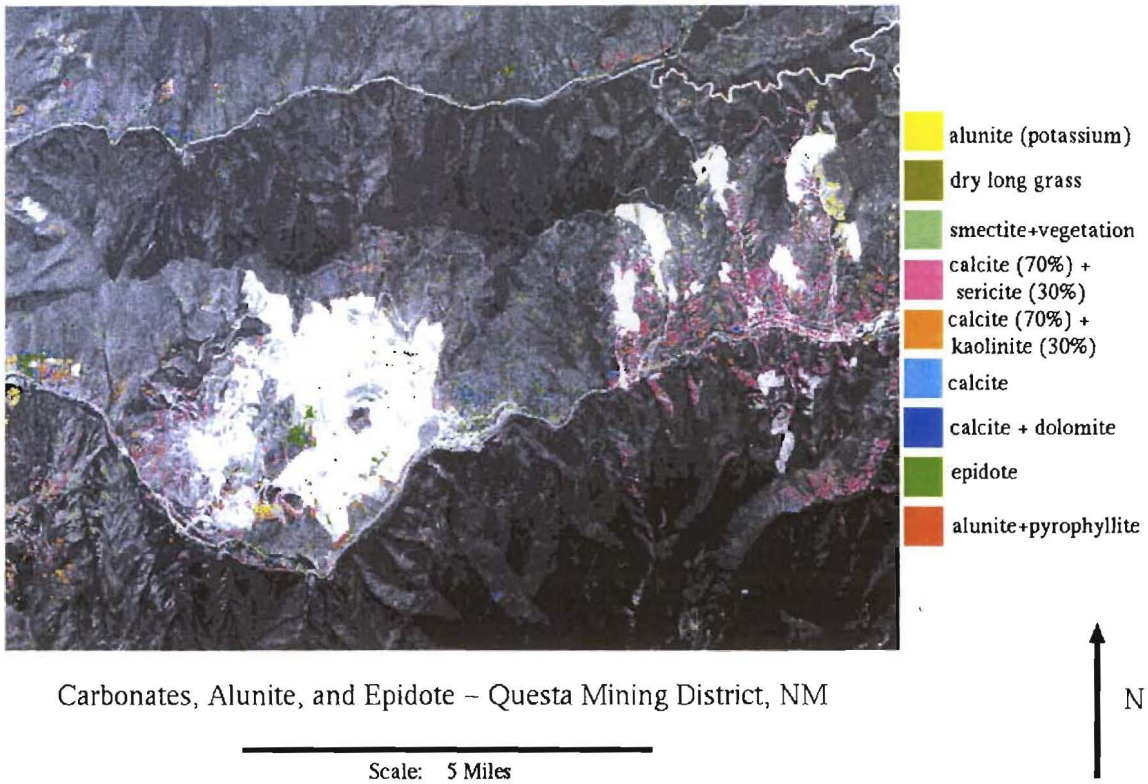

Figure 4. Carbonate, Alunite, Epidote, and Pyrophyllite altered minerals.

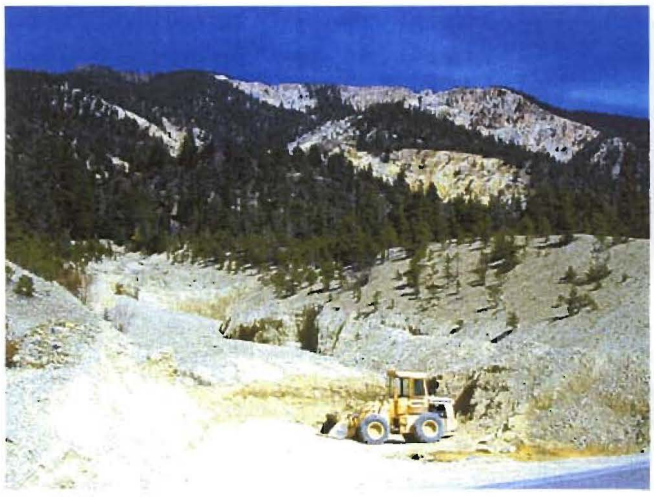

Figure 5. Eastern landslide 'Scar' areas with debris flow. Looking northeast at Lt. Hansen and Hansen landslide 'Scar' surfaces.

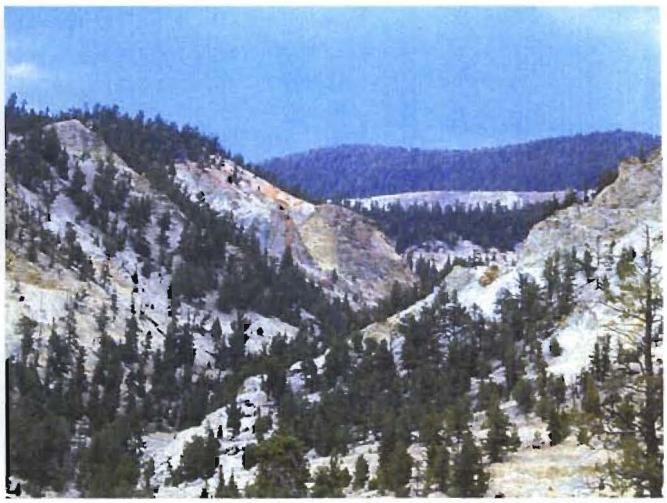

Figure 6. Goat Hill Gulch, looking north.

Results

Mineral maps of the eastern landslide 'scar' areas (Little Hansen, Hansen, Straight Creek, Hottentot, and June Bug – east side of the figs. 2, 3, and 4 image; and fig. 5) show key altered minerals that comprise the propylitic and quartz-sericite-pyrite assemblages, and the minerals due to supergene weathering. Sericite, goethite, jarosite, kaolinite, pyrophyllite, and gypsum are found in the scar areas, suggesting strong sulfide mineralization that is also expressed by the denuded terrain. Supergene jarosite, gypsum, and kaolinite signify on-going erosion and weathering of fresh steep surfaces that form the commonly seen debris flows along the steep gully floors. The weathering of altered minerals within the landslide areas breaks up the rock, weakens the slopes, and exposes metals confined within the rock to dissolution (Crowley and Zimbelman, 1997). The erosion rate in the landslide areas is moderate to high, especially during storm events, so metal leach and solid transport rates are potentially moderate to high. These conditions suggest that the potential for acid-water conditions exist with the possibility of metal leaching in these drainages. Noteably, the altered mineral package of sericite with kaolinite, jarosite with goethite, and gypsum indicate that the supergene weathering in the scar areas is in a semi-steady-state condition. Propylitically altered rock surrounds the scars, notably on the downhill side, which could mediate any acid-drainage. During storm events, however, altered mineral debris flows will overwhelm any steady-state buffering the down-gradient propylitic minerals may supply, as demonstrated by the alluvial fans at the base of each landslide drainage.

Between the Moly Mine and eastern scar areas lies a block of propylitically altered ground. Calcite (fig. 4) is identified throughout the region (where the ground surface is exposed), suggesting a break in near surface mineralization between the Moly mine and eastern scar areas.

The Moly Mine site (the large altered area in the west-central part of the image) encompasses the Goat Hill Gulch scar area (western part of area), the Sulfur Gulch (north) scar area and associated open-pit mine (northeast), and the surrounding mine waste-rock piles (north, east, and south part of the Moly Mine area). These regions are all highly altered, mainly with a quartz-sericite-pyrite assemblage, although, advanced argillic (or supergene) pods do occur peripheral to the core zone. Abundant epidote occurs at the top of the ridge that separates Goat Hill Gulch from Sulfur Gulch, suggesting that the ridge forms the top of the hydrothermal system that is exposed to the west and east, in topographically lower ground. The degree of alteration identified in the AVIRIS data is similar at the non-mined Goat Hill Gulch area (fig. 6) and Sulfur Gulch, with its mined ground and non-mined scar areas. Of note is the relation of jarosite, which indicates acid-water and metal leaching potential, with elevation at Sulfur Gulch. It appears that jarosite abundance decreases with depth from the top of the alteration system (from the pre-erosion and pre-mining surface), suggesting a strong decrease in sulfide content of the wallrock. This relation is also expressed in the waste-rock piles, with rock extracted from the top of the alteration system (and dumped topographically high) containing higher abundance of jarosite. The erosion rate of the Moly Mine scar areas appears to be similar to the eastern scar region, though open-pit mining has highly accelerated the exposure of fresh material to weathering and possible leaching of metals (Shaw, Wels, and Robertson, 2002), as seen by the high abundances of jarosite in the mine-waste rock. The overall intensity of the quartz-sericite-pyrite alteration appears to be stronger at the Moly Mine area than in the eastern scar areas. Jarosite is more abundant at the non-mined Goat Hill Gulch and the non-mined top of Sulfur Gulch, in comparison with the non-mined eastern scar areas. Similar to the eastern scar areas, calcite and chlorite occur on the downhill sides of the alteration cores, possibly buffering to an extent, any acid-drainage. The lesser amount of goethite, the abundance of jarosite, and the lower abundance of kaolinite and gypsum indicate the higher degree of mineral alteration and the lack of steady-state weathering of the Moly Mine area (mined and non-mined), compared to the landslide areas. While no mine waste pile material is seen entering the Red River in figures 2, 3, and 4, historic altered material from debris fans at Goat Hill and Sulfur Gulches do and the southwestern part of the Goat Hill altered area extends to Red River.

The northeastern extent of the Log Cabin (far southwest part of image) area of alteration shows small, dispersed occurrences of kaolinite and goethite within a highly vegetated region, indicating the occurrence of mineralization that was known to exist on the basis of previous field mapping. At the northern edge of the area (most westward part of image bisected by Red River) a small advanced argillic (or supergene weathered) center containing pyrophyllite, sericite, gypsum, and alunite, is surrounded by

propylitically altered rock containing calcite and epidote. This area suggests a potential for acid-water generation with some buffer capability.

Conclusions

Hydrothermally altered and weathered minerals were mapped at Questa, New Mexico using the AVIRIS JPL/NASA imaging spectrometer. These minerals were grouped in propylitic and quartz-sericite-pyrite mineral assemblages and as supergene minerals that were used to infer surface environmental conditions and effects on the water quality of Red River.

Altered materials from the eastern landslide areas (Hottentot, Straight Creek, June Bug, Hansen, and Little Hansen Gulches and the Moly Mine area), mined ground and Sulfur and Goat Hill gulches have the potential to adversely effect the water quality of Red River. Debris trails and fans are associated with all the gulches that have mineralized rock that produce sedimentation in Red River, which possibly could introduce metals either through mass transport or through leaching into the river. These materials have low pHs and could generate acid-water that could strongly alter water quality, especially during spring runoff or during a storm event. Both mined and non-mined Moly Mine areas appear to have slightly more intense mineral alteration and less of a steady-state supergene weathering environment compared to the eastern landslide areas, though both mineralized regions are intensely altered. The Moly Mine area is well exposed through mining in the AVIRIS data, but the landslide areas appear to have similar environmental degrading potential as expressed by similar mineral alterations and the large area of altered ground seen through the vegetation.

References

Bethke, P.M. and Lipman, P.W., 1989, Mineralization in silicic calderas: Questa, New Mexico and the San Juan Mountains, Colorado, in: 28th International Geological Congress Field Trip Guidebook T320, American Geophysical Union, 75p.

Bigham, J.M., Schwertmann, U., and Carlson, L., 1992, Mineralogy of precipitates formed by the biogeochemical oxidation of Fe (II) in mine drainage, in: Skinner, H.C.W., and Fitzpatrick, R.W., eds., Catena Supplement 21, Cremlingen-Destedt, Germany, pp. 219-232.

Clark, R.N., Swayze, G.A., and Gallagher, A.J., 1993a, Mapping minerals with imaging spectroscopy, U.S. Geological Survey, Bull. 2039, pp. 141-150.

Clark, R.N., Swayze, G.A., Gallagher, A.J., King, T.V.V., and Calvin, W.M., 1993b, The U.S. Geological Survey, digital spectral library: version 1: 0.2 to 3.0 μm, U.S. Geological Survey Open File Report 93-592, 1326 p. http://speclab.cr.usgs.gov/spectral-lib.html

Clark, R.N., Swayze, G.A., Heidebrecht, K.B., Goetz, A.F.H., and Green, R.O., 1993c, Comparison of methods for calibrating AVIRIS data to ground reflectance, in: Summaries of the fourth annual JPL airborne geosciences workshop, vol. 1: AVIRIS workshop, JPL Pub. 93-26, pp. 31-34.

Clark, R.N., Swayze, G.A., Livo, K.E., Kokaly, R.F., King, T.V.V., Dalton, J.B., Vance, J.S., Rockwell, B.W., Hoefen, Todd, and McDougal, R.R., 2002a, Surface reflectance calibration of terrestrial imaging spectroscopy data: a tutorial using AVIRIS, in: Robert O. Green, ed., Proceedings of the Eleventh JPL Airborne Earth Science Workshop, 21p., in press, this volume.

Clark, R.N., Swayze, G.A., Livo, K.E., Kokaly, R.F., Sutley, S.J., Dalton, J.B., McDougal, R.R., and Gent, C.A., 2002b, Imaging Spectroscopy: Earth and planetary remote sensing with the USGS Tetracorder and Expert Systems, Journal of Geophysical Research, in press.

Crowley, J.K. and Zimbelman, 1997, Mapping hydrothermally altered rocks on Mount Rainer, Washington, with Airborne Visible/Infrared Imaging Spectrometer (AVIRIS) data, Geology, 25(6), p. 559-562.

Gao, Bo-Cai, Heidebrecht, K.B., and Goetz, A.F.H., 1997, Atmosphere removal program (ATREM) version 3.0 user's guide, Center for the Study of Earth from Space, University of Colorado, 27p.

Green, R.O., Eastwood, M.L., Sarture, C.M., Chrien, T.G., Aronsson, M., Chippendale, B.J., Faust, J.A., Pavri, B.E., Chovit, C.J., Solis, M., Olah, M.R., and Williams, O., 1998, Imaging spectroscopy and the Airborne Visible/Infrared Imaging Spectrometer (AVIRIS), Remote Sensing of Environment, v65, pp. 227-248.

Livo, K.E. and Clark, R.N., 2002, Mapped minerals at Questa, New Mexico, using Airborne Visible-Infrared Imaging Spectrometer (AVIRIS) data – preliminary report for: First Quarterly Report of the U.S. Geological Survey Investigation of Baseline and Pre-Mining Ground-Water Quality in the Red River Valley Basin, New Mexico, November 13, 2001, U.S. Geological Survey Open-File Report 02-0026, 13p. http://greenwood.cr.usgs.gov/pub/open-file-reports/ofr-02-0026

Meyer, Jeff, and Foland, K.A., 1991, Magmatic-tectonic interaction during early Rio Grande rift extension at Questa, New Mexico, Geological Society of America Bulletin, v. 103, pp. 993-1006.

Meyer, Jeff, and Leonardson, 1990, Tectonic, hydrothermal and geomorphic controls on alteration scar formation near Questa, New Mexico, in: New Mexico Society Guidebook, 41st Field Conference, Southern Sangre de Cristo Mountains, New Mexico, pp. 417-422.

Shaw, S., Wels, C., and Robertson, A., 2002, Physical and geochemical characterization of mine rock piles at the Questa Mine, New Mexico: an overview, in: Tailings and Mine Waste '02, Swets and Zeitlinger, pp. 447-458.

Swayze, G.A., Smith, K.S., Clark, R.N., Sutley, S.J., Pearson, R.M., Vance, J.S., Hageman, P.L., Briggs, P.H., Meier, A.L., Singleton, M.J., and Roth, S., 2000, Using imaging spectroscopy to map acidic mine waste, in: Environmental Science and Technology 2000, vol. 34, No. 1, pp.47-54.

Titley, S.R., 1994, Evolution habits of hydrothermal and supergene alteration in intrusion-centered ore systems, Southwest North America, in: D.R. Lentz, ed., Short Course Notes Volume 11, Alteration and alteration processes associated with ore-forming systems, Geological Association of Canada, p. 237-260.

Decision Tree Classification of a Forest Using AVIRIS and Multi-Seasonal TM Data

Sylvio Mannel, Dong Hua, Maribeth Price, Andreas Knobloch, Xuxia Chen
South Dakota School of Mines and Technology
501 E. St. Joseph St., Rapid City, SD 57701
Sylvio@Mannel.com

Introduction

Inventories of forests are essential for managing and protecting these natural resources. Models to determine carbon cycling, global warming, etc. also depend on accurate and efficient mapping of forested areas. This paper explores different classification methods of multi- and hyperspectral data as a supplement to traditional forest inventories. Results were evaluated towards accuracy, efficiency and costs.

The success of a classification depends on the land cover and the remotely sensed data type, but also on the classification method (Kenk et al. 1988), season (Wolter et al. 1995, Schriever and Congalton 1995), and to a large extend on the reference data (Congalton 1991). In this project we tested the importance of seasonality and the relatively new method of Decision Tree classification on TM and AVIRIS data. As a general guide for preprocessing AVIRIS data we published a white paper on the web at: http://aviris.de.vu In order to increase the number of training sites needed for best decision tree performance, we developed a unique approach to extend the usefulness of the available reference dataset.

Objectives

The main objective was to generate a land cover map of the northern Black Hills, SD. Along with this main goal we pursued the following questions: 1. How well does the new classification technique Decision Tree perform in comparison to other techniques? 2. What role does seasonality play? 3. Can TM data that combines two seasons overcome the drawbacks of multispectral data and provide similar accuracies as single-season hyperspectral data?

Methods

Study Site

The study site lays in the northern Black Hills, SD. The 'black' appearance of the Hills results from dense stands of forest vegetation, particularly ponderosa pine (*Pinus ponderosa*). This conifer covers approximately 84% of the Black Hills and comprises 95% of the forested area (Bennett 1984). Other trees in the study area include, white spruce, aspen and birch. Aspen and birch usually occur as a species association and, like white spruce, form medium to dense stands.

Reference Data Acquisition

Reference (training and test) data of high quality and quantity is the foundation for a successful and robust classification (Congalton 1991). Especially for the classification of AVIRIS imagery it is important to have a sufficient number of training and test data due to the so-called dimensionality problem: A large number of bands can decrease the accuracy without sufficient

training data (Swain and Hauska 1977). We sampled species and crown cover of more than 200 plots. 30-m diameter plots were laid out with a range fork and a timber cruise prism following the techniques described in Korhonen (1979), White and Lewis (1982) and Mannel et al. (in progress). With a sighting tube we measured crown cover (as an indicator for density) and species (Ganey and Block 1994, Cook et al. 1995).

Using GIS we overlaid the field data on top of aerial Digital Ortho Quads (DOQ). On the DOQs, we identified the land cover type boundaries depicted by a field-sampled plot and picked additional points in this area. These points were labeled based on the original field plot. This procedure led to a reference data set of more than 3000 points (Figure 1).

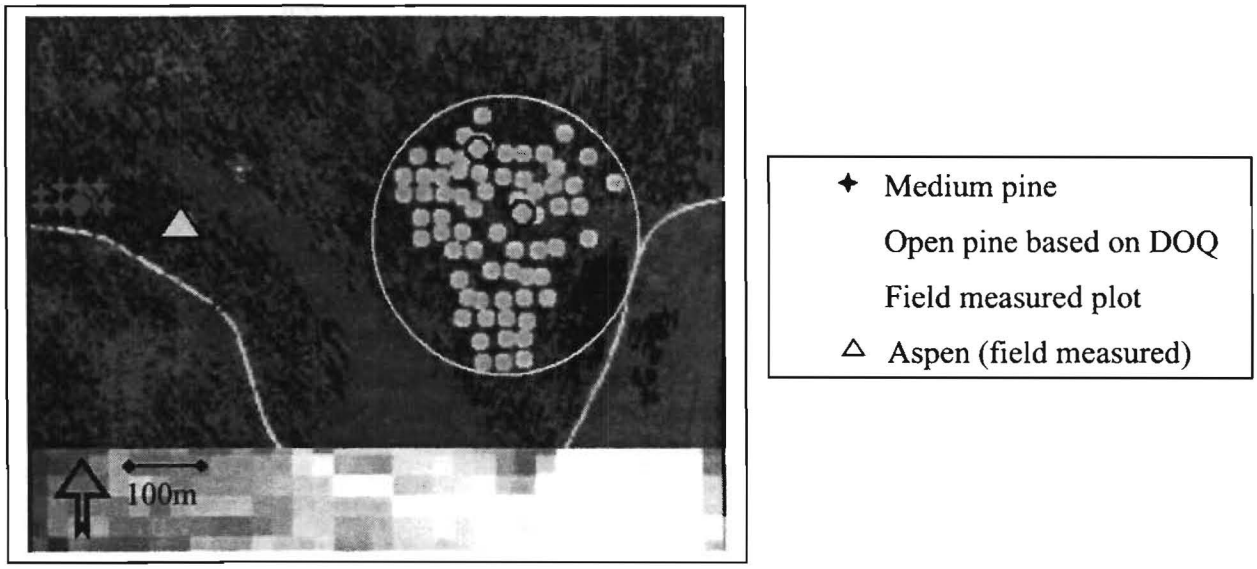

Figure 1. Additional reference points based on ground data collection and DOQ. To avoid autocorrelation, the entire cluster is either training or test data.

Densities of aspen and white spruce were combined because open white spruce and open aspen were rare (only two field plots). Mixed areas were also eliminated because mixed stands were rare and of small size, so that only an insufficient number of reference data could be generated. Furthermore, the database currently employed by the Forest Service does not include mixed classes. The final reference data set contained the following classes: open pine, medium pine, dense pine, meadow, aspen, white spruce, water and non-vegetated areas.

TM /AVIRIS

The high-altitude AVIRIS flight took place in the summer of 2000. The 7 flight lines resulted in 30 scenes. We geo-registered all scenes into the UTM Zone 13 map projection based on DOQs. We employed ACORN to correct for atmospheric absorption. As a general guide on processing AVIRIS data we published a white paper on the web at: http://aviris.de.vu. This guide explains how to prepare AVIRIS data and provides steps for atmospheric correction with ACORN and georeferencing. A good source of information is also the ACORN tutorial (Analytical Imaging and Geophysics, LLC 2001) and ENVI manual (Research Systems, Inc. 2001).

We utilized the solar bands of two Landsat TM5 images from May 5, 1998 (early spring, leaves not yet fully developed) and September 24, 1998 (early fall, "leaves on"). The images were georegistered into the UTM Zone 13 map projection using a 1:24,000 vector layer and 50 ground control points for each images. Each image was dark corrected to reduce atmospheric scatter effects. We built a "hybrid ratio composite" by adding the Normalized Difference Vegetation Index (NDVI) to the solar bands (Lillesand and Kiefer 1994). Both seasons were classified separately and as a multidate scene to test the influence of seasonality.

Decision Tree

Decision Trees for remote sensing applications were already evaluated in the 1970s (Swain and Hauska 1977). Yet, only in recent years did this method gradually emerge from business applications into natural science and provided successful land cover classifications (Hansen et al. 1996, Brodley et al. 1999, Lawrence and Wright 2001, Vogelmann et al. 2001). A decision tree is a representation of branches and nodes. Each node is connected to a set of possible answers that split the cases into subsets corresponding to different test results (Figure 2). Decision trees have similarities to other machine learning approaches. They use recursive partitioning algorithms to derive classification rules from training samples, which is often referred to as data mining (Read 2000). One of the strengths of decision trees is the flexibility in handling large datasets (De'ath and Fabricius 2000), making this approach interesting for hyperspectral data. For this study we employed the decision tree program "See5" distributed by RuleQuest (Quinlan 2002).

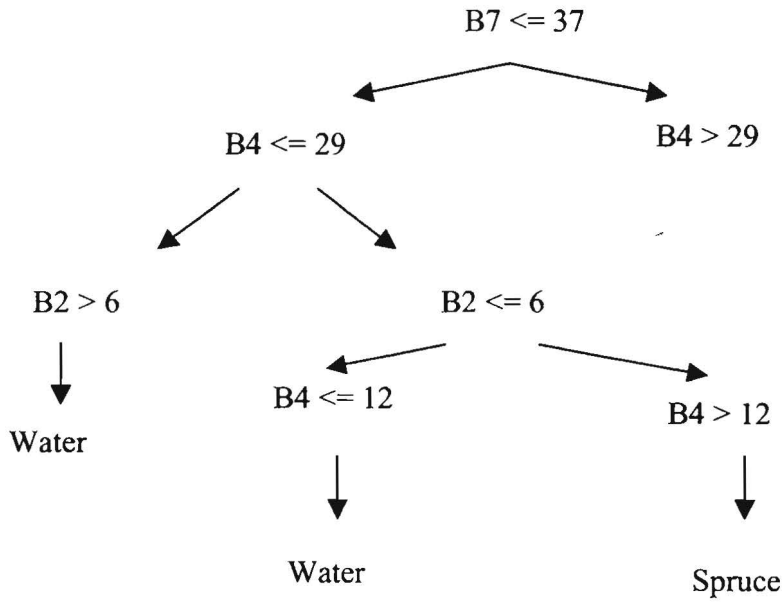

Figure 2. Example of a sub-decision tree that utilizes spring Landsat TM5 data. The tree was trained on reference data based on the summer 2000 survey.

Besides decision trees we tested Maximum Likelihood Classification on TM data and Spectral Angle Mapper (SAM) on AVIRIS data. In the case of SAM, aspen was largely overestimated and this technique was not further investigated. Mixture Tuned Matched Filtering (MTMF) is commonly applied when classifying AVIRIS data. MTMF requires a minimum noise fraction

(MNF) transformed input file (Research Systems, Inc. 2001). The MNF is area-specific, i.e. it needs to be applied to the entire study area, because it gives different results for different scenes. However, this approach quickly becomes intractable when applied over a large area. Our available computer power did not permit us to combine the 20 AVIRIS scenes covering the major part of our study area. Thus MTMF was not applied in this study.

Results

Decision tree classification was successfully applied to both TM and AVIRIS data. The overall accuracy of the AVIRIS classification was 82%, and the accuracy of the multi-date TM classification was 86%. AVIRIS was superior to TM in detecting aspen (>90%), but had difficulty separating the different densities of pine (<70% accuracy for medium and dense pine). See Table 1.

Seasonality was decisive. When classifying TM data using decision trees we found that early spring, before leaves were fully developed, gave about 5% better results than using early fall ("leaf on" before senescence set in). However, best results were achieved when combining spring and fall (86% overall accuracy). Decision tree classification of multi-date TM data was superior for non-vegetated bare areas and meadow. Maximum Likelihood Classification of the multi-date TM gave better results for separating densities of pine, but had problems with white spruce and non-vegetated bare areas.

Table 1. Comparison of different classification methods and datasets

Land cover type	Decision tree AVIRIS	Decision tree multi-date TM	Maximum-likelihood multi-date TM
Water	♦♦♦	♦♦♦	♦♦♦
Aspen	♦♦♦	-	♦♦
Pine open	♦♦♦	♦	♦♦♦
Pine medium	- (confusion med/dens)	♦♦	♦♦♦
Pine dense	- (confusion med/dens)	♦♦♦	♦
Spruce	♦♦	♦♦	♦
Non-vegetated	♦♦	♦♦♦	♦
Meadow	♦♦	♦♦♦	♦♦

	Accuracy
♦♦♦	> 90%
♦♦	>80%
♦	>70%
-	<70%

Both Maximum Likelihood and Decision Tree Classification were easily implemented. Classifications based on Decision Trees were more robust than Maximum Likelihood, because the user and producer accuracy were numerically closer, which is considered a sign of robustness (Congalton 1991).

Discussion/Conclusion

The classification technique Decision Tree was easy to implement, efficient and accurate. However, the use of AVIRIS did not offer significant advantages over TM in this particular application. The overall accuracy achieved was similar for both data types. Multiple-season imagery, easily available with TM but less practical for AVIRIS, helped offset the higher spectral resolution of AVIRIS in the classification. It is possible that AVIRIS might have done better if the data were collected in late spring or early fall. According to Schriever and Congalton (1995), summer is not the best season for a forest classification. Other studies confirm that times when leaves are either senescent or not fully developed are best for forest classification. However, the time and computer processing required to classify large areas of AVIRIS proved a significant disadvantage for applications covering many AVIRIS scenes. Atmospheric correction and georeferencing was time and computer intensive—it took about 10 hours of operator time and three CDs (2GB) to prepare one scene for the actual classification; and 20 scenes were used for a total processing time of 200 hours. Moreover, the area classified constituted only a third of the entire forest. For classification work over large areas, AVIRIS does not appear to provide sufficient improvement in results over multi-date TM that would justify the amount of work and cost required. Unfortunately, the usual procedure of reducing the data dimensionality through a MNF transform cannot be applied, because the MNF must be performed on all the scenes simultaneously. This procedure quickly becomes intractable for more than a few scenes. The development of an algorithm to perform an MNF on a collection of individual scenes, rather than on a single scene, would greatly benefit the application of AVIRIS over larger areas.

Acknowledgements

We would like to acknowledge the efforts of Mark Rumble and the USDA Rocky Mountain Forest Service Research Station for providing vegetation data and support with the reference data collection, Bruce Wylie and Chengquan Huang for assistance with the decision tree analysis, and Doug Baldwin, and Krystal Price for collecting and processing the field data. This research was supported by NASA Food and Fiber Applications of Remote Sensing Program, Grant # NAG13-99021, South Dakota School of Mines and Technology, NASA-EPSCoR, and the SD Space Grant Consortium.

References

Bennett, D.L., 1984, Grazing potential of major soils within the Black Hills of South Dakota. Master of Science Thesis, South Dakota State University, Brookings, SD.

Brodley, C.E., Lane, T., and Stough, T.M., 1999, Knowledge Discovery and Data Mining. American Scientist, 87, 54-61.

Congalton, R.G., 1991, A review of assessing the accuracy of classifications of remotely sensed data. Remote Sensing of Environment, 37, 35-46.

Cook, J.G., Stutzman, T.W., Bowers, C.W., Brenner, K.A., and Irwin, L.L., 1995, Spherical densiometers produce biased estimates of forest canopy cover. Wildlife Society Bulletin, 23, 711-717.

De'Ath, G., and Fabricius, K.E., 2000, Classification and regression trees: a powerful yet simple technique for ecological data analysis. Ecology, 81, 3178-3192.

Ganey, J.L., and Block, W.M., 1994, A comparison of two techniques for measuring canopy cover. Western Journal for Applied Forestry, 9, 21-23.

Hansen, M., Dubayah, R., and Defries, R., 1996, Classification trees: an alternative to traditional land cover classifiers. International Journal of Remote Sensing, 17, 1075-1081.

Kenk, E., Sondheim, M., and Yee, B., 1988, Methods for improving accuracy of Thematic Mapper ground cover classification. Canadian Journal of Remote Sensing, 14, 17-31.

Korhonen, J., 1979, One-person circular plot establishment. The Forestry Chronicle, 55, 51-53.

Lawrence, R.L., and Wright, A., 2001, Rule-Based Classification systems using classification and regression tree (Cart) analysis. Photogrammetric Engineering & Remote Sensing, 67, 1137-1142.

Lillesand, T.M., and Kiefer, R.W., 1994, Remote sensing and image interpretation (New York, Chichester, Brisbane, Toronto, Singapore: John Wiley & Sons, Inc.

Mannel, S., Price, M., Rumble, M., Baldwin, D., and Hua, D., in review, Using a variable-plot technique for establishing fixed-radius circular plots.

Quinlan, R., 2002, See5/C5.0. RuleQuest Research Pty Ltd, St Ives NSW 2075, Australia.

Read, B.J., 2000, Data mining and science?, CLRC Rutherford Appleton Laboratory, Chilton, Didcot, Oxon, UK, http://www.ercim.org/publication/ws-proceedings/12th-EDRG/EDRG12_Re.pdf.

Research Systems, Inc., 2001, ENVI User's Guide, 948 pp.

Schriever, J.R., and Congalton, R.G., 1995, Evaluating seasonal variability as an aid to cover-type mapping from Landsat Thematic Mapper data in the northeast. Photogrammetric Engineering & Remote Sensing, 61, 321-327.

Swain, P.H., and Hauska, H., 1977, The decision tree classifier: design and potential. GE-15, 142-147.

Vogelmann, J.E. et al., 2001, Completion of the 1990s national land cover data set for the conterminous United States from Landsat Thematic Mapper and ancillary data sources. Photogrammetric Engineering & Remote Sensing, 67, 650-662.

White, W.E., and Lewis, C.E., 1982, Establishing circular plot boundaries with a wedge prism and an adjustable target pole. Journal of Range Management, 35, 677-678.

Wolter, P.T., Mladenoff, D.J., Host, G.E., and Crow, T.R., 1995, Improved forest classification in the northern lake states using multi-temporal Landsat imagery. Photogrammetric Engineering & Remote Sensing, 61, 1129-1143.

The Evolution and Present State of Tree-Kills on Mammoth Mountain, California: Tracking Volcanogenic CO_2 and Its Lethal Effects

Brigette A. Martini and Eli A. Silver[1]

1.0 INTRODUCTION

In May 1989, a small magnitude earthquake swarm hit the east-central region of the Sierra Nevada in the state of California. The swarm was located beneath the Pleistocene-aged Mammoth Mountain - a rhyodacitic stratovolcano located on the southwestern rim of the much larger, 760,000 year-old Long Valley caldera (see Figure 1). Early earthquakes of the swarm were probably due to magmatic dike intrusion at depth (Hill et al., 1990) and recent relocations by Prejean (2001) indicate magma movement from initial depths of 7-9 km to within approximately 1 km of the mountain's surface over that six month time period.

The following spring (1990), an unusually heavy loss of needles was observed at several places on Mammoth Mt. by U.S. Forest Service personnel (Farrar et al., 1995), especially surrounding the popular recreation area of Horseshoe Lake. Approximately 4 ha of trees were dead at this lake alone, affecting all species of trees and other forest vegetation. Their deaths were initially attributed to the Sierran drought of the 1980's. In 1994 however, soil gas measurements made by the USGS confirmed that the kills were likely due to asphyxiation of the vegetation via the presence of 30-96% CO_2 in the ground around the volcano (Farrar, 1995). Current flux estimates for the entire mountain are approximately 300-500 tons/day, while flux at the Horseshoe Lake tree-kill is 93 $\pm$ 22 tons/day (Rogie, 2001). Background concentrations of CO_2 in this region are approximately 360 ppm, however concentrations in tree-kill zones can be upwards of 10,000-100,000 ppm early in the day (Rogie, pers. comm., March 2000). Many areas of CO_2-induced kills are now identified on Mammoth (Figure 2).

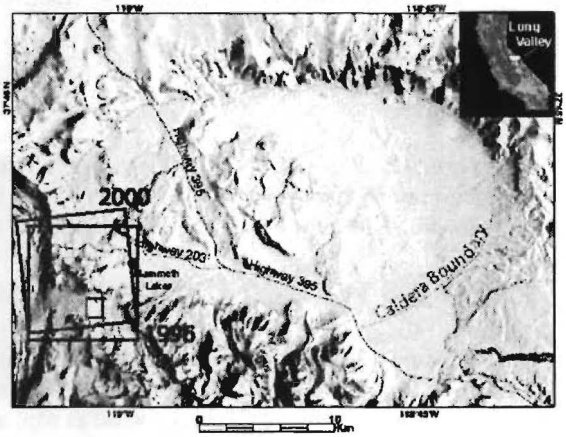

Figure 1. Shaded relief digital elevation model image of Long Valley Caldera. The scene boundaries of both years of AVIRIS data are shown as well as the approximate boundary of aerial photo and HyMap data scenes used.

Traditional mapping of CO_2 discharge zones on Mammoth Mt. is done on-foot with portable accumulation chamber instruments and GPS. The remote sensing techniques described in this study are accomplished remotely, making the spatial and temporal mapping of volcanogenic-assisted forest deaths easier and quick to do. Such mapping is vital for geological, forest, ski, and city personnel in charge of determining areas and level of hazard at Mammoth Mt. Mapping of tree-kill zones with aerial photography and hyperspectral imagery was done previously (Hausback et al., 1998; Sorey et al., 1998; de Jong, 1998; Martini et al., 2000), however this study presents the kills through time. It also attempts to utilize the superior calibration and fine spectral sampling of Advanced Visible/Infrared Imaging Spectrometer (AVIRIS) to identify and map the characteristic spectral absorptions of CO_2 gas within the near-infrared portions of the electromagnetic spectrum (2.00-2.50 μm). The following sections address the genesis of the tree-kills on Mammoth, their growth through time, and initial attempts at detection and mapping of anomalous CO_2 in the atmospheric column above Mammoth Mt. A compilation of aerial photo, HyMap data, and AVIRIS data are used in this endeavor.

[1] University of California Santa Cruz, Earth Science Department, Santa Cruz, California 95064, USA
bmartini@es.ucsc.edu

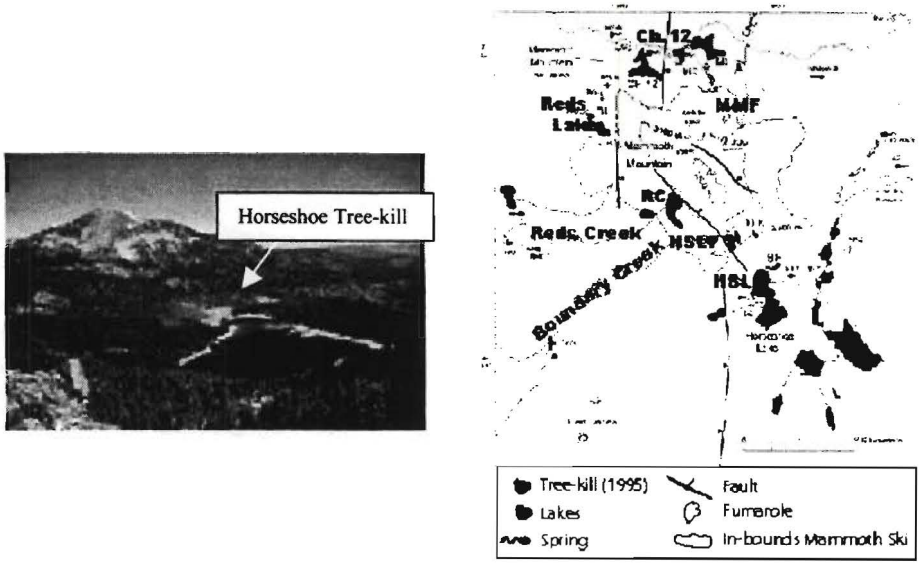

Figure 2. Picture on the left looking northeast with Horseshoe Lake in the forefront and Mammoth rising to the left. The tree-kill is visible on the northern shore of the lake. Map on the right showing known CO_2-induced tree-kills on Mammoth Mt.

2.0 PREVIOUS TREE-KILL BOUNDARY AND CO_2 MAPPING EFFORTS

The tree-kill distributions on Mammoth Mountain were initially mapped using large-scale 1:14,500 aerial photography dating from 1995 (Farrar et al., 1995; Sorey et al., 1998). The boundaries of a few specific kills were also surveyed using handheld GPS receivers, as well as two-color geodimeter measurements. Horseshoe Lake garnered early attention due to the massiveness of the kill and the large measured CO_2 flux: its boundary was measured twice using GPS; once in 1994 (Farrar et al., 1995) and once more in 1998 (Rogie and Colvard, unpub. data, 1998). The above methods are time-intensive and necessarily limited by the subjectivity of human observers on the ground.

Two separate studies in the late 1990's used hyperspectral imaging to assess the boundaries of tree-kills on Mammoth Mountain. The results of both de Jong (1996; 1998) and Hausback et al. (1998) provided initial success at mapping tree mortality using 20 meter resolution AVIRIS data. Hausback et al. also attempted to spectrally discriminate stressors or sources of tree-morbidity on the mountain (eg. the differences between trees killed by CO_2 versus those killed by drought, insects, fire, flooding, etc.). This proved to be less straightforward.

Initial attempts at mapping volcanogenic CO_2 with AVIRIS data was completed on the northern flank of Mammoth Mt. (de Jong and Chrien, 1996). Their results were inconclusive: both CO_2 endmembers acquired in the field and a ratio algorithm targeted at CO_2 band depth at 2.01 μm did not reveal zones of known CO_2 flux in 1994 or 1995 AVIRIS data. There is also ongoing work to quantify CO_2 concentrations in the atmosphere (Green, 2001). Such work has been successful, however detection of small increases or decreases in CO_2 concentration in the atmospheric column (several tens of ppm) appear difficult to track and measure.

3.0 A TEMPORAL ANALYSIS OF HORSESHOE LAKE TREE-KILL GROWTH SINCE 1989

3.1 Timeline of tree-kill growth: unanswered questions

Tree-kills were first noticed in 1991 at several locations around Mammoth Mountain including Horseshoe Lake on the southern flank and Chair 12 and Reds Lake on the northern flank. Several other kills around the mountain appeared in the years following 1991 including Reds Creek on the western flank and several kills on the north face of the mountain inbounds of the resort. Cook et al., 2001 determined through radiocarbon measurements at the Horseshoe Lake kill that almost all the trees sampled there began fixing less carbon-14 beginning in 1990. This deficiency in carbon-14 in 1990 due to magmatic CO_2 uptake was also measured at Reds Creek. The work of Cook et al. indicated that peak flux occurred in 1991, decreased steadily from 1991 to 1995, and was fairly constant till 1998. In addition, measurements of trees near cold CO_2-rich springs on the flanks of Mammoth indicate that

degassing via groundwater has been occurring in at least one tree, since 1967. This is some of the only quantitative knowledge we have about how the tree-kills have grown through the years. However, we still don't know how the tree-kills grew spatially, as none of their boundaries were actually surveyed until 1995. Knowing their initial region of death and the subsequent trajectory of growth of the kill boundaries reveals important information about the subsurface structural system and how the CO_2 propagates. We have attempted to determine a semi-quantitative measure of the growth of the tree-kill at Horseshoe Lake via a multi-temporal airborne remote sensing data analysis. Several techniques are used in this study to accurately identify the boundaries of the tree-kill at Horseshoe Lake over a period stretching from pre-kill times to recent (1977-1999). It elucidates how the kill at Horseshoe Lake began, how it grew, and whether it has continued to expand. The success of this analysis is grounds for its employment at other kills on the mountain.

3.2 Historical air photo analysis

3.2.1 Methods

Air photos of differing scales and seasonal character were acquired and analyzed for the years, 1977, 1990, 1993, 1994, and 1995. A hyperspectral 1999 HyMap image was also used in this analysis. Each photograph was scanned in at 800dpi and saved as a TIFF. The photos were subset to include the Horseshoe Lake tree-kill and 1-2 km of area surrounding the lake. The approximate location of these photos and hyperspectral image is shown by the smallest rectangle over Mammoth Mt. in Figure 1.

Several different methods were used to determine the boundaries of the kills in each photo. Simple enhancement techniques such as linear and gaussian stretching were used for delineating kill boundaries. All of the color photos were actually color-infrared, and hence dead or dying vegetation appeared less red and thus less healthy in near-infrared photography. Stretching of the data values contained in each photo allowed for simple tree-kill boundary identification and mapping. More sophisticated methods such as the Minimum Noise Fraction (MNF) algorithm contained in ENVI© were also applied to the photos. The black and white photo from 1993 was a bit more difficult. The tree-kill is visible in this photo, but doesn't stand out as well as it would in the color-infrared photography. Simple stretching didn't work well with this photo and the single panchromatic band precludes MNF analysis impossible. All the boundaries are hand-digitized into regions of interest (ROIs) and exported to separate vectors. The area of each vector polygon was calculated in hectares and is reported in the inset table of Figure 3.

Each photo was then georectified using 30-50 ground control points. RMS errors were generally below 1 to just around 2, but never went above 5. This translates to approximately 2-3 pixels (40-60 m) of error. Visual comparison of georectified photos with each other was very good.

3.2.2 Results

The MNF mapped the tree-kills well, however the simple stretching techniques were equally successful. Considering the time, storage space and effort required for an MNF, we submit that stretching routines are adequate. Figure 3 shows the vectors from all five years including the vector from the 1999 HyMap data derived from unmixing methods within ENVI©. Horseshoe Lake is placed at the bottom for reference. Minor discrepancies in boundaries are likely due to georectification error and boundary delineation error. The boundary delineation for the panchromatic 1993 photo was least successful. We erred towards the conservative with this year and hence the boundary contains less detail. Excursions in the 1999 HyMap data are due to the increased measurability of tree morbidity and sub-morbidity (the so-called "halo zones" of the tree-kill). However major boundary excursions, such as that seen between 1993 and 1994, are likely real and not due to analysis error. A plot of the growth of the tree-kill through time is shown as an inset of Figure 3.

3.3 The growth of the Horseshoe Lake Treekill: new temporal and spatial patterns revealed

The tree-kill as of 1990 was approximately 4.1 Ha including the beginnings of the northern Borrow Pit kill which was previously thought to have appeared later in 1993 (Cook et al., 2001). From 1990 to 1993, the main kill didn't change much in size. However, the Borrow Pit kill continued to grow, and a new satellite kill appeared to the south of the main kill. From 1993 to 1994, the tree-kill at Horseshoe Lake grew from approximately 5.2 Ha to 10.9 Ha, almost doubling in size. This is a previously unrecognized event. Cook et al.'s work doesn't indicate an increase in degassing in this time period. However, we may be seeing the delayed effects of the initial pulse of CO_2 degassing at Horseshoe Lake. Cook et al. indicates that trees towards the center of the kill experienced the CO_2 pulse first and hence died fastest. This is supported by the present analysis that shows initial kill in 1990 towards the center of the current kill zone (see Figure 3). Trees lying directly in ground zero of the CO_2 flux zone were

killed immediately. Transpiration and mineral and water uptake would have ceased. Initially high airborne CO_2 levels seen in the kill during this initial time period (1200 tons/day (Farrar et al., 1995)) probably led to widening of the stomata in the conifer needles to accept more CO_2 (which plants normally like) (Larcher, 1995). However, to ward off increasingly noxious levels of CO_2, plant stomata probably closed completely. The trees quickly ceased respiration and photosynthesis. They were effectively suffocated. Their cells ceased to function and the trees died.

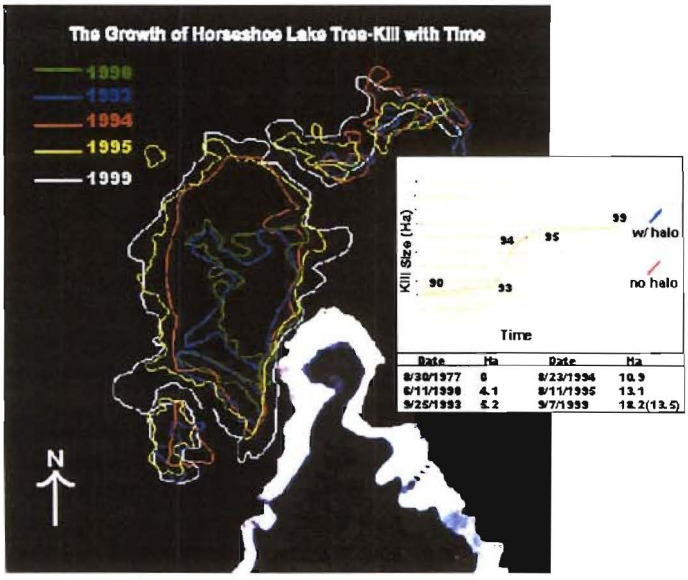

Figure 3. Tree-kill boundaries through time at Horseshoe Lake. Boundaries determined through analysis of both historical aerial photography and hyperspectral data. Inset plot shows the growth of the kill in ha.

Trees towards the boundaries of the kill away from the main CO_2 source zone, might not have received such a strong initial pulse. The CO_2 received did cause initial stress on the physiological systems of the trees. Chronic flux continued to weaken these more peripheral trees until many of them finally died after the particularly hard winter of 1993-1994. It is well known that a combination of stressors on an ecosystem is more lethal than merely one stressor and hence the heavy snows and late spring served to exacerbate the CO_2 stress problem. In addition, Cook et al. found that peripheral trees tended to die approximately four years after initial deficiencies in carbon-14 were measured. The above scenario may explain why the tree-kill is not rapidly growing at present. Constant flux from an anchored point source keeps border trees in a state of heightened physiological stress. Other stressors such as drought or insect infestation may lead to new kills, but current kills will probably remain constant in size. Future kill zones may not be due to anomalous CO_2 flux and thus possible future kill sites should be surveyed for other external stressors such as insects or drought.

The above set of analyses could easily be done for other kill sites on Mammoth Mt. As previously mentioned, Cook et al.'s radiogenic measurements on trees from Reds Creek indicated CO_2 flux in this region at least since 1967. Multi-temporal air photo analysis could reveal when trees began to die at Reds Creek historically, as well as when trees began to die around the Mammoth Mt. after the 1989 seismicity. Any correlation between timing of individual kills may indicate similar shared gas sources at depth and shared, networked, subsurface connections (such as faults and fractures). In fact, the current pattern of kills appears to coincide with hypothesized ring fractures on Mammoth Mt. (Prejean, 2001).

4.0 DETECTING AND MAPPING VOLCANOGENIC CO_2 IN THE ATMOSPHERIC COLUMN ABOVE MAMMOTH MT.

4.1 Spectroscopy of CO_2

Gas absorptions form primarily in response to vibrational absorption processes. For CO_2, there are nine fundamentals (vibrational modes). The stretching and bending of the bonds in the internal modes produces the infrared absorptions seen in CO_2 spectra. In addition, when CO_2 makes a vibrational transition, it usually makes a rotational one as well. CO_2 thence has three vibration-rotation bands (two of which are the same frequency) and a fourth band that is infrared inactive. Other absorptions are seen in CO_2 spectra, and these are due to overtones and combinations of the original fundamentals. The near-infrared absorptions of interest in this study are combination bands centered around 2.0 μm. They have centers at 1.96 μm, 2.01 μm and 2.06 μm. Each absorption is actually a doublet. The main absorption feature of interest used in this study is the 2.06 μm band whose doublet lays longward at 2.08 μm (see Figure 4). Intensity of absorptions are affected by both the level of fundamental mode (fundamentals have higher intensities of absorption than overtones and combinations do) (Gaffey et al., 1993), and the relative amount of the material causing the absorptions (the total absorptance increases with the amount of

material present)(Schurin and Ellis, 1968). Widths of bands are greatly affected by temperature and pressure, with increasing values causing absorptions to widen.

4.2 AVIRIS analysis: spectral detection of anomalous CO_2

The analysis goal was to determine whether anomalous levels of CO_2 are detectable in the atmospheric column using AVIRIS radiance data. Two separate years of data were utilized in this study; 1996 and 2000. Scene boundaries were chosen to encompass the massif of Mammoth Mt. as well as some outlying regions known to be volcanically active in the recent geologic past. Boundaries for both the 1996 and 2000 scenes are shown in Figure 1.

Both years of data were subjected to the same analysis methodologies. The data were spatially subset, spectrally subset, and analyzed for unique, repeatable, spectral features in the 2.0 μm CO_2 absorption wavelength region. In the wavelengths measured by AVIRIS, there are three CO_2 absorption regions: 1.4 μm, 1.6 μm, and 2.0 μm. This study was limited to analysis of the absorptions centered around 2.0 μm as the 1.4 μm absorptions lie too close to the H_2O absorption maximum at 1.38 μm, and the shallow 1.6 μm absorptions were not discriminated from background noise. Though the 2.01 μm feature has the highest absorption intensity, we chose the 2.06 μm absorption feature (seven bands spanning 2.04-2.10 μm). We found it to be less vulnerable to contamination from the wings of the strong 1.87 μm H_2O band. All major and minor water bodies were masked before any spectral analysis. This was done both to reduce the spectral variability encountered in the scene and to reduce the effects of the 1.87 μm water band on the 2.06 μm CO_2 absorption

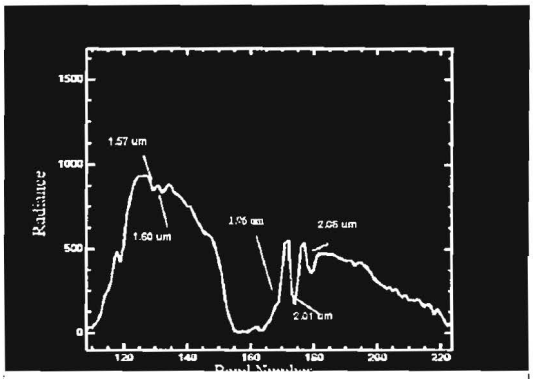

Figure 4. Spectral signature showing major CO_2 absorption regions

Continuum Removal (CR) and Minimum Noise Fraction (MNF) processing were applied to both years of AVIRIS data. We theorize that anomalous levels of CO_2 degassing from Mammoth Mt. will be detectable above background levels. Band depths in regions of elevated flux will be higher than expected given a certain elevation. Those regions with deeper than expected absorptions are possible point sources of magmatic CO_2 degassing. Normal CO_2 at these elevations is approximately 360 ppm, which is approximately 0.04% of the gasses in the atmospheric column measured by AVIRIS. Minor concentration variations from 360 ppm are difficult to measure (Green, 2002). However CO_2 concentrations at several locations on Mammoth Mt. reach levels of 10,000 – 100,000 ppm. It may be possible to detect CO_2 concentrations approaching 10 % in the atmospheric column.

4.2.1 AVIRIS analysis: Continuum Removal

CR was performed on the 2.06 μm absorption feature region in both years of AVIRIS radiance data. Theoretically, the more CO_2 there is in the atmospheric column, the deeper this absorption feature will be. Since there is a direct correlation between the amount of a gas and the relative depth of its absorption, a CR applied to the data should reveal those regions in an image dataset with higher amounts of CO_2 in the atmospheric column. Deeper absorptions should relate to increased levels of CO_2, while more shallow absorptions should relate to decreasing levels of CO_2. Differing depths of absorption were delineated with an arbitrary density slice of the final CR image.

4.2.2 AVIRIS analysis: Minimum Noise Fraction

The second analysis performed on the data was the MNF. The MNF is basically two cascaded principle component transformations, where the first transformation decorrelates and rescales the noise such that the noise has unit variance and no band-to-band correlations, and the second transform takes the noise whitened data and puts it through a standard Principle Components calculation. The MNF transformed data were analyzed on an image-by-image basis where each coherent image may emphasize a particular class of material. By focusing in on a particular absorption (2.06 μm), it was hoped the material causing said absorption would be represented in one of the coherent MNF images.

4.2.3 AVIRIS analysis: Results

Figure 5 shows the results of the CR with an eight level density slice applied. The deepest absorptions are shown in red. The next deepest are shown in green, then blue, yellow, cyan, magenta, maroon, and seagreen respectively. An elevation effect should be discernable in the data: higher elevations should have less overall CO_2 and a shallow CO_2 absorption feature while lower elevations should provide a much deeper absorption feature due to the increased amount of CO_2 in the atmospheric column (Green, 2001). Mammoth Mt. located in the lower southeast corner of the image rises approximately 600 m above the surrounding landscape. As such, higher elevations of the mountain are colored in green, blue, yellow, etc. while surrounding terrain is colored red. The blue coloration on the summit of the mountain indicates a more shallow absorption than the red coloration on its flanks, which indicates a deeper absorption. The CR algorithm appears to work at this regional scale, however regions known to host anomalously high CO_2 flux levels are not identifiable on this CR image. Average spectral signatures extracted from each density class show an expected pattern of deeper absorptions for lower elevations and more shallow absorptions for higher elevations (see Figure 5). Also of note, though the main absorption is located at 2.06 μm, CR analysis has brought out an absorption centered at 2.08 μm. Its depth appears to be conversely related to elevation, i.e. the higher elevations have a deeper 2.08 μm absorption than the lower elevations. This is opposite to the absorption depth/elevation relationship for 2.06 μm.

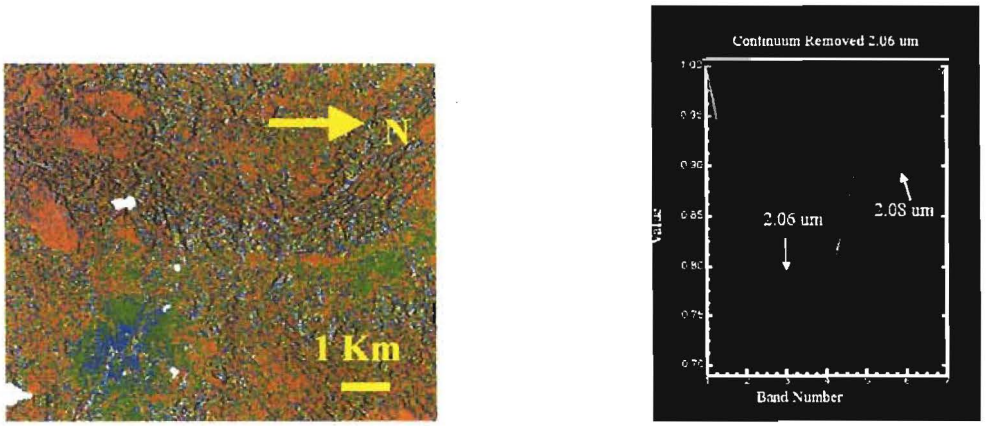

Figure 5. Subset of 2000 AVIRIS image shown on the left. A continuum removal has been applied to the 2.06 μm CO_2 absorption feature from 2.04 – 2.10 μm. The resulting image was density sliced into eight arbitrary color levels. The spectra on the right are average signatures extracted from selected density classes.

The results from the MNF analysis are more compelling than that achieved with the CR, however they are more complex. Four of the seven bands analyzed in the 2000 imagery were coherent, while only three of the seven bands were coherent in the 1996 imagery. In the 2000 AVIRIS image, MNF band 3 appears to contain a spatial distribution of degassing CO_2, while in the 1996 AVIRIS image, it's MNF band 2 that reveals a CO_2 distribution similar to that known to exist from previous field studies (Sorey et al., 1998; Rogie et al., 2001). Figure 6 shows results from the MNF analysis of 2000 AVIRIS imagery. A density slice was applied to MNF band 3. The most extreme values of the MNF (i.e. the highest density slice) were then isolated and highlighted. These areas are plotted on top of the georectified MNF band 3 image along-side mapped faults of the region.

Results from the MNF analysis on 1996 AVIRIS imagery produced similar distributions as those seen in the 2000 imagery. There are some high MNF value zones not seen in the 2000 imagery, as well as zones identified in the 1996 image that do not appear in the 2000 image. Figure 7 shows both years of extreme MNF-value zones. The zones appear around the mountain, occurring on varying rock types, differing elevations, and in both tree-covered and tree-less landscapes.

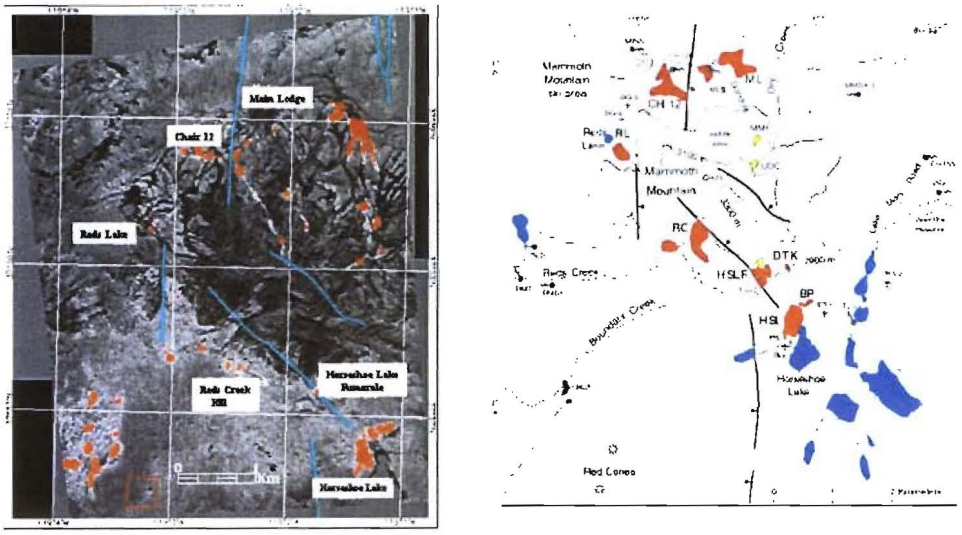

Figure 6. Results from the MNF transformation of 2000 AVIRIS imagery. MNF band 3 is shown with a density slice derived map of extreme MNF values in red. A map of known tree-kills in red is shown on the right (note different scale).

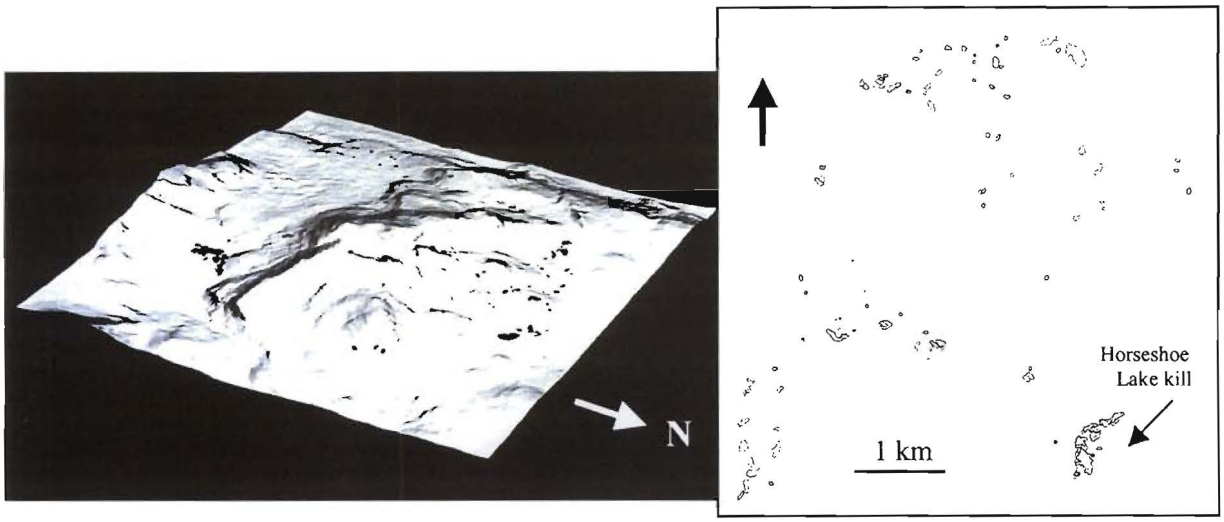

Figure 7. Left: results of MNF analysis of the 2.06 μm CO_2 absorption for 1996 (darker) and 2000 (lighter) AVIRIS imagery. Extreme MNF values from MNF band 2 (1996) and MNF band 3 (2000) shown draped on a shaded 10m USGS DEM. Right: Both years of extreme MNF values shown in plan view.

4.3 Discussion: Feasibility and problems with anomalous CO_2 detection and mapping

The general success of the CR analysis in mapping gross amounts of CO_2 in the atmospheric column is encouraging. However, the inability to map regions of extremely high concentrations of CO_2 at several major tree-kill sites with a simple CR analysis was disappointing. One problem may be that the CR/density slice analysis only measures the depth of the 2.06 μm absorption at its maximum minima. The prominence of the 2.08 μm absorption longward of the main 2.06 μm absorption may hold the key to part of the problem. This 2.08 μm absorption is probably the second half of the 2.06 μm doublet. The fact that it appears to be sensitive to elevation in a converse way to the 2.06 μm absorption is undoubtedly important. A CR analysis of just this absorption (3 bands centered on 2.08 μm) may reveal a more compelling CO_2 flux zone pattern. Another way to investigate the 2.06 μm absorption may be an area-of-absorption analysis. The calculation of band depth normalized to absorption feature areas is found to closely follow amounts of plant biochemical constituents such as water, chlorophyll, cellulose, sugar, etc.

(Kokaly and Clarke, 1999; Curran et al., 2001). Perhaps similar area calculations would prove viable for CO_2 gas absorptions.

The MNF results are quite compelling, though poorly constrained. We cannot know exactly what the MNF is detecting. It is mapping levels of coherence, but the classes produced from this procedure do not possess unique spectral signatures like other endmember classes we are used to. We initially assumed that extreme values of MNF band 3 (2000 data) were detecting anomalous levels of CO_2 via a deeper 2.06 μm absorption relative to surrounding pixels containing more shallow absorptions in this wavelength region. We theorized that these deepest absorptions were different enough from neighboring pixel values, that they produced their own MNF coherence band. The resulting spatial distributions of the extreme MNF values for both 1996 and 2000 are almost perfect matches to known zones of volcanogenic CO_2 flux, some of which host tree-kill sites. However, there are a few exceptions, which may hold the key to determining what the MNF transform analysis is actually detecting.

There are two major sites in the 2000 image mapped as extreme in MNF band 3 that do not correspond to any known zones of CO_2 flux or CO_2-induced tree-kill sites. These include zones mapped in the Rainbow Fire kill of 1992 and zones mapped at Chair 2 on the northern flank of Mammoth in-bounds of the ski area. Groundtruthing with a portable gas accumulation chamber in July, 2002 at these two sites revealed no anomalous CO_2 flux. However, both sites contained an excess of cellulose and lignin in the form of dead trees (at the Rainbow Fire site) and dry mulching grass (spread over the ski-runs at Chair 2 to increase slope stability). The grass possesses a good deal of cellulose, while the dead trees contain both cellulose and lignin within the bark and wood. The biochemicals cellulose and lignin have several distinctive absorptions, one of which is centered on 2.10 μm (see Figure 8A). The 2.06 μm CO_2 absorption lies on the shortward wing of these broad biochemical absorptions (see Figure 8B). If you only look at straight reflectance data, the lignin/cellulose absorption doesn't appear capable of greatly affecting spectral analysis. However, analysis of the data included spectrally subsetting the image to only seven bands around the absorption, and CR processing. If we apply the same analysis steps to the spectra of lignin and cellulose, prominent absorptions are revealed at 2.06 μm (see Figure 8C).

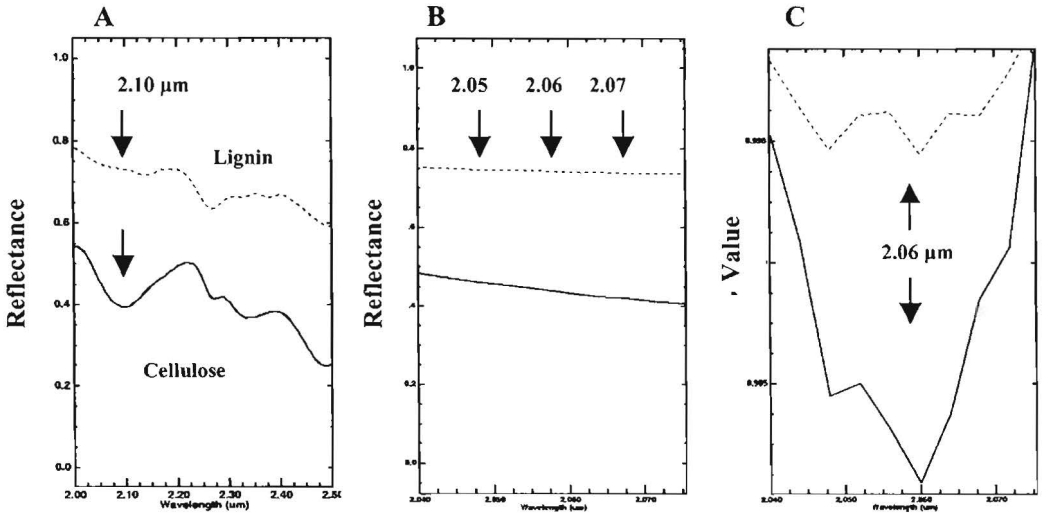

Figure 8. A: Spectral signatures of the plant biochemicals, lignin and cellulose, extracted from the USGS vegetation library B: A close up of these plant chemicals centered around 2.06 μm C: Continuum removed spectral signatures of the same chemicals shown in 8B.

This suggests that the presence of excessive dead trees and grass may create a landscape that would be preferentially mapped when using a density sliced, directed MNF transform of the 2.06 μm absorption. Most CO_2 flux zones on Mammoth have an abundance of dead or dying trees accompanying them. Perhaps the MNF analysis described in this paper is merely mapping cellulose/lignin in the form of dead trees associated with volcanogenic CO_2 emission zones. However, there is one problem with this scenario. There are a myriad of other dead tree areas on and around Mammoth measured by AVIRIS that are not highlighted with the directed MNF analysis of the 2.06 μm absorption. These include large areas of trees killed by avalanche, flooding, snow and trash burial, and insect infestations. This result suggests that there is something unique about the dead tree cellulose/lignin absorptions

highlighted with the MNF analysis in this paper. Perhaps the MNF analysis is capturing both sources of absorption, i.e. the cellulose/lignin absorption from the dead trees and grass is adding into the anomalous CO_2 absorption. We currently can't constrain how much of each spectral endmember is adding into the final spectral signature. What is unequivocal, is the creation of a map of volcanogenic CO_2 flux zones far surpassing those previously created, in detail and completeness, using standard surveying techniques.

5.0 CONCLUSIONS

Multi-temporal air photo analysis has revealed new spatial and temporal patterns of the CO_2-induced Horseshoe Lake tree-kill. The success of this analysis at Horseshoe indicates that similar analyses on other parts of Mammoth, would be an efficient way of determining the temporal growth of the kills as a whole. Our attempts at detecting and mapping anomalous volcanogenic CO_2 in the atmospheric column produced compelling spatial distributions of CO_2 flux zones that matched quite well with known, previously mapped flux zones. However, this analysis is ultimately complicated by an unknown relationship between CO_2 absorptions and those absorptions from plant biochemicals. Further work aimed at quantifying this relationship should be undertaken.

6.0 REFERENCES

Cook, A.C., L.J. Hainsworth, M.L. Sorey, W.C. Evans, J.R. Southon, 2001, "Radiocarbon studies of plant leaves and tree rings from Mammoth Mountain, CA: a long-term record of magmatic CO_2 release," Chem. Geo., v.177, pp. 117-131.

Curran, P.J., J.L. Dungan, D.L. Peterson, 2001, "Estimating the foliar biochemical concentration of leaves with reflectance spectrometry: Testing the Kokaly and Clark methodologies," Rem. Sens. Env., v.76, pp. 349-359.

De Jong, S.M. and T.G. Chrien, 1996, "Mapping volcanic gas emissions in the Mammoth Mountain area using AVIRIS," Summaries of the Sixth JPL Airborne Earth Science Workshop, March 4-8, pp. 75-81.

De Jong, S.M., 1998, "Imaging spectrometry for monitoring tree damage caused by volcanic activity in the Long Valley caldera, California," ITC Jour., 1998-1, pp. 1-10.

Farrar, C. D., M. S. Sorey, W.C. Evans, J.F. Howle, B.D. Kerr, B. M. Kennedy, C.-Y. King, and J.R. Southon, 1995, "Forest-killing diffuse CO_2 emission at Mammoth Mountain as a sign of magmatic unrest," Nature, v. 376, pp. 675-677.

Gaffey, S. J., L.A. McFadden, D. Nash, C. M. Pieters, 1993, "Ultraviolet, visible, and near-infrared reflectance spectroscopy: laboratory spectra of geologic materials," in Remote Geochemical Analysis: Elemental and Mineralogical Composition, C. M. Pieter and P.A. Englert editors, Cambridge Univ. Press, Cambridge, pp. 43-71.

Green, R. O., 2001, "Measuring the spectral expression of carbon dioxide in the solar reflected spectrum with AVIRIS," Summaries of the Tenth JPL Airborne Earth Science Workshop, February 6-9, pp. 181-192.

Hausback, B. P., M. Strong, C. Farrar, D. Pieri, D., 1998, "Monitoring of volcanogenic CO_2-induced tree kills with AVIRIS image data at Mammoth Mountain, California," in Summaries of the Seventh Annual JPL Airborne Earth Science Workshop, January 12-15.

Hill, D.P., W.L. Ellsworth, M.J.S. Johnston, J.O. Langbein, D.H. Oppenheimer, A.M. Pitt, P.A. Reasenberg, M.L. Sorey, S.R. McNutt, 1990, "The 1989 earthquake swarm beneath Mammoth Mountain, California: an initial look at the 4 May through 30 September activity," Bull. Seis. Soc. Am., v. 80, n. 2, pp. 325-339.

Kokaly, R.F. and R.N. Clark, 1999, "Spectroscopic determination of leaf biochemistry using band-depth analysis of absorption features and stepwise multiple linear regression," Rem. Sens. Env., v.67, pp. 267-287.

Larcher, W., 1995, Physiological plant ecology. 3rd ed., Springer, Berlin.

Martini, B. A., E.A. Silver, D.C. Potts, W.L. Pickles, 2000, "Geological and geobotanical studies of Long Valley Caldera, CA, USA utilizing new 5m hyperspectral imagery," in Proceedings of the Thirteenth IEEE International Geoscience and Remote Sensing Symposium, Honolulu, HI, July 2000.

Prejean, S.G., 2001, The interaction of tectonic and magmatic processes in the Long Valley Caldera, California, PhD Dissertation, Stanford.

Rogie, J. D., D.M. Kerrick, M.L. Sorey, G. Chiodini, D.L. Galloway, 2001, "Dynamics of carbon dioxide emission at Mammoth Mountain, California," Earth and Planetary Sci. Lett., v.188, pp. 535-541.

Schurin, B. D. and R.E. Ellis, 1968, "Integrated intensity measurements of carbon dioxide in the 2.0-u, 1.6-u, and 1.43-u regions," Applied Optics, v. 7, n. 3, pp. 467-470.

Sorey, M. L., W.C. Evans, B.M. Kennedy, C.D. Farrar, L.J. Hainsworth, B. Hausback, 1998, "Carbon dioxide and helium emissions from a reservoir of magmatic gas beneath Mammoth Mountain, California," J. of Geophys. Res., v.103, n. B7, pp. 15,303-15,323.

Constrained Least Squares Linear Spectral Unmixture by the Hybrid Steepest Descent Method

Nobuhiko Ogura* and Isao Yamada**

1 Introduction

A closed polyhedron is the intersection of finite number of closed half spaces, i.e., the set of points satisfying finite number of linear inequalities, and is widely used as a constraint in various application, for example specifications or constraints in signal processing or estimation problems, resource restrictions in financial applications and feasible sets of probability distributions. By the progress of the convex analysis and the fixed point theory of nonexpansive mapping, a number of convex projection based algorithms are proposed (for example, Bauschke et al, 1997; Combettes, 1993; Yamada et al, 1998–2002). In this paper, to apply efficiently such methods to problems with polyhedral constraints, we propose a simple solution to the problem of the best approximation to the certain polyhedron. By applying this solution to the the hybrid steepest descent method(Ogura et al, 2002; Yamada et al 1998; Yamada 2001), we also present two algorithms for a linear spectral unmixing problem. The proposed method enable us to deal with constraints and variety of cost function (for example, least square residual, Kullback-Leibler Divergence) as well as various a priori knowledge with great flexibility.

The rest of this paper is organized as follows. The next section contains brief preliminaries on a linear unmixing problem and the hybdid steepest descent method. In the third section, we present a simple solution to the best approximation problem. In the last section, we show the algorithmic solution to the inversion of image spectrometry data by using projection based convexly constrained pseudoinverse algorithm.

2 Preliminaries

A. Best Approximation Problem to Polyhedron

Let $\mathcal{H}$ be a real Hilbert space with inner product $\langle \cdot, \cdot \rangle$ and norm $\| \cdot \|$. Suppose that N_1 hyperplains and N_2 closed half spaces are given by $S_{1,i} := \{u \in \mathcal{H} \mid \langle \rho_{1,i}, u \rangle = c_{1,i}\}$ and $S_{2,j} := \{u \in \mathcal{H} \mid \langle \rho_{2,j}, u \rangle \geq c_{2,j}\}$ respectively, where $\rho_{1,i} \in \mathcal{H}$, $c_{1,i} \in \mathbb{R}$, $\rho_{2,j} \in \mathcal{H}$ and $c_{2,j} \in \mathbb{R}$ $(i = 1, \cdots, N_1,\ j = 1, \cdots, N_1)$. Then, the problem of our interests is

$$\text{Minimize } \|u - u_0\| \text{ over } S := \left(\bigcap_{i=1}^{N_1} S_{1,i} \right) \cap \left(\bigcap_{j=1}^{N_2} S_{2,j} \right) \neq \emptyset \tag{1}$$

for given $u_0 \in \mathcal{H}$. It is known that the problem (1) has unique minimizer. (This fact holds for general nonempty closed convex set $C(\subset \mathcal{H})$ instead of the polyhedron S. In this case the minimizer is denoted by $P_C(u_0)$.) An algorithm found in (Wolfe, 1976) gives the solution of (1) if all vertex is known. Some algorithms based on the cycric projection or the parallel projection methods (Bauscheke 1997; Combettes, 1993; Stark, 1998; Yamada 2001; Yamada et al, 1998) can be applicable to compute such a projection (which are computationaly easy but require infinitely many iterations in general). The quadratic

*Tokyo Institute of Technology (ogura@pi.titech.ac.jp)
**Tokyo Institute of Technology (isao@ss.titech.ac.jp)

programming techniques can also be available, for example general active-set methods(Gill et al, 1978;Goldfarb et al, 1983) (which are finitely convergent but somewhat complicated in handling active-sets selection). Although, the method proposed in this paper can be essentially interpreted as an active-set method, we show in Section 3 that the complete determination of the active set is possible if the polyhedron satisfies condition (2). For example, the condition is fullfilled if

$$N_1 = 0 \text{ and } \langle \rho_{2,i}, \rho_{2,j} \rangle \leq 0 \text{ for all } i \neq j,$$

(see Section 3 for other examples.) Based on this fact, we propose a simple algorithmic solution to the problem (1), which requires at most only $N_1 + N_2$ times iterations to obtain the solution.

B. Hybrid Steepest Descent Method

A *fixed point* of a mapping $T : \mathcal{H} \to \mathcal{H}$ is a point $u \in \mathcal{H}$ such that $T(u) = u$. $Fix(T) := \{u \in \mathcal{H} \mid T(u) = u\}$ denotes the set of all fixed points of T. A mapping $T : \mathcal{H} \to \mathcal{H}$ is called κ-Lipschitzian (or κ-Lipschitz continuous) over $S \subset \mathcal{H}$ if there exists $\kappa > 0$ such that $\|T(u) - T(v)\| \leq \kappa \|u - v\|$ for all $u, v \in S$. In particular, a mapping $T : \mathcal{H} \to \mathcal{H}$ is called (i) *nonexpansive* if $\|T(u) - T(v)\| \leq \|u - v\|$ for all $u, v \in \mathcal{H}$; (ii) *attracting nonexpansive* if $T : \mathcal{H} \to \mathcal{H}$ is a nonexpansive mapping satisfying $\|T(u) - f\| < \|u - f\|$ for all $f \in Fix(T) \neq \emptyset$ and $u \notin Fix(T)$. The convex projection P_C onto a nonempty closed convex set C is attracting nonexpansive. A mapping $\mathcal{F} : \mathcal{H} \to \mathcal{H}$ is called *monotone* over $S \subset \mathcal{H}$ if $\langle \mathcal{F}(u) - \mathcal{F}(v), u - v \rangle \geq 0$ for all $u, v \in S$. Indeed, a mapping $\mathcal{F}$ which is monotone over $S \subset \mathcal{H}$ is called *η-strongly monotone* or just *strongly monotone* over S if there exists $\eta > 0$ such that $\langle \mathcal{F}(u) - \mathcal{F}(v), u - v \rangle \geq \eta \|u - v\|^2$ for all $u, v \in S$ (Zeidler, 1990). Let $\| \cdot \|_{(p)}$ be the standard norm defined in Euclid space $\mathbb{R}^p$.

The following fact is an algorithmic solution to convex constrained pseudoinverse based on the hybrid steepst descent method (Yamada et al 1998; Yamada 2001).

Fact 1 *(Yamada, 1999, 2001) Suppose that* $\mathcal{C} := \arg\inf_{x \in K} \|Ax - b\|_{(m)} \neq \emptyset$ *for a given bounded linear mapping* $A : \mathcal{H} \to \mathbb{R}^m$, *a possibly perturbed vector* $b = (b_1, \cdots, b_m)^T$ *and a nonempty bounded closed convex set* $K \subset \mathcal{H}$. *Suppose* $a_i \in \mathcal{H}$ $(i = 1, \cdots, m)$ *are determined to follow* $Ax = (\langle a_1, x \rangle, \cdots, \langle a_m, x \rangle)$. *Let* $T(x) := P_K \sum_{i=1}^m \frac{\|a_i\|^2}{\sum_{j=1}^m \|a_j\|^2} \left(x - \frac{\langle a_i, x \rangle - b_i}{\|a_i\|^2} a_i \right)$. *Suppose that* $\Theta : \mathcal{H} \to \mathbb{R}$ *is convex over* K *and Gâteaux differentiable with derivative* Θ' *κ-Lipschitzian and η-strongly monotone over* K. *Then, the sequence* $(u_n)_{n \geq 0} \subset \mathcal{H}$, *generated by* $u_{n+1} = T(u_n) - \frac{1}{n+1} \Theta'(T(u_n))$ *with arbitrary* u_0, *converges to uniquely existing minimizer of* Θ *over* K. □

Remark 1 If K is bounded, $\mathcal{C} \neq \emptyset$ is ensured (Yamada et al, 1998). □

The following is a variation of the hybrid steepst descent method, which plays important role to give a flexible linear unmixing algorithm in Section 4.

Fact 2 *(Ogura et al, 2002a, 2002b) Assume that* $\mathcal{H}$ *is finite dimensional real Hilbert space. Suppose that* $T : \mathcal{H} \to \mathcal{H}$ *is an attracting nonexpansive mapping with bounded* $Fix(T)$. *Let a function* $\Theta : \mathcal{H} \to \mathbb{R}$ *be convex and Gâteaux derivative over* $T(\mathcal{H})$ *with derivative* Θ' *κ-Lipschitzian. Then, the sequence* $(u_n)_{n \geq 0} \subset \mathcal{H}$, *generated by* $u_{n+1} := T(u_n) - \frac{1}{n+1} \Theta'(T(u_n))$ *with arbitrary* u_0 *satisfies* $\lim_{n \to \infty} d(u_n, \arg\inf_{x \in Fix(T)} \Theta(x)) = 0$ *($d(u, C) := \inf_{v \in C} \|u - v\|$ denotes the distance from $u \in \mathcal{H}$ onto a nonempty closed convex set C).* □

3 Main Results

Define a closed polyhedron S as in (1) Under the assumption that $\rho_{2,i}^{(1,N_1)}$'s, defined by (3), satisfy

$$\langle \rho_{2,i}^{(1,N_1)}, \rho_{2,j}^{(1,N_1)} \rangle \leq 0 \text{ for all } i \neq j, \tag{2}$$

the following algorithm enable us to compute $P_S(u_0)$ for arbitraty $u_0 \in \mathcal{H}$ if $S \neq \emptyset$, as well as to verify S is empty or not.

Algorithm 1: Let $\rho_{1,i}^{(1,0)} := \rho_{1,i}$, $c_{1,i}^{(1,0)} := c_{1,i}$, $\rho_{2,i}^{(1,0)} := \rho_{2,i}$, $c_{2,i}^{(1,0)} := c_{2,i}$ and $u^{(1,0)} := u_0$. For simplicity, define a function $\theta : \mathcal{H} \times \mathcal{H} \times \mathbb{R} \to \mathbb{R}$ as

$$\theta(u, v, w) := \begin{cases} \dfrac{\langle u, v \rangle - w}{\|u\|^2} & (u \neq 0) \\ 0 & (\text{otherwise}). \end{cases}$$

Define the sequences $(\rho_{1,j}^{(1,i)})_{0 \leq i \leq N_1}$, $(c_{1,j}^{(1,i)})_{0 \leq i \leq N_1}$, $(\rho_{2,j}^{(1,i)})_{0 \leq i \leq N_1}$ and $(c_{2,j}^{(1,i)})_{0 \leq i \leq N_1}$ as follows:

$$\begin{array}{l} \rho_{1,j}^{(1,i+1)} := \rho_{1,j}^{(1,i)} - \theta(\rho_{1,i+1}^{(1,i)}, \rho_{1,j}^{(1,i)}, 0)\rho_{1,i+1}^{(1,i)} \\ c_{1,j}^{(1,i+1)} := c_{1,j}^{(1,i)} - \theta(\rho_{1,i+1}^{(1,i)}, \rho_{1,j}^{(1,i)}, 0)c_{1,i+1}^{(1,i)} \\ \rho_{2,j}^{(1,i+1)} := \rho_{2,j}^{(1,i)} - \theta(\rho_{1,i+1}^{(1,i)}, \rho_{2,j}^{(1,i)}, 0)\rho_{1,i+1}^{(1,i)} \\ c_{2,j}^{(1,i+1)} := c_{2,j}^{(1,i)} - \theta(\rho_{1,i+1}^{(1,i)}, \rho_{2,j}^{(1,i)}, 0)c_{1,i+1}^{(1,i)}. \end{array} \tag{3}$$

If there exists i such that $c_{1,i}^{(1,N_1)} \neq 0$, then $S = \emptyset$ and this algorithm completes. Otherwise, define $(u^{(1,i)})_{0 \geq i \geq N_1}$ by

$$u^{(1,i+1)} := u^{(1,i)} - \theta(\rho_{1,i+1}^{(1,i)}, u^{(1,i)}, c_{1,i+1}^{(1,i)})\rho_{1,i+1}^{(1,i)}.$$

and let $\rho_{2,i}^{(2,0)} := \rho_{2,i}^{(1,n)}$, $c_{2,i}^{(2,0)} := c_{2,i}^{(1,n)}$ and $u^{(2,0)} := u^{(1,N_1)}$. While it hold for some i that $\rho_{2,i}^{(2,n)} \neq 0$ and $\langle \rho_{2,i}^{(2,n)}, u_n \rangle < c_{2,i}$, repeat from $n = 0$ that

$$\begin{array}{l} \rho_{2,j}^{(2,n+1)} := \rho_{2,j}^{(2,n)} - \theta(\rho_{2,i}^{(2,n)}, \rho_{2,j}^{(2,n)}, 0)\rho_{2,i}^{(2,n)} \\ c_{2,j}^{(2,n+1)} := c_{2,j}^{(2,n)} - \theta(\rho_{2,i}^{(2,n)}, \rho_{2,j}^{(2,n)}, 0)c_{2,i}^{(2,n)} \\ u^{(2,n+1)} := u^{(2,n)} - \theta(\rho_{2,i}^{(2,n)}, \rho_{2,j}^{(2,n)}, c_{2,i}^{(2,n)})\rho_{2,i}^{(2,n)}. \end{array} \tag{4}$$

If there exists i such that $\rho_{2,i}^{(2,N_3)} = 0$ and $c_{2,i}^{(2,N_3)} > 0$ when this iteration stops at $n =: N_3$, then $S = \emptyset$, otherwise $u^{(2,N_3)}$ is $P_S(u_0)$. □

By the following lemma, it is easily verified that (a) the iterative step of (4) surely stops at some $n(= N_3) \leq N_2$; (b) if there exists i such that $c_{1,i}^{(1,N_1)} \neq 0$, then $S = \emptyset$; (c) if $c_{1,i}^{(1,N_1)} = 0$ for all $1 \leq i \leq N_1$ and there exists j such that $\rho_{2,j}^{(2,n)} = 0$ and $c_{2,j}^{(2,n)} < 0$, then $S = \emptyset$; (d) if $c_{1,i}^{(1,N_1)} = 0$ for all $1 \leq i \leq N_1$ and $\rho_{2,j}^{(2,n)} \geq c_{2,j}^{(n)}$ for all $1 \leq j \leq N_2$, then $u^{2,n} = P_S(u_0)$.

Lemma 1 *Suppose that $\rho_{2,i}^{(1,N_1)}$ satisfies (2). Let $S_{i,j}^{(k,l)} := \{u \in \mathcal{H} \mid \langle \rho_{i,j}^{(k,l)}, u \rangle \geq c_{i,j}^{(k,l)}\}$, $S^{(1,i)} := (\bigcap_{j=1}^{N_1} S_{1,j}^{(1,i)}) \cap (\bigcap_{j=1}^{N_2} S_{2,j}^{(1,i)})$ and $S^{(2,i)} := \bigcap_{j=1}^{N_2} S_{2,j}^{(2,i)}$. Then:*

(a) $\langle \rho_{2,i}^{(2,n)}, \rho_{2,j}^{(2,n)} \rangle \leq 0$ *for all* $i \neq j \Rightarrow \langle \rho_{2,i}^{(2,n+1)}, \rho_{2,j}^{(2,n+1)} \rangle \leq 0$ *for all* $i \neq j$,

(b) $|\{i \in \{1, \cdots, N_2\} \mid \rho_{2,i}^{(2,n+1)} = 0\}| \leq |\{i \in \{1, \cdots, N_2\} \mid \rho_{2,i}^{(2,n)} = 0\}| - 1$,

(c) $S^{(i,j)} = \emptyset \Leftrightarrow S^{(i,j+1)} = \emptyset$,

(d) *If* $c_{1,i}^{(1,N_1)} = 0$ *for all* i, *then* $S^{(2,0)} = \emptyset \Leftrightarrow S^{(1,N_1)} = \emptyset$,

(e) $S^{(i,j)} \neq \emptyset \Rightarrow P_{S^{(i,j+1)}}(u^{(i,j+1)}) = P_{S^{(i,j)}}(u^{(i,j)})$,

(f) *If* $c_{1,i}^{(1,N_1)} = 0$ *for all* i, *then* $S^{(1,N_1)} \neq \emptyset \Rightarrow P_{S^{(2,0)}}(u^{(2,0)}) = P_{S^{(1,N_1)}}(u^{(1,N_1)})$. □

(The proof of this lemma is omitted.)

Note: The following is an example of polyhedron satisfying (2):

$$\left\{ u = (x_1, \cdots, x_m) \in \mathbb{R}^m \;\middle|\; x_i \geq 0 \text{ for all } i \text{ and } \sum_{i=1}^{m} w_i x_i = 1 \right\}$$

where $w_i > 0$ $(i = 1, \cdots, m)$. If $w_i = 1$ for all $i = 1, \cdots, m$, this polyhedron represents the feasible set of probability distribution. The following is another example:

$$\left\{ u = (x_1, \cdots, x_m) \in \mathbb{R}^m \;\middle|\; x_i \geq 0 \text{ for all } i \text{ and } \sum_{i=1}^{m} w_i x_i \leq 1 \right\}$$

where $w_i > 0$ $(i = 1, \cdots, m)$. All closed affine spaces are also examples satisfying (2).

4 Application to the Linear Unmixing for Imaging Spectrometry

In this section, we apply the Algorithm 1 in the previous section to the problem of an inversion of image spectrometry data. In the imaging spectrometry, a pixel is generally mixed by a number of materials present in the scene as follows (Chang et al, 2000; Clark et al, 1998; Heinz et al, 2001; Settle, 1993, 1996; Shimabukuro et al, 1991):

$$r = M\alpha + e, \tag{5}$$

where $r = (r_1, \cdots, r_l)^T \in \mathbb{R}^l$ is an observed image pixel, $M \in \mathbb{R}^{l \times p}$ is a material signature, $\alpha = (\alpha_1, \cdots, \alpha_p)^T \in \mathbb{R}^p$ is an abundance vector, e is a noise or a measurement error, l is the number of spectral bands and p is the number of reference materials. Each r_i represents observed reflectance of each band, and each α_i represents abundance fraction associated with i-th material and α_i's satisfy $\sum_{i=1}^{p} \alpha_i = 1$ and $\alpha_i \geq 0$ for all $i = \{1, \cdots, p\}$, each component $m_{i,j}$ of signature matrix M is represents the reference reflectance of i-th band of the j-th material reference spectral signature.

Then, a linear unmixing method attempts to estimate the unknown abundance vector α from the observed image pixel r. Such an inversion process of the linear mixture model is required to achieve the tasks of material discrimination, detection, classification, quantification, etc.

The estimation problem is the following polyhedron constrained inverse problem:

$$\begin{array}{l} \text{Minimize } \|r - M\alpha\|_{(l)} \\ \text{subject to } \alpha \in S \end{array} \tag{6}$$

where $S := \{\alpha \in \mathbb{R}^p \mid \alpha_i \geq 0 \text{ for all } i = \{1, \cdots, p\} \text{ and } \sum_{i=1}^{p} \alpha_i = 1\}$, and $\|\cdot\|_{(l)}$ denotes the standard norm defined in Euclid space $\mathbb{R}^l$.

The quadratic programming based methods are developed in (Settle, 1993; Shimabukuro et al, 1991) to solve (6). To avoid the computational complexity of these method, an penalty function based method is employed in (Heinz et al, 2001; Chang et al, 2000). These methods assume that the matrix M has full rank. Unfortunately this assumption does not hold in some practical situations because there are so many reference signatures and sometimes signature vectors may automatically generated from observed image (Chang et al, 2000; Ren et al, 2000).

Algorithm 2: By letting $a_i := m_{i,*}$, ($m_{i,*}$ denote i-th row-vector) and $K := S$, Fact 1 realize the algorithm to Minimize a function $\Theta(u)$ over the solution of (6). □

Remark 2 This algorithm does not require for M to be full rank. In addition, unlike conventional techniques, Algorithm 2 can impose additional criteria Θ to the problem (6). Indeed, if M does not have full rank, the solution of (6) may not be unique. For such a case, Fact 1 can find unique minimizer of Θ over the set of all solution of (6). We can take Θ as energy function or other function reflecting some spatial information. □

Algorithm 3: By letting $\Theta(\alpha) := \|r - M\alpha\|_{(l)}$, Fact 2 realize the algorithm to Minimize $\|r - M\alpha\|_{(l)}$ over $Fix(T)$. □

Note: We can find a solution of (6) by using attracting nonexpansive mapping $T := P_S$ because $Fix(P_S) = S$.

Remark 3 Unlike conventional techniques, Algorithm 3 can deal with more flexible constraint than that of (6) by substituting T. By using $T := P_S \sum_{i=1}^{N} w_i P_{C_i}$, we can find a point $u \in \arg\inf_{x \in K_\Phi} \|r - M\alpha\|_{(l)}$ where C_i is nonempty closed bounded set and $w_i \in (0, 1]$ and $K_\Phi := \arg\inf_{x \in S} \sum_{i=1}^{N} w_i d^2(x, C_i)$. This T enable us to handle additional a priori knowledges reflected by $C_i's$, which is expected to be obtained from spatial or statistical information in the hyperspectral imaging. See (Yamada, 2001) for the properties of K_Φ and other example of attracting nonexpansive mapping T. Fact 2 can also take other Θ for residual minimization, which means Fact 2 potentially has capability to use various distances, which is more suitable for the hyperspectral imaging, for instance, Kullback-Leibler Divergence $\Theta(\alpha) := \sum_{i=1}^{l} \langle m_{i,*}, \alpha \rangle \log \frac{\langle m_{i,*}, \alpha \rangle}{r_i}$ or Spectral Information Divergence (Chang, 2000) $\Theta(\alpha) := \sum_{i=1}^{l} \langle m_{i,*}, \alpha \rangle \log \frac{\langle m_{i,*}, \alpha \rangle}{r_i} + \sum_{i=1}^{l} r_i \log \frac{r_i}{\langle m_{i,*}, \alpha \rangle}$. □

Numerical Experiment 1

We choose 3 independent reference spectral signature vector from USGS Digital Spectral Library: splib(vers.4) for AVIRIS. $m_{*,1}$ is record No.120 Copiapite, $m_{*,2}$ is record No.231 Jarosite, $m_{*,3}$ record No.171 Gaothite ($m_{*,j}$ denote j-th column-vector of the matrix M). These signature has band number $l = 224$. Figure 1 shows the reference spectral signature vectors $m_{*,1}$, $m_{*,2}$ and $m_{*,3}$.

Abundance of each material are set to Copiapite 60%, Jarosite 30%, Gaothite 10%, thus abundance vector is $\alpha = (0.6, 0.3, 0.1)^T$.

Sample observation data r are randomly generated by (5) with 30:1 SNR gaussian error e.

Then, inversion was made by (a) the algorithm of Fact 1 (with $\Theta(u) := \|u\|$) and (b) the algorithm of Fact 2 (with $T := P_S$) and (c) FCLS algorithm ($\delta = 10^{-5}$) proposed in (Chang et al, 2000; Heinz et al, 2001). The simulation results of 3 data are shown in Table 1.

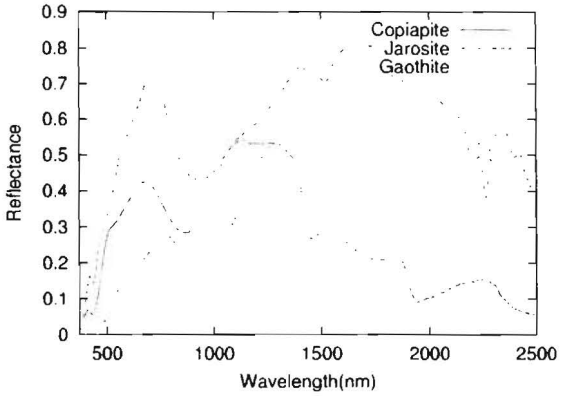

Figure 1: The reference spectral signatures.

	estimated abundance α	$\|r - MP_S(\alpha)\|^2_{(l)}$
(a), Data No.1	(0.603551, 0.305009, 0.091440)	$1.853264252604 \times 10^{-2}$
(b), Data No.1	(0.603404, 0.305436, 0.091159)	$1.853141617604 \times 10^{-2}$
(c), Data No.1	(0.603405, 0.305436, 0.091160)	$1.853141617794 \times 10^{-2}$
(a), Data No.2	(0.606399, 0.304080, 0.089520)	$2.044290704859 \times 10^{-2}$
(b), Data No.2	(0.605570, 0.304144, 0.090286)	$2.043725005123 \times 10^{-2}$
(c), Data No.2	(0.605570, 0.304144, 0.090286)	$2.043725005186 \times 10^{-2}$
(a), Data No.3	(0.596860, 0.302069, 0.101070)	$1.604000824838 \times 10^{-2}$
(b), Data No.3	(0.597202, 0.301896, 0.100902)	$1.603884893825 \times 10^{-2}$
(c), Data No.3	(0.597202, 0.301897, 0.100902)	$1.603884893852 \times 10^{-2}$

Table 1: Result of Experiment 1.

	estimated abundance α	$\|r - MP_S(\alpha)\|^2_{(l)}$
(d), Data No.1	(0.451246, 0.198576, 0.350178)	$1.902200569304 \times 10^{-2}$
(e), Data No.1	(0.638525, 0.326029, 0.035446)	$1.898692271721 \times 10^{-2}$
(d), Data No.2	(0.453241, 0.196296, 0.350463)	$2.101749344546 \times 10^{-2}$
(e), Data No.2	(0.640458, 0.324286, 0.035257)	$2.096505360051 \times 10^{-2}$
(d), Data No.3	(0.447391, 0.202981, 0.349627)	$1.622697188668 \times 10^{-2}$
(e), Data No.3	(0.636149, 0.328172, 0.035679)	$1.622479447754 \times 10^{-2}$

Table 2: Result of Experiment 2.

Numerical Experiment 2

To examine the case that signature vectors are dependent, replace $m_{*,3}$ by $0.6m_{*,1}+0.4m_{*,1}$ and make same experiment with (d) the algorithm of Fact 1 and (e) the algorithm of Fact 2. The simulation results of 3 data are shown in Table 2.

The results of Experiments 1 and 2 show that the proposed methods gives almost same accuracy as that given by conventional method although the proposed methods only requires loose assumptions and has flexibility to optimality criteria and constraints.

References

Bauschke, H. H., J. M. Borwein and A. S. Lewis, 1997, "The method of cyclic projections for closed convex sets in Hilbert space," *Contemp. Math.*, vol.204, pp.1–38.

Chang, C.-I., 2000, "An Information-Theoretic Approach to Spectral Variability Similarity, and Discrimination for Hyperspectral Image Analysis," *IEEE Trans. Information Theory*, vol.46, pp.1927–1932.

Chang, C.-I. and D. C. Heinz, 2000, "Constrained Subpixel Target Detection for Remotely Sensed Imagery," *IEEE Trans. on Geoscience and Remote Sensing*, vol. 38, pp.1144–1159.

Clark, C. and A. F. Clark, 1998, "Spectral Identification by Singular Value Decomposition," *International Journal of Remote Sensing*, vol. 19, pp.2317–2329.

Combettes, P. L., 1993, "Foundation of set theoretic estimation," *Proc. IEEE*, vol.81, pp.182–208.

Gill, P. E. and W. Murray, 1978, "Numerically stable methods for quadratic programming," *Math. Programming*, vol.14, pp.349–372.

Goldfarb, D. and A. Idnani, 1983, "A numerically stable dual method for solving strictly convex quadratic programs," *Math. Programming*, vol.27, pp.1–33.

Heinz, D. C. and C.-I. Chang, 2001, "Fully Constrained Least Squares Linear Spectral Mixture Analysis Method for Material Quantification in Hyperspectral Imagery," *IEEE Trans. on Geoscience and Remote Sensing*, vol.39, pp.529–545.

Iusem, A. N. and A. R. De Pierro, 1987 "A simultaneous iterative method for computing projections onto polyhedra," *SIAM J. Contr. Optim.*, vol.25, pp.231–243.

Ogura, N. and I. Yamada, 2002a, "Non-strictly convex minimization over the fixed point set of the asymptotically shrinking nonexpansive mapping," *to appear in Numer. Funct. Anal. Optim.* , vol.23, Nos.1&2.

Ogura, N. and I. Yamada, 2002b "Non-strictly convex minimization over the fixed point set of the bounded fixed point set of the nonexpansive mapping," *submitted for publication.*

Ren, H. and C.-I. Chang, 2000, "A Generalized Orthogonal Subspace Projection Approach to Unsupervised Multispectral Image Classification," *IEEE Trans. on Geoscience and Remote Sensing*, vol.38, pp.2515–2528.

Settle, J. J., 1993, "Linear Mixing and the Estimation of Ground Cover Proportions," *International Journal of Remote Sensing*, vol.14, 1157–1177.

Settle, J. J., 1996, On the Relationship between Spectral Unmixing and Subspace Projection, *IEEE Trans. on Geoscience and Remote Sensing*,vol.34, pp.1045–1046.

Shimabukuro, Y. E. and J. A. Smith, 1991, "The Least-Squares Mixing Models to Generate Fraction Images Derived from Remote Sensing Multispectral Data," *IEEE Trans. on Geoscience and Remote Sensing*, vol.29, pp.16–20.

Stark, H. and Y. Yang, 1998, *Vector Space Projection – A Numerical Approach to Signal and Image Processing, Neural Nets and Optics*, John Wiley & Sons.

Wolfe, P., 1976, "Finding The Nearest Point in a Polytope," *Math. Prog.*, vol.11, pp.128–149.

Yamada, I., 1999, "Approximation of convexly constrained pseudoinverse by Hybrid steepest descent method," *Proc. of 1999 IEEE International Symposium on Circuits and Systems*, vol.5, pp.37–40.

Yamada, I., 2001, The hybrid steepest descent method for the variational inequality problem over the intersection of fixed point sets of nonexpansive mappings, in *Inherently Parallel Algorithm for Feasibility and Optimization,* (D. Butnariu, Y. Censor, and S. Reich, Eds.), Elsevier.

Yamada, I., N. Ogura, Y. Yamashita and K. Sakaniwa, 1998, "Quadratic optimization of fixed points of nonexpansive mappings in Hilbert space," *Numer. Funct. Anal. Optim.* vol.19, nos.1&2, pp.165–190.

Zeidler, E., 1990, *Nonlinear Functional Analysis and its Applications, II/B — Nonlinear Monotone Operator,* Springer Verlag.

DERIVING QUANTITATIVE MONITORING DATA RELATED TO ACID DRAINAGE USING MULTI-TEMPORAL HYPERSPECTRAL DATA

Cindy Ong[1] and Thomas Cudahy[2]

Acid drainage (AD) has been recognized as one of the major problems facing the Australian mining industry. Much of Australia has a semi-arid to arid climate and is sparsely populated. The impact of AD is therefore less here than in many other countries. Nevertheless, community and shareholder expectations, and the globalization of Australian mining company activities, have ensured the industry is committed to best practice and due diligence in managing AD.

Mapping the spatial extent of the AD affected areas, let alone monitoring the effectiveness of remediation programs has been difficult because of the cost and limitations of current methods. Therefore, low cost, accurate, spatially comprehensive methods for assessing the extent of affected areas, as well as the effectiveness of any subsequent containment and remediation programs is clearly necessary. Swayze et al. (1998) have shown the great potential of AVIRIS imaging spectrometer data for locating acid-generating minerals. However, no such account has been recorded in Australia and the accurate quantification of AD using hyperspectral techniques, such as measurement of surface pH level and the amounts of associated heavy metals, has not yet been demonstrated.

This study aimed to develop and demonstrate operational methods for deriving critical environmental parameters related to AD using hyperspectral data. The study site is the Brukunga abandoned pyrite mine in South Australia where a multi-temporal dataset has been acquired from 1998 to 2001.

1 Introduction

The abandoned Brukunga Pyrite Mine is located in the Mount Lofty Ranges and is 50 kilometers east-south-east of Adelaide, the capital of South Australia. It was developed in the early 1950s to produce pyrite as a source of sulphur for the manufacturing of superphosphate fertilizer. The richest pyrite zones were mined and a concentrate was produced for processing into sulphuric acid at Port Adelaide. The acid was used to convert insoluble rock phosphate into a soluble fertilizer. About 300 000 tons of ore were mined annually, and the pyrite concentrate railed to the Sulphuric Acid Pty Ltd plant at Birkenhead, a northwestern suburb of Adelaide.

Closure of the open pit mining operations in 1972 left large exposed quarry faces and benches, waste rock dumps and tailings from the flotation treatment plant. These, along with natural rock outcrops in the area, contain remnant pyrite that will potentially oxidize and leach high levels of dissolved metals and acids.

A study conducted by Agnew (1994) found that there is potential for 300 000 tons of sulfuric acid to form. The potential health and environmental impact is considered to be one of the largest in Australia as the mine is surrounded by a town site and the nearby Dawesley Creek is used for agricultural and recreational purposes.

2 Methods

2.1 Field and Laboratory Study

The laboratory study was conducted to develop an understanding for the relationships between spectral data and physicochemistry (mineralogy, chemistry, pH). Concurrent with the 1999 airborne acquisition, field samples were collected from 43 locations across the mine environment. These were characterized in the laboratory using an ASD-Field Spec, collecting spectral data in the 350-2500 nm range, and a PIMA-SP, collecting higher resolution spectral data in the 1300-2500 nm SWIR range. Independent measurements of chemistry and mineralogy were made using XRD and chemical analysis from a commercial laboratory to measure heavy metals, pH and electrical conductivity. The pH was measured on the soil samples using a 1:5 ratio sample to water to an accuracy of 0.01.

[1] CSIRO Exploration and Mining (Cindy.Ong@csiro.au)
[2] CSIRO Exploration and Mining (Thomas.Cudahy@csiro.au)

2.2 Airborne data

Airborne hyperspectral data (HyMap (*http://www.intspec.com*) were acquired over the Brukunga Mine in April 1998. The 128 channel HyMap4 data (450-2500 nm) were acquired at 5 meter pixel resolution. Three additional datasets were acquired over the next three years at approximately the same time each year but at 3.5 meter pixel resolution.

Atmospheric correction, bi-directional reflectance distribution functions (BRDF), calibration and cross-calibration are essential issues to be considered when using airborne hyperspectral data for multi-temporal monitoring. The successful implementation of the laboratory results to the airborne data depended on successful cross-calibration of all the datasets. To achieve this, the airborne data were first processed to remove instrument, atmospheric and bi-directional reflectance distribution function (BRDF) effects. The HyMap datasets were reduced to apparent surface reflectances using Atmospheric Correction Now (ACORN) (http://www.aigllc.com). Ground validation data from three man-made invariant sites were collected proximal to the mine site. These targets consist of three homogenous large areas (>15 by 15 m each) of concrete paving bricks, concreted pavement and bitumen. These data were used to remove artifacts associated with incorrectly modeled atmospheric conditions including systematic errors in estimating the water vapor bands at 1400 and 1900 nm, the 760 nm O_2 and the 2050 nm CO_2 features, as well as residual instrument effects.

Instrument wavelength calibration was performed on each year's dataset, hence waveband centers and widths differ for each acquisition. Thus, spectral resampling was performed on the 1998, 1999 and 2000 data to produce comparable results between the four dates. After spectral resampling, each pixel's spectrum was normalized with respect to its own mean reflectance of all wavelengths. The normalization was applied to all the datasets to remove differences seen in the overlaps between adjacent flight lines. These differences are related to residual radiative transfer correction differences, topographic shading and wavelength-independent and multiplicative BRDF effects.

3 Results

3.1 Laboratory Analysis

Partial least squares (PLS) (Haaland et al., 1988) explores for linear correlations between multivariate data and a parameter of interest. In this study, PLS analysis was performed on the VNIR-SWIR spectral data and and pH measurements of the field samples. If a significant linear correlation is found, then the resultant linear comibination of bands that provides this correlation can be used to assess which wavelengths are critical. This linear combination of bands is called the final regression coefficient (FRC), which is a linear combination of weighted spectral bands that transforms each input spectrum to a predicted value of the parameter of interest. The spectral bands showing high FRC weightings, positive or negative, can be interpreted as bands that are important for the related correlation.

Figure 1 shows the results of the partial least squares analysis. To assist in the interpretation of the FRC, typical secondary minerals related to AD, namely ferrihydrite, hematite, goethite and jarosite (plotted in navy, blue, green and cyan, respectively) are also plotted. In this analysis, the wavelength regions with large weightings are centered at 437, 582, 910, 1917 and 2267 nm (black arrows show their location). Relating these high FRCs to spectral attributes of the AD-related secondary minerals, the highest contribution is attributed to the ferric iron absorption band centered at 582 nm caused by a charge transfer absorption (Curtis, 1985). Superimposed on this broad feature is a sharper and smaller excursion of the FRC related to a small feature at 437 nm attributed to jarosite. Equally important is the 910 nm ferrous iron crystal field absorption (Curtis, 1985). It is interesting to note the comparison of the contribution of the combined 910 nm and 437 nm features relative to the 2267 nm jarositefeature, which although has significant weightings, is nonetheless much smaller. Taken altogether, this result implies that pH predictions are related primarily to ferric iron mineralogy. Given that much of the correlation is driven by the wavelengths less than 550 nm, it is important that additive atmospheric effects are properly corrected when applying these FRCs to remotely sensed data. Note that the high FRC weightings at 1917 nm, related to water, would not be detectable in airborne data because of strong atmospheric absorption.

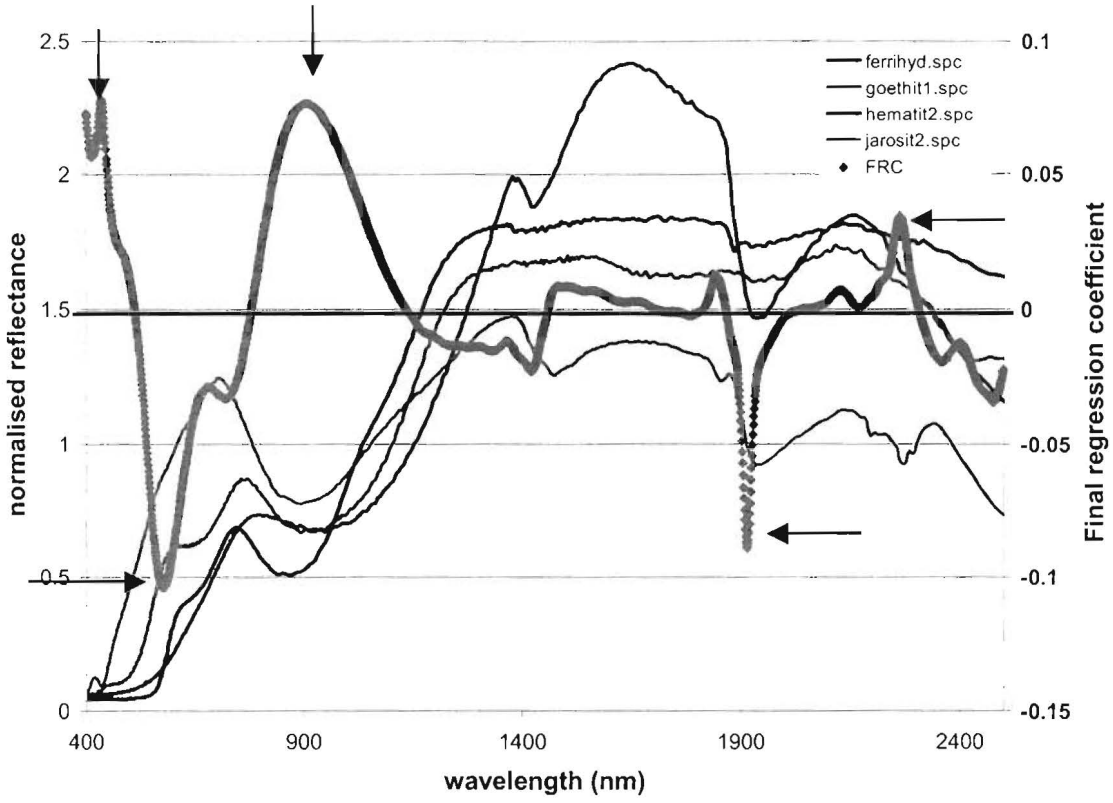

Figure 1: Final regression coefficient results from partial least squares analysis of pH (red) and spectra plotted in conjunction with typical AD related secondary minerals (blue, dark blue, cyan and dark green). The arrows illustrate high coefficients.

3.2 Airborne data

The result from the laboratory analysis was used to enable predictions of pH from the fully corrected and calibrated airborne hyperspectral imagery. The resultant pH maps are shown on Figure 2. Spectral-based masking was applied to the derived products in order to remove small commission problems, including man made materials in the township and areas of standing water. All pixels with pH >7 were also masked. These relate essentially to pixels with a significant vegetation component. The four dates of predicted pH maps are presented over gray-scale albedo image backgrounds in Figure 2. These are color coded for the range of pH values from <2 to 7 from red through to blue.

These predicted maps of surface pH effectively demonstrate the capabilities of airborne hyperspectral data for spatially mapping of critical AD information over a multi-temporal sequence. This series of maps can then be used to assess the success of rehabilitation and/or remediation procedures used as part of the mine environment management practices over the four years. For example, they may be used to assess the remediation efforts at the North-Eastern waste rock dump (marked A on Figure 2) identified previously to potentially be acid generating materials. The multi-temporal sequence shows this area to contain pH of 4-6 and this value remains constant over the monitoring period possibly showing this area to be of a fairly stable nature. Conversely, another example is the mine benches that span the Western extent of the mine and marked B on Figure 2. Major changes are mapped in this area over the four years evolving from an average pH value of 4-6 to pH of 4 and below. This sequence of pH maps is able to map the spatial extent of the areas that may need further attention or evaluation of remediation strategies as well as determine the acid generating potential of these affected areas. .

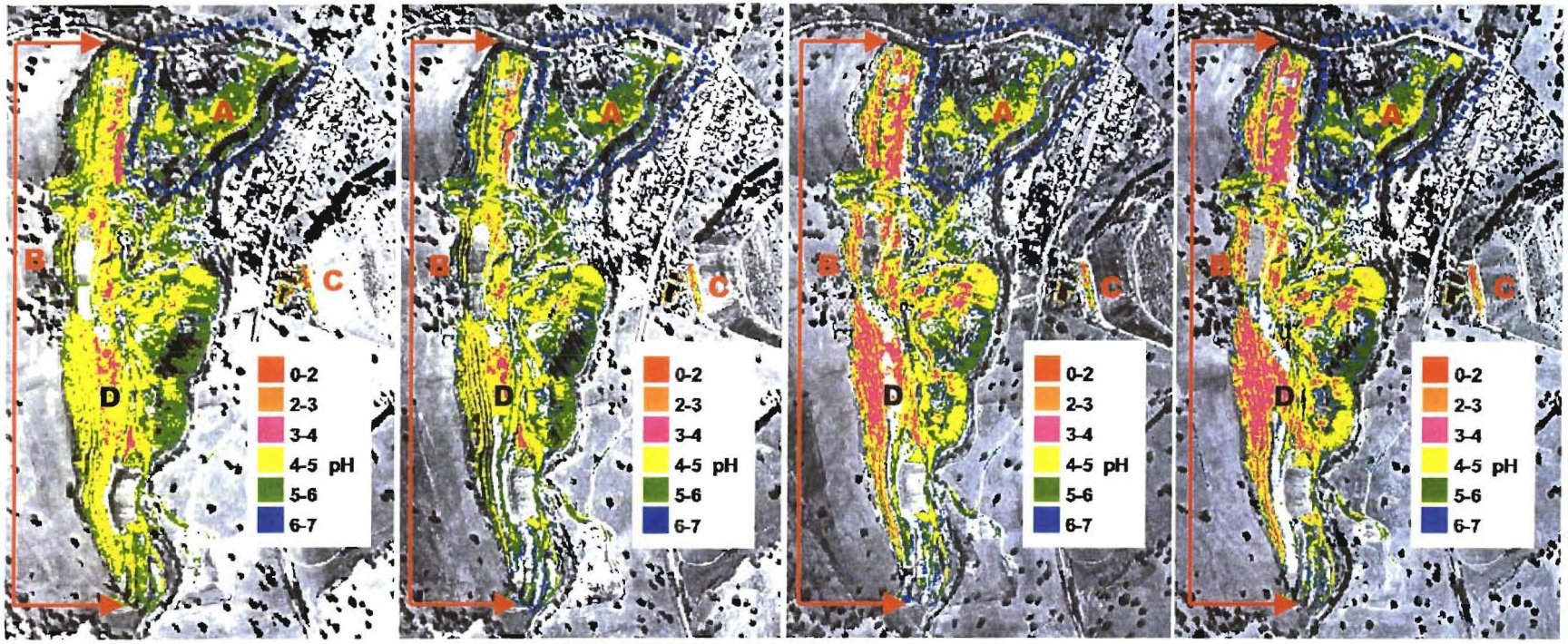

Figure 2: Time series pH predictions derived from hyperspectral data collected between 1998 to 2001. A marks the North Western waste rock dump and B marks the mine benches.

3.3 Validation of pH maps

The accuracy of the 1999 map was checked with laboratory pH measurements of field samples collected also in 1999. The first validation site consists of samples collected along a wall of a filled tailings dam at the site of the acid treatment facility (Site C in Figure 2). The pH mean and STD of samples is pH 2.31 +/- 0.44 which is consistent with the mean airborne prediction for this site of pH 2.4. The airborne and field spectra of this site also compares well, with both showing jarosite-related ferric iron absorption at 930 nm and jarosite-related hydroxyl absorption at 2265 nm. The second validation site was a transect along a mine bench (Site D in Figure 2). A total of 10 samples were collected along this transect. Comparing the transect data and the pH map, there is good correlation between the airborne predicted (pH 4.50 +/- 0.45) and field sample (pH 4.05 +/- 0.51) pH values.

4 Discussion and conclusion

The results from the laboratory study showed that pH is related to iron mineralogy. From this information, a model was developed to predict pH from hyperspectral data. It was shown that it is possible to use this laboratory-derived model to produce pH maps from a multi-temporal airborne hyperspectral dataset. However, for predictions of pH to be accurately derived from the airborne spectral data or other ground spectral data, apart from those that formed the calibration set, it is important that proper calibration of the dataset to accurate ground reflectances be obtained. Cross-calibration between airborne and laboratory sensors are also important considerations.

It was shown that is it possible to derived maps of pH from a multi-temporal dataset using the pH model developed in the laboratory. However, to be able to use the data in a quantitative manner, further work has to be undertaken. This include for the laboratory investigations: (1) the collection of a comprehensive set of calibration and validation data to build a robust model for the predictions of pH from these data; (2) understanding the secondary minerals produced from AD; and (3) the changes related to environmental conditions; and for the airborne processing: (4) methods for proper correction of the airborne dataset to accurate ground reflectances especially in view of the stability of the VIS region for mapping iron mineralogy.

5 References

Agnew, M. (1994): Weathering products and geochemistry of waste residues at the Brukunga Pyrite Mine, Adelaide Hills, S.A. in relation to environmental impacts. – Honors thesis, Dept. of Geology and Geophysics, University of Adelaide

Curtis, B. (1985) Evaluation of the physical properties of naturally occurring iron (III) oxyhydroxides on rock surfaces in arid and semi-arid regions using visible and near infrared spectroscopy. PhD thesis, University of Washington.

Haaland, D.M. and Thomas, E.V. (1988) Partial Least Squares. Anal. Chem., 60, 1193-1200.

Swayze, G.A., Clark, R.N., Smith, K.S., Hagemann, P.L., Sutley, S.J., Pearson, R.M. (1998): Using Imaging Spectroscopy to Cost-Effectively Locate Acid-Generating Minerals at Mine Sites: An Example from the California Gulch Superfund Site in Leadville, Colorado. - Summaries of the 7th JPL Airborne Earth Science Workshop, JPL Publ. 97-21, Vol. 1: 385-389

USING AVIRIS IMAGERY TO MAP INVASIVE PLANTS ON RANGELANDS: LEAFY SPURGE IN NORTHEASTERN WYOMING

Amy Parker Williams
Department of Botany
University of Wyoming
Laramie, Wyoming
and
E. Raymond Hunt, Jr.*
Hydrology and Remote Sensing Laboratory
USDA Agricultural Research Service
Beltsville, Maryland

1.0 INTRODUCTION

Invasions of exotic organisms have been proposed as one of the largest components of global environmental change, second only to habitat destruction (Vitousek et al. 1996). Leafy spurge, *Euphorbia esula* L. (sensu lato), is only one of hundreds of successful exotic plant species that have invaded North America. It is an adventive, perennial weed that infests approximately 1.2 million hectares of land in North America (Lajeuness et al. 1999). Its distribution includes the northern Great Plains of the U.S. and the prairie provinces of Canada (DeLoach 1997). It often forms dense stands that displace native vegetation and useful forage plants on rangelands and in riparian habitats. Infestations of leafy spurge destroy the quality of grazing lands for cattle and horses (Hein and Miller 1992), degrade the forage base and structure of wildlife habitat (Trammell and Butler 1995), decrease plant diversity (Belcher and Wilson 1989), and reduce land value (Leistritz et al. 1992).

Using remotely sensed data to map leafy spurge would provide a valuable tool for documenting leafy spurge distribution and infestation levels over larger regional areas. Differentiation of individual green plant species can be problematic because all green plants have similar spectral characteristics. Leafy spurge is a good candidate for detection via remote sensing because the distinctive yellow-green color of its bracts is spectrally unique when compared to the co-occurring green vegetation (Everitt et al. 1995). Because spectral detail is necessary for differentiating similar materials, high spectral resolution data is the most appropriate data for mapping individual plant species with a high level of accuracy and precision (Clark et al. 1995). Imaging spectrometers, or hyperspectral sensors, provide remotely sensed data in which each pixel in the image has a detailed set of reflectance values that allow interpretation of the pixel's spectrum. From its spectrum two primary characteristics can be identified, the physical materials of which the pixel is composed on the ground, and a quantitative estimate of their abundances. By using spectral mixture analysis to model each pixel spectrum as a linear combination of a finite number of spectrally distinct signatures or "endmembers," subpixel estimates of endmember abundance can be obtained (Adams et al. 1985, Smith et al. 1990). The main goal of this research was to map leafy spurge from hyperspectral imagery using spectral mixture analysis to obtain sub-pixel estimates of leafy spurge cover. This was compared to ground estimates of leafy spurge cover to assess the ability of hyperspectral remote sensing data to estimate leafy spurge cover.

2.0 METHODS

2.1 RESEARCH AREA

The study area for this research is in Crook County in northeastern Wyoming, on the northwestern edge of the Black Hills, a small mountain range that extends from northeastern Wyoming southeast into western South Dakota. It consists of approximately 65 square-kilometers of private land about 8 kilometers west of Devils Tower National Monument (DTNM). The land is used extensively for livestock grazing (cattle and sheep) with some areas of dryland farming and hay production.

*Building 007 Room 104, 10300 Baltimore Ave., Beltsville, Maryland 20705 (email: erhunt@hydrolab.arsusda.gov)

The vegetation of the study area is a mosaic of ponderosa pine (*Pinus ponderosa*) communities, grasslands, sagebrush-grasslands, and pine-juniper (*Juniperus scopulorum*) woodlands. Riparian areas are characterized by willow (*Salix* spp.) and plains cottonwood (*Populus deltoides*) communities, with bur oak (*Quercus macrocarpa*) and green ash (*Fraxinus pennsylvania*) commonly occurring in draws. Elevations in the study area range from 1219 m along the Belle Fourche River to 1584 m at Missouri Buttes along the northern border of the study area. The average annual precipitation is 442 mm. Leafy spurge is very well established in most of the study area.

2.2 ACQUISITION AND ATMOSPHERIC CORRECTION OF AVIRIS IMAGERY

Airborne Visible / Infrared Imaging Spectrometer (AVIRIS) imagery was acquired over the study area in northeastern Wyoming on July 6, 1999. The imagery was from a NASA ER-2 aircraft flown at an altitude of 20 km with each pixel representing a ground area of approximately 20 x 20 m (Green et al. 1998). Each AVIRIS scene was first radiometrically corrected by the Jet Propulsion Laboratory. It was atmospherically corrected to apparent surface reflectance using Version 3.1 of the ATmosphere REMoval Program, or ATREM (Gao et al. 1993, Goetz et al. 1997). Due to the limited range of field spectroradiometer data (350 – 1050 nm) and to absorption artifacts in the corrected AVIRIS data, a spectral subsample of the AVIRIS data was taken. AVIRIS bands 6 through 68 (418 – 1000 nm) were used in the final analysis. A visual comparison of AVIRIS reflectance spectra with ground reflectance spectra (Fig. 1) showed very good correspondence; therefore, we did not perform further image correction.

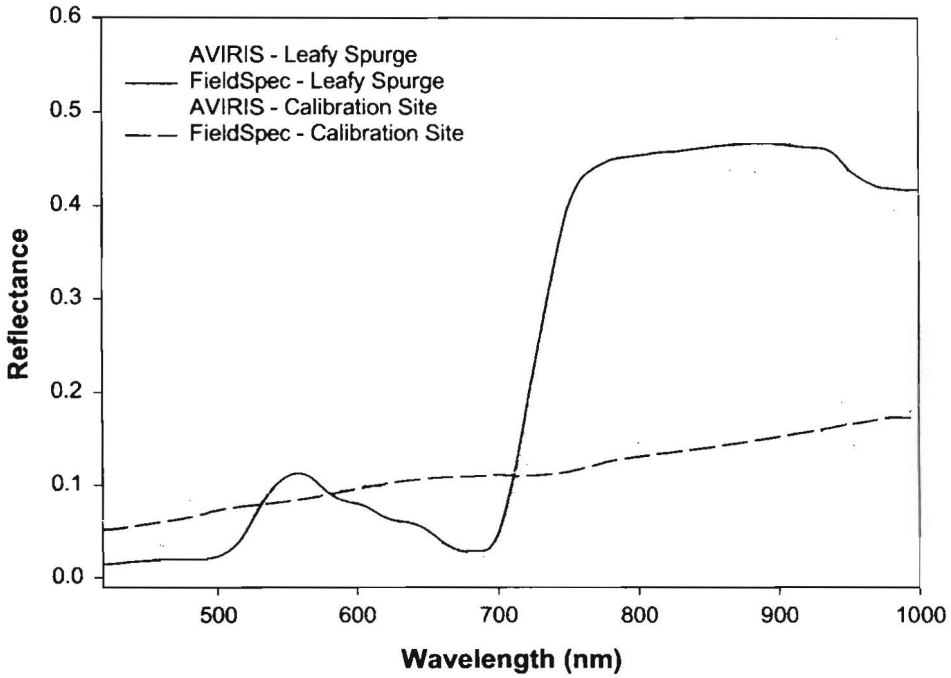

Figure 1. Correspondence of corrected Airborne Visible / Infrared Imaging Spectrometer (AVIRIS) data with averaged field spectroradiometer data.

2.3 FIELD SPECTRORADIOMETRY

Field spectroradiometer data were collected in late June 1999 about two weeks before the AVIRIS data acquisition between 10:00 am and 2:00 pm on a clear, sunny day similar to the weather and sky conditions on the day of the AVIRIS overflight. Field reflectance spectra were acquired using an Analytical Spectral Devices, Inc. (ASD, Boulder, Colorado) FieldSpec UV/VNIR Spectroradiometer. It was not possible to collect field spectroradiometer data on the day of the AVIRIS overflight due to the unavailability of the ASD spectroradiometer.

The ASD FieldSpec UV/VNIR acquires continuous spectra from 350 nm to 1050 nm. Dark current (property of the detector) and white reference (Spectralon panel) corrections were made approximately every 2-3 minutes. Each spectrum acquired in the field consisted of 25 individual measurements taken consecutively and averaged by the

FieldSpec. Measurements were acquired using the bare tip of the fiber optic cable, which had a 25 degree field of view (FOV). All measurements were made with the optic tip about 1.3 m above the target material resulting in a FOV diameter of about 0.50 m.

The final spectrum for each material in the field was calculated through postprocessing, which consisted of examining sets of 10 of the averaged field spectra, removing any extreme outliers, and averaging the remaining spectra. All field spectra were resampled to match the wavelengths and bandpass of the AVIRIS data, based on the 1999 wavelength calibration file supplied by JPL.

Two spatially and spectrally homogenous ground calibration sites were used in this study including a large gravel natural gas pumping station compound and the boulder field surrounding the base of Devils Tower. Each ground calibration site was characterized using the ASD FieldSpec Spectroradiometer along a series of transects with measurements being taken approximately every 5 meters using the same methods described previously.

2.4 GROUND DATA COLLECTION OF LEAFY SPURGE COVER

During 1999, the same year the AVIRIS data were acquired, extensive ground data collection was performed on field vegetation plots. Data were collected during the 2 weeks prior to and the 2 weeks following the AVIRIS flight. The ground plots were part of a concurrent study that documented leafy spurge percent cover in detail (Parker Williams 2001). The 67 circular vegetation plots had a radius of 23 meters and were located within areas of leafy spurge infestation. Each plot's location was recorded using a selective availability encoded Rockwell Precision Federal Global Positioning System (GPS) unit (Rockwell International Corporation, Cedar Rapids, Iowa) and digital orthophotoquads. These locations were transferred onto the AVIRIS imagery from a digital orthophoto quad with an estimated positional error of 1 pixel. It has been shown that positional error results in conservative bias of image assessments (Verbyla and Hammond 1995); therefore, the unavoidable positional error introduced into this assessment would result in lower, or conservative, correspondence between AVIRIS and ground estimates of leafy spurge cover.

Each plot was also classified on the ground into three different topographical position types, riparian, draw, or upland, and into two different vegetation types, woodland or prairie. Leafy spurge cover was estimated using broad cover classes (0-5%, 5-25%, 25-50%, 50-75%, 75-95%, and 95-100%) for five, randomly located 1-by-2-meter subplots. The mid-point value of the cover class was recorded as the leafy spurge cover for that sub-plot. Sub-plot values were then averaged to obtain an estimate of leafy spurge cover for the plot.

2.5 IMAGE PROCESSING AND ANALYSIS

The purpose of this research was to map and document leafy spurge using clear, repeatable methodology. With this goal in mind, it was unnecessary to spend time and resources trying to account for and classify all other materials and vegetation in the imagery. Therefore, Mixture Tuned Matched Filtering (MTMF) a specialized type of spectral mixture analysis was used. MTMF performs a "partial" unmixing by only finding the abundances of a few user-defined endmembers and not requiring that all image endmembers be identified (Harsanyi and Chang 1994).

With the goal of isolating and identifying the leafy spurge endmember, the AVIRIS reflectance image was used as input into the minimum noise fraction (MNF) transformation (Green et al. 1988, Lee et al. 1990). The first twelve MNF transforms were carried forward in the analysis. Eigenvalues decreased and noise increased substantially after MNF transform twelve. To identify potential endmembers in the AVIRIS imagery, the 12 MNF transforms were used as input into a Pixel Purity Index (PPI) analysis (Boardman et al. 1995). A relatively high number of iterations (3,000) and a high PPI threshold value (5) were used to eliminate large numbers of pixels and to emphasize the unique pixels. The output of "pure" pixels from the PPI procedure was examined using multidimensional visualization software (RSI 1999). Pixels were interactively clustered and grouped based on their spatial relationship to each other and upon examination of their spectral signatures. All groups of pixels that did not contain a vegetation component as identified by their spectral signatures were removed from the multidimensional plot space, allowing finer discrimination of different vegetation pixels. The spectral signatures of each remaining pixel group were systematically compared to the resampled field spectra. The average spectral signature of a tightly clustered group of pixels matched the field spectra for leafy spurge. Leafy spurge's unique color in the visible (green to red wavelengths) and NIR wavelength regions was sufficient to differentiate it from other green vegetation. The leafy spurge endmember was used as the endmember of interest in a Mixture Tuned Matched Filtering (MTMF) analysis. This procedure was performed on two AVIRIS scenes (approximately 11 km x 9 km) acquired over the study area.

In order to assess the variation between remotely-sensed and ground-measured cover of leafy spurge, data were stratified by both topographic position (riparian, draw, or upland) and vegetation type (woodland or prairie). The draw and riparian strata were combined due to a small sample size of riparian sites in the AVIRIS imagery. The relationships between MTMF estimates of sub-pixel leafy spurge abundance and ground estimates of leafy spurge cover were examined using simple linear regression analysis for all sites and for sites in each strata.

3.0 RESULTS AND DISCUSSION

3.1 FIELD SPECTRORADIOMETRY

Field spectroradiometer data collected in the study area showed that the reflectance spectrum of leafy spurge differed from other types of common green vegetation (Fig. 2). It was easily differentiated based primarily on values in the 500-700 nm wavelength region. Leafy spurge was consistently brighter than other vegetation between 500 and 650 nm. It also differed from other vegetation in the shape and magnitude of the characteristic chlorophyll absorption features between 550-685 nm.

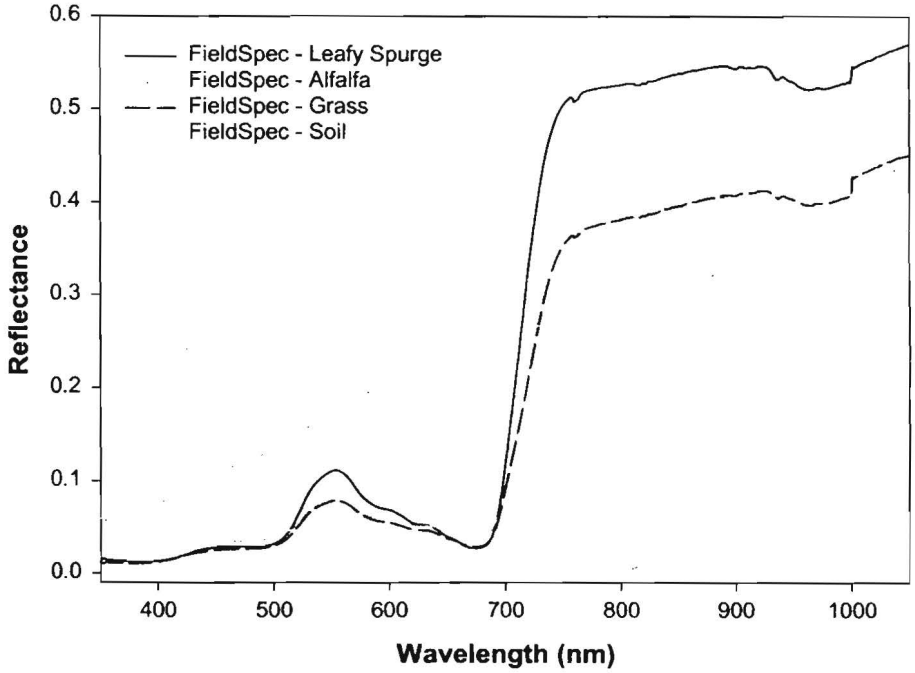

Figure 2. Comparison of averaged field spectra for vegetation and soils.

3.2 MIXTURE TUNED MATCHED FILTERING FRACTION IMAGES

The output from the mixture tuned matched filtering (MTMF) analysis was a fraction image with values for each pixel representing the relative sub-pixel abundance of leafy spurge, and an infeasibility image with values ranging from 1-12. Pixels with a high fraction value and a low infeasibility value (< 6) had a high percent cover of leafy spurge, while those with high infeasibility values were not classified as leafy spurge. All ground sites used for the MTMF comparison were located in leafy spurge infestations, and all of these sites were classified as leafy spurge in the analysis.

Overall performance of the MTMF for estimating percent cover of leafy spurge for all sites was good (Fig. 3, $r^2 = 0.69$). A definite linear relationship exists between the MTMF fraction and the ground cover estimate. The ability to discriminate leafy spurge and achieve good estimates of canopy cover may be due to the unique growth habit and color of the bracts, which are closely packed and oriented upwards, forming a dense uniform canopy that reduces shadows and de-emphasizes the contribution of green leaves to the reflectance spectrum.

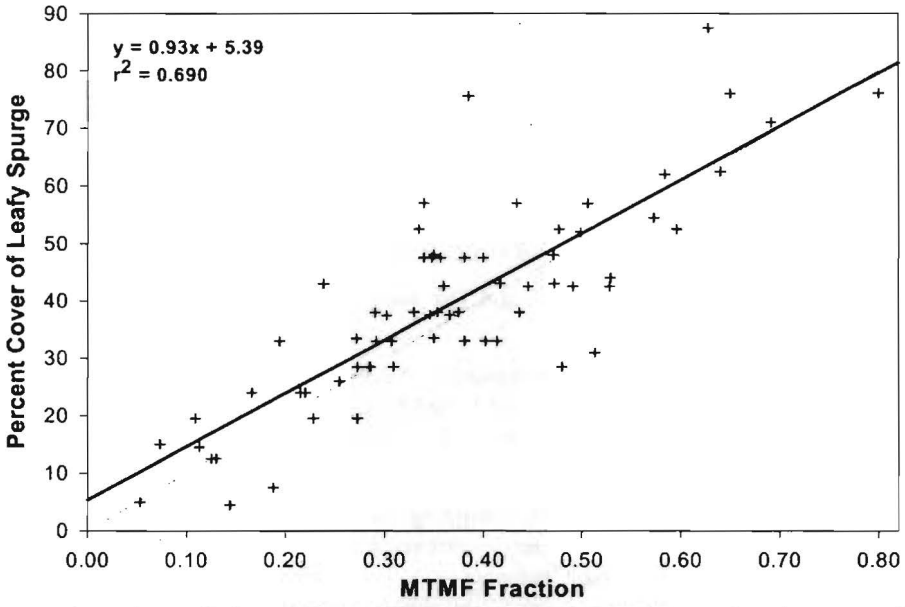

Figure 3. Regression of MTMF fraction values vs. percent canopy cover of leafy spurge from all ground data.

3.3 EFFECT OF TOPOGRAPHIC POSITION AND VEGETATION TYPE

Leafy spurge cover in sites located in draws and riparian areas ($r^2 = 0.72$) was estimated slightly better than those located in upland areas ($r^2 = 0.68$). Cover was also generally higher in draw and riparian sites than in upland sites. The better estimation of cover in draw and riparian sites may be due in part to variability in leafy spurge phenology in upland sites where moisture was less available in late June and July than in more mesic draw and riparian sites. As the summer progresses, leafy spurge bracts lose their distinctive yellow-green color and the plant is not as easily distinguished from other green vegetation.

The MTMF analysis performed very well on sites located in areas of prairie, which included all sites not in the woodland type ($r^2 = 0.79$). In contrast, the MTMF analysis performed poorly in estimating leafy spurge cover in woodland areas ($r^2 = 0.57$). These sites also had the largest variance of any of the types. This may be explained in relation to tree canopy obscuring detection from an aerial perspective and variations in tree canopy cover and view angle between sites. Materials are often obscured by forest canopies, especially when viewed at off-nadir angles. Also, positional error in woodland areas may have a larger effect on image to ground correspondence than in non-wooded prairie. However, the fact that leafy spurge can be detected in woodland areas at all is an encouraging demonstration of MTMF.

4.0 CONCLUSIONS

Mixture tuned matched filtering (MTMF) has been reported as a superior method for detection of materials in hyperspectral imagery. It can outperform spectral mixture modeling and matched filtering, especially in cases of subtle, sub-pixel occurrences (Boardman 1998). It also has the added advantage in cases of mapping individual materials of not requiring identification of all potential endmembers. MTMF performed very well for mapping leafy spurge and estimating leafy spurge canopy cover. Its sensitivity for detecting and estimating leafy spurge were surprising. Leafy spurge has several characteristics that make it an ideal species for detection from remotely sensed data, so caution must be fostered when considering mapping other invasive species using hyperspectral data. Leafy spurge grows in large dominant stands, is a robust plant with a dense canopy, and has a distinctive color for a several week period during the growing season. All of these factors make it easier to map than many other invasive species. Its habit of forming large uniform stands with a dense canopy also ameliorate problems of positional error and non-linear spectral mixing, allowing good prediction. There was also a certain amount of uncertainty in the ground data collection, because it involved estimates using broad cover classes. However, keeping these things in perspective, mapping leafy spurge using hyperspectral remote sensing data is feasible and reasonably accurate for estimating

percent cover in broad cover classes. Obviously, mapping leafy spurge under tree canopies is problematic. Although this is one limitation of the method, results demonstrated that in open canopies that have leafy spurge growing in the understory, it dominates the spectral signature sufficiently to be detectable. The techniques presented here could possibly be used for constructing leafy spurge distribution and abundance maps with satellite hyperspectral data for larger regional areas.

5.0 REFERENCES

Adams, J. B., M. O. Smith, and P. E. Johnson, 1985, "Spectral Mixture Modeling: A New Analysis of Rock and Soil Types at the Viking Lander I Site," Journal of Geophysical Research, vol. 91, pp. 8098-8112.

Belcher, J. W. and S. D. Wilson, 1989, "Leafy Spurge and The Species Composition of A Mixed-Grass Prairie," Journal of Range Management, vol. 42, pp. 172-175.

Boardman, J. W., 1988. "Leveraging The High Dimensionality of AVIRIS Data for Improved Sub-Pixel Target Unmixing and Rejection of False Positives: Mixture Tuned Matched Filtering," In: Proceedings, Eighth JPL Airborne Geoscience Workshop, JPL Publication 98-1(1). NASA Jet Propulsion Laboratory, Pasadena, California.

Boardman, J. W., F. A. Kruse, and R. O. Green, 1995, "Mapping Target Signatures Via Partial Unmixing of AVIRIS Data," In *Summaries, Fifth JPL Airborne Geoscience Workshop*, JPL Publication 95-1(1):23-26, NASA Jet Propulsion Laboratory, Pasadena, California.

Clark, R. N., T. V. V. King, C. Ager, and G. A. Swayze, 1995, "Initial Vegetation Species and Senescence/Stress Mapping in The San Luis Valley, Colorado Using Imaging Spectrometer Data. In: Proceedings: Summitville Forum '95, eds, H. H. Posey, J. A. Pendelton, and D. Van Zyl,, Colorado Geological Survey Special Publication 38, pp. 64-69.

DeLoach, C. J., 1997, "Biological Control of Weeds in the United States and Canada," In: Assessment and Management of Plant Invasions, eds, J. O. Luken and J.W. Thieret, Springer-Verlag, New York, pp. 172-194.

Everitt, J. H., G. L. Anderson, D. E. Escobar, M. R. Davis, N. R. Spencer, and R. J. Andrascik, 1995, "Use of Remote Sensing for Detecting and Mapping Leafy Spurge (*Euphorbia esula*)," Weed Technology, vol. 9, pp. 599-609.

Gao, B.-C., K. B. Heidebrecht, and A. F. H. Goetz, 1993, "Derivation of Scaled Surface Reflectances From AVIRIS Data," Remote Sensing of Environment, vol. 44, pp. 145-163.

Goetz, A. F. H., J. W. Boardman, B. Kindel and K. B. Heidebrecht, 1997, "Atmospheric Corrections: On Deriving Surface Reflectance From Hyperspectral Imagers," In: Proceedings SPIE Annual Meeting, vol. 3118, pp. 14-22.

Green, R. O., M. L. Eastwood, and O. Williams, 1998, "Imaging Spectroscopy and the Airborne Visible/Infrared Imaging Spectrometer (AVIRIS)," Remote Sensing of Environment, vol. 65, no. 3, pp. 227-248.

Green, A. A., M. Berman, P. Switzer, and M. D Craig, 1988, "A Transformation for Ordering Multispectral Data in Terms of Image Quality With Implications For Noise Removal," IEEE Transactions on Geoscience and Remote Sensing, vol. 26, no. 1, pp. 65-74.

Harsanyi, J. C., and C. Chang, 1994, "Hyperspectral Image Classification and Dimensionality Reduction: An Orthogonal Subspace Projection Approach," IEEE Transactions on Geoscience and Remote Sensing, vol. 32, no. 4, pp. 779-785.

Hein, D. G., and S. D. Miller, 1992, "Influence of Leafy Spurge on Forage Utilization By Cattle," Journal of Range Management, vol. 45, pp. 405-407.

Lajeuness, S., R. Sheley, C. Duncan, and R. Lym, 1999. "Leafy Spurge," In: Biology and Management of Noxious Rangeland Weeds, eds, R. L. Sheley and J. K. Petroff, Oregon State University Press, Corvallis, pp. 249-260.

Lee, J. B., A. S. Woodyatt, and M. Berman, 1990, "Enhancement of High Spectral Resolution Remote-Sensing Data by A Noise-adjusted Principal Components Transform." IEEE Transactions on Geoscience and Remote Sensing, vol. 28, no. 3, pp. 295-304.

Leistritz, F. L., D. E. Bangsund, and J. A. Leitch, 1992, "Economic Impact of Leafy Spurge (*Euphorbia esula*) in North Dakota," Weed Science, vol. 40, pp. 275-280.

Parker Williams, A. E., 2001, Biological Control and Hyperspectral Remote Sensing of Leafy Spurge (Euphorbia esula L.), an Exotic Plant Species in North America, Ph.D. Dissertation, Department of Botany, University of Wyoming, Laramie, 134 pp.

RSI, 1999, ENVI, The Environment for Visualizing Images, Version 3.2, Research Systems, Inc., Boulder, Colorado.

Smith, M. O., S. L. Ustin, J. B. Adams, and A. R. Gillespie, 1990, "Vegetation in Deserts: I. A Regional Measure of Abundance From Multispectral Images," Remote Sensing of Environment, vol. 31, pp. 1-26.

Trammell, M. A., and J. L. Butler, 1995, "Effects of Exotic Plants on Native Ungulate Use of Habitat," Journal of Wildlife Management, vol. 59, no. 4, pp. 808-816.

Verbyla, D. L., and T. O. Hammond, 1995, "Conservative Bias in Classification Accuracy Assessment Due to Pixel-by-Pixel Comparison of Classified Images With Reference Grids," International Journal of Remote Sensing, vol. 16, no. 3, pp. 581-587.

Vitousek, P. M., C. M. D'Antonio, L. L. Loope, and R. Westbrooks, 1996, "Biological Invasions As Global Environmental Change," American Scientist, vol. 84, pp. 468-478.

BAND RATIOS AS A RECONNAISSANCE TOOL FOR HYPERSPECTRAL DATA

Brian S. Penn
Boeing-Autometric
Colorado Springs, Colorado
brian.s.penn@boeing.com

INTRODUCTION

There are now established procedures for extracting information from hyperspectral imagery data. The Environment for Visualizing Images (ENVI) from Research Systems, Inc. it the *defacto* hyperspectral image processing software package. The following are general steps for exploiting hyperspectral imagery (HSI) data when using ENVI:

1. Compensate for atmospheric interference. The most commonly used program is the Atmospheric Removal (ATREM) program (Gao and Goetz, 1990; CSES, 1999; Gao, Heidbrecht, and Goetz, 1999).
2. Reduce the dimensionality of the data set using a Minimum Noise Transformation Boardman and Kruse (1994);
3. Find the purest pixels (apices for a hypervolume enclosing the *N*-dimensional dataset) in the hypercube representing end-members in the data set and selecting the pixels with the highest probability of being end-members (Boardman, Kruse, and Green, 1995);
4. Visualizing the highest probability end-member pixels by projecting them into two-dimensional space (Boardman, Kruse, and Green, 1995);
5. Linearly unmix the remaining pixels based on the end-members. Map the results to show relative proportions using Matched Filters, Mixture Tuned Matched Filtering™, Spectral Angle Mapper™, or some other classification procedure.

This is the most widely used approach for working with hyperspectral data by researchers external to the U.S.G.S. Spectroscopy Laboratory. The U.S.G.S. Spectroscopy Laboratory developed its own HSI image processing software. Their program, called Tetracorder, uses a significantly different paradigm to extract information from HSI data. Both ENVI and Tetracorder have much in common, but there are significant fundamental differences. Some of those differences are explored in Penn and Livo (2001).

There are other ways to extract information from HSI data. One such method uses ratios of hyperspectral data. Band ratios have been used extensively for manipulating multispectral data, but have never been embraced by the HSI community. The purpose of this paper is to present a quantitative basis for using band ratios, focusing on the optimal conditions for using band ratios.

Band ratios represent an opportunity to eliminate false-assumptions and over generalizations from the process of atmospheric removal and subsequent spectral processing. In fact, it is shown in this paper how the proper use of band ratios obviates the need for atmospheric correction for HSI data.

RADIOMETRIC CONCEPTS

The total solar irradiance reaching the earth's surface is equal to:

$$E_g = \int_{\lambda_1}^{\lambda_2} (E_{0\lambda} T_{\theta_0} \cos\theta_0 + E_{d\lambda}) d\lambda \quad (1)$$

where E_g is the global irradiance on the surface, $E_{0\lambda}$ is the spectral solar irradiance at the top of the atmosphere, $T\theta_0$ is the atmospheric transmittance at angle θ, $E_{d\lambda}$ is the spectral diffuse sky irradiance

Radiance is defined as the sum of the energy measured at the sensor including contributions from all the areas within the instantaneous field of view (IFOV), i.e., the target, surrounding areas, and the various scattering components of the atmosphere. The total radiance reaching the sensor (L_S) is the sum of the light from the target (L_T) and the contribution from the path radiance (L_P). Therefore,

$$L_S = L_P + L_T \quad (\text{W/m}^2/\text{sr}) \quad (2)$$

and,

$$L_T = L_I + L_A \quad (\text{W/m}^2/\text{sr}) \quad (3)$$

where L_I is equal to the radiance directly reflected from the target and L_A is the atmospheric contribution to the radiance coming from the target. Path radiance is the contribution to the total radiance at the sensor derived from scattering in the atmosphere and light from areas other than the target area. Also, the path radiance is not simply equal to the atmospheric contribution to the L_I, $L_A \neq L_P$, passing through the atmosphere to the sensor. A summarization of methods for computing path radiance are found in Turner and Spencer (1972), Turner (1975, 1978), and Foster (1984).

The actual amount of radiance reflected to the sensor from the target is very small and is equal to:

$$L_T = \tfrac{1}{\pi} \int_{\lambda_1}^{\lambda_2} R T_{\theta_v} \left(E_{0\lambda} T_{\theta_0} \cos\theta_0 + E_{d\lambda}\right) d\lambda \quad (\text{W/m}^2/\text{sr}) \quad (4)$$

Vincent (1997) modifies equation (4) by adding a unitless multiplicative S factor called the "shadow/slope" factor. The S factor is closely related to the bi-directional reflectance function (BDRF), i.e., all surfaces are non-Lambertian reflectors. Most equations concerning atmospheric compensation ignore this aspect of radiance calculations. The S factor is unique for each part of the earth's surface and makes a significant contribution to L_S. Vincent (1997) also adds sensor specific contributions to the L_S, including electronic gain as a multiplicative factor and electronic offset as an additive factor.

No known atmospheric models account for the contributions of these last three factors primarily because the first is completely unknown and the last two are sensor dependent. If the sensor is calibrated, then the gains and offsets for each channel are known and can be applied to the data. Vincent and Thomson (1972) helped pioneer the use of band ratios to deal with the S factor in HSI data.

DISCUSSION – CONVERTING RADIANCE TO REFLECTANCE

The previous sections on atmospheric compensation are designed to outline common thinking for converting radiance values to reflectance values. Many members of the HSI community work exclusively in the reflectance domain to the exclusion of radiance. Significant misunderstandings have occurred over the veracity of using radiance versus reflectance data. The basis for the current bias toward reflectance data has its roots in the origins of HSI. The "founders" of hyperspectral imaging at JPL (Gregg Vane, Alexander Goetz, Larry Rowan, etc.) and Johns Hopkins (Graham Hunt and John Salisbury) either were geologists by training, or had a strong geologic mindset. Consequently their interests in spectroscopy were directed to minerals. Using a Nicolet 5 DXB, Nicolet System 510 interferometer spectrometer or a Beckman 5270 Spectrometer (2 nm spectral sampling resolution) reflected light spectrum for specific minerals were measured under laboratory conditions. Once the airborne imaging spectrometers were built and flown, the desire was to relate the signals collected at altitude to the laboratory spectra for individual minerals. The logical approach was to model and remove the atmospheric contribution from the radiance data to make the signal look more like the spectra collected in the laboratory. Atmospheric models such as 6S, LOWTRAN, MODTRAN, etc. were developed to remove the atmospheric effects based on radiative transfer theory. Most atmospheric models such as LOWTRAN, MODTRAN, etc., generate a series of offsets and gains to be applied across an entire image to convert radiance data to reflectance data.

The heterogenous nature of the Earth's atmosphere requires atmospheric corrections be done on a pixel-by-pixel basis (Gao and Goetz, 1990). The development of the Atmosphere Removal (ATREM) program resulted from this idea (Gao, Heidebrecht, and Goetz, 1999). ATREM is presented here as an example of one of the premier atmospheric compensation models. Other models are based on similar physical principles and/or have less fidelity than ATREM.

ATREM has three specific assumptions (Gao, Heidebrecht, and Goetz, 1999): 1) the reflecting surface is horizontal; 2) the surface is a Lambertian reflector, i.e., light is reflected equally in all directions; and 3) CO_2, CO, CH_4, O_2, O_3, and N_2O are uniform across a hyperspectral scene (H_2O varies both spatially, vertically, and temporally).

ATREM has two shortcomings:

1. ATREM overcorrects in the blue wavelengths. The over correction in the blue wavelengths must be manually fixed.
2. To correctly generate reflectance data using ATREM, a user must go to the field and collect representative spectra using a handheld spectroradiometer either during the overflight or as soon as possible thereafter. Using the spectra gathered in the field, a series of gains and offsets are generated and applied to the output reflectance data from ATREM.

As stated in the ATREM User's Manual, ATREM uses an "approximate atmospheric radiative transfer model." Of the thirty or so atmospheric gases, only seven (H_2O, CO_2, CO, CH_4, O_2, O_3, and N_2O) have significant features in the 0.4-2.5 um region. ATREM focuses on removing the effects of H_2O because, with few exceptions, water dominates atmospheric absorptions for wavelengths from 0.4-2.5 μm. Also, the strength of the H_2O absorption features are such that they hide weaker absorption features from other gases (Clark, 1999). ATREM calculates the water content for each pixel by using a three-channel ratioing technique for water vapor features centered at 0.94 μm and 1.14 μm. Scattering terms for surface reflectance are calculated using the 6S code of Vermote, et. al. (1996) and a user selected aerosol model. Atmospheric transmittance for each gas is calculated using the Malkmus (1967) narrow band model and a user-selected standard atmospheric model (temperature, pressure, and vertical water vapor distribution).

ATREM relies on a number of assumptions that are only correct to a first approximation and, as hyperspectral instruments achieve greater spatial resolution, these assumptions will produce more pronounced output errors. Software programs like ENVI contain methods such as the Empirical Flat Field Optimal Reflectance Transformation (EFFORT) to remove cumulative corrections associated with calibration and atmospheric correction associated with ATREM (Boardman, 1998). Another source of error in ATREM is selection aerosol and standard atmosphere models to derive a reflectance spectrum by the user. If the user is not very adept with ATREM, then the resultant spectrum may not correlate with actual surface reflectance. In addition, small absorption features may be completely obliterated based on an incorrect assumption or poorly selected model. ATREM is still one of the best methods for compensating for atmospheric contributions to hyperspectral imagery, but it does have limitations, as do all radiative tranfer-based models. The solution to these shortcomings may be found in the empirically simple method of ratioing bands.

BAND RATIOS

Under certain conditions, ratioing two bands can eliminate the shortcomings of radiative transfer models and greatly expedite the processing and exploitation of hyperspectral data. Band ratios have been used extensively since the early 1970s (Vincent and Thomson, 1971; Vincent and Thomson, 1972; Vincent, 1973, Rowan et. al., 1974; Goetz, 1975; Ashley and Abrams, 1980; Rowan and Kahle, 1982; Podwysocki et. al., 1983; Fraser and Green, 1987; Crippen, 1988; Davis et. al., 1989; Rowan et. al., 1992; Crippen, 2001) to extract information from satellite imagery and airborne spectral scanners. These applications have been mostly constrained to multispectral imagery data, although recent work (Vincent, 1997; Clark, 1999; Mustard and Sunshine, 1999; Jengo, 2001) suggests that band ratios are equally applicable to HSI data.

Band ratios cannot be done haphazardly. Crippen (1988 and personal communication) detailed the problems that can occur with band ratioing and how to easily fix them. Vincent (1997, and personal communication) outlines a similar approach that essentially involves performing a dark subtraction on each band prior to ratioing the bands. Performing a dark subtraction removes additive radiance terms (electronic noise and

offset, and atmospheric path radiance) (Jengo, 2001). Using a dark subtraction assumes that the lowest Digital Number (DN) for each band should be equal to zero and the reason the first DN $\neq 0$ is due to atmospheric contribution, i.e., scatter, local slope/shadow, *S*, factor, and electronic gains and offsets. This is especially true for the near infrared wavelengths. Clear water absorbs 100% of the near infrared light, but often a spectrometer shows a DN value for water greater than zero. The atmospheric contribution for that particular channel, due to atmospheric scattering, is its DN, because there should be no reflectance value for that wavelength over water.

Another important rule for band ratios is that the bands being ratioed must not differ in wavelength by more than a few tens of nanometers. If the bands being ratioed are significantly far apart, then the atmospheric contribution, and sensor gains and offsets could be very different, invalidating the results of the ratio. For this reason most band ratios applied to HSI data are located such that one band lies in the center of a known sharp absorption feature and the other band lies nearby on the shoulder of the feature.

Stated another way, L_S values can be calculated in the following manner:

$$L_S = \int_{\lambda_1}^{\lambda_2} (L_P L_I T\theta_V) d\lambda \tag{5}$$

where L_{S_1} and L_{S_2} are sampled close together, $L_{P_1} \approx L_{P_2}$ and $T\theta_{V_1} \approx T\theta_{V_2}$, reducing the ratioed values to $\frac{L_{I_1}}{L_{I_2}}$. From this reasoning, it is understandable why band ratios eliminate the need for atmospheric corrections as long as the user knows where specific and characteristic absorption features are found in a spectrum.

Interestingly, there is no doubt as to the efficacy of using band ratios on multispectral data. There is no controversy despite the fact that the atmosphere responds to photons non-linearly over the 0.7-1.0 μm wide bands commonly ratioed in multispectral imagery data. When band ratios are utilized in HSI data, based on the rules given above, they are spectrally so close together that atmospheric effects should certainly be nearly equal for the two bands. Assumptions such as a horizontal surface and a Lambertian reflector are empirically addressed by band ratios because each is effectively the same for two closely-spaced bands (see equation 5). Band ratios are not limited to radiance data alone; they work equally well on reflectance data assuming that atmospheric compensation was done correctly.

Band ratios are a coarse, quick-check tool for examining radiance data (figure 1). This technique enables analysts to verify the presence of known materials based on absorption features. However, band ratios are not the answer to questions such as which cation, Mg^{2+} or Na^{+}, is substituted into the lattice of montmorillonite. This type of detailed chemical analysis requires reflectance data.

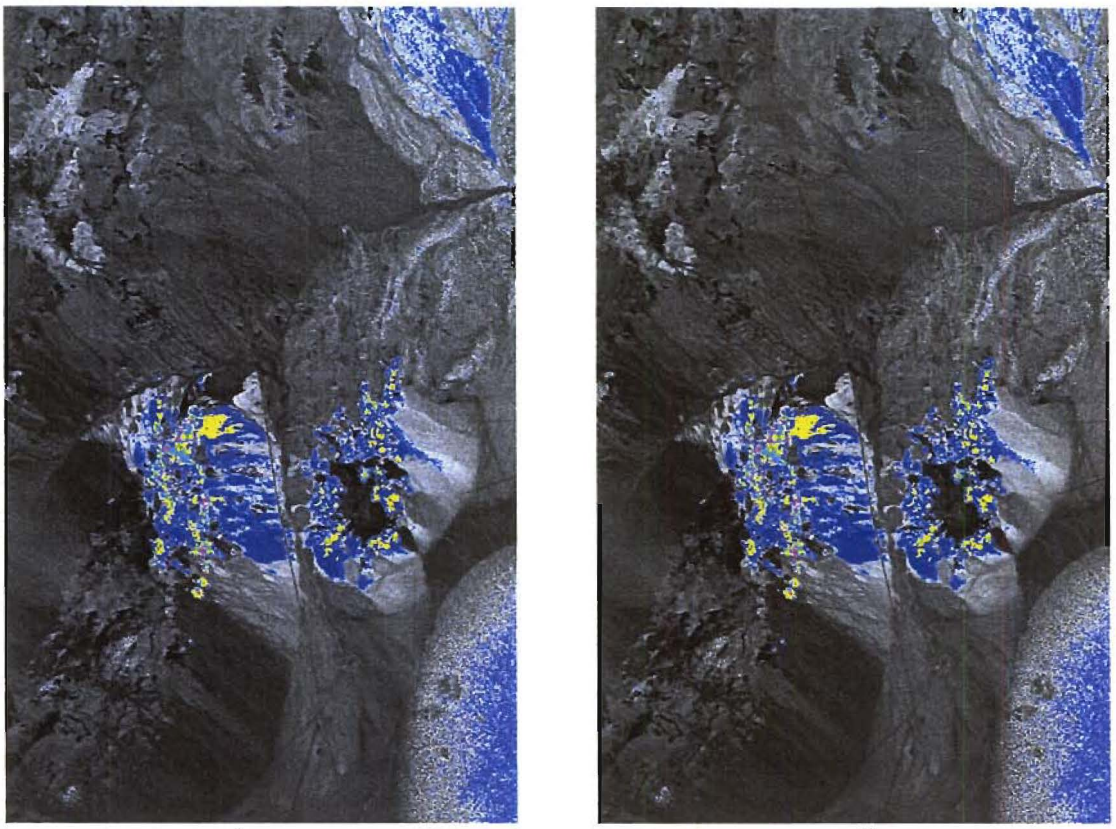

1a 1b

Figure 1 – Results of band ratios to find alunite in Cuprite 1995 AVIRIS scene.
a) radiance data, b) U.S.G.S. radiative transfer ground calibrated reflectance data

DERIVATIVE RATIO ALGORITHM

Further supporting the validity of band ratios is the work of Philpot's (1991) using derivative ratios. Derivatives have been used to analyze multispectral and hyperspectral data to extract information about minerals, plants, and soils (Foster, 1984; Bruce and Li, 2001). This more complex implementation of the band ratio concept is based on taking derivatives of the radiative transfer equation called the Derivative Ratio Algorithm (DRA) (Philpot, 1991). The goal of this approach is to determine the conditions for which the derivative algorithm is not subject to atmospheric interference. DRA uses the ratio of the *n*th derivative at λ_1 over a second derivative at λ_2. DAR demonstrated under certain conditions to obviate the need for atmospheric compensation. Equation (2) is modified by Philpot (1991) to the following:

$$L_s = TE_d R_t + L^* \tag{6}$$

Where T is atmospheric transmittance, E_d is the downwelling irradiance, R_t is target reflectance, and L^* is atmospheric path radiance. The first derivative of equation (6) is

$$\frac{dL_s}{d\lambda} = TE_d R_t \left[\frac{dRt}{R_t d\lambda} + \frac{dE_d}{E_d d\lambda} + \frac{dT}{Td\lambda} \right] + \frac{dL^*}{d\lambda}. \quad (7)$$

When the slope of the curve is sufficiently steep, the reflectance term dominates the equation yielding

$$\frac{dL_s}{d\lambda} \approx TE_d \frac{dR_t}{d\lambda}. \quad (8)$$

Eliminating the effects of the atmospheric contribution in equation (8) occurs only under certain conditions and wavelengths such that

$$\frac{T(\lambda_1)E_d(\lambda_1)}{T(\lambda_2)E_d(\lambda_2)} = 1. \quad (9)$$

If equation (9) holds, then the ratio of the first derivatives is equal to the ratio of the reflectance values at wavelengths λ_n, i.e.,

$$\frac{(dL_s/d\lambda)|\lambda_1}{(dL_s/d\lambda)|\lambda_2} \approx \frac{(dR_t/d\lambda)|\lambda_1}{(dR_t/d\lambda)|\lambda_2}. \quad (10)$$

Equation (8) can be generalized for all derivatives

$$\frac{d^n L_s}{d\lambda^n} \approx TE_d \frac{d^n R_t}{d\lambda^n}. \quad (11)$$

Equation (11) is further generalized by Bruce and Li (2001) to:

$$\frac{df}{d\lambda} = \frac{f(\lambda_2) - f(\lambda_1)}{\lambda_2 - \lambda_1} = \frac{f(\lambda_2) - f(\lambda_1)}{\Delta\lambda} \quad (12)$$

The $\Delta\lambda$ is critical because of inherent atmospheric heterogeneities. The maximum acceptable value for $\Delta\lambda \leq 50$ nm (Philpot, 1991). The other critical factor is that the curve must be sufficiently steep for this method to be valid. This is also true for band ratios in general; they function best for sharp absorption features. The DRA is more complex, yet consistent with simple band ratios.

CONCLUSIONS

Applying band ratios to radiance data has significant advantages over converting radiance data to reflectance but there remain some limitations:

1) A dark subtract must be performed on the imagery data. The requisite for a dark subtract is a large dataset with at least some areas with low reflectance values;

2) The DRA suggests that bands used for ratioing must be ≤ 50 nm apart to ensure that the numerator and denominator multiplicative factors are ≈ 1;
3) Requires sharp features associated with SWIR portion of the electromagnetic spectrum;
4) Susceptible to calibration errors.

Once these conditions are met, band ratioing provides a tool for quick assessment of materials present in hyperspectral data.

Performing high-quality utilization of hyperspectral data requires considerable effort to remove atmospheric interference effects. This type of fidelity requires accessing the target area as near as possible to the time of the sensor overflight to collect spectra using a hand-held spectrometer. Most computer programs to compensate for atmospheric interference are based on radiative transfer models of the atmosphere containing assumptions and generalizations regarding the atmosphere. Limiting the applicability of such models are there inability to account for non-Lambertian surfaces and sensor gains and offsets. Simple band ratios, when done properly, can efficiently produce high quality results from hyperspectral data.

REFERENCES

Ashley, R. P. and Abrams, M.J. 1980. Alteration mapping using multispectral images, Cuprite Mining District, Esmeralda County, Nevada, U.S.G.S. Open File Report 80-367, U.S. Geological Survey, Washington, D.C.

Boardman, J.W., and Kruse, F.A. 1994. Automated spectral analysis: A geologic example using AVIRIS data, north Grapevine Mountains, Nevada, in Proceedings of the 10th Thematic Conference on Geologic Remote Sensing, Environmental Research Institute of Michigan, Ann Arbor, Michigan, I – 407 – I – 418.

Boardman, J.W., Kruse, F.A., and Green, R.O., 1995. Mapping Target Signatures va partial unmixing of AVIRIS data in Summaries, 5th JPL Airborne Earth Science Workshop, JPL Publication 95-1, vol. 1, 23-26.

Boardman, J.W., 1998. Post-ATREM polishing of AVIRIS apparent reflectance data using EFFORT: a lesson in accuracy versus precision, in Summaries of the Seventh JPL Airborne Earth Science Workshop, Vol. 1, p. 53.

Bruce, L.M., and Li, J. 2001. Wavelets for Computationally Efficient Hyperspectral Derivative Analysis, IEEE Transactions in Geoscience and Remote Sensing, 39(7), 1540- 1546.

Clark, R. N. 1999. Spectroscopy of Rocks and Minerals, and Principles of Spectroscopy in Remote Sensing for the Earth Sciences: Manual of Remote Sensing, 3rd edition, volume 3, Rencz, A. N. (ed.), John Wiley and Sons, Inc., New York, New York, 707 pages.

Center for the Study of Earth from Space (CSES) 1999. Atmosphere Removal Program (ATREM) User's Guide, Version 3.1. 31p.

Crippen, R. E. 1988. The dangers of underestimating the importance of data adjustments in band ratioing, International Journal of Remote Sensing, 9(4):767-776.

Crippen, R.E. 2001. Unveiling the Lithology of Vegetated Terrains in Remotely Sensed Imagery, Photogrammetric Engineering & Remote Sensing, 67(8), 935- 943.

Davis, P.A., Mullins, K.F., Berlin, G.L., Al-Farasani, A.M., and Dini, S.M. 1989. Phosphorite exploration in the Thaniyat and Sanam districts, Kingdom of Saudi Arabia, using Landsat thematic mapper data. Proceedings of the 7th Thematic Conference on Remote Sensing for Exploration Geology, Vol. II, Environmental Research Institute of Michigan, Ann Arbor, Michgan, 1205-1221.

Foster, B. C. 1984. Derivations of Atmospheric Correction Procedures for Landsat MSS with Particular Reference to Urban Data, International Journal of Remote Sensing, vol. 5, 799-817.

Fraser, S.J, and Green, A.A. 1987, A software defoliant for geological analysis of band ratios. International Journal of Remote Sensing, 8, 525-532.

Gao, B. -C., and Goetz, A.F.H. 1990. Column Atmospheric Water Vapor and Vegetation Liquid Water Retrievals from Airborne Spectometer Data, Journal of Geophysical Research, 95, 3549-3564.

Gao, B.-C., Heidbrecht, K.G., and Goetz, A.F.H. 1999. Atmospheric Removal Program (ATREM) Users Guide Version 3.1: Center for the Study of Earth from Space (CSES), University of Colorado at Boulder, 31 p.

Goetz, A.F.H., 1975, Imaging for geothermal exploration, Geothermal Workshop on Geophysical Methods Applied to Detection, Delineation and Evaluation of Geothermal Resources, 13-18, Dept. of Geology and Geophysics,University of Utah, Salt Lake City, U. S. Geological Survey, Snowbird, Utah.

Jengo, C. 2001. Hyperspectral Imaging of Ancient Hydrocarbon Seeps, Wind River Basin, Wymoing. M.S. Thesis, Bowling Green State University, Bowling Green, Ohio, 202 p.

Malkmus, W. 1967. Random Lorentz Band Model with exponential-tailed S line intensity distribution function, Journal of the Optical Society of America, vol. 57, 323-329.

Mustard, J.F., and Sunshine, J. M. 1999. Spectral Analysis for Earth Science: Investigations Using Remote Sensing Data. In Remote Sensing for the Earth Sciences:

Manual of Remote Sensing, 3rd ed., Vol. 3., A. M. Rencz (ed.), John Wiley & Sons, New York, New York, 251- 306.

Penn, B.S., and Livo, K.E. 2001. Using AVIRIS Data to Map Geologic Signatures of Copper Flat Porphyry Copper Deposit, Hillsboro, New Mexico, in Proceedings of the Tenth JPL workshop on Airborne Earth Science Workshhop, Jet Propulsion Laboratory, California Institute of Technology, February 28 - March 2, 2001.

Philpot, W. D. 1991. The Derivative Ratio Algorithm: Avoiding Atmospheric Effects in Remotes Sensing, IEEE Transactions on Geoscience and Remote Sensing, 29(3), 350-357.

Podwysocki, M.H., Segal, D. B., and Abrams, M.J. 1983. Use of multispectral scanner images for assessment of hydrothermal alteration in the Marysvale, Utah mining areas, Economic Geology, 78, 675-687.

Rowan, L.C., Wetlaufer, P.H., Goetz, A.F.H., Billingsley, F.C., and Stewart, J.H. 1974. Discrimination of Rock Types and Detection of Hydrothermally Altered Areas in South-Central Nevada by Use of Computer-Enhanced ERTS Images, U.S.G.S. Professional Paper 883, U.S. Geological Survey, Washington, D.C., 35 p.

Rowan, L.C., and Kahle, A.B. 1982. Evaluation of .46-2.36 um multispectral scanner image of the East Tintic mining district, Utah for mapping hydrothermally altered rocks, Economic Geology, 77, 441-452.

Rowan, L.C., Pawlewicz, M.J., and Jones, O.D. 1992. Mapping Thermal Maturity in the Chainman Shale, near Eureka, Nevada, with Landsat Thematic Mapper images. American Association of Petroleum Geologists Bulletin, 76(7):1008-1023.

Turner, R. E. 1975. Signature Variations Due to Atmospheric Effects in Proceedings, 10th International Symposium on Remote Sensing of the Environment, Ann Arbor, MI, Environmental Research Institute of Michigan, 671-682.

_____ 1978. Elimination of Atmospheric Effects from Remote Sensing Data, in Proceedings, 12th International Symposium on Remote Sensing of the Environment, Ann Arbor, MI, Environmental Research Institute of Michigan, 783.

Turner, R.E. and Spencer, M.M. 1972. Atmospheric Model for Correction of Spacecraft Data in in Proceedings, 8th International Symposium on Remote Sensing of the Environment, Ann Arbor, MI, Environmental Research Institute of Michigan, 895-934.

Vermote, E., Tanre, D., Deuze, J.L., Herman, M., and Morcrette, J.J. 1996. Second Simulation of the Satellite Signal in the Solar Spectrum (6S), 6S User's Guide Version 1, NASA-GSFC, Greenbelt, Maryland, 134 pages.

Vincent, R. K, and Thomson, F. 1971. Discrimination of Basic Silicate Rocks by

Recognition Maps Processed from Aerial Infrared Data. In Proceedings of the Seventh International Symposium on Remote Sensing of the Environment, Ann Arbor, Environmental Research Institute of Michigan, 247-252.

Vincent, R. K., and Thomson, F. 1972. Rock Type Discrimination from Ratioed Infrared Scanner Images of Pisgah Crater, California. Science 175:986-988.

Vincent, R. K. 1973. A Thermal Infrared Ratio Imaging Method for Mapping Compositional Variation Among Silicate Rock Types. Ph.D. University of Michigan, Michigan.

_____ 1997. Fundamental of geological and environmental remote sensing. Prentice-Hall, Upper Saddle River, New Jersey, 366p.

USING THE SEMI-AUTOMATED PLUG-IN TOOL FOR FEATURE IDENTIFICATION, RECOGNITION, AND EXTRACTION (SPITFIRE) TO EXTRACT ROADS AND SURFACE MATERIAL TYPES FROM AVIRIS IMAGERY

Brian S. Penn
Boeing-Autometric
Colorado Springs, Colorado
brian.s.penn@boeing.com

K. Eric Livo
United States Geological Survey
Denver, Colorado

INTRODUCTION

Effective tactical troop deployment can be negatively impacted by a lack of current and accurate lines of communication (LOC) information. For example, little, if any NIMA and ADRG data exist for locations such as East Timor, Bosnia, Somalia, or Afghanistan. Because of funding constraints and the sheer size of the problem, this situation is unlikely to change in the near term and will continue to unnecessarily complicate the already difficult task of troop deployment and logistical support for troop deployment. Additionally, while some engagements occur in rural areas, the trend is toward engagements in urban areas.

Over the past several years, a variety of military, government, and civilian organizations have developed tools for automated feature extraction to significantly speed up the task of identifying and extracting LOC information from imagery for use in mapping applications (Maillard and Cavayas, 1989; Zlotnick and Carnine, 1993; Gee, 1994; Kahrig et. al., 1994; Lersch, Iverson, and West, 1994; Bullock et al., 1996; Couloigner and Ranchin, 2000). While some of these efforts have had limited success, constraints in computing power and the availability of data containing the requisite spatial as well as spectral characteristics have significantly hampered achievement of a complete solution.

The primary goal of this system described here is to quickly extract LOC for use by military forces. They don't need the quintessential map, they need roads, and they need them fast. For this reason the threshold for success is based on the Pareto Principle or the 80/20 rule. The Pareto Principle states that the first 80% of whatever is being done is achieved with the first 20% of the total effort. The converse is also true: 80% of the effort is expended completing the final 20% of a task. This is the metric used to determine the success for LOC extraction.

Spatial resolutions of satellite imagery data have improved to the point that it is now possible to automatically map LOCs for most environments. These data are readily available in differing spatial and spectral resolutions and can be merged to provide the range of data products necessary to produce LOC maps. Moreover, computer speed

continues to increase dramatically, permitting even computationally intensive tasks like satellite image processing to be performed on a desktop computer. Consequently, the primary technological barriers to developing fast, efficient, and effective LOC recognition systems no longer exist.

Hyperspectral imagery (HSI) offers significant advantages over panchromatic and multispectral imagery. Hyperspectral imagery is not a new type of imagery; it really is just more of the same data at finer spectral resolution. Previously interpreters were limited to broad bands of the electromagnetic spectrum (EMS). These bands "smeared" subtle features in the integrated signatures representing information about an imaged material. These details are only apparent when the wide bands of the EMS are split into 100s and 1000s of samples. This type of resolution requires a hyperspectral sensor. HSI data provides unprecedented capability for extracting previously hidden information from imagery.

Hyperspectral imagery complements high spatial resolution imagery by providing high spectral resolution data. Instead of having several very wide bands ranging in the tens of micrometers (μm), hyperspectral sensors have many bands with sampling measured in the tens of nanometers (nm). Sensors like the Jet Propulsion Laboratory's Airborne Visible & Infrared Imaging Spectrometer (AVIRIS) are regularly providing high-fidelity hyperspectral images composed of 224 samples at 10 nanometer (nm) intervals over the EMS from 400 to 2500 nm wavelengths.

The Semi-automated Plug-In Tool for Feature Identification, Recognition, and Extraction (SPITFIRE) extracts lines of communication (LOC), i.e., roads and rivers, from digital imagery of urban environments and generates centerline vectors in ArcView shapefile format. SPITFIRE is capable of quickly extracting LOCs from digital imagery ranging from panchromatic to hyperspectral imagery (HSI). When HSI data is provided, SPITFIRE can also provide surface material types. This paper explores the techniques used to extract LOCs and determine material types using AVIRIS HSI data.

BACKGROUND

During fiscal year 1999, Army Space Command in Colorado Springs, Colorado drafted a proposal to the Military Exploitation of Reconnaissance and Intelligence Technology (MERIT) Board to develop a prototype tool for LOC extraction. The successful completion of the multispectral phase of SPITFIRE led to the development of a hyperspectral version implemented as a plug-in to Research System's Environment for Visualizing Images (ENVI) during fiscal year 2001. The basic ideas for extracting LOCs were carried over from Phase I. The significant difference in Phase II involved using HSI data to identify road surface material types.

To take full advantage of the information in hyperspectral data, it was necessary to develop a hybrid knowledge-based system to identify surface material types. The tremendous range in urban surface material types led to the development of general categories of surface material types used for LOC extraction in urban environments, i.e.,

concrete, asphalt, bare soil, and water. These general categories provided the basis for material identification using a combination of rules, neural networks, and fuzzy logic. The hyperspectral component of SPITFIRE was developed and tested using an AVIRIS scene acquired in July of 1997 west of Denver over the Front Range of Colorado. The AVIRIS scene was atmospherically corrected by the U.S.G.S. at the Spectroscopy Laboratory in Lakewood, Colorado.

EXTRACTING LINES OF COMMUNICATION

Lines of communication, i.e., roads, rivers, etc. have certain spatial and spectral characteristics. The chief requisite among these characteristics needed is spectral contrast between the road surface material and the off-road material. Finding the LOCs requires proper image preparation. Image preparation and extraction of the LOC is a three-step process:

1) Finding the bands with the highest amount of contrast between the road surface and the non-road surface;
2) Reduce the amount of information to only include the roads of interest;
3) Connect adjoining pixels of interest along the LOC.

Wavelengths with the maximal contrast can be found either empirically, using a statistical function like the Bhattacharyya distance (Chulhee and Landgrebe, 1993), or by performing a change of basis on the data set, i.e., a principle component transformation. Visual inspection of the average spectra of two areas of interest is a simple way to find those wavelengths providing the best contrast (Figure 1). Only the visual inspection technique and principle component transformations are covered here.

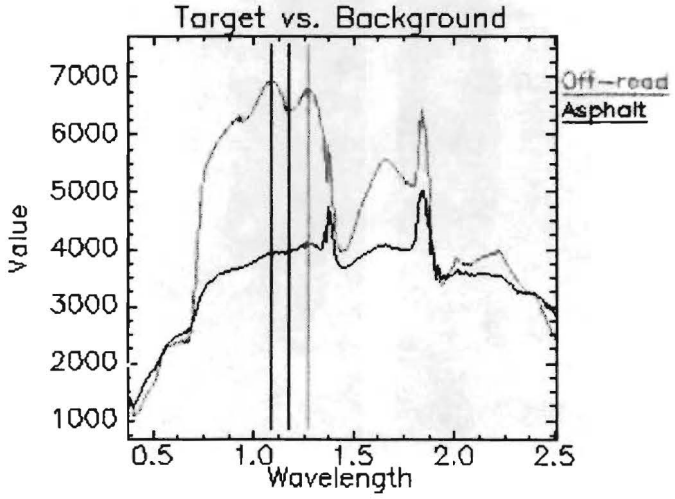

Figure 1 – Average spectra showing largest contrast between road surface and non-road surface

PRINCIPLE COMPONENT TRANSFORMATION

Finding a maximal contrast between road surface materials and non-road materials can be achieved by performing a principle component (PC) transformation. PC transformations are useful because of the high positive correlation normally found between bands in imagery data. The number of PC bands generated is equal to the total number of bands, n, in the image. A PC transformation rotates the coordinate axes around such that the first PC is parallel to the maximum amount of variance in the imagery data set. The second PC is orthogonal to the first PC and is parallel to that portion of the data containing the second largest amount of variance. The is process is continued until the nth axis is perpendicular to the $(n\text{-}1)^{th}$ and contains the next least amount of variance. The last couple of PCs generally contain mostly noise.

It was empirically determined that subtracting the 4th PC from 2nd PC generated a good contrast between the road surface and non-road surface materials. The complexity and time required to perform a PC transformation compared to simply using a visual test to find the bands with the highest contrast makes doing a PC transformation untenable.

LOC EXTRACTION

Once the bands with the highest contrast were found, it was obvious that even with the contrast there was too much high-frequency information in the imagery. This problem of high-frequency information was addressed by applying a low-pass filter to the image (Figure 2).

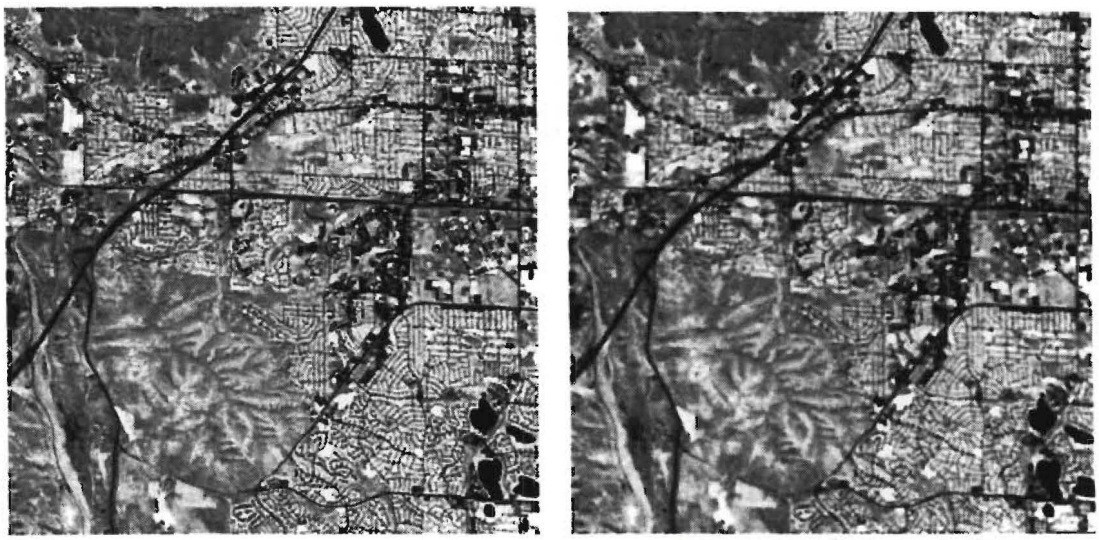

a b

Figure 2 – a) False-color image of bands shown in Figure 1;
b) Figure 2a smoothed with 3x3 low-pass filter.

Once the image is prepared, the LOC extraction process is performed with a simple flood-fill. A flood-fill should be familiar to anyone using a computer paint program. A

flood-fill works by selecting the starting point of the feature to fill with the fill tool. Because the fill procedure is done using simple statistics it is quite rapid (Figure 3). The primary benefit of this approach is that it uses both the spectral and spatial nature of LOCs to constrain the bounds of the LOC.

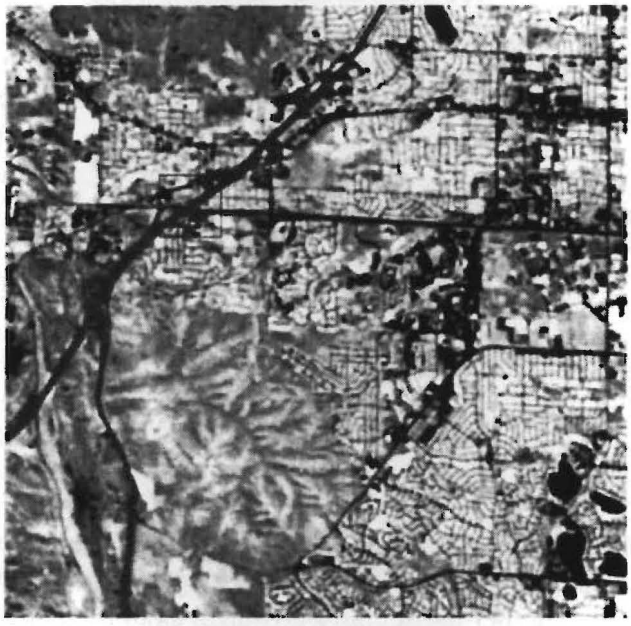

Figure 3 – LOCs found using flood-fill method

LIMITATIONS OF LOC EXTRACTION

Spatial resolution restricts the size of LOCs that can be effectively extracted. A single lane road is approximately 3-4 m wide, a two-lane road is 6 – 8 m, and a four-lane road with a turning lane is approximately 25 m wide. While it is possible to extract subpixel features, this can lead to inaccuracies. The AVIRIS sensor when flown at 20 km has an instantaneous field of view (IFOV) of 1 milliradian yielding a nominal pixel size of $\approx$ 20 m. At this pixel size four-lane roads are slightly larger than individual pixels making them easy to unambiguously identify and extract. Using the success metric of the Pareto Principle described above, most four-lane and some two-lanes can be extracted quickly. Extracting smaller LOCs can be easily achieved by flying the sensor lower with the same IFOV yielding pixels sufficiently small to extract one- and two-lane roads.

Once the flood-fill finds the appropriate LOC, the next task is to generate centerline vectors. Using Able Software's R2V, commercial off-the-shelf raster to vector conversions tool, the LOCs are converted to vectors and exported as shapefiles for use in GIS systems.

MATERIAL IDENTIFICATION

The primary reason for using hyperspectral data is to extract material types. Urban areas are spectrally complex (Gardner et al., 2001; Small, 2001). For most researchers in HSI spectral complexity equates to collecting vast amounts of spectra for every possible substance that might be encountered and storing these spectra in a reference library. This is equivalent to carrying around an album containing a picture of every person you have ever met and comparing everyone you meet to this photo album! Humans don't do this; they have the capability of generalizing about faces. An example of our ability to generalize is demonstrated by the number of people who see a face on the surface of Mars. There are techniques pioneered in artificial intelligence that permit satisfactory generalization such as neural networks and fuzzy logic.

REPRESENTATION

In artificial intelligence (AI), it is generally understood that problem complexity is usually a function of representation. All intelligent human tasks involve some form of problem solving which is fundamentally a search problem. Recasting problems into different representations is just another way of constraining the search space. Seemingly intractable problems in one representation when recast into a different domain are easily solved (Raphael, 1976; Rich, 1983; Winston, 1984). In the current context, using a flood-fill to extract LOCs is an example of how recasting a problem into another domain makes it easily solvable. Another particularly powerful example is Fourier transforms. Fourier transforms convert signals from the time domain into the frequency domain. In the frequency domain all signals can be represented as a series of sine waves that are much easier to work with than other waveforms.

It should be clear that how the problem is perceived or represented determines the ease by which it is solved. That is the controlling mechanism behind the solution presented below for road surface material identification.

The alternative to collecting individual spectrum of all surfaces to identify materials is to do what comes naturally to humans, i.e., generalize. As was alluded to above regarding the recognition of faces, one of the skills our brains naturally possess is the ability to generalize. The first task in developing a system capable of generalizing about spectral properties of road surface material types is to collect representative spectra of the surficial material types of interest. Once the spectra were collected, a small library of average spectrum for each material type was developed (Figure 4).

REFLECTANCE RULES FOR SURFACE MATERIAL TYPES

Roadway surfaces are generally composed of aggregate (bare soil), asphalt, and/or concrete. Other material types include vegetation and water. Several heuristics (rules of thumb, i.e., generalizations) were developed. One rule was that bare soil and concrete have significantly higher albedos than water and asphalt. Using this rule, bright

reflectors are easily separated from dark reflectors. Average albedos were useful enough for this first pass. Any spectrum with an average albedo below 10% was considered

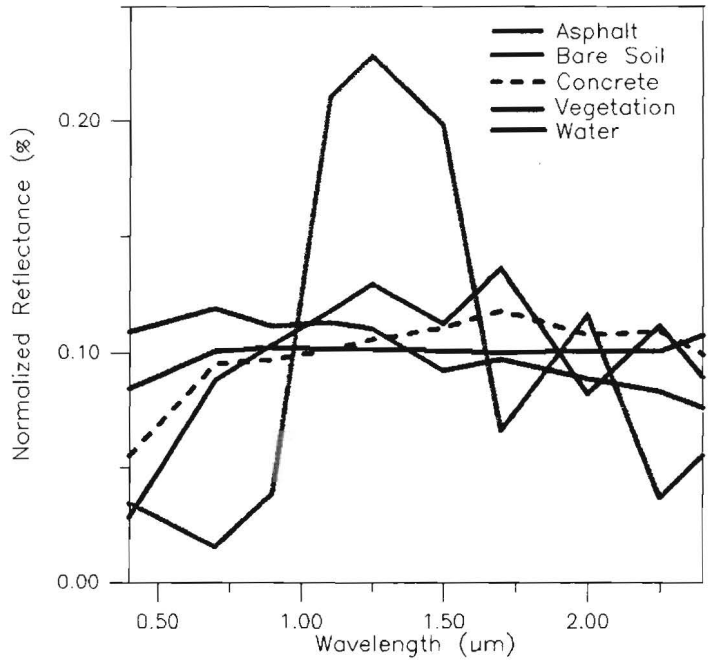

Figure 4 – Normalized averages for spectra collected using and ASD-FR hand held spectrometer of primary surface material types resample to ten wavelengths.

either water or fresh asphalt. Water and fresh asphalt are distinguished by the fact that water may have a slight spike in the blue wavelengths and the overall spectrum has a negative slope. Fresh asphalt is practically flat over the range of wavelengths from 400-2500 nanometers (nm). Spectra with reflectance values greater than 25% were considered either pure concrete or pure soil. Since concrete and bare soil don't have any unique absorption features it was necessary to use the overall spectral shape to distinguish between them. It was determined empirically that all 224 channels of AVIRIS data were more data than necessary to distinguish between these material types. The necessary spectral information was reduced to 10 bands. These 10 bands equally spaced over 400-2500 nm were enough to discriminate between bare soil and concrete. The problem then reduced to one of pattern matching. One of the best tools for pattern matching and recognition is a neural network (Lippman, 1987, 1989; Fukushima, 1988; King, 1989).

NEURAL NETWORK

A feed-forward neural network was designed with ten input nodes and two output nodes (Rummelhart, 1986). The network was trained using back propagation. Several hundred training sets of spectra of concrete and bare soil were presented to the neural network during the training process and convergence generally occurred within one thousand iterations.

FUZZY RULE

Spectra of road surface material types with average reflectance values between 10% and 25% were determined to be mixtures of either asphalt and concrete or asphalt and bare soil. It was possible to distinguish whether the mixture was either concrete or bare soil by the shape of the curve, but not how much was present. To address this question, a fuzzy rule was developed and applied to the spectrum. Fuzzy rules are based on fuzzy set theory (Zadeh, 1965). The fuzzy rule is show in Figure 5.

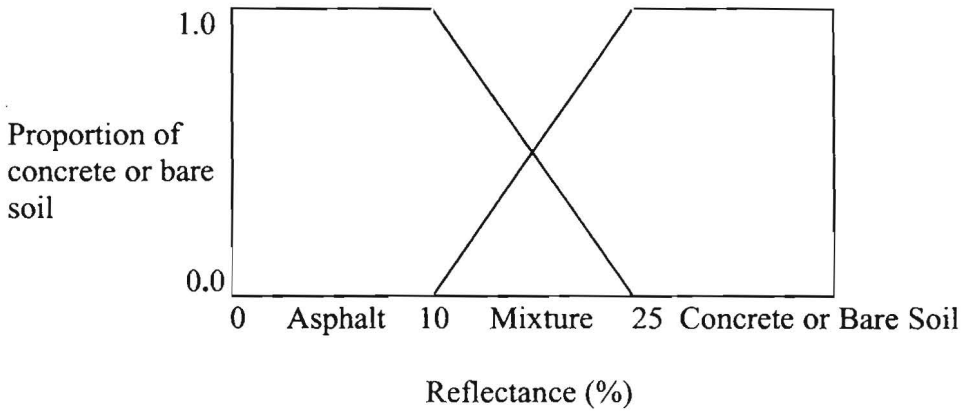

Figure 5 – Fuzzy rule for determining proportions of asphalt and bare soil or concrete

The rule in Figure 5 is over-simplified. The diagonal lines representing relative proportions should really be exponential curves concave downward with steep slopes nearly parallel to the y-axis and rolling over near 0.85 and becoming asymptotic with the upper x-axis. This shape is more consistent with what is understood regarding non-linear mixtures between dark and light materials and the effect dark materials have on the reflectance values of lighter materials. The exact shape of these curves is the subject of current research.

The general reflectance rules, neural network, and fuzzy rule were combined into a hybrid knowledge-based system and integrated into the SPITFIRE plug-in module to ENVI.

CONCLUSIONS

The Semi-automated Plug-In Tool for Feature Identification, Recognition, and Extraction (SPITFIRE) was designed and implemented to extract lines of communication from digital imagery. The initial version operated on multispectral imagery. SPITFIRE was later migrated to ENVI to operate on hyperspectral imagery.

Extracting LOCs involves locating wavelengths with sufficient spectral contrast between the desired road surface and non-road surface (background). Once these wavelengths are found, then a simple flood-fill algorithm is used to follow the road. A raster to vector

tool is then used to find centerlines and generate vectors as shapefiles for ease of incorporation in to a Geographic Information Systems like Arc/Info or Arc/View.

The chief benefit of using hyperspectral imagery is the ability to discriminate and identify material types. SPITFIRE achieves road surface material identification using a hybrid knowledge-based system using a combination of rules, neural networks, and fuzzy logic.

The basis for this approach of classifying road surface materials is generalization and pattern recognition. This approach obviates the need to develop large spectral libraries because it mimics what humans do in terms of pattern recognition. A smaller set of characteristic spectra are still needed to develop generalizations about the different surface material types.

REFERENCES

Bullock, M.E., Fairchild, S.R., Patterson, T.J., and Haxton, R. 1996. Automated map generation and update from high-resolution multispectral imagery, SPIE vol. 2758, 91-103.

Chulhee L. and Landgrebe, D. A. 1993. "Decision Boundary Feature Extraction for Non-Parametric Classification," IEEE Transactions on System, Man, and Cybernetics, Vol. 23(2), 433-444.

Couloigner, I. and Ranchin, T. 2000. Mapping of Urban Areas: A Multiresolution Modeling Approach fro Semi-Automatic Extraction of Streets, Photogrammetric Engineering & Remote Sensing, vol. 66 (7), 867-874.

Fukushima, K. 1988. Neural Networks for Visual Pattern Recognition, IEEE Computer, vol. 21(3), 65-75.

Gardner, M. E., Roberts, D. A., Funk, C., and Noronha V. 2001. Road Extraction from AVIRIS using Spectral Mixture and Q-Tree Filter Techniques in Proceedings of the 10th JPL Airborne Earth Science Workshop, Green, R. O. (ed.), JPL Publication 02-1, 145-150.

Gee, S.J. 1994. Lines of Communication in LANDSAT TM Imagery, SPIE vol. 2231, 27-35.

Kahrig, A.H., Abeloe, K.A., Teschan, P.E. 1994. Model-based approach to Landsat-TM scene linear LOC segment detection using morphology, SPIE vol. 2231, 7-18.

King, T. 1989. Using Neural Networks for Pattern Recognition, Dr. Dobb's Journal, January, 14-28.

Lersch, J.R., Iverson, A.E., and West, K.F. 1994. Multispectral Lines of Communication, SPIE vol. 2231, 36- 47.

Lippman, R. P. 1987. An Introduction to Computing with Neural Networks, IEEE Transactions in Acoustics, Speech, and Signal Processing Magazine, April, 4-22.

---------- 1989. Pattern Classification Using Neural Networks, IEEE Communications Magazine, November, 47-64.

Maillard, P. and Cavayas, F. 1989. Automatic map-guided extraction of roads from SPOT imagery for cartographic database updating, International Journal of Remote Sensing, vol. 10(11), 1775-1787.

Raphael, B. 1976. The Thinking Computer: Mind inside Matter, W.H. Freeman and Company, San Francisco, CA, 322 p.

Rich, E. 1983. Artificial Intelligence. McGraw-Hill, New York, New York, 436 p.

Rummelhart, D.E., Hinton, G.E., and Williams, R.J. 1986. Learning Internal Representations by Error Propagation, *in* Parallel Distributed Processing: Explorations in the microstructure of cognition-Volume 1: Foundations, Feldman, J.A., Hayes, P.J., and Rummelhart, D.E. (eds.). MIT Press, Cambridge, MA, 318-362.

Small, C. 2001. Spectral Dimensionality and Scale of Urban Radiance in Proceedings of the 10th JPL Airborne Earth Science Workshop, Green, R. O. (ed.), JPL Publication 02-1, 375-385.

Winston, P.H. 1984. Artificial Intelligence, 2nd edition, Addison-Wesley, New York, New York, 524 p.

Zadeh, L.A. 1965. Fuzzy Sets, Information and Control, vol. 8, 338-353.

Zlotnick, A., and Carnine, P.D. 1993. Finding Road Seeds in Aerial Images, CVGIP: Image Understanding, vol. 57(2), 243-260.

A COMPARATIVE ANALYSIS OF ENDMEMBER EXTRACTION ALGORITHMS USING AVIRIS HYPERSPECTRAL IMAGERY

Antonio Plaza, Pablo Martínez, Rosa M. Perez, Javier Plaza[1]

1. Introduction

Spectral unmixing techniques are widely used for hyperspectral data analysis and quantification. Many novel applications have been developed from the unmixing point of view, including surface constituent identification for land use mapping, disaster assessment, geology, biological process analysis and change detection (Keshava and Mustard, 2002). All existing unmixing approaches require a previous step where the spectral signatures of ground constituents (endmembers) are identified (Kruse, 1998; Boardman et al., 1995), and then a mixture model is used to estimate the abundance fractions of these signatures by expressing individual pixels as a linear or non-linear combination of endmembers (Bateson et al., 2000). The accuracy of the quantification depends strongly on how accurate endmembers are identified in the first step.

Several different strategies have been proposed to evaluate the quality of selected endmembers for spectral unmixing. The simplest approach has been direct comparison to reference signatures contained in a spectral library of ground measurements (Winter, 2000; Sweet et al., 2000). Another alternative has been focused on analyzing the abundance of endmembers in the scene, which is usually expressed as a series of greyscale images where the grey level value at each pixel represents a combined amount of the abundance of endmembers contained in the pixel. Then, the quality of a set of endmembers may be evaluated by comparing their associated abundance fractions to reference abundance planes, either by visual comparison (Winter, 2000; Kneubuehler et al., 1998) or, more reliably, by statistical measures like the average root mean square error (RMSE) (García and Ustin, 2001) or the Pearson correlation coefficient (Maselli, 1998).

The previous approaches are possible when ground truth data is available and contains information about the abundance of materials in each pixel of the scene. Nevertheless, it should be noted that the obtention of reliable ground truth is difficult, expensive and very time-consuming, a fact that has traditionally prevented the existence of reliable ground measurements for a large number of datasets.

Some approaches have been previously considered in order to assess endmember extraction accuracy when no ground truth information is available. Most of them are based on a reconstruction process of the original hyperspectral image, using the set of extracted endmembers and their estimated abundance maps, according to linear spectral mixture model definitions. The generated image may be compared to the original one by several statistical measures (Bowles et al., 2000).

However, in many reconstruction-oriented approaches, an important question arises: the number of endmember vectors required to accurately approximate or regenerate the pixels of the original image. In order to answer this question, several authors have proposed to consider multiple sets of endmembers simultaneously for spectral unmixing (Roberts et al., 1998, Okin et al., 1998, Bateson et al., 2000). Following this idea, some studies have demonstrated that models based on three endmembers generally provide satisfactory results although, in some applications, models based on four and more endmembers improve considerably the results found using only three endmembers (Segl et al., 2000; Garcia and Ustin, 2001). In general terms, it is expected that the quality of the reconstruction process would improve as the number of reference signatures used increases, even though mixed pixels are used in the reconstruction process. Nevertheless, the goal should be the identification of a reduced subset of pure spectral signatures which are able to provide a reconstruction which is similar enough (i.e., under a certain error tolerance threshold) to the original image.

Although several comparative efforts have been proposed in recent years, no unified criterion has been accepted for rigorous and impartial comparison of endmember extraction algorithms. The importance of this issue cannot be understated since, without effective evaluation criteria, the performance of any new algorithm cannot be substantiated. In this paper, we take a first step by conducting a comparative study of performance analysis among several existing endmember extraction algorithms, including the Pixel Purity Index (Boardman et al., 1995), the N-FINDR algorithm (Winter, 2000) and our custom-designed method Automated Morphological Endmember Extraction, AMEE (Plaza et al., 2002; Plaza et al., 2001a; Plaza et al., 2001b). A novel comparative framework is introduced, allowing detailed quantitative assessment of endmember

[1] Neural Networks and Signal Processing Group (GRNPS), Computer Science Department, University of Extremadura. Avda. de la Universidad s/n, 10.071 Cáceres, SPAIN. E-mail: aplaza@unex.es, pablomar@unex.es, rosapere@unex.es.

extraction accuracy. The significance of these experimental results is to offer a performance evaluation of endmember detection algorithms in a rigorous fashion so that each algorithm is fairly compared to others on the same common context. Several different situations are considered in the above framework, regarding the availability or not of ground truth data and the intrinsic characteristics of such information.

The paper is organized as follows. Section 2 defines an objective framework for evaluation of endmember extraction and subsequent classification accuracy. Section 3 presents a comparative performance analysis for the above-mentioned algorithms, and section 4 concludes with some remarks.

2. Comparative framework for evaluation of endmember extraction algorithms

In this section, a schema to evaluate endmember extraction algorithms is proposed. The framework has into account the following situations:

1) Ground truth (GT) is available in the form of a spectral library of constituent signatures.
2) GT contains the abundance of endmember materials for each pixel of the scene.
3) GT is not available.

We proceed to describe the evaluation approach to validate extracted endmembers in each situation.

2.1. Evaluation by Comparison to GT Spectral Signatures

Before addressing the metrics used to evaluate endmember quality in this case, the following definitions are introduced:

N	Total number of pixels in the original hyperspectral image.
$\Gamma_E = \{E_i\}_{i=1}^K$	Set containing X endmembers extracted from the hyperspectral image.
$E_i = (E_i(\lambda_1), E_i(\lambda_2), ..., E_i(\lambda_S))^T$	A particular endmember of Γ_E.
$\Gamma_R = \{R_i\}_{i=1}^K$	Set containing Y GT signatures.
$R_i = (R_i(\lambda_1), R_i(\lambda_2), ..., R_i(\lambda_S))^T$	A particular GT signature of Γ_R.

A correlation matrix of spectral angle distances (SAM matrix) is used to perform the comparison in this situation. Figure 1 shows an example of the construction of a SAM matrix between extracted endmembers and GT signatures. In this representation, we denote $SAM_{nm} = SAM(E_n, R_m)$, where SAM refers to the cosine of the spectral angle.

		Endmember signatures			
		$\mathbf{E_1}$	$\mathbf{E_2}$		E_X
GT signatures	$\mathbf{R_1}$	SAM_{11}	SAM_{21}	...	$\mathbf{SAM_{X1}}$
	$\mathbf{R_2}$	SAM_{12}	SAM_{22}	...	$\mathbf{SAM_{X2}}$
	⋮	⋮	⋮		⋮
	R_Y	$\mathbf{SAM_{1Y}}$	$\mathbf{SAM_{2Y}}$	...	$\mathbf{SAM_{XY}}$

Figure 1. SAM matrix between extracted and reference signatures.

2.2. Evaluation by Comparison to GT Abundance Planes

This schema is based on the assumption that each evaluated endmember E_i has an associated GT signature R_i. Both E_i and R_i have associated abundance maps, $G(E_i)$ and $G(R_i)$, which respectively contain the fractional abundance of the spectral signature in the pixels of the original image. Before addressing the quality measures used in this situation, the following definitions are introduced:

$I = \{P_j\}_{j=1}^{N}$	Original hyperspectral image expressed as a set of N hyperspectral pixels.
$P_j = (P_j(\lambda_1), P_j(\lambda_2), ..., P_j(\lambda_S))^T$	A particular pixel of the image.
$\Phi_j(E_i)$	Fractional abundance of endmember material E_i at pixel P_j of the original image.
$\Phi_j(R_i)$	Fractional abundance of reference material R_i at pixel P_j of the original image.
$G(E_i) = \{\Phi_j(E_i)\}_{j=1}^{N}$	Greyscale abundance map of endmember E_i.
$G(R_i) = \{\Phi_j(R_i)\}_{j=1}^{N}$	Greyscale abundance map of reference signature R_i.

Each E_i, R_i pair is compared at a pixel level by calculating the root mean square error between their associated abundance maps using the following expression.

$$RMSE_I\{G(E_i), G(R_i)\} = \sqrt{\sum_{i=1}^{N} (\Phi_j(E_i) - \Phi_j(R_i))^2}$$

2.3. Evaluation when ground truth is not available

The approach that we present to compare endmembers when no ground truth information is available is only applicable when the linear mixture model is suitable to perform the analysis and classification of the scene. The linear approach has been demonstrated in numerous applications to be a useful technique for interpreting the variability in remote sensing data. Nevertheless, it is only strictly valid for the situation where the endmembers are arranged in discrete, segregated patches on the surface (Keshava and Mustard, 2002). This condition is hardly met in nature, and many constituents of interest for earth science investigations exist in soils, or at smaller scales, in intimate association with one another. In this work, we rely on the linear model as an initial attempt to validate our framework, but we are aware that the use of this model may introduce errors in the comparison.

Once this initial statement has been made, we proceed to describe our comparative framework in this situation. Using the previously defined notations, a particular pixel P_j in the original hyperspectral image can be approximated by the following expression:

$$P_j \approx P_j' = \sum_{i=1}^{p} \Phi_j(E_i) \cdot E_i ,$$

where $\Phi_j(E_i)$ denotes the abundance fraction of endmember material E_i at pixel P_j. The accuracy of the approximation in (12) for a single P_j using a set of endmembers Γ_E can be quantified by the root mean square error:

$$RMSE_I(\Gamma_E) = \sqrt{\sum_{i=1}^{N} \left(P_j - \sum_{i=1}^{p} \Phi_j(E_i) \cdot E_i \right)^2}$$

In order to study the capacity of extracted endmembers to provide an accurate reconstruction of the original image, we consider a variable number of endmembers to perform the reconstruction. Our goal is to analyze the optimum number of endmembers needed to reconstruct the original image, and also to evaluate the accuracy of such reconstruction. In order to achieve the previously addressed objectives, the following algorithm is used.

Step 1) Set a tolerance threshold T.

Step 2) Calculate the abundance of each endmember E_i in image I: $\forall Ei,\ G(E_i) = \{\Phi_j(E_i)\}_{j=1}^{N}$.

Step 3) Order the endmembers in set Γ_E according to their total abundance in the original image. The total abundance of endmember E_i in image I is calculated as: $\sum_{j=1}^{N} \Phi_j(E_i)$.

Step 4) Construct a new set Γ_N which contains the three most abundant endmembers of Γ_E, and remove such endmembers from Γ_E.

Step 5) If $RMSE_I(\Gamma_N) < T$ then stop (a satisfactory reconstruction is achieved).

Step 6) Remove the most abundant endmember in Γ_E and incorporate it to Γ_N.

Step 7) Repeat from step 5 until $\Gamma_E = \varnothing$ (in this case, no satisfactory reconstruction was possible).

3. Results and discussion

The following endmember extraction methods: PPI, N-FINDR and AMEE were applied to hyperspectral datasets obtained by the NASA/JPL-AVIRIS imaging spectrometer (Green et al., 1988). Also, a preliminary evaluation of the above methods was performed using data from the DAIS 7915 and ROSIS imaging spectrometers from DLR (Müller et al., 2001).

- The AVIRIS hyperspectral dataset corresponds to the well-known mining region of Cuprite in Nevada. This area is well-understood mineralogically and has reliable ground truth in several forms (Clark et al., 1993; Swayze, 1997). This fact has made this region a standard test site for comparison of classification algorithms, since not many scenes with such quality ground truth measurements are available for public use. The Cuprite scene we have selected for this work was acquired in 1995, and has been reduced to 50 bands in the 2-2.5 nm region.
- The DAIS 7915 and ROSIS hyperspectral datasets were acquired near the town of Caceres, Spain, in 2001. These data are a good example of Dehesa agroecosystems, typical of the south-western part of Spain and mainly formed by cork-oak trees, pasture and bare soils (semi-arid environment). Our knowledge of the field, obtained after several ground campaigns, make these dataset suitable to test algorithm accuracy. Next, we proceed to describe the experiments performed over these datasets.

3.1. Experiments with AVIRIS hyperspectral dataset

a) First experiment: comparison of the spectral shape

In order to perform this experiment we have selected a set of ground spectral signatures contained in the USGS Digital Spectral Library splib04 (available at http://speclab.cr.usgs.gov/spectral.lib04/spectral-lib04.html) as ground truth references for the comparison. In particular, we have used the AVIRIS-convolved version of this library (http://speclab.cr.usgs.gov/spectral.lib04/lib04-AVIRIS.html).

Figure 2 shows a plot of the GT signatures from the USGS spectral library and the endmembers extracted by PPI, N-FINDR and AMEE algorithms. PPI endmembers were obtained and made public by Research Systems. N-FINDR endmembers were obtained by Dr. Michael E. Winter, author of the algorithm. Finally, AMEE endmembers were extracted by our research group. The USGS spectra are labeled in the plot with their correspondent names in the library. PPI endmembers were labeled with the names that appear in the plot, while N-FINDR and AMEE spectra are not labeled. The colors used in figure 2 have been selected so that the similar spectral signatures can be visually matched. It is appreciated in figure 2 that there are some differences in the absolute value of the reflectances and spectral shape that are likely due to atmospheric transmission effects. In order to avoid these effects, we use the SAM distance measure, which is invariant to ilumination details.

Tables I, II and III respectively show the confusion matrices of spectral angle distances between USGS GT signatures and the endmembers extracted by PPI, N-FINDR and AMEE. Table IV shows the number of correctly detected endmembers, redundant endmembers, missed GT signatures and mean error for the considered endmember extraction algorithms using three different similarity threshold values. In order to understand the results shown in this table it should be noted that perfect performance for a certain algorithm would be correct detection of all endmembers and no missed GT signatures or redundant endmembers, independently of the similarity threshold considered. The results shown in table IV reveal that, when a strong similarity threshold is imposed, the three tested algorithms perform similarly. When the similarity constraint is relaxed, AMEE performs better than the other approaches, detecting all endmember signatures and producing only 2

redundant endmembers, which correspond to the ones labeled as AMEE_ENDMEMBER_8 and AMEE_ENDMEMBER _9 in figure 2. It should be noted that AMEE_ENDMEMBER_9 is a typical shade endmember, while AMEE_ENDMEMBER_8 is associated to the brightest parts of the Silica mineral (a similar endmember is also detected by the PPI algorithm).

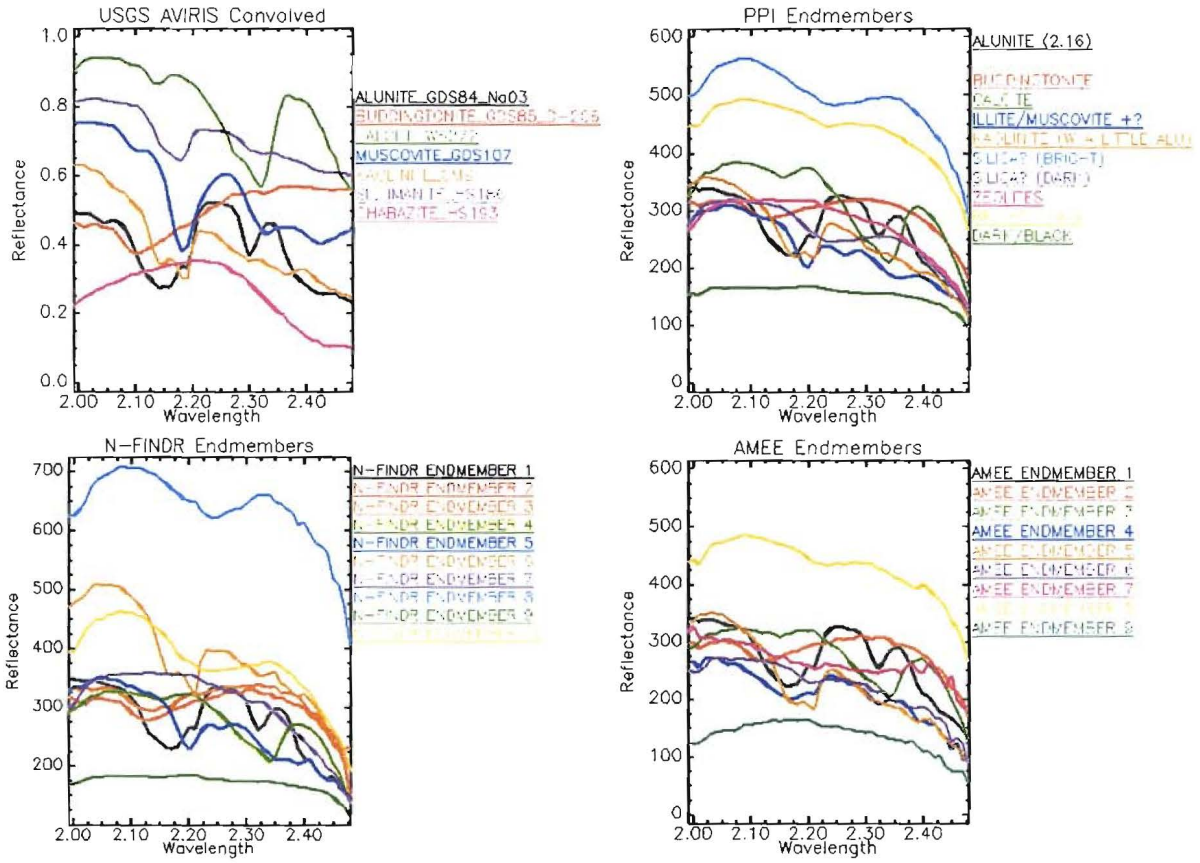

Figure 2. Clockwise, reference GT signatures extracted from AVIRIS-convolved USGS Digital Spectral Library and endmembers extracted for the Cuprite dataset by PPI, N-FINDR and AMEE methodologies.

Table I. Confusion matrix of spectral angle distances between endmembers extracted by PPI and USGS GT references.

	PPI:										
USGS:	**E1**	**E2**	**E3**	**E4**	**E5**	**E6**	**E7**	**E8**	**E9**	**E10**	E11
Alunite	0.119	0.155	0.208	0.178	0.265	0.207	0.238	0.208	0.216	0.230	0.206
Buddingtonite	0.286	0.269	0.228	0.188	0.319	0.208	0.343	0.359	0.231	0.302	0.287
Calcite	0.136	0.104	0.085	0.093	0.149	0.088	0.140	0.157	0.084	0.124	0.132
Muscovite	0.256	0.229	0.232	0.263	0.234	0.241	0.238	0.268	0.247	0.223	0.167
Kaolinite	0.164	0.178	0.223	0.233	0.208	0.236	0.139	0.093	0.218	0.189	0.226
Sillimanite	0.151	0.149	0.181	0.199	0.186	0.197	0.103	0.090	0.177	0.161	0.194
Chabazite	0.194	0.151	0.112	0.142	0.095	0.114	0.148	0.183	0.103	0.117	0.144

Table II. Confusion matrix of spectral angle distances between endmembers extracted by N-FINDR and USGS GT references.

	N-FINDR:									
USGS:	**E1**	**E2**	**E3**	**E4**	**E5**	**E6**	**E7**	**E8**	**E9**	E10
Alunite	0.211	0.233	0.119	0.241	0.182	0.208	0.180	0.225	0.205	0.282
Buddingtonite	0.192	0.338	0.283	0.283	0.178	0.300	0.167	0.279	0.320	0.247
Calcite	0.085	0.137	0.132	0.121	0.113	0.143	0.092	0.105	0.121	0.175
Muscovite	0.255	0.235	0.256	0.227	0.276	0.146	0.279	0.234	0.257	0.319
Kaolinite	0.243	0.141	0.164	0.210	0.249	0.226	0.240	0.195	0.127	0.284
Sillimanite	0.201	0.102	0.149	0.181	0.219	0.196	0.205	0.159	0.098	0.251
Chabazite	0.117	0.152	0.191	0.083	0.159	0.154	0.148	0.109	0.147	0.179

Table III. Confusion matrix of spectral angle distances between endmembers extracted by AMEE and USGS GT references.

	AMEE:								
USGS:	**E1**	**E2**	**E3**	**E4**	**E5**	**E6**	**E7**	**E8**	E9
Alunite	0.119	0.213	0.179	0.243	0.232	0.162	0.248	0.216	0.213
Buddingtonite	0.286	0.227	0.125	0.289	0.297	0.316	0.415	0.311	0.226
Calcite	0.194	0.109	0.153	0.087	0.173	0.158	0.230	0.136	0.084
Muscovite	0.151	0.178	0.212	0.184	0.234	0.127	0.122	0.155	0.147
Kaolinite	0.164	0.221	0.244	0.211	0.268	0.136	0.100	0.185	0.183
Sillimanite	0.136	0.081	0.145	0.127	0.169	0.128	0.213	0.129	0.058
Chabazite	0.256	0.237	0.270	0.225	0.143	0.221	0.298	0.194	0.284

Table IV. Mean error, number of matched endmembers, redundant endmembers and missed GT signatures for each method using three different tolerance threshold errors.

		T = 0.10				T = 0.15				T = 0.20			
Method:	**NE**	**MEr**	**MEn**	**MG**	**RE**	**MEr**	**MEn**	**MG**	**RE**	**MEr**	**MEn**	**MG**	**RE**
PPI	11	0.090	3	4	8	0.105	5	2	6	0.115	6	2	5
N-FINDR	10	0.091	3	4	7	0.106	5	2	5	0.110	6	1	4
AMEE	9	0.081	3	4	6	0.101	7	0	2	0.108	7	0	2

NE – Number of extracted endmembers MEr – Mean error MEn – Number of matched endmembers
MG – Number of missed GT signatures T – Tolerance threshold RE – Number of redundant endmembers

b) Second experiment: comparison of fractional abundance maps

In this experiment, we have focused on comparing the fractional abundance maps derived from the endmembers shown in figure 2. Abundance maps of GT USGS signatures, obtained using Fully Constrained Linear Spectral Unmixing (FCLSU) are used as ground truth information. The experiment presented in the previous subsection revealed that five USGS signatures are easily detected by all the studied endmember extraction algorithms: Alunite, Buddingtonite, Calcite, Kaolinite and Muscovite. Following this result, we have calculated the abundance planes of the endmembers obtained by PPI, N-FINDR and AMEE for the previously addressed minerals, using a FCLSU approach.

Table V. Root Mean Square Error (RMSE) obtained by comparing FCLSU fractional abundances of selected USGS GT signatures to FCLSU abundance maps of correspondent extracted endmembers. The average RMSE for the signatures considered is also addressed.

USGS-derived Abundance Map	PPI Map	N-FINDR Map	AMEE Map
Alunite	0.071	0.072	0.070
Buddingtonite	0.170	0.150	0.157
Calcite	0.011	0.023	0.020
Kaolinite	0.048	0.089	0.009
Muscovite	0.042	0.045	0.063
Average	0.068	0,075	0.064

A detailed quantitative study of the quality of derived abundance planes has been carried out by calculating the RMSE between pairs of correspondent abundance maps. The results obtained are shown in Table V, which also addresses the mean error for each method. This table reveals that the similarity between the obtained abundance maps is very high in general, although the performance is slightly different depending on the mineral considered. AMEE algorithm obtains the best result for the Alunite and Kaolinite materials, while PPI is the most successful algorithm with the Calcite and Muscovite and N-FINDR is the best approach with Buddingtonite.

c) Third experiment: reconstruction of the original image

In this experiments we test the accuracy of the considered approaches to provide a reconstruction of the original image. Table VI shows a comparison of the RMSE errors obtained by the considered approaches, using the algorithm shown in section 2.3.

Table VI. RMSE errors obtained by the proposed endmember extraction algorithms in the reconstruction of AVIRIS Cuprite dataset.

	Number of endmembers used in the reconstruction (ordered by total abundance):								
	3	**4**	**5**	**6**	**7**	**8**	**9**	**10**	**11**
PPI	0.197	0.168	0.144	0.123	0.100	0.075	0.060	0.045	0.032
N-FINDR	0.197	0.115	0.098	0.086	0.073	0.063	0.054	0.049	
AMEE	0.174	0.128	0.102	0.074	0.055	0.046	0.042		

From this table, PPI is the most accurate method when all extracted endmembers are used in the reconstruction (3.2% error versus 4.9% of N-FINDR and 4.2% of AMEE). Nevertheless, when the number of endmembers used in the reconstruction is reduced, both N-FINDR and AMEE outperform PPI. For instance, if 7 endmembers are used for the reconstruction, the use of PPI results in a 10% error, while N-FINDR reduces the error to 7.3% and AMEE results in just a 5.5% error, which is a significant improvement over PPI. Further experiments are required to validate the previously addressed results using additional datasets and different conditions.

3.2. Experiments with DAIS 7915 and ROSIS hyperspectral datasets

In this section, we address some preliminary results obtained after applying our AMEE algorithm to DAIS 7915 and ROSIS hyperspectral datasets, obtained over the town of Cáceres, Spain, in July 2001. These results are showed just for illustrative (not comparative) purposes. In the future, the development of several ground campaigns will allow us to make these images, along with quality ground measurements, available to the scientific community dedicated to hyperspectral data analysis as test images to validate endmember extraction and classification algorithms. Figures 3 and 4 show extracted endmembers and corresponding abundance maps for DAIS 7915 and ROSIS imagery, respectively.

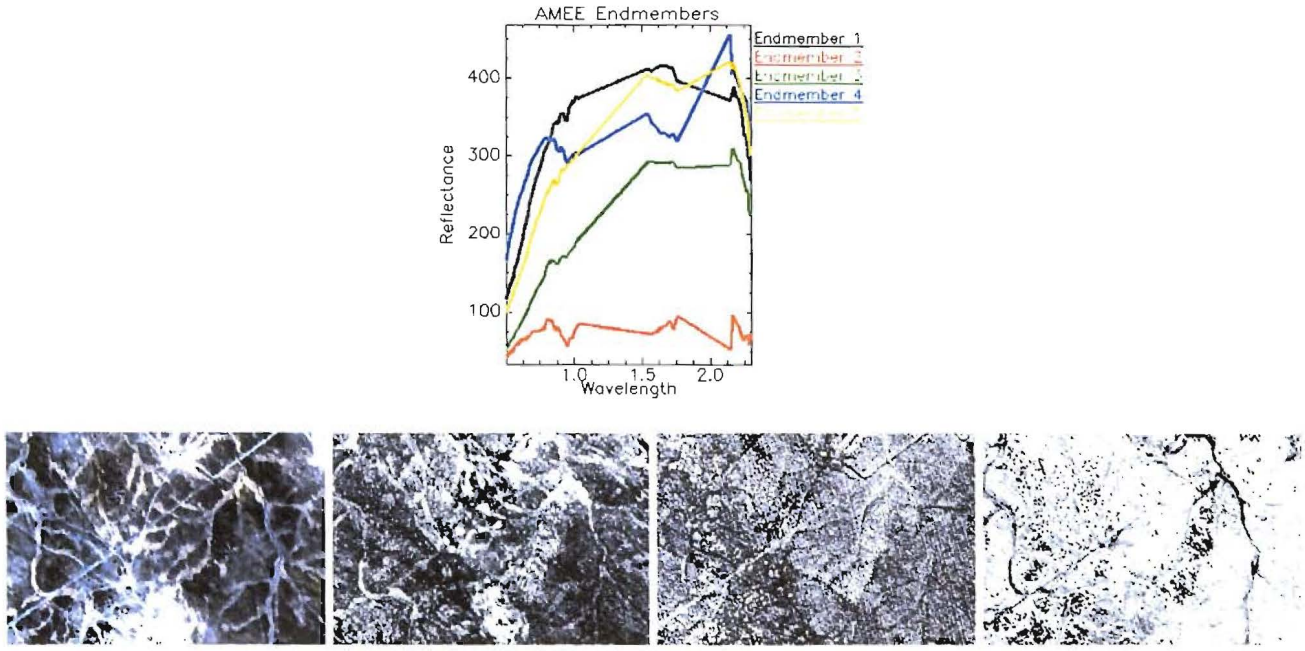

Figure 3. Preliminary endmember extraction results of AMEE algorithm applied to DAIS 7915 hyperspectral data. Top: extracted endmembers. Bottom, left to right: original image; abundance map for Endmember_1 (soil-pasture); abundance map for Endmember_2 (cork-oak trees); abundance map for Endmember_3 (shadow).

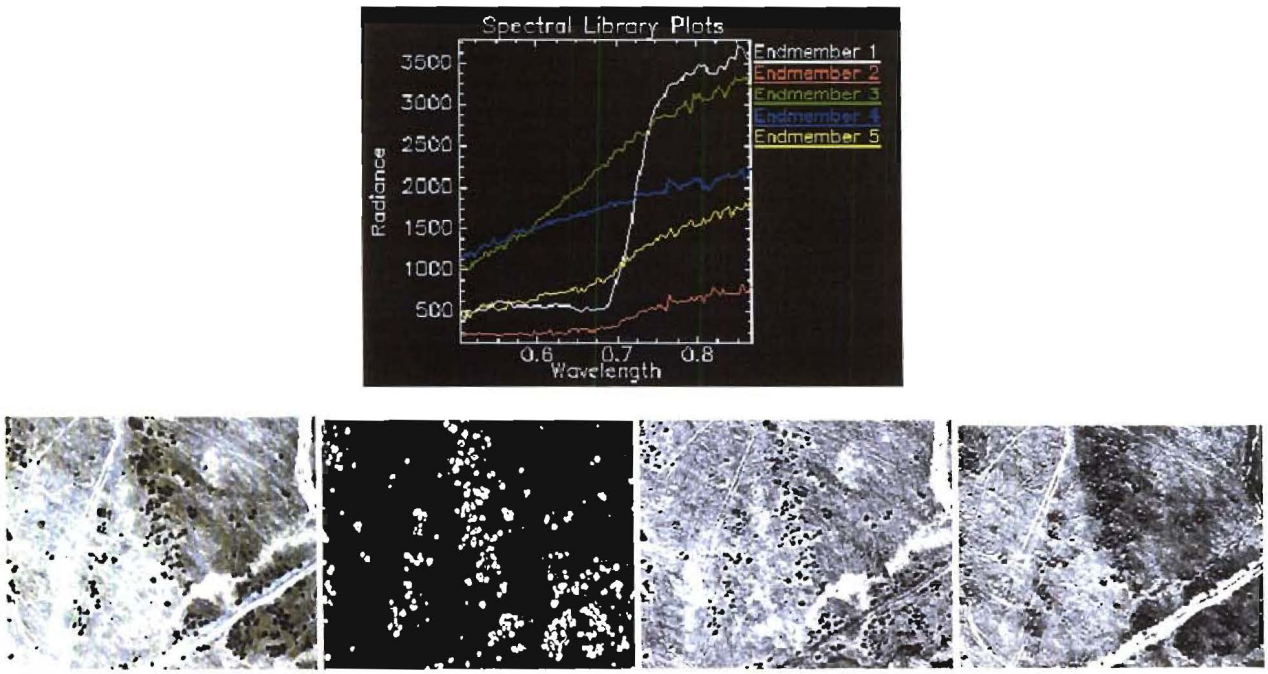

Figure 4. Preliminary endmember extraction results of AMEE algorithm applied to ROSIS hyperspectral data. Top: extracted endmembers. Bottom, left to right: original image; abundance map for Endmember_1 (cork-oak trees); abundance map for Endmember_2 (soil); abundance map for Endmember_3 (pasture).

4. Conclusions and future lines

Many endmember extraction algorithms have been proposed in the literature over the last decade. Comparison of these approaches has been a challenging task due to a lack of rigorous criteria to substantiate any new algorithm. Another difficulty arises from the fact that there is no standardized data to perform the comparison. In this paper, we have conducted a first attempt to impartially evaluate the accuracy of several well-known endmember extraction algorithms. The study focuses on two hyperspectral datasets: the famous AVIRIS dataset of the Cuprite mining region in Nevada (a well-understood mineralogically region which has been extensively mapped and truthed) and a DAIS 7915 dataset containing a typical Spanish Dehesa environment (pasture and cork-oak trees).

Comparison of endmembers has been carried out from several points of view. Firstly, the problem was tackled under the assumption that reliable ground truth information is available. In this sense, we performed a simple preliminary experiment based on comparing the spectral shape of extracted endmembers to available reference signatures. A further attempt from the perspective of a mixed pixel classification problem was also conducted by comparing abundance planes of endmember constituents to reference maps. Finally, a new schema to compare algorithms when no ground truth measurements are available was presented and discussed. Since reliable ground truth is generally expensive and difficult to obtain, we believe this approach may be of interest to the community.

Despite our effort to conduct comprehensive, impartial and rigorous comparative analysis of various algorithms, completion is not claimed. In particular, the number of algorithms compared in this work is limited to three methods. Also, the number of comparative measures is reduced to linear distances. Plausible future research should include a comparative analysis of linear and non linear distances, as well as comparative measures that include second order statistics.

Acknowledgments

The authors would like to acknowledge Robert O. Green and Roger Clark for their comments on this comparative effort. Also, the contribution of Michael and Ed Winter, who provided results and an evaluation version of the N-FINDR method, is gratefully acknowledged. Finally, Antonio Plaza would like to personally thank Robert O. Green and the whole AVIRIS team for their guidance, support and warm hospitality during his research visit to JPL.

References

Bateson, C.A., Asner, G.P., Wessman, C.A., "Endmember Bundles: A New Approach to Incorporating Endmember Variability into Spectral Mixture Analysis," *IEEE Transactions on Geoscience and Remote Sensing*, vol. 38 issue 2 part: 2 , pp. 1083 –1094, March 2000.

Boardman, J.W., Kruse, F.A. & Green, R.O., "Mapping Target Signatures via Partial Unmixing of AVIRIS Data," *Summaries of the V JPL Airborne Earth Science Workshop*, 1995.

Bowles, J., Gillis, D., Palmadesso, P., "New improvements in the ORASIS algorithm," *Aerospace Conference Proceedings*, vol. 3, pp. 293-298, 2000.

Clark, R. N., Swayze, G. A., Gallagher, A., King, T. V. V., and Calvin, W. M., "The U. S. Geological Survey Digital Spectral Library: Version 1: 0.2 to 3.0 m," *U. S. Geological Survey, Open File Report* 93-592, 1340 p, 1993.

Garcia, M., Ustin, S.L., "Detection of interannual vegetation responses to climatic variability using AVIRIS data in a coastal savanna in California," *IEEE Transactions on Geoscience and Remote Sensing*, vol. 39, pp. 1480-1490, 2001.

Green, R.O. et al., "Imaging Spectroscopy and the Airborne Visible/Infrared Imaging Spectrometer (AVIRIS)," *Remote Sensing of Environment*, vol. 65, pp. 227-248, 1998.

Keshava, N., Mustard, J.F., "Spectral unmixing,". IEEE Signal Processing Magazine, vol. 19, pp. 44-57, 2002.

Kneubuehler, M., Schaepman, M.E., Kellenberger, T.W., "Comparison of different approaches of selecting endmembers to classify agricultural land by means of hyperspectral data (DAIS7915)," *Proceedings International Geoscience and Remote Sensing Symposium*, vol. 2 , pp. 888-890, 1998.

Kruse, F.A., "Spectral Identification of Image Endmembers Determined from AVIRIS Data," *Summaries of the VII JPL Airborne Earth Science Workshop*, 1998.

Maselli, F., "Multiclass spectral decomposition of remotely sensed scenes by selective pixel unmixing," *IEEE Transactions on Geoscience and Remote Sensing*, vol. 36, pp. 1809 -1820, 1998.

Müller, A., Hausold, A., Strobl, P., "HySens – DAIS / ROSIS Imaging Spectrometers at DLR," *Proc. SPIE Image and Signal Processing for Remote Sensing VII*, Toulouse, France, 2001.

Okin, G.S, Roberts, D.A., Murray, B., "Multiple Endmember Spectral Mixure Analysis: Application to an Arid/Semi-arid Landscape," *Summaries of the IX JPL Airborne Earth Science Workshop*, 1998.

Plaza, A., Martinez, P., Perez, R.M., "Spatial/Spectral Endmember Extraction by Multidimensional Morphological Operations," *IEEE Transactions on Geoscience and Remote Sensing*, vol. 40, no. 9, Sept. 2002.

Plaza, A., Martínez, P., Gualtieri, J.A., Pérez, R.M., "Spatial/Spectral Endmember Extraction from AVIRIS Hyperspectral Data Using Mathematical Morphology," *Summaries of the XI JPL Airborne Earth Science Workshop*, 2001a.

Plaza, A., Martinez, P., Gualtieri, J.A., Perez, R.M., "Automated identification of endmembers from hyperspectral data using mathematical morphology," *Proc. SPIE Image and Signal Processing for Remote Sensing VII,* Toulouse, France, 2001b.

Roberts, D.A., Gardner, R., Church, R., Ustin, S., Scheer, G., Green, R.O., "Mapping Chaparral in the Santa Monica Mountains Using Multiple Endmember Spectral Mixture Models," *Remote Sensing of Environment*, vol. 65, pp. 267-279, 1998.

Segl, K., Roessner, S., Heiden, U., "Differentiation of urban surfaces based on hyperspectral image data and a multi-technique approach," *Proceedings International Geoscience and Remote Sensing Symposium*, vol. 4 , pp. 1600-1602, 2000.

Swayze, G., *The hydrothermal and structural history of the Cuprite Mining District, Southwestern Nevada: an integrated geological and geophysical approach*.Ph. D. Dissertation, University of Colorado, Boulder, 1997.

Sweet, J., Granaham, J. and Sharp, M., "An Objective Standard for Hyperspectral Image Quality," *Summaries of the XII JPL Airborne Earth Science Workshop*, 2000.

Winter, M.E., "Comparison of approaches for determining end-members in hyperspectral data," *Aerospace Conference Proceedings*, vol. 3 , pp. 305 -313, 2000.

COMANCHE and COCHISE: two reciprocal atmospheric codes for hyperspectral remote sensing

Laurent Poutier,* Christophe Miesch, Xavier Lenot, Véronique Achard, Yannick Boucher
Office National d'Etudes et de Recherches Aérospatiales, Département d'Optique Théorique et Appliquée

1. INTRODUCTION

This paper describes two reciprocal codes developed for hyperspectral imagery in remote sensing. The first one is called COMANCHE and computes the incoming spectral radiance at the sensor level, for an instrument operating in the VIS - LWIR spectral range and observing a target over a background. COMANCHE uses an analytical formulation of the upwelling radiance at the sensor level in which the atmospheric parameters are independent of the ground parameters. The formulation includes the environmental effects due to scattering (trapping effects and diffuse transmission). The atmospheric parameters are extracted from MODTRAN 4 computations and the environment functions are obtained using two Monte-Carlo codes. The second code is called COCHISE and retrieves the 2D ground spectral reflectance from a calibrated hyperspectral image. The actual version of COCHISE is limited to the reflective domain. It performs the inversion of the COMANCHE analytical formulation and includes a 2D estimation of the columnar water vapor amount directly from the radiance hypercube. The COMANCHE and COCHISE algorithms are presented and preliminary validation results based on comparisons with reference radiative transfer codes and an AVIRIS data set are given.

2. ANALYTICAL FORMULATION OF THE AT-SENSOR RADIANCE

This section presents the formulation that is used in COMANCHE and that addresses the following scenario: the scene consists of a circular uniform lambertian target of radius R_t, albedo ρ_t and temperature T_t, laying on a uniform lambertian background, infinite in size, of albedo ρ_b and temperature T_b. The spectral radiance is simulated for a target pixel (Fig. 1), centered on the target and a background pixel, located at such a distance from the target that adjacency effects involving the target material can be neglected.

For the target pixel, the incoming radiance, $L_{tot}^{tp}(\lambda)$, can be written as the sum of three contributors:

$$L_{tot}^{tp}(\lambda) = L_{atm}(\lambda) + t_{dir}(\lambda) L_0^{tp}(\lambda) + t_{dif}(\lambda) L_0^{env}(\lambda) \tag{1}$$

The first contributor, $L_{atm}(\lambda)$, represents the atmospheric radiance, without any interaction with the ground. The second one represents the upwelling radiance directly transmitted from the ground, which is the product of the direct transmission from the target to the sensor, $t_{dir}(\lambda)$, and the upwelling radiance at the ground level leaving the target pixel, denoted $L_0^{tp}(\lambda)$. The third contributor describes the photons that have reached the ground and then have been scattered towards the sensor. This contributor is the product of the diffuse upwelling transmittance $t_{dif}(\lambda)$ and the upwelling radiance of the target environment at the ground level, $L_0^{env}(\lambda)$.

The radiance leaving the target pixel is the sum of reflective and emissive terms, as written below:

$$L_0^{tp}(\lambda) = \tilde{\rho}^{tp}(\lambda) \frac{E_{tot}^{tp}(\lambda)}{\pi} + \tilde{\varepsilon}^{tp}(\lambda) L_{BB}\left(\lambda, \tilde{T}^{tp}(\lambda)\right) \tag{2}$$

* ONERA Centre de Toulouse, 2 av. Edouard Belin, BP 4025, 31055 Toulouse Cedex 4, France
Phone: (33) 5 62 25 26 25; Fax: (33) 562 25 25 88; E-mail : Laurent.Poutier@onecert.fr; Web: http://onera.fr/dota-en/

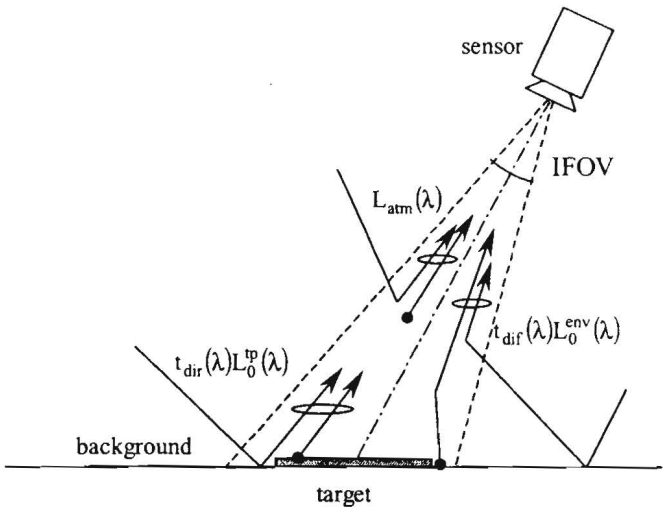

Figure 1. Illustration of the three contributors in the target pixel upwelling radiance.

In Eq. 2, $E_{tot}^{tp}(\lambda)$ represents the total irradiance incoming at the target pixel, $L_{BB}(\lambda,T)$ is the black body spectral radiance at temperature T, given by the Planck's law:

$$L_{BB}(\lambda,T)=\frac{A(\lambda)}{\exp[B(\lambda)/T]-1} \tag{3}$$

The terms $\tilde{\rho}^{tp}(\lambda)$, $\tilde{\varepsilon}^{tp}(\lambda)$ and $\tilde{T}^{tp}(\lambda)$ are respectively the albedo, the emissivity and the temperature averaged on the target pixel. Let α be simply the fraction of the target pixel corresponding to the target material. The three average thermo-optical characteristics of the target pixel are obtained as follow:

$$\tilde{\rho}^{tp}(\lambda)=\alpha\rho_t(\lambda)+[1-\alpha]\rho_b(\lambda) \tag{4}$$

$$\tilde{\varepsilon}^{tp}(\lambda)=\alpha\varepsilon_t(\lambda)+[1-\alpha]\varepsilon_b(\lambda) \tag{5}$$

$$\tilde{T}^{tp}(\lambda)=\frac{B(\lambda)}{\ln\left(\frac{A(\lambda)\tilde{\varepsilon}^{tp}(\lambda)}{\alpha\varepsilon_t(\lambda)L_{BB}(\lambda,T_t)+[1-\alpha]\varepsilon_b(\lambda)L_{BB}(\lambda,T_b)}+1\right)} \tag{6}$$

The total downward irradiance can be written as:

$$E_{tot}^{tp}(\lambda)=\left[E_0(\lambda)+\pi\tilde{\varepsilon}_{dn}^{tp}(\lambda)L_{BB}\left(\lambda,\tilde{T}_{dn}^{tp}(\lambda)\right)S(\lambda)\right]\frac{1}{1-\tilde{\rho}_{dn}^{tp}(\lambda)S(\lambda)} \tag{7}$$

The first factor corresponds to the ground downward irradiance without ground reflection phenomena. It is the sum of $E_0(\lambda)$ which accounts for sun and atmospheric sources of irradiance, and of the surface emission scattered back to the ground through the atmospheric spherical albedo $S(\lambda)$. The second factor describes the trapping effects between the ground and the atmosphere.

The three quantities denoted as $\tilde{X}_{dn}^{tp}$ (albedo, emissivity and temperature) correspond to an averaging over the area participating in the trapping effect. Let the environment function $G_\lambda(r)$ describe the probability that the last reflection involved in the trapping effects comes from a distance r from the target center (there is no azimuthal dependence in the density function G_λ). The environment function describing the ground-atmosphere coupling should take into account the spatial distribution of the multiple rebounds that finally reach the target pixel. Meanwhile, as this function acts as a second order on the global irradiance (the spherical albedo being typically around or less than 10^{-1} in magnitude), it remains fully valid to describe it only by the last rebound, the multiple

trapping effects acting as a second order on the environment function, compared to the single rebounds. The average quantities can be obtained by the following formulas:

$$\tilde{\rho}_{dn}^{tp}(\lambda) = \alpha_{dn}(\lambda).\rho_t(\lambda) + [1 - \alpha_{dn}(\lambda)].\rho_b(\lambda) \tag{8}$$

$$\tilde{\varepsilon}_{dn}^{tp}(\lambda) = \alpha_{dn}(\lambda).\varepsilon_t(\lambda) + [1 - \alpha_{dn}(\lambda)].\varepsilon_b(\lambda) \tag{9}$$

$$\tilde{T}_{dn}^{tp}(\lambda) = \frac{B(\lambda)}{\ln\left(\dfrac{A(\lambda).\tilde{\varepsilon}_{dn}^{tp}(\lambda)}{\alpha_{dn}(\lambda)\varepsilon_t(\lambda)L_{BB}(\lambda,T_t) + [1 - \alpha_{dn}(\lambda)]\varepsilon_b(\lambda)L_{BB}(\lambda,T_b)} + 1\right)} \tag{10}$$

where $\alpha_{dn}(\lambda)$ expresses the weight of the target material participating to the coupling effect:

$$\alpha_{dn}(\lambda) = 2\pi.\int_0^{R_t} G_\lambda(r).r.dr \tag{11}$$

The environment upwelling radiance $L_0^{env}(\lambda)$ is almost similar to the target pixel upwelling radiance. The main difference is that the averaging of the thermo-optical properties of the ground are governed by an environment function describing the spread out of the upwelling diffused radiance that reaches the sensor target pixel. In the same manner as in the trapping effect processes, let $F_\lambda(r,\theta)$ denote the 2D density function giving the probability that the upwelling diffuse paths come from the position (r,θ) expressed in polar coordinates relatively to the center of the target. The azimuthal dependence is observed for off-nadir viewing angles. In a similar way to Eq. 11, the weight of the target material involved in the diffuse radiance, $\alpha_{up}(\lambda)$, is derived by the following integration:

$$\alpha_{up}(\lambda) = \int_0^{2\pi}\int_0^{R_t} F_\lambda(r,\theta).r.dr.d\theta \tag{12}$$

The average thermo-optical properties implied in the environment upwelling radiance are given by:

$$\tilde{\rho}_{up}^{tp}(\lambda) = \alpha_{up}(\lambda).\rho_t(\lambda) + [1 - \alpha_{up}(\lambda)].\rho_b(\lambda) \tag{13}$$

$$\tilde{\varepsilon}_{up}^{tp}(\lambda) = \alpha_{up}(\lambda).\varepsilon_t(\lambda) + [1 - \alpha_{up}(\lambda)].\varepsilon_b(\lambda) \tag{14}$$

$$\tilde{T}_{up}^{tp}(\lambda) = \frac{B(\lambda)}{\ln\left(\dfrac{A(\lambda).\tilde{\varepsilon}_{up}^{tp}(\lambda)}{\alpha_{up}(\lambda)\varepsilon_t(\lambda)L_{BB}(\lambda,T_t) + [1 - \alpha_{up}(\lambda)]\varepsilon_b(\lambda)L_{BB}(\lambda,T_b)} + 1\right)} \tag{15}$$

Finally, the environment upwelling radiance can be written as:

$$L_0^{env}(\lambda) = \tilde{\rho}_{up}^{tp}(\lambda)\frac{E_{tot}^{env}(\lambda)}{\pi} + \tilde{\varepsilon}_{up}^{tp}(\lambda)L_{BB}\left(\lambda, \tilde{T}_{up}^{tp}(\lambda)\right) \tag{16}$$

In the latter equation, the downward irradiance is denoted $E_{tot}^{env}(\lambda)$. In a strict formulation, the downwelling irradiance should include a position dependence, due to the coupling effects that, as mentioned before, involve an environment function related to the environment of the surface element where the irradiance is calculated. Considering that the joint effect of the ground-atmosphere coupling and the upwelling scattering are negligible, the downward irradiance is supposed to be uniform and equal to $E_{tot}^{tp}(\lambda)$ given by Eq.7.

Concerning the background pixel, the target interaction is neglected and the radiance is simply given by the precedent formulas where the coefficients α, $\alpha_{up}(\lambda)$ and $\alpha_{dn}(\lambda)$ are equal to zero.

3. DIRECT MODEL: COMANCHE IMPLEMENTATION

COMANCHE uses the precedent equations to simulate target/background at-sensor spectral radiances. These equations separate atmospheric radiative properties and ground characteristics. The atmospheric parameters are the upwelling atmospheric radiance without any interaction with the ground $L_{atm}(\lambda)$, the downwelling irradiance at ground level $E_0(\lambda)$, also with no interaction with the ground, the atmospheric spherical albedo $S(\lambda)$, the diffuse and direct upward transmittances, respectively $t_{dif}(\lambda)$ and $t_{dir}(\lambda)$, and the two environment functions $F_\lambda(r,\theta)$ and $G_\lambda(r)$.

The first five parameters are computed using the radiative transfer code MODTRAN 4.1 (Anderson et al., 2000) in radiance mode, considering a uniform ground with four different boundary conditions: $\{\rho = 0, T = 0K\}$; $\{\rho = 0.5, T = 0K\}$; $\{\rho = 1, T = 0K\}$; $\{\rho = 0, T = 300K\}$. Let $L_{tot}^{\rho,T}(\lambda)$ and $L_{ref}^{\rho,T}(\lambda)$ be respectively the total and reflected radiances associated to each simulation run. The direct transmittance is directly obtained as an output of the MODTRAN simulations. The atmospheric radiance is straightforward:

$$L_{atm}(\lambda) = L_{tot}^{0,0}(\lambda) \tag{17}$$

The spherical albedo is given by the relation:

$$S(\lambda) = \frac{L_{tot}^{1,0}(\lambda) + L_{tot}^{0,0}(\lambda) - 2.L_{tot}^{1/2,0}(\lambda)}{L_{tot}^{1,0}(\lambda) - L_{tot}^{1/2,0}(\lambda)} \tag{18}$$

The downward irradiance is given by:

$$E_0(\lambda) = \pi \frac{1 - S(\lambda)}{t_{dir}(\lambda)} . L_{ref}^{1,0}(\lambda) \tag{19}$$

The diffuse transmission is given by the following relation:

$$\begin{cases} t_{dif}(\lambda) = \dfrac{L_{tot}^{0,300}(\lambda) - L_{tot}^{0,0}(\lambda)}{L_{BB}(\lambda,300)} - t_{dir}(\lambda) & \text{if } \lambda \geq 3\mu m \\ t_{dif}(\lambda) = \left[L_{tot}^{1,0}(\lambda) - L_{tot}^{0,0}(\lambda)\right] \dfrac{1 - S(\lambda)}{E_0(\lambda)} - t_{dir}(\lambda) & \text{if } \lambda < 3\mu m \end{cases} \tag{20}$$

The environment functions $F_\lambda(r,\theta)$ and $G_\lambda(r)$ result from very complex and chaotic physical processes. Thus they are difficult to obtain directly from analytical expressions. Monte Carlo methods are well adapted to compute them in a robust way. Indeed, the Monte Carlo principle consists in modeling statistically the elementary phenomena to reproduce the global physical ones. In order to compute both environment functions, the method consists in simulating the paths of photons inside the atmosphere, considering a flat ground. Actually, the two algorithms developed here (one for each function) are derived from an existing radiative transfer code (Miesch et al., 1999). This radiative transfer code is able to simulate paths of photons inside the earth-atmosphere system and reproduce absorption, scattering and reflection phenomena. It considers a plane-parallel and horizontally invariant atmosphere divided into elementary homogeneous layers, and the extinction and scattering coefficients for both molecules and aerosols are computed at a specific monochromatic wavelength. The scene is represented by a digital elevation model associated to a bidirectional reflectance map. Each pixel of the ground model is assumed to be homogeneous.

To compute the environment function $F_\lambda(r,\theta)$, the existing algorithm is adapted so that the photons are launched from the sensor, in the viewing solid angle. The ground surface is digitized along the (r,θ) coordinates, in relation to the center of the observed ground pixel. Then, the photons that have been scattered by atmosphere and that have reached the ground surface are collected in each surface element. After having simulated enough paths to reach an acceptable convergence in the statistical process, the number of photons associated to a surface element divided by the total number of photons that have reached the ground is directly related to the values of the function $F_\lambda(r,\theta)$ over this surface element.

Concerning the environment function $G_\lambda(r)$, the photons have to be launched from a fixed point of the ground surface. As the ground is here supposed lambertian, the distribution of the emission direction is isotropic. Similarly to the previous computation, the ground surface is again digitized along the coordinate r, in relation to the initial emission point (there is here no dependence on the θ coordinate). The photons that are scattered back to the ground are collected in each annulus element. With an acceptable convergence, the values of the function $G_\lambda(r)$ are derived from the ratio of the photons collected in a given annulus and the photons received on the whole surface.

4. INVERSE MODEL: COCHISE IMPLEMENTATION

The global equation giving a pixel radiance in the reflective part of the spectrum can be rewritten as:

$$L_{tot}(x,y) = L_{atm} + t_{dir}\cdot\left[\frac{E_0.\rho(x,y)}{\pi[1-\rho_G(x,y).S]}\right] + t_{dif}\cdot\left[\frac{E_0.\rho_F(x,y)}{\pi[1-\rho_G(x,y).S]}\right] \quad (21)$$

This expression, limited to the VIS-NIR-SWIR, is reduced to the well-known 6S formulation (Vermote et al., 1997). The seven atmospheric parameters are obtained as in COMANCHE code except that the $L^{0,300}$ computation is no longer useful.

In Eq. 21, we have voluntarily omitted the wavelength dependence for clarity. Moreover, as this equation is to be inverted, the spatial dependence has been added through the (x,y) position of the pixel. The albedo $\rho(x,y)$ represents the averaged pixel albedo and the albedos $\rho_F(x,y)$ and $\rho_G(x,y)$ are the averaged values given by the convolutions with the environment functions introduced in the first section:

$$\rho_F(x,y) = \rho(x,y) \otimes F(x,y) \quad (22)$$

$$\rho_G(x,y) = \rho(x,y) \otimes G(x,y) \quad (23)$$

The inversion technique is iterative. In a first step, the adjacency effects are neglected and a first estimate of $\rho(x,y)$ is obtained by the following equation:

$$\hat{\rho}(x,y) = \frac{L_{tot}(x,y) - L_{atm}}{\frac{E_0}{\pi}.(t_{dir}+t_{dif}) + S\left(L_{tot}(x,y) - L_{atm}\right)} \quad (24)$$

Using Eq. 22 and Eq. 23 a first estimate of environment albedos $\hat{\rho}_F(x,y)$ and $\hat{\rho}_G(x,y)$ is calculated and reinjected in Eq. 21. A second estimate of $\rho(x,y)$ is then obtained by the straightforward inversion of Eq .21:

$$\hat{\rho}'(x,y) = \frac{\pi[1-\hat{\rho}_G(x,y).S]}{E_0.t_{dir}}.\left(L_{tot}(x,y) - L_{atm} - t_{dif}\cdot\left[\frac{E_0.\hat{\rho}_F(x,y)}{\pi[1-\hat{\rho}_G(x,y).S]}\right]\right) \quad (25)$$

This last expression usually gives a satisfactory result. Meanwhile other iterations consisting in convoluting $\hat{\rho}'(x,y)$ with F and G and then reprocessing Eq. 25 could be performed to get a more accurate convergence.

As in COMANCHE, the seven atmospheric parameters, $t_{dir}(\lambda)$, $t_{dif}(\lambda)$, $E_0(\lambda)$, $L_{atm}(\lambda)$, $S(\lambda)$, $F_\lambda(x,y)$ and $G_\lambda(x,y)$ are first computed. The code also includes the inversion of the columnar water vapor amount on a pixel basis using spectral channels in an absorption band. As in FLAASH code (Adler-Golden et al., 1998), the retrieval uses a 2D Look-Up-Table depending on both reflectance and water vapor. The LUT is obtained in a preliminary training step: the at-sensor radiance in the appropriate channels is computed for a set of water vapor amounts and for different values of spectrally flat reflectances. A linear regression ratio (LIRR) and the mean radiance in the out-band channels (L_{REF}) are then computed and finally the LUT expresses the water vapor amount as a function of a regularly resampled grid {LIRR;L_{REF}}.

5. PRELIMINARY VALIDATION RESULTS

COMANCHE and COCHISE implement an analytical formulation relating ground properties and at-sensor radiances, where the atmospheric parameters are extracted from computations with a radiative transfer code (currently MODTRAN 4.1) in four specific configurations (three for COCHISE). The first step of the validation consisted in verifying that the at-sensor radiance computed with COMANCHE was in good agreement with the one delivered by the radiative transfer code itself. Figure 2 gives the obtained differences between COMANCHE and MODTRAN 4 for five different values of spectrally flat reflectance (0.0, 0.25, 0.5, 0.75 and 1.0), over the 0.4-13μm region. The comparison was performed for a homogeneous ground, a sensor located at 1.5 km above the ground and viewing at the nadir direction, a 30° sun zenithal angle, and a midlatitude summer model with 23 km visibility rural aerosols. The differences remain less than 0.4% and validate the at-sensor formulation for a homogeneous scene.

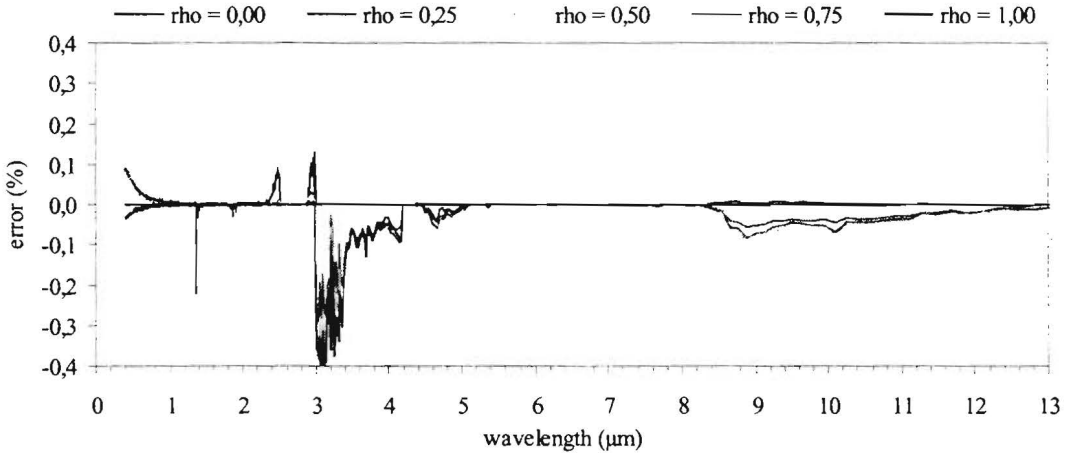

Figure 2. Comparisons between MODTRAN and COMANCHE at-sensor radiances for 5 reflectance values.

The second step consisted in verifying the reciprocity between COCHISE and COMANCHE in the COCHISE spectral domain (up to 2.5 μm). A uniform scene was simulated by duplicating COMANCHE outputs computed for the 224 AVIRIS channels in the environmental and geometric conditions of the previous validation step, for five reflectance values (0.1, 0.3, 0.5, 0.7, 0.9) and for four columnar water vapor amounts (1, 2, 3 and 4 g/cm^2). Figure 3 shows the water vapor then the reflectance sequentially retrieved by COCHISE. Residual errors for reflectance estimation in absorption bands are attributed to the spectral integration over the AVIRIS channels.

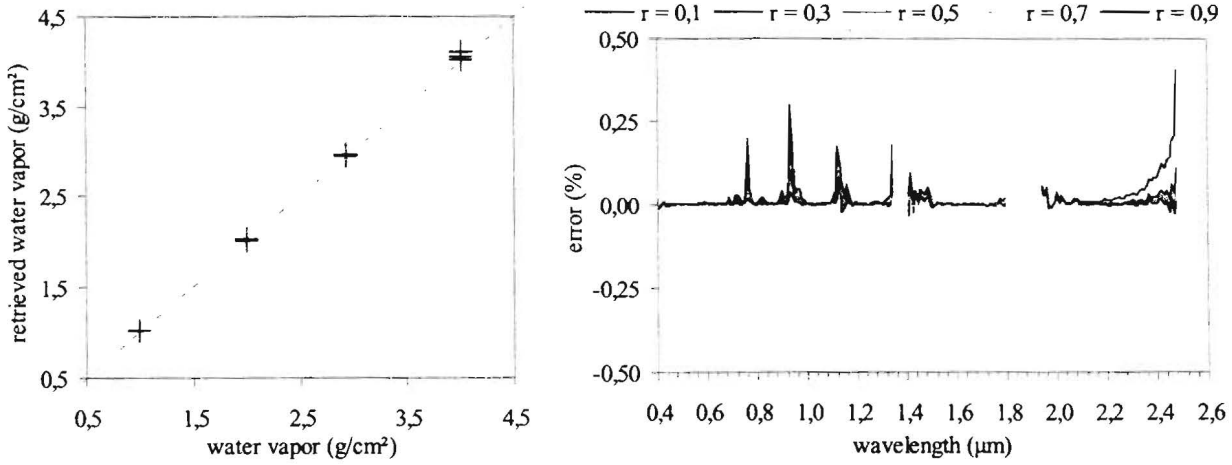

Figure 3. Evaluation of COCHISE on images simulated with COMANCHE for different water vapor and reflectance values. Retrieved water vapor (left), error on retrieved reflectance (right).

Further validations against a reference code have been carried out for heterogeneous scenes. They were based on AMARTIS that simulates at-sensor images in the VIS-NIR for heterogeneous 3D scenes including BRDF effects (Miesch et al., 2000). Figure 4 gives the comparison between AMARTIS and COMANCHE for a concrete target that fits exactly the target pixel, then occupies 1/9 of the same target pixel, the background being a standard vegetation. The simulation was done with the same conditions as the previous ones except the sensor altitude which was set to 3km. As AMARTIS is not dedicated to hyperspectral imagery, it was run for eight single wavelengths. The differences for the at-sensor radiance remain less than 5%. This amplitude is attributed to a difference in the spectral resolution of the two codes and a difference between the two top of atmosphere sun irradiance databases. Meanwhile, the observed differences keep the same amplitudes for the target and the background pixels. This validates the heterogeneous formulation applied to the target pixel which does not degrade the results compared to the standard homogeneous formulation for the background.

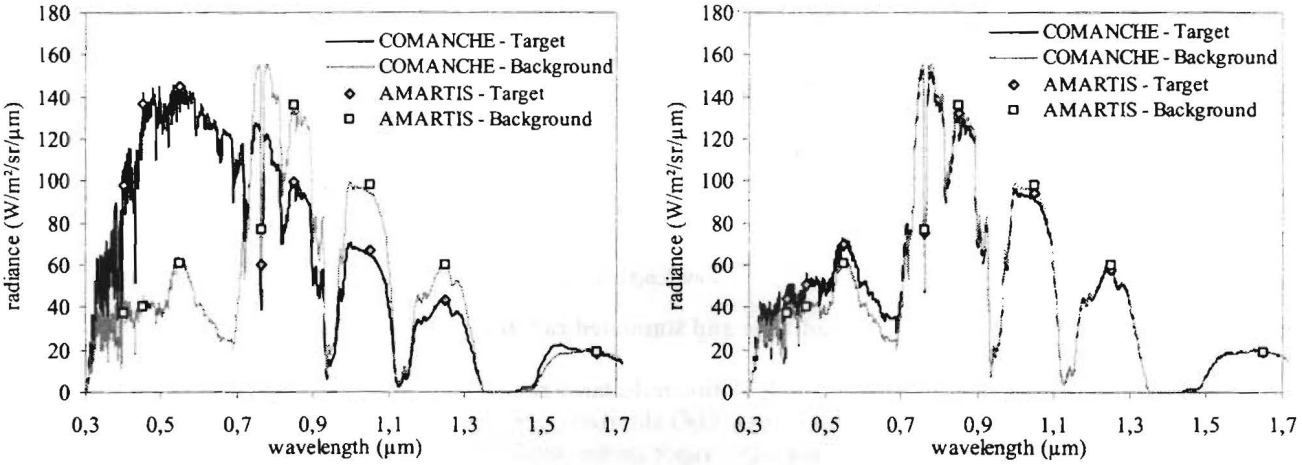

Figure 4. COMANCHE-AMARTIS comparisons for a heterogeneous scene. Target material coincident with target pixel (left) ; target material = 1/9 of target pixel pixel (right).

Concerning COCHISE, an image was simulated in the same conditions as before with AMARTIS, except that the geometry of the scene was an edge. Figure 5 shows the retrieved reflectance profile, normal to the edge. The adjacency effects are clearly apparent in the raw retrieval (after Eq. 23) and the convolution by the two environment kernels computed by the Monte-Carlo modules lead (after Eq. 25) to very satisfactory results, after only one iteration.

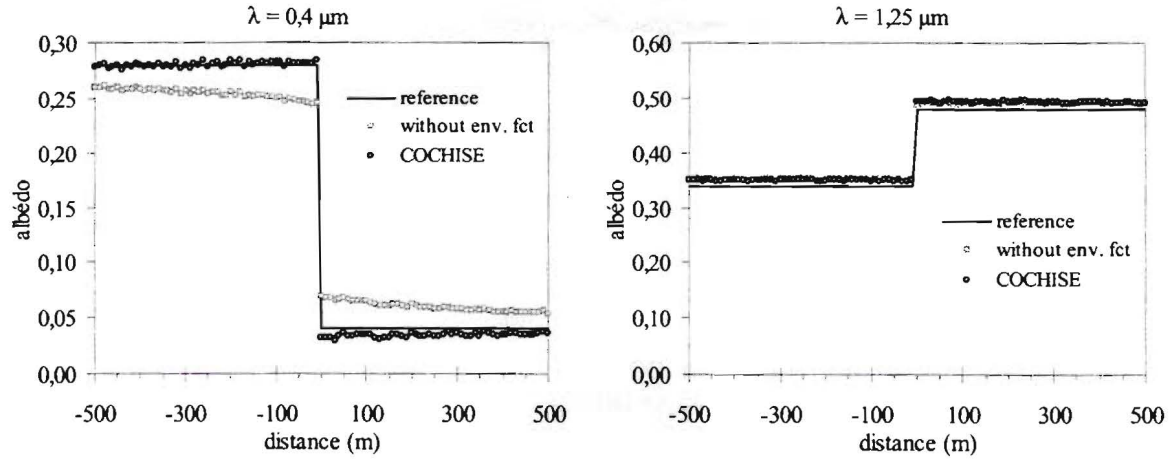

Figure 5. Retrieved reflectance with COCHISE, applied to an edge simulated by AMARTIS. Grey squares show the intermediate results without environment averaging.

Finally, COMANCHE and COCHISE have been applied to an AVIRIS data set composed of an AVIRIS radiance hypercube acquired over the Railroad Valley Playa on the 17 June 1998, a reflectance spectrum of the ground measured in laboratory and atmospheric characteristics including a radiosounding and optical depths measured at different wavelengths for constraining the aerosol behavior. The at-sensor radiance estimated by COMANCHE is shown on Figure 6, along with the radiance extracted from the pixel # (88, 463). The agreement is very good except for the first three channels and the difference is typically less than a few percents.

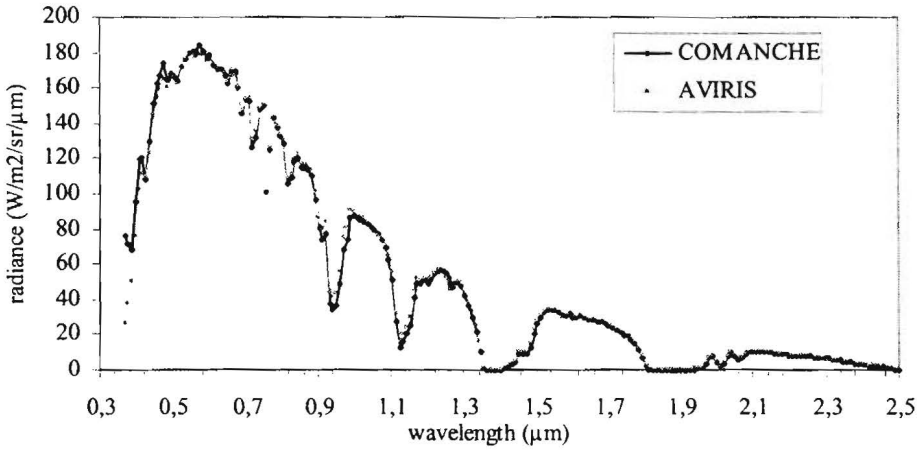

Figure 6. AVIRIS radiance and simulated radiance with COMANCHE.

The same data set is used for COCHISE. A first reflectance retrieval was computed using the water vapor included in the data set. Artifacts are observed in the H_2O absorption regions at 0.94 and 1.13µm. COCHISE was then rerun with a preliminary estimation of the water vapor content based on the 0.94µm absorption band. The restituted amount was 0.99g/cm² in the area of interest, with spatial variability of less than 5% within an extension of approx. 2x2 km. This value underestimates the original value (1.3 g/cm²) by nearly 25%. Meanwhile, the retrieved reflectance leads to a better fit in these two absorption bands. Figure 7 illustrates both reflectance spectra along with the ground truth. Correlatively to the radiance results (Figure 6) the retrieved reflectance is very close to the ground truth. The difference between the measured and estimated water vapor is currently under investigation.

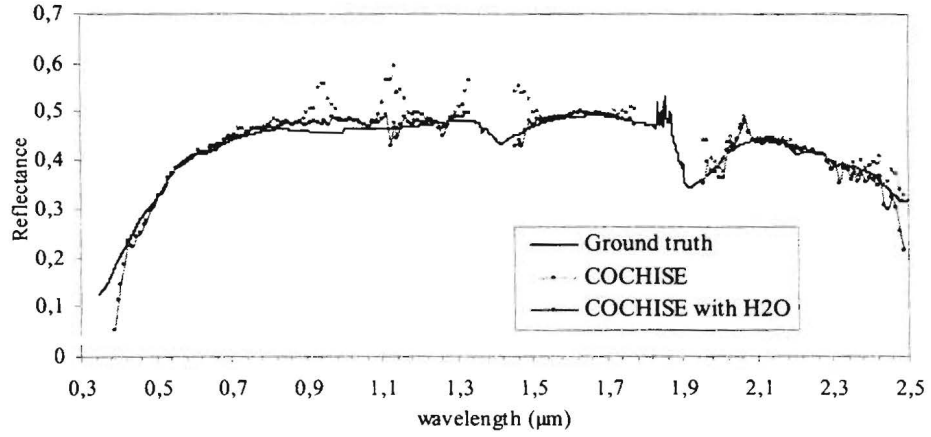

Figure 7. Reflectance retrieval with COCHISE, with and without water vapor correction, and AVIRIS ground truth.

6. CONCLUSION

A simple analytical formulation of the at-sensor radiance including reflective and emissive contributors is proposed for a target over a background. This formulation separates the atmospheric terms from the ground thermo-optical properties. This formulation has been implemented in a direct code, called COMANCHE, that is dedicated to hyperspectral contrasts evaluation in the VIS-LWIR domain. The atmospheric parameters are computed using the MODTRAN4.1 radiative transfer code and two Monte-Carlo modules estimate the spectral environment functions. The inversion of this formulation is straightforward in the reflective region and is implemented in COCHISE that also includes a water vapor retrieval module based on a 2D LUT. This code is devoted to large scale optical ground properties collection from hyperspectral remote sensing acquisitions.

Preliminary evaluations of these two reciprocal codes have been carried out: i) by confrontation with reference codes such as MODTRAN4 for homogeneous scenes and AMARTIS for heterogeneous scenes, ii) by comparison with an AVIRIS data set. The evaluation gave very satisfactory results in all of the studied cases. We then conclude that COMANCHE and COCHISE are validated in the VIS-NIR-SWIR region. Further comparisons will be completed on other experimental data sets including AVIRIS and HYMAP measurements. Moreover water vapor retrieval with COCHISE is still under investigation in order to compare results between the 0.94 and 1.13 μm.

Finally, the validation is still limited to homogeneous scenes in the infrared spectrum. An opportunity to overcome this limitation is to carry out comparisons with the MATISSE code developed at ONERA and that will be soon available (Simoneau et al., 2001).

7. ACKNOWLEDGEMENTS

The work associated with this paper is supported by the DGA, DSP/STTC/OP (Délegation Générale de l'Armement, Direction des Systèmes de forces et de la Prospective, Service Technique des Technologies Communes, Département Optronique). AVIRIS data on Railroad Valley Playa and ground-based measurements are courtesy of K. Thome, Optical Science Center, Remote Sensing Group, University of Arizona.

8. REFERENCES

Adler-Golden, S., A. Berk, L.S. Bernstein, S. Richtsmeier, P.K. Acharya, M.W. Matthew, G.P. Anderson, C.L. Allred, L.S. Jeong, J.H. Chetwynd, 1998, "FLAASH, a MODTRAN 4 atmospheric correction package for hyperspectral data retrievals and simulations," 1998 AVIRIS Workshop Proceedings.

Anderson, G.P., A. Berk, P.K. Acharya, M.W. Matthew, L.S. Bernstein, J.H. Chetwynd, H. Dothe, S.M. Adler-Golden, A.J. Ratkowski, G.W. Felde, J.A. Gardner, M.L. Hoke, S.C. Richtsmeier, B. Pukall, J. Mello, L.S. Jeong, 2000, "MODTRAN 4: Radiative transfer modeling for remote sensing," Algorithms for Multispectral, Hyperspectral, and Ultraspectral Imagery VI, Proceedings of SPIE, vol. 4049, pp. 176-183.

Miesch, C., X. Briottet, Y.H. Kerr, F. Cabot, 1999, "Monte Carlo approach for solving the radiative transfer equation over mountainous and heterogeneous areas," Applied Optics, Vol. 38, No. 36, pp. 7419-7430, 20 December 1999.

Miesch, C., X. Briottet, Y.H. Kerr, F. Cabot, 2000, "Radiative transfer solution for rugged and heterogeneous scene observations," Applied Optics, Vol. 39, No.36, pp. 6830-6846, 20 December 2000.

Simoneau, P., R. Berton, K. Caillault, G. Durand, T. Huet, L. Labarre, C. Malherbe, C. Miesch, A. Roblin, B. Rosier, 2001, "MATISSE: Advanced earth modeling for imaging and scene simulation," Europto European Symposium on Remote Sensing, Toulouse, 17–21 September 2001.

Vermote, E., D. Tanré, J.L. Deuzé, M. Herman, J.J. Mocrette, 1997, "Second Simulation of the Satellite Signal in the Solar Spectrum (6S)," 6S User Guide Version 2.

LEAF AREA INDEX MAPPING USING RETRIEVED REFLECTANCE FROM AVIRIS DATA

Ruiliang Pu, Peng Gong and Greg S. Biging

1. INTRODUCTION

Leaf area index (LAI) has been an important driver to some ecosystem models applied at landscape to global scales. Study on the spatial distribution of LAI on the Earth's surface is helpful to understanding various biological and physical processes within a terrestrial ecosystem, such as photosynthesis, respiration, transpiration, carbon and nutrient cycle, and rainfall interception (Chen and Cihlar, 1996; Fassnacht et al., 1997; Gong et al., 1995; White et al., 1997; Hu et al., 2000). Direct measure of canopy LAI is labor-intensive and, thus, is only practicable on experimental plots of limited size. Consequently, estimating LAI over large areas is problematic (Gobron et al., 1997). Remote sensing techniques, particularly the use of satellite imagery, may offer a practical means to measure LAI at the landscape scale or even global scale (Running et al., 1989). With remote sensing techniques, scientists have made progress in developing methods that correlate remotely sensed data with regional estimates of a number of forest ecosystem variables, including LAI, absorbed fraction of photosynthetically active radiation (APAR), canopy temperature, and community type.

Since the advent of imaging spectrometers, various approaches have been developed for estimation of forest biophysical (e.g., LAI) and biochemical (e.g., chlorophyll content) parameters using hyperspectral data. They can be divided into three categories: statistical regression, physical modeling and bio-parameters mapping. So far, most attempts to estimate the LAI on the basis of airborne hyperspectral remote sensing data have relied on empirical relationships (i.e., statistical correlations) between values of LAI measured *in situ* and the values of a particular vegetation index computed from remote sensing data (e.g., Spanner et al., 1994), derivative spectra (e.g., Gong et al., 1992) or some spectral position parameters (e.g., "red edge" optical parameters, extracted from an inverse Gaussian model by Miller et al. (1990)). The physically based models rest on a theoretical basis consisting of developing a leaf scattering and absorption model that involve canopy characteristics, such as LAI (e.g., Jacquemoud et al., 1996). Imaging spectroscopy has made it possible to study the spatial distribution of biophysical and biochemical parameters because the pixel-based parametric value can be easily calculated in terms of the relationships between spectra from hyperspectral remote sensing images and biophysical and biochemical parameters measured and/or inverted from physical models (e.g., Curran et al., 1997; Hu et al., 2000). Of these three categories, empirical relationships between ground-based LAI values and various forms of multispectral and hyperspectral data are the most successful and popular. In this study, we still use the empirical regression model to predict pixel-based LAI value for LAI mapping.

The atmosphere can modify the information of the Earth's surface in several ways (Richter, 1992; Gao et al., 1993; Sturm, 1992). It contributes a signal independent of the ground (path radiance); it absorbs some fractions of the ground reflected radiance; and the atmospheric scattering (Rayleigh & aerosol) modifies the radiances of adjacent fields of different reflectance (adjacency effect). Therefore, dark areas surrounded by bright areas appear to have a higher reflectance than the intrinsic reflectance. Since the effects of atmospheric scattering and absorption on high spectral resolution remote sensing data are critical, the atmospheric correction is particularly important to imaging spectrometer data (Vane and Goetz, 1993; Green et al., 1998) for retrieval of surface reflectance and atmospheric constituents. For this reason, we will use retrieved surface reflectance to study the spatial distribution of LAI. During the 2001 EO-1 campaign in Argentina, two high spectral resolution image scenes of AVIRIS were acquired at two study sites in southern Argentina, and relevant ground truth data were collected for estimating and mapping LAI. In this study, we retrieved surface reflectance spectra from AVIRIS hyperspectral data with the atmospheric transfer code —MODTRAN4 (Berk et al., 2000). We used the retrieved pixel-based reflectance spectra to estimate and map LAI. The objectives of this study were to (1) develop an LAI mapping approach with the

Center for Assessment & Monitoring of Forest & Environmental Resources (CAMFER)
145 Mulford Hall, University of California, Berkeley, California 94720-3114, USA
Email: rpu@nature.berkeley.edu

AVIRIS hyperspectral data; and (2) compare the effectiveness of AVIRIS data at different processing stages of atmospheric correction used for estimating and mapping LAI.

2. STUDY SITES AND DATA COLLECTION

2.1 Study Sites

During the 2001 EO-1 campaign in Argentina, we set up two study sites, the south site (41° 51' 23" S / 71° 24' 44" W) and the north site (41° 10' 59" S / 71° 20' 27" W), in Rio Negro province of southern Argentina. The study areas are located on a relatively flat area, semiarid region with many patches of conifer forest plantations. The species are young- to mid-aged ponderosa pine, lodgepole pine, and Oregon pine. Besides these forest plantations, the study sites are covered by some broad-leaf species and shrub and grasses (mainly consisting of nire brush acaena, coiron, barberis, laura, rosa mosquede). The relative elevational difference within the study areas is less than 100 m and the average elevation is approximately 850 m.

2.2 Data Acquisition and Measurement

(1). AVIRIS data

At the both the north and south study sites, AVIRIS data were acquired on February 15, 2001, around 14:50 p.m. local time. The AVIRIS were acquired at an altitude of 5029 m and this led a spatial resolution of 3.6 m. A standard scene of AVIRIS image consists of 614 pixels X 512 lines X 224 bands.

(2). Spectroradiometric measurements

From March 27-29, 2001, we took reflectance measurements in the field from road surface (gravel material), bare soil, young tree canopy (ponderosa pine and lodgepole pine), grasses and shrubs using a FieldSpec®Pro FR (Analytical Spectral Devices, Inc., USA). The spectral range covered by the instrument is 350 - 2500 nm with three separate spectrometers. The first spectrometer has a spectral resolution of 3 nm while the second and the third have the same spectral resolution of approximately 10 nm. All spectra were measured at the nadir direction of the radiometer with a 25° FOV. The distance between the spectroradiometer and targets was 20 to 100 cm to allow within-target-area radiance measurement. White reference radiance was measured every 5-10 minutes. Each sample was repeatedly scanned 10 times. These spectral reflectance measurements were used for atmospheric correction for the retrieval of surface reflectance from AVIRIS data.

(3). LAI collection

An LAI-2000 Plant Canopy Analyzer (PCA) was used in the field to measure forest LAI. The PCA is based on the amount of canopy light transmittance measured across a hemispherical field by five concentrically nested sensors (Welles and Norman, 1991). The LAI measurement taken by the PCA has been termed 'effective' LAI because of the contamination of this measure by self-shading at the needle-to-shoot level, branch and canopy levels, and stand level (White et al., 1997; Chen and Cihlar, 1996). The operation instructions for the LAI instrument were followed carefully to ensure each LAI point measured correctly. From March 27 to 29, 2001, a total of 70 LAI measurements were taken at both sites. Each LAI measurement represents an average of ten PCA readings which were taken in an area between 100 to 1000 m^2. The locations of PCA readings in each plot were selected based on the canopy closure, age of stands and nutrient level so as to make them representative of the variability in the plot. After taking one LAI measurement, its exact location (i.e., a plot) was marked on the color composite image of AVIRIS data or on forest inventory polygon map. This has been used as references for subsequent spectral data extraction from the AVIRIS images. Since the effective LAI is less variable and easier to measure than LAI, and is also an intrinsic attribute of plant canopies (Chen and Cihlar, 1996), we directly used the effective LAI in our analysis.

3. METHODS

Figure 1 illustrates a flowchart of our analytical procedure, which consists of two parts, retrieval of surface reflectance from AVIRIS data and LAI mapping with the AVIRIS data at three different processing stages. The detailed description to the flowchart is given below.

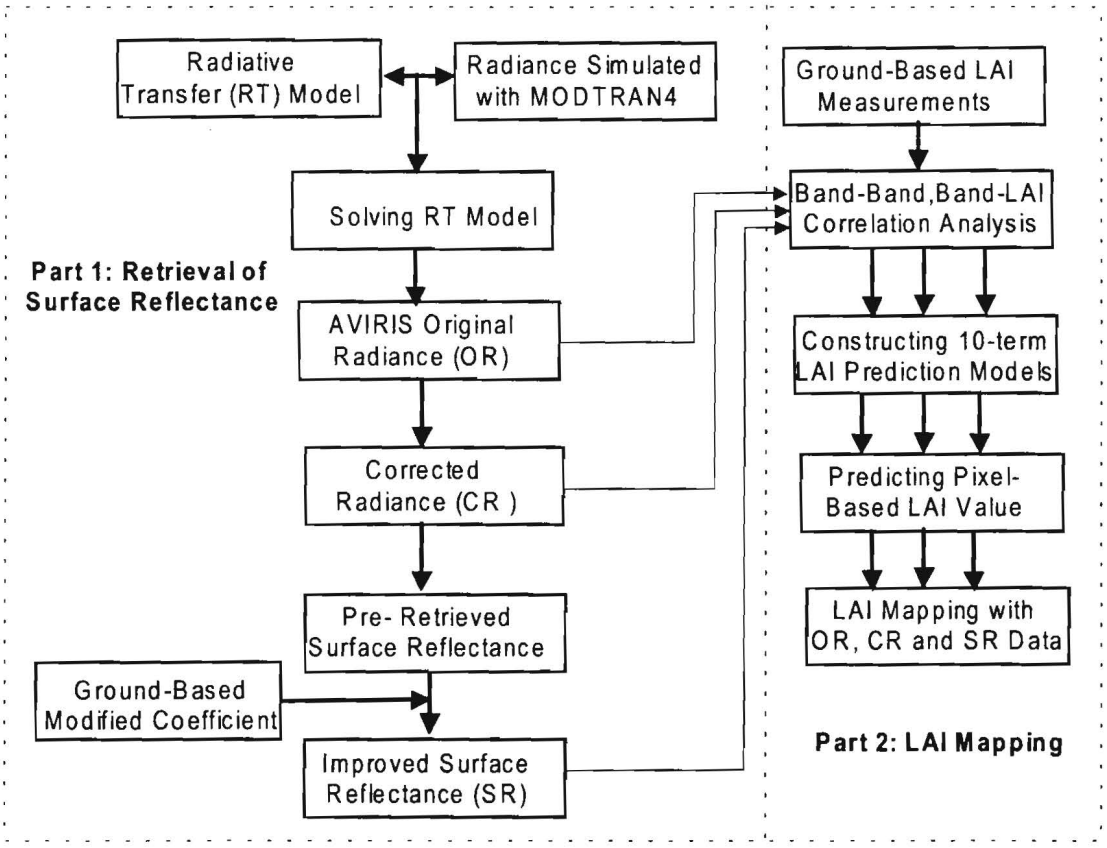

Figure 1. A flowchart of retrieval of surface reflectance and LAI mapping

3.1 Retrieval of Surface Reflectance

According to Gao et al. (1993), Sturm (1992), Green (1992) and Qu et al. (2001), a simplified radiative transfer (RT) model based on the same principles (see Tanré et al., 1986) is applied here. In a simplified form, the at-sensor radiance L can be a combination of the radiance reflected from Lambertian surface and scattered from atmosphere by

$$L = L_a + \frac{T_2 \rho}{1 - \rho S} \cdot \frac{E_s \cdot Cos(\theta_s)}{\pi}, \tag{1}$$

where, T_2 is the Sun-surface-sensor two-way transmittance in consideration of the total gaseous transmittance effect, L_a is the path radiance caused by atmospheric scattering, S is the spherical albedo of the atmosphere, ρ is the earth's surface reflectance, E_s is the exoatmospheric solar irradiance, and θ_s is the solar zenith angle. Eq. (1) can be rewritten for retrieval of surface reflectance, ρ, as

$$\rho = \frac{L - L_a}{(L - L_a)S + T_2 \cdot \frac{E_s \cdot Cos(\theta_s)}{\pi}}. \tag{2}$$

Once solving Eq. (1) for parameters, T_2, S, and L_a through simulation with an atmospherically radiative transfer code such as MODTRAN4 and giving a satellite measured radiance, L, a surface reflectance spectrum can be retrieved with Eq. (2). In this study, a procedure, as shown in Figure 1, for retrieving surface reflectance from AVIRIS data can be described as following.

Through MODTRAN4, three at-sensor total radiances were first simulated with inputs of 3 surface reflectance values (e.g., 0.0, 0.3, 0.5) and other parameter values necessary for calculating the total radiance, such as water vapor (0.7 in this experiment), aerosols, and atmospherically geographical-seasonal model. Since the water vapor is of a parameter very critical to radiance output, a principle of the "smoothness test" (Qu et al., 2001) was adopted to

determine water vapor value. The simulated output radiance was used as L in Eq. (1). With the three simulated at-sensor total radiances, we can solve the RT model (Eq. (1)) for parameters T_2, S, and L_a. Using AVIRIS image pixel value (radiance) as at-sensor radiance and the solved T_2, S, and L_a, we can easily calculate pixel-based surface reflectance from AVIRIS image radiances through Eq. (2). In this paper we refer to the original pixel-based radiance simply subtracted by the L_a as the corrected radiance. Since the input parameter values for MODTRAN4 cannot completely satisfy atmospheric conditions over the study sites during flight overpasses, the retrieved surface reflectance is not prefect at this stage. With a set of ratio coefficients across all spectral bands calculated by dividing the ground reflectance by the corresponding retrieved reflectance, pixel-based surface reflectance can be scaled to ground measured reflectance and improved in accuracy.

3.2 LAI Estimation and Mapping

With the AVIRIS data of three different processing stages: the original radiance (OR), corrected radiance (CR) and retrieved surface reflectance (SR), the following procedure was used in this study for LAI estimation and mapping.

Step 1. Pxel-based field spectra from 15 to 225 homogenous pixels were extracted for each of the 70 LAI measurement plots from the OR, CR and SR images. An average was taken from all pixel spectra extracted for each individual plot.

Step 2. A linear correlation coefficient is calculated between each band and the LAI measurements. The purpose of this step was to select those bands with high correlations to construct LAI prediction models.

Step 3. We selected 20 bands from the AVIRIS data of OR, CR and SR. The following band combinations were considered: (a) selecting 2 - 3 bands from each band group in terms of the correlogram (Jia and Richards, 1999); (b) selecting those bands corresponding to peak values of the correlation curve; and (c) selecting those bands with known absorption features.

Step 4. Using the piecewise regression procedure of SAS we further selected an optimal set (10 bands) of bands from the 20 bands determined at Step 3 to construct LAI prediction model. In order to evaluate the capabilities of the AVIRIS data at the three processing stages for LAI estimations, we tested the power of a regression model constructed using only 46 or 47 samples in estimating LAI values of the remaining 24 or 23 test samples. We repeated LAI model construction and estimation three times by splitting the total 70 samples into three non-overlapping test sample sets (24, 23, 23). We used all 70 samples to finally construct a 10-term prediction model for each type of the AVIRIS data to predict pixel-based LAI values for LAI mapping.

Step 5. LAI estimated from the AVIRIS data were sliced into classes and colored with a legend referencing the value ranges for each class.

3.3 Effectiveness Assessment Criteria

The capabilities of the three types of AVIRIS data for estimating LAI can be evaluated using the following three criteria:

- Multi-correlation coefficient (determination coefficient), R^2, of an LAI prediction model;
- LAI prediction accuracy evaluated based on the overall average accuracy (*OAA*) from validation samples (three sets of non-overlapping test samples), from corresponding training samples or from all 70 training samples, *OAA* is defined as

$$OAA = \left(1 - \frac{SDR}{Y_{mean}}\right) * 100.00\% \qquad (3)$$

where, $SDR = \sqrt{\frac{\sum_{i=1}^{n}(y_i - y_i)^2}{n-m-1}}$; $y_{mean} = \frac{\sum_{i=1}^{n} y_i}{n}$; $y_i (i = 1,2,..,n)$ are actual LAI measurements;

$y_i (i = 1,2,\ldots,n)$ are LAI values estimated from the validation samples or training samples by the constructed regression models; n is the number of samples; and m is the number of predictors in a regression model. The greater OAA is, the better is the regression result.

- Visual examination of LAI maps by comparing with a pseudo-color composite image of AVIRIS to assess the reasonability of LAI spatial distribution.

4. RESULTS AND ANALYSIS

4.1 Retrieval of Surface Reflectance

With MODTRAN4 (Berk et al., 2000), when we chose three surface reflectance values: 0.0, 0.3, and 0.5, a water vapor value of 0.7, a mid-latitude summer atmospheric geographical-seasonal model, and other necessary parameters as inputs for the code, three at-sensor total radiances were simulated for solving the simplified RT model (Eq. (1)). Figure 2 presents three total radiance curves corresponding to surface reflectance, 0.0, 0.3 and 0.5, respectively. Some absorption features along the curves of 0.3 and 0.5 reflectance, especially for those caused by water vapor, appear clearly in Figure 2. With the three simulated at-sensor total radiances and three surface reflectance values, the path radiance (L_a), the Sun-surface-sensor two transmittance (T_2), and the spherical albedo of atmosphere (S) could be obtained by solving the 3-equation group of Eq. (1). When replacing the simulated at-sensor radiance by the sensor image pixel value, a corrected radiance image could be produced (suppose $L_{img} \approx L$) by deducting the L_a (i.e., $L_{img} - L_a$). Further, with the two other parameters (T_2 and S), a retrieved surface reflectance image could be produced in terms of Eq. (1). The retrieved surface reflectance image was called as primary retrieved surface reflectance image at this stage.

Figure 3 (a-c) present atmospheric correction results at different processing stages. Figure 3 (a) is the original radiance (OR) and (b) the corrected radiance (CR) of (a). Comparing (a) with (b), we can see clearly that the atmospheric effect (scattering) influences more on the visible and near infrared region than on the longer wavelength regions. Since the surface reflectance curve is retrieved only with solved L_a, T_2 and S, there are a lot of 'spikes' along the reflectance curves, especially near 0.76 μm (O_2), 0.94 μm and 1.14 μm (H_2O), and the 2.0 μm (CO_2) absorption bands in addition to the 1.4 and 1.9 μm where water vapor absorption is strong. These might be caused by MODTRAN4 input parameters whose values are not totally adequate, especially for those sensitive gases such as water vapor. It is therefore necessary to further modify the primary retrieved reflectance with ground spectroradiometeric measurements. We used ground spectrometer data measured from road surface (high way) and plant canopy (lodgepole pine) and the primary surface reflectances retrieved from the corresponding locations on the images to calculate a set of ratio coefficients, then applied the ratio coefficients to the primary retrieved surface reflectance to obtain the final version of retrieved surface reflectance (SR) images (see Figure 3 (c)). From Figure 3 (c), it is evident that most portions of the reflectance curve are close to their ground-measured version although a few 'spikes' still remain. The 'spikes' near 0.94 and 1.14 μm indicate the water vapor effect was not completely removed. To efficiently remove the water vapor effect, a three-channel ratioing technique (Gao et al., 1993) may be tested as an alternative.

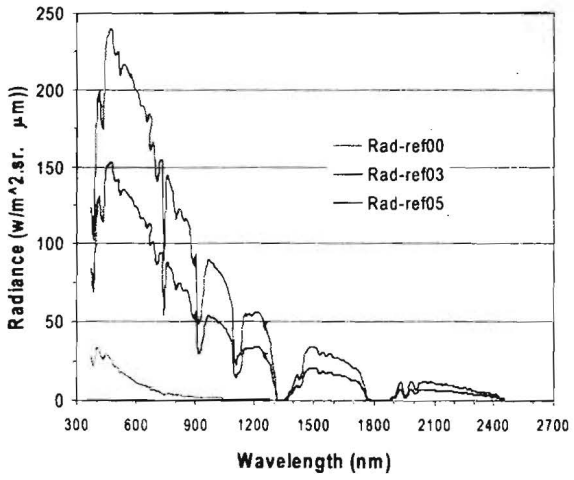

Figure 2. Total at-sensor radiance simulated using MODTRAN4 with inputs of three surface reflectances (0.0, 0.3 and 0.5) and a water vapor value of 0.7.

4.2 LAI Estimation

(1). Correlation between AVIRIS data and LAI

Linear correlations between the three types of AVIRIS data and field LAI measurements were calculated. The three correlation curves of OR, CR and SR along the wavelengths are presented in Figure 4. For AVIRIS SR data, some bands in the visible and short wave infrared (SWIR) regions have higher correlation compared to other

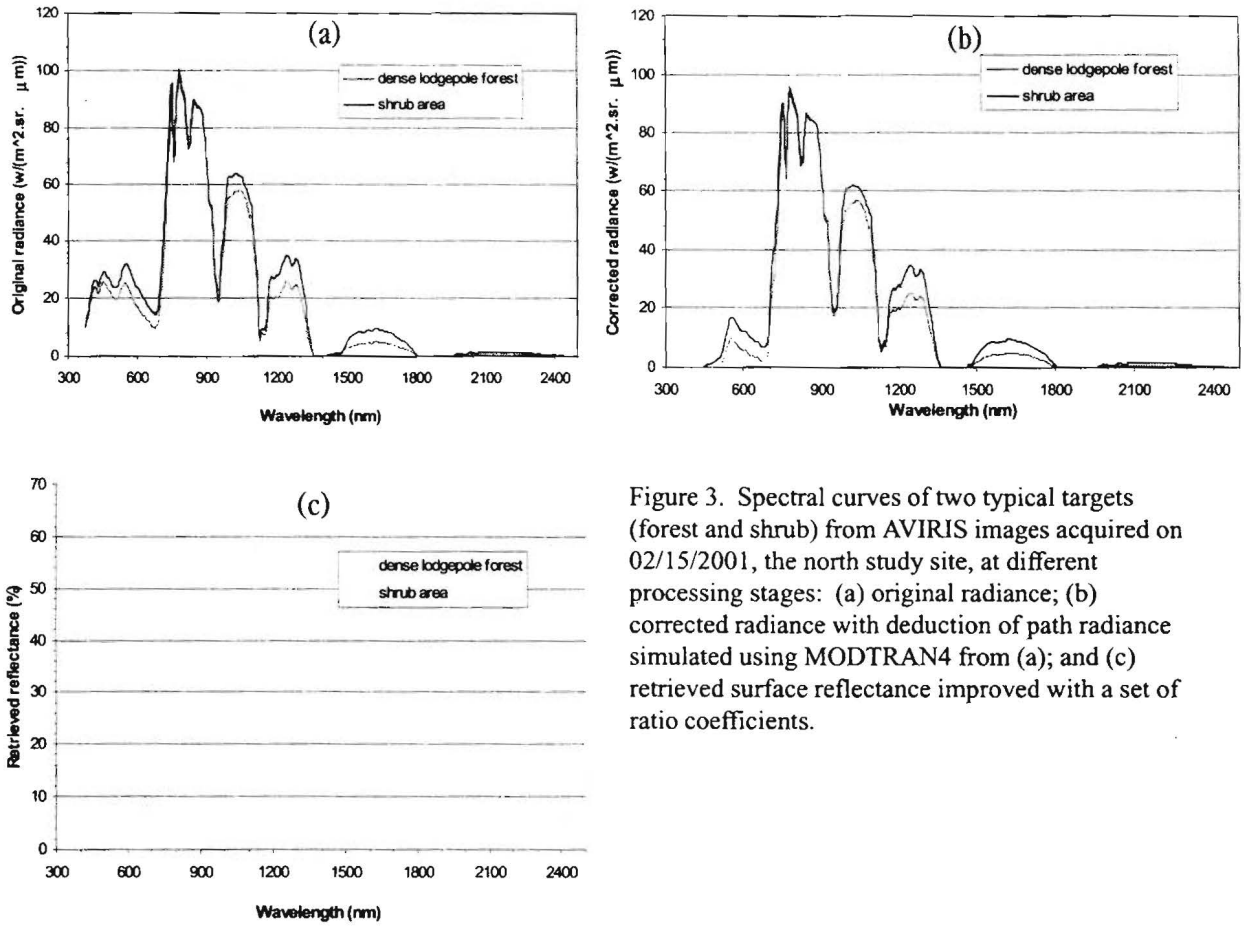

Figure 3. Spectral curves of two typical targets (forest and shrub) from AVIRIS images acquired on 02/15/2001, the north study site, at different processing stages: (a) original radiance; (b) corrected radiance with deduction of path radiance simulated using MODTRAN4 from (a); and (c) retrieved surface reflectance improved with a set of ratio coefficients.

AVIRIS data, especially in the visible region. This indicates that the atmospheric correction has effectively reduced the scattering effect of the atmosphere on the sensor data in the visible region. In the region of SWIR 2.05 – 2.4 μm, there is also a certain degree of effectiveness. However, since we have not considered a gain factor that consolidates all the multiplicative influences such as atmospheric transmission, solar irradiance and instrument response (Goetz et al., 1997), a simple deduction of the effect of atmospheric path radiance from the OR data has not improved the correlation. For all the three types of data, the SWIR bands can be used as a potential range for LAI estimation because the effect of atmosphere is relatively weak in this region except two strong water absorption bands centered near 1.4 and 1.9 μm.

(2) LAI prediction models

In order to construct LAI prediction models, we first selected 20 relatively important bands from all AVIRIS bands according to the three criteria mentioned earlier. Using the piecewise regression procedure from SAS, an optimal set (10 bands) of bands from the 20 bands was selected to construct LAI prediction models for the three types of AVIRIS data. The optimal number of bands selected was determined based on Figure 5. When all three types of data were considered, 10 bands were sufficient because the R^2 almost no longer increases if more bands were used. Therefore, we used all 70 samples to finally construct one 10-term prediction model for each type of the data. Table 1 lists some indices for model evaluation and band wavelengths selected for each type of data. Note that all spectral data selected were transformed into logarithmic values. All model indices including R^2, overall accuracy (OAA) and standard deviation (SD) show that the AVIRIS SR data are the best among the three. This indicates that the atmospheric correction executed to OR data and the procedure of retrieving surface reflectance are helpful in estimating forest LAI. According to Curran (1989), most of the bands used relate to biochemical absorption features and account for biological significance because canopy LAI is considered to have a direct or indirect relation with most of the biochemical absorption features. For example, 2 - 3 bands selected for each type of the data (539 and 626 nm for OR; 539, 558 and 626 nm for both CR and SR) locate in the visible region and, therefore, can relate to the chlorophyll absorption features; most of the other bands in the SWIR region are affected by water, protein,

nitrogen, starch, oil, lignin, and cellulose absorption features (1080, 1174, 1274, 1653, 1763, 1792 and 2221 nm); and only 780 nm for all three types of the data and 2420 nm for SR seem to have no causal association with those known absorption features (> 50 nm away). Among the three types of data, there are 6 common bands (539, 626, 780, 1763, 1792, and 2221 nm). We regard these 6 common bands more important than the others in the selected 20-band group.

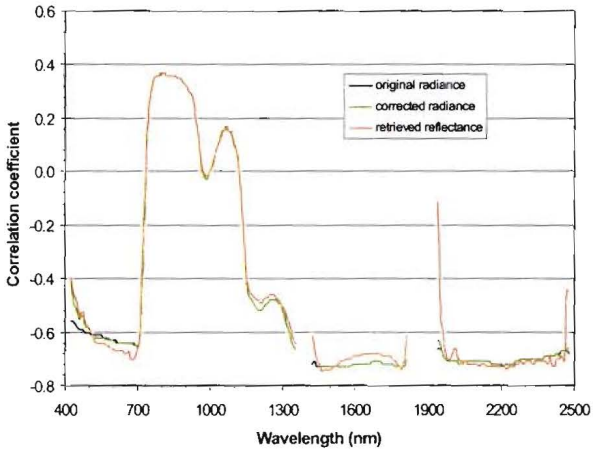

Figure 4. Comparison of correlation coefficients among the AVIRIS data at the three different processing stages: original radiance, corrected radiance and retrieved surface reflectance.

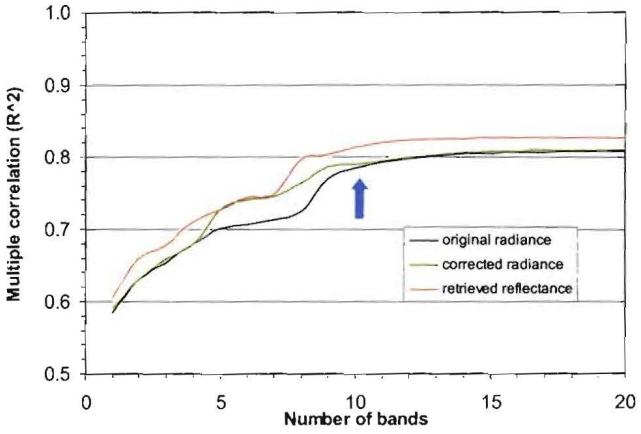

Figure 5. R^2 value varying with the increase of the number of bands included in a regression model.

(3). Test of LAI prediction models

Table 2 lists evaluation indices of training (from 46 or 47 samples) and test sets (remaining 23 or 24 samples) for the three types of data. All results listed were obtained through averaging the results from training or testing. All indices for AVIRIS SR are better than those of the other two (OR and CR) with training samples. For the results obtained from the test sets, it seems that atmospheric correction did not improve the accuracy of LAI estimation. In fact, the accuracies for CR and SR data are lower by a little bit than those of OR data. This may have two explanations: the atmospheric correction is insignificant; or the results are inconclusive because the training and test

Table 1. LAI prediction models (10-term) of the three types of AVIRIS data, original radiance (OR), corrected radiance (CR), and retrieved surface reflectance (SR). N = 70 samples

	Logarithm of OR	Logarithm of CR	Logarithm of SR
R^2	0.7854	0.7904	0.8130
Wavelengths (nm)	539 626 780 1080 1174 1274 1653 1763 1792 2221	539 558 626 780 1080 1212 1274 1763 1792 2221	539 558 626 780 1174 1653 1763 1792 2221 2420
OAA (%)	76.63	76.91	78.19
SD	0.5677	0.5609	0.5297

Note: All of R^2 are significant at 0.99 confident level; OAA-overall average accuracy; SD-standard deviation

Table 2. Comparison of the effectiveness of LAI estimation with 10-term regression models from the three types of AVIRIS data. 46 or 47 training samples and 24 or 23 test samples were used. All test results were obtained through averaging the three non-overlapping test sets.

Effectiveness indiex		Logarithm of OR	Logarithm of CR	Logarithm of SR
Training set	R^2	0.8119	0.8225	0.8306
	OAA(%)	78.24	78.88	79.34
	SD	0.5283	0.5125	0.5020
Test set	OAA(%)	67.19	62.33	66.71
	SD	0.7931	0.9232	0.8126

Note: All of R^2 are significant at 0.99 confident level; OAA-overall average accuracy; SD-standard deviation

sample sizes are not big enough. Nevertheless, based on the results shown in Table 1, the retrieved surface reflectance data should be expected to have the potential to improve the accuracy of LAI estimation compared to the use of OR or CR data. The expectation can also be supported by LAI mapping result analyzed below.

4.3 LAI Mapping

A unique color or a gray level was assigned to a class of pixel-based LAI value, and corresponding legend was also added onto the pixel-based LAI maps. These LAI maps reflect spatial distribution of different LAI classes (see Figure 6). Figure 6 consists of 8 parts of the two study sites (N – north site and S – south site): (a-N, -S) are false-color composite images with AVIRIS bands 45 (NIR), 24 (Red), and 12 (Green); (b-d, -N and -S) are LAI maps mapped using AVIRIS OR, CR and SR, respectively. For the false color composite images the areas with the highest LAI are in red color while the lowest LAI in blue-green-white color and the medium LAI in reddish and dark-red colors. Compared to the false color composite images, the LAI maps produced by SR are the most reasonable because the spatial distribution of LAI patches on the maps matches the false color image very well, and the maps reflect detailed LAI variation, especially for patches at the low and high ends of LAI when compared with those from the CR and OR. From Figure 6 (a-N, -S), it is evident that the range of LAI mapped from the OR is narrow. For LAI maps produced from CR, they are better than those from the OR, but, obviously, worse than those with the SR. This could be due to the results of atmospheric correction and use of the retrieved surface reflectance.

5. SUMMARY AND CONCLUSIONS

In this study, we compared the effectiveness of AVIRIS data processed at three levels for LAI estimation. The three data levels are original radiance (OR), corrected radiance (CR) and retrieved surface reflectance (SR) images. AVIRIS images were acquired on February 15, 2001 at the north and south study sites during an EO-1 campaign in Argentina. Spectraoradiometric measurements were taken from road surface, vegetation and bare soil with a FieldSpec®Pro FR spectrometer. A total of 70 LAI measurements with an LAI-2000 Plant Canopy Analyzer were also taken in the field. We first simulated the total at-sensor radiances using MODTRAN4. Then, we solved a

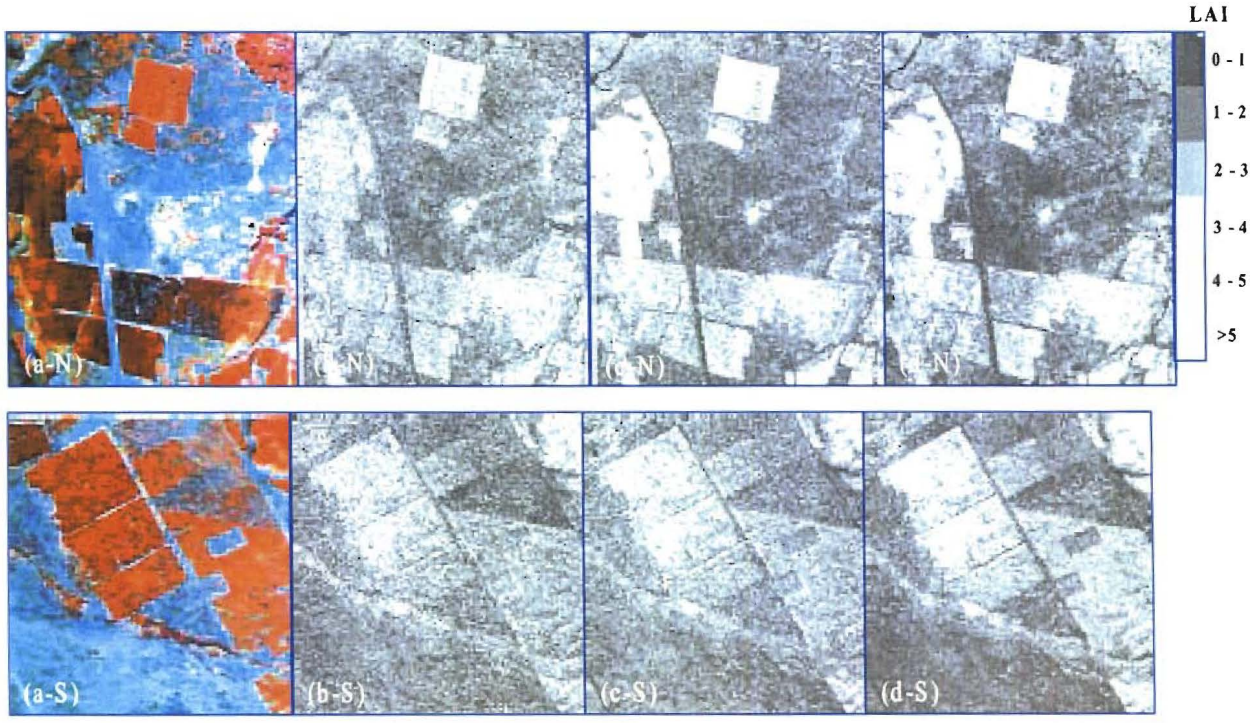

Figure 6. LAI mapping using three types of AVIRIS images. The upper four subimages are from the north site and the lower four subimages from the south site. (a-N, a-S) False color composite (AVIRIS bands 45, 24, 12); (b-N, b-S) LAI mapping with original radiance; (c-N, c-S) with corrected radiance; and (d-N, d-S) with retrieved surface reflectance data.

simplified radiative transfer model for three parameters of the path radiance, the Sun-surface-sensor two transmittance, and the spherical albedo of atmosphere, followed by using the ground spectroradiometric measurements to improve the retrieved surface reflectance from the AVIRIS images. The CR images were obtained by simply deducting path radiance from the OR images. A 10-term LAI prediction model for each type of the data was constructed to predict pixel-based LAI value. Finally, the pixel-based LAI values were used to make LAI maps for all the three types of images.

The results indicate that the LAI mapped with SR is the most reasonable among those derived from the three types of data. The worst LAI map is from OR. According to the results of correlation analysis, the SR data type generated the greatest correlation coefficients with measured LAI. In general, we conclude that the retrieved surface reflectance data is more effective for forest LAI estimation compared to the other two types of data. Additional field LAI measurements may be needed to test the 10-term prediction models for LAI estimation.

ACKNOWLEDGEMENTS

This research was partially supported by a NASA EO-1 science validation grant (NCC5-492) and field support provided by the forest plantation inventory section of the agricultural department of the government of Argentina. Assistance in field work by Mirta Rosa Larrieu, Gillsermo Defossé, Florencia Farias, and Maria Cristina Frugoni is appreciated.

REFERENCES

Berk, A., G. P. Anderson, P. K. Acharya, J. H. Chetwynd, L. S. Bernstein, E. P. Shettle, M. W. Matthew, and S. M. Adler-Golden, 2000, *MODTRAN4 User's Manual,* Air Force Research Laboratory, Hanscom AFB, MA, pp. 1-93.

Chen, J. and J. Cihlar, 1996, "Retrieving Leaf Area Index of Boreal Conifer Forests Using Landsat TM images," *Remote Sens. Environ.*, vol. 55, pp. 153-162.

Curran, P. J., 1989,"Remote Sensing Of Foliar Chemistry," *Remote Sens. Environ.*, vol. 30, pp. 271-278.

Curran, P. J., J. A. Kupiec, and G. M. Smith, 1997, "Remote Sensing The Biochemical Composition of A Slash Pine Canopy," *IEEE Transactions on Geoscience and Remote Sensing*, vol. 35, no. 2, pp. 415-420.

Elvidge, C. D., and F. P. Portigal, 1990, "Change Detection in Vegetation Using 1989 AVIRIS Data," In *Proceedings of SPIE: Imaging Spectroscopy of the Terrestrial Environment*, vol. 1298, pp. 178-189.

Fassnacht, K. S., S. T. Gower, M. D. MacKenzie, E. V. Nordheim, and T. M. Lillesand, 1997, "Estimating the Leaf Area Index of North Central Wisconsin Forests Using the Landsat Thematic Mapper," *Remote Sens. Environ.*, vol. 61, pp. 229-245.

Gao, B. C., K. B. Heidebrecht, and A. F. H. Goetz, 1993, "Derivation of Scaled Surface Reflectances from AVIRIS Data," *Remote Sensing of Environment*, vol. 44, pp. 165-178.

Gobron, N., B. Pinty, and M. M. Verstraete, 1997, "Theoretical Limits to the Estimation of the Leaf Area Index on the Basis of Visible and Near-Infrared Remote Sensing Data," *IEEE Trans. Geosci. Remote Sensing*, vol. 35, pp. 1438-1445.

Goetz, A. F. H., J. W. Boardman, B. Kindel, and K. B. Heidebrecht, 1997, "Atmospheric Corrections: On Deriving Surface Reflectance from Hyperspectral Images," In *Proceedings of SPIE: Imaging Spectrometry III*, vol. 3118, pp. 14-22.

Gong, P., R. Pu, and J. R. Miller, 1992, "Correlating Leaf Area Index of Ponderosa Pine with Hyperspectral CASI Data," *Canadian Journal of Remote Sensing*, vol. 18, pp. 275-285.

Gong, P., R. Pu, and J. R. Miller, 1995, "Coniferous Forest Leaf Area Index Estimation along the Oregon Transect Using Compact Airborne Spectrographic Imager Data," *P. E. & R. S.*, vol. 61, no. 9, pp.1107-1117.

Green, R. O., 1992, "Retrieval of Reflectance from Calibrated Radiance Imagery Measured by The Airborne Visible Infrared Imaging Spectrometer (AVIRIS) for Lithological Mapping," *Imaging Spectroscopy: Fundamentals and Prospective Application,* pp. 61-71.

Green, Robert O, M. L. Eastwood, C. M. Sarture, T. G. Chrien, M. Aronsson, B. J. Chippendale, J. A. Faust, B. E. Pavri, C. J. Chovit, M. Solis, M. R. Olah, and O. Williams, 1998, "Imaging Spectroscopy and the Airborne Visible/Infrared Imaging Spectrometer (AVIRIS)," *Remote Sens. Environ.*, vol. 65, pp.227-248.

Hu, B, K. Inannen, and J. R. Miller, 2000, "Retrieval of Leaf Area Index and Canopy Closure from CASI Data over the BOREAS Flux Tower Sites," *Remote Sens. Environ.*, vol. 74, pp. 255-274.

Jacquemoud, S., S. L. Ustin, J. Verdebout, G. Schmuck, G. Andreoli, and B. Hosgood, 1996, "Estimating Leaf Biochemistry Using the PROSPECT Leaf Optical Properties Model," *Remote Sens. Environ.*, vol. 56, pp. 194-202.

Jia, X. and J. A. Richards, 1999, "Segmented Principal Components Trasformation for Efficient Hyperspectral Remote-Sensing Image Display and Classification," *IEEE Transactions on Geoscience and Remote Sensing*, vol. 37, no. 1, pp. 538-542.

Miller, J. R., Hare, E. W., and Wu, J., 1990, "Quantitative Characterization of the Vegetation Red Edge Reflectance. 1. An Inverted-Gaussian Reflectance Model," *International Journal of Remote Sensing*, vol. 11, pp. 1775-1795.

Qu, Z., A. F. H. Goetz, and K. B. Heidebrecht, 2001, High-accuracy atmosphere correction for hyperspectral data (HATCH), 2000, *AVIRIS 2000 Workshop Proceedings*, http://popo.jpl.nasa.gov/docs/workshops/00_docs/tos_html, pp. 1-8.

Richter, R., 1992, "Atmospheric Correction of Imaging Spectrometer Data," *Imaging Spectroscopy: Fundamentals and Prospective Application,* pp. 259-266.

Running, S. W., R. R. Nemani, D. L. Peterson, L. E.Band, D. F. Potts, L. L. Pierce, and M. A. Spanner, 1989, "Mapping Regional Forest Evapotranspiration and Photosynthesis by Coupling Satellite Data with Ecosystem Simulation," *Ecology*, vol. 70, no. 4, pp. 1090-1101.

Spanner, M. A., L. Jphnson, J. R., R. McCreight, J. Freemantle, J. Runyon, and P. Gong, 1994, "Remote Sensing of Seasonal Leaf Area Index across the Oregon Transect," *Ecological Applications,* vol. 4, pp. 258-271.

Strum, B, 1992, "Atmospheric and Radiometric Corrections for Imaging Spectroscopy," *Imaging Spectroscopy: Fundamentals and Prospective Application*, pp. 47-60.

Tanré, D., C. Deroo, and P. Duhaut et al., 1986, "Simulate the Satellite Signal in the Solar Spectrum (5S)," *User's Guide*, Laboratory d'Optique Atmospherique, U. S. T. de Lille, 59655 Villeneuve D'ascq, France.

Vane, Gregg and Alexander F. H. Goetz, 1993, "Terrestrial Imaging Spectrometry: Current Status, Future Trends," *Remote Sens. Environ.*, vol. 44, pp. 117-126.

Welles, J. M., and J. M. Norman, 1991, "Instrument for Indirect Measurement of Canopy Architecture," *Agron. J.*, vol. 83, pp. 818-825.

White, J. D., S. W. Running, R. Nemani, R. E. Keane, and K. C. Ryan, 1997, "Measurement and Remote Sensing of LAI in Rocky Mountain Montane Ecosystems," *Can. J. For. Res.*, vol. 27, pp. 1714-1727.

COMPARISON OF AVIRIS AND EO-1 HYPERION FOR CLASSIFICATION AND MAPPING OF INVASIVE LEAFY SPURGE IN THEODORE ROOSEVELT NATIONAL PARK

Ralph Root,[1] Susan Ustin,[2] Pablo Zarco-Tejada,[2] Carlos Pinilla,[2] Raymond Kokaly,[3] Gerry Anderson,[4] Karl Brown,[5] Kay Dudek,[6] Steve Hager,[7] and Edmond Holroyd[8]

1. Introduction

Invasive species are rapidly becoming a threat to the world's biodiversity. In the United States alone, non-native species are causing environmental damage and economic losses estimated to exceed $100 billion per year (Pimentel *et al.*, 2000). Morse *et al.* (1995) estimate that approximately 5,000 plant species that have escaped from cultivation have subsequently invaded natural ecosystems in the United States. One of these species, leafy spurge (*Euphorbia esula* L.), entered North America from Eurasia in 1829 (Council for Agricultural Science and Technology (CAST), 2000). Some years later, during the Homestead Period, it found its way into North Dakota and subsequently has spread throughout the upper Midwest and northern Rocky Mountain States, causing estimated annual losses of revenue in excess of $200 million. Leafy spurge causes severe ecosystem alteration due to its aggressive growth relative to that of native flora, its ability to invade unaltered habitats, and its persistence once established. It forms nearly monotypic stands and has the capacity to alter ecological processes and visitor perceptions of Theodore Roosevelt National Park and the surrounding region (Trammell, 1994).

Control of leafy spurge infestations has become a primary resources management issue at Theodore Roosevelt National Park, resulting in years of research to develop efficient and cost effective methods for detection, mapping, and monitoring of this plant (Anderson, *et al.*, 1997; O'Neill *et al.*, 2000; Root and Wickland, 2001).

2. Study area description

Theodore Roosevelt National Park (Fig. 1) was established April 25, 1947. The park consists of three separate units totaling 70,416.39 acres of which 245 acres are directly linked in historical significance to the life of Theodore Roosevelt. Management is directed toward protection and interpretation of the badlands ecosystems surrounding the Little Missouri River and the cultural resources resulting from human habitation of the area. Approximately 42 percent of the park has been designated as a wilderness. Local variations in geology, soil, and topography along the Little Missouri River have created an abrupt scenic contrast to the gently rolling panorama of the northern Great Plains. Sandstones, siltstones, and clays interspersed with beds of coal -- some of which have burned, baking the overlaying clays into bright pink to deep purple "scoria" -- have been sculptured into a landscape of seemingly infinite variety. The badlands formations are rich in fossils of Paleocene forests and swamp life including petrified trunks of giant Metasequoia and remains of ancient alligators. Under the influence of today's climate, the park is mantled by a rich and diverse mosaic of plant communities that provide habitats for an equally diverse variety of animal life.

Approximately 500 species of vascular plants are found in the park. While the majority of plants are typical of those found in the rolling plains of the Missouri Plateau, species of the southwestern desert and Great Basin regions, as well as from the boreal forests are represented here. Of these, 59 species are not native to the park's total flora. The most invasive exotic with the greatest potential for damage to native plant communities is leafy spurge.

Leafy spurge is found throughout the park in all habitat types, although it prefers streambeds, drainages, and wooded draws. The plant was first discovered a the western boundary of the park on Knutson Creek, and spread east along the drainage from an established National Grasslands infestation. From just a few plants in the late-

[1] U.S. Geological Survey, Rocky Mountain Mapping Center, Denver, Colorado (Ralph_root@usgs.gov)
[2] Center for Spatial Technologies and Remote Sensing (CSTARS), Department of Land, Air and Water Resources (LAWR), University of California, Davis
[3] U.S. Geological Survey, Spectroscopy Laboratory, Denver, Colorado
[4] U.S. Department of Agriculture, Agricultural Research Service, Northern Plains Agricultural Research Laboratory, Sidney, Montana
[5] U.S. Geological Survey, Center for Biological Informatics, Denver, Colorado
[6] Colorado State University, College of Forest Sciences, Fort Collins, Colorado
[7] National Park Service, Theodore Roosevelt National Park, Medora, North Dakota
[8] U.S. Bureau of Reclamation, Remote Sensing and Geographic Information Group, Denver, Colorado

1960s, the infestation grew to an estimated 10 ha by 1970. During the next twenty years, sporadic attempts at containment and eradication with herbicides were limited to manual ground spraying in rugged terrain while the infestation increased dramatically. In the late 1980s, the park embarked on an aggressive eradication campaign in cooperation with the United States Department of Agriculture (USDA) Agricultural Research Service (ARS), Animal and Plant Health Inspection Service (APHIS), and North Dakota State University. An integrated approach utilizing helicopter-based herbicide application, ground spraying, and release of host-specific insect species (biological control) was adopted and remains in use to date.

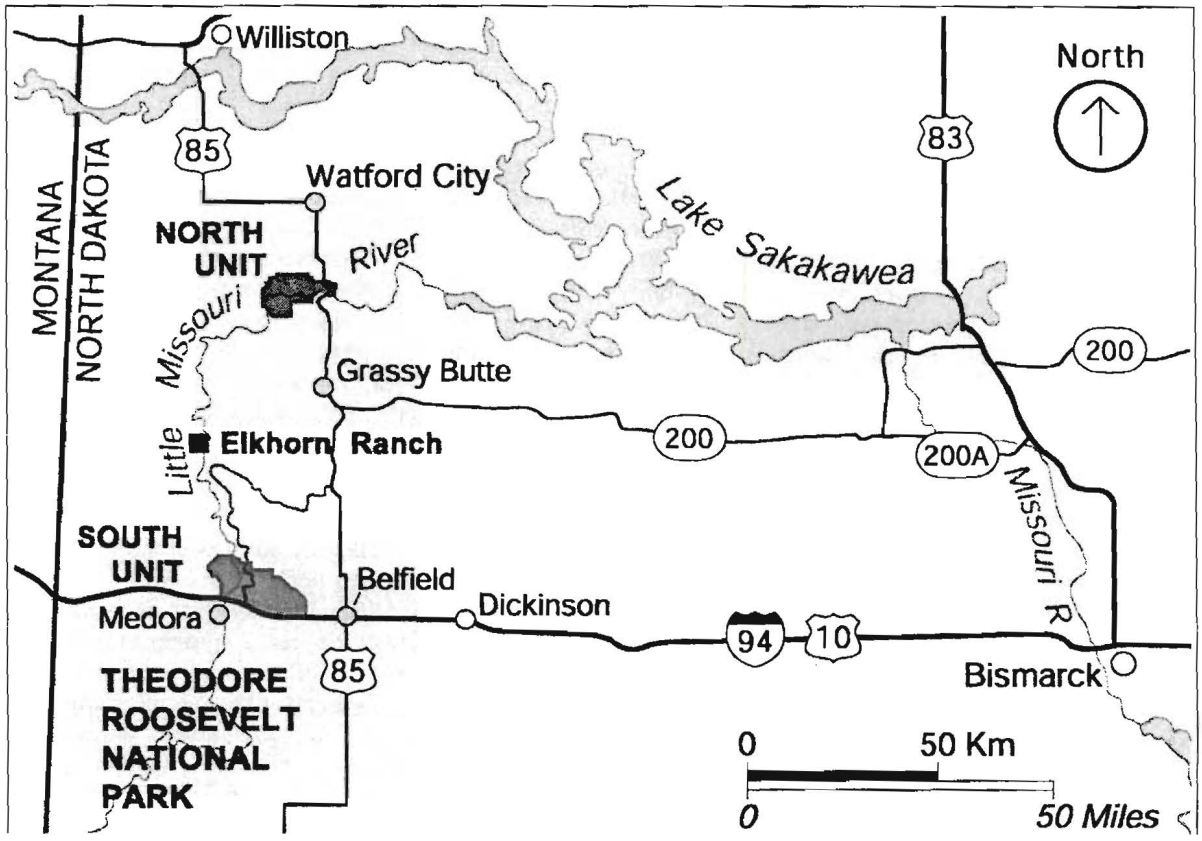

Figure 1. Location of study area. The South Unit of Theodore Roosevelt National Park is situated immediately north of Medora, ND, bordering Interstate Highway 94.

Biological control insectories located in North Dakota and Montana provided increasing numbers of insects for release in the park beginning in 1994. By the late 1990s, more than 2000 insect release sites had been established, forming a dense network of insectories throughout the infestation. Recently, the park has seen landscape-scale reduction in leafy spurge infestation as the insect network coalesces; however, leafy spurge still infests an estimated 10 percent of the land base. To effectively monitor the infestation and improve the application of controls, state-of-the-art remotely sensed data are being used at frequent intervals to quantify areas of reduction/eradication and identify remaining infestations.

3. Previous leafy spurge mapping efforts

In 1993, the USDA ARS flew low-altitude aerial photography at a scale of 1:10,000 over the South Unit of Theodore Roosevelt National Park, and mapped the leafy spurge infestation with visual photointerpretation (Anderson *et al.*, 1997). Maps depicting 750 ha of leafy spurge were digitized, georeferenced, and imported into a geographic information system (GIS). Using this base of spatial information, map products were generated that allowed park managers to more efficiently gather and direct resources toward infestation control (National Park Service, 1992; Redente, 1993). In 1998 the South Unit of the park was reflown, and an updated leafy spurge map

was created, again by manual photointerpretation. In Figure 2 the level of infestation by 1993 is illustrated in yellow, with additional infestations from 1993 to 1998 mapped in red. Because different photointerpreters were used in 1998, the areas of infestation are more generalized, giving the impression of greater spread than may have actually occurred.

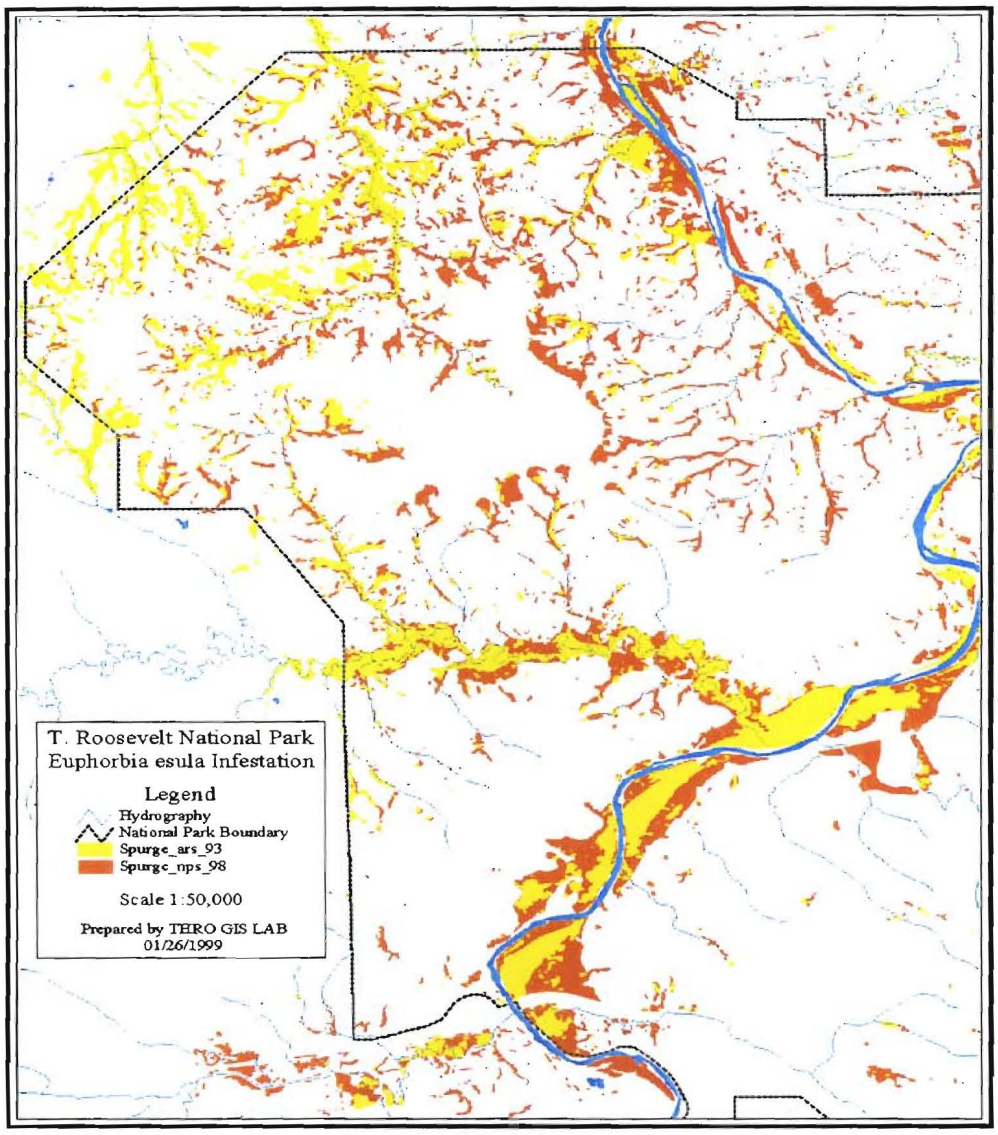

Figure 2. Manually interpreted aerial photo maps of leafy spurge illustrating infestation levels in 1993 (yellow), and 1998 (red).

For this reason, a variety of digital remote sensing techniques have been examined since 1998 with the aim of achieving more quantitative and consistent analysis of leafy spurge spread over time.

4. Data acquisition

Testing of state-of-the art remote sensing technology for detection and mapping of leafy spurge at Theodore Roosevelt National Park began in 1998 as part of a cooperative demonstration project between the National Aeronautics and Space Administration (NASA) and the United States Department of Interior. (DOI). Within the NASA/DOI Hyperspectral Technical Transfer Project (Root and Wickland, 2001), high altitude Airborne Visible and Infrared Imaging Spectrometer (AVIRIS) data were collected over the South Unit of the park in July, 1999.

Preliminary analysis of these data demonstrated that leafy spurge could be identified and mapped (O'Neill *et al.*, 2000).

Examination of the potential for mapping leafy spurge from a space-based platform was supported by NASA in 1999 with the incorporation of leafy spurge mapping research into the Earth Observing-1 (EO-1) science validation program. EO-1 Hyperion data were obtained over the extreme western part of the South Unit of Theodore Roosevelt National Park on May 21, July 6, and September 24 of 2001, along with a second high altitude AVIRIS mission on 21 June 2001 for comparison purposes. Because leafy spurge was close to full bract development in early July, the 6 July 2001 Hyperion data set was selected for in-depth analysis. Fully developed bracts produce a uniform greenish-yellow canopy, making infestations visibly stand out from surrounding native vegetation.

5. Data pre-processing and calibration to surface reflectance

The EO-1 Hyperion data, collected on 6 July 2001, were corrected to radiance (Level 1) at NASA Goddard Space Flight Center. The radiance corrected data, initially in hierarchical data format (HDF), were then sent to the USGS Rocky Mountain Mapping Center and previewed for spatial and spectral data integrity.

At the time of EO-1 data collection on 6 July 2001, field crews used two ASD-FR spectrometers to gather several hundred ground spectra over a pre-selected calibration site at the estimated time of satellite overpass. The site was a 1 ha. level asphalt parking surface with uniform medium reflectance. Consistency of spectral responses between the two spectrometers was verified by single path measurements through a calibrated mylar sheet. Close agreement of sharp absorption feature responses from both instruments justified merging the spectra.

The mean calibration reflectance spectrum collected from the ground was then corrected for Spectralon panel absorption features, to achieve the best possible approximation of true reflectance. Noise associated with the 1,370 and 1,870 nm water vapor regions was eliminated using lab-measured spectra from asphalt samples obtained from the parking area. Minor smoothing was also done in the 2,200 to 2,500 nm region where field instrument signal-to-noise was at a minimum. The spectrum was then convolved to Hyperion and AVIRIS wavelength and bandpass, and processed in ACORN (Atmospheric CORrrection Now) (Analytical Imaging and Geophysics, 2001), to ratio the data to surface reflectance. The final edited and smoothed ground spectrum was input into ACORN for Single Spectrum Enhancement (SSE) along with the arithmetic mean of corresponding AVIRIS and Hyperion pixels. These were selected after examination of their spectra to assure that they were consistent and positioned fully within the boundaries of the asphalt calibration surface. Because calibration site ground spectra collected at the time of the AVIRIS overflight on 21 June 2001 were virtually the same as those collected on 6 July 2001, only the 6 July 2001 ground spectra were used for calibration of both sensors. Close agreement (+/- 1 percent) between the EO-1 and AVIRIS calibration spectra indicated consistent calibration to surface reflectance enabling direct comparisons between the two sensors.

6. Comparison of AVIRIS and EO-1 spectra

Figure 3 shows comparisons of 21 June 2001 and 6 July 1999 AVIRIS and 6 July 2001 EO-1 Hyperion spectra over identical ground locations at: the calibration site, the Medora sewage lagoon (low reflectance water), Little Missouri River (turbid water), non-vegetated road fill, a 0.5 ha patch of leafy spurge, and a 4 ha grassland area. All areas clearly show the difference in noise levels of the two instruments, but they also show the consistency of Hyperion in approximating the spectra obtained by AVIRIS. Over highly reflective surfaces there are consistently lower reflectance levels in the 950-1,900 nm range for Hyperion. Although the reasons for this difference are unclear, it may be a result of a small scaling error in the Hyperion calibration or it might indicate variations in Hyperion detector response in this portion of the spectrum.

7. Collection of vegetation spectra and verification data from the ground

Throughout the course of this study ground spectra were collected at multiple sites representing varying densities of leafy spurge ranging from 25 to 100 percent canopy cover, and at other locations representing native grasses and shrubs. Each measured site was delineated by global positioning system (GPS) measurements and entered into the park's GIS database. Spectrometer measurements were collected by walking over the entire site with the collection probe to obtain a mean spectrum with both a strong signal and good spatial variation within the site. Numbers of individual spectra collected at each site were usually in excess of 200, with a minimum of 50. Mylar panels were used to document the spectral calibration of each spectrometer used in the study to assure uniformity of spectra.

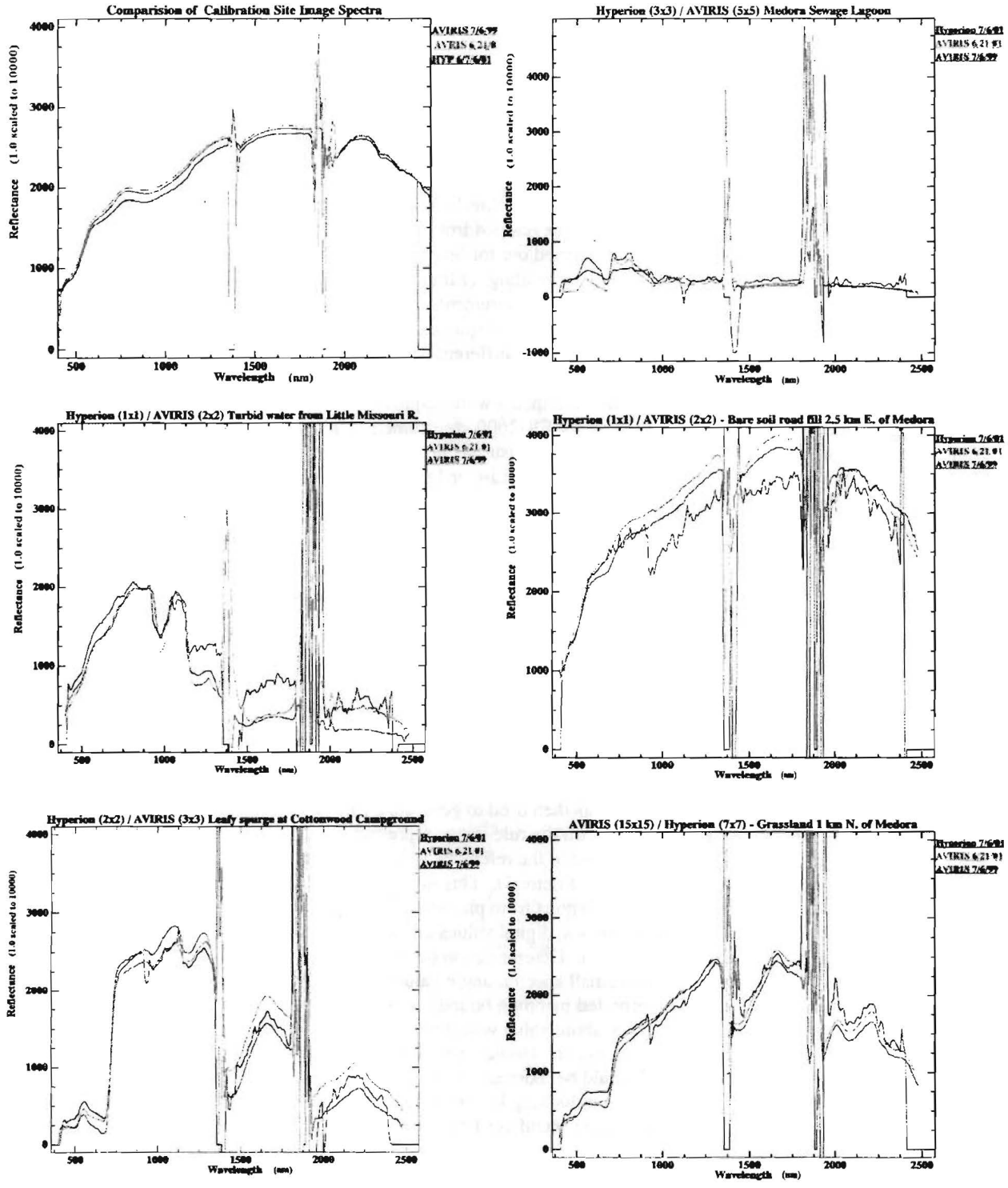

Figure 3. Comparisons of Hyperion (2001) and AVIRIS (1999 and 2001) spectra at selected locations.

During the summer of 2001, field crews at Theodore Roosevelt National Park trained in vegetation identification and GPS field procedures conducted detailed ground surveys of major leafy spurge infestation areas. Using a sampling scheme of 32 by 32 m grid cells, percent cover of leafy spurge and up to 28 other vegetation types was recorded in several areas containing extensive leafy spurge infestations (National Park Service, 2001). These data were gathered to characterize both presence and density of leafy spurge in spatial context with associated native vegetation. A second field survey was conducted for three consecutive growing seasons from 1999 through 2001 to

monitor responses of leafy spurge to chemical and biological control measures. This project entailed collection of data from a total of 550 3 by 5 m plots to geographically document presence/absence of leafy spurge, and to produce detailed estimates of canopy cover (via stem counts) and biomass for leafy spurge and associated native vegetation types. Plots containing leafy spurge were a combination of known bio-control measure locations and stratified random samples from areas previously mapped as leafy spurge (Anderson, et al., 1997). Plots not containing leafy spurge were randomly selected from a buffer zone extending 250 meters in all directions from previously mapped leafy spurge infestations (Anderson, et al., 1997). Ground data obtained from the first of these surveys were used for determining classification training inputs and setting of thresholds. Data from the second survey will be used to perform accuracy assessments on the classifications developed from both the Hyperion and AVIRIS imagery.

Leaf-level spectral measurements were also carried out for biochemical analysis of leaf chlorophyll concentrations through SPAD-502 chlorophyll meter readings (Minolta Camera Co., Ltd., Japan) and leaf reflectance and transmittance. Leaf and bract optical measurements were acquired from leafy spurge samples collected at different locations in order to use reflectance and transmittance for red edge characterization and modeling leafy spurge canopy reflectance as a function of different densities.

Single leaf reflectance and transmittance measurements were acquired on all leaves and bracts using a Li-Cor 1800-12 Integrating Sphere apparatus coupled by a GER-2600 spectrometer yielding a 0.5 nm sampling interval and 2.5 nm spectral resolution in the 340-2500 nm range. Measurements were collected with the integrated sphere following the methodology described in the manual of the Li-Cor 1800-12 system in which five signal measurements are required: transmittance signal, reflectance signal, reflectance internal standard, reflectance external reference, and dark measurements.

8. Preliminary classification analyses

Minimum noise fraction (MNF) principal components analyses were performed on the 1999 and 2001 AVIRIS and 2001 Hyperion surface reflectance data to reduce overall data dimensionality. Both years of AVIRIS data yielded approximately 30 useable components compared to 10 from Hyperion. The Spectral Angle Mapper (SAM) algorithm in the Environment for Visualizing Images (ENVI) was applied to selected components of each set of imagery that gave clear visual indications of known leafy spurge infestations. Two leafy spurge infestations that had been observed on the ground were selected for training areas. Both were approximately 100 m square, and represented dense-(50%) and moderate-(35%) canopy cover. Pixels representing these areas were located in the Hyperion imagery by visual interpretation and comparison of image spectra with mean ground spectra obtained from these sites. The SAM classification algorithm was then used to generate a rule image for the high- and moderate-density training areas. Gray-scale density values on the rule image represent spectral angle values, with smaller angles (i.e., darker areas) indicating closer matches to the reference spectrum. The two rule images were then added to each other, producing an integrated rule image (Figure 4). This image was then georeferenced and visually compared with the GPS field survey data and polygons from photointerpreted leafy spurge maps created with 1993 aerial photographs. Using these visual comparisons, digital values on the summed rule image were thresholded to produce a leafy spurge occurrence map (Figure 5). Determination of the threshold value was based on interactive contrast stretching of the rule image to match small spectral angle values with GPS ground surveyed areas (National Park Service, 2001) and previous photointerpreted mapping boundaries of leafy spurge (Anderson *et al.*, 1997). From a statistical point of view, an optimal threshold value would result in a classification where there is a balance between errors of commission and errors of omission. However, a classification with a looser threshold that minimizes or eliminates errors of omission would be more useful from a land management and monitoring perspective, because of the importance of not overlooking locations of existing and newly developing infestations. Further analysis with accuracy assessments using ground verification data is expected to assist in making a final and best determination of the threshold.

Spectral feature fitting, applied to a continuum-removed version of the chlorophyll absorption zone, has been successfully demonstrated for mapping leafy spurge using Compact Airborne Spectrographic Imager (CASI) data calibrated to surface reflectance (Kokaly *et al.*, 2001a, 2001b, 2001c). A library of ground spectra, collected from several leafy spurge infestations, was used for reference spectra. Similar analyses of the 1999 and 2001 AVIRIS surface reflectance data using these same library spectra are also expected to produce viable classifications of leafy spurge infestations.

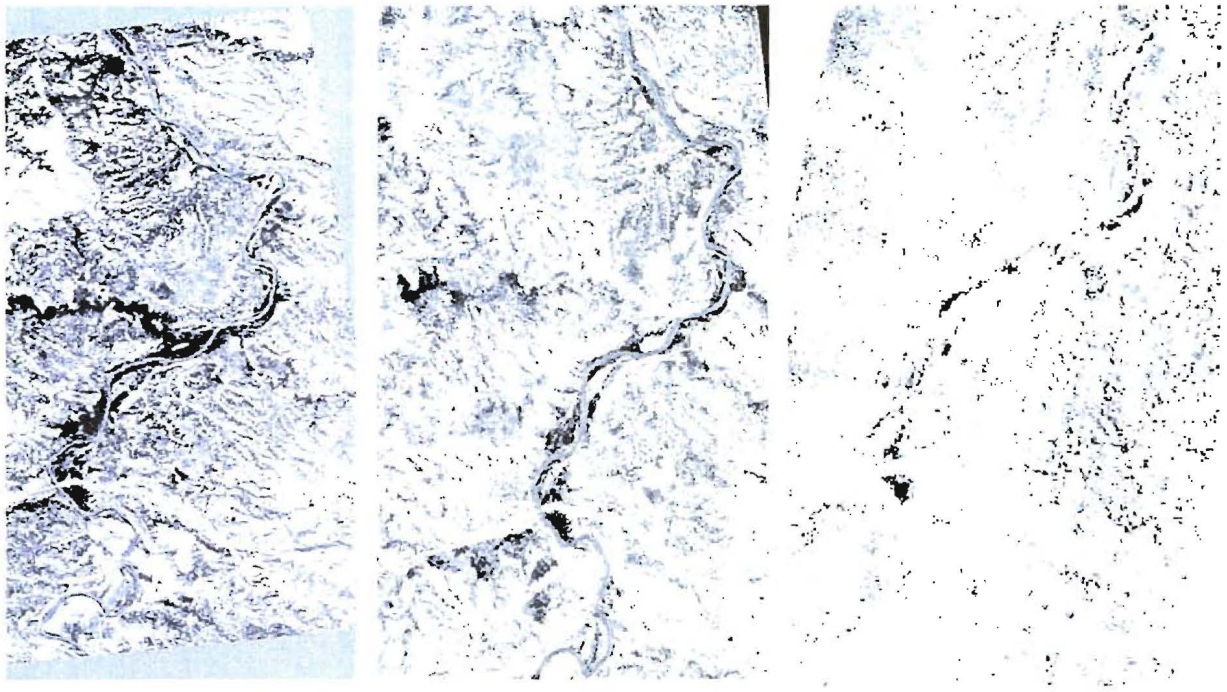

Figure 4. Summed spectral angle mapper rule images from 1999 AVIRIS (left), 2001 AVIRIS (middle), and 2001 Hyperion (right). Note the absence of leafy spurge in the lower Knutsen Creek drainage (center of image) in the 2001 images, resulting from chemical control measures taken in late 1999.

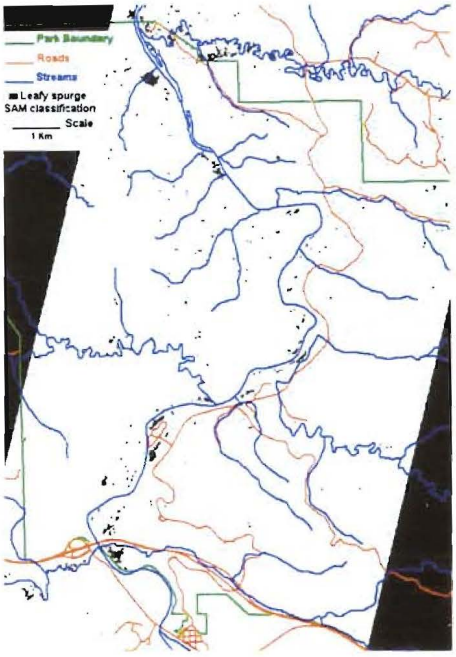

Figure 5. Example of a tightly thresholded spectral angle mapper classification of the 2001 Hyperion data, showing only the closest matches to the reference spectrum (i.e. very small spectral angles). Although other vegetation that might be mis-classified as leafy spurge is virtually eliminated, many less dense infestations and those mixed with other types of vegetation are more likely to be omitted from the classification.

A third approach being investigated is based on the calculation of red edge spectral parameters from hyperspectral data, which are related to biophysical and biochemical constituents of the vegetation canopy. A method for the classification of land cover has recently been reported that exploits systematic differences in species within the shorter wavelength infrared spectral regions sensitive to foliar chemistry (Martin *et al.*, 1998). Zarco-Tejada and Miller (1999) described classification of vegetated land cover based on spectral parameters that characterize the red edge reflectance region, which are responsive to foliar chlorophyll pigment levels. Classification with three red edge spectral parameters, red edge inflection point (λ_p), the wavelength at the

reflectance minimum (λ_o), and a shape parameter (σ) as defined by the inverted-gaussian red-edge curve-fit model (Hare *et al.*, 1984; Miller *et al.*, 1990, 1991), was carried out with the surface reflectance calibrated Hyperion data. The separation of land cover types and location of leafy spurge patches using this classification method is based on cover-type systematic differences in the variables known to affect red edge spectral parameters: vegetation chlorophyll content, canopy structure, canopy cover, and illumination. Preliminary classifications from the inverted-gaussian red-edge curve-fit model for red-edge spectral parameter calculation, adapted for Hyperion reflectance data, also compare favorably with the preliminary results from the first two methods described above.

9. Further research tasks ahead

During the next year finalized classifications developed by the methods described above will be completed and compared by applying accuracy assessments to each technique. In combination with precise georeferencing procedures, classifications for all four AVIRIS flight lines will be merged, producing leafy spurge maps for the entire South Unit of the park. These maps will then be used to quantify the effects of integrated pest control efforts undertaken by the park from 1999 through 2001.

10. Conclusions

AVIRIS has been a central element of four years of imaging spectroscopy research in detection and mapping of invasive leafy spurge at Theodore Roosevelt National Park in southwestern North Dakota. The exceptionally high signal-to-noise ratios, well-defined system calibrations, and recently improved geospatial positioning capabilities of AVIRIS have provided an excellent reference point for comparison with the Hyperion imager on the orbital side, and CASI on the low altitude aircraft side, for effectiveness of mapping leafy spurge with imaging spectrometers spanning a wide range of spatial resolution. Preliminary results of three different classification techniques indicate that leafy spurge is generally separable from its associated vegetation types. Further research is expected to quantify classification results and explore the potential for generating more regional, multi-flightline maps of leafy spurge infestations that will provide valuable contributions to monitoring and controlling efforts.

11. Acknowledgments

The authors acknowledge the substantial contributions of the National Park Service and Theodore Roosevelt National Park for field, logistical, laboratory, and GPS ground survey support, Diane Larson of the USGS Northern Prairie Science Center for providing field plots data, Joe Boardman of Analytical Imaging and Geophysics LLC for assistance in georeferencing and terrain correction, and John R. Miller and James Freemantle (York University and CRESTech, Canada) for sharing the computer code for red-edge parameter calculation.

12. References

Analytical Imaging and Geophysics 2001, ACORN User's Guide. Version 3.12. Analytical Imaging and Geophysics LLC. 4450 Arapahoe Ave. Suite 100. Boulder, CO 80303 USA. acorn@aigllc.com.

Anderson, G.L., J.H. Evert, D.E. Escobar, N.R. Spencer, and R.J. Andrascik. 1997, Mapping leafy spurge (*Euphorbia esula*) infestations using aerial photography and geographic information systems. Geocarto International, vol 11, no. 1, pp. 81-89.

Council for Agricultural Science and Technology (CAST). 2000, Invasive Plant Species. Issue Paper Number 13. Council for Agricultural Science and Technology , Ames, Iowa.

Hare, E. W., J. R. Miller, and G. R. Edwards. 1984. Studies of the vegetation red reflectance edge in geobotanical remote sensing, in *Proceedings of the 9th Canadian Symposium on Remote Sensing*, pp. 433-440, Can. Remote Sens. Soc., Can. Aeronaut. and Space Inst., Ottawa, 1984.

Kokaly, R., R. Root, K. Brown, G. L. Anderson, and S. Hager. 2001a, Calibration of Compact Airborne Spectrographic Imager (CASI) Data to Surface Reflectance at Theodore Roosevelt National Park. Abstract: 221st Annual Meeting of the American Chemical Society. April 1-5, 2001. San Diego, CA.

Kokaly, R., R. Root, K. Brown, S. Hager, and G. L. Anderson. 2001b, Discriminating leafy spurge spectral signature from native vegetation using field reflectance measurements from Theodore Roosevelt National Park, North Dakota. Abstract: 221st Annual Meeting of the American Chemical Society. April 1-5, 2001. San Diego, CA.

Kokaly, R. F., R. Root, and K. Brown. 2001c, Mapping the Distribution of the Invasive Species Leafy Spurge (*Euphorbia esula*) in Theodore Roosevelt National Park Using Field Measurements of Vegetation Spectra and CASI Imaging Spectroscopy Data. Third International Conference on Geospatial Information in Agriculture and Forestry. Denver, Colorado. 5-7 November, 2001. Poster presentation.

Martin, M. E., S. D. Newman, J. D. Aber, and R. G. Congalton. 1998, Determining forest species composition using high spectral resolution remote sensing data, Remote Sensing of Environment, 65, 249-254, 1998.

Miller, J. R., E. W. Hare, and J. Wu. 1990, Quantitative characterization of the vegetation red edge reflectance I. An inverted-Gaussian reflectance model, International Journal of Remote Sensing., 11, 121-127, 1990.

Miller, J. R., J. Wu, M. G. Boyer, M. J. Belanger, and E.W. Hare. 1991, Seasonal patterns in leaf reflectance red edge characteristics, International Journal of Remote Sensing., 12, 1509-1524, 1991.

Morse, L.E., J.T. Kartesz, and L.S. Kutner, 1995, Native vascular plants. Pages 205-209 in LaRoe, E.T., Farris G.S., Puckett, C.E., Doran, P.D., Mac, M.J., eds. Our Living Resources: a Report to the Nation on the Distribution, Abundance, and Health of U.S. Plants, Animals and Ecosystems. Washington, DC: U.S. Department of the Interior, National Biological Service.

National Park Service. 1992, Statement for Management – Theodore Roosevelt National Park. Theodore Roosevelt National Park, Medora, ND. 73 p.

National Park Service. 2001, Ground truthing remotely sensed leafy spurge infestations at Theodore Roosevelt National Park: Methodology for mapping project using global positioning systems and geographic information systems. Internal Report. U.S. Department of the Interior, National Park Service. Theodore Roosevelt National Park. Medora, ND. 6 p.

O'Neill, M., S.L. Ustin, S. Hager, and R. Root. 2000, Mapping the Distribution of Leafy Spurge at Theodore Roosevelt National Park using AVIRIS. Proceedings of the 9th Jet Propulsion Laboratory (JPL) Airborne Earth Science Workshop. NASA JPL Publication 00-18, pp. 339-347.

Pimentel, D. L. Lach, R. Zuniga, and D.Morrison. 2000, Environmental and Economic Costs of Non-Indigenous Species in the United States. BioScience 50:53-65.

Redente, E.F. 1993, "Restoration management plans for National Park Service prairie sites in Colorado, South Dakota, North Dakota, and Wyoming." Colorado State University, Fort Collins.

Root, R., and D. Wickland. 2001, Hyperspectral Technology Transfer to the U.S. Dept. of Interior: Summary of Results of the NASA/DOI Hyperspectral Technology Transfer Project. Proceedings of the Tenth JPL Airborne Earth Science Workshop. NASA JPL Publication 02-1, pp. 331-342.

Trammell, M.A. 1994, Exotic Plants of Theodore Roosevelt National Park: Extent, distribution, and ecological impact. Master Thesis. University of South Dakota, Vermillion. 175 p.

Zarco-Tejada, P. J., and J.R. Miller, 1999, Land cover mapping at BOREAS using red edge spectral parameters from CASI imagery, Journal of Geophysical Research. 104:27921-27933.

Environmental Processes in the Monterey Bay National Marine Sanctuary: Studies Integrating AVIRIS and Synoptic In Situ Sensing

John Ryan,[1] Francisco Chavez,[1] James Bellingham,[1] Erich Rienecker,[1] Heidi Dierssen[1]
Raphael Kudela,[2] Andrea Vander Woude[2]
Robert Maffione[3]
Andrew Fischer[4]

[1]Monterey Bay Aquarium Research Institute, Moss Landing, California 95039
[2]Department of Marine Sciences, University of California Santa Cruz 95064
[3]Hydro-Optics, Biology, and Instrumentation Laboratories, Tucson, Arizona 85749
[4]Department of Earth and Atmospheric Sciences, Cornell University, Ithaca, New York 14853

Abstract

AVIRIS observations of the Monterey Bay National Marine Sanctuary are presented in light of oceanic processes studied in multidisciplinary field efforts. Field studies in the Monterey Bay region occurred during the second half of August and on October 10-11, 2000. AVIRIS acquisition of the Monterey Bay region was planned to coincide with the field studies. High-altitude AVIRIS overflight on October 13, 2000 spanned near coastal to deep oceanic waters. During the overflight, hyperspectral measurements of downwelling irradiance and upwelling radiance were made at the ocean surface over a large region of the bay. High-resolution *in situ* measurements from an autonomous underwater vehicle during the August field studies revealed complex small-scale processes of significance to coastal ocean ecology. These processes related to upwelling of iron-bearing (fertilizing) sediments, vertical fluxes of carbon at convergent fronts, topographic influences on coastal circulation, and small-scale frontal dynamics. AVIRIS observations captured near-surface structure related to complex small and mesoscale processes, including eddies, filaments, plumes and frontal dynamics, and they defined environmental structure consistent with the *in situ* observations. Application of these advanced sensing methods emphasize the necessity of high spatial and spectral resolution sensing in the dynamic coastal ocean environment and the value of combining remote and *in situ* sensing in studying coastal ocean complexity.

Introduction

The coastal ocean off western North America has received considerable oceanographic study because of its fisheries and proximity to large human populations. The region is strongly influenced by the process of coastal upwelling through which deep waters are drawn to the surface in response to wind-driven transport of surface waters away from the coast. Upwelled waters are nutrient-rich and support high levels of phytoplankton (Figure 1) and higher trophic level production (Ryther, 1969; Barber and Smith, 1981). Dynamic currents of the upwelling system transport upwelled waters and their associated productivity horizontally and vertically by diverse circulation phenomena ranging from the scale of an eastern boundary current to mesoscale eddies and filaments and small-scale frontal dynamics. Off the western United States and Baja California, coastal upwelling occurs seasonally (Bakun et al., 1974; Bakun, 1990). In spring, the Aleutian low pressure system moves northwest and the North Pacific high moves north, resulting in upwelling favorable winds. Equatorward winds continue to force persistent upwelling through spring and early summer; they weaken in late summer and fall and are eventually interrupted by northward winter storm winds, resulting in the cessation of upwelling (Strub et al., 1987a, b).

The Monterey Bay National Marine Sanctuary (MBNMS) lies in the heart of the productive upwelling system off central California (Figure 1). Within this dynamic coastal ocean setting, the Monterey Bay Aquarium Research Institute (MBARI) is developing an Ocean Observing System (MOOS) to advance observational methods and capabilities across the disciplines of geological, chemical, physical and biological oceanography, and spanning research from the ocean surface to the sea floor. MOOS upper-ocean research is founded in sustained observations from moorings and ships that have extended for over a decade (Pennington and Chavez, 2000). These long-term observations provide a framework for understanding local ecosystem function, perturbation by remote forcing such as El Niño (Chavez et al., 2002), and the important ecological questions that may be addressed by advances in methods of remote and *in situ* observation.

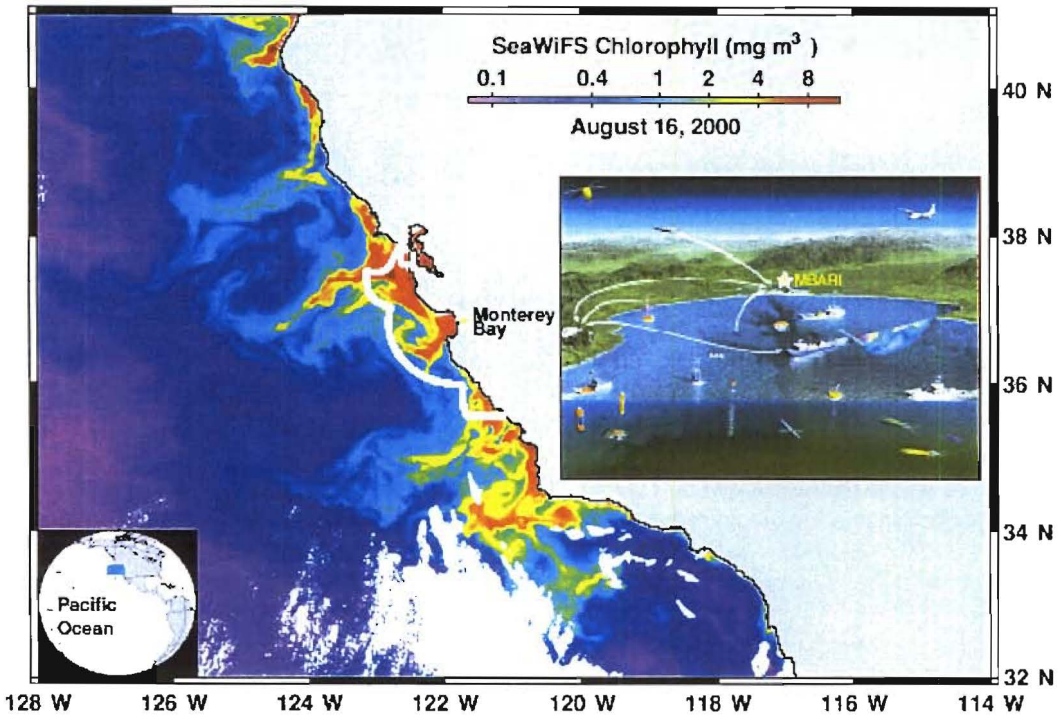

Figure 1. Environmental and experimental context. Main image shows space-based estimates of surface ocean chlorophyll concentrations from SeaWiFS, illustrating the highly productive coastal upwelling system. The white contour overlay defines the boundaries of the MBNMS. Inset image represents activities of the MUSE studies in the Monterey Bay region during August 2000 (see text).

An important approach of MOOS development is to integrate and apply emergent technologies in major field efforts that enable unprecedented ocean sensing while testing the new technologies. During the most recent of these observatory experiments in August 2000, the MOOS Upper-water-column Science Experiment (MUSE; http://www.mbari.org/MUSE), oceanic process studies were focused on the nature and consequences of natural iron fertilization of the coastal food web that occurs through transport of iron-bearing sediments from deep shelf waters into the shallow, sunlit euphotic zone. Iron is a limiting nutrient for phytoplankton, and its importance to oceanic productivity and ecosystem structure in open ocean (Coale et al., 1996; Kudela and Chavez, 1996) and coastal systems (Johnson et al., 1999) is clear. During MUSE participants from 12 research institutions employed a wide array of advanced observing technologies (Figure 1, inset) to pursue diverse science. One of the key technologies was the autonomous underwater vehicle (AUV), an unmanned, untethered robotic submarine programmed to autonomously survey the marine environment (2 yellow submarines at the lower right of Figure 1 inset). Because of their high degree of maneuverability, wide range of flight behaviors, capacity for carrying a multidisciplinary suite of sensors, and relatively rapid propulsion, AUVs are capable of capturing synoptic measurements of the ocean interior that permit greater understanding of complex processes. Most of the *in situ* observations presented here were made using an AUV.

During MUSE there were two primary goals for overflight by the Airborne Visible/Infrared Imaging Spectrometer (AVIRIS; Green et al., 1998). The first was to resolve variability at spatial scales between the high-resolution observations of various moored and mobile *in situ* platforms that cover small regions, and periodic images of satellite ocean color and temperature that cover larger regions at relatively coarse resolution (~1 km). AVIRIS acquisition was intended to fill a scale of observation unachievable by any other means. The second goal was to explore spectral structure of the coastal waters and the science enabled by a highly resolved reflectance spectrum. Having ~2500 times the spatial resolution of a satellite ocean color or infrared image, far greater spectral coverage and resolution than multispectral satellite ocean color sensors, and greatly enhanced signal to noise ratio (Asner and Green, 2001), AVIRIS offers a tremendous opportunity to study near-coastal optical properties, oceanic structure, and processes. Concurrence of AVIRIS and multi-platform *in situ* observation is synergistic.

Methods

The ocean observatory experiment called MUSE occurred as scheduled during the second half of August 2000. AVIRIS acquisition in the Monterey Bay region was planned to coincide with MUSE, however atmospheric conditions precluded high altitude remote sensing of the surface ocean during the experiment (Figure 1 shows conditions immediately before the experiment). Thus a second, shorter research cruise was planned for October 10-11, also intended to coincide with an AVIRIS overflight. The cruise occurred as scheduled on the *R/V Pt. Sur* and included hydro-optical station profiles and continuous underway measurements of temperature, salinity, fluorescence, and spectral absorption and attenuation. The cruise track is shown over regional bathymetry in Figure 2. Conditions during this 2-day cruise were again unsuitable for AVIRIS acquisition. However, on October 13 conditions were favorable, and the overflight occurred. The AVIRIS data spanned near coastal to deep oceanic waters (flight line centers in Figure 2). Coincident with the overflight on October 13, *in situ* hyperspectral measurements of downwelling irradiance and upwelling radiance were made at 18 stations (Figure 2) in a rapid small-boat survey extending into all but the most seaward AVIRIS swath. Additionally, moored hyperspectral and hydrographic measurements were taken within the center flight swath (mooring location in Figure 2). All *in situ* hyperspectral measurements were made with HOBI Labs Hydrorad-4 hyperspectral radiometers.

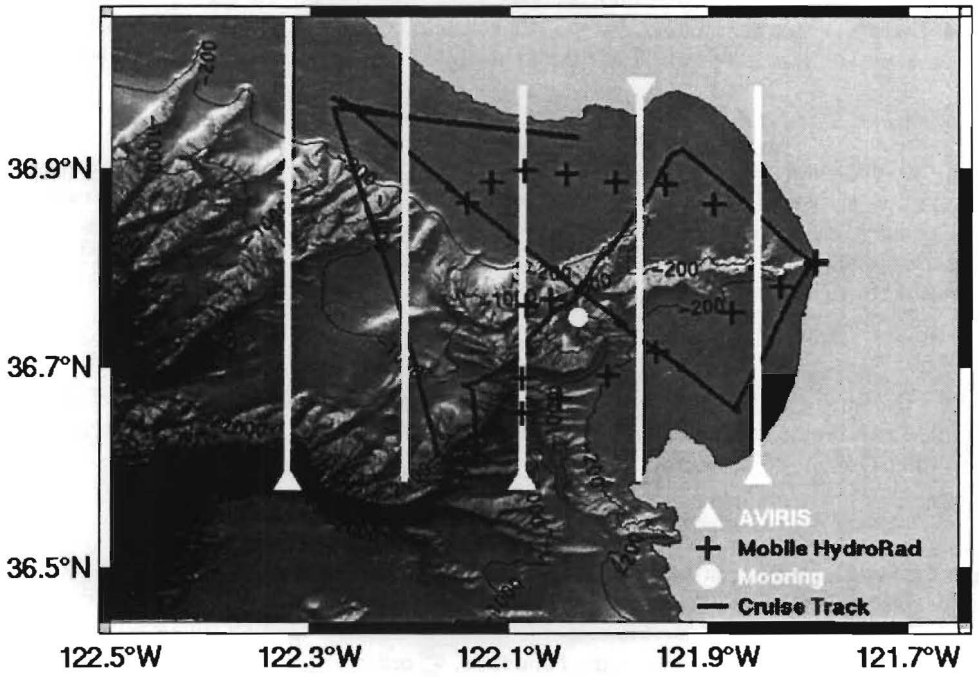

Figure 2. AVIRIS flight lines and ship-based sampling locations shown over bathymetry of the Monterey Bay region (depth contours are 200, 1000, and 2000 m). AVIRIS flight lines and mobile hydrorad stations are from October 13, 2000; cruise track is for the October 10-11 cruise; mooring-based measurements were continuous.

Processing of AUV and ship observations are detailed elsewhere (Ryan et al., in prep). Here we focus on processing of the AVIRIS data. AVIRIS flight line data were obtained from JPL as 512-scanline scenes (Green et al, 1998). The data set consisted of 33 scenes in the five north-south flight lines having ~1 km overlap along their east-west boundaries (Figure 2).

Cross-Track Illumination Correction

Irregularities in cross-track illumination may be due to vignetting effects, instrument scanning, off-nadir view angle and solar reflection, or other non-uniform illumination effects (RSI, 2001b). To avoid sun glint, flight lines for this Monterey Bay region overflight were oriented north-south and intended for acquisition near local noon, which occurred at 12:55 pm on October 13, 2000. AVIRIS acquisition occurred after local noon, between approximately 1:27 and 2:10 pm local time, and some cross-track illumination irregularities were evident in all but

the eastern-most flight line. To reduce cross-track illumination effects in the other four flight lines, we applied a polynomial fit correction method (RSI 2001b).

Atmospheric Correction

Atmospheric correction was accomplished using the Fast Line-of-Sight Atmospheric Analysis of Hyperspectral cubes (FLAASH) atmospheric correction program on each of the flight lines individually. FLAASH is based on the atmospheric physics and spectroscopy of the MODTRAN4 radiative transfer code (Andersen et al., 2000) and models the scattering and absorption processes in the atmosphere with user-supplied parameters. Visibility can be retrieved from the aerosol calculations. However, the assumptions of the aerosol retrieval method (RSI, 2001b), while appropriate for land applications, do not work well over water. We found that this method over-corrected for aerosols and resulted in negative reflectance retrievals. We therefore disabled the aerosol retrieval calculation and specified visibility values using an iterative empirical approach comparing retrieved reflectances with *in situ* surface reflectance measurements made at 18 locations during the AVIRIS overflight. While the scene average visibility calculated by FLAASH was approximately 30 km for all flight lines, the visibility value yielding the closest comparison with *in situ* spectra was 60 km. FLAASH was run in the ISAACS MODTRAN multiple-scattering mode using the atmospheric model of mid-latitude summer and a maritime aerosol profile. In addition to 60 km visibility, we specified a CO_2 mixing ratio of 390 ppm, and an aerosol scale height of 2 km. Corrected flight lines were then joined using pixel-based, overlap-feathering to produce a mosaic image of 3070 x 3914 pixels.

Geometric Correction

An irregular grid of ground control points (GCPs) was constructed from geographic positions provided in the AVIRIS navigation files and supplemented with data from National Ocean Service shoreline data set. GCPs were determined for the center line and edges of each flight line. The flight lines were then transformed into geographic space (latitude and longitude) using the WGS-84 datum and a polynomial warping function in ENVI (RSI 2001a). Nearest-neighbor sampling (Richards and Jia, 1999) was used to assign pixel brightness values.

Other Corrections

The composite image was normalized to account for remaining glint and sea foam effects. For this correction, the reflectance value at 810 nm, a rather flat, low reflectance region of the spectrum, was subtracted from all wavelengths (S. Adler-Golden, communication).

Derived Characteristics of the Marine Environment

Considering the focus of the ocean process studies on phytoplankton ecology, we applied the radiometrically and geometrically corrected AVIRIS oceanic reflectances to derive ocean surface chlorophyll estimates based on algorithms developed for the SeaWiFS satellite sensor (Figure 1). The SeaWiFS OC2 version 4 (OC2V4) modified cubic polynomial and the OC4 version 4 maximum band ratio, 4th order polynomial algorithms were applied (Appendix 1). We present chlorophyll maps from the OC2V4 algorithm. Further algorithm development is underway for suspended sediments, colored dissolved organic matter (CDOM), and characterization of phytoplankton functional groups.

Results

Oceanic Process Studies

In situ observations from the AUV extended over 8 days and provided valuable observations related to upwelling of iron-bearing (fertilizing) sediments, vertical fluxes of carbon at convergent fronts, topographic influences on coastal circulation, and small-scale frontal dynamics resolved in 3-D. Here we present only two examples of AUV observations that illustrate the importance of high-resolution observations.

Physical-Biological Coupling in 3-D

On August 31 2000, an oceanic front was located via underway surface mapping by ship in northern Monterey Bay, and an AUV was deployed to survey a volume around and through the front. Taking nearly 60,000 measurements from each of 6 instruments, the AUV surveyed a volume 7 km x 3 km x 70 meters (Figure 3a). The

gray surface in Figure 3b is a constant density surface (isopycnal) within the volume surveyed, showing a ridge-trough structure in the density field that was aligned with and inshore of the Monterey Canyon shelfbreak. The density ridge coincided with a surface slick that extended as far as the eye could see. The colored contours show mean temperature in the layer 10 to 20 m (11° to 12°C; 0.2° interval). The coldest waters (dark blue contours) were above the isopycnal ridge. There was a temperature front south of the ridge and small-scale cool/warm eddy-like features south of the front (labeled C and W).

The outer boundary of a concentrated phytoplankton layer is shown as a green isosurface in Figure 3b. Inside this surface, chlorophyll fluorescence was equal to or greater than that along its outer boundary, and fluorescence was much lower everywhere outside this boundary. The highest chlorophyll fluorescence was observed along the southern end of the survey (Chl_{max}), over the trough in the density field. Property distributions are consistent with the concentration of phytoplankton in the trough of an internal wave (Lennert-Cody and Franks, 1999; Pineda, 1999; Franks, 2001). Phytoplankton samples in this region showed high abundance of harmful algal species, thus phytoplankton concentration and patchiness indicated by these observations have implications for transfer of biologically produced toxins through the coastal ocean food web. This complex environmental structure and physical-biological coupling became evident only with a 3-dimensional snapshot of a volume captured from synoptic AUV survey.

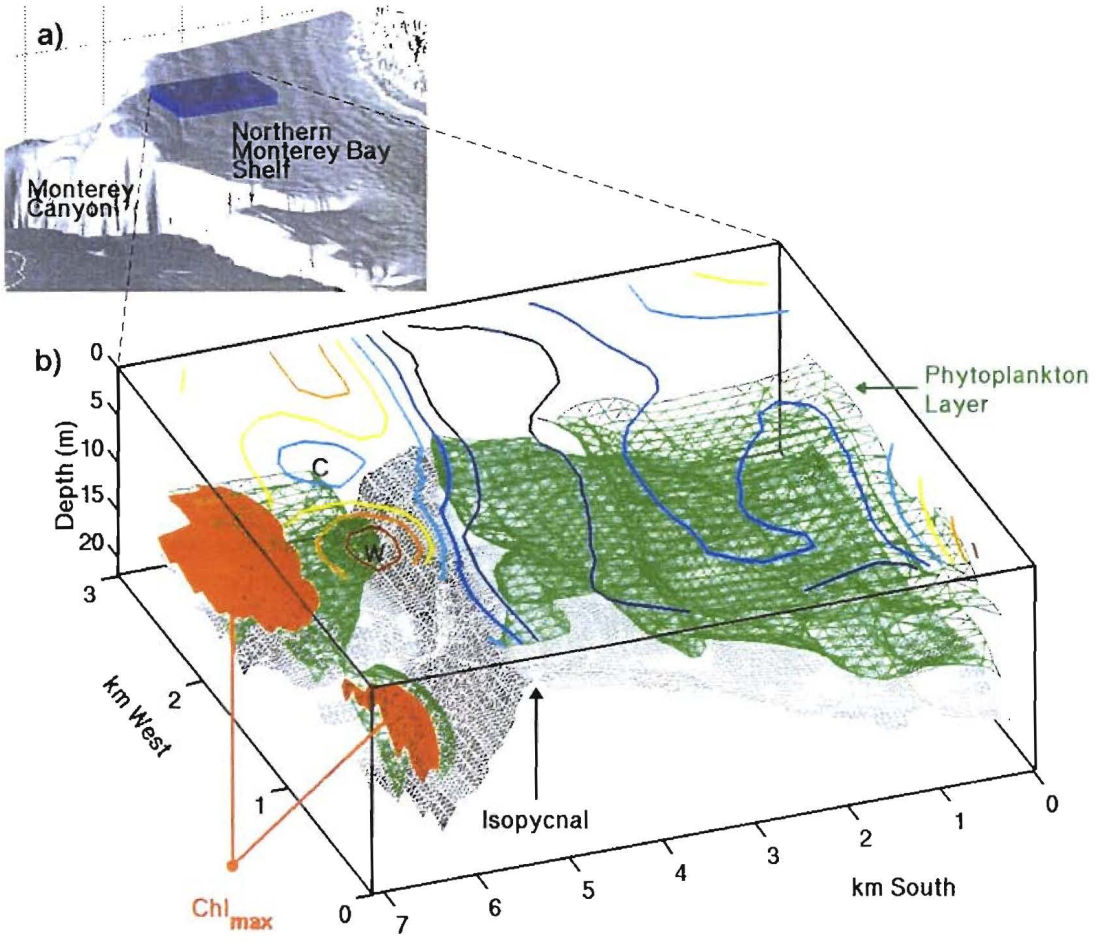

Figure 3. Volume view around a front / density field perturbation on the northern Monterey Bay shelf, 31 August 2000. a) ocean volume (blue) relative to bathymetry (gray); the survey region was near the shelfbreak of Monterey Submarine Canyon. b) observations within volume: the gray isosurface is an isopycnal; the green isosurface is a phytoplankton-rich layer; maximum chlorophyll concentrations are shown in red. The contours are mean temperature between 10 and 20 m (see text).

Exchange between Submarine Canyon and Continental Shelf

Even on scales of a few kilometers, bottom topography can strongly influence ocean circulation on continental shelves; this is an important research area in coastal ocean science (NSF Ocean Sciences Decadal Committee, 2001). Submarine canyons carved into the continental shelf and slope are a ubiquitous feature along the US West Coast (Figure 2). Observational and model studies indicate that cross-shelf exchange and upwelling patterns are profoundly influenced by canyons (Shea and Broenkow, 1982; Freeland and Denman, 1982; Allen 1996; Klinck, 1996; She and Klinck, 2000). AUV-based observations near Monterey Canyon illustrate strong influence of the canyon on regional ecology of benthic and pelagic habitat. During MUSE we mapped physical and bio-optical distributions where a phytoplankton bloom dominated by the diatom *Pseudo-nitzschia australis* was developing. This species produces domoic acid, a neurotoxin harmful to marine life and humans. In 1998, a bloom of *P. australis* resulted in widespread mortality of marine mammals and seabirds (Scholin et al., 2000). On August 30, 2000, in only two hours, we surveyed at high resolution the upper 60-m along an 8-km transect south of Monterey Canyon (Figure 4). This survey allowed examination of the environment and processes surrounding the bloom.

The bloom was concentrated in a subsurface layer approximately 10 m thick. Its vertical distribution closely followed a constant density surface throughout the domain surveyed (Figure 4a,b), indicating close association between the physical environment and the distribution of the phytoplankton. Beneath the bloom was a plume of suspended particulate material emanating from Monterey Canyon (Figure 4c). Particulate material from the bottom can contain iron-bearing sediments that fertilize productivity of the pelagic ecosystem and may contain resting stages of phytoplankton that can initiate blooms when they are transported to shallow, sunlit waters. Iron is thought to be a key regulator of toxin production in *Pseudo-nitzschia* (Maldonado et al., 2002). The lack of toxicity of this bloom may relate to iron supply from canyon upwelling. The patterns observed within the water column, and at the surface (aircraft-mapped SST, not shown) are remarkably consistent with circulation patterns forced by the interaction of flow with the topography of the canyon (Klinck, 1996).

In these case studies, high-resolution, synoptic sensing of the ocean interior with a diverse suite of sensors was essential to understanding processes. We now turn from high-resolution *in situ* sensing to the high spatial and spectral resolution remote sensing from AVIRIS.

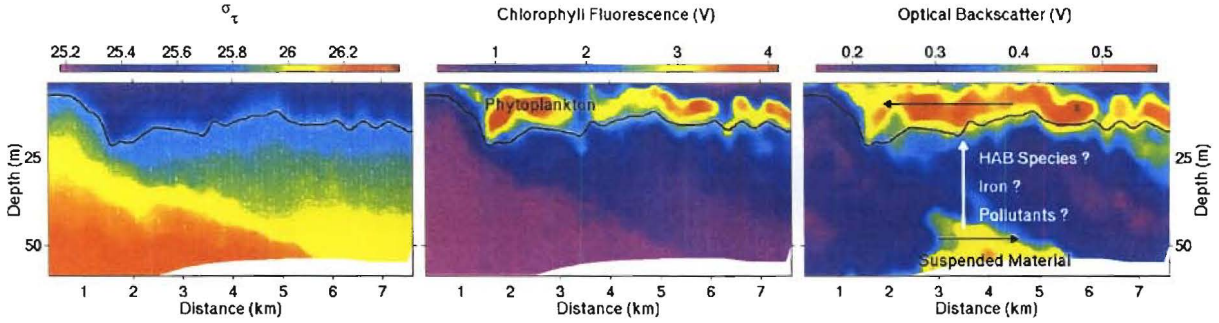

Figure 4. High-resolution vertical sections of 3 of the 6 properties measured using an AUV adjacent to Monterey Canyon on August 30, 2000. The same density level (black contour) is repeated in all panels for reference.

Atmospheric Correction Results

At nearly all *in situ* measurement locations the comparison of ground-truth and image spectra showed good correspondence of spectral shape except in the blue (400-440 nm) region of the spectrum where AVIRIS is less well calibrated (Gao et al., 2000). An example comparison is shown in Figure 5a. At 15 of the 18 stations, comparison of image and *in situ* spectra showed similar characteristics. These are summarized in Figure 5b. The error is characterized as the percent difference between the *in situ* spectra and the spatially-coincident atmospherically corrected image spectrum ([image-*in situ*]/*in situ*). The temporal offset of remote and *in situ* measurements varied between the stations, and this complicates the comparison somewhat; temporal offsets ranged from less than 10 minutes to ~90 minutes. The thick black line in Figure 5b is the median error for the 15 stations. The median error increased from a minimum of ~ 5% at 450 nm to a maximum of ~ 80% toward the IR. We are further examining how atmospheric correction issues (cross-track illumination and glint) affect these comparisons.

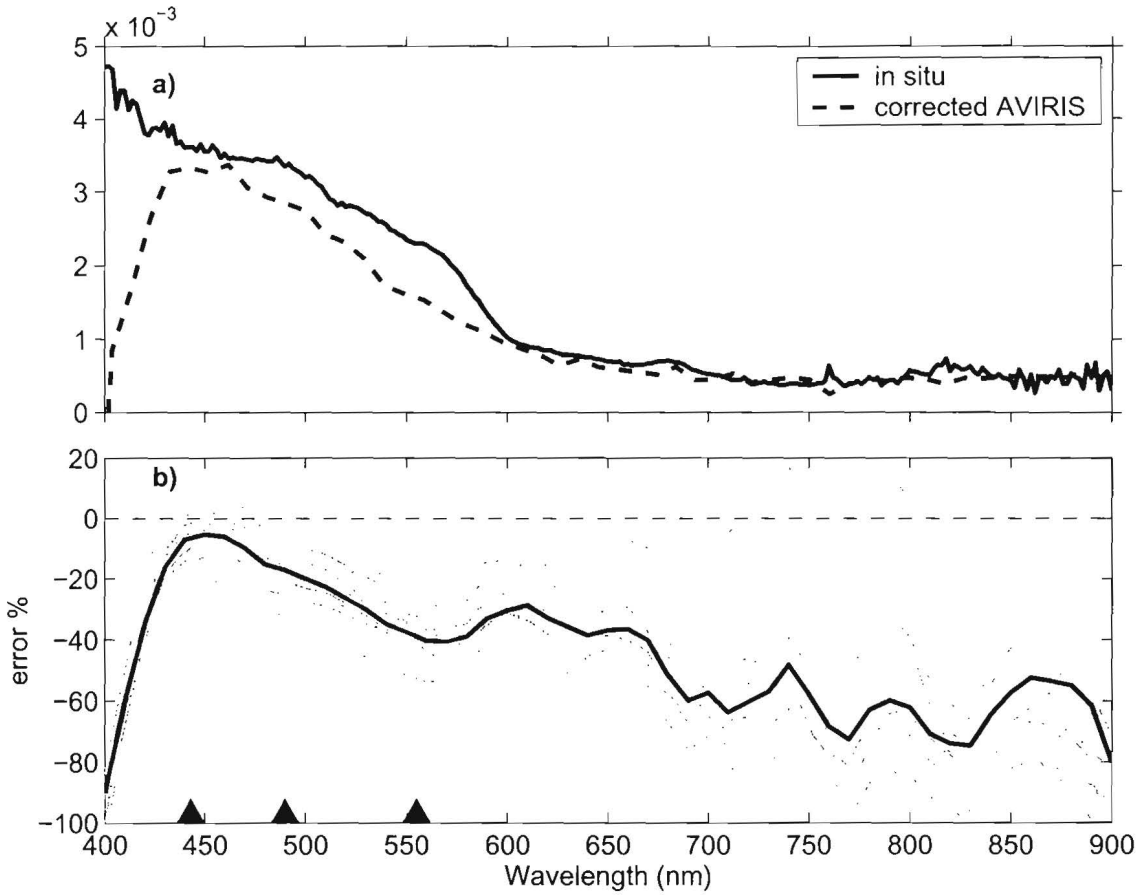

Figure 5. Characterization of error in atmospherically corrected spectra based on ocean surface measurements at 15 locations on the day of AVIRIS overflight. a) example comparison of an *in situ* and AVIRIS corrected spectum, and b) summary for 15 stations; triangles mark wavelengths used for initial chlorophyll estimates (Figure 6).

Surface Chlorophyll Calculated from AVIRIS Data

The surface chlorophyll map derived from the atmospherically corrected reflectance data revealed phenomenal small and mesoscale structure in the Monterey Bay region. A mesoscale hammer-head shaped region of low chlorophyll concentrations extended into the northern and southern shelf waters (Figure 6a). These low chlorophyll plumes were flanked on their seaward sides by relatively high chlorophyll filaments extending from the northern and southern shores toward the bay interior. A high chlorophyll filament extended out of the southern bay into an anticyclonic (clockwise spinning) eddy immediately outside the bay. The highest chlorophyll estimates were in near coastal waters of the northern bay, extending in a plume from the mouth of the Pajaro River. Of course, chlorophyll estimates in this region must be treated carefully as river-borne matter can strongly influence the color of coastal waters.

At the very center of the Monterey Bay crescent is the mouth of Elkhorn Slough (Figure 6b). At this location, the AVIRIS-derived chlorophyll estimates showed a small-scale plume extending from the mouth of the estuary (P label at western boundary of plume). At the core of this plume was a narrow band of high chlorophyll estimates, perhaps indicative of sediments influencing the reflectance and hence calculated chlorophyll. We are currently examining sediment algorithms to study this signature more closely. The highest chlorophyll estimates in this plume region were along the western (seaward) boundary of the plume, consistent with concentration of phytoplankton or other colored organic matter at the outer plume boundary.

Seaward of the Monterey Peninsula (Figure 6c) the map shows a ring of kelp canopy following the topography (labeled k) and fine-scale filaments (labeled F) indicating complex circulation features within the high-chlorophyll filament east of the peninsula. Like the *in situ* observations from the AUV these remotely sensed signatures

emphasize the importance of high spatial resolution in understanding the complex processes of the dynamic coastal ocean.

Spatial Structure from Ship-Based Measurements

Underway surface mapping from the R/V Pt. Sur on October 10 and 11 (ending less than 2 days before the AVIRIS acquisition) revealed surface structure consistent with the AVIRIS chlorophyll map (Figure 7). High chlorophyll fluorescence levels were observed in the region of the northern bay nearshore plume, while low fluorescence and relatively high salinity (relative to the rest of the bay interior) prevailed over the region of the southern bay low-chlorophyll plume evident in the AVIRIS chlorophyll map (Figures 6a,7). The eddy evident in the AVIRIS chlorophyll map (Figure 6a) coincided with warm SST (Figure 7). The warmest, freshest waters surveyed were immediately outside the mouth of Elkhorn Slough (Figure 7), the same plume that showed very complex optical structure (Figure 6b). There are also compelling differences in the region of this plume. While the AVIRIS chlorophyll map suggests relatively low chlorophyll concentrations within the plume (Figure 6b; yellow plume region lower in chlorophyll estimates than the adjacent near-coastal waters), some of the highest chlorophyll fluorescence mapped by the ship were within this plume (Figure 7c). This suggests that either conditions changed between the underway mapping of that region on October 11 and the AVIRIS observations of October 13, or perhaps that absorption in the blue by dissolved substances of estuarine or terrestrial origin affected the chlorophyll estimate based on AVIRIS spectral reflectance.

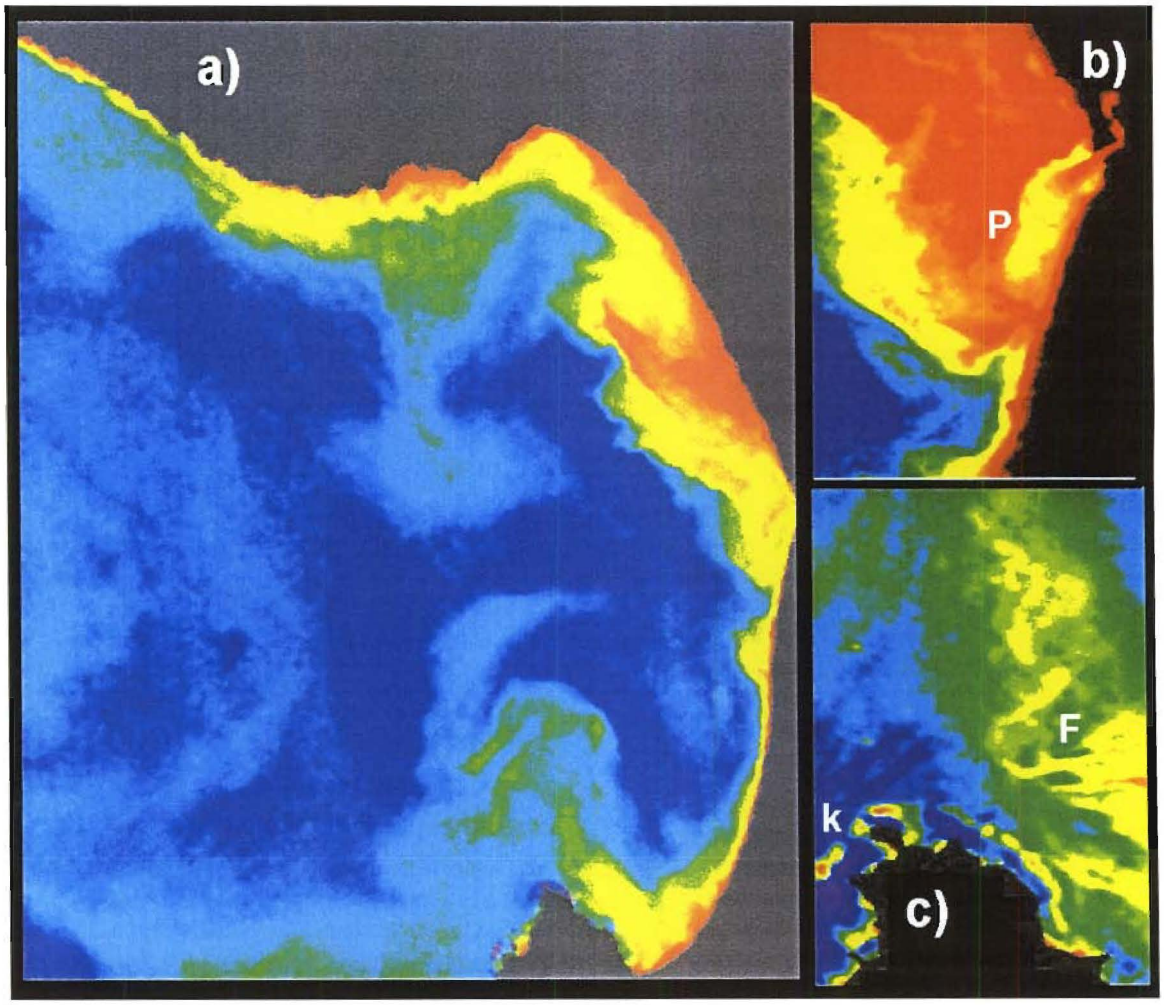

Figure 6. Surface chlorophyll calculated from AVIRIS atmospherically corrected reflectance spectra; ranges differ between the large-area view in a), and the enhanced zoom images around Elkhorn Slough outflow in b) and the Monterey peninsula in c). The range calculated over the entire region was ~0.2 to 8 mg m^{-3}.

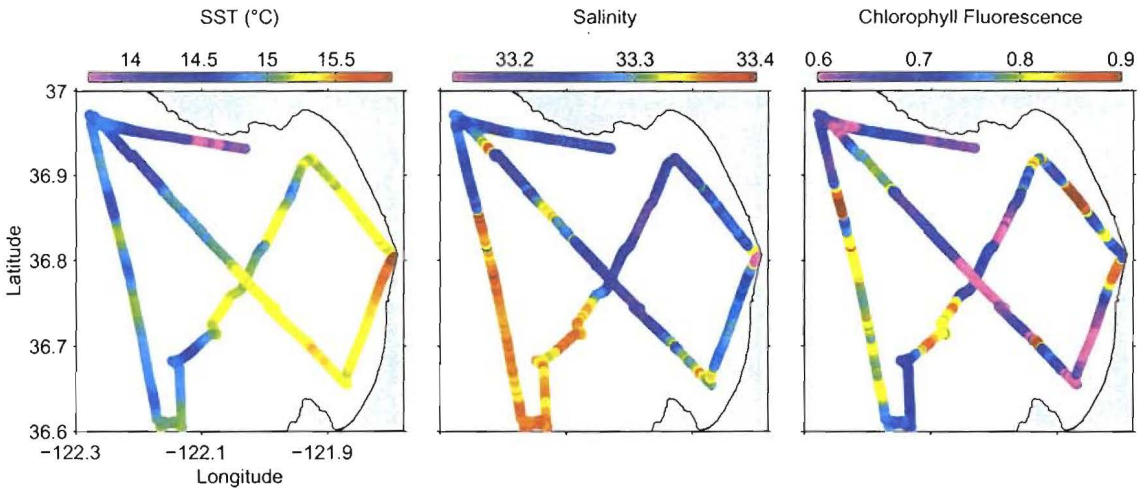

Figure 7. Maps of ocean surface properties measured via the continuous flow system of the R/V Point Sur on October 10-11.

Exploring Spectral Resolution

When and where the color of ocean waters in the upper optical depth is dominated by specific functional groups of phytoplankton, distinct spectral signatures resulting from their unique pigment assemblages may permit mapping of their spatial distributions, as has been shown for Florida Bay (Richardson and Kruse, 1999). We are using a unique time series including moored surface ocean hyperspectral reflectance measurements, moored hydrographic measurements, and regular 3-weekly samples characterizing the pigment and species composition of surface waters at the MBARI M1 mooring in outer Monterey Bay (location shown in Figure 2). Figure 8a shows variability in the shape of the reflectance spectrum over nearly one year at M1 and suggests five periods when the spectrum was markedly different. Changes in the spectrum were clearly related to changes in the underlying ocean structure. For example a sudden change occurred in the spectrum (Figure 8a) as the ocean temperature and salinity fields shoaled in the second period (Figure 8b,c), indicative of the presence of upwelled waters. The third period defined by spectral distinction coincided with hydrographically distinct conditions when surface waters were most persistently cold and saline. There are also indications of relationships between the reflectance spectra and both pigment concentrations and abundance of important phytoplankton groups. For example, chlorophyll was highest during the 3rd and 5th periods of the time series, and the spectral shape during these periods were similar to each other and unique from the other periods. Synechococcus also showed their highest abundance during these periods. Similarly, the 2nd and 4th periods showed similar spectral shapes and were unique compared with the other periods, and they coincided with high abundance of autotrophic flagellates. These patterns are being further examined with a focus on species and functional groups that can dominate the phytoplankton assemblage. Robust relationships from single-location time series will be extended to explore spatial patterns in the spectral gradients of the AVIRIS data relative to the distributions and ecology of important microalgae of this dynamic coastal upwelling environment.

Ongoing and Future Work

Further examination of the AVIRIS atmospheric correction is planned, as described in the results. It is anticipated that improvements to FLAASH specifically for ocean applications (S. Adler-Golden, communication) may improve the atmospheric correction of these data. We are also evaluating the Tafkaa model (Gao et al., 2000) developed by the Naval Research Lab for ocean applications. Motivated by the structure around river and estuarine plumes evident in the AVIRIS-derived chlorophyll maps, we are testing algorithms for sediments and CDOM.

Conclusion

Application of imaging spectroscopy to the coastal ocean is a young science with tremendous promise for delving into the complexity inherent in ocean margin environments so crucial to societal well being. The Monterey Bay region of this dynamic coastal upwelling system, with its history and ongoing development in ocean observing systems, provides a solid basis on which to explore the potential of imaging spectroscopy and its integration with other sensing methods.

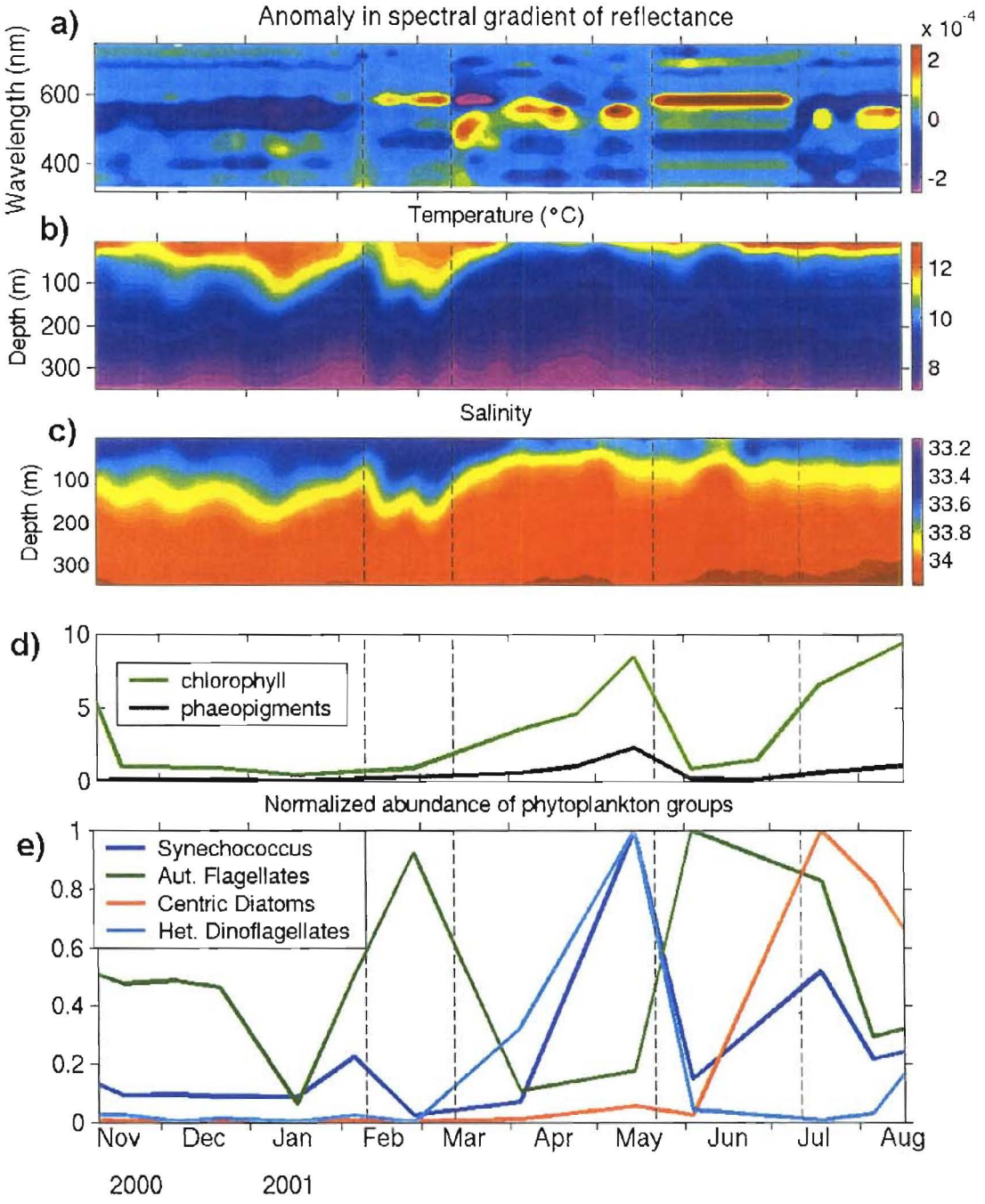

Figure 8. A time series of hyperspectral *in situ* measurements (a) at the mooring location shown in Figure 2 relative to hydrography of the water column (b,c), surface pigments (d) and important local phytoplankton groups (e). The anomaly in the spectral gradient of reflectance (sr^{-1} nm^{-1} x 5) in a) was calculated as follows: A daily reflectance spectrum (calculated from upwelling radiance just below the surface and downwelling irradiance just above the surface) was calculated for the two hour period of each day having the highest downwelling irradiance. To take advantage of the spectral resolution and emphasize variability in spectral shape, the spectral gradient (difference in reflectance / difference in wavelength) was computed. Finally, the anomaly in the spectral gradient was calculated by removing the spectrally resolved temporal mean of the spectral gradient.

Acknowledgments

The observatory research presented was funded by the David and Lucile Packard Foundation. We thank Robert Green (JPL) and Charles McClain (Goddard) for funding the AVIRIS overflight. S. Adler Golden of Spectral Sciences provided invaluable consultation on atmospheric correction. Hydrorad data processing was provided by P. Coenen and E. Palomino.

References

Allen, S.E., 1996. Topographically generated, subinertial flows within a finite length canyon. J. Phys. Oceanogr., 26, 1608-1632.

Andersen, G.P., A. Berk, P.K. Acharya, M.W. Matthew, L.S. Bernstein, J.H. Chetwynd, H. Dothe, S.M. Adler-Golden, A.J. Ratkowski, G.W. Felde, J.A. Gardner, M.L. Hoke, S.C. Richtsmeier, B. Pukall, J. Mello, and L.S. Jeong (2000). MODTRAN4: Radiative transfer modeling for remote sensing, In Algorithms for Multispectral, Hyperspectral, and Ulraspectral Imagery VI, Sylvia S. Chen, Michael R. Descour, Editors, Proceedings of SPIE Vol. 4049, pg. 176-183.

Asner, G. P. and R. O. Green, 2001. Imaging Spectroscopy Measures Desertification in United States and Argentina. EOS 82(49): 601-606.

Bakun, A., 1990. Global climate change and intensification of coastal ocean upwelling. Science 247, 198-201.

Bakun, A., McLain, D.R., Mayo, P.V., 1974. The mean annual cycle of coastal upwelling off western North America as observed from surface measurements. Fish. Bull. 72, 843-844.

Barber, R. T., & Smith, R. L., 1981. Coastal upwelling ecosystems. In Analysis of Marine Ecosystems, (pp. 31-68). New York: Academic Press.

Chavez, F. P., J. T. Pennington, C. G. Castro, J. P. Ryan, R. P. Michisaki, B. Schlining, P. Walz, K. R. Buck, A. McFadyen, and C. A. Collins. 2002. Biological and chemical consequences of the 1997-98 El Niño in central California waters. Progress in Oceanography, 54:205-232.

Coale K. S., K. S. Johnson, S. E. Fitzwater, R. M. Gordon, et al., 1996. A massive phytoplankton bloom induced by an ecosystem-scale iron fertilization experiment in the equatorial Pacifi Ocean. Nature, 383: 495-501.

Franks, P.J.S., 2001. Spatial patterns in dense algal blooms. Limnology and Oceanography, in press.

Freeland, H.J. and K.L. Denman, 1982: A topographically controlled upwelling center off southern Vancouver Island. J. Mar. Res., 40, 1069-1093.

Gao, B-C, M.J. Montes, Z Ahmad, C.O. Davis (2000). Atmospheric correction algorithm for hyperspectral remote sensing of ocean color from space. Applied Optics 39(6) 887-896

Green, R. O. et al., 1998. Imaging Spectroscopy and the Airborne Visible/Infrared Imaging Spectrometer (AVIRIS). Remote Sensing of Environment 65:227-248.

Johnson, K. S., F. P. Chavez, and G. E. Friederich. 1999. Continental-shelf sediment as a primary source of iron for coastal phytoplankton. Nature, 398, 697-700.

Klinck, J.M., 1996: Circulation near submarine canyons: A modeling study. J. Geophys. Res., 101, 1211-1223.

Kudela, R. M. and F. P. Chavez, 1996. Bio-optical properties in relation to an algal bloom caused by iron enrichment in the equatorial Pacific. Geophysical Research Letters, 23(25):3751-3754.

Lennert-Coty, C. E. and P. S. J. Franks, 1999. Plankton patchiness in high-frequency internal waves. Marine Ecology Progress Series, 186: 59-66.

Maldonado, M. T., M. P. Hughes, E. L. Rue, and M. R. Wells, 2002. The effect of Fe and Cu on growth of domoic acid production by Pseudo-nitzschia multiseries and Pseudo-nitzschia australis. Limnol. Oceanogr. 47(2):515-526.

NSF Ocean Sciences Decadal Committee, 2001, Ocean Sciences at the New Millennium, 152 pp.

Pennington, J. T. and F. P. Chavez, 2000. Seasonal fluctuations of temperature, salinity, nitrate, chlorophyll, and primary production at station H3/M1 over 1989-1996 in Monterey Bay, California. Deep-Sea Research, Part II, 47:947-973.

Pineda, J., 1999. Circulation and larval distribution in internal tidal bore warm fronts. Limnology and Oceanography 44(6):, 1400-1414.

Richards, J.A and X. Jia, 1999. Remote Sensing Digital Image Analysis: An Introduction. 3rd Edition. Springer.

Richardson, L. L. and F. A. Kruse, 1999. Identification and classification of mixed phytoplankton assemblages using AVIRIS image-derived spectra. Summaries of the Eighth JPL Airborne Earth Science Workshop, Pasadena, CA, JPL Publication 99-17.

RSI, 2001a, ENVI User's Guide. September 2001 edition. Research Systems.

RSI,2001b, FLAASH User's Guide. Version 1.0. Research Systems.

Ryan, J., F. Chavez, J. Bellingham, C. Scholin, J. Bellingham, J. Paduan, S. Ramp. Phytoplankton layers and related processes in Monterey Bay, California, in prep.

Ryther, J. H., 1969. Photosynthesis and fish production in the sea. *Science* **166**: 72-76.

Scholin, C. A. et al., 2000. Mortality of sea lions along the central California coast linked to a toxic diatom bloom. Nature, 403:80-84.

She, J. and J.M. Klinck, 2000: Flow near submarine canyons driven by constant winds. J. Geophys. Res., 105, 28,671-28,694.

Shea, R. E. and W. W. Broenkow, 1982. The role of internal tides in the nutrient enrichment of Monterey Bay, California. Estuarine, Coastal and Shelf Science, 15:57-66.

Strub, P.T., Allen, J.S., Huyer, A., Smith, R.L., 1987a. Large-scale structure of the spring transition in the coastal ocean off western North America. Journal of Geophysical Research 92, 1527-1544.

Strub, P.T., Allen, J.S., Huyer, A., Smith, R.L., Beardsely, R.C., 1987b. Seasonal cycles of currents, temperatures, winds, and sea level over the northeast Pacific continental shelf. Journal of Geophysical Research 92, 1507-1527.

Appendix 1.

Chlorophyll algorithms used for corrected AVIRIS reflectances.

***Table 1*: Version 4 of SeaWiFS chlorophyll algorithms OC4 and OC2 used for initial chlorophyll estimates from corrected AVIRIS data.**

Coefficients for OC4 version 4 (Maximum Band Ratio, 4th Order Polynomial)

a = [0.366,-3.067,1.930,0.649,-1.532]

R = ALOG10((Rrs443>Rrs490>Rrs510)/Rrs555)

Chl a (ug/l) = 10.0^(a(0) + a(1)*R + a(2)*R^2 + a(3)*R^3 + a(4)*R^4)

Coefficients for OC2 version 4 (Modified Cubic Polynomial)

a = [0.319, -2.336, 0.879, -0.135, -0.071]

R = ALOG10(Rrs490/Rrs555)

Chl a (ug/l) = 10.0^(a(0) + a(1)*R + a(2)*R^2 + a(4)

http://seawifs.gsfc.nasa.gov/SEAWIFS/RECAL/Repro3/OC4_reprocess.html

HYPERSPECTRAL IMAGE ANALYSIS FOR OIL SPILL DETECTION

Foudan Salem,[1] Menas Kafatos,[1] Tarek El-Ghazawi,[2] Richard Gomez,[1] and Ruixin Yang[1]

[1]Center for Earth Observing and Space Research
George Mason University, Fairfax, VA USA.
fsalem@scs.gmu.edu
[2] Department of Electrical and Computer Engineering
George Washington University, Washington DC, US

1. Introduction

During the last several decades, the Chesapeake Bay has suffered from several large oil spill events have threatened coastal habitats and species. Chesapeake Bay's marine resources remain vulnerable as they share the coastal areas with major interstate commerce routes, underground pipelines, extensive development, large industrial facilities, and heavy shipping traffic to the ports of Norfolk and Baltimore. In order to effectively protect communities and species in jeopardy, fast and accurate determination of oil spill hazard areas is needed, particularly if monitoring large quantities of oil spilled. Where oil-handling infrastructure is aging, this need is amplified. This research addresses remote sensing, especially hyperspectral image analysis applicable to the Chesapeake Bay.

This case study is a prototype of oil spill leaks in Patuxent River in Maryland (Darrell and Brebbia, 1996) and the associated image analysis for detecting oil spills using hyperspectral imagery and the effect of oil contaminants on soil, water quality, wetland, and vegetation. Hyperspectral airborne images, as an effective survey tool, are a main source for getting real-time data. In the event of an oil spill, this information can be retrieved in a short time to help authorities plan the quickest route to the spill and formulate an effective environmental protection plan that could be a way to reduce damages. Hyperspectral sensor affords the potential for detailed identification of materials and better estimates of their abundance. This can eliminate the false alarms of features that have the same color and appearance of oil, such as large algae blooms or jellyfish. These phenomena may be identified by visual interpretation as a suspected oil spill using some conventional sensors. Some other types of light fuel, such as gasoline and diesel, cannot be identified visually because of their changing appearance with time.

Hyperspectral sensing can record over 200 selected wavelengths of reflected and emitted energy. With this spectral information one can exploit the spectral signature of oil and also distinguish between different concentrations of crude oil dispersant. HSI observations with high spectral and spatial resolution can be used to detect oil using the spectral signature matching to identify oil spectra based on chemical composition. Oil signatures can be extracted for deferent oil concentration to identify the level of oil contamination of polluted areas, which is necessary for determining proper cleaning processes.

In this research, some of the problems of the conventional techniques can be minimized, when using more advanced methodology to identify oil spill based on the spectral signature matching not by visual interpretation of the image. New techniques such as HSI should be used in order to make the proper distinctions between oil spills and to properly identify natural phenomena. Preliminary results of this research show that with HSI spectral information, the signature of oil can be used to detect minute concentrations of hydrocarbon (crude oil) on the sea and it can distinguish between different levels of oil dispersant on water. The first part of this study also includes the monitoring of oil slicks movements, dispersion in water, and identifying spills on the shoreline. The second part will emphasize the oil contaminates in wetland, soil, vegetation, and grass in the Patuxent River basin in Chesapeake Bay due to oil pollution.

A number of remote sensing systems are available (e.g., side-looking airborne radar, laser fluorescence, microwave radiometer, infrared-ultraviolet line scanner, SAR, ERS 1, 2 and LANDSAT satellite systems). However, problems associated with each of these systems preclude their exclusive use during oil spills. Although remote sensing data can be a valuable tool in the response effort, results from different sensors can vary widely (Fingas, 1991). This problem is particularly apparent during major spills, when many interpretative analyses for satellite images are based on oil color or oil film appearance on water. Many of these analysis techniques have many problems identifying and quantifying oil floating on the sea. As the spill progressing, a surprising number of false positive sightings may be seen. Ice, internal waves, kelp beds, natural organics, pollen, plankton blooms, cloud shadows, jellyfish, algae, and guano washing off rocks all appear as oil (Pavia and Payton, 1983) (McFarland et al., 1993). Weather conditions are one of the limitations when using some sensors such as radar imagery, wind speed and high waves usually cause difficulties inherent in estimating area of coverage (Payne et. al., 1984). Waves will

increase natural dispersion during the early parts of the spill, break the surface tension that causes the oil to look "slick," and mix some of the oil into the surface layer temporarily. Observers should note that as the wind speed increases, the ability to detect the oil decreases (Ministry of Transport 1992). Visual observation of submerged oil is extremely difficult unless the water is very clear and shallow. Spill characteristics appear differently under low light conditions and under strong winds conditions (Fingas, 1991). Observations in an up-sun direction are typically difficult to interpret. Glare due to very low sun angles and sunlight directly overhead can make observations particularly difficult due to poor contrast between the oil sheen and water. After oil spends even a short time floating on the ocean surface, it starts to change its physical characteristics due to various physical, biological, and chemical processes (Schriel, 1987). The false reports obscure knowledge of the actual location and description of the spill. In additional to other factors that make some conventional remote sensing techniques unreliable.

One of these conventional methods was used for tracking oil spill movements by using space shuttle photography, the images was taken in sequentional order in the same time of the oil spill even, The visual interpretation of the four images was based on the shape and the size of the oil spill, and the oil color. The enlargement of the spill with the time indicated the oil dispersant rate and the spill movement direction towards the shoreline. Also the oil type can be identified as a crude oil based on the slick color and shape.

1.1 Space Shuttle Photography

The four Space Shuttle images (from mission STS- 41C) were selected for the Saudi Arabia shoreline. The images were taken consecutively in a short period of time for the different stages of an oil slick. The oil spill appears black in the images; any slick in the image is significantly darker (> 2dB difference) than the surrounding sea surface water. The Space Shuttle photography has the advantage of taking images, with direct human visualization, which is not possible with other satellite techniques (Figure (1) a,b).

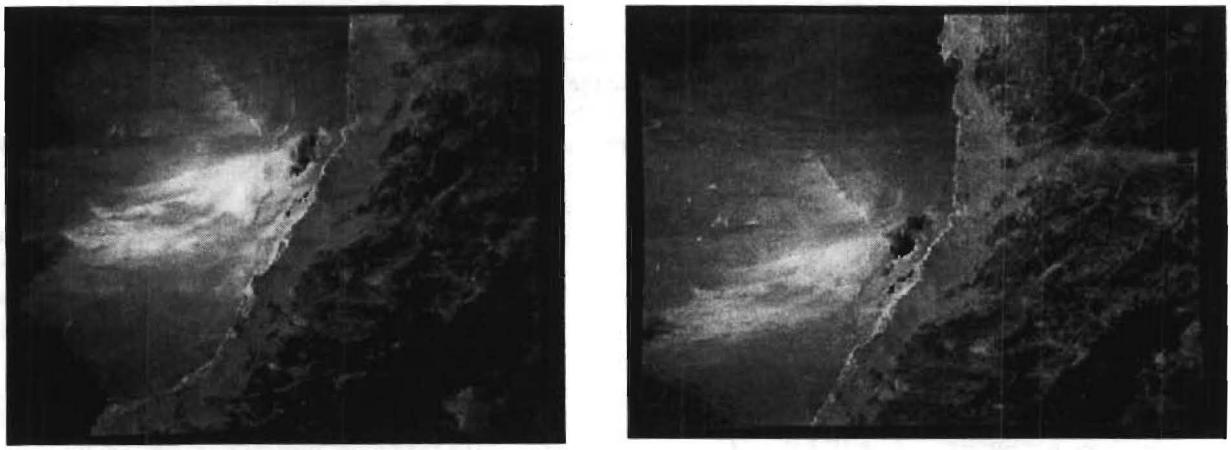

Figure (1) a, b

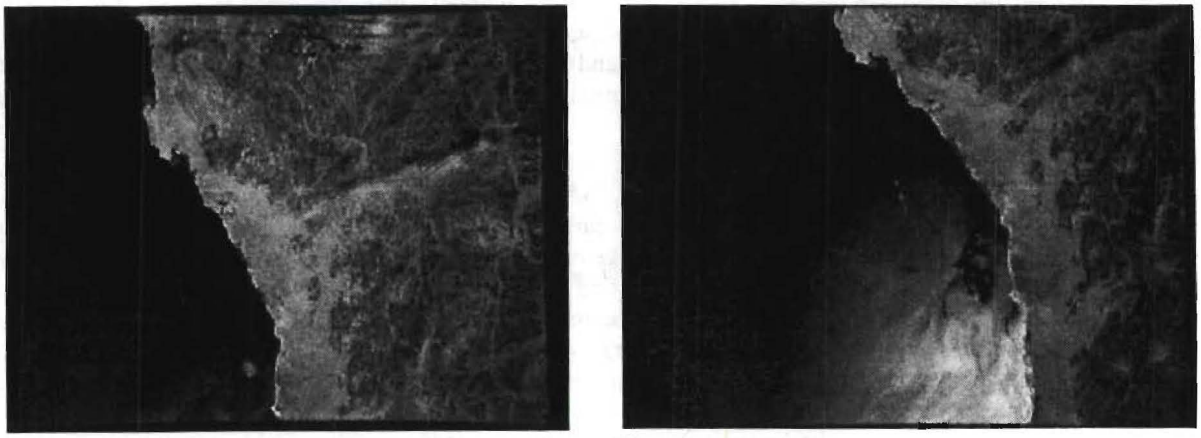

Figure (2) a, b

The four Space Shuttle images (numbers 2340, 2341, 2342, 2343) were taken consecutively of the same oil spill from different angles and locations, show extensive oil slick, in the shallow water surface, close to the shore. The first image shows the initial stage of the spill. The oil slick appeared larger in each image as it is spreading with respect to time. The dark heavy oil spill seems to be sufficiently thick, which can be identified as crude oil, as there was no significant gapes exist in the main slick (Figure (2) a,b).

Winds and current forces pushed three small oil slicks to the shore. The sea wave patterns show that the wave's direction in curved lines paralleled to the shore boundaries and two long oil streaks appear related to wave direction. The upper right line, appears perpendicular on the waves direction, which seams to be traces of a ship track moving away from the spill, the line seems sharper toward the slick direction and thinner as it go further away from the spill location. The wave patterns grow and persist for a long time after a ship passes (Figures 1,2).

1.2 AISA Hyperspectral Sensor

The AISA Airborne Imaging Spectrometer is a push-broom style, hyperspectral system measuring up to 288 bands of continues visible to IR wavelengths. 25 bands were selected for our image processing. The data was derived from the Pipco oil company project for pollution protection for Patuxent River in Maryland (Figure 3). For high spatial and spectral resolution requirements, the Airborne Imaging Spectro-radiometer for Applications (AISA) sensor system gets more information out of each pixel of data -more detail, finer imagery and faster turnaround than from other multi-spectral systems or traditional methods of monitoring. The use of AISA data for identifying spectral signatures for oil spill and oil contaminated areas, can be more successful than traditional methods. Time sequence images of the oil can guide efforts in real-time by providing relative concentrations and accurate locations (Galt, 1994). Environmentally sensitive sites such as wetland can be quickly and accurately mapped, measured, and characterized. AISA can be used to build a spectral library for oil spill on water and land for areas, which contaminated by oil. The Spectral signature can be used for identifying shoreline features specially areas which are environmentally sensitive, and determine the level of oil contamination (heavy or moderate) areas onshore. This can be useful for focusing cleanup processes.

Figure (3) shows an AISA hyperspectral image in Patuxent River for an oil spill due to a petroleum pipeline break, and also the contaminated offshore areas (Maryland April 2000)

1.3 Hyperspectral Data

Hyperspectral sensors such as the Airborne Imaging Spectroradiometer for Applications (AISA) enabled the construction of an effective, continuous reflectance spectrum for every pixel in the scene. These systems can be used to discriminate among earth surface features. Hyperspectral sensors afford the potential for detailed identification of materials and better estimates of their abundance. This can eliminate the false alarms of features, which may be

identified by mistake as a suspected oil spill with other conventional sensors (McFarland et. al.,1993). Hyperspectral sensing can record over 200 selected wavelengths of reflected and emitted energy. With this spectral information one can exploit the spectral signature of oil to detect minute concentrations of hydrocarbon on the sea surface, and also to distinguish between different crude oil concentrations. Applications of the hyperspectral sensing include determination of contaminated soil wetlands, shallow water, sand beaches, and shoreline that enables the identification of features with high spatial and spectral resolution. HSI can provide high quality data for analyzing the complex variability of landscape surface cover in different global environments. However, The application of traditional multispectral data analysis tools to hyperspectral data has not yielded satisfactory results because of mathematical and practical limitations.

2. Methodology

The Hyperspectral images are used to detect oil spill and determine characteristics of the substance spilled, and to make predictions of the spread or mitigation success. The tasks involved are:

1. **Predict oil spill spread direction and flow rate characteristics:** Hyperspectral image analysis for oil spills must be fast and timely for operational environmental monitoring. The airborne HSI temporal image process predicts how oil spills disseminate within a particular body of water, under current environmental conditions, and where it might affect sensitive sites, such as coastal wetlands.

2. **Identify shoreline features and the severity of oil spills:** With its high spectral and spatial resolution, HSI can be used to identify shoreline features, and areas damaged due to spilled oil. Areas impacted are environmentally sensitive, e.g., wetlands with shallow water, sea-grass, salt marshes, tidal-flats, waterways, or sandy beaches with significant biodiversity therein.

3. **Determine the pollutant type**: The oil characteristics (e.g., oil types and concentration) are important to help the cleanup crews identify the best cleanup method, the environmental impacts of burning oil, and the modeling techniques (to predict the flow path, dispersion rates, and time before the slick hits the shoreline) (Jordan and Payne, 1980). For example, an oil type can be crude or light oil and the evaporation rate of the light fuel is faster than crude oil, but it could be more toxic for the marine species (Massin, 1998).

2.1 Spectral Angle Mapper (SAM) Method

The Spectral Angle Mapper (SAM) is a signature matching method is used for identifying oil spills and oil dispersant in water and shoreline. Real time analysis of the images allows field checks in the rapidly changing water conditions due to wind, current and tides. HSI is used to extract specific spectral signatures in order to build a spectral library for different oil types on water, wetland, and vegetation contaminated by oil spills. It can also be used to determine the level of oil contamination onshore (Figure 4). Spectral Angle Mapper (SAM) classification is a physically based spectral classification that uses the N-dimensional angle to match pixels to reference spectra. The algorithm determines the spectral similarity of two spectra by calculating the angle between them. The advanced image processing software, ENVI, is used for image analysis.

2.2 Information Extraction of Hyperspectral Data

The basic approach has been to seek a more fundamental understanding of high dimensional signal spaces in the context of multispectral remote sensing, and then to use this knowledge to extend the methods of conventional multispectral analysis to the hyperspectral domain in an optimal or near optimal fashion. The introduction of hyperspectral sensors that produce much more detailed spectral data than those previously provide much enhanced abilities to extract useful information from the data stream that they produce. In theory, it is possible to discriminate successfully between any specified set of classes of data by increasing the dimensionality of the data far enough. In fact, current hyperspectral data, which may have from a few 10's to several hundreds of bands, essentially make this possible (Landgrebe, 1998). However, it is also the case that this more detailed data requires more sophisticated data analysis procedures if their full potential is to be achieved. Much of what has been learned about the necessary procedures is not particularly intuitive, and indeed, in many cases is counter-intuitive. In this paper, we shall attempt not only to illuminate some of these counter-intuitive aspects, but also to point the direction for practical methods to make optimal analysis procedures possible.

Extracting Oil Spectrum

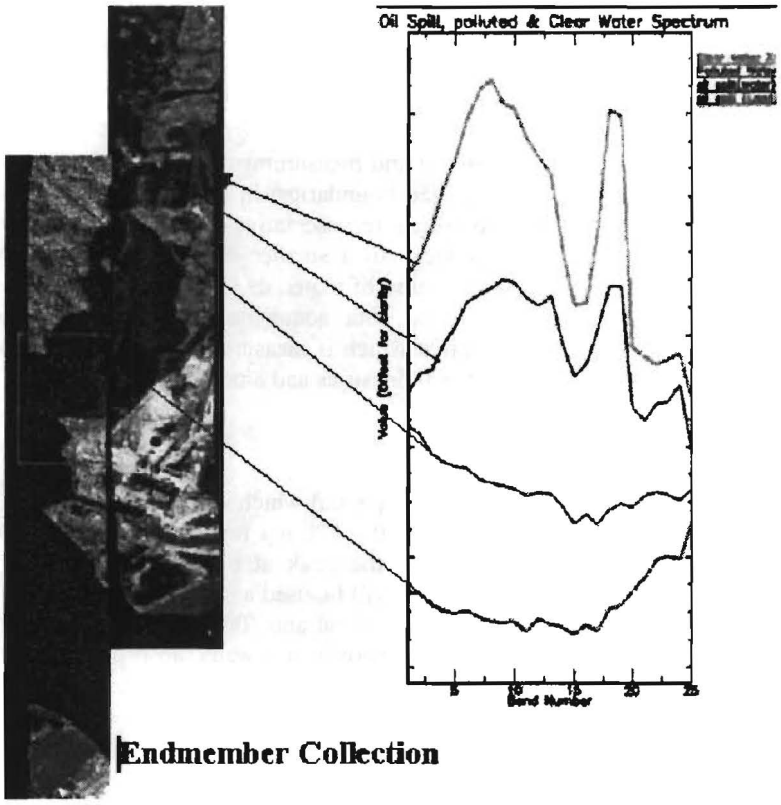

Figure (4) shows the oil on water spectra in red, oil on land spectra in green, polluted water spectra in gray and clear water spectra in cyan. The oil and water spectra extracted from the image create the spectral library; the spectra are used as an endmember collection to train the Spectral Angle Mapper classifier.

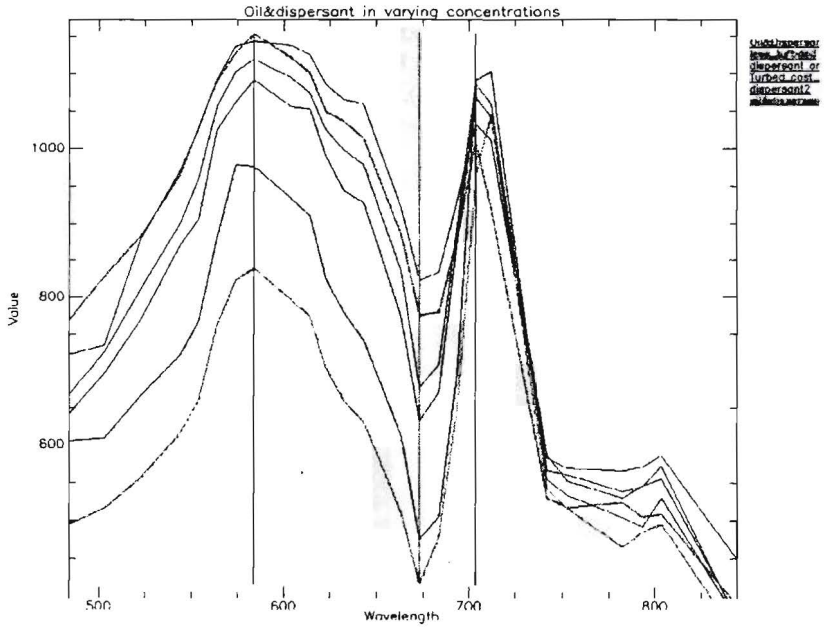

Figure (5) Oil dispersant spectra appeared in red, cyan and green shows that high absorption at 670 nm indicated high oil concentrations compared with the turbid water spectra (appeared in brown, light green, and blue) which shows high reflectance at 580 nm.

As shown in Figure (5) that high oil concentration increases the absorption of light and decrease the reflectance in the visible bands. In the opposite of turbid water have higher reflectance in the visible bands and less absorption in the near IR bands. The water reflectance range is between the two other types.

2.3 Ground Truth

Photography of locations of all zones of sampling and measurement from the air, were used to familiarize the analyst with the materials that exist within the imaged boundaries. In order to successfully identify classes from unsupervised classification results or to create appropriate representative classes (or training sites). Such efforts also allow us to narrow the processing, and analysis focus to a smaller region of the imagery. For extracting the endmembers signatures, the identification and distribution of materials in the field is suggested. In addition, ground truth information that corresponds with the day of data acquisition allows the developing of quantitative relationships between materials on the ground and that which is measured by the remote sensing instrument. These relationships may allow for actual estimates of material densities and amounts.

2.4 Oil Spectra Features Analysis

There are a number of interesting features in the oil spectral which will enable algorithms to be formed for this oil type (Salisbury, 1993). There is a specific peak at 580 – 600 mμ represent the absorption of the dispersant oil, increasing concentration of oil causes a linear dip in the peak at 675-685 mμ (Figure 5). At increasing the concentration of oil on water the dip levels out so that it will be used a good marker for high and low concentration of oil. The dispersant oil give very strong reflectance at 580 mμ and 700 mμ in the visible and near IR . In the blue band there is a reflectance for water at 800 mμ and there is the water absorption at 670 mμ which provides information about the total concentration of oil and water turbidity near shore line.

3. Results

It was demonstrated from our results that by using Spectral Angle Mapper classification technique, the signatures for different concentrations of crude oil and oil dispersant can be matched as long as the sample has high concentration of hydrocarbons as shown in Figure (6) and may not match for light oils such as diesel or gasoline. The model is reliable for distinguishing between different concentrations of crude oil based on the oil spectra for each type of oil spills as shown in Figure (7). Using oil spectra on land allows us to identify the contaminated areas with oil spill on the shoreline (Figure 8). The classified image also indicated that features similar to oil was appeared in areas used for storing coal inside the Maryland Power station, the results confirmed that materials which have the same chemical composition such as coal (carbon), have the same signature as oil (hydrocarbons). Finally, ground truth information (Figure 9) provides the basis for post-processing accuracy assessments.

Figure (6) The class image shows heavy oil slicks appeared in red color on the river and the small streams

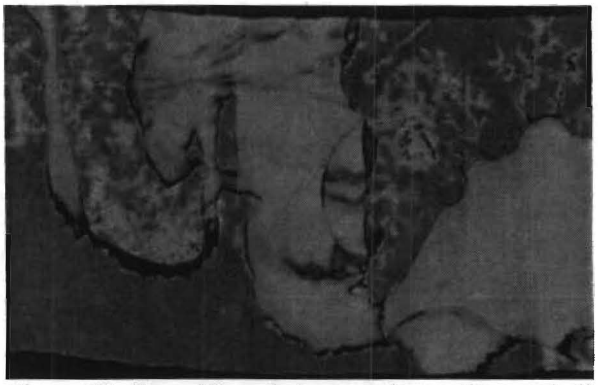

Figure (7) One of the rule images shows dispersed oil and polluted water appeared in black

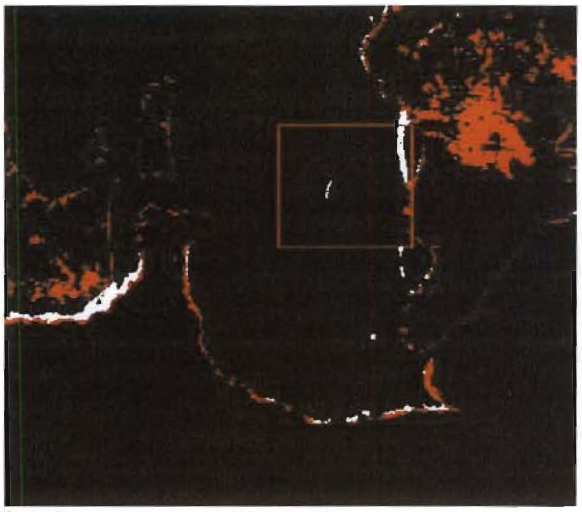

Class Image Figure (8)

Figure (9)

Figure (8) shows two classes, white indicted heavy oil slicks on water, it appear close to the shore outline, and red color represents oil spills on land and on the river edges due to the pipeline break.

Figure (9) shows picture was taken on the same time of oil spill event is used as ground truth for comparing results.

4. Summary and Conclusions

1. Using hyperspectral imagery as an advanced remote sensing technology is more reliable to minimize the limitations of conventional remote sensing techniques for detecting oil spill.
2. The visual interpretation of the space shuttle images shows many limitations such as changing in oil appearance with time, image glare due to sun angle, and other natural phenomena would result in the same appearance as oil spill due to weather difficulties.
3. The results of this research show that the signature matching method is more accurate than the conventional techniques, which base on the visual interpretation of oil color and the appearance in the space shuttle images.
4. HSI spectral information is used to distinguish between different concentrations of oil dispersant for different levels of oil pollution. The signature of oil is used to detect minute concentrations of hydrocarbon (crude oil).
5. For oil spill image analysis, Spectral Angle Mapper classification is more accurate than other supervised classification techniques. When the training samples are selected from the image based on the pixels color, the classification may be misled. Signatures matching technique can distinguish between materials based on its chemical composition not by visual appearance. This allows more confidence in the classification results.
6. Hyperspectral imagery is fast and timely for operational environmental monitoring for oil compared with space-borne systems. The airborne HSI temporal image processes predicts how oil spills disseminate within a particular body of water, under current environmental conditions, and where it might affect sensitive sites, such as coastal wetlands.

5. Future work

1- Accuracy assessment will be applied on the classification results for several techniques, and evaluation for each classification performance will show the accuracy level for each method.

2- The linear un-mixing signature method will be used to identify contaminated coastal features, to distinguish between mixed signatures for different materials such as grass, water, and soil contaminated with oil.

6. References

Darrell, L., Majedi, B., Lizárraga, J., and Blomquist, J. (1996). Nutrient and suspended-sediment concentrations, trends, loads, and yields from the non tidal part of the Susquehanna, Potomac, Patuxent, and Chop tank rivers, 1985-96 By USGS Water-Resources Report 98-4177

Galt, J. A. (1994). Trajectory Analysis for Oil Spills, J.Adv. Mar.T. Conf.11, pp.91-126

Fingas, Merv (1991). The Technology of Oil Spill Remote Sensing, U.S. Coast Guard Oil Spill Remote Sensing Workshop, ERIM Report # 213259.

Jordan, R. and Payne, J.R. (1980). Fate and Weathering of Petroleum Spills in the Marine Environment. Science. P. 1-12.

Landgrebe, D. (1998). Information Extraction Principals and Methods for Multispectral and Hyperspectral Image Data, Information processing for Remote Sensing, World Scientific Publishing Co. Inc., NJ, USA.

Massin, J. (1998). Remote Sensing for the control of Marine Pollution. Plevum. P 237-295.

McFarland, B., Murphy, J. and D. Simecek-Beatty (1993). Conventions for reporting and Displaying over flight Observations, proceedings from the 1993 Oil Spill Conference, (Prevention, Behavior, Control, Cleanup), Tampa, Florida, Mar. 29-Apr. 1, 1993, pp.789-790

Ministry of Transport (1992). Visibility Limits of Oil Discharges: Investigation into the Visibility Limits of Operational Oil Discharges from Ships, Ministry of Transport. Public Works and Water Management, The Netherlands, pp. 43.

Pavia, R. and D. Payton (1983). An Approach to Observing Oil at Sea, Proceedings from the 1983 Oil Spill Conference, (Prevention, Behavior, Control, Cleanup), San Antonio, Texas, Februry.28- Marsh 3, 1983, pp.345-348.

Payne, J. and D. Mcnabb, Jr. (1984). Weathering of Petroleum in the marine environment, Marine technical society journal, and 18(3), pp.24-42.

Salisbury, John W., Dana M. D'Aria, and Floyd F. Sabins, Jr. (1993). Thermal infrared remote sensing of crude oil slicks. Remote Sens Environ. 45:225 231.

Schriel, R. (1987). Operational Air Surveillance and experiences in the Netherlands, Proceedings from the 1987 Oil Spill conference, Tenth Biennial, (Prevention, Behavior, control, Cleanup), Baltimore, Maryland, April 6-9, 1887, pp.129-136.

EFFECTS OF GEO-ATMOSPHERIC PREPROCESSING ON IMAGING SPECTROSCOPY DATA QUALITY AND METHODS

Daniel Schläpfer, Philipp Meier, and Michael Schaepman

Remote Sensing Laboratories (RSL),
Department of Geography, University of Zurich, CH-8057 Zurich, Switzerland
Phone: +41 1 635 52 50, Fax: +41 1 635 68 46, E-mail: dschlapf@geo.unizh.ch

1. INTRODUCTION

Advanced methods of geo-atmospheric preprocessing have become available in the past years and increasingly are applied to AVIRIS airborne imagery. Both, the geometric as well as the atmospheric part of the preprocessing have their specific impact on data quality which should be aware to scientists using such corrected data. An integral geo-atmospheric correction has been developed in a joint effort by the Remote Sensing Laboratories of the University of Zurich and the German Aerospace Agency of Wessling, Germany. It combines the parametric orthorectification program PARGE (Schläpfer et al., 1998) with the atmospheric and topographic correction program ATCOR4 (Richter et al. 2000). The method has been successfully tested on AVIRIS and other airborne imaging spectrometry data such as DAIS, HyMap, and CASI. The method has been described in the abovementioned papers and thus is not further explained herein. In the following, two specific radiometric problems inhere to geometric as well as to atmospheric and topographic correction are explained and potential solutions are depicted.

In the first experiment, the impact of spatial resampling on the spectral accuracy is determined by comparing resampled AVIRIS imagery to its original counterparts. The spectral artefacts appearing while applying resampling technologies during the geometric processing lead to conclusions on how to perform geometric resampling in hyperspectral imagery. The comparison of nearest neighbor resampling to interpolation procedures shows how the spectral and spatial accuracy is affected after applying any of these methods in the parametric geometric correction process.

Second, the impact of radiometric processing on the performance of hyperspectral methods such as spectral angle mapping and spectral unmixing is analysed. The tests are performed on AVIRIS low altitude and high altitude over the Ray Mine area in Arizona, using the geo-atmospheric correction chain PARGE/ATCOR4 (ReSe, 2002). The impact of various processing stages on the recognition of jarosite as well as differences between low and high altitude imagery is investigated.

2. IMPACT OF SPATIAL INTERPOLATION ON SPECTRAL ACCURACY

Whenever geometric corrections are performed, image data are to be resampled to a regular grid before the data are stored in a final geometry. This best kind of resampling has already lead to extensive discussions for the geocoding of multispectral satellite imagery. Cubic resampling has been found to lead to the spatially most accurate results for such data, while having a negative impact on the radiometric integrity (Schowengerdt, 1997). For airborne imaging spectrometry, the paradigm so far was to leave the spectra 'as is' in order to avoid interpolated (artificial) spectra in final data products. The arguments for such nearest-neighbor based interpolation are twofold. First, the spectrometric accuracy and spectral uniformity is higher weighted than the spatial accuracy. Second, the interpolation processing of full image data cubes may be very time consuming if, e.g., cubic convolution would be applied to such data. Using an exemplary set of AVIRIS data it has now been tested how various interpolation methods affect the spatial as well as the spectral accuracy of the data.

2.1 Methods

The tests performed within this analyses are based on real data sets which have been chosen for proper representation of the errors involved with spatial resampling. The spatial analysis is done in a non-quantitative way by visual comparison of results from resampling options within the geocoding process (see below). The radiometric analysis is done by a method as also described in Schläpfer et al. 2001.

Six types of resampling are compared:

- nearest neighbor (direct neighbors of the original pixels in a 'first come first serve' procedure),
- triangulated nearest neighbor (nearest neighbor with respect to a triangulation of the original pixels),
- across track linear interpolation,
- along track linear interpolation,
- bilinear interpolation (strictly bilinear in two explicit directions), and
- triangulation (equals a multilinear interpolation).

Any higher order interpolations such as 'cubic convolution' or 'quintic interpolation' (IDL, RSI Inc.) are not further analysed due to their tremendeous requirements in processing ressources and their high impact on radiometric accuracy. The interpolation methods have been implemented in the parametric geocoding application PARGE.

For the radiometric analysis, four types of masks are used for partial mapping of the data which represent missing individual pixels, missing lines, or groups of missing lines respectively (cf Figure 3). All masked pixels are then replaced by interpolated spectra from the neighboring pixels. Radiometrically equivalent resampling procedures are treated as one (i.e. the two nearest neighbor or the two linear interpolation options). The systematically resampled spectra are then compared to the real spectra at the very same spatial position over masked image areas. The mean relative deviation between the original pixel and the interpolated value is then taken as measure for the error which is related to the interpolation method. For comparison, the maximum relative error is defined as mean deviation of the original spectra under the mask to the average image spectrum. If interpolation results are achieved close to this generic error, the interpolation obviously has failed to create an improved replacement of mis-registered image pixels. The obtained deviations may be interpreted with regard to the resampling of apparent gaps after the geocoding process.

2.2 Tests on AVIRIS data

Effects on Spatial Pattern

The spatial effects are investigated on an exemplary low altitude AVIRIS data set from the Navarro River Watershed, Mendocino County, California collected in July 2000 (provided by UC Davis). The results of various interpolation methods are depicted in Figure 1 and Figure 2. Artefacts are evident if the initial geocoding procedure leads to an undersampled image as given in Figure 1. The gaps between the 'original' pixels need to be interpolated by the best suited resampling procedure. However, in order to take respect to the argument not to change radiometric measurements, the initial spectra at the center pixel positions are forced to remain unchanged. This oversampled situation is often preferred since it keeps the amount of data losses minimal and usually leads to higher spatial accuracy. If the data amount must be kept minimal while preserving most of the original data, the output grid resolution is taken according to the original image resolution (see Figure 2). Hence, only few pixels are missing after geocoding and need to be replaced.

For the undersampled output grid, it is obvious from Figure 1 that all linear interpolation methods fail to properly reconstruct a realistic spatial pattern in the image. Only a triangulated interpolation can solve the issue satisfyingly. The spatial pattern is also kept if nearest neighbour resampling is applied, but the texture suffers from this kind of resampling by introducing non-realistic 'crispy' artefacts. The triangulated nearest neighbor still shows such artefacts although being more accurate by considering triangulated distances between the original pixels. If only few pixels have to be replaced as given in Figure 2, the triangulated interpolation looses its advantage over linear interpolations. A simple and fast linear interpolation can lead to good results, as long as it's done in across-track direction (for this AVIRIS case example).

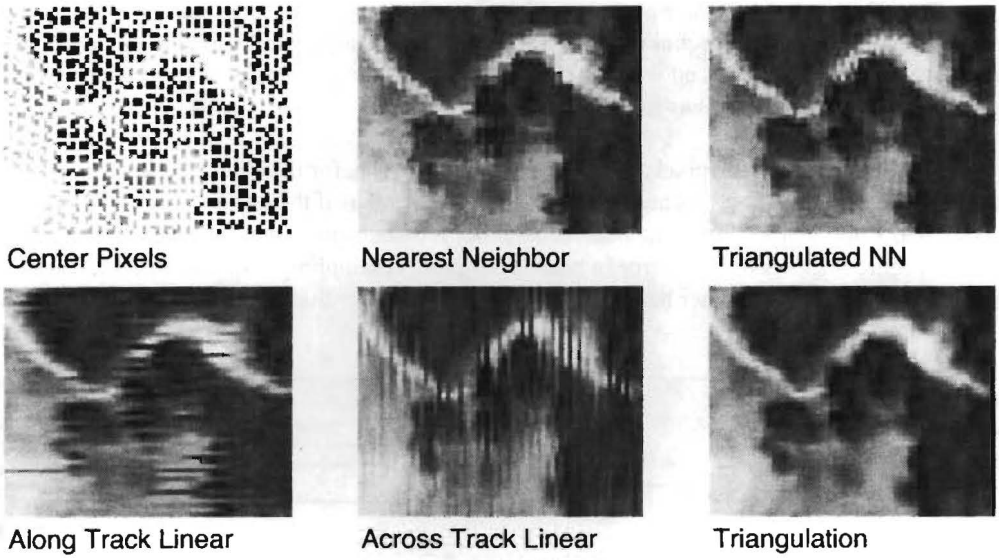

Figure 1: **Spatial effects of resampling methods in an oversampled grid.**

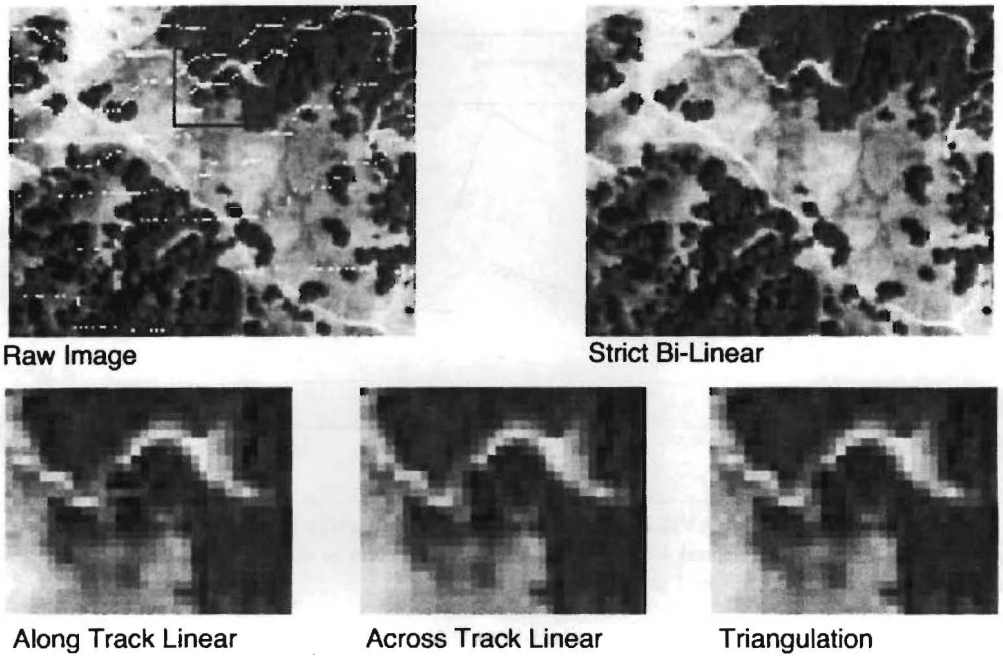

Figure 2: **Spatial effects of interpolation methods in an equally sampled grid (on AVIRIS data).**

Radiometric Effects

The radiometric effects have been investigated with the method as described above. Investigation have been done on a combined AVIRIS low altitude and high altitude data set over the Ray Mine, Arizona, The low altitude data is dating from 10/3/1998 (low altitude) at a nominal ground sampling distance of 3.6 m, while the high altitude dates from 6/5/ 1998, at a ground sampling distance of 20.2 m.

The radiometric errors due to the applied interpolation are between 5 and 20% for the replacement of single pixels and lines, dependent on the wavelength and the interpolation method (see Figure 3). The peak at lowest wavelengths is directly related to the high noise observed in these bands while the second peak at 680 nm is rather related to the

maximal absorption of vegetation at this wavelength. Bilinear and triangulated interpolation both proved to be superior to nearest neighbor replacement techniques by a factor of 2 in average. The triangulation yields best results if only individual pixels have to be replaced while there is no significant improvement in comparison to linear interpolation for the replacement of whole lines as for masks 2 to 4.

If pixels of a distance higher than the pixel size have to be replaced (i.e. for the black pixels of mask4), the interpolation becomes very inaccurate. The errors are almost on the same level as if the average spectrum would have been taken as interpolated value. For all cases, the nearest neighbor replacement is significantly worse than any other interpolation method. Figure 4 shows that the error in nearest neighbor resampling is almost independent on the mask pattern. The triangulation error on the other hand is only significantly lower than the nearest neighbor-error for the

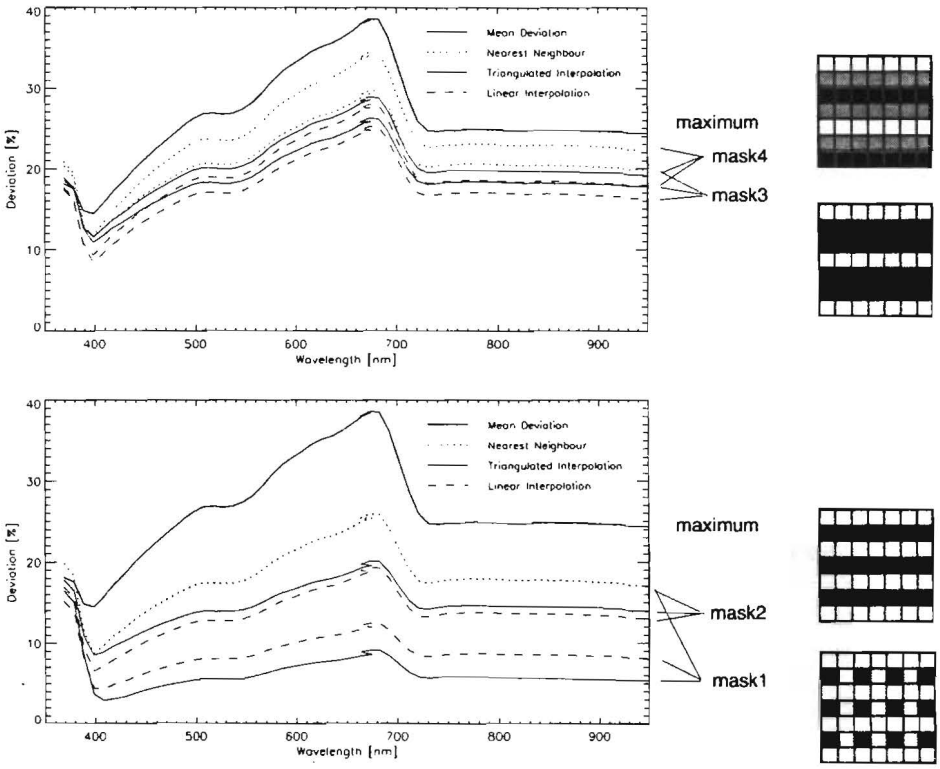

Figure 3: Resampling errors for AVIRIS low altitude data in comparison to the maximum error (most upper curve). The upper graphic refers to masks 3 and 4 while the lower graphic refers to masks 1 and 2. The lower lines per interpolation kind correspond to masks 1 and 3, respectively.

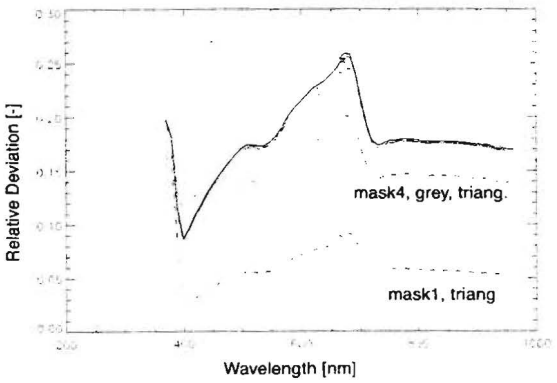

Figure 4: Comparison of triangulation (dashed) and nearest neighbor (solid) resampling for mask1 and mask4. The uppermost dashed line corresponds to the black pixels only of mask 4 while the middle dashed line represents the greyed pixels (masks see Figure 3).

replacement of pixels directly adjacent to the original values. However, the relative advantage of triangulation decreases drastically for pixels 'in the second line' (black pixels of mask4 as of Figure 3).

The analysis is extended to AVIRIS high altitude data where the validation is restricted to a reduced number of masks and methods for the intercomparison to AVIRIS low altitude data. Bilinear interpolation can be skipped due to the mask patterns which only allow for interpolations in y-direction. Only 'mask1' has been used for cross comparison of the results between low and high altitude imagery. Figure 5 shows that the absolute deviations are reduced by about one third in comparison to the low altitude data. Nearest neighbor resampling is still viable although the linear interpolation yields better results for the whole wavelength range. The general lower level of errors while interpolating the high altitude data can be explained by the more homogeneous patterns in the imagery at 20 meters resolution in comparison to 4 meters. The scattered vegetation observed in low altitude data is smoothed out and does no longer lead to discontinuities in the imagery.

In general, the best interpolation method leads to an error level of 3-5% for high altitude data, while for low altitude data the error is in a range of 5-10%. This error levels may be attributed to the expected errors for the replacement of individual AVIRIS pixels at an interpolation of1 pixel distance.

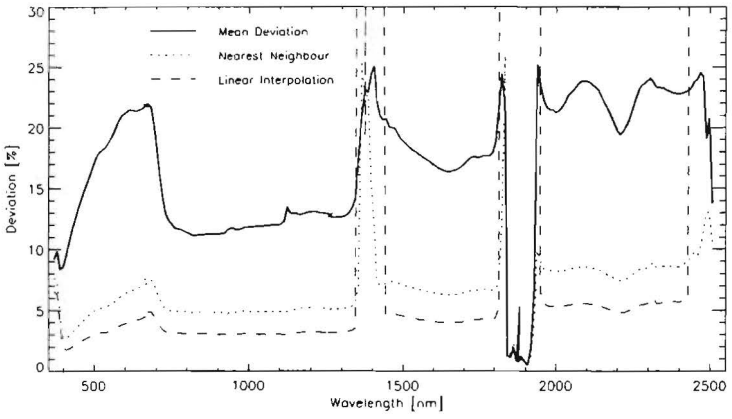

Figure 5: AVIRIS high altitude results for mask2 and the whole wavelength range.

3. IMPACT OF PREPROCESSING ON SPECTRAL ANALYSIS RESULTS

The second part of this paper summarizes effects of the atmospheric/topographic correction on spectral data analysis methods. Standard methods for data processing include the spectral angle mapper (SAM) or spectral unmixing (SUM). All these methods rely on radiometric comparison of reference spectra from any sources (such as standard reflectance libraries) to the images. Theoretically, such comparison can only be done on a physical basis, if the image data itself has been converted to surface reflectance by atmospheric and topographic correction. The ATCOR4 program has been used to perform the correction of the above-mentioned test data set at Ray Mine, Arizona. The effect of the atmopheric correction on the mean spectrum is given in Figure 6. The engaged atmospheric correction program does not apply any 'spectral polishing' leaving the physically derived reflectance data untouched while terrain effects are reduced. Spectral bands with low atmospheric transmittance (i.e. $\tau < 0.3$) have been eliminated from the data set, since atmospheric correction can not fully compensate such strong distortions. A short analysis showed a high distorting impact if such bands are included in spectral processing methods.

The atmospheric correction of the two datasets over the same spatial extent leads to a minimal relative difference of the retrieved spectra. This fact is illustrated by the example scatterplots in Figure 7. The high altitude and the low altitude image are on a disjunctive data space before applying an atmospheric correction. After the atmospheric correction, both images share the same space. The figure also clearly depicts, that the spectral variation in the high altitude is lower than in the low altitude image of the same area. The data range for the low altitude spectra is significantly larger due to the integrating effect of the larger FOV in the high altitude image.

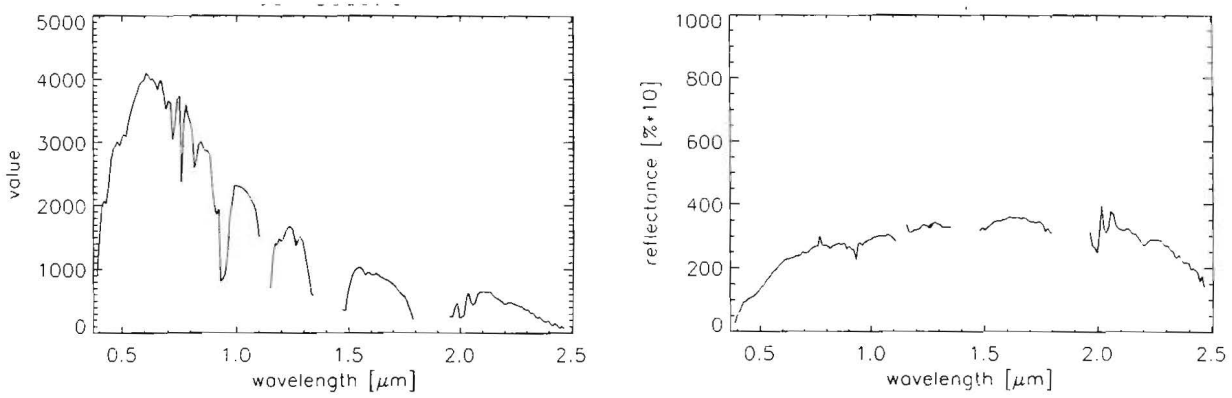

Figure 6: Spectral influence of the atmospheric correction on the mean image spectrum. Left: Calibrated and scaled raw AVIRIS imagery, Right: atmospherically corrected. Strong absorbing bands have been mapped out for spectral analysis.

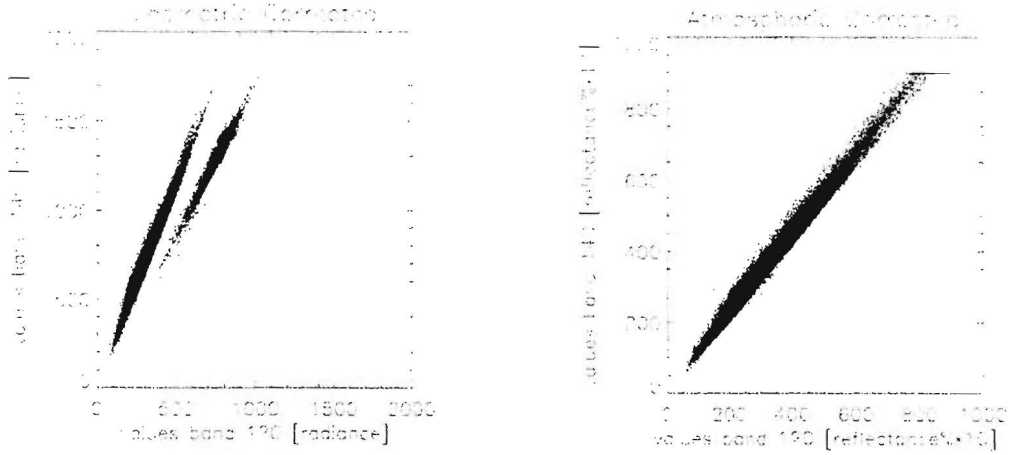

Figure 7: Scatterplot of two exemplary spectral bands of the low altitude imagery (black) and the high altitude imagery (red) before and after atmospheric correction.

3.1 Spectral Angle Mapper

Spectral angle mapping has been performed for the detection of jarosite using three kind of processing status. The number of detected pixels and the mean spectral angles for these situations are given in Table 1. The high sensitivity of the spectral angle mapping procedure can be illustrated by various facts:

- smallest spectral angles are achieved if the library reflectance spectra are compared to the geo-atmospherically corrected reflectance image,
- the uncertainty in radiative modelling leads to slightly larger spectral angles, if the method is done on at-sensor radiance level instead of reflectance, and
- applying reflectance endmembers directly to the calibrated radiance cube leads to useless results showing SAM angles beyond the necessary accuracy.

The comparison of the low altitude image to the high altitude images (see Figure 8) lead to the following results: in the high altitude image, a far larger number of pixels is classified as jarosite pixels than for the low altitude image at a the same constant threshold angle. This is due to the fact that the low altitude image shows larger spectral variations and thus its average spectral angle towards a quite uniform spectrum (as jarosite is) in average are larger. This fact is also underlined by Figure 7, which shows the higher spectral variability in the low altitude image. The case is inverse for SAM on radiance images. The less accurate (or even wrong) radiometry for those cases leads to a higher number of pixels detected in the low alittude image due to its higher variation. The spatial analyses of these results shows that the detected pixels rather depict arbitrary jarosite signals than a consistent mineralogical product.

Table 1: Differences in number of classified pixels and Spectral Angle between various processing stages and between low altitude and high altitude AVIRIS imagery over the same area. The 'mean' angle is calculated within the detected area in relation to the atmospherically corrected low or high altitude image.

jarosite spectrum	low altitude image match to jarosite [SAM angle, rad] within threshold area	high altitude image match to jarosite [SAM angle, rad] within threshold area
reflectance endmember on atmospheric corrected reflectance image	*threshold=0.09:* mean = 0.089; #pixels: 37 *threshold=0.10:* mean = 0.096; #pixels: 4 649	*threshold=0.09:* mean = 0.082. #pixels: 25 959 *threshold=0.10:* mean = 0.087; #pixels: 88 228
reflectance endmember on geometric correcte calibrated radiance image	*threshold=0.74:* mean = 0.222; #pixels: 2 955 *threshold=0.80:* mean = 0.190; #pixels: 14 229	*threshold=0.74:* no values detected *threshold=0.80:* mean = 0.176; #pixels: 3 296
simulated radiance endmember on geometric correcte calibrated radiance image (indirect)	*threshold=0.10:* mean = 0.138; #pixels: 643 *threshold=0.13:* mean = 0.122; #pixels: 36 677	*threshold=0.10:* no values detected *threshold=0.13:* mean = 0.089; #pixels: 495

3.2 Spectral Unmixing

The robustness of the linear spectral unmixing approach has been tested on the atmospherically corrected image. The selected concurrent endmember minerals to jarosite are kaolinite, hematite, and goethite. The latter represents a dark mineral with flat spectral characteristics (a suited spectrum instead of a 'shadow' endmember). Figure 8 shows a larger area detected in the high altitude images than in the low altitude image under the same prerequisites for both SAM and SUM classification. While for the SAM classification the detected area grows vastly, the detected are in the SUM are growin moderately but are almost disjunctive between the low altitude and the high altitude image. The effect of spatial resolution is stronger in the spectral angle mapper than in spectral unmixing. The concurrent endmembers in the SUM limit the difference due to resolution changes whereas the SAM only displays relative differences between one endmember and the real spectrum.

Discrepancies between low and high altitude images are also found to origin in the time delay between the two images, being about 4 months. During this time period, the surface has changed significantly in this active mining district. The dust roads (e.g.) are almost completely differently mapped by the two methods. This is assumed to be a temporal change detected in that area which is obvious in the true color images of the critical area. Anyhow, the differences between SUM and SAM unmixing are significant and still are not completely understood.

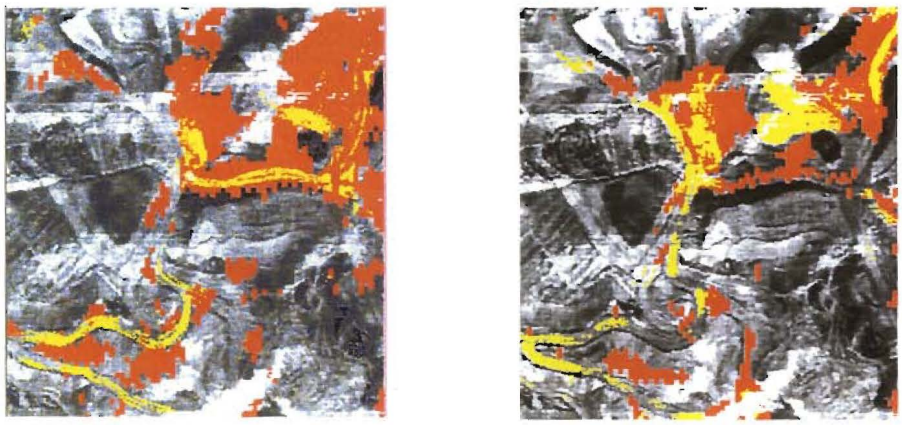

Figure 8: Differences in detected jarosite pixels using the spectral angle mapper (left) and the linear spectral unmixing (right) on low altitude imagery (yellow) and high altitude imagery (red).

4. CONCLUSIONS

The described experiments give an order of magnitude for the expected errors if interpolations need to be done in spectral processing and if the 'same' spectral analysis is done on various kind and processing status of spectral data. The results point towards important issues to be considered in data preprocessing. The radiometric analysis of spatial interpolation processes questions an often-heard paradigma in imaging spectroscopy that no 'artificial' spectra shall be produced by using interpolations. A significant higher error in the spectra derived by nearest neighbour resampling is observable in comparison to other interpolation methods. Thus, linear interpolations can be recommended for the replacement of individual pixels or missing lines. Furthermore, it has been shown that the replacement of pixels outside the reach of the pixel PSF is very questionable and should be avoided wherever possible. The choice of interpolation method depends on the target grid resolution. For undersampled grids, triangulated interpolation leads to superior results, while for regularly sampled grids the more efficient linear interpolations are sufficient.

The short analysis of spectral unmixing and spectral angle mapper methods for the detection of jarosite in an open pit mine showed, how heavily radiometric effects can influence the results of spectroscopic analysis. It is indicated that the preprocessing status as well as the spatial resolution of the image have a significant impact on the discernability of abundant minerals in geological imaging spectroscopy. The mineral detection can completely be distorted, if no attention is paid towards processing status and quality of the input data. Stability of both, spectral unmixing and spectral angle mapping proved to be critical towards atmospheric preprocessing, number of spectral bands, as well as spatial resolution. These issues may be solved by careful tuning of the spectral analysis methods using absolute reflectance data corrected to hemispherical reflectance units (including approximate corrections for BRDF effects).

The values have been derived from exemplary real imaging spectrometer data and thus are only of limited generic validity. Anyhow, the results of this analysis will be used to improve the capabilities of current geo-atmospheric processing systems such as PARGE and ATCOR4. On the geometric side, flexible options for interpolation of imaging spectrometry data in the processing chain need to be provided to the data users. On the radiometric side, the importance of highest accuracy atmospheric and topographic corrections for consistent results in imaging spectroscopy applications once more has been illustrated.

5. ACKNOWLEDGEMENTS

Part of this work has been supported by the ESA/ESTEC contract 14906/00/NL/DC. NASA/JPL and the AVIRIS team is thanked for providing the AVIRIS 1998 data and Carlos Ramirez of the UC Davis is thanked for providing some of the more recent AVIRIS data examples.

6. REFERENCES

ReSe, 2002: PARGE v1.3.4, ATCOR4 v2.1, distributed by ReSe Applications Schläpfer, software available from http://www.rese.ch.

Richter R., 1997: Correction of atmospheric and topographic effects for high spatial resolution satellite imagery. *Int. J. Rem. Sens.*, 18(13):1099-1111.

Richter, R., 2000: *Atmospheric / Topographic Correction for Wide FOV Airborne Imagery: Model ATCOR4*. DLR Internal Report, DLR-IB 552-05/00, Wessling, Germany, pp. 62.

Schläpfer D., Schaepman M., and Itten K.I., 1998: PARGE: Parametric Geocoding Based on GCP-Calibrated Auxiliary Data. Descour, M.R. and Shen, S.S. (Eds.), *Imaging Spectrometry IV*, SPIE, San Diego, Vol. 3438:334-344.

Schläpfer D., Schaepman M., and Strobl P., 2001: Impact of Spatial Resampling Methods on the Radiometric Accuracy of Airborne Imaging Spectrometer Data. 5th Int. Airb. R. S. Conf. and Exh., VERIDIAN, San Francisco / Miami, CD-ROM, pp.8.

Schowengerdt R.A., 1997: *Remote Sensing: Models and Methods for Image Processing*. Academic Press, 2nd Ed., pp. 522.

COUPLING HYPERSPECTRAL REMOTE SENSING WITH FIELDSPECTROMETER TO MONITOR INLAND WATER QUALITY PARAMETERS

Naseer A. Shafique,[1] Florence Fulk[2] and Susan M. Cormier,[2] Bradley C. Autrey[1]

INTRODUCTION

Stream ecosystems around the world are being impacted by eutrophication. Eutrophication is the state of having high nutrient content and high organic production (Wetzel, 1995). It diminishes water quality by promoting the excessive growth of algae, cyanobacteria (blue-green algae) and macrophytes. Environmental researchers have been making efforts to monitor, simulate and control eutrophication for more than two decades. Various mathematical models have been developed and applied to rivers, lakes and estuaries (Lung, 1986; Thomann and Mueller, 1987; Kuo and Wu, 1991; Kuo et al., 1994). Most water quality models simulate increases in eutrophication based on initial conditions of the water body, therefore, demanding comprehensive water quality sampling programs. However, the conventional measurement of water quality requires in situ sampling and expensive and time-consuming laboratory work. Due to these limitations, the sample size often cannot be large enough to cover the entire water body. Therefore, the difficulty of synoptic and successive water quality sampling becomes a barrier to water quality monitoring and forecasting.

Remote sensing could overcome these constraints by providing an alternative means of water quality monitoring over a range of temporal and spatial scales. A number of studies have shown that applications of remote sensing can meet the demand for the large sample sizes required of water quality studies conducted on the watershed scale. Imagery from satellite and aircraft remote sensing systems have been used in the assessment of water quality parameters such as temperature, chlorophyll *a*, turbidity, and total suspended solids (TSS) for lakes and reservoirs (Lillesand et al., 1983; Lathrop and Lillesand, 1989; Ritchie and Cooper, 1991), estuaries (Verdin, 1985; Harding et al., 1995) and tropical coastal areas (Ruiz-Azuara, 1995).

Previous studies have focused on the discovery of the relationship between remote sensing data and in-situ measurements. To make remote sensing tools useful for practical applications, water quality modeling must be incorporated with water quality monitoring programs. Moreover, integrating a geographic information system (GIS) allows for the display of refined monitoring simulation results, rather than the use of traditional numerical figures. This provides a means by which water quality modeling data can be presented in a way that is practical for water quality management. The specific objectives of this study were to: 1) establish a model to process remote sensing data and provide a rapid and efficient water quality monitoring technique for a wide area, 2) present predicted water quality conditions temporally and spatially on a georeferenced map and 3) display sequential (temporal) images of water quality predictions to provide decision makers with easily understandable information.

Study Area

The study site is located in southwest Ohio and includes the Great Miami River (a tributary of the Ohio river), as well as adjacent water bodies, including fishponds, reservoirs and other rivers that are tributaries of the Ohio River.

The Great Miami River is situated in the Miami basin, which encompasses the drainage basins of both the Little and Great Miami Rivers (Figures 1 and 2). The Miami basin includes most of southwestern Ohio and portions of Indiana. The major waterways are the Great Miami River (including the tributaries, the Stillwater and Mad Rivers), the Little Miami River, and Whitewater River in Indiana.

Landforms in the Great Miami River Watershed have been shaped by glaciations, which left flat-to-gently-rolling terrain, glacial till, and in some areas, exposed limestone and shale. Soils in the watershed tend to be neutral-to-slightly alkaline and drainage varies from well drained to very poorly drained, depending on parent material and topography. The river lies within a broad valley with a wide flood plain (Ohio EPA, 1997). The area drained by the

[1] SoBran Environmental Inc: Shafique.Naseer@epa.gov
[2] US Environmental Protection Agency: Fulk.Florence@epa.gov

major waterways includes both agricultural and urban lands (Ohio EPA, 1997). The Miami basin includes the major cities of Cincinnati and Dayton, Ohio, and the smaller cities of Hamilton and Middletown, Ohio along the Great Miami River. Currently, it is estimated that 70% of the total land area is used for agriculture, dominated by row crops of corn and soybeans. Urban areas occupy 13% of the land, forested areas occupying 7%, and wetlands and water bodies occupy 1% of the total land area in the Miami basin (USGS, unpublished report).

The Ohio Environmental Protection Agency (Ohio EPA) noted that most industries and municipalities near the Great Miami River utilize groundwater as a principal water source but discharge treated wastewater to the river. Surface run off from agricultural or urban areas and industries along the river is not treated or impeded prior to entering the river (Ohio EPA, 1997).

Both the U.S. Environmental Protection Agency (USEPA) and the U.S. Geological Survey (USGS) have identified six important water quality issues in the Miami basin. These include: 1) the degradation of surface-and ground-water quality by urban and agricultural sources of fertilizer and pesticides, 2) assessing the relative importance of point and non-point sources to contaminant loads in the Great and Little Miami River basins, 3) habitat degradation and decreases in stream biodiversity as a result of urbanization, 4) the occurrence of water-borne pathogens in streams and shallow ground water in rural and urban land-use settings, 5) the effect of septic systems and combined sewer overflows on surface and shallow ground-water quality, and 6) the disruption and fragmentation of stream habitats by low dams and impoundments and their effects on fish and benthic invertebrate communities (Ohio EPA, 1997).

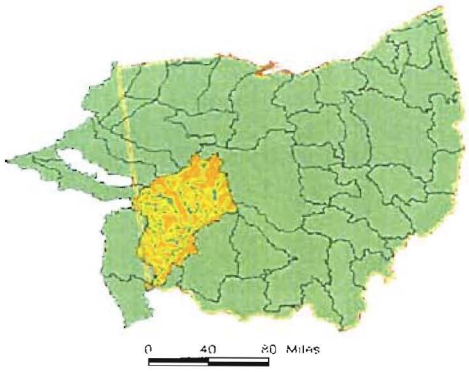

Figure 1: Location map.

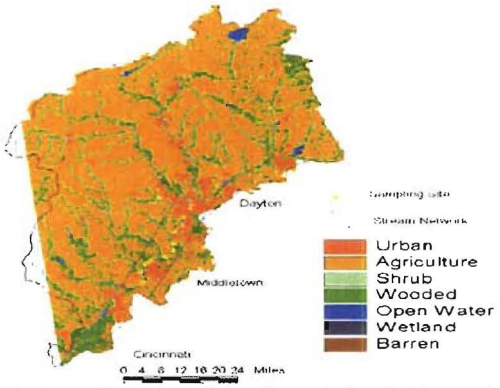

Figure 2: Sampling site of the Great Miami River within the Miami River basin.

The presence of these environmental concerns in the Miami basin and the availability of ancillary data in the offices of the USEPA, OEPA, Ohio Department of Natural Resources (ODNR), Natural Resources Conservation Commission (NRCS) and USGS make the Miami basin an appropriate pilot study site for this type of research. A map of the study locations within the Miami basin is shown in Figure 2.

DATA

Ground truth (reference) and spectral data were collected from 26 January 1999 to 30 September 1999. The data can be roughly divided into two sets, preliminary and pilot, based on the date and location from which the data were collected and the amount of data collected. The preliminary data sets were collected from 26 January 1999 to 12 April 1999 and the pilot data sets were collected from 14 May 1999 to 30 September 1999. In addition, all pilot data were collected from the Great Miami River between river miles (RM) 45 and 92, where remote sensing imagery was acquired in the latter part of the study period. The purpose of the preliminary data was to examine the response of the Full Range Field Spectroradiometer (FieldSpec FR, Range 350-2,500 nm) to different water quality conditions found in the various water bodies. Generally, the preliminary spectral reading was accompanied by turbidity measurements using a field turbidimeter. In addition, in-vivo chlorophyll measurements were made on two additional dates. The other major data set for this project includes two sets of hyperspectral imagery. The airborne sensor that acquired the imagery was the Compact Airborne Spectrometer Imager (CASI), taken on 8 and 9 September 1999. The CASI acquired imagery in 19 spectral bands and the HyMap acquired imagery in 126 spectral bands.

Spectral Data Collection

Two types of spectral data were collected during the study period: above water reflectance spectra and underwater radiance or irradiance spectra. The reflectance data represent the ratio of reflected energy to incident energy with values ranging from 0.0 to 1.0. The irradiance data represent actual energy received by the sensor as downwelling (irradiance) or upwelling (radiance) in units of power per unit area per unit wavelength ($W/m^2/sr/nm$). The above water reflectance data were collected using the FieldSpec FR instrument from Analytical Spectra Devices (ASD), Inc., 1999. The underwater radiance spectra were collected using two methods. The first method used the FieldSpec FR instrument fitted with an underwater extension cord and an Underwater Remote Cosine Receptor (UWRCR). The second method used a Li-Cor brand light meter (LI-189) with an underwater sensor (LI-1000). While the FieldSpec FR samples energy (reflected or radiant) at 1-nm intervals, the Li-Cor measured an aggregate energy in the visible range between 400 and 700 nm. Due to the amount of time it takes to assemble and disassemble the underwater extension to the FieldSpec FR, the underwater extension was used only during the first day of the CASI flyover. Thus, the instrument of choice for most underwater light measurement was the Li-Cor meter. An apparatus was constructed to position the sensors at the desired depth, pointing upward to measure downwelling irradiance and downward to measure upwelling radiance).

Imagery

On 8 and 9 September 1999, Hyperspectral Data International (HDI) flew the CASI sensor over the Great Miami River from approximately RM 45 to approximately RM 92. This sensor acquired data in 19 spectral bands with a spatial resolution of 2 m. Twenty three flightlines covered approximately 80 km (49.7 miles) of the Great Miami River, from Middletown, Ohio to the Taylorsville Dam, approximately 15 km (9.3 miles) north of Dayton, Ohio. The imagery was delivered on 36 compact discs (CDs) in a band sequential (BSQ) file format that was imported with the Environment for Visualizing Images (ENVI) processing software. Some of the flight lines were split into several segments for the purpose of pre-processing (Hyperspectral Data International, 2000). Data obtained with the hand-held spectroradiometer were analyzed, revealing seven spectral bands that demonstrated usefulness for water quality studies. These include, bands 2 (440 nm), 7 (625 nm), 11 (672 nm), 14 (705 nm), 16 (740 nm), 17 (816 nm) and 18 (840 nm). These are the minimum number of bands that could be used to develop preliminary water quality maps.

METHODS

Criteria of Band Selection

Absorption

Through the components of light absorption and scattering coefficients, the water body controls the ratio between light scattering and absorption values, and thus determines the subsurface reflectance and in turn the emergent flux that will be sensed by radiometers (Jupp et al., 1994). Because the medium composition affects the absorption and scattering coefficients differently at various wavelengths, the resulting spectral distribution can be mathematically modeled and/or measured by a spectroradiometer from above and under the water's surface, and thus can be used to provide information about the water body.

Both field and laboratory spectrometric measurements of reflectance and absorbance are essential to developing semi-empirical and analytical (radiative transfer) models that can describe the interactions of light and in-water materials (Dekker, 1997). Field spectrometry is the quantitative measurement of radiance, irradiance, reflectance or transmission of light in the field. There are many reasons why it is desirable to perform spectral measurement in the field. Field spectra of ground and water targets that are homogeneous at the scale of the imaging sensor and collected using ambient solar illumination can be used to convert radiance images to reflectance (Conel et al., 1987a,b). Often, field spectra of target materials are collected to allow for more precise image analysis and interpretation (Goetz and Srivastava, 1985). Hand-held spectroscopy is also used as a tool to perform feasibility studies to understand if and how a process or material of interest can be detected using remote sensing. Field spectra of both the material(s) of interest and spectra of other materials present in the environment can be used to address such issues as what spatial and spectral resolutions are required for detection. Lab spectroscopy measurements are also desirable because they are used for the determination of the inherent optical properties of water by measuring the absorption and scattering spectra of dissolved materials and particulate matter.

Correlation

The correlation between temporally pooled groundtruth and spectral data was used to locate spectral signatures for water quality parameters. Replicate groundtruth data at a sampling point were averaged before conducting the correlation. Thus, when available, a data point represented the mean of three replicates. There were two spectral samples, taken a few seconds apart, for each sampling point. These values were averaged before calculating the correlation with the groundtruth data. A statistical summary of all groundtruth data was first computed using descriptive statistical parameters (e.g., mean, maximum value, minimum value). This allowed the data sets to be examined for the detection of the extreme outliers.

One of the tools used to quantify the relationship between the spectral data and the groundtruth data was a correlation matrix. Scatter plots of groundtruth data against spectral data and of groundtruth parameters of interest against each other were made to investigate relationship trends that may not be captured by correlation values. Depending on the magnitude of the correlation values and the trend in the scatter plots, linear and non-linear equations were developed to predict water quality parameters from spectral indices.

First Derivative

Spectroscopic derivatives are tools that can be used in spectroscopy (Philpot, 1991). They are obtained by taking the difference between the reflectance of two bands and dividing that value by the difference between the wavelengths separating the two bands. Then, a correlation test is performed between derivative reflectance and the field measurement of turbidity. When the two bands used in the calculation are adjacent to one another, the result is the first derivative. It is assumed that the components of variation are additive constants acting in a spectrally independent way over a spectral range of a few nanometers (nm). This assumption fits well with knowledge of the behavior of radiation and reflectance in the atmosphere and water, moreover it is much less demanding than the assumption made for the use of broad waveband indices. The mathematical basis of derivative spectroscopy has been reviewed (Dixit and Ram, 1985) and applied to the remote sensing of vegetation (Curran, 1989; Demetriades-Shah et al., 1990; Curran et al., 1991).

The use of derivative spectroscopy for estimating turbidity and suspended particles is not frequently reported in the literature, however its potential can be inferred from previous studies (Dick and Miller, 1991; Philpot, 1991) and demonstrated using three laboratory spectra (Chen et al., 1991). The derivative reflectance spectra vary in a regular way with turbidity. Three regions of the spectrum at wavelengths near 450-550 nm, 675-750 nm and 800-1000 nm show particularly large changes in derivative reflectance with turbidity and these are, therefore, candidate spectral regions for the estimation of turbidity with derivative spectroscopy.

RESULTS AND DISCUSSION

The evaluation of band selection criteria leads to the selection of certain channels from the whole dataset for various water quality parameters. The bands integral to the most significant parameters, chlorophyll *a* and turbidity, are discussed below.

Chlorophyll a

Chlorophyll *a* is a phytopigment present in all algae groups in inland waters and shows distinct absorption bands in the blue wavelength range at 440 nm and in the red wavelength range from 672-678 nm (Figure 3), leaving a maximum green reflectance due to an internal cell scattering process. The red edge ascent near 705 nm that is narrowed to a peak by growing water absorption in the infrared is also correlated to increasing chlorophyll *a* contents (Figure 4).

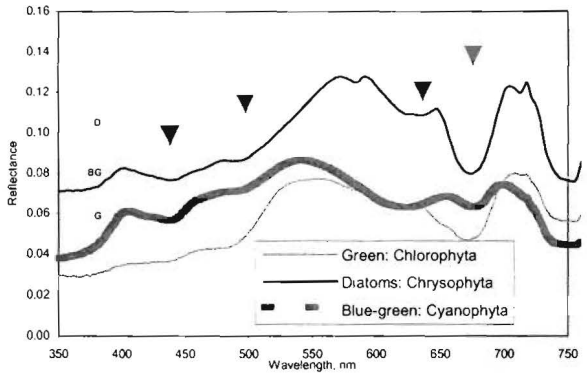

Figure 3: Absorption maxima and minima in reflectance spectra of pure algal culture.

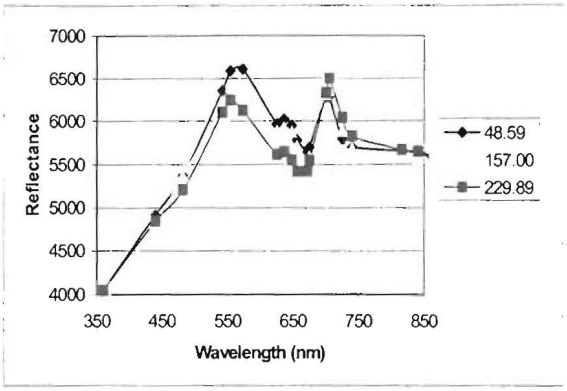

Figure 4: Reflectance spectra for known chlorophyll *a* values from CASI data.

Based on the correlation with the ground truth data, one of the most important relationships observed in this study was the relationship between turbidity, TSS, and chlorophyll. Turbidity was positively correlated with TSS ($r = 0.76$) and less positively correlated with chlorophyll ($r = 0.37$). Turbidity was negatively correlated with Secchi disk depth ($r = -0.55$), river depth ($r = -0.19$), and pH ($r = -0.64$). TSS was moderately correlated with chlorophyll parameters (up to $r = 0.51$). Of the chlorophyll parameters, turbidity and TSS generally appear to correlate better with a chlorophyll parameter that combines chlorophyll *a* and pheophytin data. Dissolved oxygen showed a low positive correlation ($r = 0$ to 0.49) with most parameters, but with a relatively stronger value with chlorophyll variables ($r = 0.44$), asserting that more living algal activity enriches the water with DO through the process of photosynthesis.

The two most significant bands, 672 nm and 705 nm, were selected for the calibration of chlorophyll *a* concentration. The ratio of 672 and 705 nm wave bands produced a good correlation ($r = 0.86$) with the chlorophyll *a* concentration (Figure 5). Using this linear model, a chlorophyll-a distribution map of the river was made (Figure 6). It is interesting to see that a plume of relatively clean water (lower chlorophyll-a concentration) is entering the river from the wastewater treatment plant.

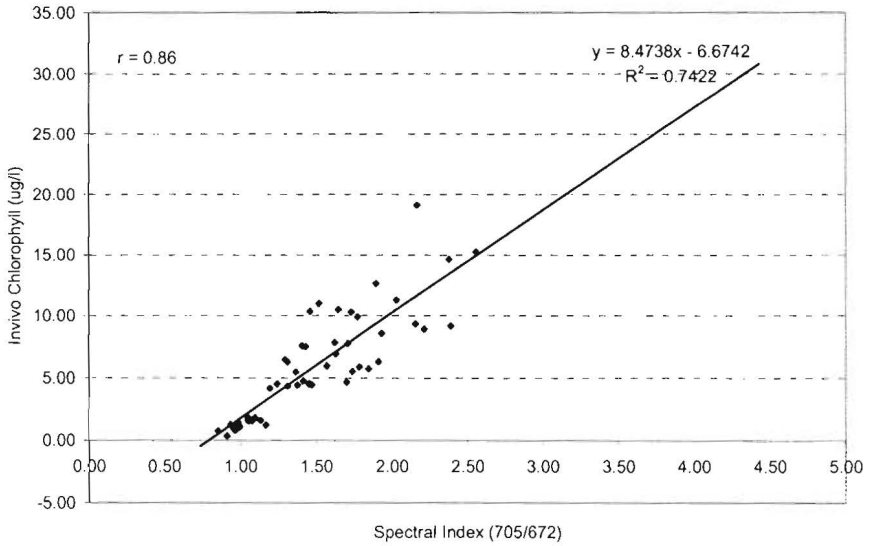

Figure 5: Correlation between spectral index and chlorophyll concentration obtained from the ground truth data.

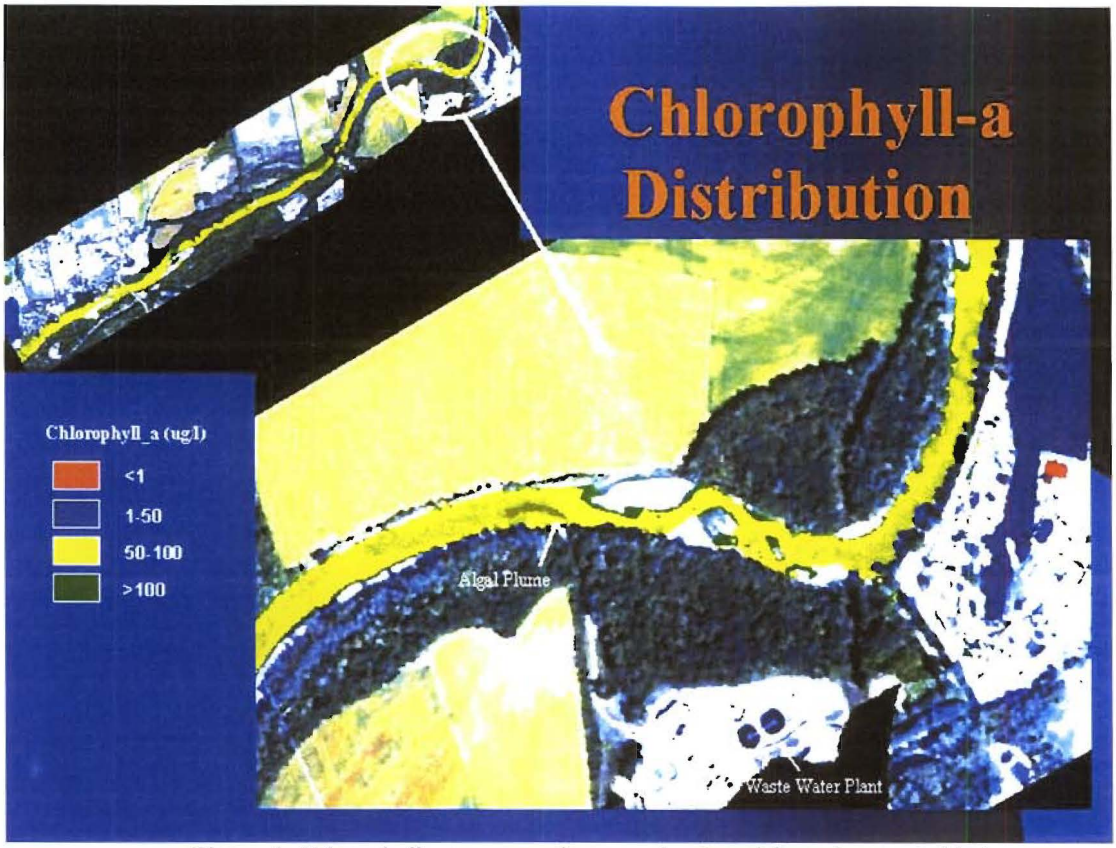

Figure 6: Chlorophyll *a* concentration map developed from the spectral index.

Turbidity

To examine the association between spectral reflectance and turbidity, correlation analyses were applied to the Fieldspec FR channels between 400 and 880 nm. A strong relationship existed between turbidity and reflectance with r = 0.8 at (625-440)*705/672. However, this relationship resulted in much higher predicted values of turbidity in the river than the turbidity values that were actually collected on the ground. In an effort to improve results, first derivatives were calculated by dividing the difference between successive reflectivity values by the wavelength interval separating them. A correlogram for turbidity was developed using the first derivative and normal reflectance at a particular wavelength. Figure 7 illustrates the difference between the correlation coefficients from the raw reflectance data and the first derivative method.

The maximum correlation, r = 0.76 was found at the derivative of (700-675)/25 nm (Figure 7). Therefore, the bands at this wavelength were selected for the turbidity measurement.
The first derivative reflectance and turbidity scatter plot (Figure 8) fits with a linear model:

$$\text{Turbidity} = 1224.4^{*} (R(685)) + 3.9561 \qquad \text{with } R^2 = 0.7917$$

Using this linear model, a turbidity map of the river was made (Figure 9). This model showed a strong agreement between observed and estimated turbidity values (Figure 10).

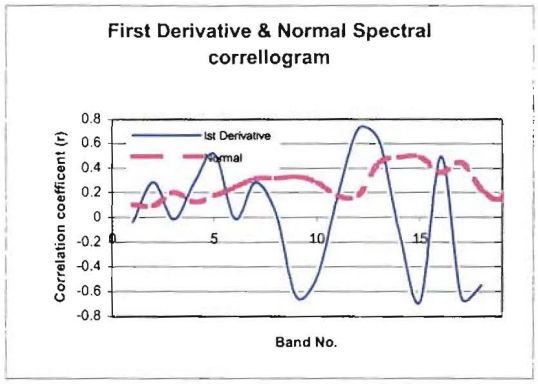

Figure 7: Comparison of first derivative and normal correlogram, higher correlation obtained from the first derivative.

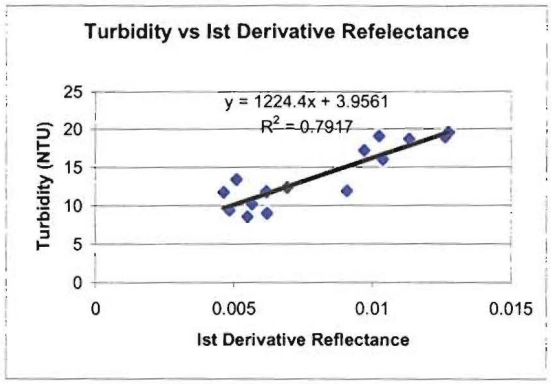

Figure 8: Correlation between first derivative reflectance and turbidity obtained from the field spectrometer data.

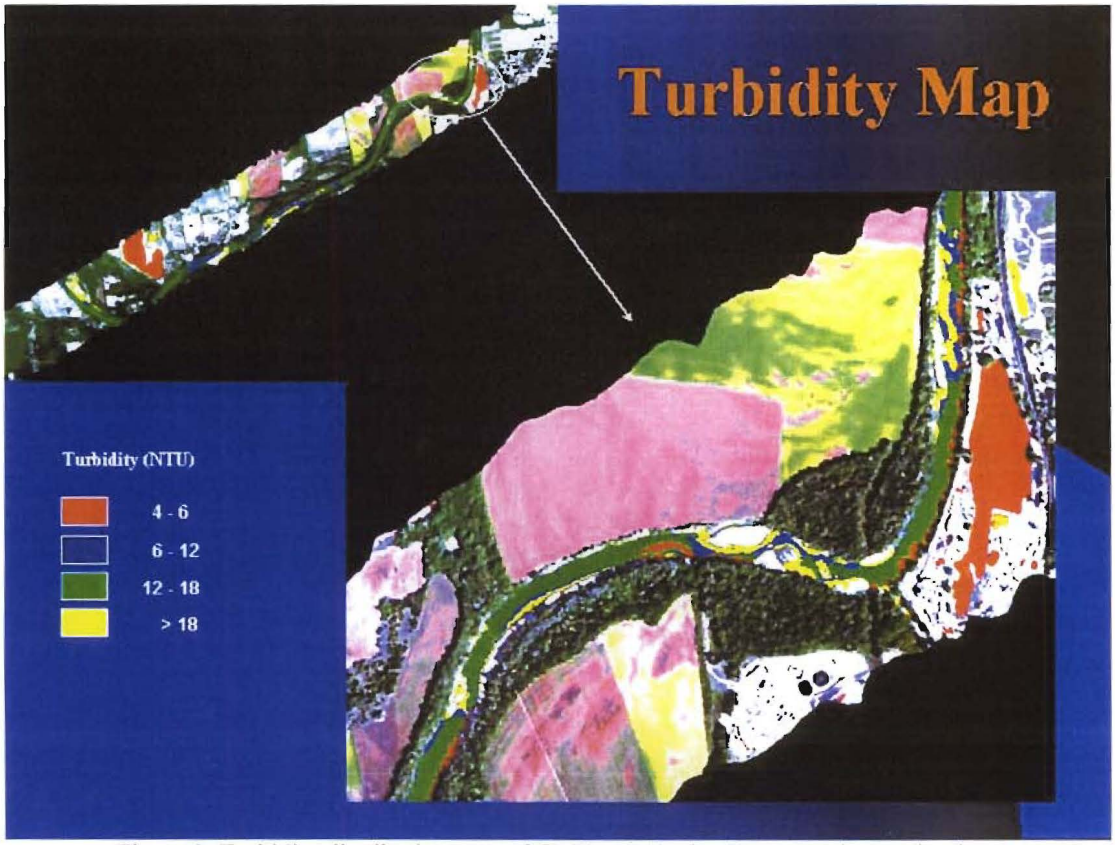

Figure 9: Turbidity distribution map of GMR, relatively clear water is entering into the river from the wastewater treatment plant.

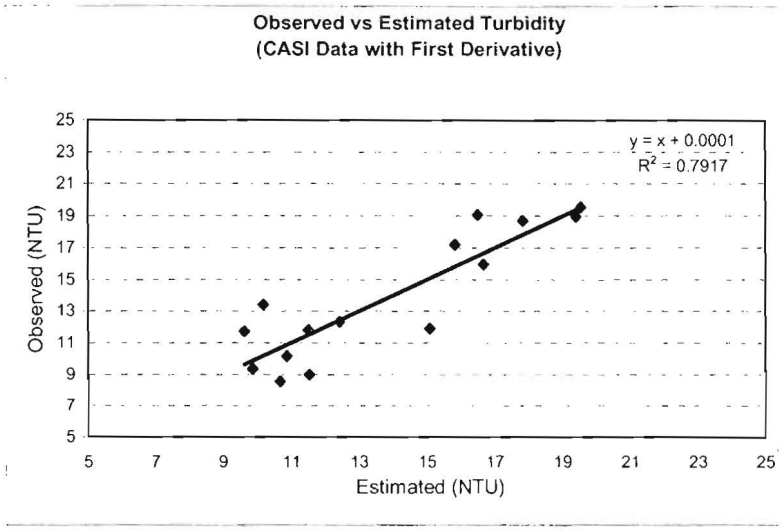

Figure 10: Observed and estimated turbidity plot, high R^2 reflects the validity of the results.

CONCLUSIONS

Remotely sensed hyperspectral data have been used successfully to map the spatial distribution of chlorophyll *a* concentrations and turbidity in the Great Miami River, Ohio. Spectral signatures from the hand-held spectrometer and airborne hyperspectral imagery showed promising correlations with ground truth water quality parameters such as algal chlorophyll concentrations, turbidity values, secchi disk depths and light extinction coefficients. Due to the presence of the strong correlation between laboratory-measured TSS and derivative reflectance with both field spectrometer data and CASI data, a first derivative spectrometry was used which showed promising results for the low-turbidity conditions of the Great Miami River. This was not possible with normal (i.e., ratio or combination) indices due to the lack of gradient in actual turbidity measurements. The imagery and the final map confirmed this uniformity in the distribution of turbidity for most of the river. Finally, maps of relative spatial distributions of chlorophyll and turbidity were created from the selected signatures derived from the imaging spectrometer data.

The hyperspectral chlorophyll and turbidity map demonstrate the spatial variability of the contents of chlorophyll and suspended matter that help determining the point and non point sources responsible for the spatial variability for the Great Miami River. As a result these maps may help to obtain more representative monitoring locations of suspended matter and related parameters as chlorophyll and secchi depth. Overall conclusion of this study was that the combined use of water quality model results, hyperspectral data and field spectrometer in situ data leads to better monitoring and understanding of suspended matter and transparency in the Great Miami River.

REFERENCES

Chen, Z., J.D. Hanson, and P.J. Curran, 1991, "The form of the relationship between suspended sediment concentration and spectral reflectance and its implications for the use of Daedalus 1268 data", *Int. J. Remote Sens,* 12:15-222.

Conel J.E., C.J. Bruegge, and B. Curtiss, 1987a, "Correcting airborne imaging spectrometer measurements for the atmosphere: A comparison of methods." Proc. 31st. S.P.I.E. International Technical Symposium on Optical and Optoelectronic Applied Science and Engineering.

Conel J.E., R.O. Green, G. Vane, C.J. Bruegge, R.E. Alley, and B. Curtiss, 1987b, "AIS-2 Radiometry and a comparison of methods for the recovery of ground reflectance." Proc. 3rd Airborne Imaging Spectrometer Data Analysis Workshop.

Curran, P.J., 1989, "Remote sensing of foliar chemistry," *Remote Sens. Environ.* 29:271-278.

Curran, P.J., J.L. Dungan, B.A. Macler, and S.E. Plumer, 1991, "The effect of a red leaf pigment on the relationship between red edge and chlorophyll concentration," *Remote Sens. Environ.* 35:69-76.

Dekker, A.G., 1997, "Operational tools for remote sensing of water quality: A prototype tool kit. Vrije Universiteit, Amsterdam Institure for Environmental Studies." BCRS Report 96-18, ISBN 90 5411 215 8.

Demetriades-Shah, T.H., M.D. Steven, and J.A. Clark, 1990, "High resolution derivative spectra in remote sensing," *Remote Sense. Environ.* 33:55-64.

Dick, K., and J. Miller, 1991, "Derivative analysis applied to high resolution optical spectra of freshwater lakes." Proc. 14th Canadian Symposium on Remote Sensing, Canadian Remote Sensing Society, Ottawa, pp. 400-418.

Dixit, L. and S. Ram, 1985, "Quantitative analysis by derivative electronic spectroscopy," *Appl. Spectrosc. Rev.* 21:311-418.

Goetz, A.F.H. and V. Srivastava, 1985, "Mineralogical mapping in the Cuprite mining district, Nevada," Proc. Airborne Imaging Spectrometer Data Analysis Workshop, April 1985, JPL Publication, no. 85-41.

Harding, L.W., E.C. Itsweire, and W.E. Esalas, 1995, "Algorithm development for recovering chlorophyll concentrations in the Chesapeake Bay using aircraft remote sensing, 1989-91," Photogrammetric *Engineering & Remote Sensing*, 61(2):177-185.

Hyperspectral Data International (HDI), Inc., 2000, "Final Report: Great Miami River Remote Sensing Project." Work Number 99RD037R. Hyperspectral Data International, Inc., Dartmouth, Nova Scotia, Canada. 57 pp.

Jupp, D.L.B., J.T.O Kirk, and G.P. Harris, 1994, "Detection, identification and mapping of cyanobacteria: Using remote sensing to measure the optical water quality of turbid inland waters, Aust. J. Mar. Freshwater Res., 45:801-828.

Kuo, J.T., J.H. Wu, and W.S. Chu, 1994, "Water quality simulation of Te-Chi Reservoir using two-dimensional models." *Wat. Sci. Tech* 30(2):63-72.

Kuo, J.T., and J.H. Wu, 1991, "A nutrient model for a lake with time-variable volumes." *Wat. Sci. Tech* 24(6): 133-139.

Lathrop, R.G., and T.M. Lillesand, 1989, "Monitoring water quality and river plume transport in Green Bay, Lake Michigan with SPOT-1 imagery." *Photogrammetric Engineering & Remote Sensing*, 55(3): 349- 354.

Lillesand, T.M., W.L. Johnson, R.L. Deuell, O.M. Lindstrom, and D.E. Meisner, 1983, "Use of Landsat data to predict the trophic state of Minnesota Lakes." *Photogrammetric Engineering & Remote Sensing*, 49(2):219-229.

Lung, W.S., 1986, "Assessing phosphorus control in the James River Basin." *Journal of Environmental Engineering*, 112(1): 44-60.

Ohio EPA, 1997, "Biological and water quality study of the Middle to Lower Great Miami River and Selected tributaries." Division of Surface Waters, Monitoring and Assessment Section, Columbus, OH. Ohio EPA Technical Report MAS/1996-12-8.

Philpot, W.D., 1991, "The derivative ratio algorithm: Avoiding atmospheric effects in remote sensing," *IEEE Trans. Geosci. Remote Sens.* 29:250-357.

Ritchie, J.C., and C.M. Cooper, 1991, "An algorithm for estimation surface suspended sediment concentrations with Landsat MSS digital data," *Water Resources Bulletin*, 27(3): 373-379.

Ruiz-Azuara, P., 1995, "Multitemporal analysis of "simultaneous" Landsat imagery (MSS and TM) for monitoring primary production in a small tropical coastal lagoon," *Photogrammetric Engineering & Remote Sensing*, 61(2):877-898.

Thomann, R.V. and Mueller, J.A., 1987, Principles of Surface Water: Quality Modeling and Control, Addison-Wesley Publishing Company: 694 pp., Facsimile edition (June, 1987).

Verdin, J.P., 1985, "Monitoring water quality conditions in a large western reservoir with Landsat imagery," *Photogram. Eng. Rem. Sens.*, 51, 343-353.

Wetzel, R. G., 1995, "Death, detritus and energy-flow in aquatic ecosystems." *Freshwater Biology*, 33, 83-89.

MULTISCALE OPPONENT APPROACH FOR HYPERSPECTRAL TEXTURE RECOGNITION USING AVIRIS DATA

Miaohong Shi and Glenn Healey*

1 Introduction

Hyperspectral sensors measure spectral radiance for a number of contiguous spatial locations to form an image. Several imaging spectrometers provide spectral coverage with hundreds of bands over the visible through short-wave infrared from 0.40 to 2.45 micrometers (Basedow et al., 1995) (Vane et al., 1993) (Simi et al., 2000). Hyperspectal data with its high spectral resolution may be used to identify specific features on the earth's surface such as soils with different composition.

Developing efficient methods to process hyperspectral data becomes important as the number of spectral bands increases. Many existing algorithms for processing hyperspectral data are the direct outgrowth of algorithms that were developed for single band or multispectral sensors where the number of bands is small. These approaches resort to a variety of approximations to reduce the computational burden. Important questions for these approaches include which data-reduction procedure to use and which features to compute.

A large number of techniques for analyzing image texture have been proposed (Haralick, 1979) (Reed et al., 1993). Recent work on texture analysis mainly focuses on statistical approaches and filter-based approaches. The statistical approach characterizes textures as arising from probability distributions on random fields. This approach typically uses a small number of parameters to provide a concise representation for textures. Markov random fields (MRF) (Cross et al., 1983) (Li, 1995) are a popular statistical model for texture. However, these models require prior selection of spatial structure. Multiband correlation models allow for a more generic representation and have been used for geometry-invariant recognition (Kondepudy et al., 1994) and illumination-invariant recognition (Healey et al., 1996) (Healey et al., 1995). Filter-based approaches (Daugman, 1985) (Mallat, 1989) are inspired by multi-channel filtering mechanisms in human vision. Gabor filters have been used extensively to compute texture features for image interpretation tasks (Bovik et al., 1990) (Jain et al., 1991) (Manjunath et al., 1996). These filters achieve optimal joint localization in space and spatial frequency (Daugman, 1985) and can be used to decompose images into components corresponding to different scales and orientations.

The modeling of hyperspectral textures is important for many applications including terrain classification and material identification. The number of spectral bands in hyperspectral imagery provides a large number of spectral/spatial correlations that can be exploited for texture modeling. There have been few attempts to

*Department of Electrical and Computer Engineering, University of California, Irvine, CA 92697 (mshi@ece.uci.edu;healey@ece.uci.edu)

exploit texture information in hyperspectral images. Schweizer and Moura (Schweizer et al., 2001) used Gaussian Markov random fields to model hyperspectral textures to support detection applications.

In this paper, we introduce a representation for hyperspectral textures using unichrome and opponent features computed from Gabor filter outputs. The unichrome features are computed from the spectral bands independently while the opponent features combine information across different bands at different scales. Using an AVIRIS data set acquired at Indian Pines in 1992, we evaluate the performance of the multiscale approach using opponent features for recognizing hyperspectral textures.

2 The Gabor Texture Features

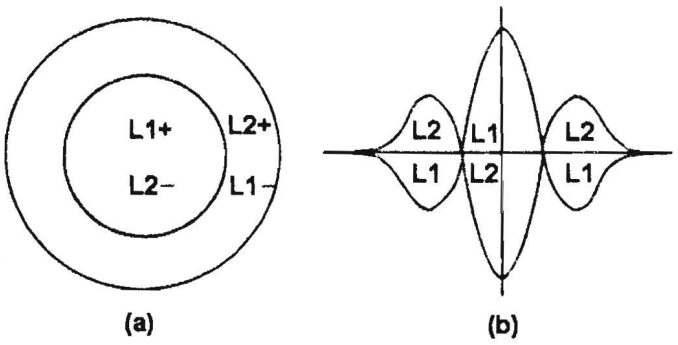

Figure 1: Gabor function approximation of type II opponent cell

Gabor filters are defined in the spatial domain by

$$f_{mn}(x,y) = \frac{1}{2\pi\sigma_m^2} \exp\left(-\frac{x^2+y^2}{2\sigma_m^2}\right) \times \cos(2\pi(u_m x \cos\theta_n + u_m y \sin\theta_n)) \quad (1)$$

where m is the index for the scale and n is the index for the orientation. We consider a filter bank with two scales and four orientations ($0°, 45°, 90°$ and $135°$).

2.1 Unichrome features

Unichrome features are extracted from a single spectral band. Let $L_i(x,y)$ be the ith spectral channel of a hyperspectral image and let $f_{mn}(x,y)$ be a filter in the filterbank. Denote the filtered image

$$h_{imn}(x,y) = L_i(x,y) * f_{mn}(x,y) \quad (2)$$

and the unichrome feature U_{imn} by

$$U_{imn} = \sqrt{\left(\sum_{x,y} h_{imn}^2(x,y)\right)} \quad (3)$$

For C spectral channels, M scales, and N orientations, a set of CMN unichrome features can be computed.

2.2 Opponent features

Hering's opponent process theory (Goldstein, 1996) of human color vision was formulated in the 1800's and later experimentally tested by Hurvich and Jameson (Hurvich et al., 1957). The theory is still a subject of strong interest (Masland, 1996). We can use Gabor functions to model receptive field structure on the retina. For example, we can approximate a type II cell response (Wiesel et al., 1966) using the difference of Gabor functions at the same scale (see Fig. 1). For filtered bands $h_{imn}(x,y)$ and $h_{jmn}(x,y)$, we consider the normalized difference

$$d_{ijmn}(x,y) = \left(\frac{h_{imn}(x,y)}{U_{imn}} - \frac{h_{jmn}(x,y)}{U_{jmn}} \right) \tag{4}$$

Then the type II opponent feature ψ_{ijmn} (Wiesel et al., 1966) (Jain et al., 1998) is obtained by

$$\psi_{ijmn} = \sqrt{\left(\sum_{x,y} d^2_{ijmn}(x,y) \right)} \tag{5}$$

By normalization in (4), we remove information that is already contained in the unichrome features of (3). The opponent features capture the spatial correlation between different spectral channels at a certain scale and orientation.

3 Experiments

3.1 Data set

We used AVIRIS (Vane et al., 1993) hyperspectral data for our experiments from Purdue University's MultiSpec web site[1]. The 20m GSD data was acquired over the Indian Pine Test Site in Northwestern Indiana in 1992. Band 8 (0.58–0.62μm) of this data is shown in Fig. 2. From the data, we obtained 50 test texture images of size 10 × 10 pixels which belong to the following 8 texture classes: Corn-notill, Corn-min, Soybean-notill, Soybean-min, Grass/Trees, Grass/Pasture, Woods, and Hay-windrowed.

3.2 Band reduction

As the number of spectral channels increases, the ability to discriminate similar ground cover classes should also increase. Often the number of pixels available to texture classification techniques is limited, thus limiting the accuracy with which texture characteristics can be estimated. From the 220 AVIRIS bands, we chose a 126 band subset by excluding bands with low signal due to water absorption or the solar radiance function. Fig. 3 plots an AVIRIS spectral radiance function using the 126-band data set. In order to reduce the dimension of the spectral space, we average every three adjacent spectral bands of the 126 spectral bands to get 42 spectral bands. This significantly reduces feature computation requirements. Fig. 4 shows the spectral radiance function corresponding to figure 3 in the reduced band system using the 42 spectral bands.

3.3 Feature subset selection

For filters defined using 2 scales and 4 orientations, there are a total of 336 unichrome features for the 42 spectral bands. We compute opponent features ψ_{ijmn} for all i,j with $i = 1,2,\ldots,42$; $j = 1,2,\ldots,42$ and $i \neq j$

[1] http://dynamo.ecn.purdue.edu/~biehl/MultiSpec/

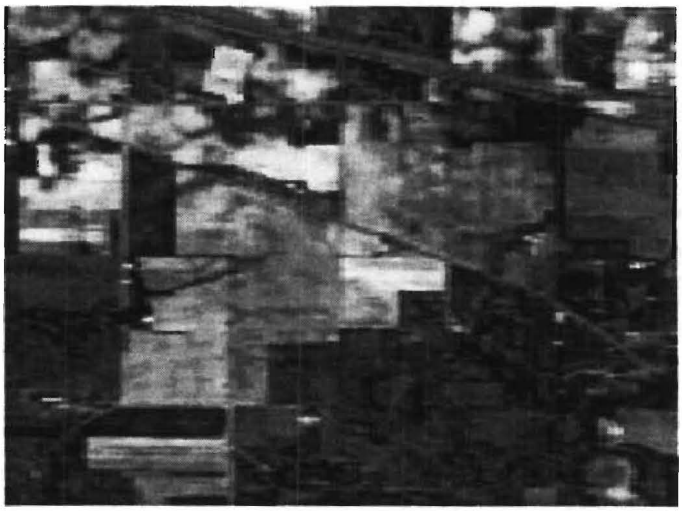

Figure 2: Band 8 (0.58–0.62μm) of AVIRIS Indian pine test site image

to get 6888 opponent features. Thus, a test texture image can be represented by a vector of 7224 unichrome and opponent features. We compute a mean feature vector for each of the 8 texture classes by averaging the feature vectors for all of the test texture images of that texture class.

We define a distance metric between two feature vectors by

$$d_{ij} = \sum_{k=1}^{p} \left(\frac{f_k^i - f_k^j}{\gamma(f_k)} \right)^2 \tag{6}$$

where $(f_1^i, f_2^i, \ldots, f_p^i)$ is the feature vector for texture image i and $(f_1^j, f_2^j, \ldots, f_p^j)$ is the feature vector for texture image j. $\gamma(f_k)$ is the standard deviation of f_k over the 8 texture classes. For each test texture image, we compute the distance of the test texture image from the mean feature vector for each of the eight texture classes using (6). We classify a test texture image as an instance of nearest class. We can use a stepwise optimal algorithm to build up approximately optimal feature subsets. At each step, we add a new feature that leads to a maximum increase in classification rate.

3.4 Classification results

We show a comparison of the classification performance for the best subsets of six feature sets in Fig. 5. The first feature set includes the 42 mean features and 42 variance features. The mean feature is defined by $m_i = \frac{1}{100} \sum_{x,y} L_i(x,y)$ with $L_i(x,y)$ denoting the ith spectral band. The variance feature is defined by $var_i = \frac{1}{100} \sum_{x,y} (L_i(x,y) - m_i)^2$. The second feature set includes only the 42 mean features. The third feature set includes only the 42 variance features. The fourth feature set includes the 336 unichrome features. The fifth feature set includes the 6888 opponent features. The sixth feature set includes all 7224 unichrome and opponent features. We see that for a given number of features, the mean and variance feature set performs better than only the mean or only the variance feature set. The unichrome feature set performs better than the mean and variance feature set. We also see that using the opponent features significantly improves the classification accuracy over only using the unichrome features.

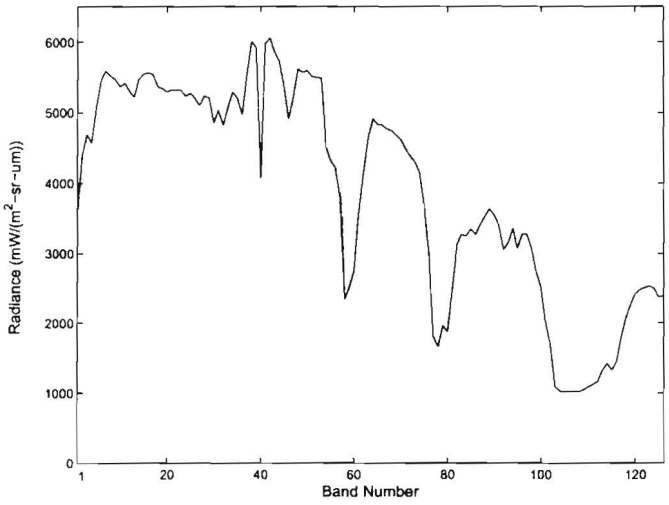

Figure 3: AVIRIS spectral signature (bands 1–126)

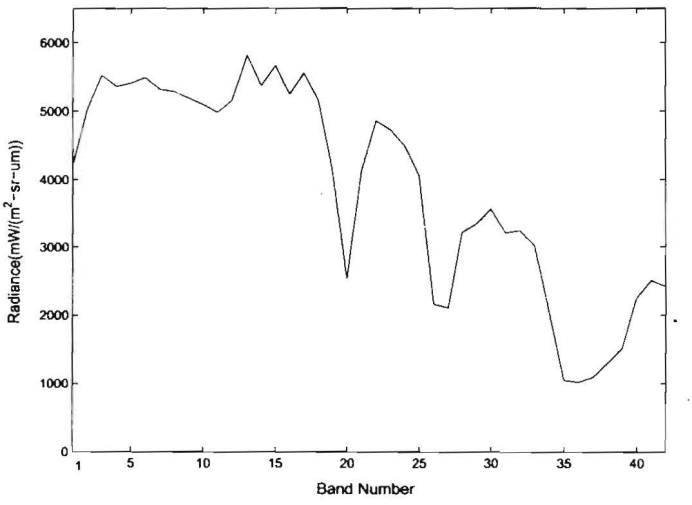

Figure 4: Spectral signature in the reduced band system (bands 1–42)

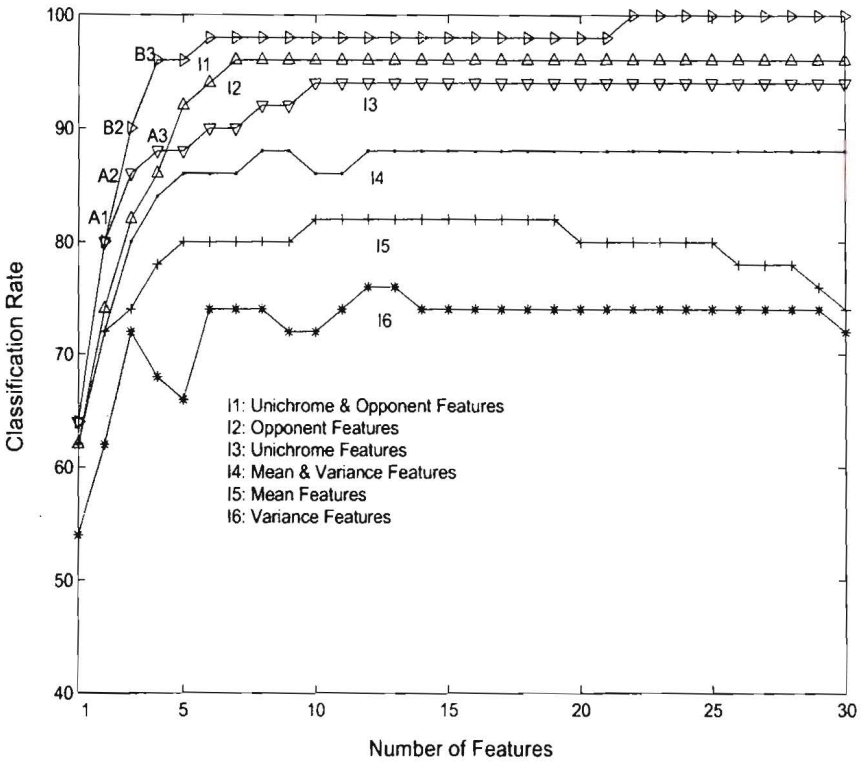

Figure 5: Best classification rate for each of six feature sets

3.5 An example

Texture class 1 (Corn-notill) and texture class 2 (Corn-min) are taken as an example to illustrate how the use of opponent features improves classification performance. There are seven test texture images of size 10×10 in class 1 and five test texture images of size 10×10 in class 2. We define a unichrome filtered image by $|h_{imn}(x,y)|$ and an opponent filtered image by $|d_{ijmn}(x,y)|$ so that the square of the unichrome feature defined by (3) is the energy of the unichrome filtered image and the square of the opponent feature defined by (5) is the energy of the opponent filtered image. We label several points in figure 5 with A_i or B_i symbols. We denote the best two unichrome features at A_1 as μ_1, μ_2, the added unichrome feature at A_2 as μ_3, and the added unichrome feature at A_3 as μ_4. Point B_1 coincides with point A_1 since the best two selected features from the unichrome and opponent feature set are only unichrome features. We then denote the added opponent feature at B_2 as ψ_1 and the added opponent feature at B_3 as ψ_2. Fig. 6 displays the filtered images for the seven 10×10 instances of texture 1. From top to bottom in Fig. 6 are filtered images corresponding to $\mu_1, \mu_2, \mu_3, \psi_1$ and ψ_2. Similarly, the filtered images for the five instances of texture 2 are shown in Fig. 7. We see that while the unichrome filtered images for the two texture classes are quite similar, the opponent filtered images are significantly different. The opponent filtered images for texture class 1 have more energy than the opponent filtered images for texture class 2. This can also be seen by examining the computed features shown in Table 1. The values of μ_1, μ_2, and μ_3 are close for the two classes while the values of ψ_1 and ψ_2 are significantly larger for class 1 than for class 2.

Using (6), we also compute the distance between the mean of the seven instances of texture class 1 and the mean of the five instances of texture class 2 at points A_1, A_2, A_3, B_2 and B_3. The results are shown in Table 2. For a fixed number of features, the distance increases greatly with the opponent features added to the feature

set. This indicates that texture classes 1 and 2 are more easily discriminated when using the opponent features versus only unichrome features.

To show why the opponent features improve classification performance, we consider the first selected opponent feature ψ_1 which captures the spatial correlation between band 9 and band 28 at a certain scale and orientation. ψ_1 is much larger for texture class 1 than for texture class 2 which suggests that the band 9 and band 28 intensities across rows are more correlated for texture class 2 than for texture class 1. If normalized band 9 and band 28 are equal, then from (4) the opponent feature ψ_1 will be zero. We compute normalized intensities of band 9 and band 28 for texture class 1 along a row by averaging the rows of the filtered image for these two bands respectively. The normalized intensities are plotted in Fig. 8. Similarly, we plot the normalized intensities for texture class 2 in Fig. 9. As we can see, the normalized band 9 and band 28 curves are more similar for texture class 2 than for texture class 1.

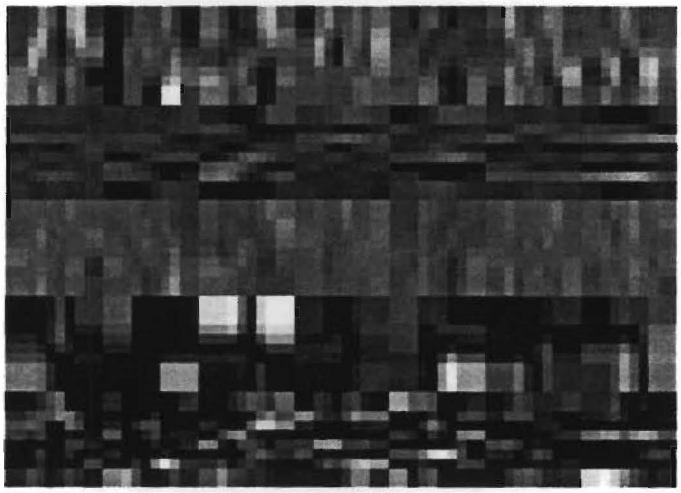

Figure 6: Filtered images for texture 1 (from top to bottom: $\mu_1, \mu_2, \mu_3, \psi_1, \psi_2$)

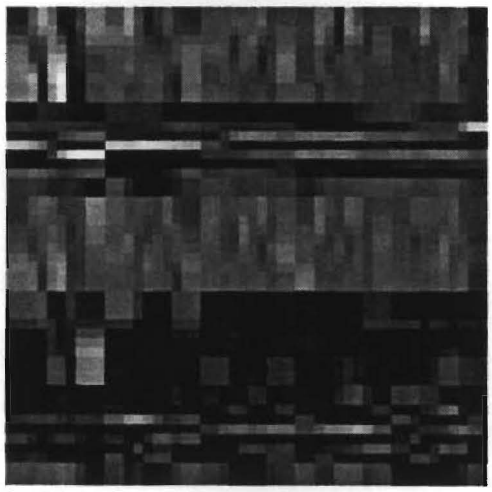

Figure 7: Filtered images for texture 2 (from top to bottom: $\mu_1, \mu_2, \mu_3, \psi_1, \psi_2$)

Table 1: Selected features for texture 1 and 2

	Texture 1	Texture 2
μ_1	0.0320	0.0312
μ_2	0.0228	0.0258
μ_3	0.0133	0.0132
ψ_1	0.0452	0.0256
ψ_2	0.1335	0.0964

Table 2: Distance metrics between texture 1 and 2

	Number of Features	Distance Metrics
A_1	2 uni	1.6203
A_2	3 uni	1.6260
A_3	4 uni	1.6298
B_2	2 uni 1 oppo	1.8742
B_3	2 uni 2 oppo	2.1826

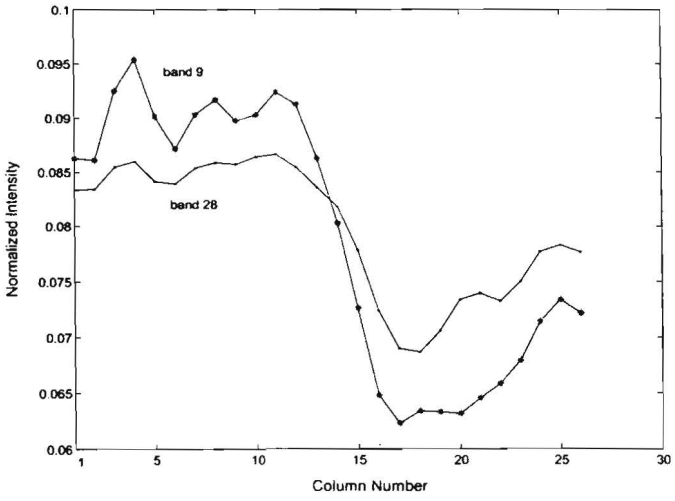

Figure 8: Normalized intensities of band 9 and band 28 across rows for texture 1

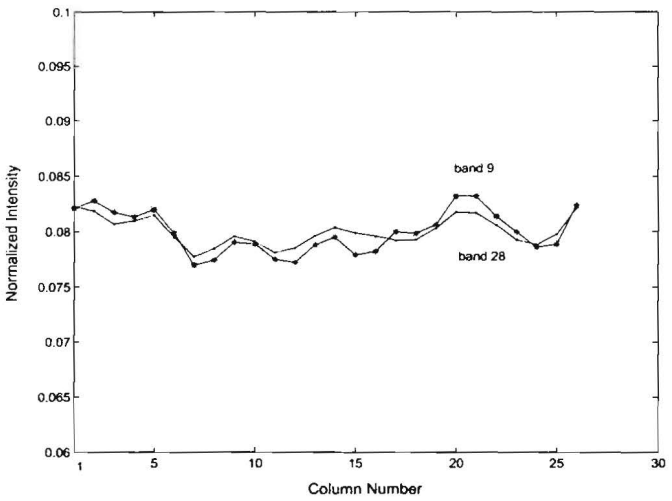

Figure 9: Normalized intensities of band 9 and band 28 across rows for texture 2

4 SUMMARY

In this paper, we have examined feature subspaces for texture recognition in hyperspectral imagery using unichrome and opponent features computed from Gabor filter outputs. The opponent color features are motivated by opponent processes in human vision. With the unichrome and opponent features, we can capture the spatial information within and between spectral bands. Using an AVIRIS data set, we demonstrated the discriminatory power of optimized feature sets that include opponent features for texture recognition. We have shown that using both unichrome and opponent features significantly improves the performance of texture classification over only using the same number of unichrome features.

5 ACKNOWLEDGMENTS

This work has been supported by the National Science Foundation and the Air Force Office of Scientific Research.

References

Basedow, R. W., D. C. Armer, and M. E. Anderson, 1995, "HYDICE system: Implementation and Performance," *SPIE Proceedings*, Vol. 2480, 258–267.

Bovik, A. C., M. Clark, and W. S. Geisler, 1990, "Multichannel texture analysis using localized spatial filters," *IEEE Trans. Pattern Anal. Machine Intell.*, Vol. 12, pp. 55–73.

Cross, G. R. and A. K. Jain, 1983, "Markov random field texture models," *IEEE*, PAMI, 5: 25–39.

Daugman, J. G., 1985, "Uncertainty relation for resolution in space, spatial frequency and orientation optimized by two-dimensional visual cortical filters," *J. Opt. Soc. Amer.*, Vol. 2, pp. 1160–1169.

Goldstein, E. B., 1996, *Sensation & Perception*, 4th ed. Pacific Grove, Calif., Brooks/Cole Publishing Company.

Haralick, R. M., 1979, "Statistical and structural approaches to texture," *Proc. IEEE*, Vol. 67, 786–804.

Healey, G. and A. Jain, 1996, "Retrieving multispectral satellite images using physics-based invariant representations," *IEEE Trans. Pattern Anal. Machine Intell.*, Vol. 18, pp. 842–848.

Healey, G. and L. Wang, 1995, "Illumination-invariant recognition of texture in color images," *J. Opt. Soc. Amer. A*, Vol. 12, pp. 1877–1883.

Hurvich, L. M. and D. Jameson, 1957, "An Opponent-Process Theory of Color Vision," *Physiological Rev.*, Vol. 64, pp. 384–404.

Jain, A. K. and F. Farrokhnia, 1991, "Unsupervised texture segmentation using Gabor filters," *Pattern Recognit.*, Vol. 24, pp. 1167–1186.

Jain, Amit and G. Healey, 1998, "A Multiscale Representation Including Opponent Color Features for Texture Recognition," *IEEE Trans. Image Processing*, Vol. 7, No. 1.

Kondepudy, R. and G. Healey, 1994, "Use of invariants for recognition of three-dimensional color textures," *J. Opt. Soc. Amer.*, Vol. 11, pp. 3037–3049.

Li, S. Z., 1995, *Markov Random Field Modeling in Computer Vision*, Springer.

Mallat, S., 1989, "Multi-resolution approximation and wavelet orthonormal bases of $L^2(R)$," *Trans. Amer. Math. Soc.*, 315: 69–87.

Manjunath, B. S. and W. Y. Ma, 1996, "Texture features for browsing and retrieval of image data," *IEEE Trans. Pattern Anal. Machine Intell.*, Vol. 18, pp. 837–842.

Masland, R. H., 1996, "Unscrambling Color Vision," *Science*, Vol. 271, No. 2, pp. 616–617.

Reed, T. R. and J. M. Hans du Buf, 1993, "A review of recent texture segmentation and feature extraction techniques," *Computer Vision Graphics and Image Processing*, Vol. 3, No. 57, 359–372.

Schweizer, S. and J. Moura, 2001, "Efficient Detection in Hyperspectral Imagery," *IEEE Trans. Image Processing*, Vol. 10, No. 4, 584–597.

Simi, C. G., S. G. Beaven, E. M. Winter, C. LaSota, J. Parish, and R. Dixon, 2000, "Night vision imaging spectrometer (NVIS) performance parameters and their impact on various detection algorithms," *SPIE Proceedings, Algorithms for Multispectral, Hyperspectral, and Ultraspectral Imagery VI*, Vol. 4049.

Vane, G., R. Green, T. Chrien, H. Enmark, E. Hansen and W. Porter, 1993, "The airborne visible infrared imaging spectrometer,"*Remote Sensing of Environment*, Vol. 44, 127–143.

Wiesel, T. N. and D. H. Hubel, 1966, "Spatial and Chromatic Interactions in the Lateral Geniculate Body of the Rhesus Monkey," *J. Neurophysiology*, Vol. 29, pp. 1,115–1,156.

HYPERSPECTRAL REMOTE SENSING OF THE BRAZILIAN PANTANAL LAKES

Lênio Soares Galvão,[1] Waterloo Pereira Filho,[2] Myrian de Moura Abdon,[1]
Evlyn M. M. L. Novo,[1] João S. V. da Silva,[3] and Flávio Jorge Ponzoni[1]

1. INTRODUCTION

Located in the center of South America, mostly in Brazil, the Pantanal is considered the largest complex of wetlands of the world (Alho et al., 1988; Tundisi, 1994). From the ecological, biological and economical points of view, thousands of small shallow fresh and salt water round lakes are responsible for the supply of water and food for human beings and animals and of salt for cattle. They have also a very important role as temporary or unique habitats for several native species of mammals, reptiles and aquatic birds (Brum and Souza, 1985; Pott et al., 1987; Campos, 1991).

The Pantanal is one of the least known regions of the planet. The difficulty to access many areas is one of the major factors responsible for the scarce scientific knowledge on the lakes. In the study of the lakes, remote sensing investigations are restricted to a very small number of published papers. For example, Abdon et al. (1998) reported the discrimination of aquatic plant covers especially in areas with *Salvinia auriculata* and *Scirpus cubensis* through the use of multispectral remote sensing (TM/Landsat 5 and HRV/SPOT images). However, to address the difficulty to distinguish areas occupied by different mixtures of aquatic plants, they suggested the use of data with better spatial and spectral resolution. In this sense, hyperspectral remote sensing introduces new perspectives for the study of the Pantanal lakes. The possibility of comparing pixel spectra with field spectra of water or aquatic plants, retrieving narrow absorption bands on a per-pixel basis, and of relating the spectral characteristics of the Pantanal lakes with physico-chemical databases is essential to understand the relationships between reflectance and water constituents.

In August 1995, at the peak of the regional dry season, the Airborne Visible/Infrared Imaging Spectrometer (AVIRIS) acquired images in the Brazilian Pantanal region in 224 bands (400-2500 nm) with 20 meters of spatial resolution. By inspection of these images, a subset of 12 lakes with distinct characteristics was selected for field investigation and spectral and physico-chemical data collection. The objective of this article is to discuss the spectral behavior of these lakes face to variations in water constituents.

2. METHODOLOGY

The location of the study area (approximately 10 x 20 km) is depicted in Figure 1. AVIRIS data were acquired in August 1995, at the peak of the regional dry season, from an altitude of 20 km. Images were obtained in 224 bands (10 nm in width) positioned in the 400-2500 nm interval, with a solar zenith angle of 34° and a nominal spatial resolution of 20 m. AVIRIS radiance values were converted to surface reflectance data, that is, corrected for the scattering and absorption atmospheric effects, through the use of the Atmosphere Removal (ATREM) technique (Gao et al., 1993). After calculating the surface reflectance data, the Empirical Flat Field Optimal Reflectance Transformation (EFFORT) technique (Boardman, 1998) was applied over the images at selected spectral intervals to smooth noisy data resulting from the atmospheric correction procedure.

[1] Instituto Nacional de Pesquisas Espaciais - INPE
Caixa Postal 515, 12201-970, São José dos Campos, SP, Brasil (lenio@ltid.inpe.br).
[2] Universidade Federal de Santa Maria – UFSM
Departamento de Geociências, 97119-900, Santa Maria, RS, Brasil.
[3] Empresa Brasileira de Pesquisa Agropecuária – Embrapa
Caixa Postal 6041, 13083-970, Campinas, SP, Brasil.

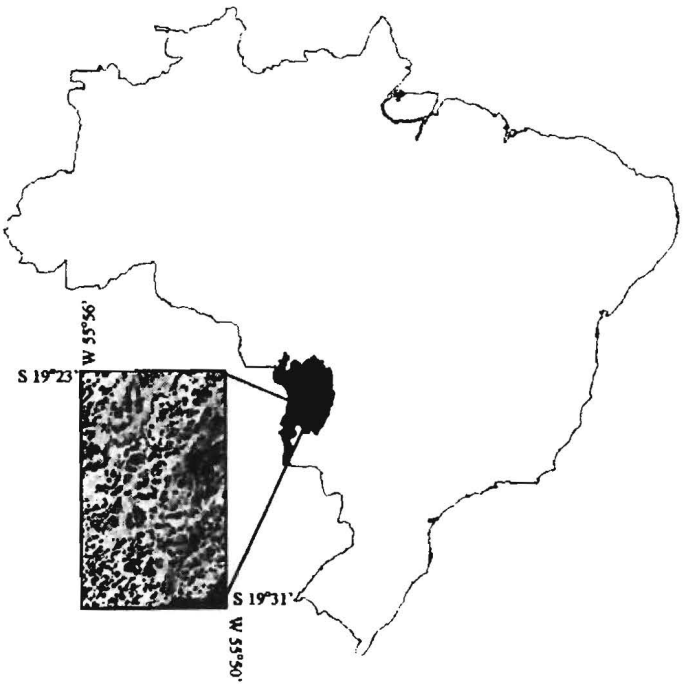

Figure 1 - Spatial distribution of the Pantanal in Brazil and location of the study area.

The selection of the lakes for field inspection was based on the analysis of true color composites and of pixel spectra. The Bidirectional Reflectance Factor (BRF) at 39 sampling sites of seven fresh water and five salt water lakes were collected from a boat using a portable spectrometer (SPECTRON SE-590). The sensor collected data in the 400-900 nm range at spectral intervals of 3 nm and with 15° FOV lens. A $BaSO_4$ plate of known reflectance was used as reference. Each one of the 39 collected spectra was the average of five continuous readings.

At each site, besides the reflectance data, the following in-situ measurements were performed: electrical conductivity, pH, total depth of the lake and Secchi disk transparency or Secchi depth. In laboratory, 33 water samples were submitted to chemical analysis. The methods used for determination of the water constituents were: calcium (Ca), total iron (Fe), magnesium (Mg), potassium (K) and sodium (Na) (atomic absorption spectrometric method); total phosphorous (P) (colorimetric and ascorbic acid method); total organic nitrogen (N) (Kjeldahl method); dissolved organic carbon (DOC) (colorimetric method); and total concentration of chlorophyll *a* plus phaeophytin (Chl) (spectrophotometric method). Details on these methods are described in Eaton et al. (1985). The total suspended solids (TSS) was determined by filtering samples onto 0.45 μm filters of known weight, drying them, and measuring the weight gain due to sediment concentration.

To characterize variations in depth of the main absorption bands present in pixel spectra, the continuum removal method (Clark and Roush, 1984) was applied to normalize the curves, to isolate the features, and to allow their comparison from a common baseline. Straight line segments connecting the edges (reflectance maxima) of the absorption band centered at 630 nm were chosen to define the continuum. The depth of the absorption band (D) was computed from the equation "D = 1 – Rb/Rc", where Rb is the reflectance value at the center of the absorption band, and Rc is the reflectance of the continuum at the same wavelength as Rb.

3. RESULTS AND DISCUSSION

Figure 2 shows a true color composite (AVIRIS bands centered at 667 nm, 559 nm and 480 nm displayed in red, green and blue colors, respectively) and the location of the lakes selected for field inspection. Despite the non-existence of AVIRIS data for lake 7, which is located very close to the border of lake 6, its selection for investigation is due to its similarity in field with the bluish lake 3 indicated in Figure 2.

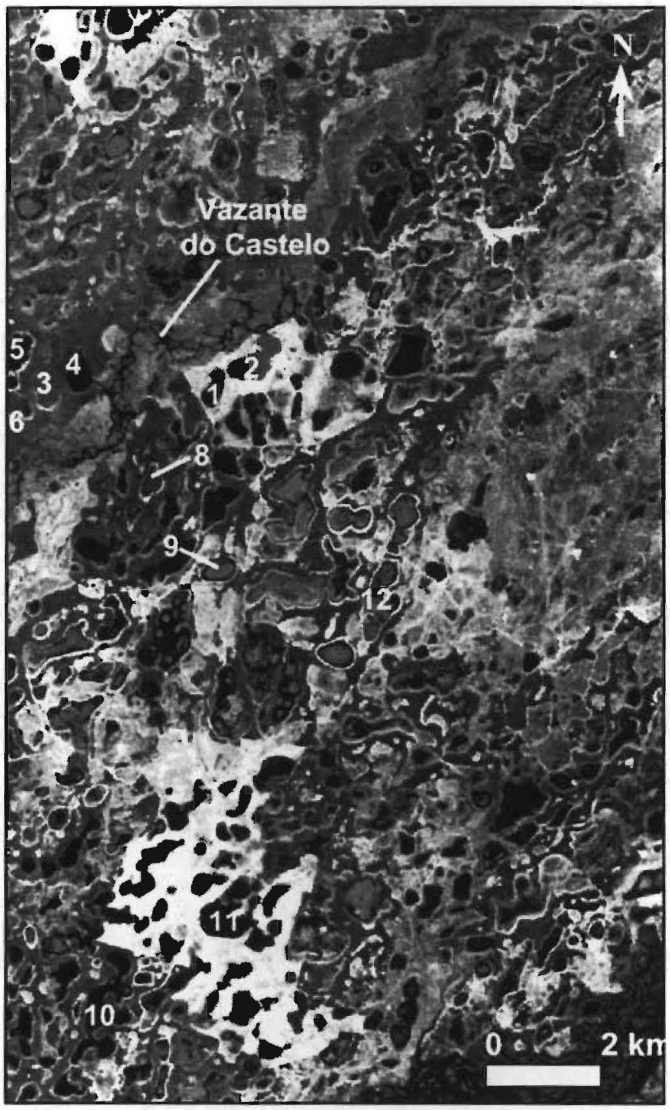

Figure 2 - True color composite of the study area with the AVIRIS bands centered at 667 nm, 559 nm and 480 nm depicted in red, green and blue colors, respectively. The location of the lakes selected for investigation (except lake 7) is indicated. The location of the "*Vazante do Castelo*", a temporary drainage channel, is also shown.

The fresh water lakes 1, 2 and 4, which display dark or light green colors in Figure 2, are characterized by the occurrence of small amounts of aquatic macrophytes (e.g., *Eichhornia azurea* and *Salvinia auriculata*) in their margins. On the other hand, the surface of the fresh water lakes 9 and 12 are dominated by a dense cover of floating vegetation, composed of *Nymphaea amazonum*, *Nymphaea lingulata* and *salvinia auriculata*. These aquatic plants

are responsible for the green colors observed in the color composite of Figure 2. A lesser dense cover of aquatic plants, composed of *Eicchornia azurea*, *Oxycaryum cubense* and *Nymphaea amazonum,* are predominant in lakes 10 and 11.

The salt water lakes appear in greenish (lakes 5, 6 and 8) and bluish (lake 3) colors in the true color composite of Figure 2. However, the green color of lake 8 is the result of the strong background influence of the submerse rooted macroscopic algae *Chara rusbyana* that densely covers the bottom of this shallow lake.

Table 1 shows average and standard deviation values of the physico-chemical characteristics of the studied lakes. In general, when compared with the fresh water lakes, the salt water lakes, especially the more saline water bodies (lakes 3, 5 and 6), tend to present lower values of total depth and Secchi depth, and higher contents of DOC, TSS, Ca, Mg, Na and K. As illustrated in Table 1, the salt water lakes are composed of alkaline waters (pH > 9) with high values of electrical conductivity that may reach more than 3500 µS/cm in the more saline lakes.

Table 1 – Average and Standard Deviation (in Parentheses) Values of the Physico-Chemical Characteristics of the 12 Studied Fresh Water (F) and Salt Water (S) Lakes.

L	Chl µg/L	DOC mg/l	TSS mg/l	Secchi m	Depth m	pH	EC µS/cm	Ca mg/l	Fe_t mg/l	P_t mg/l	Mg mg/l	N_t mg/l	K mg/l	Na mg/l	N
1	724.6	0.13	3.07	0.35	0.97	8.99	97.1	1.07	0.63	0.12	0.63	120.3	8.60	2.37	3
(F)	(570.9)	(0.02)	(0.42)	(0.00)	(0.25)	(0.36)	(2.44)	(0.06)	(0.04)	(0.04)	(0.27)	(9.52)	(0.56)	(0.23)	
2	579.4	0.13	2.17	0.30	0.83	8.87	62.5	1.40	2.73	0.08	0.27	79.9	4.43	2.20	3
(F)	(429.5)	(0.02)	(0.19)	(0.00)	(0.21)	(0.60)	(0.15)	(0.61)	(0.31)	(0.02)	(0.27)	(40.0)	(0.46)	(0.44)	
4	68.0	0.11	16.41	0.40	0.87	6.68	72.2	1.97	3.85	0.65	0.29	121.6	4.02	1.75	4
(F)	(25.9)	(0.01)	(2.30)	(0.00)	(0.09)	(0.17)	(1.60)	(0.09)	(0.93)	(0.62)	(0.14)	(44.0)	(0.40)	(0.90)	
9	62.4	0.05	5.25	0.80	0.88	6.37	105.0	4.10	2.00	0.01	0.25	22.2	3.20	9.20	2
(B)	(35.7)	(0.00)	(2.33)	(0.00)	(0.04)	(0.04)	(38.0)	(0.14)	(0.00)	(0.00)	(0.08)	(7.92)	(0.28)	1.13	
10	468.8	0.02	0.80	1.32	1.57	6.11	37.5	1.75	0.80	0.01	0.30	12.5	4.70	2.27	4
(F)	(395.5)	(0.00)	(0.58)	(0.09)	(0.15)	(0.26)	(2.01)	(0.01)	(0.40)	(0.00)	(0.09)	(5.30)	(0.22)	(0.29)	
11	62.0	0.03	1.10	1.10	1.10	6.29	34.9	1.80	1.60	0.01	0.14	9.80	5.10	2.00	1
(F)	-	-	-	-	-	-	-	-	-	-	-	-	-	-	
12	183.7	0.06	3.40	0.70	0.70	6.14	105.2	6.30	2.75	0.01	0.61	16.75	6.05	7.95	2
(F)	(96.5)	(0.01)	(4.24)	(0.00)	(0.00)	(0.11)	(2.90)	(0.28)	(1.06)	(0.00)	(0.19)	(8.84)	(6.86)	(0.07)	
3	95.6	1.05	39.16	0.07	0.42	9.33	4907	13.66	28.9	4.55	9.11	66.3	188.5	394.4	7
(S)	(73.9)	(0.04)	(10.9)	(0.00)	(0.07)	(0.03)	(55.0)	(1.35)	(4.42)	(0.45)	(5.78)	(23.7)	(26.9)	(56.4)	
5	538.3	0.62	200.6	0.08	0.45	10.19	3882	9.08	1.22	0.02	0.87	66.3	117.2	255.5	5
(S)	324.9	(0.01)	(51.4)	(0.00)	(0.28)	(0.11)	(25.9)	(1.28)	(1.67)	(0.03)	(0.91)	(64.9)	(64.0)	(142)	
6	778.9	0.43	220.3	0.09	0.45	10.44	4293	8.73	0.38	0.01	1.47	42.2	165	384.4	3
(S)	(34.3)	(0.02)	(9.81)	(0.00)	(0.05)	(0.07)	(130)	(2.31)	(0.16)	(0.00)	(0.55)	(5.91)	44.2	(123)	
7	267.3	2.07	42.70	0.06	1.10	9.07	1530	9.40	105.3	0.39	5.87	17.5	46.1	145.6	2
(S)	(-)	(0.05)	(37.2)	(0.00)	(0.21)	(0.17)	(14.1)	(0.00)	(0.00)	(0.11)	(0.64)	(1.13)	(0.14)	(7.07)	
8	103.6	0.06	5.88	0.30	0.30	9.91	1590	5.33	0.35	0.01	0.26	12.7	73.6	88.2	3
(S)	(30.5)	(0.01)	(5.07)	(0.00)	(0.00)	(0.47)	(70.0)	(1.15)	(0.31)	(0.00)	(0.32)	(1.75)	(7.52)	(7.91)	

Figure 3 exhibits water reflectance spectra representative of the saline lakes (Fig. 3a), of the fresh water lakes affected by the floods of the *Vazante do Castelo* (Fig. 3b), and of the fresh water lakes covered by aquatic plants (Fig. 3c). In Figure 3a, the greenish salt water lakes 5 and 6 show spectra with well-defined chlorophyll absorption bands at 450 nm and 667 nm, a green reflectance peak at 556 nm, a narrow absorption band at 630 nm due to phycocyanin, and a broad spectral feature around 750 nm due to water absorption. The phycocyanin feature is not present in the spectrum of lake 8, which is a mixed spectral response of relatively transparent water and algae (*Chara rusbyana*). The featureless spectra of lakes 3 and 7 and their resulting blue colors in the images are produced by an increase in the DOC concentration, which masks absorption bands due to other constituents, and by a decrease in the content of chlorophyll (Table 1). In Figure 3b, the larger concentration of TSS in lake 4 (Table 1), in relation to lakes 1 and 2, produces an increase in reflectance in the red interval.

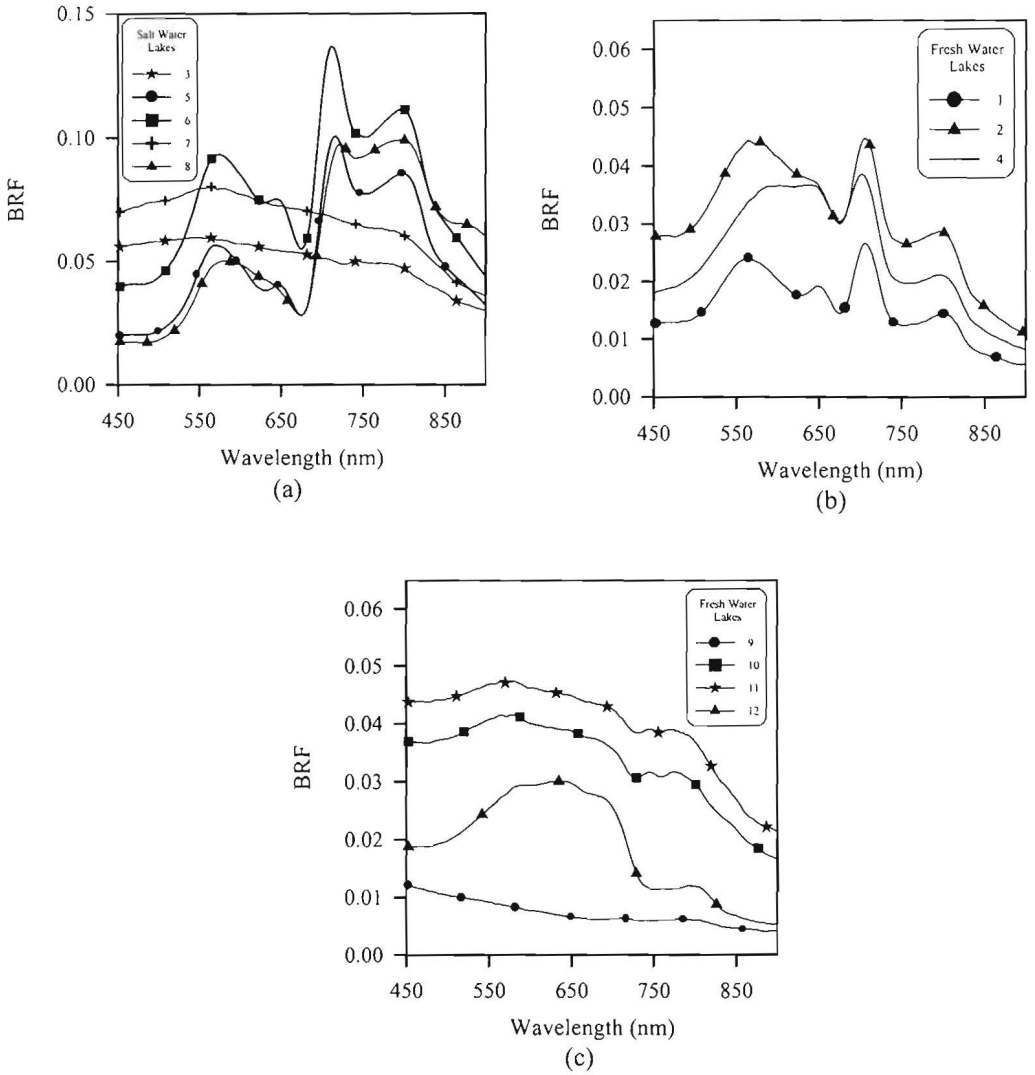

Figure 3 - Field bidirectional reflectance factor (BRF) values for the (a) salt water lakes, (b) fresh water lakes without dense aquatic plant covers at the *Vazante do Castelo* drainage, and (c) for the fresh water lakes with extensive aquatic plant covers.

The comparison between field (Spectron) and airborne (AVIRIS) data reveals interesting aspects. The capability of AVIRIS in retrieving the narrow 630 nm absorption band is shown in Figure 4, which displays variations in the depth of the 630 nm absorption band derived from the continuum removal method. The characterization of this feature is important because it can be useful in the identification of broad algae group of species (Jupp et al., 1994). As indicated in Figure 4, the deepest 630 nm absorption band occurs in pixel spectra of the fresh water lakes 1 and 2 and of the greenish salt water lakes 5 and 6, which is consistent with the results of Figure 3.

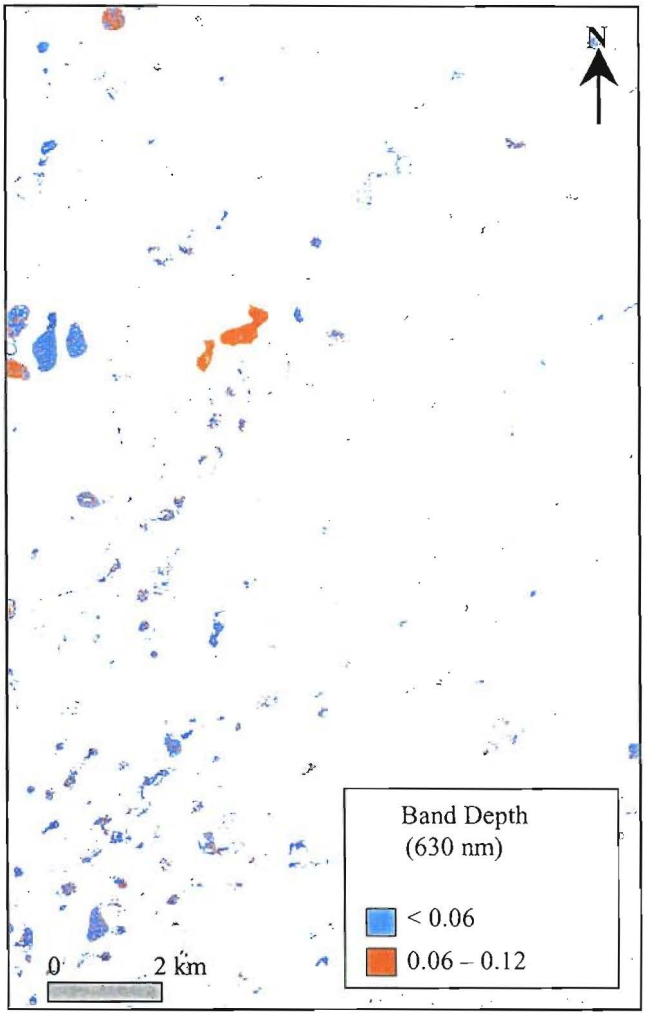

Figure 4 - Variations in the depth of the 630 nm absorption band for lakes without dense covers of aquatic plants.

On the other hand, the strong spectral influence of the macrophytes on the lakes 9 to 12 is illustrated in Figure 5 that displays AVIRIS pixel spectra. Lakes 9 and 12 are densely covered by *Nymphaea amazonum*, *Nymphaea lingulata* and *Salvinia auriculata* that completely obliterate the spectral response of the water. The pixel spectra of these lakes exhibits a well-defined green reflectance peak. Lakes 10 and 11 are dominated by *Eicchornia azurea*, *Oxycaryum cubense* and *Nymphaea amazonum* that show a different spectral pattern. As a result, spectra of Figure 5 are very different from those displayed in Figure 3c that shows field water reflectance spectra of lakes 9 to 12.

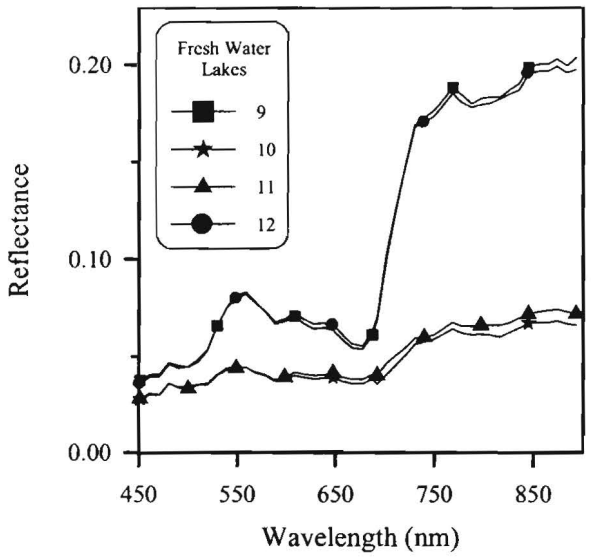

Figure 5 – AVIRIS pixel spectra representative of lakes 9 to 12 with covers of aquatic plants.

4. CONCLUSIONS

The transition from the fresh water lakes to the salt water lakes in the study area is characterized by lower values of total depth and Secchi depth, greater concentrations of DOC, TSS, Ca, Mg, Na and K, and higher values of pH and electrical conductivity. The saline lakes presented a higher overall reflectance than the fresh water lakes. In comparison with the greenish salines, the bluish salt water lakes show an increase in the DOC concentration, which masks absorption bands due to other constituents, and a decrease in the content of chlorophyll. In some fresh water lakes, the presence of dense covers of aquatic plants restricts the spectral response of water to a small number of pixels.

Hyperspectral data are very important in the selection of the Pantanal lakes with distinct spectral characteristics for field sampling, which facilitates the subsequent construction of empirical relationships or more elaborated methods for the remote estimate of water constituents. They allow a better characterization of the variations in reflectance and in related absorption band parameters due to changes in water constituents. Major spectral features present in field spectra, such as the narrow 630 nm absorption band, were also observed in AVIRIS spectra of some lakes and mapped on a per-pixel basis. Hyperspectral sensors can provide also an important contribution in the characterization of aquatic plant covers in the Pantanal lakes because of the well-defined spectral signatures of some species.

ACNOWLEDGEMENTS

The authors are grateful to *Fundação de Amparo à Pesquisa do Estado de São Paulo* (FAPESP) for the financial support in this investigation (Project 2000/04966-7). Thanks are also due to the *Empresa Brasileira de Pesquisa Agropecuária* (Embrapa) for assistance in the field activities.

REFERENCES

Abdon, M.M., V.J. Pott, and J.S.V. Silva, 1998, Evaluation of aquatic plant covers in lakes from the Nhecolândia Pantanal by Landsat and SPOT data. *Pesquisa Agropecuária Brasileira*, vol. 33, pp. 675-1683 (in Portuguese).

Alho, C.J.R., T.E. Lacher, and H.C. Gonçalves, 1988, Environmental degradation in the Pantanal ecosystem. *Bioscience,* vol. 38, pp. 164-171.

Boardman, J. W., 1998, Post-ATREM polishing of AVIRIS apparent reflectance data using EFFORT: a lesson in accuracy versus precision. In *Proceedings of the 7th JPL Airborne Earth Science Workshop,* Jet Propulsion Laboratory, 12-16 January, Pasadena California, vol. 1, p. 53.

Brum, P.A.R., and J.C. Souza, 1985, Levels of mineral nutrients in the Pantanal lakes ("baías" and "salinas") from Mato Grosso do Sul. *Pesquisa Agropecuária Brasileira*, vol. 20, pp. 1451-1454 (in Portuguese).

Campos, Z.M.S., 1991, Female fecundity, egg survival and sex of newborn *Caiman crocodilus yacare* (Crocodilia, Alligatoridae) in the Pantanal, Brazil. Master Thesis. Manaus: INPA/FUA, 1991. 61 p. (in Portuguese).

Clark, R. N., and T.L. Roush, 1984, Reflectance spectroscopy: quantitative analysis techniques for remote sensing applications. *Journal of Geophysical Research,* vol. 89, pp. 6329-6340.

Eaton, A.D., L.S. Clesceri, and A.E. Greenberg, 1985, Standard methods for the examination of water and wastewater. United Book Press, Baltimore.

Gao, B.C., K.B. Heidebrecht, and A.F.H. Goetz, 1993, Derivation of scaled surface reflectance from AVIRIS data. *Remote Sensing of Environment,* vol. 44, pp. 165-178.

Jupp, D.L.B., J.T.O Kirk, and G.P. Harris, 1994, Detection, identification and mapping of cyanobacteria using remote sensing to measure the optical quality of turbid inland waters. *Australian Journal of Marine and Freshwater Research,* vol. 45, pp. 801-828.

Pott, E.B., P.A.R. Brum, I.L. Almeida, J.A. Comastri Filho, and J.F. Dynia, 1987, Mineral nutrition of bovines from the Mato Grosso Pantanal: survey of macro-nutrients in central Nhecolândia. *Pesquisa Agropecuária Brasileira*, vol. 22, pp. 1093-1109 (in Portuguese).

Tundisi, J.G., 1994, Tropical South America: present and perspectives. In Limnology now: a paradigm of planetary problems (R. Margalef, Ed.). Elsevier, New York, pp.353-424.

LOW-ALTITUDE AVIRIS DATA FOR MAPPING LANDFORM TYPES ON WEST SHIP ISLAND, MISSISSIPPI

Joseph P. Spruce,[1] Ervin G. Otvos,[2] and Marco J. Giardino[3]

1. INTRODUCTION

Barrier islands help protect the southern and southeastern U.S. shoreline from hurricanes and severe storms. They are important for coastal resource management and geologic research, especially in studies that involve changes in island areas and surface environments, and they display a dynamically changing and diverse mix of landform and vegetative cover habitats. Many Gulf Coast barrier islands have undergone dramatic decreases in areal extent, often due to hurricane and severe storm damage. For example, Louisiana's barrier islands have lost 55 percent of their surface area over the past 100 years (Williams et al., 1992; Louisiana Department of Natural Resources, 1998).

Aerial photography and Landsat data have been used to monitor changes in barrier island areal extent, although neither data source is optimal for making maps of detailed landform types at site-specific scales. High-spatial-resolution hyperspectral imagery, such as that obtained from the high-spatial-resolution Airborne Visible/Infrared Imaging Spectrometer (AVIRIS) sensor, may enable improved mapping of landform types, which would benefit studies of the dynamics of barrier island environments.

During the summers of 2000 and 2001, a study was conducted to assess low-altitude AVIRIS data for mapping the landform types of West Ship Island, a barrier island in Harrison County, Mississippi (Figure 1). Otvos et al. (2001) submitted an internal report on this work to the National Aeronautics and Space Administration (NASA). This study area was selected because of the availability of low-altitude AVIRIS data acquired on July 22, 1999, and because of the area's accessibility to the investigating team. West Ship Island is one of six barrier islands that belong to the Gulf Shores National Seashore, which is managed by the National Park Service. This island contains an impressive range of landform categories. Surface types include beach, dune, and sand flat environments (Otvos, 1995; Otvos et al., 2001). West Ship Island also harbors Fort Massachusetts, a historic fort used during the Civil War. Because it is located near Stennis Space Center, the island is frequently imaged by NASA's airborne and spaceborne sensors.

West Ship Island was formed when Hurricane Camille split the former Ship Island in half on August 17, 1969. Between 1849 to 1974, Ship Island lost 463 acres due to segmentation and shoreline erosion. As of 1991, West Ship Island was about 3.5 miles long by 0.4 miles wide and 555 acres in extent (Otvos et al., 2001). West Ship Island further diminished in size in 1998 when erosion caused by Hurricane Georges decreased the island area to about 468 acres (Schmid, 2001). At the same time, East Ship Island was temporarily split into two segments (Otvos et al., 2001; Schmid, 2001). Otvos (1981; 1995) provides much additional information on island formation processes for Ship Island and related barrier islands along the Mississippi Sound.

2. RATIONALE FOR RESEARCH

Aerial photography is frequently used in geomorphologic mapping, including the mapping of coastal landforms (Way and Everett, 1997). Aerial photography is a standard data source for wetland mapping for the U.S. National Wetland Inventory. Landsat data have been used for monitoring change compared to pre-existing wetland maps (Wilen and Smith, 1996; Tiner, 1997; Koeln and Bissonnette, 2000). Aerial photography is also used for mapping general vegetative cover types of barrier islands (e.g., Army Corp of Engineers, 1981; Tiner, 1997; Torres-Pulliza et al., 2002). In addition, aerial photography is frequently employed to map shoreline change (e.g., Gorman

[1] Lockheed Martin Space Operations – Stennis Programs, John C. Stennis Space Center, Joseph.Spruce@ssc.nasa.gov
[2] University of Southern Mississippi, Gulf Coast Research Laboratory, ervin.otvos@usm.edu
[3] NASA Earth Science Applications Directorate, Marco.Giardino@ssc.nasa.gov

et al., 1998), although some scientists have used Landsat data to assess shoreline and/or wetland change at regional scales (e.g., Dobson et al., 1995; Wilen and Smith, 1996; Tiner, 1997; Shao et al., 1998; Koeln and Bissonnette, 2000).

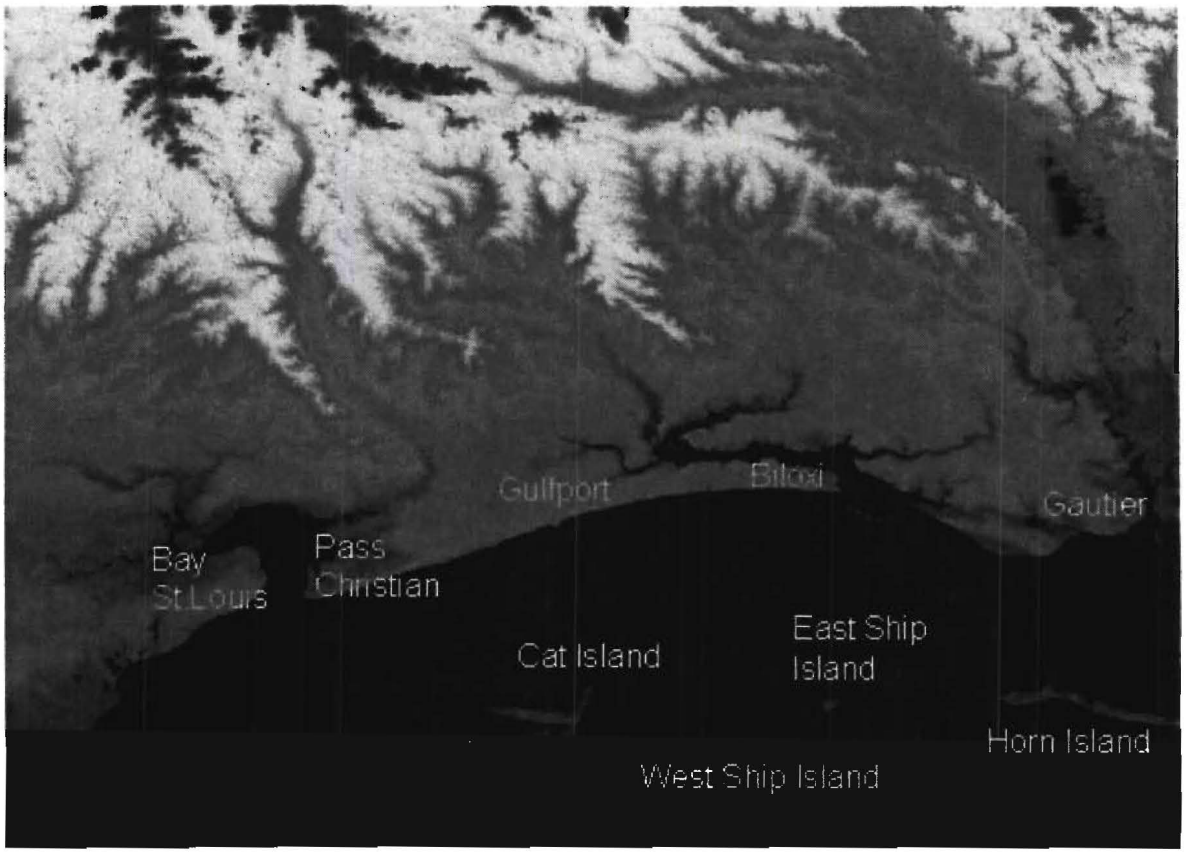

Figure 1. Oblique View of U.S. Geological Survey 30-Meter Digital Elevation Model for Mississippi Gulf Coast Showing Study Area Location

While aerial photography is commonly used in coastal wetland studies, it is not without its shortcomings (Wilen and Smith, 1996; Tiner, 1997). For example, the use of aerial photography for accurate mapping of land cover categories requires a trained analyst to interpret and delineate cover types, usually stereoscopically. This process is highly subjective and time-consuming and can be confounded by poor contrast between spectrally similar features. In many cases, panchromatic, true color, or color infrared aerial photographs provide insufficient contrast for identifying spectrally similar cover types, especially monoscopically, and often even with stereoscopic viewing. Hyperspectral remote sensing offers an alternative method that can be more automated and less subjective in that the analyst does not have to delineate and identify each polygonal surface cover feature.

With numerous narrow contiguous bands recording visible through short-wave reflective infrared energy, airborne hyperspectral imagery, such as AVIRIS, can be useful in separating spectrally similar cover types. However, detection can depend on data quality, on reference training data, and on processing technique. More recently, hyperspectral remote sensing has been tested for improving maps and for assessing coastal habitats (e.g., Bachman et al., 2001; Donato et al., 2001; Garcia and Ustin, 2001; Neuenschwander et al., 1998; Ustin, 2001). Ustin (2001) and Bachman et al. (2001) have mapped invasive plants in coastal environments with some success. Carter and Young (1993) conducted hyperspectral analyses of stressed vegetation on a barrier island.

A few of the hyperspectral studies were in regard to classifications of barrier island environments (Bachman et al., 2001; Donato et al., 2001; Neuenschwander et al., 1998), although none employed low-altitude

hyperspectral data for mapping landforms. The study by Neuenschwander et al. (1998) applied high-altitude AVIRIS data with 20-meter spatial resolution to produce highly accurate coastal land cover maps of Kennedy Space Center. Neuenschwander et al. (1998) reported that the best map produced from AVIRIS data used the 13 most signal-rich minimum noise fraction bands, subjected to a supervised neural net classifier. This map contained seven upland and five wetland categories with an overall accuracy of 93.5 percent. The results provided some indication that low-altitude AVIRIS data of 3.4-meter spatial resolution could produce high-quality maps of landform types over West Ship Island.

Depending on the data type, the use of low-altitude, high-spatial-resolution airborne sensor data can enable smaller minimum mapping units as well as more detailed maps of island landforms, vegetative communities, and elevation. This study utilized the high spatial resolution of low-altitude hyperspectral and multispectral imagery for mapping barrier island landform types and also employed digital terrain models for mapping landform elevation.

3. GEOSPATIAL DATA ACQUISITION

A wealth of remote sensing and other geospatial data exists for West Ship Island, mostly originating from Federal and State agency sources. Several remote sensing datasets were downloaded from NASA's data archive for use in the study, including 1) low-altitude AVIRIS hyperspectral imagery acquired July 29, 1999, at 3.4-m ground sampling distance (GSD); 2) Airborne Data Acquisition and Registration (ADAR) multispectral imagery acquired November 9, 1997, at 0.5-m GSD; and 3) Star-3*i* Digital Terrain Map data acquired November 11, 1999, at 10-m GSD. The ADAR and Star-3*i* datasets were acquired by NASA as part of the Scientific Data Purchase program from Positive Systems, Inc., and Intermap, respectively.

Additional geospatial datasets were acquired for use in a reference capacity, including 1) digital orthophoto quarter quadrangle (DOQQ) imagery acquired by the U.S. Geological Survey (USGS) on January 11, 1997, and produced at 1-m spatial resolution; 2) Digital National Wetland Inventory map; 3) 1:24,000 scale USGS digital raster graphic topographic map; and 4) field survey data collected August 2, 2001, in the form of locations determined with a Global Positioning System receiver, with digital handheld photography, and with field-annotated hardcopies of remote sensing imagery and related mapping products.

4. MAPPING METHODS

The AVIRIS and Star-3*i* data came as preregistered segments, whereas the ADAR imagery was in the form of seven nonregistered frames of image data. The AVIRIS, ADAR, and Star-3*i* data were subsequently mosaicked to provide complete coverage of the island. Doing so was straightforward for the AVIRIS and Star-3*i* data but required additional image-to-image coregistration of ADAR data frames prior to mosaicking. Once mosaicked, the path-oriented AVIRIS mosaic was atmospherically corrected with Atmosphere Removal (ATREM) Program software (Gao et al., 1993), which outputs data scaled to apparent ground reflectance. Insufficient information was available for atmospheric correction of the ADAR data. The data were scaled in terms of raw digital numbers. Analysts later georeferenced the AVIRIS and ADAR data to fit the Universal Transverse Mercator map projection (WGS84 spheroid and datum). Doing so required use of USGS DOQQ data as reference data for selecting ground control points (GCPs). The AVIRIS data was georeferenced with a second order polynomial fit, 52 GCPs, and a +/- 3.4-m root mean square error (RMSE). The ADAR data needed additional effort to georeference, requiring a fourth order polynomial fit, 195 GCPs, and +/- 3.7-m RMSE.

The AVIRIS datasets were then classified into cluster classes, using the unsupervised Iterative Self-Organizing Data Analysis Technique (ISODATA) clustering algorithm resident to ERDAS IMAGINE software. This approach was selected because it requires much less information for effective application in comparison to the supervised method. The latter approach puts the burden on the analyst to derive spectral training statistics (i.e., signatures) for segmenting the landscape into discrete land cover types. When the study began, the research team knew of the landforms that occur in the study area but was largely unaware of the spectral variability of these features; consequently, the unsupervised approach was selected. In doing so, each ISODATA classification run was performed by using 50 iterations, 99 percent convergence between iterations, cluster means initialization along the first principal component axis, automatic scaling, and sampling of every pixel.

Classification was performed on a subset of AVIRIS bands rather than on the entire spectrum of 224 bands. In particular, the AVIRIS data cube was subset into a file of 15 select bands (Table 1). The selected bands appeared to offer comparatively high spectral separability between common land and water surface cover types. Analysts assessed spectral signature separability across bands by visualizing and interpreting AVIRIS-based spectral signatures for several upland and wetland forest, shrub, grass, barren, and water surface types using AVIRIS data from a previous study described by Spruce (2001) and Spruce et al. (2001). ISODATA classifications of land cover can be quite effective with quality multispectral datasets of 15 bands or less. The use of 15 select AVIRIS bands was expected to result in a similar if not better classification, especially if the bands had high spectral contrast between land cover types of interest and acceptable signal resolution.

Table 1. Bands of AVIRIS Data Selected for Classification

1	15	508.02	Left side of green
2	20	557.14	Green peak
3	32	675	Red absorption well
4	35	673.25	Red absorption well
5	36	682.79	Lower part of red edge
6	45	768.66	Upper part of red edge
7	56	873.67	NIR plateau, left side
8	66	974.58	NIR plateau, right side
9	77	1078.06	NIR, transition to SWIR
10	91	1209.73	NIR, transition to SWIR
11	102	1305.43	NIR, transition to SWIR
12	137	1654.04	SWIR-1 (Landsat TM 5)
13	194	2211.8	SWIR-2 (Landsat TM 7)
14	204	2311.49	SWIR-2
15	212	2391.06	SWIR-2

NIR = near-infrared
SWIR = short-wave infrared

The AVIRIS data were classified initially into 20 clusters, which analysts subsequently recoded into a binary mask containing land and water categories. Additional masking techniques were then employed to isolate the raw data obtained from the land cover. The masked raw data was then reclassified with ISODATA cluster busting (Jensen, 1996) into 30 cluster classes. These classes were described and assigned to apparent landform types by an experienced coastal geomorphologist.

Unsupervised classification proceeded similarly for ADAR multispectral data, except that it was based on four broad multispectral bands in the visible/near-infrared portion of the electromagnetic spectrum. Only one classification was performed on the ADAR data and no attempt was made to reclassify the raw data corresponding to the land features, because the 1997 ADAR data were believed to be out of date because of the land cover change caused by Hurricane Georges in 1998. Fortunately, the AVIRIS data collection occurred after Hurricane Georges and the island had suffered no subsequent hurricane damage. Consequently, more effort went into developing the AVIRIS classifications.

The Star-3*i* digital terrain model was used to create a shaded relief map for the island. This was a trial and error process because of the subtlety of the terrain, over which vertical microtopographic differences of 0.5 feet might result in different landform and/or vegetation type. The local relief was not apparent on the shaded relief map until the elevation height was stretched 25 times in the "Z." This information was subsequently utilized in refining the AVIRIS and ADAR classifications.

Hardcopies of resulting landform maps and remote sensing imagery were produced for field validation on August 2, 2001. The field survey occurred about two years after AVIRIS data collection. Land cover changes were evident in the lowest lying areas. Approximately 70 percent of the island area was visited during the survey and many points of interest were noted on hardcopy imagery and maps for subsequent entry into a GIS-based coverage. Handheld photography was taken at each point of interest. GPS locations were also collected for areas that were difficult to locate on hardcopy imagery and maps.

The field survey data were then used to refine descriptions of cluster classes on the AVIRIS and ADAR classifications. Publications by Duncan and Duncan (1987) and by Tiner (1993) were consulted in describing vegetation-dominated landforms. Work by Otvos (1995) and Godfrey (1976) were also used in developing class descriptions.

5. PRELIMINARY ANALYSIS OF RESULTS

Figure 2 shows a low-altitude AVIRIS Red, Green, Blue (RGB) composite image that has been enhanced with the raw data for the land stretched independently of the raw data for the water using masking techniques to isolate the raw data for the land cover and water features, respectively. The enhancement enabled clear visualization of the comparatively sparse vegetation in the beach and dune zones of the island perimeter. This enhancement is an important tool in assessing the AVIRIS landform classification shown in Figure 3. This figure also provides a map legend and summarizes the areal extent of each cluster class. This preliminary map displays all of the common landforms on the island. Both the island perimeter and the interior include numerous landform and environment categories.

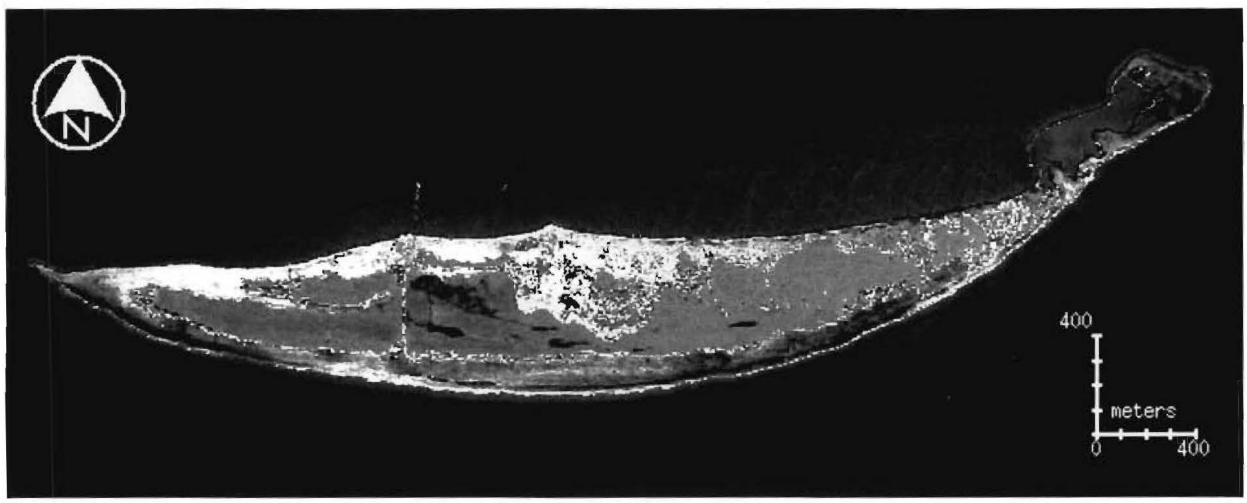

Figure 2. AVIRIS Color Composite Image of Study Area with Bands 56 (873 nm), 32 (675 nm), and 20 (557 nm) Assigned to RGB

Based on comparisons to AVIRIS imagery and field checks, the AVIRIS map of the island exterior clearly separates the foreshore and backshore environments. The island perimeter includes several landform classes with bare sand and with sand covered by various types of sparse vegetation. Among the foreshore sand cover categories, the AVIRIS map distinguishes between bright siliceous, slightly calcareous sand that occurs mainly on the Mississippi Sound side and dark sand concentrates of heavy minerals found commonly on the Gulf beaches. For the backshore, the AVIRIS map shows barren sand flats as well as partially vegetated dunes containing pioneering herbaceous vegetation, low shrubs, or xeric grasses. Although sand cover types usually occur predominantly on the beach, sand sheets created by storm overwash and eolian blow out extend from the north shore southward to the island interior in some areas. Major eolian sand accumulations can also be found near Fort Massachusetts.

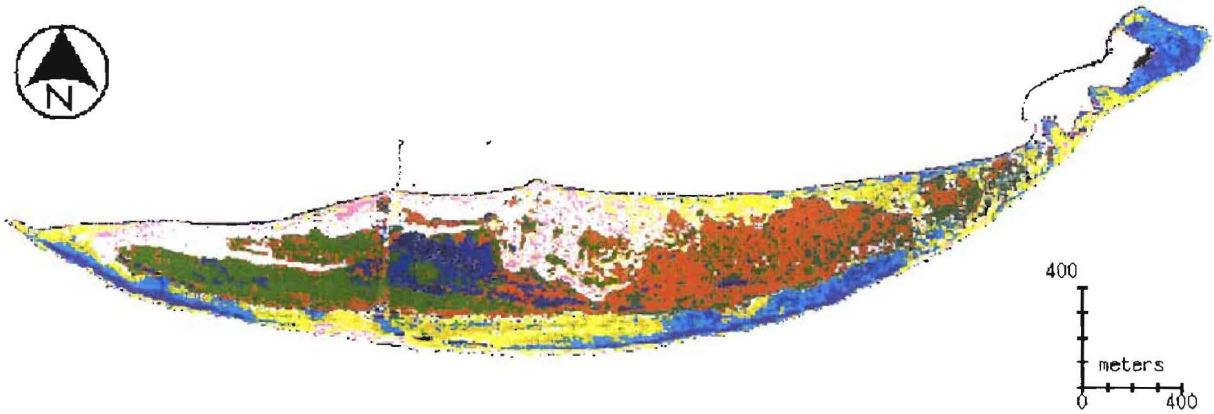

Color	Cluster #	Acres	Landform	Land Cover
	1	7.4	beach on Sound side	moist sand
	2	3.7	foreshore on Sound side	wet sand
	3	5.0	interior flat	lowest marsh
	4	13.5	interior flat	high marsh
	5	45.1	interior sheet	moist grassland
	6	1.6	beach	moist sand
	7	29.1	interior sheet, ridge	marsh
	8	63.1	interior flat	shrub/scrub
	9	28.5	interior flat	marsh
	10	15.8	interior flat	disturbed edge vegetation
	11	11.8	backshore flat on Gulf side	sand
	12	16.1	backshore flat	sand
	13	17.3	exterior flat, spit	sand
	14	1.6	exterior flat	sand
	15	10.8	interior patch	disturbed edge vegetation
	16	16.0	backshore flat	sand
	17	11.1	dune patch	sparse, disturbed vegetation
	18	9.3	interdune or dune flat	sparse vegetation and sand
	19	16.4	exterior flat, spit	sand
	20	18.5	backshore flat	wet sand
	21	12.6	dune flats	sparse vegetation and sand
	22	19.1	beach flat, some on cuspate spit	sand
	23	11.6	dune flats	sparse vegetation and sand
	24	15.9	backshore flat, dune ridge - on Gulf side	sand
	25	13.7	exterior flat, minor amounts on spit	sand
	26	10.9	dune patch - small areas	sparse vegetation and sand
	27	17.0	backshore sheet - interridge location	sand
	28	12.1	dune patch - small areas	sparse vegetation and sand
	29	20.6	high backshore sheet, parabolic dunes	sand
	30	17.5	backshore sheet - moderately high	sand

Figure 3. AVIRIS Classification of Landform Type

The AVIRIS classification of the island interior identifies many land cover types. Several vegetation categories were identified mainly on the interior sand flats, including various types of marsh dominated by sedges and rushes. Grassland, shrub/scrub, very low-forested swamp, shallow ponds occurring in swales between old beach ridges, and a few small patches of slash pine forest were among the surface cover categories. The interior also included beach ridges, indicative of ancient island shoreline positions and the dynamic nature of barrier island changes. Such landforms of the island interior can be viewed on the Star-3*i* shaded relief map (Figure 4). The shrub/scrub type often grows on the higher ground, including relict beach ridges and the higher sand sheet surfaces. In this case, land cover type is not necessarily the same as landform. Land cover on the island is in part affected by the site conditions: wetness, salinity, tidal influence, and level of disturbance. However, at least for the island interior, the same vegetation type can occur on multiple landforms that are of interest to coastal geomorphologists.

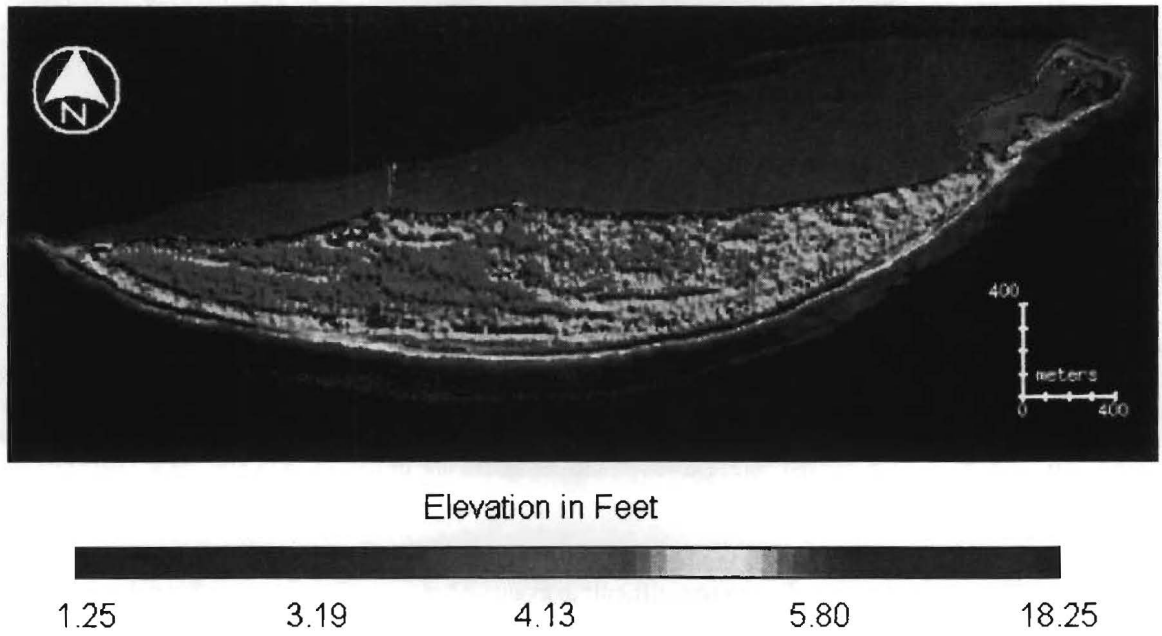

Figure 4. Hillshaded Digital Terrain Model Derived from Star-3*i* Radar Data and Draped Over AVIRIS RGB Shown in Figure 2

The field survey enabled common landforms and cover types evident on the AVIRIS classification to be visited and documented for further research. These field checks indicated that the AVIRIS color composite imagery displays island landforms: foreshore, backshore, vegetated dunes, and island interior zones. The AVIRIS classification does not distinguish between backshore and dune landforms when covered by dry bright sand and does not show interior vegetated beach ridges as a distinct landform type. The AVIRIS map is a consistent and reliable predictor of common cover types as compared to field checks. However, rare cover types, such as the relict pine forest, were not uniquely identified. Some of the sparsely vegetated dunes appeared to be misclassified as barren sand types. Such problems can be addressed through additional cluster busting techniques as described by Jensen (1996) and Spruce (2001). The field survey also confirmed the finding of Schmid (2001) that Hurricane Georges resulted in significant land cover change. These changes made it difficult to evaluate the landform classification produced from the 1997 ADAR multispectral dataset. However, certain areas showed only minor land cover change. In those areas one could use hardcopies of ADAR color composite imagery in the field. These image maps were especially useful in locating the few small patches of remnant pine forest that were difficult to see on the AVIRIS color composites because of the coarser spatial resolution.

The research focused on the mapping of landforms in the intertidal zone and higher terrestrial landform environments of the island. It was difficult to map land cover in more specific terms because of the lack of timely *in*

situ data on vegetation community distributions, especially in the marshlands. The dynamic nature of barrier island environments made it impractical to map specific plant communities, particularly in the marshy island interior. Marsh cover type distributions did not correspond well with the field survey, largely because of the 2-year time difference between the AVIRIS data collection and the field survey. No attempt was made to map subtidal geomorphologic environments using the AVIRIS data. A quantitative accuracy assessment of the AVIRIS landform classification is underway and will be reported at a later date.

6. CONCLUDING REMARKS

Preliminary results suggest that low-altitude AVIRIS data can be effective for mapping landform-specific environments of both the island's exterior and interior. In particular, the AVIRIS classification enabled multiple cover types to be identified on the beaches and dunes on the island's exterior. AVIRIS classification also enabled mapping of multiple environments (i.e., cover types) in the island's interior, including vegetated land cover types occupying relict beach ridges, inter-ridge swales, and sand flats. The AVIRIS classification did not always clearly identify all landforms in specific terms. However, this classification supplied a great deal of information on land cover associated with barrier island landforms.

The unsupervised classification method employed in this study appeared to be effective, although refinement and perhaps other techniques would be needed to identify land cover types in more specific terms. While the band selection approach worked, in retrospect it would have been better to include a blue band for classification and for AVIRIS color composite screen displays.

The Star-3*i* digital terrain model was useful for aiding the assessment of the AVIRIS classification as it enabled viewing of the subtle island interior landforms (e.g., ancient beach ridges) that were difficult to see on the AVIRIS imagery. Its 10-meter spatial resolution was not optimal for this task, although it was much better than the alternative 30-meter USGS Digital Elevation Model. The current landform map of West Ship Island could perhaps be improved by using a much higher-spatial-resolution digital elevation map than the Star-3*i* product in conjunction with the AVIRIS classification discussed here. However, the combined use of the AVIRIS and Star-3*i* data could also enable a better landform map to be produced.

Hardcopies of the 0.5-meter ADAR multispectral imagery were effective in aiding the field survey. However, the classification of the ADAR data was difficult to evaluate because of hurricane-induced land cover changes that had impacted the island after the ADAR data were acquired. Despite this shortcoming, the ADAR data did provide general information on land cover types and a useful estimate of the areal extent of the island prior to Hurricane Georges.

This study enabled assessment of low-altitude AVIRIS data for mapping landform environments of barrier islands in the Gulf Coast region of the United States. Based on initial results, high-spatial-resolution hyperspectral imagery, such as AVIRIS, appears to be a useful tool for mapping the landform and land cover of barrier island and other coastal environments. Additional work is underway to confirm these preliminary observations.

7. ACKNOWLEDGEMENTS

This work was supported by the NASA Earth Science Applications Directorate under contract number NAS 13-650 at the John C. Stennis Space Center, Mississippi.

8. REFERENCES

Army Corp of Engineers, 1981, Recommended Scales of Aerial Photography for Mapping Barrier Island Vegetation, Coastal Engineering Technical Note, USACE Technical Report TN-V-8, January 1981, 2 pp. Also online [accessed 27 August 2002]: http://chl.wes.army.mil/library/publications/chetn/pdf/cetn-v8.pdf.

Bachman, C. M., T. F. Donato, K. Dubois, R. A. Fusina, M. Bettenhausen, J. H. Porter, and B. R. Truitt, 2001, "Automatic Detection of Invasive Plant Species on a Barrier Island in the Virginia Coastal Reserve Using HYMAP and IKONOS Data," Proceedings for IGARSS 2001, CD-ROM, 3 pp.

Carter, G. A., and D. R. Young, 1993, "Foliar Spectral Reflectance and Plant Stress on a Barrier Island," Int. J. Plant Sci., vol. 154, pp. 298-305.

Dobson, J., E. A. Bright, R. L. Ferguson, D. W. Field, L. L. Wood, K. D. Haddad, H. Iredale III, J. R. Jensen, V. V. Klemas, R. J. Orth, and J. P. Thomas, 1995, NOAA Coastal Change Analysis Program (C-CAP): Guidance for Regional Implementation, NOAA Technical Report NMFS 123, U.S. Department of Commerce, April 1995. Also online [accessed 14 September 2002]: http://www.csc.noaa.gov/crs/lca/protocol.html.

Donato, T. M., C. M. Bachman, and R. A. Fusina, 2001, "High Resolution Remote Sensing Observations at the Virginia Coastal Reserve Long-Term Ecological Site," Proceedings for IGARSS 2001, CD-ROM, 3 pp.

Duncan, W. H., and M. B. Duncan, 1987, The Smithsonian Guide Seaside Plants of the Gulf and Atlantic Coasts from Louisiana to Massachusetts, Exclusive of Lower Peninsula Florida, Smithsonian Institution Press, 409 pp.

Gao, B., K. Heidebrecht, and A. Goetz, 1993, "Derivation of Scale Surface Reflectances from AVIRIS Data," Remote Sens. Environ., vol. 44, pp. 165-178.

Garcia, M., and S. L. Ustin, 2001, "Detection of Interannual Vegetation Responses to Climatic Variability Using AVIRIS Data in a Coastal Savanna in California," IEEE Transactions of Geoscience and Remote Sensing, vol. 39, no. 7., pp. 1480-1490.

Godfrey, P. J., 1976, "Barrier Island of the East Coast," Oceanus, vol. 19, no. 5, pp. 27-40.

Gorman, L., A. Morang, and R. Larson, 1998, "Monitoring the Coastal Environment; Part IV: Mapping, Shoreline Changes, and Bathymetric Analysis," J. Coastal Res., vol. 14, no. 1, pp. 61–92.

Jensen, J. R., 1996, Introductory Digital Image Processing: A Remote Sensing Perspective, Prentice-Hall, Inc., 231 pp.

Koeln, G., and J. Bissonnette, 2000, "Cross-Correlation Analysis: Mapping Land Cover Change with a Historic Land Cover Database and a Recent, Single-Date Multispectral Image," Proc. 2000 ASPRS Annual Convention, Washington, D.C. Also online [accessed 18 June 2002]: http://www.glc.org/monitoring/wetlands/subcommittees/CCA_Paper.doc.

Louisiana Department of Natural Resources, 1998, Coast 2050: Toward a Sustainable Coastal Louisiana, Louisiana Coastal Wetlands Conservation and Restoration Task Force and the Wetlands Conservation and Restoration Authority, Baton Rouge, Louisiana, 161 pp. Also online [accessed 27 August 2002]: http://www.coast2050.gov/report.pdf.

Neuenschwander, A. L., M. M. Crawford, and M. J. Provancha, 1998, "Mapping of Coastal Wetlands via Hyperspectral AVIRIS Data," Proceedings of the 1998 International Geoscience and Remote Sensing Symposium, Seattle, Washington, July 6-10, 1998, pp. 189-191.

Otvos, E. G., 1981, "Barrier Island Evolution and History of Migration, North Central Gulf," Mar. Geol., vol. 43, pp. 195-243.

Otvos, E. G., 1995, "Coastal Field Trip: New Orleans, Louisiana to Pensacola Beach, Florida," Geological Society of America Annual Meeting, Field Trip Guidebook No. 4, pp. 95-128.

Otvos, E. G., J. P. Spruce, and M. J. Giardino, 2001, Remote-Sensing Mapping of West Ship Island Surface Environments, Coastal Mississippi, Final Report Submitted to NASA Summer Faculty Program, Stennis Space Center, Mississippi, 19 pp.

Schmid, K., 2001, West Ship Island Evolution, Morphology, and Hurricane Response – 1995 to 2000, Mississippi Department of Environmental Quality, Office of Geology, Open File Report 133, 36 pp.

Shao, G., D. R. Young, J. H. Porter, and B. P. Hayden, 1998, "An Integration of Remote Sensing and GIS to Examine the Responses of Shrub Thicket Distributions to Shoreline Changes on Barrier Islands," J. Coastal Res., vol. 14, pp. 299-307.

Spruce, J. P., 2001, "Low-Altitude AVIRIS Data for Mapping Land Cover in Yellowstone National Park: Use of ISODATA Clustering Techniques," Proceedings of the Tenth JPL Airborne Earth Science Workshop, February 27-March 2, Jet Propulsion Laboratory, Pasadena, California, pp. 387-396. Also online [accessed 2 September 2002]: http://popo.jpl.nasa.gov/docs/workshops/01_docs/2001Spruce_web.pdf.

Spruce, J. P., A. S. Warner, and G. Terrie, 2001, "Development of Ground Reference GIS for Assessing Land Cover Maps of Northeast Yellowstone National Park," Poster, 2001 ESRI Conference, San Diego, California.

Tiner, R. W., 1993, Field Guide to Coastal Wetland Plants of the Southeastern United States, University of Massachusetts Press, 329 pp.

Tiner, R., 1997, Identifying and Monitoring Wetlands, In: Manual of Photographic Interpretation, second edition, W. R. Phillipson (ed.), ASPRS, Bethesda, Maryland, pp. 475-494.

Torres-Pulliza, D., J. Brock, C. Lea, and M. Duffy, 2002, "Classification of Barrier Island Land Cover Using Aerial Photography and Lidar Airborne Remote Sensing," Proceedings of the 5th International Airborne Remote Sensing Conference and Exhibition, Miami, Florida, Ann Arbor, Michigan, CD-ROM, 8 pp.

Ustin, S., 2001, "Hyperspectral Techniques for Identification of Invasive Weeds," Poster, Proceedings of 2001 Strategic Environmental Research and Development Program Symposium. Also online [accessed 2 September 2002]: poster at http://www.serdp.org/symposiums/2001/presentations/2C-Ustin.pdf and abstract at http://www.serdp.org/symposiums/2001/PosterAbstracts.pdf.

Way, D. S., and J. R. Everett, 1997, Landforms and Geology, In: Manual of Photographic Interpretation, second edition, W. R. Phillipson (ed.), ASPRS, Bethesda, Maryland, pp. 117-165.

Wilen, W., and G. Smith, 1996, "Assessment of Remote Sensing/GIS Technologies to Improve National Wetlands Inventory Maps," Proceedings of the Sixth Biennial Remote Sensing Conference, April 29-May 3, Denver, Colorado, pp. 50-64.

Williams, S. J., S. Penland, and A. H. Sallenger, Jr. (eds.), 1992, Louisiana Barrier Island Erosion Study: Atlas of Shoreline Changes in Louisiana from 1853 to 1989, U.S. Geological Survey and Louisiana Geological Survey, 103 pp.

Mineral Mapping Mauna Kea and Mauna Loa Shield Volcanos on Hawaii Using AVIRIS Data and the USGS Tetracorder Spectral Identification System: Lessons Applicable to the Search for Relict Martian Hydrothermal Systems

Gregg A. Swayze,[1] Roger N. Clark,[1] Stephen J. Sutley,[1] Carol A. Gent,[1] Barnaby W. Rockwell,[1] Diana L. Blaney,[2] James L. Post,[3] and Brian P. Farm[4]

INTRODUCTION

The Hawaiian AVIRIS campaign conducted during the spring of 2000 provided an opportunity to collect hyperspectral data over a unique geologic environment on the sides of two of the Earth's largest shield volcanos. High altitude AVIRIS data were collected on April 14, 2000 along a 75 km NE traverse passing over the summits of Mauna Kea (4205 m) and Mauna Loa (4064 m) encompassing the saddle (1940 m) between them. This traverse covers diverse climatic and ecological zones extending from tropical coastal forests to alpine tundra over an elevation range of 3200 m. The summits of both volcanos are among the highest and driest readily accessible areas in the world with the summit of Mauna Kea chosen as the site for the largest collection of telescopic observatories in the world. In the cool-dry atmosphere atop these shield volcanos, rocks are nearly devoid of macroscopic life and chemical weathering is relatively low. These extreme climatic conditions and extensive basalt outcrops combine to form one of the best terrestrial analogues to the Martian shield volcanos. Several studies have suggested that certain palagonitic soils from Mauna Kea are good spectral analogues of Martian surface materials (Singer et al., 1979, Singer, 1982; Evans and Adams, 1979, 1980; Allen et al., 1981, 1982). Other studies suggest that hydrothermal systems may have been sanctuaries for ancient life on Mars (Walter et al., 1993; Farmer and DeMarais, 1994; Wade et al., 1999). Examples of relict hydrothermal systems exist at the summits of both Mauna Kea and Mauna Loa, and these areas were measured by AVIRIS as terrestrial analogues of the mineral associations and spatial extent of hydrothermal systems developed in mafic volcanic rocks.

VOLCANIC HISTORY OF THE BIG ISLAND

There are five distinct volcanos that grew and merged to form the Big Island of Hawaii. The loci of volcanism (Fig. 1) has shifted progressively southeastward over time reflecting the NW motion of the Pacific plate over the Hawaiian hot spot (Clague and Dalrymple, 1987). The most intense subaerial volcanic activity is now centered at the two southernmost volcanos, Mauna Loa and Kilauea. The youngest and smallest volcano in the Hawaiian chain is Loihi which is growing beneath the sea 30 km SE of the Big Island (Wolfe and Morris, 1996 and references therein). Ideally a Hawaiian shield volcano goes through four stages during it life: preshield, shield, postshield, and rejuvenation (Clague and Dalrymple, 1987, 1989). Accordingly, the preshield stage involves initial eruption of alkalic basalt, followed by the shield building stage eruption of tholeiitic basalts (low in alkalis), which eventually gives way to the postshield stage eruption of more SiO_2-rich alkali hawaiite lavas. The rejuvenated stage involves the eruption of SiO_2-poor lava after a few million years

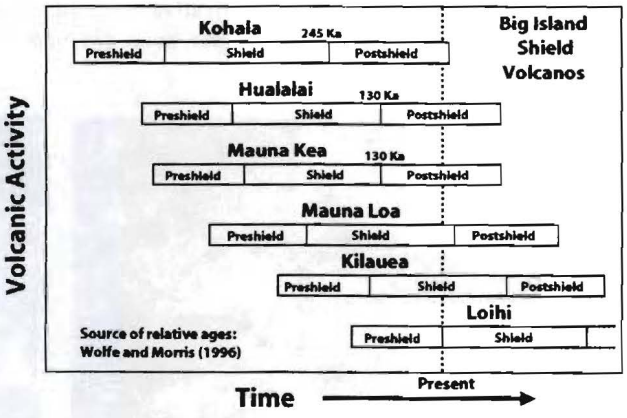

Figure 1. Growth stages of the Big Island shield volcanos.

[1]U.S. Geological Survey, MS964 Box 25046 DFC, Denver, Colorado 80225; gswayze@speclab.cr.usgs.gov
[2]Jet Propulsion Laboratory, 4800 Oak Grove Drive, Pasadena, California 91109
[3]Vector Engineering, Inc., 12438 Loma Rica Drive, Suite C, Grass Valley, California 95945
[4]Previously at the U.S. Geological Survey, Kilauea Volcanic Observatory, Hawaii

of quiescence, but no volcanos on the Big Island have reached this stage. Loihi is thought to be in transition from the preshield stage to the shield stage (Moore et al., 1982). Mauna Loa and Kilauea are in the shield building stage, which produces 95 to 98% of a volcano's volume (Wolfe and Morris, 1996) and typically lasts for about 500,000 years (Moore and Clague, 1992). Kohala, Hualalai, and Mauna Kea, being the oldest, are in the postshield stage and are capped by alkalic lavas. Shield volcanos grow from lava erupted at the summit of the volcano and from vents aligned along rift zones extending out from the summit, forming mountains elongated parallel to the rift zones (Wolfe et al., 1997). The Big Island has grown by addition of lavas to its SE flank and by seaward displacements along its active NE-trending rift zones. Mauna Loa has a fault-bounded caldera approximately 5 km in diameter (Fig. 2) which is a relatively recent feature only active for several centuries (Wolfe and Morris, 1996). Postshield eruptions transform broad, smoothly sloping shields into steeper, more irregularly-shaped edifices, by addition of more viscous lavas (Wolfe et al., 1997). The summit of Mauna Kea has numerous scoria cinder cones formed from the explosive eruption of more viscous and volatile-rich alkalic lavas typical of postshield volcanism.

Figure 2. View of Mokuaweoweo Caldera (looking SW) on the summit of Mauna Loa. Argillic alteration possibly produced by a small relict hydrothermal system is visible as a bleached area along the SW wall of the caldera.

IMAGING SPECTROSCOPY

Solar radiance, atmospheric absorptions, and scattering were removed from the AVIRIS data using the ATREM program (Gao et al., 1993). Artifacts from the ATREM processing were then removed by first subtracting a path radiance correction from the data and then multiplying by correction factors derived from field spectra of a ground calibration site using the method of Clark et al. (this volume). Because we were most interested in the geologic materials exposed near the summits of both volcanos, a calibration site at high elevation was chosen to minimize the effects of imperfect removal of atmospheric CO_2. Landsat 7 ETM+ data were analyzed and a spectrally bland, non-hydrothermally altered area was chosen as a field calibration site. Field spectral measurements of a relatively flat post-glacial alluvial fan deposit located near the summit of Mauna Kea at 4000 m and 0.45 km SE of the Puu Poliahu Cinder Cone were used to derive a multiplicative correction (Figs. 3 and 4). A total of 233 spectral measurements were collected with an ASD FR spectrometer, averaged, and corrected to absolute reflectance using a NIST traceable

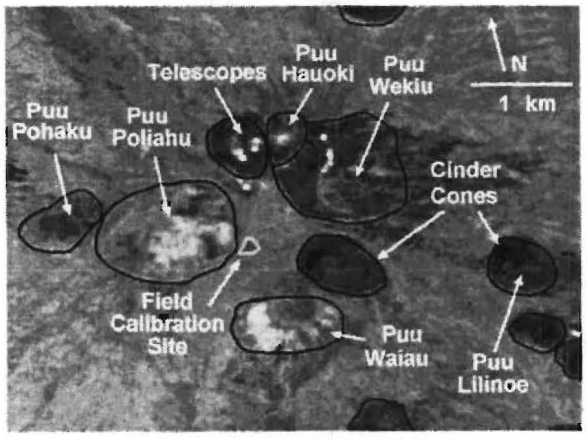

Figure 3. True color composite AVIRIS image of the summit of Mauna Kea. Cinder cones are circled in black and the field calibration site is circled in yellow. Strongly altered areas show up as bleached areas.

Figure 4. Collection of field calibration spectra at the base of the Puu Poliahu cinder cone near the summit of Mauna Kea. Erosion has exposed a zone of argillic alteration produced by a relict hydrothermal system seen as a bleached area.

spectralon reflectance correction. Shadowed areas below the SE margin of the Mauna Loa summit caldera (about 4000 m elevation) were used to derive a path radiance correction.

AVIRIS data calibrated to apparent reflectance were spectrally mapped using the USGS Tetracorder System (Clark et al., 2003). Tetracorder uses a modified least-squares band-shape fitting technique to spectrally identify materials and create maps of their distribution. The primary algorithm works by scaling a library spectrum to an observed spectrum using a modified least-squares solution to derive a numerical value called "*fit.*" The algorithm derives *fits* for all of the spectra in its library and selects the material with the highest *fit* as the best spectral match. Comparisons are done only in the wavelength regions of diagnostic absorptions. In most cases Tetracorder identifies the spectrally-dominant material in each spectral region (e.g. electronic and vibrational), but it is capable of identifying mixtures if representative spectra of those mixtures are added to its library. When Tetracorder identifies a material as spectrally dominant that material does not have to be pure, it can also be intimately or aerially mixed with other phases. Spectral dominance means the diagnostic absorptions of that material are the strongest features in a given spectral region and are not obscured beyond recognition by absorptions from other phases. Other parameters like *depth* and *fit*depth* are determined for each comparison, and if the highest *fit*, *depth*, or *fit*depth* falls below a threshold then *no match* is found and the observed spectrum is not identified. Mineral maps of the electronic (0.4 - 1.35 μm) and vibrational (1.35 - 2.5 μm) spectral regions were produced for the entire flight line.

DISCUSSION

Types of Alteration

Alteration of mafic volcanic rocks can occur in a number of ways: 1) pervasive supergene alteration caused by weathering and oxidation of minerals when they are exposed to atmospheric oxygen, 2) widespread deuteric alteration related to degassing of the host lava or alteration caused by interaction with meteoric water or the atmosphere during emplacement of hot lava, and 3) localized hydrothermal alteration caused by hot fluids that circulate along fractures or other conduits after extrusion of the lava. These processes create a continuum of alteration mineral associations superimposed on each other. Supergene alteration cause by weathering forms palagonitic soils nearly devoid of phyllosilicates but containing nanocrystalline ferric oxide and hematite (Morris et al., 2001). Dueteric alteration may also lead to the formation of palagonite and various Fe-minerals. Hydrothermal alteration can usually be recognized by the presence of characteristic mineral associations that vary depending on the chemistry and temperature of the fluids, and composition of the host rock (Guilbert and Park, 1986). The types of hydrothermal alteration present on Mauna Kea and Mauna Loa are characteristic of the argillic and advanced argillic associations formed when hot, sometimes acidic, fluids or vapors percolate up through cinder cones or along caldera walls leaching iron from host rocks leaving bleached zones rich in clays like kaolinite, montmorillonite, ferruginous smectite, saponite, and in a few places hydroxysulfates like alunite and jarosite (Table 1). Ugolini (1974) investigated the altered materials from the summit cinder cones and found evidence of montmorillonite and saponite formed during hydrothermal alteration due to influx of hypogene fluids causing Mg-enrichment of saponite relative to non-hydrothermally altered tephra.

Table 1. Generalized chemical formulas for some clays and hydroxysulfates discussed in this paper.

Montmorillonite	$(Na,Ca_{0.5})_{0.33}(Al,Fe^{3+},Mg)_2Si_4O_{10}(OH)_2 \cdot nH_2O$
Ferruginous smectite	$(Na,Ca_{0.5})_{0.33}(Al,Fe^{3+},Mg)_2(Si,Al)_4O_{10}(OH)_2 \cdot nH_2O$
Nontronite	$(Na,Ca_{0.5})_{0.33}(Fe^{3+})_2(Si,Al,Fe^{3+})_4O_{10}(OH)_2 \cdot nH_2O$
Saponite	$(Na,Ca_{0.5})_{0.33}(Fe^{2+},Fe^{3+},Mg)_3(Si,Al)_4O_{10}(OH)_2 \cdot nH_2O$
Kaolinite	$Al_2Si_2O_5(OH)_4$
Alunite	$(Na,K,H_3O)Al_3(SO_4)_2(OH)_6$
Jarosite	$(Na,K,H_3O)Fe_3(SO_4)_2(OH)_6$

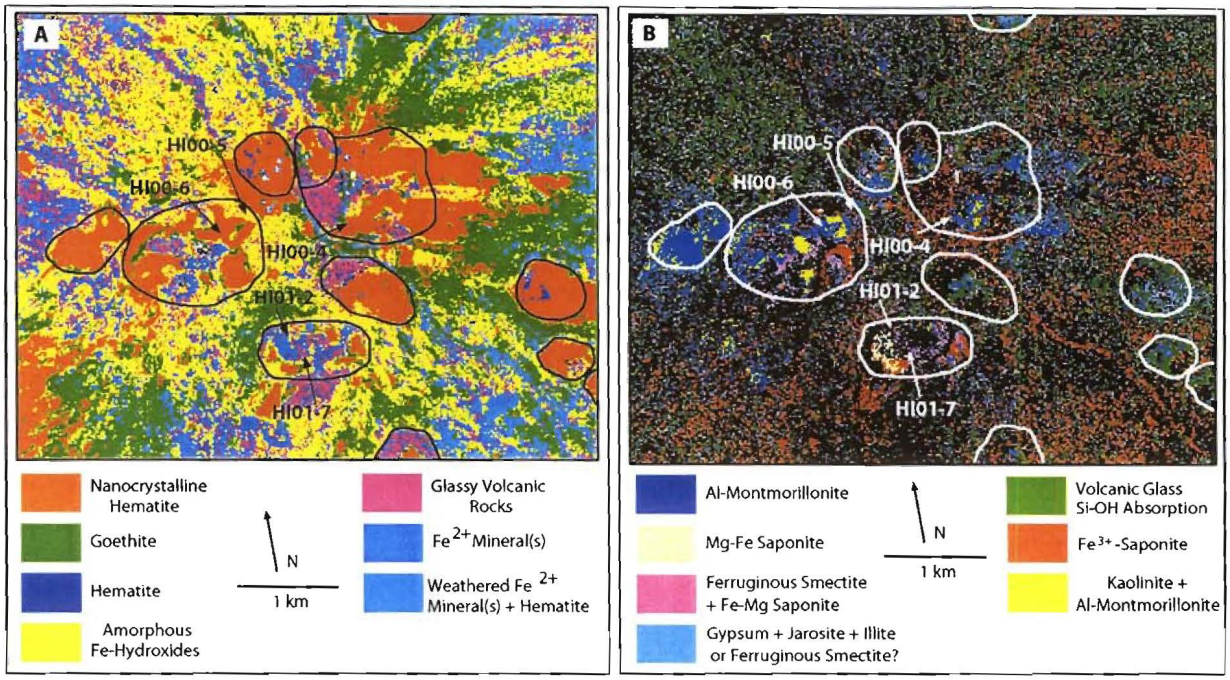

Figure 5. A) Electronic region (0.4 - 1.35 μm) minerals on the summit of Mauna Kea. Cinder cones are outlined in black. Arrows show collection locations of samples. B) Vibrational region (1.35 - 2.5 μm) minerals on the summit of Mauna Kea. Cinder cones are outlined in white.

Mauna Kea Mineral Maps

Five hydrothermally altered cinder cones were identified at the summit of Mauna Kea: Puu Pohaku, Puu Poliahu, Puu Hauoki, Puu Wekiu, and Puu Waiau. Formation of the Puu Waiau (107 ka) and Puu Poliahu (53 ka) cinder cones during the Pleistocene was subaerial and not subglacial as once believed with their once cone-like profiles rounded by subsequent glacial erosion (Wolfe et al., 1997). Alteration occurred during or soon after the eruptions that formed the cones. The mineral map of the electronic region shows that the cinder cone hydrothermal alteration is characterized by nanocrystalline hematite, hematite, goethite, and amorphous Fe-minerals in this spectral region (Fig. 5A). The hydrothermally altered cinder cones have the same types of Fe-minerals as non-hydrothermally altered cones and surrounding lava flows, therefore in this case Fe-mineralogy determined by AVIRIS cannot be used to distinguish between alteration as a result of supergene oxidation due to weathering and oxidation due to interaction with hydrothermal fluids.

The mineral map of the vibrational region shows the distribution of the alteration minerals more clearly. The hydrothermal alteration is characterized by zones of spectrally dominant kaolinite, Al-montmorillonite, ferruginous smectite, and saponite (Fig. 5B). The task of interpreting the relative positions of these mineral zones is made difficult because the alteration zones have been variably exposed by erosional dissection of the original cinder cone topography. Figure 6 shows a very generalized model of the relative sequence of spectrally determined mineral zones. Kaolinite + Al-montmorillonite alteration is limited in extent while the other alteration minerals are more widespread within the areas of hydrothermal alteration. The Al-montmorillonite zones (blue) usually enclose smaller kaolinite + Al-montmorillonite zones (yellow), and are themselves bordered, in places, by ferruginous smectite + Fe-Mg saponite zones

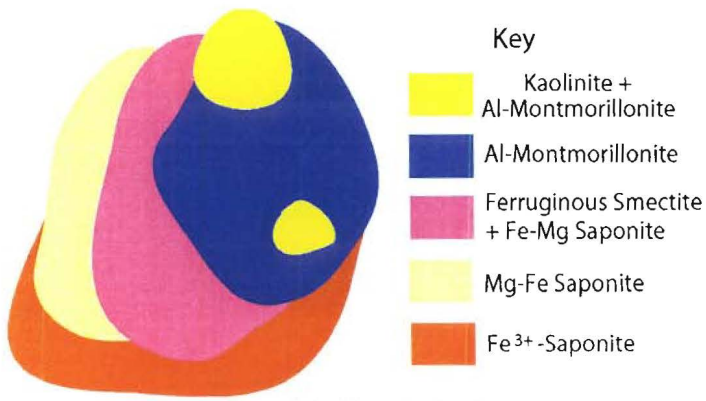

Figure 6. Idealized model of spectrally determined mineral zones.

(magenta) as seen on Puu Poliahu. On Puu Waiau a Mg-Fe saponite zone (tan) borders the southwestern side of a donut-shaped ferruginuous smectite + Fe-Mg saponite zone (Fig. 5B), which is bordered on the east by a Fe^{3+}-saponite zone (red). Nontronite-like Fe^{3+}-saponite is the only spectrally detectable clay widely dispersed among the non-hydrothermally altered volcanic rocks. The large bleached area on the western slope of Puu Waiau was initially identified as either saponite, hectorite, or talc because absorption features of these minerals look spectrally similar at AVIRIS spectral resolution. Analysis of field samples was needed to confirm that we were indeed mapping Mg-Fe saponite in this area (Fig 5B).

The absence of alunite is conspicuous at the spatial scale of AVIRIS on Mauna Kea and Mauna Loa when compared to alteration formed in continental settings, and may be explained by the possible lack of H_2S in Hawaiian magmatic gasses required for alunite formation near the surface (Robert Rye, personal comm.). Some alunite, however, has been identified in hand samples collected from the altered rocks of the Puu Poliahu cinder cone on Mauna Kea (Wolfe et al., 1997). Spectra from three pixels on this cinder cone did show possible evidence of alunite but its spectral features are nearly concealed by more abundant kaolinite. It is possible that the dry nature of tholeiitic magmas and rapid migration of meteoric water through highly porous volcanic rocks down to sea level and out into the ocean may not allow the formation of large circulating hydrothermal systems (Don Thomas, personal comm.). Indeed, it is the presence of clays produced by alteration of the Puu Waiau cone that has allowed surface waters to accumulate forming Lake Waiau in an otherwise arid landscape (Wolfe et al., 1997). Jarosite may also be present mixed with gypsum and illite on the slopes of Puu Lilinoe, but due to its marginal detection there in the AVIRIS data, this possible occurrence needs field verification.

Guinness et al. (2001) also spectrally analyzed the AVIRIS data acquired over Mauna Kea and found that the alteration systems in the cinder cones had central cores of montmorillonite, surrounded by saponite zones, in turn surrounded by outer kaolinite zones. Their findings differ from those discussed here by our identification of ferruginous smectite and only minor amounts of kaolinite. We were unable to detect kaolinite outside of the hydrothermally altered areas when we extracted spectra from pixels that corresponded to the areas they identified as containing kaolinite. Our field calibration site coincides with a cluster of kaolinite pixels on their map; examination of our field spectra revealed no spectrally detectable kaolinite. Apparently the kaolinite they mapped in unaltered rock was an artifact of simultaneously mapping ferric minerals in the 1-μm region and kaolinite in the 2-μm region using Spectral Angle Mapper that has been eliminated from their more recent maps (Guinness, pers com.). Two levels of verification were used to check the mineral maps: 1)

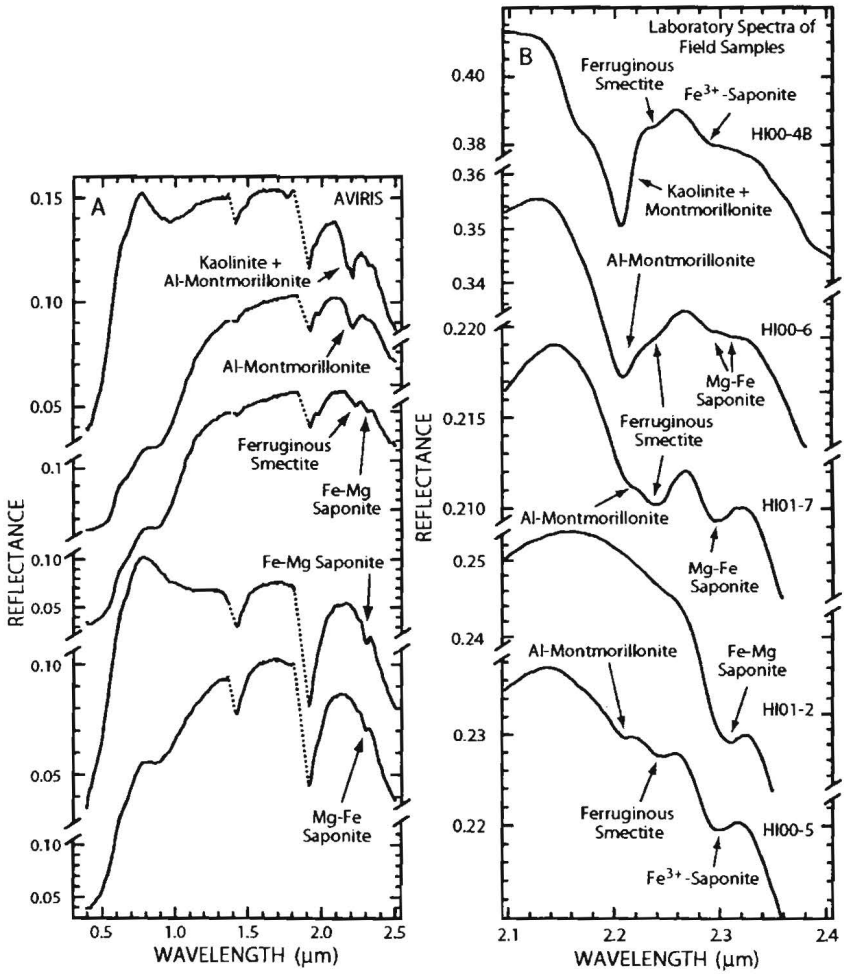

Figure 7. A) Averaged AVIRIS spectra extracted from alteration mineral zones in hydrothermal systems on Mauna Kea. Spectra offset vertically for clarity. B) Laboratory reflectance spectra of alteration minerals in field samples collected from the hydrothermal systems on Mauna Kea.

extraction and comparison of AVIRIS spectra to library spectra of well-characterized minerals, and 2) mineralogic analyses of field samples. Because of the remoteness of most areas in the flight lines comparison of extracted spectra to library spectra was used as the primary means of mineralogic verification of the mineral maps. Field samples were collected from hydrothermal systems on Puu Poliahu, Puu Waiau, and Puu Wekiu cinder cones (Fig. 3). Five samples from the alteration zones on Mauna Kea were subjected to X-ray diffraction analysis (XRD). These samples were also measured spectroscopically in the laboratory with results compared to those from XRD (see Fig. 7 and Table 2).

Table 2. Field sample verification of mineralogy derived from imaging spectroscopy.

Sample ID	Sample location		Tetracorder result	Verification
HI00-4F	N19° 49' 15" W155° 28' 18"	West side Puu Wekiu Cinder Cone	**Nanocrystalline hematite**[1], **kolinite + Al-montmorillonite**	*XRD:* albite (M), microcline (m), smectite (m) consistent with **montmorillonite**, nontronite or saponite (m), **kaolinite** (tr). *LS*: **nanocyrstalline hematite** or goethite, **kaolinite, Al-montmorillonite**, Fe-saponite, ferruginous smectite.
HI00-6F	N19° 49' 17" W155° 28' 55"	Northeastern Puu Poliahu	**Nanocrystalline hematite, Al-montmorillonite**	*XRD*:albite (M), microcline (m), smectite (m) consistent with **montmorillonite**, nontronite or saponite (tr), hematite (tr). *LS*: **nanocrystalline hematite, Al-montmorillonite**, ferruginous smectite, Mg-Fe saponite.
HI01-7	N19° 48' 37" W155° 28' 46"	Western top of Puu Waiau	Glassy volcanics, **ferruginous smectite + Mg-Fe-saponite**	*XRD:* Anorthite (M), nontronite or **saponite** (m), **montmorillonite** (m), kaolinite (tr). *LS:* **ferruginous smectite, Mg-Fe saponite,** Al-montmorillonite.
HI01-2	N19° 48' 43" W155° 28' 47"	Western slope of Puu Waiau	**Fe-minerals, Fe-Mg saponite**	*XRD:***saponite** from glycolation of clay separate. Main fraction not measured. *LS:* trace **Fe-minerals, Fe-Mg saponite**.
HI00-5F	N19° 49' 23" W155° 28' 48"	Northeastern Puu Poliahu	Amorphous Fe-hydroxide, **Fe-saponite**	*XRD:*albite (M), microcline (m), **saponite** by glycolation of clay sep. (m), hematite(tr). *LS:* trace Fe-mineral(s), **Fe-saponite,** ferruginous smectite, Al -montmorillonite.

XRD = X-ray diffraction analysis; *LS* = laboratory spectroscopy; clay sep. = clay separate; **bold** mineral names in "Tetracorder results" column also verified in field samples; (M) = major component 20wt% or more; (m) = minor 5-20 wt%; (tr) = trace < 5 wt%. [1]Trace hematite, goethite, jarosite and other Fe^{3+}-bearing minerals can be difficult for XRD to detect, even when red and yellow Fe^{3+} colors are present in the sample. Sample position is ± 50m (positions based on NAD83 datum).

Burns (1993, and references therein) suggest that deep weathering of mafic and vitric tuffs initially forms Fe^{2+}-saponite that subsequently oxidizes to partially dehydroxylated Fe^{3+}-Mg saponite, Fe^{3+}- montmorillonite, and nontronite intimately intergrown with ferrihydrite, nanocrystalline hematite, or FeOOH phases. A 2.232-μm band of variable strength often forms a shoulder or a completely independent absorption on the longward side of the 2.213-μm montmorillonite Al-OH combination band in many of the Mauna Kea samples, and may be caused by the presence of ferruginous smectite. In Fe-rich dioctahedral smectites some or all of the octahedral Al is replaced by Fe^{3+} with total replacement occurring in nontronites. The term ferruginous smectite applies to dioctahedral smectites when Fe^{3+} > 3% whereas montmorillonites have Fe^{3+} < 1% (Frost and Kloprogge, 2000). Ferruginous smectite may be an Fe-montmorillonite equivalent formed by oxidation and dehyroxylation of the Fe^{2+}-saponite on Mauna Kea. Both saponite and ferruginous smectite (a.k.a. Fe-montmorillonite) are present in variable proportions in nearly all of the samples collected from the Mauna Kea alteration systems (Fig. 7B) at concentrations much higher than in the surrounding non-hydrothermally altered rock (Fig. 5B). Burns suggest that intracrystalline oxidation of

Fe^{2+} to Fe^{3+} in cation clusters with metal vacancies creates additional absorptions that can form shoulders on the main combination bands in the 2 - 2.5 μm region resulting in broader but weakened absorptions that might be difficult to identify with remote sensing. Dehydration may also be an important mechanism for reducing H_2O-related band strengths in ferrihydrite-bearing smectites (Bishop et al., 1993). A combination of both mechanisms may be at work in the saponites and ferruginous smectites observed at Mauna Kea as their absorption bands rarely have depths greater than a few percent but XRD indicates abundances of 5 - 20 wt% in these relatively bright soils with 20 - 40% reflectance in the 2- 2.5 μm region. Nanocrystalline hematite and ferrihydrite have been identified in individual samples of palagonitized tephra and soil from Mauna Kea (Morris et al., 1993, 2001; Golden et al., 1993). The apparent lack of ferrihydrite at the spatial scale of AVIRIS may be explained by its tendency to dissolve and reprecipitate as goethite (Bigham et al., 1992), its spectral obscurity when intimately mixed with other Fe-minerals, or its nanocrystalline character (Morris et al., 1996) causing it to be classified into the more generic amorphous Fe-hydroxides category.

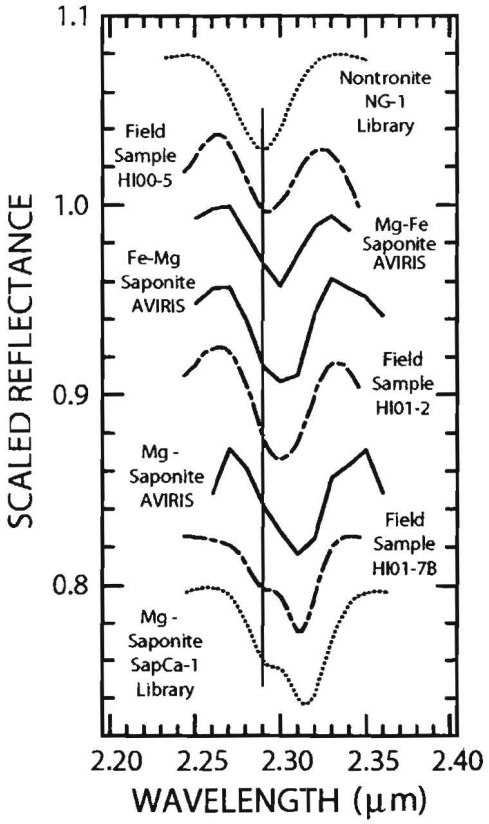

Figure 8. Comparison of continuum-removed absorptions from spectra of nontronite and saponites. Vertical line is a reference from which to measure the wavelength shift of the band centers. Spectra offset vertically for clarity.

Spectrally differentiating between nontronite and Fe^{3+}-saponite is difficult because their diagnostic absorptions overlap in some cases. Mg-rich saponites have an Fe-OH combination band that forms a shoulder at 2.292 μm (see sample SapCa-1in Fig.8) on the short wavelength side of the 2.312 μm Mg-OH combination band. This shoulder and absorptions at intermediate wavelength positions may be due to octahedral layer hydroxyl groups adjacent to cation clusters with vacancies (V) like $Fe^{3+}Fe^{3+}$(V), $MgFe^{3+}$(V), and fully occupied clusters like $MgFe^{2+}Fe^{3+}$ formed by the intracrystalline oxidation described above. Oxidized Fe-Mg saponite has two bands at intermediate positions between these endmember band positions that overlap significantly forming one broad composite absorption centered at 2.305 μm (e.g. see sample HI01-2 in Fig. 8). The spectrum of sample HI00-5 has a 2.292-μm absorption at the same wavelength position as that of nontronite (source clay mineral standard NG-1) but is missing an Mg-OH absorption at 2.312 μm. Differentiation was equally challenging using XRD on non-glycolated samples because of over-lapping saponite and nontrontite peaks. Thinking this sample contained nontronite we tested for the presence of saponite by analyzing a glycolated clay separate of this sample with XRD. Saponite was identified as the dominant smectite in the glycolated clay fraction of both HI00-5 and HI01-2 based on the appear-ance of a peak at 10.5° 2θ characteristic of glycolated saponite and lacking in the other smectites. Spectroscopy suggests the presence of nontronite in HI00-5 while XRD indicates saponite; perhaps this is evidence of an intermediate di- and tri-octahedral nontronite-like Fe^{3+}-saponite phase in this sample (Guven, 1988). Thus it appears that Fe^{3+}-saponite produced by intracrystalline oxidation is geochemically and spectrally a defacto nontronite with the original crystal lattice of a trioctahedral Fe^{2+}-saponite. It is possible to detect compositional variations of saponite with AVIRIS (see Fig. 5B). The spectral map key is coded to indicate the spectrally dominant cation in saponite: Fe^{3+}-, Mg-Fe, Fe-Mg, and Mg-saponite categories are listed here in order of increasing Mg content. It may be that Fe^{2+}-saponite is oxidized to Fe^{3+}-saponite where there is no hydrothermal Mg-enrichment, possibly accounting for the observed widespread nontronite-like 2.29-μm spectral signatures outside of the hydrothermally altered areas (Fig. 5B) in weathered rocks. In contrast, Mg-rich saponite, like kaolinite, may be indicative of hydrothermal alteration on Mars.

A tentative model for the alteration zones present in the summit cinder cones on Mauna Kea is presented in Fig. 9. This model was constructed from the mineral assemblages present in the vibrational mineral map (Fig. 5B) and spectra of field samples (Fig. 7B). Multiple clay phases exist in variable proportions in nearly all of the samples, therefore the alteration mineral associations were arranged into zones named after the spectrally dominant mineral

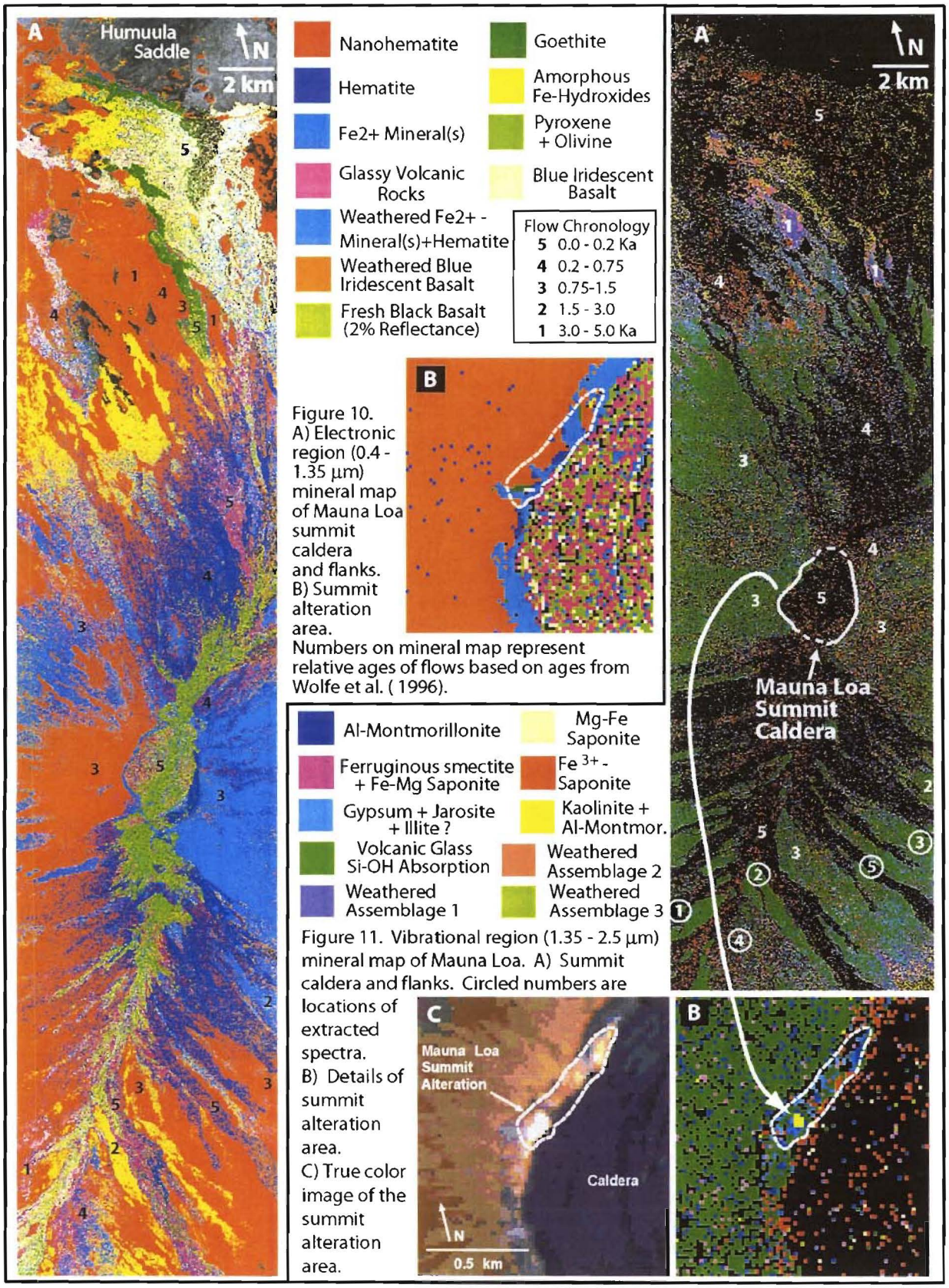

Figure 10. A) Electronic region (0.4 - 1.35 μm) mineral map of Mauna Loa summit caldera and flanks. B) Summit alteration area. Numbers on mineral map represent relative ages of flows based on ages from Wolfe et al. (1996).

Figure 11. Vibrational region (1.35 - 2.5 μm) mineral map of Mauna Loa. A) Summit caldera and flanks. Circled numbers are locations of extracted spectra. B) Details of summit alteration area. C) True color image of the summit alteration area.

μm (Fig. 13) reminiscent of the diffraction scattering peak seen at ultraviolet wavelengths in common opal and at visible wavelengths in precious opal (Darragh et al., 1976). The blue iridescence appears to be related to the initial stages of basalt weathering in the relatively moist environment at lower elevations because spectra of the same flows at higher elevations (> 3000 m) on the mountain and older flows (> 0.7 ka) at lower elevations have no peaks.

In the vibrational spectral region, older flows show spectral evidence of a 2.24-μm Si-OH absorption probably related to hydration of basaltic glass whereas the younger flows lack this spectral feature (Fig.14). A possible explanation is that over time, water diffuses into the surface of a flow forming a water-rich hydration rind that increases in thickness with time. Studies have shown that growth of hydration rinds is a non-linear function of time, relative humidity, temperature, and lava composition (Friedman and Smith, 1960, Friedman and Obradovich, 1981, Friedman et al., 1994). Various techniques have been developed to date obsidian archeological artifacts using the thickness of hydration rinds as an indicator of relative age. Based on analysis of the mineral patterns in Fig. 11A, it appears that spectral maps of the Si-OH absorption can be used to perform the same type of relative dating using hyperspectral data collected by airborne or orbital instruments. Hydration rinds are either spectrally concealed or destroyed by accelerated weathering at lower, more humid, elevations below about 2600 m on the N and SW flanks of Mauna Loa. A comparable mineral map pattern of Si-OH absorptions is absent at the summit of Mauna Kea probably because of the relatively older (generally >10,000 years based on the geologic map of Wolfe and Morris, 1996) and more weathered flows exposed there (Fig 5B). Possible application of this technique to date Martian lava flows would depend on how fast volcanic glass hydrates in the cold-thin atmosphere of Mars. The spectral signature of hydrated volcanic glass is similar to those of chert, chalcedony, opal, hydrated cristobalite, and coesite in the 2.2 - 2.3 μm region, but can be differentiated with adequate spectral resolution and signal-to-noise ratio. This is a potentially important distinction to make when searching for hydrothermally-altered areas on Mars.

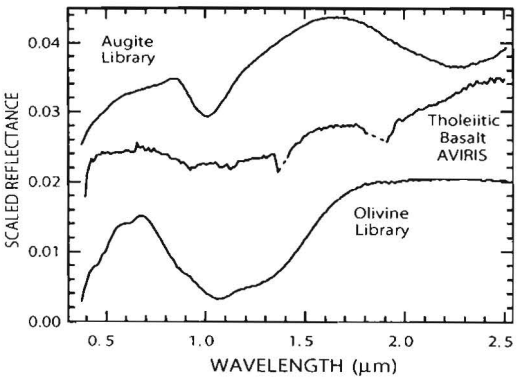

Figure 12. Averaged AVIRIS spectra extracted from an area where a recent flow (< 0.1 Ka) near the summit of Mauna Loa (Fig. 10A) that mapped as pyroxene + olivine compared to library spectra of pyroxene (augite) and olivine. The intimate mixture of these two minerals can explain the broad upward sloping absorption seen in the AVIRIS spectrum.

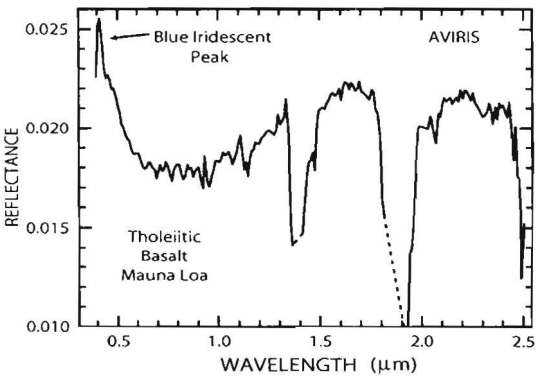

Figure 13. Averaged AVIRIS spectra extracted from a portion of a recent flow (< 0.2 Ka) on the NW flank of Mauna Loa just above the saddle that mapped as weathered blue iridescent basalt (Fig.10A).

Hydrothermal Alteration as a Function of Tectonic Setting

Over the past two decades geologists have analyzed hyperspectral data collected over 15 relict and 3 active hydrothermal systems ranging from those developed on hot spot shield volcanos, to those on continental margin stratovolcanos and continental interior calderas (Goetz and Strivastava, 1985; Kruse and Huntington, 1990; Simon, 1990; Swayze et al., 1992; King et al., 1995; Kruse et al., 1996; Crowley and Zimbelman, 1997; Swayze, 1997; Livo et al., 1999; Dalton et al., 2000; Rockwell et al., 2000; Martinez-Alonso, 2000; Smailbegovic et al., 2001; Martini et al., 2001; Vaughan et al., 2001). Some useful patterns emerge when the characteristics of hydrothermal systems developed in these three tectonic environments are compared (Fig. 15). It is apparent that the composition and volatile content of magmas influence the duration, mineral associations, size, and geometry of hydrothermal systems with drier, more mafic, magmas producing smaller, short-lived hydrothermal systems and wetter, more silicic, magmas producing larger, long-lived systems characteristic of continental interior calderas. Most notable is the

greater diversity of spectrally detectable alteration minerals, including alunite, and the presence of large propylitic zones and silica caps in hydrothermal systems of the continental interior calderas compared to the handful of alteration minerals, little to no alunite, and lack of propylitic zones or silica caps in hydrothermal systems on shield volcanos. In summary, very small hydrothermal systems develop along fault bounded caldera walls of tholeiitic basalt shield volcanos during the shield-building stage as seen at Mauna Loa and Kilauea. Small systems develop in summit and flank cinder cones during the postshield-building stage of alkalic volcanism on shield volcanos as seen at Mauna Kea. Medium-sized hydrothermal systems develop at the summits and on the flanks of andesitic stratovolcanos along subduction margins as seen at Mt. Rainer (Crowley and Zimbelman, 1997) and the Nansatsu District in Japan (Hedenquist et al., 1994). And large hydrothermal systems develop in or along the margins of continental interior bimodal rhyolite/basalt calderas as seen at Cuprite (Swayze, 1997) and Goldfield, Nevada (Ashley and Silberman, 1976).

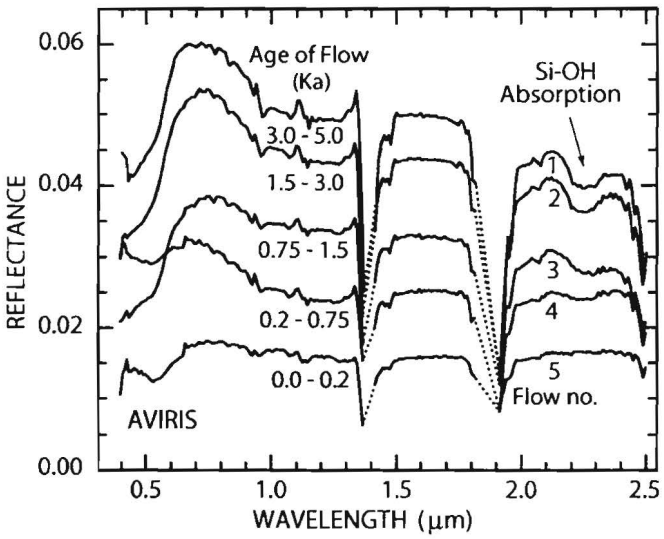

Figure 14. Averaged AVIRIS spectra of tholeiitic basalt flows of different age from the southwestern flank of Mauna Loa. Spectra were extracted from sites shown in Fig. 11A (circled numbers). Note that older flows have deeper 2.24-μm Si-OH absorptions. 1.0 Ka = one thousand years ago.

There are exceptions to these trends with large continental interior-style hydrothermal systems occurring in subduction margin island arcs like the Philippines (Reyes, 1990). Likewise, many of the alteration minerals observed in hydrothermal systems of continental interior calderas are present in the subduction margin systems but at spatial scales too small to spectrally dominate entire pixels.

THE SEARCH FOR MARTIAN HYDROTHERMAL SYSTEMS

The spectral search for alteration minerals will undoubtably continue to play a critical role in the search for relict hydrothermal systems on Mars (Farmer, 1996). Results of this study suggest that the classical set of alteration mineral associations found in active continental interior calderas like Yellowstone, Wyoming or relict systems like Goldfield, Nevada, are not all likely to be found in Martian volcanic hydrothermal systems given the lack of comparable tectonic settings on Mars. Alternatively, the Hawaiian alteration mineral

Tectonic Setting	Oceanic Hotspot Shield Volcanoes	Subduction Margin Stratovolcanoes	Continental Interior Calderas
Magmatic Composition	Mafic	Intermediate	Silicic
Volcanic Rock Composition	Tholeiitic Basalt	Andesite	Bimodal Rhyolite / Basalt
Magmatic Volatile Content	Dry		Wet
Structural Setting	Caldera Basins & Walls Rift Zones & Cinder Cones	Volcanoe Summit and Flanks	Caldera Basins & Margins
Duration of Hydrothermal Centers	Few Years to Decades	1000 - 10,000 Years	Up to Millions of Years
Spectrally Detectable Alteration Mineral Associations (0.4 - 2.5 microns) at > 14x14 m pixel scale	Cristobalite Goethite Gypsum Hematite Jarosite Kaolinite + smectite Al-Montmorillonite Ferruginous Smectite Saponite	Alunite Chlorite Cristobalite Cryptocrystalline Quartz Goethite Gypsum Hematite Jarosite Kaolinite Montmorillonite Opal Sericite/Illite Smectite	Alunite Buddingtonite Chlorite Chalcedony Cristobalite Dickite Goethite Gypsum Halloysite Hematite Jarosite Kaolinite Montmorillonite Opal Pyrophyllite Sericite/Illite Smectite
Size of Hydrothermal Centers	0.006 - 0.3 km^2	1 - 8 km^2	2-10 km^2
Geometry of Hydrothermal Centers	No Silica Cap No Alunite Zones No Propylitic Zones	Some Silica Caps Small Alunite Zones Propylitic Zones	Large Silica Cap Large Alunite Zones Propylitic Zones
Spectral evidence of acid-sulfate alteration (at > 14 x 14 m pixel scale)	Absent		Abundant

Figure 15. Hydrothermal alteration as a function of host rock composition, tectonic setting, and magmatic volatile content.

associations are probably closer to what we should expect to find on Mars. Alteration minerals such as chalcedony, chlorite, dickite, halloysite, opal, pyrophyllite, and sericite are absent in the Hawaiian systems at the spatial scale of AVIRIS (14 m pixels). The presence of only small hydrothermal systems on Hawaii at the surface may be an observation biased by what is exposed. Larger systems formed at depth, if they exit, have little chance of being exposed due to rapid subsidence of the islands (Don Thomas, personal comm.). If large hydrothermal systems have developed at depth on Mars, they may have been subsequently exposed by erosion, edifice collapse, or exhumation during meteorite impact.

Successfully locating Martian hydrothermal systems will require the identification of alteration minerals with enough spectral contrast to avoid confusion with minerals formed by weathering in non-hydrothermally altered areas. Unfortunately many of the alteration minerals found in the Hawaiian hydrothermal systems also form during weathering of mafic volcanic rocks. Nontronite-like Fe^{3+}-saponite is a weathering product of the non-hydrothermally altered basaltic rocks surrounding the hydrothermal centers on Mauna Kea (Fig. 5B). Similarly hematite and goethite form as products of weathering of non-hydrothermally altered sulfide-rich volcanic rocks on both mountains (Figs 5A and 10A). The most reliable indicator of hydrothermal alteration in mafic volcanic rocks, from a remote sensing perspective, is the presence of kaolinite. It is present in the hydrothermal centers on both Mauna Kea and Mauna Loa, in the most intensely altered areas. The process of hydrothermal alteration must hasten the formation of Fe^{2+}-saponite from basaltic rocks with resulting oxidation and dehyroxylation to form Fe^{3+}- and Mg-saponites, and ferruginous smectite. Although this assemblage is normally present in weathered basalts (Burns, 1993), it seems that hydrothermal action may enhance the weathering process, creating areas with higher than background concentrations of these minerals. And if the mineral associations in the cinder cones on Mauna Kea are an applicable spectral analogue, then Mg-rich saponites may also be indicative of hydrothermal alteration on Mars. Care must be exercised to avoid potential confusion between the spectral signatures of hydrated volcanic glass, which might be widespread on Mars, and hydrated SiO_2 minerals indicative of localized hydrothermal alteration systems.

The duration of activity in a hydrothermal system also varies as a function of tectonic setting, lasting a few orders of magnitude longer in more silicic magmatic systems like those formed in continental interior calderas (Fig. 15). It seems logical that long-lived hydrothermal systems would provide a better shelter for Martian life and may be more likely to preserve evidence of that life than short-lived systems. This observation has important implications for the search for past life on Mars: the largest and best-developed hydrothermal systems may be those associated with postshield basalts or andesites on Mars. Cinder cones and exhumed altered rocks formed during the postshield stage of volcanism may be the best targets for remote detection of hydrothermal systems and for exobiology sample collection missions. These would be the areas to concentrate on in the search for sample return sites at spatial resolutions no coarser than 30 meters. Exopalaeontological studies may also benefit from studying the biota of active and relict hot springs of the Hawaiian and Icelandic oceanic hotspot hydrothermal systems. Areas of reduced permeability may be necessary for the formation of large hydrothermal convection cells at the surface.

Volcanism may not be the only mechanism for forming hydrothermal systems on Mars. Newsom (1980) has suggested that hydrothermal systems may have developed in meteorite impact melt sheets on Mars. Studies of terrestrial impact structures in continental settings have found evidence of extensive long-lived hydrothermal systems and their associated calc-silicate alteration mineral associations (McCarville and Crossey, 1996). For the same reasons discussed above, host-rock composition may influence the type of alteration minerals formed during impact induced heating. Unfortunately, terrestrial analogues of impact-driven hydrothermal alteration applicable to Martian mafic volcanic rocks may not exist because plate subduction has probably destroyed the oceanic impact structures they reside in, biasing the terrestrial geologic record toward those preserved in silicic cratons. Nevertheless, the alteration minerals formed in the hydrothermal systems on Mauna Kea and Mauna Loa may be useful guides in deducing the effects of heat and water on mafic rocks expected during impact heating.

ACKNOWLEDGMENTS

Special thanks is given to Robert O. Green and the AVIRIS team for collecting and providing the imaging data. Ideas were clarified by helpful discussions with Trude King, Jim Crowley, Bob Tilling, Don Thomas, Sara Martinez-Alonso, Ed Guinness, Dick Morris, Ray Arvidson, Geoff Plumlee, Charlie Alpers, Skip Cunningham, and Blair Jones. The manuscript benefitted greatly from reviews by Eric Livo, Robert Rye, and Todd Hoefen. Funding was provided by the USGS Minerals Program. Any use of trade, product, or firm names in this publication is for descriptive purposes only and does not imply endorsement by the U.S. Government.

REFERENCES

Allen, C.C., J.L. Gooding, M. Jercinovic, and K. Keil, Altered basaltic glass: A terrestrial analog to the soil of Mars, *Icarus, 45*, 347-369, 1981.

Allen, C.C., J.L. Gooding, K. Kiel, Hydrothermally altered impact melt rock and breccia: Contributions to the soil of Mars, *Journal of Geophysical Research, 87*, 10083-10101, 1982.

Ashley, R.P., and M.L. Silberman, Direct dating of mineralization at Goldfield, Nevada, by Potassium-Argon and fission-track methods, *Economic Geology, 71*, 904-924, 1976.

Bigham, J.M., U. Schwertmann, L. Carlson, Mineralogy of precipitates formed by the biogeochemical oxidation of Fe(II) in Mine Drainage, *in* Biomineralization: Processes of Iron and Manganese, H.C.W. Skinner, R.W. Fitzpatrick (eds.), *Catena Supplement 21*: Cremlingen-Destedt, Germany, 219-232, 1992.

Bishop, J.L., C.M. Pieters, R.G. Burns, Reflectance and Mössbauer spectroscopy of ferrihydrite-montmorillonite assemblages as Mars soil analog materials, *Geochimica et Cosmochimica Acta, 57*, 4583-4595, 1993.

Burns, R.G., Rates and mechanisms of chemical weathering of ferromagnesian silicate minerals on Mars, *Geochimica et Cosmochimica Acta, 57*, 4555-4574, 1993.

Clark, R.N., G.A. Swayze, K. E. Livo, R.F. Kokaly, S.J. Sutley, J. B. Dalton, R.R. McDougal, and C. A. Gent, Imaging spectroscopy: Earth and planetary remote sensing with the USGS Tetracorder and Expert Systems, *J. Geophys. Res.*, 2003, in press.

Clark, R.N., G.A. Swayze, K.E. Livo, R.F. Kokaly, T.V.V. King, J.B. Dalton, J.S. Vance, B.W. Rockwell, T. Hoefen, R.R. McDougal, Surface reflectance calibration of terrestrial imaging spectroscopy data: a tutorial using AVIRIS, Proceedings of the Eleventh JPL Airborne Earth Science Workshop, *Jet Propulsion Laboratory Publication*, this volume, 2003.

Clague, D.A., G.B. Dalrymple, The Hawaiian-Emperor volcanic chain. Part I. Geologic evolution, chap. 1 of R.W. Decker, T.L. Wright, P.H. Stauffer (eds.), Volcanism in Hawaii*: U.S. Geological Survey Professional Paper 1350, 1*, 5-54, 1987.

Clague, D.A., G.B. Dalrymple, Tectonics, geochronology, and origin of the Hawaiian-Emperor Chain *in* E.L. Winterer, D.M. Huson, R.W. Decker (eds.), The eastern Pacific Ocean and Hawaii, v. N *of* The geology of North America, Geological Society of America, 188-254, 1989.

Crowley, J.K., D.R. Zimbelman, Mapping hydrothermally altered rocks on Mount Rainier, Washington, with Airborne Visible/Infrared Imaging Spectrometer (AVIRIS) data, *Geology, 25*(6), 559-562, 1997.

Dalton, J.B., T.V.V. King, D.J. Bove, R.F. Kokaly, R.N. Clark, J.S. Vance and G.A. Swayze, Distribution of acid-generating and acid-buffering minerals in the Animas River Watershed as determined by AVIRIS spectroscopy, *Proceedings of the ICARD 2000 Meeting*, Denver Colorado, 1541-1550, 2000.

Darragh, P.J., A.J. Gaskin, J.V. Sanders, Opals, *Scientific American, 234(4)*, 84-95, 1976.

Duke, E.F., Near infrared spectra of muscovite, Tschermak substitution, and metamorphic reaction progress: implications for remote sensing, *Geology, 22*, 621-624, 1994.

Evans, D.L., J.B. Adams, Composition of Viking Lander multispectral images and laboratory reflectance spectra of terrestrial samples, *Proc. Lunar Planet. Sci. Conf., 10th*, 1829-1834, 1979.

Evans, D.L., J.B. Adams, Amorphous gels as possible analogs to martian weathering products, *Proc. Lunar Planet. Sci. Conf. 11th*, 757-763, 1980.

Farmer, J.D., D.J. De Marais, Exopaleontology and the search for a fossil record on Mars, *Lunar Planet. Sci., 25*, 367-368, 1994.

Farmer, J.D., Hydrothermal systems on Mars: an assessment of present evidence, in Evolution of hydrothermal ecosystems on Earth (and Mars?), *Ciba Foundation Symposium 202*, Wiley and Sons, 273-299, 1996.

Friedman, I., R.L. Smith, A new dating method using obsidian: Part I, The development of the method., *American Antiquity, 25*, 476-522, 1960.

Friedman, I., J. Obradovich, Obsidian hydration dating of volcanic events, *Quaternary Research, 16*, 37-47, 1981.

Friedman, I., F.W. Trembour, F.L. Smith, and G.I. Smith, Is obsidian hydration dating affected by relative humidity? Quaternary Research, 41(2), 185-190, 1994.

Frost, R.L., J.T. Kloprogge, Vibrational spectroscopy of ferruginous smectite and nontronite, *Spectrochimica Acta Part A, 56*, 2177-2189, 2000.

Gao, B-C, K.B. Heidebrecht, and A.F.H. Goetz, Derivation of scaled surface reflectances from AVIRIS data, *Remote Sensing of Environment, 44(2)*, 165-178, 1993.

Goetz, A.F.H., and Vinay Strivastava, Mineralogical mapping in the Cuprite mining district, Proceedings of the Airborne Imaging Spectrometer (AIS) Data Analysis Workshop, *Jet Propulsion Laboratory Publication 85-*

41, 22-29, 1985.

Golden, D.C., R.V. Morris, and D.W. Ming, Mineralogy of three slightly palagonitized basaltic tephra samples from the summit of Mauna Kea, Hawaii, *J. Geophys. Res., 98(E2)*, 3401-3411, 1993.

Guinness, E.A., R.E. Arvidson, B.L. Ljolliff, R.V. Morris, and D.W. Ming, Mapping alteration minerals exposed on the summit of Mauna Kea Volcano using AVIRIS data: implications for mapping Mars mineralogy, Lunar and Planetary Science XXXII, 1659.pdf, 2001.

Guven, N., Smectites, in Hydrous Phyllosilicates, Reviews in Mineralogy, v. 19, chapter 13, S.W. Bailey (ed.), Mineralogical Society of America, 497-559, 1988.

Guilbert, J.M., C.F. Park, Jr., Ore Deposits, W.H. Freeman and Company, New York, 985pp., 1986.

Hedenquist, J.W., E. Izawa, N.C. White, W.F. Giggenbach, M. Aoki, Geology, geochemistry, and origin of high sulfidation Cu-Au mineralization in the Nansatsu District, Japan, *Economic Geology, 89(1)*, 1-30, 1994.

King, T.V.V., R.N. Clark, C. Ager, G.A. Swayze, Remote mineral mapping using AVIRIS data at Summitville, Colorado, and the adjacent San Juan Mountains: in Proceedings: Summitville Forum '95, eds. H.H. Posey; J.A. Pendelton; and D. Van Zyl, *Colorado Geological Survey Special Publication 38*, 59-63, 1995.

Kruse, F.A., K.S. Keirein-Young, and J.W. Boardman, Mineral mapping at Cuprite, Nevada with a 68-channel imaging spectrometer, *Photogrammetric Engineering and Remote Sensing*, *56*(1), 83-92, 1990.

Kruse, F.A., J.H. Huntington, The 1995 AVIRIS geology group shoot, Proceedings form the Airborne Earth Science Workshop, Jet Propulsion Publication, 1996.

Livo, K.E., R.N. Clark, F.A. Kruse, and R.F. Kokaly, Characterization of hydrothermally altered rock and hot spring deposits at Yellowstone National Park using AVIRIS data, Summaries of the Eight JPL Airborne Science Workshop, *Jet Propulsion Laboratory Publication 99-17*, 259-266, 1999.

Martinez-Alonso, S.E., Study of the infrared spectra of phyllosilicates through direct measurements, quantum mechanical modeling, and analysis of AVIRIS imaging spectrometer data: relationships with environment of mineralization, Ph. D. Dissertation, University of Colorado Boulder, 232 pp., 2000.

Martini, B.A., E.A. Silver, D.C. Potts, Hyperspectral remote sensing in Long Valley Caldera: issues of scale resolution, and signal to noise, Proceedings of the Tenth JPL Airborne Earth Science Workshop, *Jet Propulsion Laboratory Publication 02-1*, 275-282, 2001.

McCarville, P., L.J. Crossey, Post-impact hydrothermal alteration of the Manson impact structure, *Geological Society of America Special Paper 302*, 347-376, 1996.

Moore, J.G. D.A. Clague, W.R. Normark, Diverse basalt types from Loihi Seamount, Hawaii: *Geology, 10(2)*, 88-92, 1982.

Moore, J.G., D.A. Clague, Volcano growth and evolution of Island of Hawaii: *Geological Society of America Bulletin, 104(11)*, 1471-1484, 1992.

Morris, R.V., D.C. Golden, J.F. Bell, H.V. Lauer, and J.B. Adams, Pigmenting agents in Martian soils: Inferences from spectral, Mossbauer, and magnetic properties of nanophase and other iron oxides in Hawaiian palagonitic soil PN-9, *Geochimica et Cosmochimica Acta, 57*, 4597-4609, 1993.

Morris, R.V., D.W. Ming, D.C. Golden, J.F. Bell, III, An occurrence of jarositic tephra on Mauna Kea, Hawaii: Implications for the ferric mineralogy of the Martian surface, *in* Mineral Spectroscopy: A Tribute to Roger G. Burns, Geochemical Society special Publication No.5, M.D. Dyar, C. McCammon, M.W. Schaefer (eds.), 327-336, 1996.

Morris, R.V., D.C. Golden, D.W. Ming, T.D. Shelfer, L.C. Jorgensen, J.F. Bell, III, T.G. Graff, S.A. Mertzman, Phyllosilicate-poor palagonitic dust from Mauna Kea Volcano (Hawaii): A mineralogical analogue for magnetic Martian dust?, *Journal of Geophysical Research, 106(E3)*, 5057-5083, 2001.

Newsom, H.E., Hydrothermal alteration of impact melt sheets with implication for Mars, *Icarus, 44*, 207-216, 1980.

Rockwell, B.W., R.N. Clark, C.F. Cunningham, S.J. Sutley, C. Gent, R.R. McDougal, K.E. Livo, and R.F. Kokaly, Mineral mapping and verification in the Marysvale volcanic field, Utah using AVIRIS data, in Summaries of the 9th Annual JPL Airborne Earth Science Workshop, *Jet Propulsion Laboratory Publication 00-18*, 407- 418, 2000.

Reyes, A.G., Petrology of Philippine geothermal systems and the applicaton of alteration mineralogy to their assessment, *Journal of Volcanology and Geothermal Research, 43*, 279-309, 1990.

Simon, J.H., The combined use of multispectral remotely sensed data from the short wave infrared (SWIR) and thermal infrared (TIR) for lithological mapping and mineral exploration, *Fifth Australasian Remote Sensing Conference*, Perth, Western Australia, *1*, 371-380, 1990.

Singer, R.B., Spectral evidence for the mineralogy of high-albedo soils and dust on Mars, *Journal of Geophysical Research, 87*, 1,159-10168, 1982.

Singer, R.B., T.B. McCord, R.N. Clark, J.B. Adams, and R.L. Huguenin, Mars surface composition from reflectance spectroscopy: A summary, *Journal of Geophysical Research, 84*, 8415-8425, 1979.

Smailbegovic, A., J.V. Taranik, W.M. Calvin, Preliminary results of hydrothermal alteration assemblage classification in Aurora and Bodie Mining Districts, Nevada and California, with airborne hyperspectral data, Proceedings of the Tenth JPL Airborne Earth Science Workshop, *Jet Propulsion Laboratory Publication 02-1*, 367-374, 2001.

Swayze, G.A., R.N. Clark, S. Sutley, and A.J. Gallagher, Ground-truthing AVIRIS mineral mapping at Cuprite, Nevada, Summaries of the Third Annual JPL Airborne Geosciences Workshop, Volume 1: AVIRIS Workshop, *Jet Propulsion Laboratory Publication 92-14, 1*, 47-49, 1992.

Swayze, G.A., The hydrothermal and structural history of the Cuprite Mining District, southwestern Nevada: an integrated geological and geophysical approach, Ph. D. Dissertation, University of Colorado Boulder, 399 pp., 1997.

Ugolini, F.C., Hydrothermal origin of the clays from the upper slopes of Mauna Kea, Hawaii, *Clays and Clay Minerals, 22*, 189-194, 1974.

Vaughan, R.G., W.M. Calvin, J.V. Taranik, Anaylsis of sub-pixel mixing in high-altitude AVIRIS data over Virginia City, Nevada, using systematic field-based observations, Proceedings of the Tenth JPL Airborne Earth Science Workshop, *Jet Propulsion Laboratory Publication 02-1*, 421-426, 2001.

Walter, M.R., D.J. De Marais, Preservation of biological information in thermal spring deposits: developing a strategy for the search for fossil life on Mars, *Icarus, 101*, 129-143, 1993.

Wade, M.L., D.G. Agresti, T.J. Wdowiak, L.P. Armendarez, A Mossbauer investigation of iron-rich terrestrial hydrothermal vent systems: Lessons for Mars exploration, *Journal of Geophysical Research, 104(E4)*, 8489-8507, 1999.

Wolfe, E.W., J. Morris, Geologic Map of the Island of Hawaii, *Miscellaneous Investigation Series Map I-2524-A*, U.S. Geological Survey, 18 pp., 1996.

Wolfe, E.W., W.S. Wise, G.B. Dalrymple, The geology and petrology of Mauna Kea Volcano, Hawaii – A study of postshield volcanism, *U.S. Geological Survey Professional Paper 1557*, 129 pp., 1997.

TERRAIN NORMALIZATION OF AVIRIS AND HYPERION IMAGERY IN FORESTED LANDSCAPES

Philip A. Townsend and Jane R. Foster[1]

1. INTRODUCTION

The effects of topographic shadowing in satellite and aerial imagery can be substantial in rugged landscapes with steep hills or mountains. These effects can affect interpretations and quantitative analyses of imagery, and in forested areas can complicate the classification of forest types or the extraction of biophysical parameters from the reflectance data. Because of this, numerous techniques have been devised to correct for terrain illumination differences, including the simple cosine (or Lambertian) correction, the Minnaert correction (Minnaert, 1941), and a variety of other approaches (e.g., Civco, 1989; Conese et al., 1993; Meyer et al., 1993). The purpose of this study is to demonstrate the application of one technique, the empirical approach of Meyer et al. (1993) to high altitude AVIRIS and Hyperion imagery. Previous work by Martin et al. (1999) compared the application of two techniques – the Lambertian (simple cosine) and Minnaert corrections – on AVIRIS, finding superior performance by the Minnaert correction. Neither of these approaches is used here, as the cosine correction is generally recognized to over-correct on shaded slopes, while the Minnaert correction requires the derivation of a cover-type specific correction coefficient, which is especially difficult when cover types are either not known or not mapped (see Allen, 2000). The empirical approach also has the benefit of providing several tools (described below) for the quantitative evaluation of the correction.

2. STUDY AREA AND METHODS

2.1 Study Area

The study area is the 15,700 ha Green Ridge State Forest (GRSF) in western Maryland (Figure 1). GRSF is located in the Ridge and Valley physiographic province of the central Appalachian Mountains, and is characterized by steep southwest-northeast trending mountains with gently sloping to steeply incised valley bottoms. Elevation ranges from 250-700 m. The forests are comprised largely of deciduous oaks, with Virginia pine on some west-facing slopes and hemlock in some valley bottoms. This research was undertaken as a component of a larger project to compare multiple sensor combinations for mapping and modeling forest composition and structure.

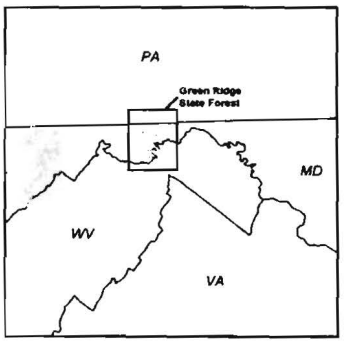

Figure 1. Location of Green Ridge State Forest in western Maryland.

Table 1. Image Characteristics

Sensor	Date	Time (UTC)	Solar Azimuth	Solar Elevation
AVIRIS	5/14/2000	15:42:46	133.8	62.62
AVIRIS	7/13/2001	15:47:47	134.94	66.72
Hyperion	7/24/2001	16:09:30	126.35	61.13

2.2 Image Preprocessing

The research presented here uses two AVIRIS images, acquired on 14 May 2000 and 13 July 2001 from an altitude of ~19,900 m, and one EO-1 Hyperion image acquired on 24 July 2001 (Table 1). The images were atmospherically corrected using the ATmospheric REMoval program (ATREM) (Gao et al., 1993) followed by an empirical line calibration (e.g., Moran et al., 2001) developed from measurements taken by an Analytical Spectral Devices (ASD) FieldSpec spectroradiometer. The AVIRIS imagery exhibited a cross-track view-angle dependent brightness gradient. This gradient of increasing brightness on the west side of the images results from the AVIRIS

[1] University of Maryland Center for Environmental Science, Appalachian Laboratory, Frostburg, Maryland 21532; townsend@al.umces.edu

scan angle and direction, flight path orientation and solar azimuth, and was corrected by fitting a first-order additive quadric curve to the mean radiance by view angle (Kennedy et al., 1997). The images were georeferenced to UTM coordinates using a triangulation method with > 70 GCPs per scene and nearest neighbor resampling.

2.3 Terrain Normalization

All of the images used in this research exhibited substantial terrain effects (Figure 2). To determine the effects of differential illumination, we modeled solar illumination for each image using slope and aspect derived from a digital elevation model (DEM) and solar altitude and azimuth information for the time of imaging (Table 1). The incidence angle of solar radiation is defined as *cos(i)*, i.e. the angle between the normal to the surface and the source of light (the sun). A linear model was then constructed to predict reflectance (on a pixel-by-pixel basis) as a function of illumination (Figure 2). The influence of illumination was then removed through detrending based on the slope of the regression equation. In general, the approach removes the slope between reflectance and illumination, while the variance in reflectance at any given incidence angle remains unchanged. The approach assumes that illumination differences are constant among cover classes (Allen, 2000). However, the training pixels used to determine the regression equation (i.e., Figure 3) are sampled from sites with similar canopy composition. For this research, the regression equations were developed using reflectance data from leafed-out mature oak forests, the dominant cover type in the region. Following Meyer et al. (1993), reflectance on the normalized image is then computed as:

$$L_H = L_T - cos(i)\ m - b + L_\mu + e \qquad \text{(Equation 1)},$$

where L_H is the normalized reflectance, L_T is the observed reflectance on sloped terrain, L_μ is the mean L_T for a channel, m is the slope and b is the y-intercept of the linear regression model; e represents model error. This regression-based approach allows the reporting of a variety of diagnostics to evaluate the efficacy of any corrections that are applied. In particular, the R^2 of the regression equation indicates the strength of the linear relationship

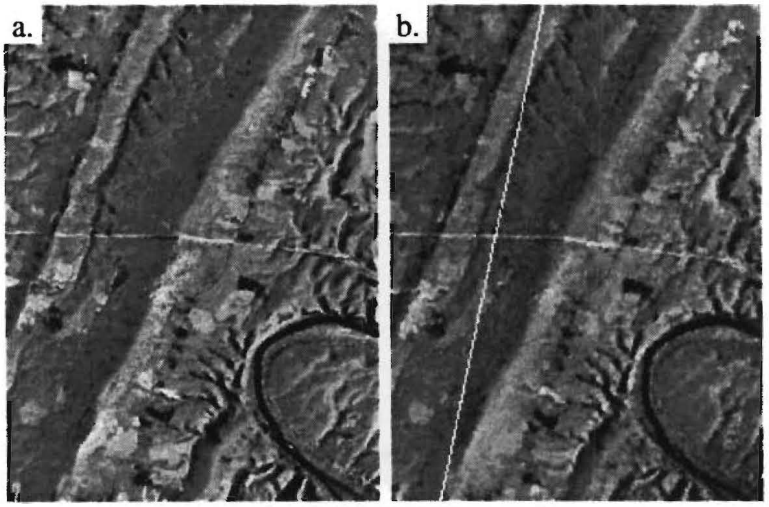

Figure 2. (a) AVIRIS image of GRSF from 14 May 2000. Bands shown in RGB are 1663 nm, 1089 nm, and 549 nm. (b) Hyperion image of the same area from 24 July 2001, showing 1659 nm, 1256 nm and 570 nm. Note the strong illumination effects along the mountain ridges.

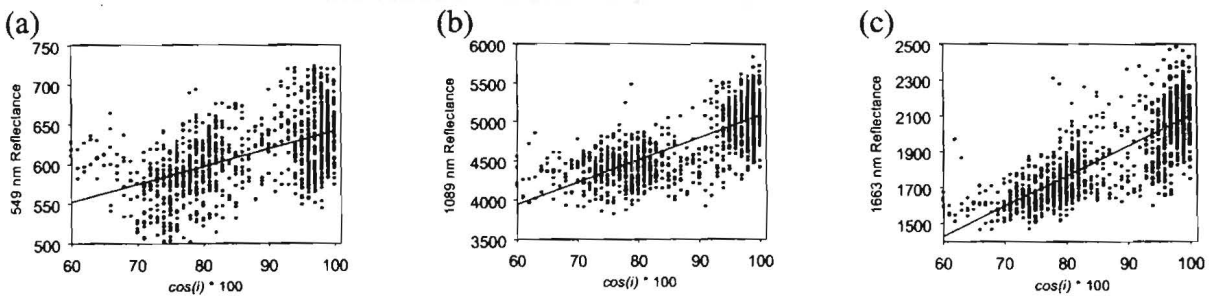

Figure 3. Relationship between illumination and reflectance for the three bands in the AVIRIS image shown in Figure 2a (14 May 2000). Values on the y-axis are 10000 * reflectance. The data shown here are for deciduous oak forests.

between reflectance and *cos(i)*. In addition, the steepness of the slope of the regression equation for any particular band denotes the relative amount of shadowing in that band, with steeper slopes indicating greater amounts of shadowing and illumination.

3. RESULTS

Regression relationships between reflectance and illumination were developed using automated routines for all bands in the AVIRIS and Hyperion images. The fit (R^2) between *cos(i)* and reflectance for all bands is shown in Figure 4. Excluding the water absorption wavelengths, most bands exhibited some relationship between *cos(i)* and reflectance (i.e., $p < 0.05$) that allowed the implementation of the normalization. For example, the R^2 for AVIRIS Band 19 (549 nm) shown on Figure 3a was 0.3; even so, implementing Equation 1 still resulted in the detrending of the data so that reflectance was no longer related to *cos(i)* (Figure 6). Most notable, however, was that the strength of the relationship between illumination and reflectance appeared to parallel the general reflectance curve for forests in GRSF. That is, the ability to correct for illumination is greater at wavelengths where the reflectance is the greatest, e.g., the near infrared where R^2 was around or above 0.6 for most bands. For example, the improved correction at the reflectance peak in the green wavelengths (558 nm) (compared to other visible bands) is especially notable on the 13 July 2001 AVIRIS image. These results are not surprising; they simply indicate that topographic effects are most readily corrected at wavelengths where the signal to the sensor is greatest. However, these results also show that robust corrections can be developed at wavelengths with low reflectance.

From a statistical perspective, an examination of R^2 only indicates how strong the relationship between illumination and reflectance is, but not the magnitude of the effect of illumination. On a band-by-band basis, the degree of terrain effect is best illustrated by examining the slope of the relationship between illumination and reflectance. That is, the greater the effect of illumination, the higher the slope between less illuminated pixels (low *cos(i)*) and more illuminated pixels (high *cos(i)*). The effects of illumination are most pronounced at those wavelengths with the highest reflectance (Figure 5). Again, this result is not surprising; it simply indicates that effects of shading are more dramatic where there is greater reflectance by the surface and hence signal strength at the sensor.

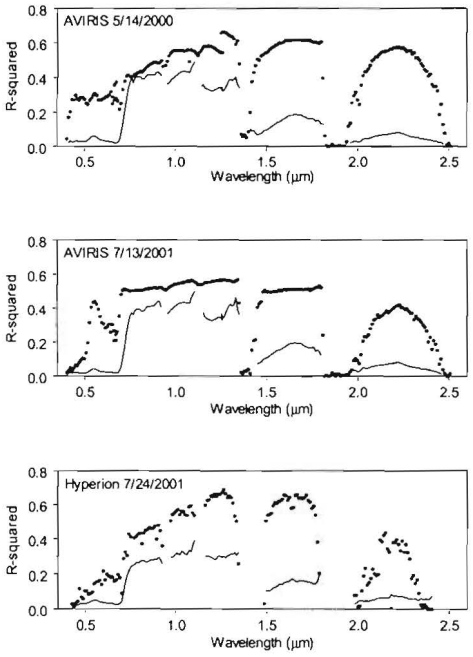

Figure 4. R^2 of reflectance as a function of illumination by wavelength (dots) for the images. Also shown is the average reflectance for oak forests in each image (lines).

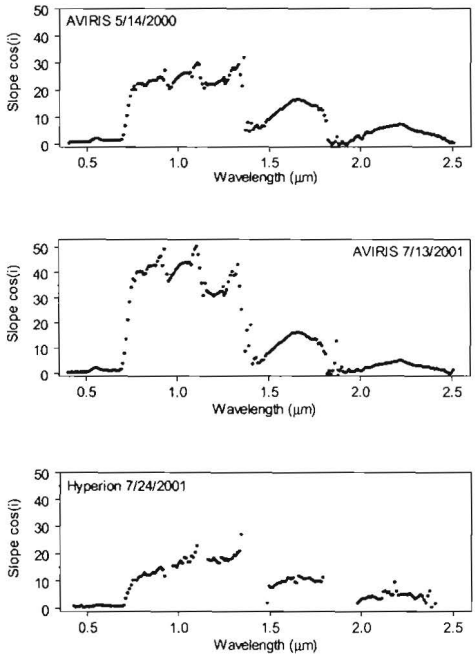

Figure 5. Slope of the regression line between reflectance and illumination by wavelength.

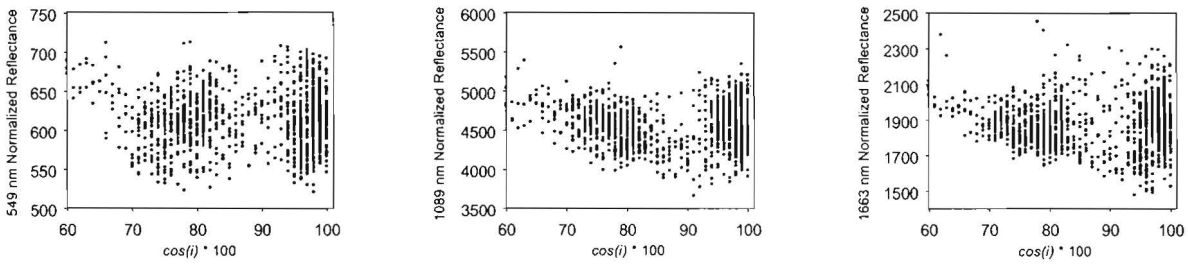

Figure 6. Relationship between illumination and reflectance following normalization for the 14 May 2000 AVIRIS image. Reflectance values on the y-axis are 10000 * reflectance.

The terrain normalization resulted in a substantial reduction of the effects of solar illumination in the AVIRIS and Hyperion images (Figures 6 and 7). In particular, areas on the illuminated and shadowed sides of steep ridges now exhibit comparable reflectance. It is notable that some areas along the ridges do not appear to have been corrected; in most cases these represent areas characterized by pines rather than oaks and as such have lower reflectance than surrounding areas. However, some areas were undercorrected, meaning that shaded slopes appear to remain shaded. These problems occur in areas where the images and DEM are slightly misregistered. An offset of even 2 pixels along the top of a steep ridge will result in a thin band of undercorrected pixels along the top of the ridge. Other DEM errors can also create problems; for example, our DEM, which was acquired from the National Elevation Database (NED), exhibited some regular striping that was corrected using a low-pass filter. However, this filtering has the effect of reducing slopes and thereby lowering apparent illumination differences as modeled from the DEM. This leads to the potential for underestimating the slope of the regression between *cos(i)* and reflectance. Nevertheless, the net effect of the correction was to reduce the effects of solar illumination, which should improve the ability to interpret the images and quantify differences in reflectance between forests with different properties.

4. CONCLUSIONS

An empirical method of terrain normalization (Allen, 2000; Meyer et al., 1993) was applied to AVIRIS and Hyperion images for a forested area of steep topography in the central Appalachian Mountains. The effects of differential illumination of the landscape were reduced in the corrected images, but were not eliminated altogether because of potential misregistration between DEMs and images. The empirical fit between reflectance and illumination was best at the near infrared wavelengths having the highest reflectance. However, statistically significant relationships between illumination and reflectance were found at almost all wavelengths. The greatest amount of correction – indicated by the steepness of the slope of the regression equation – was applied at wavelengths having highest reflectance. Therefore, we conclude that topographic effects are greatest when reflectance is highest and that those effects are also most easily modeled and corrected at the same wavelengths.

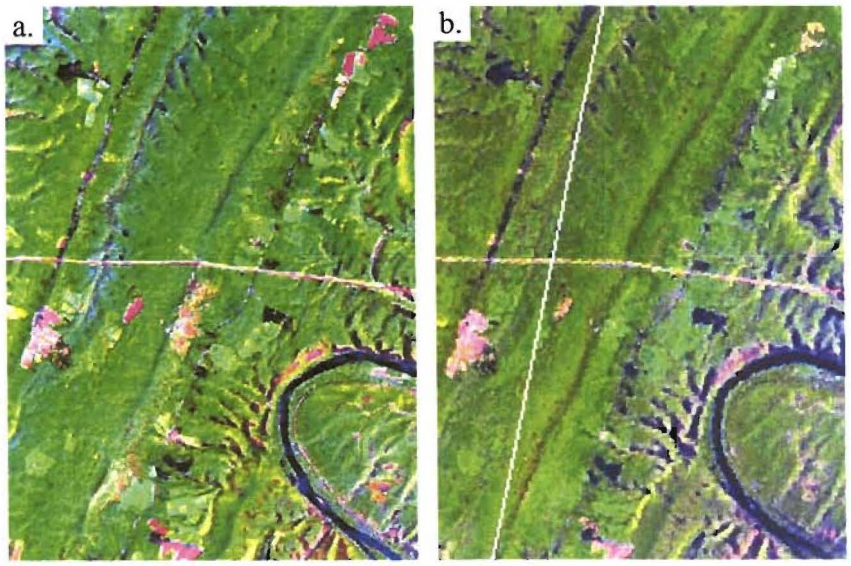

Figure 7. Normalized images of those shown in Figure 2: (a) AVIRIS from 14 May 2000 showing 1663 nm, 1089 nm, and 549 nm; (b) Hyperion from 24 July 2001, showing 1659 nm, 1256 nm and 570 nm. When compared with Figure 2, the illumination effects are greatly reduced. Dark areas on these images are generally pine forests; some areas are under-corrected due to mis-registration between the DEM and images.

Because the approach is rapid, and – with the exception of the selection of training pixels – automated, it can be readily applied to large hyperspectral data sets. Further, once training sites are established for a given area, the extraction of training data can also be automated. This approach is especially relevant for sites where the detailed information on tree physiognomy and bi-directional reflectance factors (BRDF) necessary for canopy based models are unavailable. Topographic normalization is essential for analyses of forests in rugged terrain, and the approach described here provides a simple approach with effective results.

5. ACKNOWLEDGMENTS

This research was supported by NASA EO-1 Science Validation Team grant NCC5-493. Thanks to Tom Allen for valuable discussions of terrain normalization, and to Clayton Kingdon, Carol Garner, Clay Baros and Robert Chastain for their contributions to this work. This paper is Scientific Series Contribution Number 3550-AL, University of Maryland Center for Environmental Science.

6. REFERENCES

Allen, T.R., 2000. Topographic normalization of Landsat Thematic Mapper data in three mountain environments. *Geocarto International*, 15(2): 13-19.

Civco, D.L., 1989. Topographic normalization of Landsat Thematic Mapper digital imagery. *Photogrammetric Engineering and Remote Sensing*, 55(9): 1303-1309.

Conese, C., Gilabert, M.A., Maselli, F. and Bottai, L., 1993. Topographic normalization of TM scenes through the use of an atmospheric correction method and digital terrain models. *Photogrammetric Engineering and Remote Sensing*, 59(12): 1745-1753.

Gao, B.C., Heidebrecht, K.B. and Goetz, A.F.H., 1993. Derivation of scaled surface reflectances from AVIRIS data. *Remote Sensing of Environment*, 44(2-3): 165-178.

Kennedy, R.E., Cohen, W.B. and Takao, G., 1997. Empirical methods to compensate for a view-angle-dependent brightness gradient in AVIRIS imagery. *Remote Sensing of Environment*, 62(3): 277-291.

Martin, M. E., Smith, M.L., Ollinger, S.V., Hallett, R.A., Goodale, C.L. and Aber, J.D., 1999. Applying AVIRIS at the sub-regional scale: Forest productivity and nitrogen and cation cycling. In: R.O. Green (Editor), *Proceedings of the Eighth JPL Airborne Earth Science Workshop*, Pasadena, California, pp. 275-279.

Meyer, P., Itten, K.I., Kellenberger, T., Sandmeier, S. and Sandmeier, R., 1993. Radiometric corrections of topographically induced effects on Landsat TM data in an Alpine environment. *ISPRS Journal of Photogrammetry and Remote Sensing*, 48(4): 17-28.

Minnaert, N., 1941. The reciprocity principle in lunar photometry. *Astrophysics Journal*, 93: 403-410.

Moran, M.S. et al., 2001. A refined empirical line approach for reflectance factor retrieval from Landsat-5 TM and Landsat-7 ETM+. *Remote Sensing of Environment*, 78(1-2): 71-82.

MAPPING NON-NATIVE PLANTS USING HYPERSPECTRAL IMAGERY

Emma Underwood,[1] Susan Ustin,[1] Deanne Dipietro[1]

1. INTRODUCTION

One of the significant threats to global biodiversity and ecosystem functioning is the spread of invasive plant species (Mooney and Cleland, 2001). Continuing anthropogenic related disturbances such as land conversion, grazing, and habitat fragmentation, combined with international trade and climate change indicate that these trends are likely to continue (Zedler and Scheid, 1988). In this context, the major challenge for land managers and ecologists is how to effectively manage non-native plants to preserve native biodiversity. Being able to delineate the spatial extent and ascertain the severity or intensity of the invasion is essential for resource management (Byers et al., 2001). This information provides a baseline for monitoring future expansion, the effectiveness of control efforts, and assists in identifying targets for control activities, such as satellite populations and 'invasion fronts.'

Techniques such as remote sensing offer significant opportunities for providing timely information on invasions of non-native species into native habitats. To date, there have been two divergent approaches (Everitt et al., 1996, Dewey et al., 1991). The first approach uses imagery with a high spatial, but low spectral resolution, such as black and white or color infrared aerial photographs. These photographs have the benefit of being relatively cheap, large amounts of archival data are available for many sites, and photographs are available at hyperspatial resolutions (0.1–2 m). However, the major disadvantage is that they rely on the non-native plant possessing visually detectable unique characteristics, extensive manual labor for processing and, finally, the resolution means that it is only feasible to collect data over a relatively small spatial area. The second approach uses digital images with greater spectral resolution, although coarser spatial resolution have been utilized—predominantly various airborne or spaceborne multispectral instruments. The use of digital multispectral imagery offers the opportunity for automated image processing, access to recent historical data for time series analyses, and large spatial coverage. However, the spatial resolutions of these sensors, such as TM and AVHRR imagery, mean that invasive species populations can often only be detected once, dense and widespread (Carson et al., 1995). In addition, traditional classification techniques like isodata or maximum likelihood, usually identify vulnerable land cover classes, rather than the non-native species itself. Consequently, maps have only a general applicability.

The availability of Airborne Visible/Infrared Imaging Spectrometer (AVIRIS) imagery with both increased spatial, but in particular spectral, resolution offers an enhanced potential for mapping invasive species. Because of the large number of wavebands (224) image processing is able to capitalize on both the biochemical and structural properties of the target invader. However, to date, there has been little evaluation of different processing techniques suitable for imaging spectrometry data for identifying invasive plants. The objective of this research is to investigate the use of AVIRIS imagery to detect the invasive species iceplant (*Carpobrotus edulis*) and jubata grass (*Cortaderia jubata*). More specifically, to compare three techniques for processing the imagery: Minimum Noise Fraction, Continuum Removal, and Band Ratio Indices, and to critically evaluate the relative ease of processing and repeatability of each method.

2. METHODS

2.1. Study Site and Vegetation Descriptions

The study site for this research is Vandenberg Air Force Base (VAFB) located along the central coast of California. VAFB is 39,800 ha in size and is used primarily for developing and testing missiles and satellite launches for the Department of Defense and NASA. Consequently, there are still significantly sized intact blocks of land representing one of the last undeveloped open areas of coastal California (Keil and Holland, 1998). There are 836 vascular plants documented at VAFB, of which almost a quarter are invasive species. In particular, *Carpobrotus edulis* and *Cortaderia jubata* have successfully invaded two native community types: coastal dune scrub community and maritime chaparral (Keil and Holland, 1998). The coastal scrub community forms a relatively

[1] Center for Spatial Technologies and Remote Sensing (CSTARS), Dept. of Land, Air & Water, University of California, Davis, One Shields Avenue, Davis, California 95616, USA. Corresponding author: eunderwoodrussell@ucdavis.edu

continuous cover of low to medium shrubs (< 1m tall), subshrubs, and herbs (Keil and Holland, 1998), and is dominated by California sagebrush (*Artemisia californica*), coyote bush (*Baccharis pilularis*), and mock heather (*Ericameria ericoides*). It is one of the most threatened community types in California, being rapidly fragmented and replaced by suburban developments, which makes the extensive iceplant invasion into remaining habitats of particular concern. The second community that iceplant is encroaching on is the maritime chaparral community characterized by broad-leafed and needle-leafed sclerophyllous shrubs, such as manzanita (*Arctostaphylos purissima, A.rudis*) and chamise chaparral (*Adenostoma fasciculatum*). An extensive area of this community—the Burton Mesa chaparral—is noted as one of the rarest and most threatened chaparral types in California, harboring extraordinary biodiversity (The Nature Conservancy, 1991). Invading iceplant, jubata grass, and other invasive species such as veldt grass (*Ehrharta calycina)* form mosaics with the native species. The focus of this research is the encroachment of iceplant and jubata grass into these native communities and specifically on the ability of AVIRIS to identify pixels of different densities of these species—the premise being that lower densities at the margins of the distribution, represent invasion fronts, and thus critical areas for management attention.

Iceplant (*Carpobrotus edulis*) (Figure 1) is native to South Africa and was introduced into California in ballast sand. By the 1950s it was used extensively for stabilizing land adjacent to roads. *C. edulis* is a succulent perennial forming mats up to 20 m wide and 50 cm deep (D'Antonio, 1993). The species' success is due to its tolerance of a range of soil moisture and nutrient conditions, and utilizing a number of mammals for seed dispersal (D'Antonio, 1993). Ecological impacts of iceplant include aggressive competition with native species, such as Tidestrom's lupine (*Lupinus tidestromii*), destabilizing native dune communities, and modifying soil pH. Economic impacts stem from the time and financial costs associated with both manual and mechanical control. Jubata grass (*Cortaderia jubata*), the second species of concern, is a perennial tussock grass from the Andes Mountains, characterized by huge creamy-pink plumes and long leaves (Figure 2). Introduced as an ornamental species it now dominates much of the coastal habitat of California. Jubata grass poses a significant threat to Mediterranean ecosystems because of its prolific wind dispersed seeds, tolerance of a broad range of habitats, and its competitiveness for light, moisture, and nutrients (Cowan, 1976).

2.2. Description of Fieldwork and Global Positioning System (GPS) Data Collection

Existing Geographic Information System (GIS) data layers were acquired from VAFB, including topographic maps, vegetation maps, road layers, and land use history, which were converted into a common Universal Transverse Mercator (UTM) projection. A field sampling methodology was designed and implemented in summer 2000 to coincide with the acquisition of the AVIRIS imagery. Sampling was undertaking in five community types identified *a priori*: intact coastal dune scrub, intact maritime chaparral, invaded scrub, invaded chaparral, and chaparral invaded by jubata grass. The location of the 352 fieldwork plots was random, but consideration was given to ease of access and location within the flightline. Field data was collected at three different scales to provide information from the plot through to the community level: measurements included percent cover by species, species height, type and size of disturbances, and soil characteristics. GPS readings (Trimble Pro-XRS, Trimble Navigation, Inc.) were taken of plot centers and around pure polygons of iceplant, jubata grass, and intact community types. Fieldwork also involved the acquisition of field-based reflectance spectra of the dominant native and non-native plant species and soil types in the area. Data were acquired at the time of the overflights using a GER 2500 (Geophysical Research, Corp.) field-portable spectrometer (400–2500 nm). Owing to almost continual coastal fog during the period around the overflight, only 80 individual spectra of target species at VAFB were acquired. AVIRIS data was acquired by the NOAA Twin Otter aircraft on 9 September, 2000 at 3,810 m, providing a nominal pixel resolution of 4 m.

2.3. Data Processing Techniques

The imagery was atmospherically corrected from radiance to reflectance with ACORN (Analytical Imaging and Geophysics LLC v.4) a commercial package based on MODTRAN, using the reflectance of target features from spectrometer data acquired in the field. The AVIRIS scenes were spectrally and spatially sub-setted to allow for rapid georeferencing and noisy bands were removed (ENVI software v.3.4; Research Systems Inc.). Masks were created to limit processing to vegetated areas - identified as pixels with an NDVI > 0.2, to reduce the number of classes in the classification process. GPS points and polygons of known community types and species were differentially corrected (Pathfinder Office v.2.8; Trimble Navigation, Inc.) and used to generate regions of interest (ROIs). These ROIs then served as training polygons for conducting supervised classifications.

Three processing techniques were compared: a supervised classification based on the results of a Minimum Noise Fraction, an unsupervised classification using the results of the Continuum Removal applied to the 932 nm

water absorption feature (875 – 1032 nm), and finally a supervised classification performed on a dataset composed of selected Band Ratio Indices.

2.3.1. Minimum noise fraction classification

A Minimum Noise Fraction (MNF) was performed on each flightline to reduce and compress the data and to increase the speed of data processing. The MNF sequentially performs two Principle Component Analyses (PCA) on the data: the first separates white noise (i.e., uninformative data), the second recombines these bands into new composite bands which account for most of the variance in the original data (informative data). Based on the MNF output graph of eigenvectors and visually inspecting the new bands, a conservative noise floor was established and the first 12 bands were selected as inputs for the classification. The results of the MNF were georegistered and a maximum likelihood supervised classification performed. Twelve intact and invaded community classes were generated for VAFB, including five different densities of iceplant, three densities of jubata grass, and a class for intact scrub.

2.3.2. Continuum removal for water bands

The second technique investigated to classify specifically iceplant was a Continuum Removal of the water absorption bands, which was assumed to be particularly applicable to the fleshy succulent leaves of *C. edulis* (Figure 3). The Continuum Removal technique isolates spectral features and standardizes reflection across the liquid water absorption features so that they may be intercompared (Clark and Roush, 1984). The advantage is that values are independent of differences across the image such as illumination or shadow. The process involved spectrally subsetting 34 bands of the image; 17 around 932 nm (between the wavelengths 875–1032 nm) and 17 around 1155 nm (1070–1221 nm). Water absorption is calculated from the area under the absorption feature divided by the area under the continuum, resulting in a range of values from 0 to 1; the lower the value, the greater the absorption. This is illustrated in Figure 3, which shows a comparison of the reflectance spectra of pixels having two different densities of iceplant compared to a pixel of intact coastal scrub. The graph shows two distinctive absorptions for dense iceplant centered on the 932 nm and 1155 nm wavelengths. Visual inspection of the resulting images showed greater accuracy when using wavelengths centered around 932 nm than the 1155 nm feature due to the atmospheric water vapor absorption at 1240 nm. An unsupervised classification (K-means method) was then conducted using the derived image, classifying five community classes for VAFB.

2.3.3. Band ratios indices

Finally, use of selected vegetation indices that emphasize bands containing important biochemical and biophysical properties of the vegetation. Vegetation indices are clearly correlated with foliage chlorophyll absorption as well as Leaf Area Index, percent green cover and biomass, productivity, and photosynthetic capacity (Ustin et al., 1999). The NDVI is perhaps the most well known of these vegetation indices, while the water band index has been shown to be a good indicator of leaf and canopy water content (Peñuelas et al., 1997; Serrano et al., 2000), and the red-edge spectral parameters for chlorophyll concentration (Zarco-Tejada and Miller, 1999). Even so, using a combination of vegetation indices for a classification has received limited application for ecological studies (Fuentes et al, 2001). We seek to assess how well a land cover classification based on data from this technique compares to the results using MNF and Continuum Removal approaches. Five indices were calculated on the calibrated image, capturing NDVI, water absorption, greenness, and pigment properties (Table 1), and combined into a single image. A maximum likelihood supervised classification was performed on the results.

3. RESULTS

A visual comparison of the three classification results (Figures 4, 5, 6) shows iceplant is clearly distinguished in all analyses with a similar spatial configuration: highest densities parallel to the coastline and tapering off with increasing distance inland (in a northeast direction). Separation of different density levels of iceplant is evident in all three images. Field validation was undertaken in August 2001 to perform ocular cover estimates by species of the classification performance and also acquire GPS polygons for a formal verification of image classes.

A total of twenty-three regions of interest were acquired during the second period of fieldwork across intact scrub and iceplant at four different densities (≤ 50%, 51-75%, 76-90%, 91-100%) to provide the reference data for validation (Table 2). An evaluation of the three images for simply classifying presence/absence of iceplant of any density had very high success: 99% for the MNF, and 98% for the Continuum Removal and Band Ratio

techniques—indicating that the distinctive succulent characteristics of iceplant are being identified in each method. It is more informative; however, to compare the accuracy assessment for the intact scrub class and each of the different densities of iceplant classes in turn using a confusion matrix (Congalton, 1991). For intact scrub and any density of iceplant the Band Ratios and MNF results achieved comparable levels of accuracy: 92% and 91% respectively. When this assessment was limited to intact scrub and iceplant with densities > 50% and then further refined to intact scrub and iceplant density > 75% the Band Ratios technique performed marginally better in both cases: 90% v. 88% and 90% v. 86%. The Continuum Removal approach also performed well - achieving 89% and 84% respectively. But in a comparison of intact scrub and the densest class of iceplant (> 90%) the MNF approach performed best.

Significant differences between the three approaches were only revealed by looking at the overall accuracy across all four density classes: intact scrub, iceplant 51%-75%, 76%-90%, and 91%-100%. In this case, the MNF result was superior, achieving a 55.2% overall accuracy and a kappa value of 0.36, compared to Band Ratios with 44% accuracy (kappa = 0.26), and finally Continuum Removal with a 39% accuracy (kappa = 0.20%). It is interesting to note the percent of iceplant pixels that were confused as scrub pixels is relatively low for all methods, on average 8% and 4%, and 13% for MNF, Band Ratios, and Continuum Removal respectively. This illustrates that the primary source of confusion is in classifying different densities of iceplant, rather than confusing iceplant with scrub pixels.

Although no formal accuracy assessment was performed for the results of the jubata grass classification, fieldwork verification indicated that the results from the MNF and Band Ratio Indices performed similarly. The MNF method did distinguish three density classes although it overestimated the total extent, in some cases confusing jubata grass with areas of eucalyptus trees (Figure 5). The Band Ratio technique provided a more realistic estimate of extent of jubata grass (Figure 6), identifying the major infestations in the northeast corner of the image where jubata grass has rapidly invaded areas of disturbed chaparral.

4. DISCUSSION

Effective management of invasive species requires accurate knowledge of their spatial distribution and density, which all three processing methods succeeded in capturing, producing some encouraging results. The following discussion evaluates the three methods in terms of accuracy, logistics of processing, and ease of interpretation.

The techniques were extremely successful in detecting the presence of iceplant and jubata grass. However, the MNF and Band Ratio techniques were better able to distinguish different densities of iceplant. This is because these two techniques utilize significantly more information from the image. The MNF classification utilized the 12 most informative transformed bands while the Band Ratios used five key indices capitalizing on the physiological properties of the species. In contrast, the Continuum Removal method relies solely on the seventeen bands around the 932 nm water absorption feature, which explains why it performed relatively well for classifying areas of dense iceplant, but poorly when the iceplant forms more complex mosaics with the scrub species. The confusion matrices demonstrate that the MNF and Band Ratio methods performed equally as well, one disadvantage of the Band Ratio classification is that it produced a speckled image with single and double pixels scattered throughout. Even after a sieving and clumping of the image was performed to generalize the spatial patterns, the accuracy only increased by 1.8%. This improvement in accuracy is not significant and not warranted at the expense of losing information, particularly along critical invasion boundary areas. Also, a proportion of the inaccuracies occurring in the classification are most likely attributable to a combination of errors in both the georegistration of the image and the accuracy of the GPS polygons despite differentially correcting the acquired positions.

Interpretation of the different techniques varied markedly. The MNF method was the most difficult to interpret. Although values from each of the eigenvectors generated by the PCA can be graphed, interpreting the basis of spectral variation was difficult. Even in wavelengths of water absorption there were no consistently high eigenvalues. Alternatively, using the Band Ratios has the advantage of being more intuitive, highlighting ecophysiological information about the vegetation that can be readily related to the data collected in fieldwork.

From a processing perspective, the Continuum Removal method was by far the most efficient, which involved running a single standard procedure in the ENVI software. In contrast, the MNF procedure was time and processing intensive, taking several hours to run and creating a 1.8 GB file for each of the two processing modes. In terms of identifying repeatable methods for future use, the Continuum Removal and Band Ratio techniques are easily transportable for images acquired at different times or over different geographic areas. In contrast, the MNF approach cannot be applied to new data as it is unique to the variance of each flightline.

In brief, the Continuum Removal method is a reliable method for depicting presence/absence of iceplant within a scrub community. Coupled with this is the ease and efficiency of processing, which makes it an attractive approach for inexperienced users of hyperspectral data. Such a method is also likely to be applicable to other invasives such as the giant reed (*Arundo donax*) which has a high water content in the stem. In contrast, the MNF and Band Ratio approaches were most accurate in delineating the spatial extent and density of iceplant and jubata grass. This might be particularly important for management activities, where the early detection of iceplant encroachment into endangered native scrub communities is important for prioritizing control methods and activities. By using field derived polygons as inputs for the supervised classification, these techniques also had the additional advantage of classifying all communities across the image.

Land managers wishing to use imagery for mapping and monitoring invasive plants have a tradeoff between spatial and spectral resolutions and costs. At one extreme the virtues of low spectral, high spatial resolution imagery (aerial photos) are well known, while this research illustrates that AVIRIS imagery offers improved opportunities for mapping invasive plants in a matrix of other vegetation types. The improved spectral resolution of the AVIRIS imagery permits identification of vegetation characteristics that are not possible using multispectral wavebands traditionally used in remotely sensed imagery. However, one interesting question is whether further improvements in resolutions are necessary. Interestingly, we found for the target species that it was possible to achieve adequate results using only a portion of wavebands available (Band Ratios and Continuum Removal), which could potentially mean fewer bands need to be acquired and processed, with possibly lower associated costs. However, the specific bands needed to map the full range of land cover types may still require a hyperspectral imager. Similarly, the 4 m resolution of the AVIRIS data also proved sufficient for detecting *C. edulis* and *C. jubata*. Despite the common belief that higher spatial resolutions are necessarily better, in this case it might have produced only marginally improved results, but disproportionately increased the computing and processing requirements. Although the current costs of hyperspectral data means that frequent acquisitions over large areas are probably not feasible, it is a highly appropriate technique for monitoring hotspots of invasions along selected transects. In addition, various data nesting strategies might be employed to optimize the spatial and spectral resolutions required.

5. CONCLUSIONS

This research describes encouraging findings for using hyperspectral imagery to map iceplant and jubata grass in California's Mediterranean-type ecosystems. The next step is to evaluate how well these approaches can be applied to invasions of these species in different habitat types and also their ability to detect other invasive species. Given the ecological and economic impacts of invasive plants, together with their rates of spread, they constitute one of the most critical issues for many land managers (Goodall and Naude, 1998). The immediate benefit of this research has been to contribute to the knowledge base of land managers at VAFB by providing improved information on the spatial extent and density of the iceplant and jubata grass, that will lead to better protection of the native biodiversity. Additionally, the project evaluated three different methods for processing AVIRIS imagery which can now be tested in other geographic locations or for other invasive species.

6. ACKNOWLEDGEMENTS

We would like to thank George Scheer, Pablo Zarco-Tejada, and Karen Olmstead from CSTARS at U.C. Davis for assistance in processing of the imagery; Teresa Magee at Dynamac for providing input and advice on the project and John Brooks; and Amparo Rifa for helping to conduct fieldwork. Funding for this project was provided by the Department of Defense's Strategic Environmental Research and Development Program.

7. REFERENCES

Byers, J.E., Reichard, S.H., Randall, J.M., Parker, I.M., Smith, C.S., Lonsdale, W.M., Atkinson, I.A.E., Seastedt, T.R., Williamson, M., Chornesky, E., and Hayes, D., 2001, "Directing research to reduce the impacts of nonindigenous species," Conservation Biology (in press).

Carson, H.W., Lass, L.W., and Callihan, R.H., 1995, "Detection of yellow hawkweed with high resolution multispectral digital imagery," Weed Technology, vol. 9, pp. 477-483.

Clarke, R.N. and Roush, T.L., 1984, "Reflectance spectroscopy: quantitative analysis techniques for remote sensing applications," Journal of Geophysical Research, vol. 89, pp. 6329-6340.

Cowan, B., 1976, "The menace of pampas grass," Fremontia, vol. 4, no. 2, pp. 14-16.

Congalton, R.G., 1991, "A review of assessing the accuracy of classifications of remotely sensed data," Remote Sensing of Environment, vol. 37, pp. 35-46.

D'Antonio, C., 1993, "Mechanisms controlling invasion of coastal plant communities by the alien succulent *Carpobrotus edulis*," Ecology, vol. 74, no. 1, pp. 83-95.

Dewey, S.A., Price, K.P., and Ramsey, D., 1991, "Satellite remote sensing to predict potential distribution of dyers woad (*Isatis tinctoria*)," Weed Technology, vol. 5, pp. 479-484.

Everitt, J.H., Escobar, D.E., Alaniz, M.A., Davis, M.R., and Richerson J.V., 1996, "Using spatial information technologies to map Chinese tamarisk (*Tamarix chinensis*) infestations," Weed Science, vol. 44, pp. 194-201.

Fuentes D.A,. Gamon, J.A., Qiu, H.L., Sims, D.A., and Roberts, D.A., 2001, "Mapping Canadian boreal forest vegetation using pigment and water absorption features derived from the AVIRIS sensor," Journal of Geophysical Research-Atmospheres, vol. 106, no. D24, pp. 33565-33577.

Keil, D.J. and Holland, V.L., 1998, "The vegetation of Vandenberg Air Force Base", report prepared for The Nature Conservancy and Vandenberg Air Force Base.

Mooney, H.A. and Cleland, E.E., 2001, "The evolutionary impact of invasive species," Procedures of National Academy of Science, vol. 98, no. 10, pp. 5446-5451.

Peñuelas, J., Pinol, J., Ogaya, R., and Filella I., 1997, "Estimation of plant water concentration by the reflectance Water Index WI (R900/R970)," International Journal of Remote Sensing, vol. 18, no. 13, pp. 2869-2875.

Serrano, L., Ustin, S.L., Roberts, D.A., Gamon, J.A., and Peñuelas, J., 2000, "Deriving water content of chaparral vegetation from AVIRIS data," Remote Sensing of Environment, vol. 74, no. 3, pp. 570-581.

The Nature Conservancy, 1991, "Fish and wildlife management plan for Vandenberg Air Force Base," revision number 3 for Plan Period August 1991 to August 1996.

Ustin, S.L., Smith, M.O., Jacquemoud, S., Verstraete, M, and Govaerts, Y., 1999, "Geobotany: vegetation mapping for earth sciences," in: A.N. Rencz (Ed.), Remote sensing for the earth sciences: manual of remote sensing. John Wiley and Sons, New York, vol. 3, pp. 189-248.

Zarco-Tejada, P. and Miller, J.R., 1999, "Land cover mapping at BOREAS using red edge spectral parameters from CASI imagery," Journal of Geophysical Research, vol. 104, no. D22, pp. 921-933.

Zedler, P.H. and Scheid, G.A., 1988, "Invasion of *Carpobrotus edulis* and *Salix lasiolepis* after fire in a coastal chaparral site in Santa Barbara county, California", Madrono, vol. 35, no. 3, pp. 196-201.

8. FIGURES AND TABLES

Fig. 1. Iceplant

Fig. 2. Jubata grass

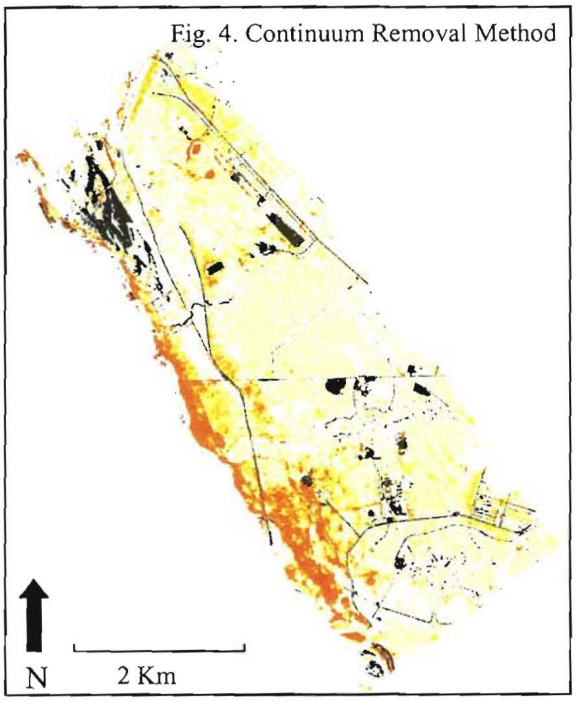

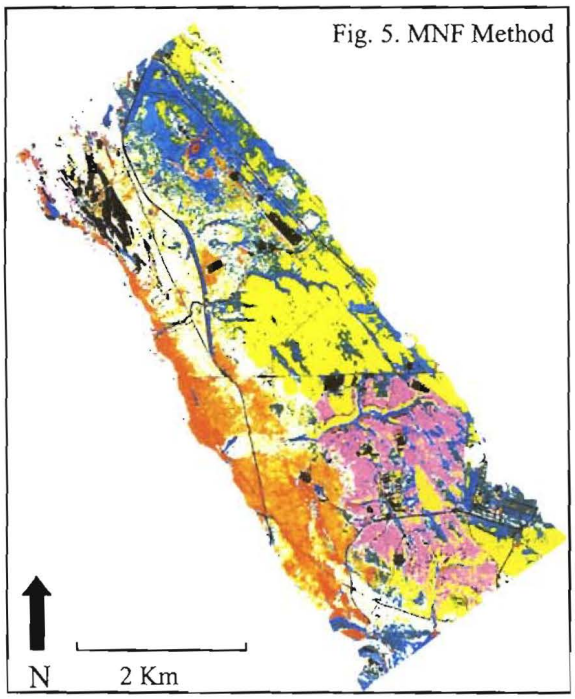

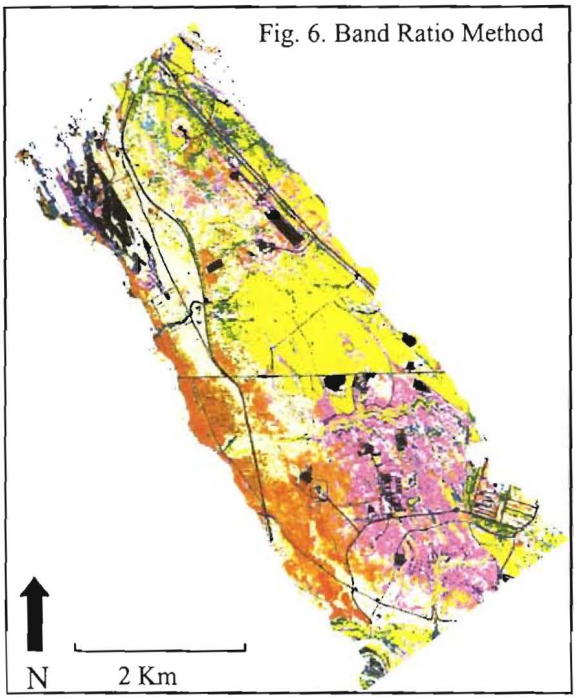

Intact scrub
Iceplant 91-100%
Iceplant 76-90%
Iceplant 51-75%
Iceplant 26-50%
Iceplant 0-25%
Jubata grass 0-33%
Jubata grass 34-66%
Jubata grass 67-100%
Chaparral with Iceplant
Intact chaparral
Masked

Table 1. Wavebands used to calculate vegetation indices (adapted from Fuentes, 2001)

Index	Bands	Wavelengths	Source
Red/green ratio	Chlorophyll	683/510	Gamon and Surfus (1999)
Index of pigment	Pigment	750/710	Gamon and Surfus (1999)
Index of water 1	Water content	970/900	Penuelas et al. (1997)
Index of water 2	Water content	1193/1126	Image inspection
NDVI	Green vegetation	895-675/895+675	Modified from Tucker (1979)

Table 2. Summary of confusion matrix results for the three methods

Class	MNF	Kappa	Continuum Removal	Kappa	Band Ratios	Kappa
Single Class						
Iceplant 0-100%	98.98%	N/A	97.95%	N/A	97.98%	N/A
Scrub & 1 iceplant class						
Scrub and iceplant 0-100%	91.3%	0.50	N/A	N/A	92.3%	0.51
Scrub and iceplant > 50%	87.5%	0.44	89.1%	0.60	90.3%	0.50
Scrub and iceplant > 75%	86.4%	0.55	84.9%	0.63	89.7%	0.63
Scrub and iceplant > 90%	82.4%	0.56	77.5%	0.58	80.3%	0.57
Scrub & all 3 density classes	55.2%	0.36	38.5%	0.20	44.2%	0.26

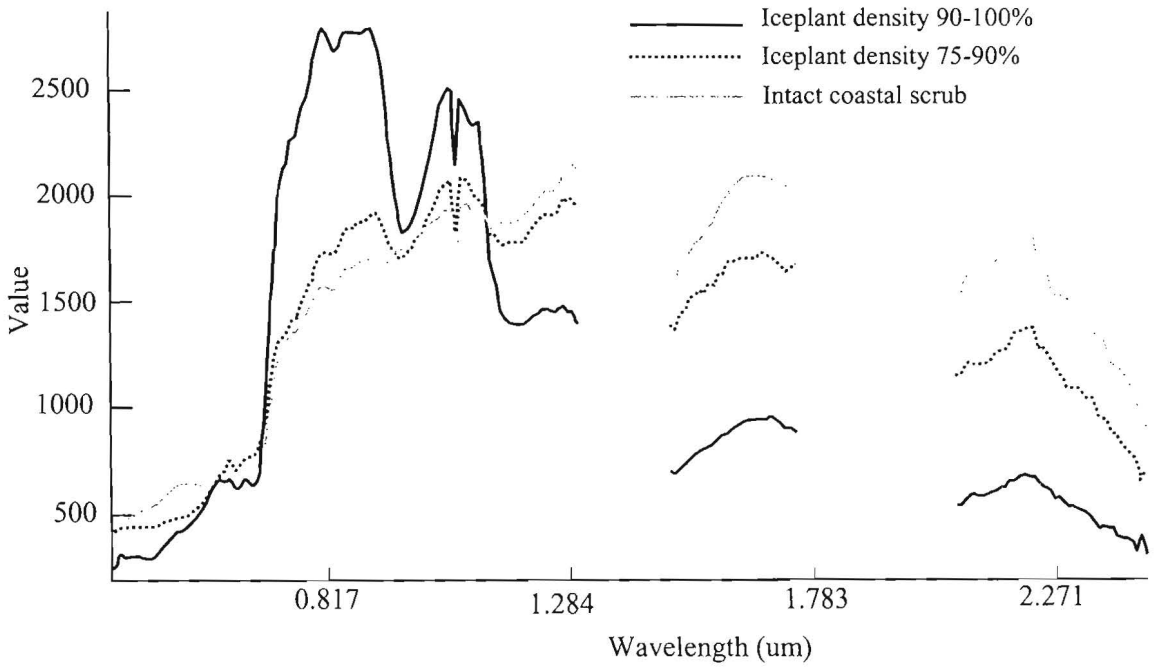

Fig. 3. Reflectance Spectra Showing Absorption in the Water Band

An Integrated Approach to the Discrimination of Riparian Vegetation in the Navarro River Watershed, Mendocino County, California, USA

Joshua H. Viers,[1] Charlene T. Sailer,[2] Carlos M. Ramirez,[1] James F. Quinn,[1] AND Michael L. Johnson[3]

In July of 2000, the Information Center for the Environment (ICE) and Center for Spatial Technologies and Remote Sensing (CSTARS) collaborated with National Aeronautics and Space Administration – Jet Propulsion Laboratory (NASA – JPL) to obtain Airborne Visible InfraRed Imaging Spectrometer (AVIRIS) data of the Navarro River watershed. The Navarro River watershed is located in southern Mendocino County, California, USA. This watershed, 820 km^2 in size, drains into the Pacific Ocean and provides a unique opportunity to investigate a closed hydrologic system (Figure 1). A mixture of redwood and mixed conifer forests, oak woodlands, open grasslands, and agricultural areas provides an array of land uses from which to analyze interactions with aquatic and riparian habitats. The Navarro River watershed supports a resource-based economy; timbering, grazing, and limited cropping are the primary land use activities in the watershed. However, recent changes in the California economy have resulted in increased viticultural activities and an increase in the local human population (ca. 3500) within this watershed. These combined factors have resulted in pervasive land use change in the last 150 years, from which researchers have sought to inventory, catalogue, and provide a synopsis of the ecological state of the watershed.

Using a large area, high spatial resolution collection of AVIRIS data for the Navarro River watershed, a classification of riparian vegetation was initiated using a combination of traditional ecological assessment techniques and hyperspectral data analysis. The Navarro River watershed is the focal point of many ongoing, multidisciplinary investigations concerning anthropogenic disturbance of watershed processes, such as logging, road building, and land conversion to vineyards and other agriculture, and resulting ecological responses. Namely, these studies have focused on the role that land use activities play in perturbing anadromous salmonid populations and habitat. Riparian vegetation is a key habitat parameter in that it regulates many of the ecosystem components necessary for salmon reproduction, rearing, and migration through its effect on stream shading, contribution of large woody debris, and allocthonous inputs to the stream system, none which can be assessed comprehensively from ground studies due both to the size of the area and limited access to private lands. The primary goal of this project was to test the suitability of hyperspectral analytical techniques to identify and asses riparian vegetation over an area with complex topography and land use. In particular, our goals were to use ecological field data to 1) provide *a priori* expectations of vegetation classifications, 2) serve as a verification for spectral classification, and 3) to serve as a basis from which to nest the classification results within ongoing, national efforts of cataloging vegetation.

A series of traditional vegetation classification methods were employed on field data to determine the expected species composition of vegetation communities within the riparian zone. The traditional methods of vegetation classification from field collections are based on clustering algorithms and factor analyses, such as TWINSPAN (Hill, 1979), and these methods were used to establish an expected distribution of species for the watershed. To limit spectral feature extraction of possible riparian vegetation to locations near waterways, a riparian zone was delineated by using topographic features generated from a digital elevation model of the watershed. The process results in a hierarchical framework with expected species distributions that represent field conditions; this framework was then integrated with hyperspectral feature extraction methods, such as endmember selection, to discriminate different vegetation communities within the riparian zone.

Efforts to bridge vegetation community ecology and spectral technologies are not new; however, the use of hyperspectral data analysis to elucidate both specific constituents of vegetation communities and intra-community differences is a dynamic, adaptive science (Roberts et al., 1998). Techniques of both vegetation ecologists and spectrometrists are directed toward pattern detection. Vegetation ecologists typically do not test *a priori* hypotheses – studies are far more often observational or descriptive, with a focus on inductive, multivariate methodologies. Similarly, spectrometry relies on the multi-, or hyper-, variate differences among materials to effectively discriminate and identify classes of objects. In this paper, we engage in methods to identify physical relationships that are evident in both ecological and spectral space. Namely, riparian plant species were identified and categorized into communities on the ground. AVIRIS data were used to both classify vegetation communities within the riparian

[1] Department of Environmental Science and Policy, University of California, Davis (jhviers@ucdavis.edu)
[2] Crocker Nuclear Laboratory, University of California, Davis
[3] John Muir Institute of the Environment, University of California, Davis

zone and to identify diagnostic species spectrally. The results of our study indicate that the composition of species within vegetation communities is reflected in both variable spaces: ecological and spectral.

Methods:

The following software packages were necessary for the procedures detailed below: ESRI ArcInfo v. 8.0.2 (Environmental Systems Research Institute, Inc.); ERDAS Imagine v. 8.5(Leica Geosystems, Atlanta, Georgia); RSI ENVI v. 3.5 (Research Systems Inc., Boulder, Colorado); RSI IDL v. 5.5 (Research Systems Inc., Boulder, Colorado); PARGE v. 1.3 and ATCOR4 v. 2.0 (ReSe Application Schläpfer, Zurich, Switzerland), and PC ORD v. 4.14 (MjM Software, Gleneden, Oregon).

In all, NASA flew 26 of the 29 proposed flightlines over a period of three days in late July of 2000. For this preliminary hybrid classification analysis, we have chosen one representative flightline (FL) from the collection to process: FL 18 (Figure 1). Elevation of the study site ranges from sea level to 1054 m with most ridge tops paralleling the San Andreas Fault in a southeast to northwest direction toward the Pacific Ocean.

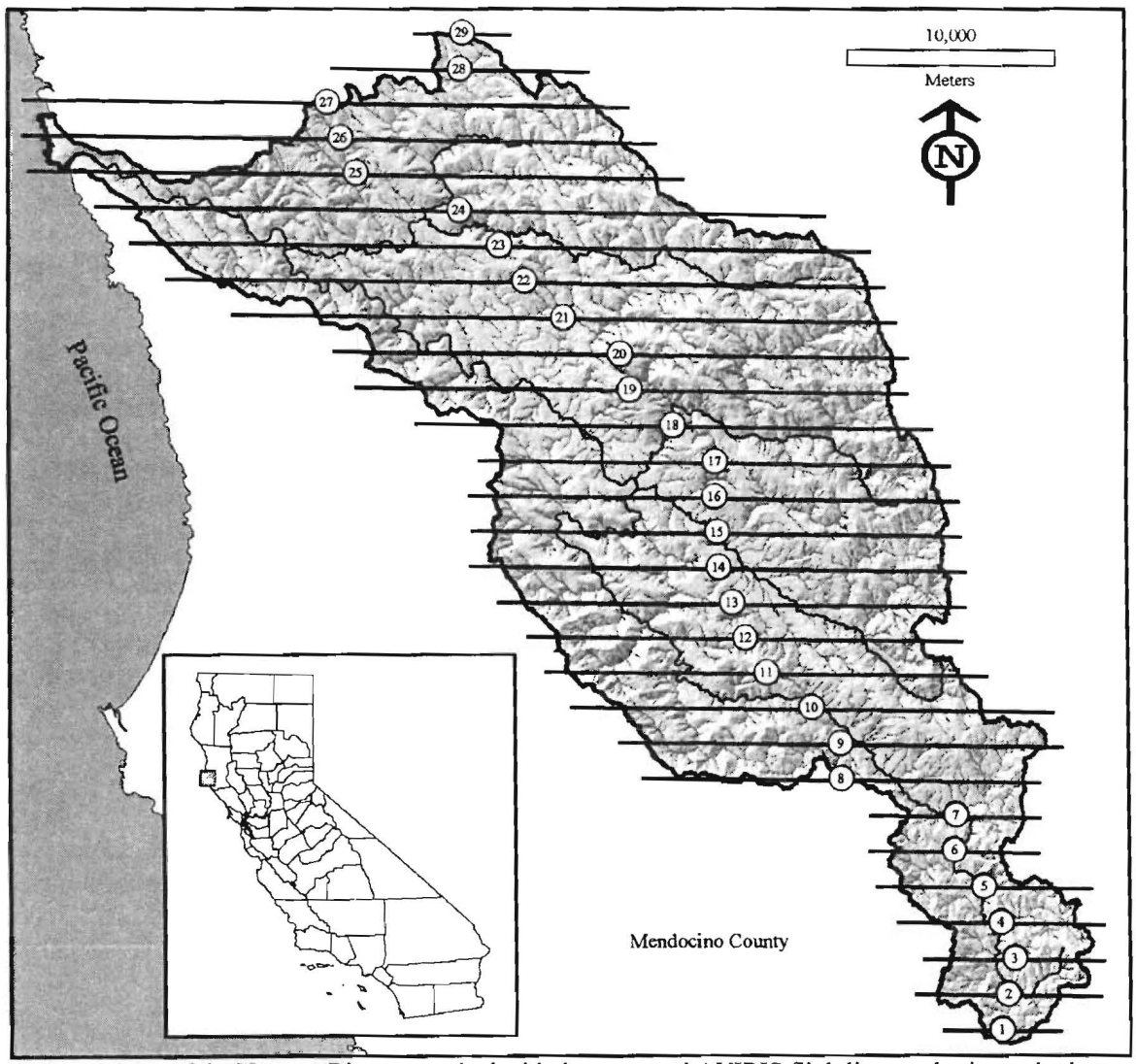

Figure 1. Map of the Navarro River watershed with the proposed AVIRIS flightlines and primary hydrographic features. All but flightlines 1-3 were flown in July 2000. Flightline 18 is the focus of this study. Inset Map shows position of watershed in Mendocino County, California.

NASA – JPL supplied the AVIRIS data in radiometrically corrected format on 8mm tape. Tape contents were uncompressed to a common file space on a sixteen-processor SGI Origin 2000 supercomputer; each flightline

totals approximately 1.5 – 2.5 gigabytes. To geometrically correct flightline data, a terrain correction software package, Parametric Geocoding (PARGE) (Schläpfer, 2000), was used. PARGE integrates the inertial navigation unit readings, flight GPS positions, and ground control points (GCPs) to correct for pitch, roll, heading, and yaw. This procedure also incorporates a Digital Elevation Model to adjust for topographic effects. Prior to initiating PARGE, each frame was mosaicked in ENVI to create a seamless flightline. AVIRIS data were converted from BIP to BSQ in ENVI. GCPs were collected by using a combination of ENVI and Imagine tool sets and Digital Orthophoto Quarter Quadrangles as a visual anchor. GCPs were systematically eliminated based on their X and Y coordinate offsets until the GCP Residual (RMSE) was less than 5.0 m. A 10-m USGS Digital Elevation Model of the watershed was resampled to 5 m cell resolution using bilinear interpolation and converted in ArcInfo from a grid to a DEM in USGS format (ESRI, 2001). The USGS format DEM was imported into ENVI to be used with PARGE, along with the GCPs. The final AVIRIS data were resampled to 5m from the native 3.3-m to 4.2-m spatial resolution. The geo-corrected results from PARGE, in addition to field spectra of pseudo-invariant targets, such as Navarro Beach and the Boonville Airport, were incorporated into ATCOR4, an atmospheric correction software package (Richter, 2000). ATCOR4 corrects for sun angle, atmospheric moisture and particulates, topography, off-nadir viewing angles, and shadows. Once the FLs were geometrically and atmospherically corrected, "noisy" bands were eliminated. Bands were visually inspected and dropped from the analysis if their respective response signatures for a known material deviated from the expected response. The following bands were chosen as acceptable for further analysis: 2–104, 116–152, 168–220 (384.46 nm–1324.15 nm, 1443.7 9 nm–1802.45 nm, 1950.66 nm–2469.24 nm, respectively) and resulted in a final spectral product.

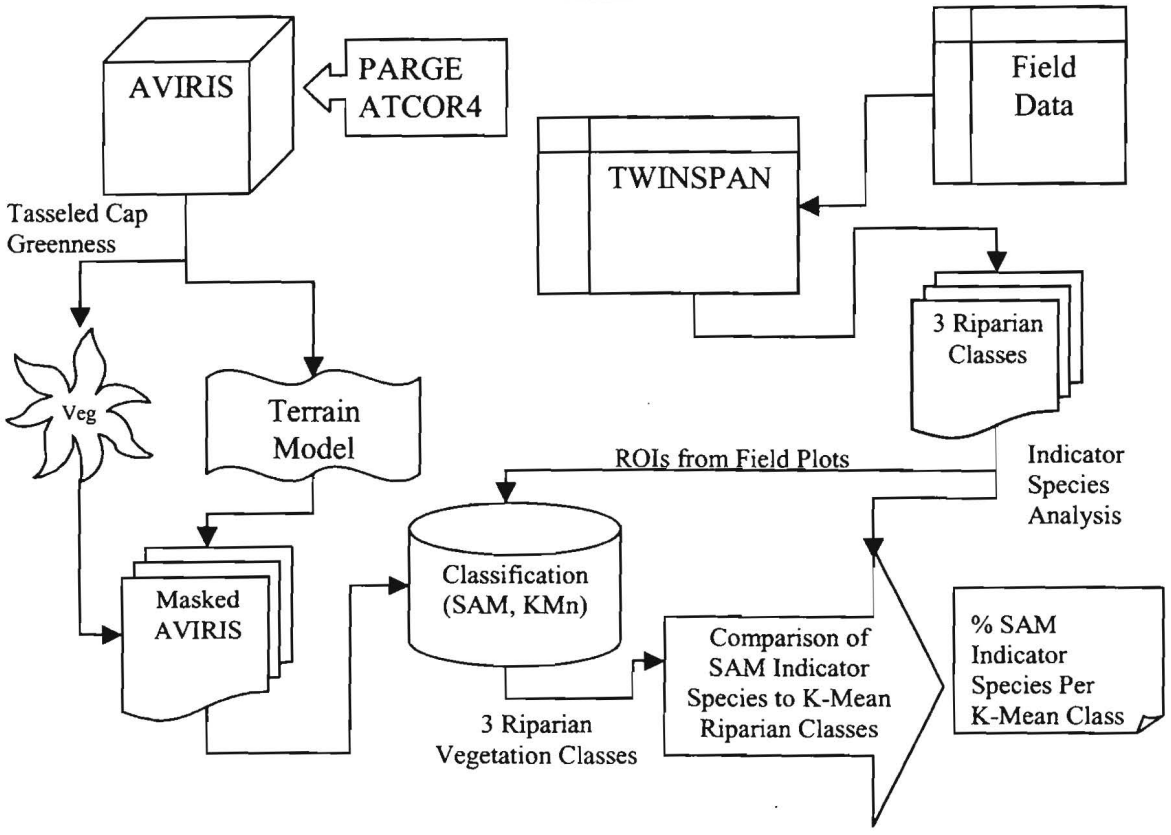

Figure 2. Processing flow diagram for the hybrid methodology to discriminate riparian vegetation.

The process for isolating riparian vegetation relies on a hybrid methodology, which incorporates an intersection of two masks, an ecological field data classification, a field-integrated spectral classification, an ecological field data indicator species analysis, and a final spectral comparison of indicator species within classes (Figure 2). The dual masking procedure is part terrain analysis and part spectral transformation. The spectral masking involved the transformation of the spectral array into three data planes using the Tasseled Cap transformation (Jackson, 1983, Richards and Jia, 1999). A processing script was developed in Interactive Data

Language (IDL) to extract data planes via the Tasseled Cap procedure for soil brightness, vegetation greenness, and water saturation (Jackson, 1983, Richards and Jia ,1999). The IDL script uses Regions of Interest (ROIs) as inputs for each data plane and the spectral downselected bands are used in the input array. To develop a series of ROIs, FL 18 was transformed using Boardman and Kruse's (1994) Minimum Noise Fraction (MNF) routine to collapse the input data array into 92 dimensions; ultimately the twenty dimensions with the highest eigenvalues were used for classification. ROIs were defined for pixels encoded by the Pure Pixel Index (1000 iterations) (Boardman et al., 1995) on the MNF transformed arrays. ROIs, in this case, were selected to represent soil brightness, vegetation greenness, and water saturation. Flightline 18 was examined for the distribution of values from the three-band transform array and each plane was bisected to separate materials based on its modal distribution. Vegetation was determined to have a "greenness" array value greater than the least first standard deviation from the mean.

To reduce spectral variability and errant classification of riparian vegetation in upland vegetation communities, the vegetation pixels were further segmented with a Riparian Extent Mask. The Riparian Extent data grid was created as a combination of two inputs. The first input is a Euclidean distance from streams data grid that was natural log transformed and rescaled from 1–100. A break point of 37.4 was chosen; it represents one standard deviation less than the mean. The second input represents the least cost path away from streams where Degree Slope is the cost. The results were natural log transformed and rescaled 1–100. A break point of 76.6 was chosen; it represents one standard deviation less than the mean. The Riparian Extent Mask represents the intersection of these two grids. This Riparian Extent Mask was then used to limit the influence of upslope vegetation on the spectral classification of the AVIRIS data and the Tasseled Cap Greenness plane was used as a mask to restrict the spectral classification to vegetation solely.

The hyperspectral classification incorporated the results of ecological data analysis of fieldwork conducted in the summer of 2000. The riparian fieldwork consisted of 6–10 m x 10 m quadrats randomly placed along each study reach at sixteen study sites throughout the watershed (Figure 3). Study sites were stratified to represent major tributaries in the watershed and position in the watershed, in terms of upstream accumulative drainage area. This stratification also recognizes differences in elevation, geologic substrates, and distance to the Pacific Ocean—a primary climatological determinate. We identified all woody species, estimated percent cover of each woody species, measured all stems greater than 10cm at diameter breast height, measured tree heights with a LaserTech Impulse 2000 Rangefinder, and located quadrat boundaries with a Trimble ProXRS DGPS. Additional field verification plots and individual species locations were geographically located with DGPS as well.

The species cover data were analyzed using Two-Way Indicator Species Analysis (Hill, 1979, McCune and Mefford, 1999). TWINSPAN can be described as dichotomized ordination analysis, in that an iterative character weighting is used to separate species affinities based on the incorporation of *pseudo-species* to represent differences in abundance for each observed species (van Tongeren, 1995). Similarly, sample sites are dichotomized and, ultimately, added to a species-by-site matrix. The result of this ordination is a fidelity matrix with an approximate positive diagonal, from upper-left to lower-right, which can be used to characterize un-sampled sites (van Tongeren, 1995); in this exercise, it is used as an *a priori* guide to vegetation communities within the riparian zone and resulted in three broad classes (Appendix I). Lastly, in terms of the ecological field data analysis, an Indicator Species Analysis was performed using the three Riparian Vegetation classes derived from TWINSPAN (Dufrene and Legendre, 1997). Indicator Species Analysis is a method that combines information on the concentration of species abundance for a particular group and the faithfulness of occurrence of a species in that group, as a function of frequency (McCune and Mefford, 1999). It produces indicator values for each species in each group, reflecting abundance and frequency, and this score is tested for statistical significance using a Monte Carlo technique (McCune and Mefford, 1999).

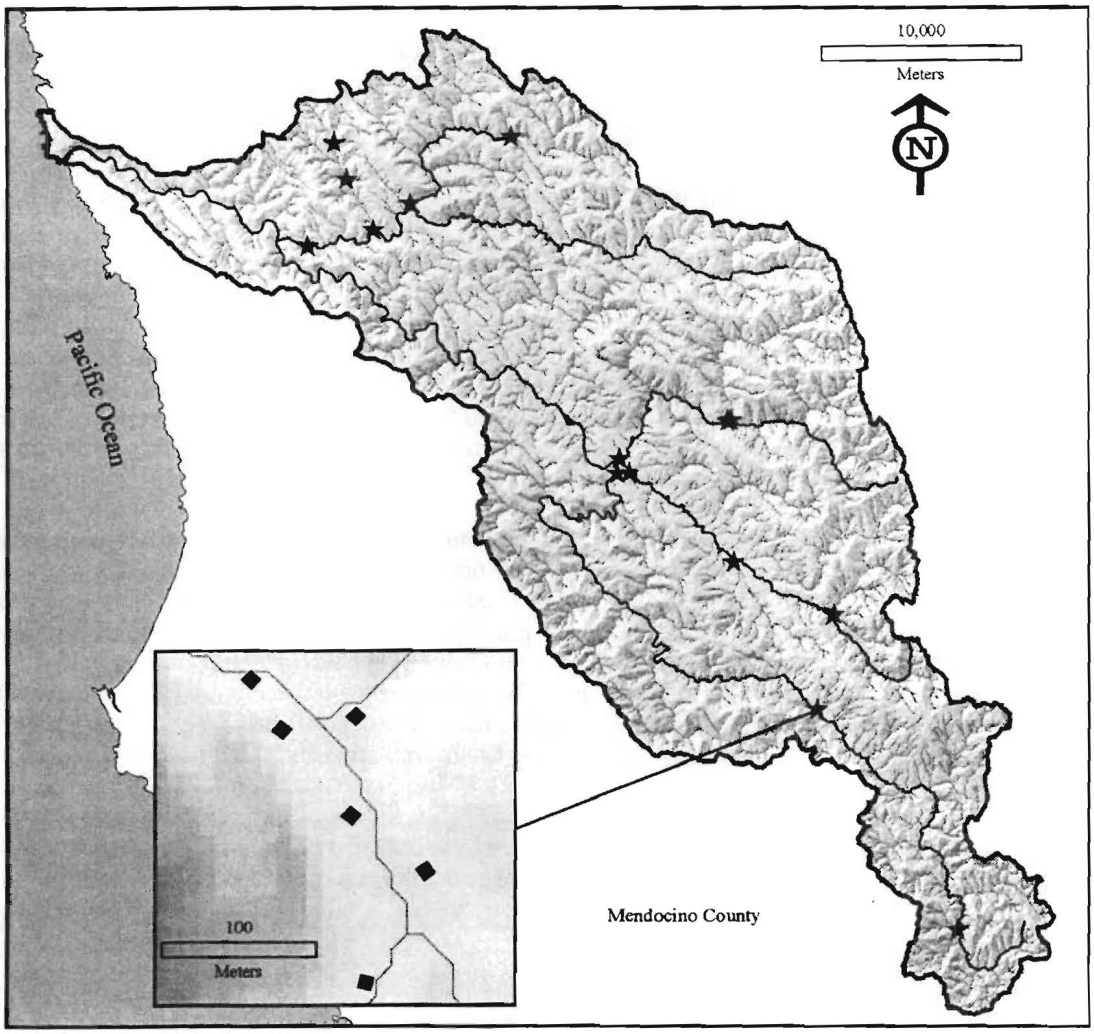

Figure 3. Map of field vegetation plots in the Navarro River watershed depicts a stratification based on major tributaries and watershed position. Study plots are 10 m x 10 m and are in clusters of six plots per site, as shown in the inset map.

Two classification methods were performed on the AVIRIS data to accomplish two separate, but related, objectives: 1) an unsupervised classification to establish vegetation communities within the riparian extent; and 2) a supervised classification of Indicator Species reference spectra to establish distributions of plant species indicative of vegetation communities. The purpose of this two-staged approach is to determine if hyperspectral data analysis can be used to identify patterns of species indicative of vegetation communities observed in the field; essentially, this two-stage method tries to establish whether vegetation communities observed in the field, in terms of composition and constancy, are reflected in the spectral characteristics of AVIRIS. A Spectral Angle Mapper (SAM) supervised classification was performed in ENVI using ROIs defined by the field quadrat boundaries and ancillary field identifications. The SAM classification (Kruse et al., 1993) was seeded to represent Indicator Species from the TWINSPAN classification using ROI endmembers for coast redwood, California bay laurel, and arroyo willow with a 0.1 radian deviance threshold from the reference spectra for classification. For each diagnostic species, a series of ROIs were identified, mean and standard deviation spectra were collected, and spectral libraries created to be used in the SAM classification. Additionally, a K-Means unsupervised classification was implemented on the twenty-band MNF in ENVI to classify vegetation communities within the riparian extent (Figure 4.1). A total of four classes were chosen to represent vegetation within the riparian extent (Figure 4.2); three classes are described in field plot results, and one class represents cultivated crops. The K-Means classification was performed with five hundred iterations and a 2% class deviance. Field plots and individual species' locations were geographically located with a Trimble ProXRS GPS unit, differentially corrected, and brought into ENVI as vector data for verification.

Results:

Using minimum criteria for TWINSPAN classification of field data, three broad classes of vegetation emerged. Two classes are typically considered upland vegetation; however, they are well represented in the riparian zone (Class A & B). These two classes have three species that are ubiquitous and representative: California bay laurel (*Umbellularia californica*), Douglas-fir (*Pseudotsuga menziesii*), and tanoak (*Lithocarpus densiflorus*). These two classes are separated by two diagnostic species: coast redwood (*Sequoia sempervirens*), and big-leaf maple (*Acer macrophyllum*); representing wetter and drier climes respectively. Other species that are marginally diagnostic are Pacific madrone (*Arbutus menziesii*) for wetter environments and coast live oak (*Quercus agrifolia*) for drier environments. The riparian class (Class C) is represented by a heterogeneous mixture of species; however, arroyo willow (*Salix lasiolepis*), Himalayan blackberry (*Rubus discolor*), and white alder (*Alnus rhombifolia*) emerged as diagnostic species. Other indicator species in this riparian class are: California blackberry (*Rubus vitifolius*), Pacific dogwood (*Cornus nuttallii*), and white willow (*Salix alba*). Furthermore, many of these species have significant Indicator Values in determining riparian class as determined by Indicator Species Analysis (Table 1), which determines a species Indicator Value as a function of abundance and frequency (Dufrene and Legendre, 1997). For Class A, redwood had the highest Indicator Value. For Class B, California bay laurel was the best indicator species. Arroyo willow had the highest Indicator Value for Class C.

The results of the K-Means classification of the MNF transformed flightline 18 showed an overall accuracy of 71.77% and a Kappa Coefficient of 0.58 when using post-classification verification field plots. Class A (*Sequoia*) had a Producer's / User's Accuracy of 66.7% / 86.5%. Class B (*Umbellularia*) had a Producer's / User's Accuracy of 71.1% / 63.4%. Class C (*Salix*) had a Producer's / User's Accuracy of 78.9% / 72.3%. The results of the Spectral Angle Mapper classification for the three class diagnostic species (Table 1, in bold), determined from Indicator Species Analysis (results in Table 2), describe the relationship between vegetation community class, as defined by K-Means, and spectral libraries developed from field observation ROIs. The comparison of the SAM Indicator Species classification to the K-Means Community classification had overall accuracy 97.82% of and a Kappa Coefficient of 0.7471. These results are further detailed in Table 1.

Table 1. Results of Spectral Angle Mapper Classification on Discriminated Riparian Vegetation using field mean and standard deviation spectra for selected Indicator Species defined by K-Means Classification.

Class	Indicator Species	No. SAM Pixels	No. Class Pixels	Pct. Indication by SAM
A	***Sequoia sempervirens***	**46551**	**65822**	**70.72**
B	*Sequoia sempervirens*	17745	46766	37.94
C	*Sequoia sempervirens*	4849	38890	12.47
A	*Umbellularia californica*	531	65822	0.81
B	***Umbellularia californica***	**13486**	**46766**	**28.84**
C	*Umbellularia californica*	1801	38890	4.63
A	*Salix lasiolepis*	15589	65822	23.68
B	*Salix lasiolepis*	13892	46766	29.71
C	***Salix lasiolepis***	**20777**	**38890**	**53.43**

Discussion:

Riparian vegetation communities identified in the field were identified spectrally via a restricted K-Means classification on MNF transformed AVIRIS data. The results of this classification, with an overall accuracy of 71.77%, suggest that the three vegetation classes within the riparian extent largely represent field observations (Figure 4.3) and the association with the field plots, classified by TWINSPAN to cluster communities of plant species, was generally correct. Thus, each spectral class had a representative surrogate field class that was verified via cluster analysis of field data plots. Additionally, and perhaps more significantly, SAM classification of AVIRIS data for selected species shows similar patterns of species associations observed in the field. In particular, Indicator Species Analysis, a method using species' observed abundance and frequency in relation to developed classes or communities, produced three diagnostic species for the three observed riparian communities. Spectral libraries of these diagnostic species were used in the SAM classification, which in turn were compared to the K-Means classified riparian communities. The overall accuracy of this comparison was 97.82%. Ultimately, these results indicate that the cross-comparison of individual species to classes was accurate in both field and spectral settings.

Table 2. Indicator Species Analysis Values and Probabilites for Sampled Riparian Plant Species in the Navarro River Watershed by Spectral Class.

	Taxon Name	Common Name	Class	Indicator Value	p*
1	*Salix lasiolepis*	arroyo willow	C	53.7	0.001
2	*Acer macrophyllum*	big-leaf maple	B	30.7	0.015
3	*Umbellularia californica*	California bay	B	68.1	0.001
4	*Quercus kelloggii*	California black oak	B	13.2	0.069
5	*Rubus ursinus*	California blackberry	C	20.8	0.121
6	*Aesculus californica*	California buckeye	B	2.4	1
7	*Rhamnus californica*	California coffeeberry	A	10.8	0.109
8	*Corylus cornuta var. californica*	California hazelnut	A	11.9	0.225
9	*Torreya californica*	California nutmeg	B	7.1	0.481
10	*Vitis californica*	California wild grape	B	7.3	0.415
11	*Quercus chrysolepis*	canyon live oak	B	10.5	0.159
12	*Quercus agrifolia*	coast live oak	B	17	0.069
13	*Sequoia sempervirens*	coast redwood	A	83.4	0.001
14	*Ceanothus incanus*	coast whitethorn	B	7.9	0.189
15	*Salix hookeriana*	coastal willow	C	6.6	0.327
16	*Arctostaphylos manzanita*	Common manzanita	B	2.6	1
17	*Baccharis pilularis*	coyote brush	C	14.3	0.023
18	*Pseudotsuga menziesii var. menziesii*	Douglas-fir	A	45.4	0.005
19	*Abies grandis*	grand fir	A	10.7	0.143
20	*Rubus discolor*	Himalayan blackberry	C	70.4	0.001
21	*Arbutus menziesii*	Madrone	A	9	0.587
22	*Fraxinus latifolia*	Oregon ash	B	3.4	0.762
23	*Cornus nuttallii*	Pacific dogwood	C	15.4	0.021
24	*Taxus brevifolia*	Pacific yew	B	5.1	0.579
25	*Toxicodendron diversilobum*	poison oak	B	13.8	0.119
26	*Alnus rubra*	red alder	B	4.7	0.662
27	*Salix laevigata*	red willow	C	7.7	0.139
28	*Rubus spectabilis*	salmon berry	B	5.3	0.498
29	*Salix sessilifolia*	sandbar willow	B	2.6	1
30	*Salix sitchensis*	Sitka willow	C	7.7	0.15
31	*Lithocarpus densiflorus*	Tanoak	A	63.2	0.001
32	*Heteromeles arbutifolia*	Toyon	C	5.1	0.447
33	*Quercus lobata*	valley oak	B	10.5	0.103
34	*Myrica californica*	wax-myrtle	A	5.4	0.311
35	*Rhododendron occidentale*	western azalea	A	15.4	0.038
36	*Plantanus racemosa*	western sycamore	C	7.7	0.135
37	*Alnus rhombifolia*	white alder	C	51	0.001
38	*Salix alba*	white willow	C	23.1	0.006

* proportion of randomized trials with indicator value equal to or exceeding the observed indicator value (Dufrene and Legendre 1997).

P = (1 + number of runs >= observed)/(1 + number of randomized runs)

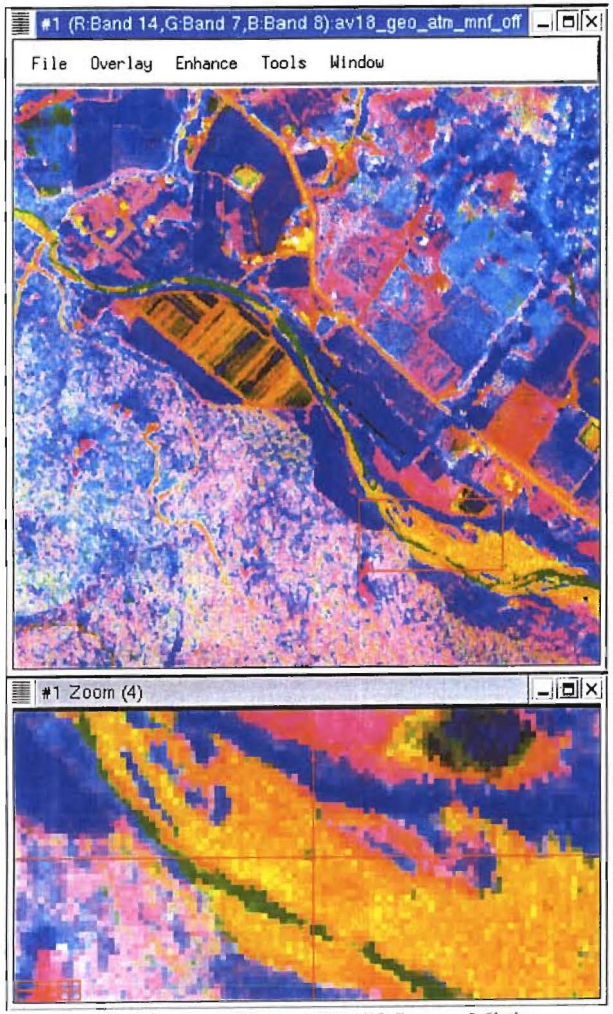

Figure 4.1. Navarro River AVIRIS Image Minimum Noise Fraction Transform (Planes 14, 7, 8).

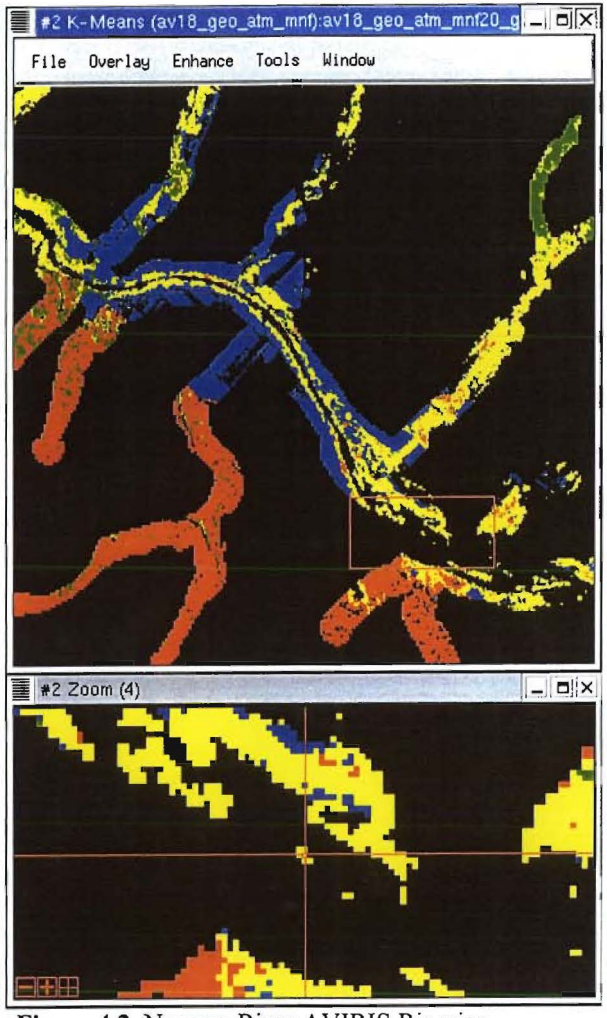

Figure 4.2. Navarro River AVIRIS Riparian Vegetation Classification (Class A in Red, Class B in Green, Class C in Yellow, and Cultivated Crops in Blue).

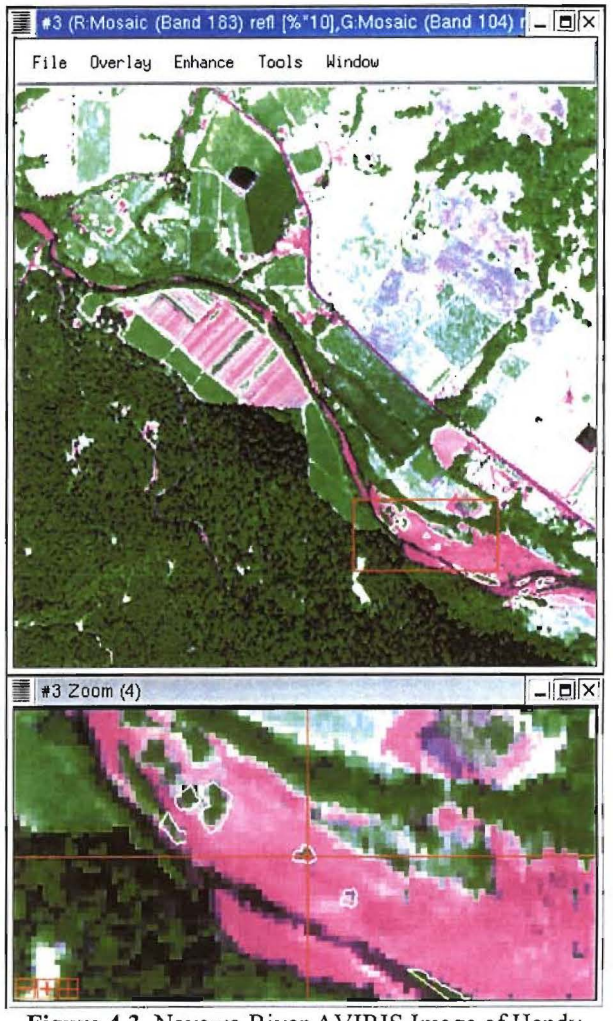

Figure 4.3. Navarro River AVIRIS Image of Hendy Woods State Park (Bands 183, 104, 195) with GPS Verification Overlay (White Polygons) targeting Class C pixels

Comparatively, California bay laurel (*Umbellularia californica*) was the only Indicator Species to not represent more than 50% of its associated Class pixels; it represented only 28.84% of Class B. Without additional fieldwork, it is difficult to determine if the SAM performed poorly for bay laurel or if the incorporation of other diagnostic species, such as big leaf maple (*Acer macrophyllum*), would be more appropriate for this class. Class B must also be considered a "mixed hardwood" community and, as such, would naturally have a great number of possible species in its class. Regardless, each Indicator Species had the predominate percent of its pixels within its associated K-Means class. Coastal redwood (*Sequoia sp.*) performed the best at 70.72% of its SAM pixels in Class A. Furthermore, it is also apparent that traditional riparian vegetation, as represented by willow (*Salix spp.*) for example, are true to their ecological form in terms of being generally interspersed within other vegetation communities; this is evidenced by each of the three K-Means riparian classes having more than 20% of its pixels classified as arroyo willow (*S. lasiolepis*) by SAM. Arroyo willow represented 53.43% of Class C. In the case of true riparian vegetation, additional diagnostic species will need to be incorporated into future SAM classification efforts if the identification of species will be used as a surrogate for classifying vegetation communities.

These results are for a limited portion of the watershed and could change with the incorporation of other flightlines and other field plots. Some considerations for addressing possible error include: 1) the mixed composition of vegetation communities are difficult to separate spectrally by species; 2) the "ribbon" forest nature of riparian vegetation can be overwhelmed by upland species; and 3) canopy structure, especially with 80–100 m tall coastal redwood trees, can obscure other vegetation features. The preliminary results of this effort indicate that hybrid methods of feature extraction work best in this varied landscape of topography, climate, and vegetation communities. Additional research will be focused on assessing other discriminatory methods for feature extraction within the riparian zone and other feature types. However, assessing the distribution and composition of riparian vegetation at a watershed scale is essential to protecting salmonid habitat and guiding restoration efforts. The methods outlined here, as they are improved, will aid land use managers in their ability to inventory, restore, and monitor riparian ecosystems. This is particularly true for north, coastal California watersheds where recent policy determinations under the federal Clean Water Act and Endangered Species Act require regulatory agencies to assess ecosystem integrity in a comprehensive and timely manner.

Acknowledgements:

We would like to thank the following entities and individuals for the support in this project: Lisa Levien, Chris Keithley, Bruce Gwynne, David Leland, Zhi-Wei Lu, George Scheer, Susan Ustin, Eric Lehmer, Derek Masaki, Bob Brewer, Anni Schairer, the Information Center for the Environment, UC Davis Department of Environmental Science and Policy, the John Muir Institute of the Environment, the Center for Spatial Technologies and Remote Sensing, the Center for Image Processing and Integrated Computing, and the University of California. This work was partially supported by funding from the North Coast Regional Water Quality Control Board, California Department of Transportation, California Department of Forestry and Fire Protection, and United States Department of Agriculture – Forest Service.

Citations:

Boardman, J.W. and Kruse, F.A., 1994. Automated Spectral Analysis: A Geological Example Using AVIRIS Data, North Grapevine Mountain, Nevada: in *Proceedings, ERIM Tenth Thematic Conference on Geologic Remote Sensing*, Research Institute of Michigan, Ann Arbor, MI, ppd. I-407 – I-408.

Boardman, J.W., Kruse, F.A and Green, R.O., 1995. Mapping Target Signatures Via Partial Unmixing of AVIRIS data: in Summaries, *Fifth JPL Airborne Earth Science Workshop*, JPL Publication 95-1, V. 1, ppd. 23-26.

Dufrene, M. and P. Legendre. 1997. Species assemblages and indicator species: the need for a flexible asymmetrical approach. Ecological Monographs 67:345-366.

Environmental Systems Research Institute, Inc. 2001. Version 8.1 Redlands, CA 92373-8100, USA.

Environment for Visualizing Images (ENVI), Version 3.5. Research Systems, Inc., Boulder, CO, 2001.

Hill, M.O. 1979. TWINSPAN–A FORTRAN program for arranging multivariate data in an ordered two-way table by classification of the individuals and attributes. Ithaca, NY: Ecology and Systematics, Cornell University.

Jackson, R.D., 1983. Spectral Indices in *n*-Space. *Remote Sensing of the Environment*, 13, ppd. 409-421.

Kruse, F.A., Lefkoff, A.B., Boardman, J.B., Heidebrecht, K.B. Shapiro, A.T., Barloon, P.J. and Goetz, A.F.H., 1993.

The Spectral Image Processing System (SIPS) - Interactive Visualization and Analysis of Imaging Spectrometer Data: Remote Sensing of the Environment, Special Issue on AVIRIS, May-June 1993, V. 44, p. 145-163

McCune, B. and M.J. Mefford. 1999. Multivariate Analysis of Ecological Data Version 4.14. MjM Software, Gleneden Beach, Oregon, USA.

Richards, J.A. & Jia, X., 1999. *Remote Sensing Digital Image Analysis: An Introduction*. Berlin, Germany, Springer-Verlag.

Richter, R. 2000, Atmospheric / Topographic Correction for Wide FOV Airborne Imagery: Model ATCOR4, DLR-German Aerospace Center, Wessling, Germany.

Roberts, D. A., M. Gardner, R. Church, S. Ustin, G. Scheer and R. O. Green. 1998. Mapping Chaparral in the Santa Monica Mountains Using Multiple Endmember Spectral Mixture Models, *Remote Sensing of Environment*, Volume 65(3) ppd. 267-279

Schläpfer, D. 2000, Parametric Geocoding User Guide, Version 1.3, Remote Sensing Laboratories, University of Zurich, Zurich, Switzerland.

van Tongeren, O.F.R. 1995. Cluster analysis in *Data Analysis in Community and Landscape Ecology*. R.H.G. Jongman, C.J.F. ter Braak, and O.F.R. van Tongeren, editors. Pudoc, Wageningen, The Netherlands.

Appendix I
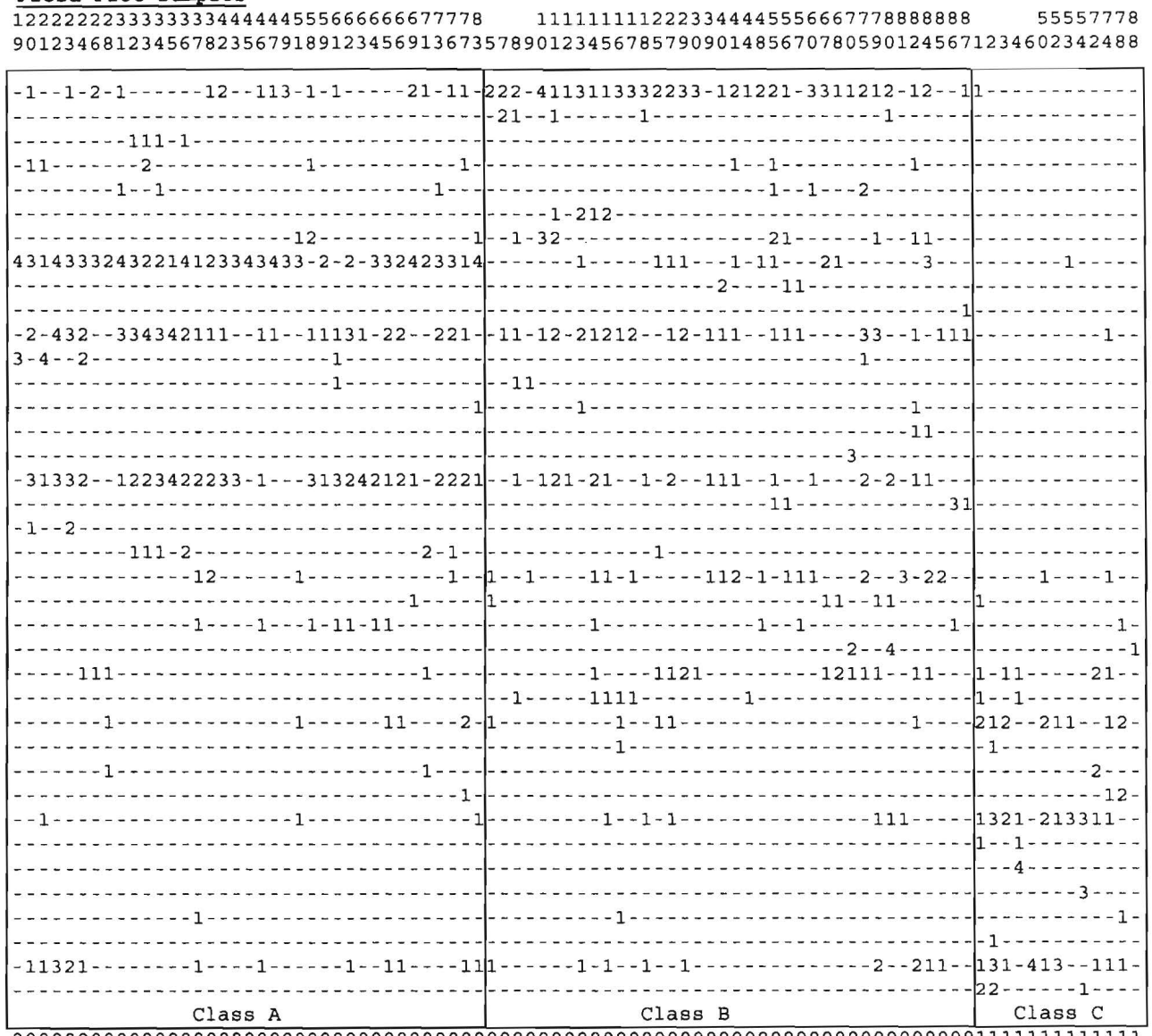
Field Plot Samples